Search for light charged Higgs bosons with the $H^{\pm} \to \tau^{\pm}\nu_{\tau}$ decay in the fully hadronic final state

A thesis presented

by

Alexandros Attikis

to

The Department of Physics

in partial fulfilment of the requirements

for the degree of

Doctor of Philosophy

in the subject of

Physics

University of Cyprus

Nicosia, Cyprus

June, 2012

2012

Approval Page

Doctor of Philosophy Dissertation

Search for light charged Higgs bosons
with the $H^{\pm} \to \tau^{\pm}\nu_{\tau}$ decay in the fully hadronic final state

Presented by

Alexandros Attikis

Research Supervisor

Professor Panos A. Razis
(University of Cyprus)

Committee Member Chair

Associate Professor Fotios K. Ptochos
(University of Cyprus)

Committee Member

Associate Professor Nicolaos Toumbas
(University of Cyprus)

External Committee Member

Professor Pantelis Damianou
(University of Cyprus)

External Committee Member

Dr. Christophe Royon, Director of Research
(IRFU CEA Saclay, France)

University of Cyprus
June, 2012

Στους γονείς μου, Ινώ και Ξένιο
και στη μνήμη του αγαπημένου μου θείου Πάρη

Abstract

This thesis describes the work conducted for the search for light charged Higgs bosons at the Large Hadron Collider (LHC) with the Compact Muon Solenoid (CMS) experiment, in $t\bar{t}$ events. In particular, the fully hadronic final state of the signal processes $t\bar{t} \to bW^{\pm}bH^{\mp}$ and $t\bar{t} \to bH^{\pm}bH^{\mp}$ was investigated, with the $H^{\pm} \to \tau^{\pm}\nu_{\tau}$ decay mode. The search was based on data corresponding to an integrated luminosity of $2.3\,\text{fb}^{-1}$, recorded in the early part of 2011 with the CMS detector at a centre-of-mass-energy of $\sqrt{s} = 7\,\text{TeV}$. The Minimal Supersymmetric Standard Model (MSSM) maximal mixing scenario $m_{\text{h}}^{\text{max}}$ was tested in a cut-based analysis, by fitting a background-only hypothesis to the transverse mass shape reconstructed using the missing transverse energy $E_{\text{T}}^{\text{miss}}$ and τ jet objects, after all signal selection requirements. Model-independent upper limits for the branching ratio $\text{BR}(t \to bH^{\pm})$ were calculated, and were consequently transformed to upper limits in the $(\tan\beta, m_{A^0})$ plane, under the assumption that the light charged Higgs boson decays exclusively to a τ-lepton and a neutrino, with a branching ratio $\text{BR}(H^{\pm} \to \tau^{\pm}\nu_{\tau}) = 1$.

A significant part of the present work concentrated on the determination of the dominant background contributing to the signal region, found to be attributed to Quantum Chromodynamics (QCD) multi-jet processes, whereby a hadronic jet is falsely identified as a τ jet and the presence of transverse energy imbalance is primarily caused by jet resolution or jet mis-measurement effects. The determination of the QCD multi-jet background was achieved by employing data-driven factorisation techniques, with crucial steps of the signal selection requirements being factorised out of the cut-flow and then re-introduced in the form of applied efficiencies. This factorisation procedure was conducted within selected bins of the τ jet candidate transverse momentum, to account for the fact that the probability of a quark or gluon jet to pass the chosen τ-jet isolation criteria was found to be dependent on the jet transverse momentum. An additional physics-motivated incentive for this procedure was to minimise the small correlations that were observed to exist between the τ jet candidate transverse momentum and the missing transverse energy, in a given event. Using similar techniques, the transverse mass shape of QCD multi-jet processes after all signal selection requirements was also extracted with data-driven methods. In parallel, a complete evaluation of the uncertainties associated with all the measurements was also conducted, which included all relevant systematic and statistical contributions.

The transverse mass shape extracted for QCD multi-jet processes, along with all other related background processes, were subsequently employed in a binned maximum likelihood fit to the transverse mass shape observed in the data, after all signal selection requirements.

As a result, model-independent upper limits were evaluated for the branching ratio BR($t \to bH^{\pm}$), as a function of the light charged Higgs boson mass ($m_{H^{\pm}}$). The observed and expected upper limits were found to be $2.2 - 7.3\%$ and $1.5 - 5.2\%$, respectively, for the light charged Higgs mass range of $80\,\mathrm{GeV}/c^2 \leq m_{H^{\pm}} \leq 160\,\mathrm{GeV}/c^2$. The corresponding upper limits were transformed to the ($\tan\beta$, $m_{H^{\pm}}$) and ($\tan\beta$, m_{A^0}) parameter space of the MSSM maximal mixing scenario $m_{\mathrm{h}}^{\mathrm{max}}$, and were found to exclude a significant region of the parameter space that had previously remained unexplored.

Abstract in Greek

Η παρούσα διδακτορική διατριβή περιγράφει τη μελέτη που διεξήχθηκε για την αναζήτηση του ελαφρού και ηλεκτρικά φορτισμένου μποζονίου Higgs στο Μεγάλο Επιταχυντή Αδρονίων (LHC) με το πείραμα CMS, σε γεγονότα $t\bar{t}$. Ειδικότερα, διερευνήθηκε η πλήρως αδρονική τελική κατάσταση των διεργασιών $t\bar{t} \to bW^{\pm}bH^{\mp}$ και $t\bar{t} \to bH^{\pm}bH^{\mp}$, με περαιτέρω διάσπαση $H^{\pm} \to \tau^{\pm}\nu_{\tau}$. Η αναζήτηση βασίστηκε σε δεδομένα που αντιστοιχούν σε $2.3\,\text{fb}^{-1}$ ολοκληρωμένης φωτεινότητας, όπως καταγράφηκαν κατά την αρχική περίοδο του έτους 2011 με τον ανιχνευτή CMS σε ενέργεια κέντρου μάζας $\sqrt{s} = 7\,\text{TeV}$. Το Ελάχιστο Υπερσυμμετρικό Καθιερωμένο Πρότυπο (MSSM) , υπό το σενάριο με μέγιστη ανάμειξη $m_{\text{h}}^{\text{max}}$, εξετάστηκε μέσα από μια ανάλυση βασισμένη σε περικοπές, με προσαρμογή στην κατανομή εγκάρσιας μάζας, όπως αυτή ανακατασκευάστηκε με τη χρήση του τ-πίδακα και της χαμένης εγκάρσιας ενέργειας μετά από όλες τις επιλογές, υπό την υπόθεση παρουσίας μόνο υπόβαθρου στα δεδομένα. Υπολογίστηκαν ανώτατα όρια για το λόγο διακλάδωσης $\text{BR}(t \to bH^{\pm})$, ανεξαρτήτως μοντέλου, τα οποία και μετατράπηκαν σε ανώτατα όρια στο επίπεδο $(\tan\beta, m_{A^0})$ υπό την υπόθεση ότι το ελαφρύ φορτισμένο μποζόνιο Higgs διασπάται αποκλειστικά σε ένα τ-λεπτόνιο και ένα νετρίνο, με λόγο διακλάδωσης $\text{BR}(H^{\pm} \to \tau^{\pm}\nu_{\tau}) = 1$.

Η κύρια εργασία της παρούσας διατριβής επικεντρώθηκε στην εκτίμηση του δεσπόζοντος υποβάθρου στην περιοχή του σήματος το οποίο βρέθηκε να πηγάζει από Κβαντοχρωμοδυναμικές διεργασίες με πολλαπλούς αδρονικούς πίδακες (QCD multi-jet), στις οποίες ένας εκ των αδρονικών πιδάκων λανθασμένα χαρακτηρίζεται ως τ-πίδακας, ενώ η παρουσία χαμένης εγκάρσιας ενέργειας οφείλεται κυρίως σε λανθασμένες μετρήσεις στην ενέργεια των διαφόρων πίδακων, ή σε επιδράσεις της πεπερασμένης διακριτικής ικανότητας μέτρησης της ενέργειας τους. Ο προσδιορισμός του εν λόγω υπόβαθρου επιτεύχθηκε με τη χρησιμοποίηση των πειραματικών δεδομένων με βάση τις τεχνικές παραγοντοποίησης. Αυτή η διαδικασία παραγοντοποίησης διεξήχθη σε επιλεγμένα διακριτικοποιημένα διαστήματα εγκάρσιας ορμής των υποψηφίων τ-πιδάκων, ούτως ώστε να ληφθεί υπόψη το γεγονός ότι η πιθανότητα ενός πίδακα προερχόμενου από κουάρκ ή γκλουόνιο για να περάσει τα απαιτούμενα κριτήρια απομόνωσης ενός τ-πίδακα, βρέθηκε να εξαρτάται από την εγκάρσια ενέργεια του εν λόγω πίδακα. Ένα επιπρόσθετο κίνητρο για την υιοθέτηση της προαναφερθείσας μεθόδου απετέλεσε η ελαχιστοποίηση των μικρών συσχετίσεων που παρατηρήθηκαν ανάμεσα στην εγκάρσια ορμή του υποψήφιου τ-πίδακα και της χαμένης εγκάρσιας ενέργειας ενός γεγονότος. Χρησιμοποιώντας παρόμοιες τεχνικές, καθορίστηκε επίσης και η κατανομή της εγκάρσιας μάζας για Κβαντοχρωμοδυναμικές διεργασίες με πολλαπλούς αδρονικούς πίδακες, μετά από όλες τις επιλογές για την εξαγωγή του σήματος από τα πειραματικά δεδομένα. Παράλληλα, πραγματοποιήθηκε μια πλήρης αξιολόγηση των

αβεβαιοτήτων που συνδέονται με όλες τις μετρήσεις, η οποία περιελάμβανε όλα τα σχετικά συστηματικά και στατιστικά σφάλματα.

Η κατανομή εγκάρσιας μάζας από Κβαντοχρωμοδυναμικές διεργασίες με πολλαπλούς αδρονικούς πίδακες, αλλά και όλων των σχετικών διαδικασιών του υποβάθρου, χρησιμοποιήθηκαν στη συνέχεια για την προσαρμογή τους στην κατανομή της εγκάρσιας μάζας μέσω της μεθόδου του maximum likelihood κατά διακριτικοποιημένα διαστήματα, μετά από όλες τις επιλογές για την εξαγωγή του σήματος. Ως αποτέλσμα, εξήχθηκαν ανώτατα ορία ανεξαρτήτως μοντέλου για το λόγο διακλάδωσης $\mathrm{BR}(t \to bH^{\pm})$, ως συνάρτηση της μάζας του ελαφρού και ηλεκτρικά φορτισμένου μποζονίου Higgs ($m_{H^{\pm}}$). Τα παρατηρηθέντα και τα αναμενόμενα ανώτατα όρια βρέθηκαν να είναι $2.2 - 7.3\%$ και $1.5 - 5.2\%$, αντιστοίχως, για μάζες $80\,\mathrm{GeV}/c^2 \leq m_{H^{\pm}} \leq 160\,\mathrm{GeV}/c^2$. Τα εν λόγω όρια μετατράπηκαν σε όρια στο επίπεδο $(\tan\beta, m_{H^{\pm}})$ και $(\tan\beta, m_{A^0})$ του MSSM σεναρίου με μέγιστη ανάμειξη $m_{\mathrm{h}}^{\mathrm{max}}$, και βρέθηκαν να εξαιρούν μια σημαντική περιοχή του παραμετρικού χώρου που είχε προηγουμένως παραμείνει ανεξερεύνητη.

Acknowledgements

I find it impossible to try to encapsulate all aspects that contributed to the completion of this doctoral thesis. Nevertheless, I will attempt my best efforts to pay a deserving tribute to all the people that contributed in one way or another to me finally getting through graduate school, in a journey that started as far as September of 2007.

I would like to express my deepest and sincerest gratitude to my advisor, Professor Panos Razis, who has supervised all possible aspects of this research work throughout its duration. His support and guidance in overcoming the numerous obstacles that emerged along this winding and exhaustively long journey has been truly heartwarming. I consider it extraordinary that, whenever and wherever I required assistance he was there to provide a swift and direct solution to my problems. His mere presence has always inspired me, and somehow conveyed to me a feeling that everything will fall in place eventually. And I guess it finally did. I consider him an exceptional person and tremendously charismatic leader, of great integrity and an everlasting desire and dedication for disseminating his knowledge and wisdom to other people. I also consider myself very fortunate to have had the opportunity and privilege to turn to Professor Fotios Ptochos for guidance, concerning any kind of physics problem that cropped up in my path, even at the oddest hours, or rather the normal hours as the common physics researcher would say. I am short for words to express my indebtedness to him for his openness, his patience and his willingness to help any ignorant experimental high-energy physicist that knocks on his door, such as myself.

This doctoral thesis is based on research conducted with the CMS experiment of the LHC at the European Organisation for Nuclear Research (CERN), during the years 2009 – 2012, in close collaboration with the CMS Physics Analysis group of the Helsinki Institute of Physics (HIP), and under the mentoring of a truly inspirational and gifted leader, Professor Alexandre Nikitenko. I will forever be indebted to him for trusting in me, always patiently directing me into the right path but also always pushing forward. I have been honoured to work with him, and I consider his masterful direction of this beautiful analysis to be of such grace that can be compared to the grace with which a conductor guides an orchestra. Most importantly, however, I am grateful for the bottles of champagne he so generously offered to us after every milestone of the analysis.

I would also like to express my deepest appreciation and my eternal gratitude to the group of brilliant and wonderful people comprising the HIP analysis team, especially Lauri Wendland, Sami Lehti, Ritva Kinnunen and Matti Kortelainen. It is hard to describe the warmth and kindness with which I was taken on as a member of the team, and I would not

be exaggerating if I said that I could not have asked for better colleagues. I would especially like to thank Lauri Wendland, who from day one took me under his wing and openly offered me his constant support and guidance, and shared with me his immense knowledge in physics. I feel the need to also express a special thanks to Matti Kortelainen, who as I am typing this, is also writing his doctoral thesis and who I consider a truly brilliant young researcher with limitless potential, a belief strongly manifested by the fact that I just recently characterised him as "almost better than Google as a search engine". The conversations we have had during the last weeks have been incredibly constructive and pleasant. In addition, it would be a pitty not to thank Lauri and Matti for the special experience that all collaborating physicists share; the 24-hour long marathon before a deadline.

Of course, to complete a doctoral thesis, one not only needs a fantastic work environment, but also good friends to whom he can turn to for the out-of-office hours. Luckily, I was fortunate to have plenty of friends who have genuinely contributed in the completion of this doctoral thesis. Because, at the end of the day, what really stays with us is the personal relations with people we love and the experiences we share with them. Firstly, I would like to say thanks to the amazing, the incredible and -above all- the unpredictable "Suspenders": Georgios Konstantinou, Marco Bonvini, Matias Hernandez, Samir Arfaoui, Valerio Rossetti and Lillian Smestad. It is absolutely incredible to think that "The Suspenders" were formed as a result of a just-for-fun "Δεν χωράς πουθενά" music video at the CERN Music Club, some dozens of beers, a couple of Ζιβανία bottles, and a handful of Band-Hero nights. Yet, we stuck with it, made it through thick and thin, through numerous workshops, conferences and paper deadlines, and of course one storm-out incident, to finally become a decent rock band. It has been an absolute pleasure and true privilege to be around you guys, and I only have one thing to say to you: "Merci Genève, à demain Lausanne!".

I would also like to say thanks to my friends from the amazing Cypriot community at CERN: Christos Hadjivasiliou, Constantinos Melachrinos, Natalie Heracleous, Nikiforos Nikiforou and Zinonas Zinonos. I could think of no better persons to represent Cyprus in the international scientific community, and I am grateful for everything you have given to me. Constantinos, for introducing me to Cashmere and conveying to me the meaning of being "with the people, for the people". Natalie, for one amazing smile and one summer school, Nikiforos for being a worthy Σύντροφος in Πιλόττα and for being an amazing chef and host. Zinonas, for the lovely coffee conversations and his unparalleled integrity. I would like to also express my thanks, appreciation and love to a very dear friend of mine, that was with me both in the in-office and out-of-office hours, Loukas Gouskos. For the past $\sim$ 3 years he has shared with me an office and his endless knowledge on physics, he provided me with an unlimited pool of mental strength, and most importantly, has offered me a genuine and strong friendship. It would be understatement to say that he has been the best office-mate I could have wished for, although I could have lived without the occasional dreadful joke and the constant complaints about keyboard-related noise.

Finally, I would like to thank the Cyprus Research Promotion Foundation (RPF), and in particular its Framework Programme for Research, Technological Development and Innova-

tion 2008 (ΔΕΣΜΗ 2008), which was co-funded by the Republic of Cyprus and the European Regional Development Fund. It provided me with the means to address my research ambitions and set the foundations for the career I have always dreamed of. I can only wish and hope that it will continue to support and promote all the bright young physicists who aspire to embark on a research career in physics.

June, 2012,
Nicosia, Cyprus.

List of Publications

1. CMS Collaboration, "Search for a light charged Higgs boson in top quark decays in pp collisions at $\sqrt{s} = 7$ TeV", arXiv:1205.5736 – *Submitted to the Journal of High Energy Physics*.

2. CMS Collaboration, "Search for the light charged Higgs boson in top quark decays in pp collisions at $\sqrt{s} = 7$ TeV", *CMS PAS* **HIG-11-019** (2011).

3. CMS Collaboration, "Search for the charged Higgs boson with $H^+ \to \tau^+ \nu$ decay mode in top quark decays", *CMS PAS* **HIG-11-008** (2011).

4. A. Attikis et al., "Search for light charged Higgs bosons with the $H^\pm \to \tau^\pm \nu_\tau$ decay in the fully hadronic final state", *CMS AN* **2011/470** (2012).

5. A. Attikis et al., "Search for the light charged MSSM Higgs bosons with the $H^\pm \to \tau^\pm \nu_\tau$ decay in fully hadronic final state", *CMS AN* **2011/126** (2011).

6. The Higgs PAG, "Trigger strategies for Higgs searches", *CMS AN* **2011/065** (2011).

7. A. Attikis, "QCD backgrounds in charged Higgs boson searches", Conference Report CMS-CR-2010-303, CERN, Geneva, (Dec, 2010).

List of Acronyms

ALICE A Large Ion Collider Experiment

AOD Analysis Object Data

APD Avalanche Photo-Diode

ATLAS A Toroidal LHC Apparatus

BPix Barrel Pixel

BSM Beyond the Standard Model

BTI Bunch and Track Identifier

CDF Collider Detector at Fermilab

CDF Cumulative Distribution Function

CERN European Organisation for Nuclear Research

CKM Cabibbo-Kobayashi-Maskawa

CL Confidence Level

CMS Compact Muon Solenoid

CRAB CMS Remote Analysis Builder

CSCTF CSC Track Finder

CSC Cathode Strip Chamber

CT Calorimeter Trigger

DAQ Data Acquisition

DQM Data Quality Monitoring

DTTF Drift Tube Trigger Track Finder

DT Drift Tube

EB ECAL Barrel

ECAL Electromagnetic Calorimeter

EE ECAL Endcap

EM Electromagnetic

ES Endcap preShower

EWK Electroweak

FDL Final Decision Logic

FED Front-End Driver

FES Front-End System

FPix Forward Pixel

FSR Final State Radiation

FU Filter Unit

GCT Global Calorimeter Trigger

GMT Global Muon Trigger

GPT Global Phase Transformation

GSF Gaussian Sum Filter

GTFE Global Trigger Front-End

GTL Global Trigger Logic

GT Global Trigger

GUTs Grand Unified Theories

HB HCAL Barrel

HCAL Hadronic Calorimeter

HD Higgs Doublet

HEP High-Energy Physics

HE HCAL Endcap

HF HCAL Forward

HIP Helsinki Institute of Physics

HLT High-Level Trigger

HO HCAL Outer

HPD Hybrid Photo-Diode

HPS Hadron plus Strips

IBS Intra-Beam Scattering

ISO Isolation

ISR Initial State Radiation

IP Interaction Point

JER Jet Energy Resolution

JES Jet Energy Scale

JSON Java Script Object Notation

L1 Level-1

L2.5 Level-2.5

L2 Level-2

L3 Level-3

LCT Local Charged Track

LEIR Low Energy Ion Ring

LEP Large Electron-Positron Collider

LHC-*b* Large Hadron Collider beauty

LHC Large Hadron Collider

LINAC LINear ACcelerator

LO Leading Order

LPT Local Phase Transformation

LSP Lighest Supersymmetric Particle

LT Lorentz Transformation

LandS Limits and Signifcance

L1A Level-1 Accept

MB Muon Barrel

MC Monte-Carlo

ME Muon Endcap

MIP Minimum Ionising Particle

MPI Multiple Parton Interactions

MSSM Minimal Supersymmetric Standard Model

MT Muon Trigger

MWPC MultiWire Proportional Chamber

NLO Next-to-Leading Order

NNLL Next-to-Next-to-Leading Logarithm

NNLO Next-to-Next-to-Leading Order

PACT Pattern Comparator Trigger

PCC Pixel Cluster Counting

PDF Parton Distribution Function

PD Primary Dataset

PF Particle Flow

PMT Photomultiplier Tube

POG Physics Object Group

PSB Proton Synchrotron Booster

PS Parton Shower

PS Proton Synchrotron

PDF Probability Density Function

QCD Quantum Chromodynamics

QED Quantum Electrodynamics

QFT Quantum Field Theory

QPS Quench Protection System

RCT Regional Calorimeter Trigger

RECO Reconstructed

RF Radio Frequency

RHIC Relativistic Heavy Ion Collider

RCT Regional Muon Trigger

ROC Readout Chip

RPC Resistive Plate Chamber

RPF Research Promotion Foundation

RR Run Registry

SC SuperCrystal

SIP Impact Parameter Significance

SL SuperLayer

SM Standard Model

SPS Super Proton Synchrotron

SSB Spontaneous Symmetry Breaking

SUSY Supersymmetry

SC Sector Collector

TCHE Track Counting High Efficiency

TCS Trigger Control System

TEC Tracker EndCap

TIB Tracker Inner Barrel

TID Tracker Inner Disks

TOB Tracker Outer Barrel

TOTEM ToTal Elastic and diffractive cross-section Measurement

TPG Trigger Primitive Generator

TRACO Track Correlator

TS Trigger Server

TTC Timing, Trigger and Control

TT Trigger Tower

UE Underlying Event

VBF Vector Boson Fusion

VEV Vacuum Expectation Value

VPT Vacuum Photo-Triode

vdM Van der Meer

WIMP Weakly Interacting Massive Particle

WLCG Worldwide LHC Computing Grid

WLS WaveLength-Shifting

***p*QCD** Perturbative Quantum Chromodynamics

Contents

List of Figures

List of Tables

Chapter 1

The Standard Model and beyond

1.1 Introduction

The field of particle physics has made enormous leaps since the idea of the existence of quarks as elementary constituents of Strongly interacting particles was independently set forth by Gell-Mann and Zweig in 1963. In the past 5 decades, the consequent theory known as the Standard Model (SM) has acquired immense momentum and is now the accepted theory for describing fundamental particles and their interactions, through 3 of the 4 known fundamental forces.

Table 1.1: The SM particle content.

Type	Particles		
Left-handed leptons	$\begin{pmatrix} \nu_e \\ e \end{pmatrix}_L$	$\begin{pmatrix} \nu_\mu \\ \mu \end{pmatrix}_L$	$\begin{pmatrix} \nu_\tau \\ \tau \end{pmatrix}_L$
Right-handed leptons	e_R	μ_R	τ_R
Left-handed quarks	$\begin{pmatrix} u \\ d \end{pmatrix}_L$	$\begin{pmatrix} c \\ s \end{pmatrix}_L$	$\begin{pmatrix} b \\ t \end{pmatrix}_L$
Right-handed quarks	u_R d_R	c_R s_R	t_R b_R
Vector bosons	γ	Z^0 , $W^\pm$	G_a
Scalar bosons	H^0		

In the SM, all the phenomena of particle physics are described in terms of the properties and interactions of 12 elementary particles of 2 distinct types; quarks and leptons. Quarks and leptons are all fermions and are grouped into 3 families, comprising the fundamental building blocks of matter, as shown in Table 1.1. Their interactions, which arise from the exchange of field quanta, are described by 3 forces and their associated force carrying particles, known as gauge bosons, as shown in Table 1.2. The Electromagnetic (EM) force describes the interactions between electrically charged particles, through the exchange of massless particles known as photons (γ). The Quantum Field Theory (QFT) for EM interac-

Table 1.2: The SM forces.

Quantity	Strong nuclear	Weak nuclear	EM	Gravitational
Charge	colour	flavour	electric	mass/energy
Vector boson	G_a	$W^{\pm}$, Z^0	γ	graviton (?)
Boson mass $\left(\mathrm{GeV}/c^2\right)$	0	80.399 , 91.188	0	0
Boson spin	1	1	1	2
Range (m)	10^{-15}	$< 10^{-18}$	∞	∞
Relative strength	1	10^{-5}	10^{-2}	10^{-38}

tions is known as Quantum Electrodynamics (QED), which employs the Lagrangian formalism in deriving the equations of motion describing electrically charged particles and their interactions with the EM force field. A summary of the Lagrangian formalism and a brief overview of QED is given in Appendices A and B, respectively.

The massive $W^{\pm}$ and Z^0 bosons mediate the Weak interaction between all quarks and leptons. The equivalent particles for the Strong interaction, which describes interactions between the colour charged quarks, are called gluons (g or G_a) and, like the photon, are massless. A brief summary of Quantum Chromodynamics (QCD) is given in Appendix C. To-date all experimental observations are described to remarkable accuracy by the SM, which now serves as the descriptive framework for understanding the structure and evolution of the universe from the Big Bang to the present.

1.2 Spontaneous symmetry breaking

Within the SM, the EM and Weak interactions are now understood to be manifestations of a single Electroweak (EWK) interaction, for which a brief overview is given in Appendix D. The associated EWK Lagrangian however, is not as elegant as that of QED or QCD, since its structure is imposed by hand to satisfy experimental facts. Most importantly, the EWK Lagrangian does not have any predictive power, due to the fact that all the EWK gauge bosons in the Lagrangian are assumed to be massless, quite contrary to experimental results. Therefore, unless a way is found to break the $\mathrm{SU}(2)_L \otimes \mathrm{U}(1)_Y$ symmetry and allow a mass to be acquired by the EWK gauge bosons, the EWK Lagrangian cannot be of any practical use. The only way this can be done, while preserving the intrinsic symmetry of EWK Lagrangian, is through a Spontaneous Symmetry Breaking (SSB) mechanism.

Many systems undergoing SSB exist in nature, like for example the direction in which a uniform cylindrical plastic rod chooses to bend when a force is exerted on it. A priori, the rod is invariant under rotations, a symmetry which is however spontaneously broken as soon as the rod chooses a direction to bend into. Another example would be a ferromagnet, which if above a critical temperature $T > T_C$ is just a collection of electrons with their spins randomly oriented. Upon cooling however, the thermal motion of electrons decreases, and when the

temperature of the ferromagnet goes below the critical temperature $T < T_C$, the electron spins align. This very weak interaction between electron spins causes them to align in a direction which is random. Therefore, the perfect rotational symmetry of the Hamiltonian of the ferromagnet is spontaneously broken by the system choosing a specific alignment direction, when the temperature is below the critical value. Moreover, any higher-energy state, which can be built from the ground state through a finite number of excitations, shares this anisotropy.

1.2.1 The Goldstone theorem

The basic premise of this concept can be used in QFT, by considering a Lagrangian which is invariant under a group of transformations $\mathcal{G}$, which transform a degenerate set of states with minimal energy. Thus, if any single one of those states is arbitrarily chosen as the ground state of the system (i.e. the vacuum), the symmetry is spontaneously broken. In this way the SSB mechanism appears from a symmetric Lagrangian that has a non-symmetric vacuum. Let us consider a complex scalar field $\phi(x)$, with a Lagrangian of the form

$$\mathcal{L}_\phi = \partial_\mu \phi^\dagger(x)\, \partial^\mu \phi(x) - V[\phi(x)] \tag{1.1}$$

where the potential $V[\phi(x)]$ takes the form

$$V[\phi(x)] = \mu^2 \phi^\dagger(x)\, \phi(x) + \lambda \left[\phi^\dagger(x)\, \phi(x)\right]^2 . \tag{1.2}$$

Under Global Phase Transformations (GPTs) of the scalar field $\phi(x)$

$$\phi(x) \overset{\mathrm{U(1)_{global}}}{\longrightarrow} \phi'(x) \equiv e^{i\theta}\phi(x) , \tag{1.3}$$

the Lagrangian in Eq. (1.1) remains invariant. This symmetry however can be spontaneously broken.

A closer examination on the form of the potential in Eq. (1.2), reveals that, in order for the potential to have a ground state it must be bounded from below. Therefore, the values $\lambda < 0$, which provide the unbounded ground states are rejected and thus the potential parameter can only take values such that $\lambda > 0$. Furthermore, the potential's quadratic nature, originating from the μ term, allows for the 2 possibilities shown in Fig. 1.2; For the case where $\mu^2 > 0$, the potential has a minimum at $\phi(x) = 0$ and it describes a massive scalar particle with mass μ and quartic coupling λ. The situation is strikingly different though for the case where $\mu^2 < 0$, with the potential minimum obtained at the points

$$\phi_0(x) = \sqrt{\frac{-\mu^2}{2\lambda}} \equiv \frac{v}{\sqrt{2}} > 0 \quad , \quad V[\phi_0(x)] = -\frac{\lambda}{4} v^4 \tag{1.4}$$

Since the Lagrangian describing the scalar field remains invariant under GPTs, there must

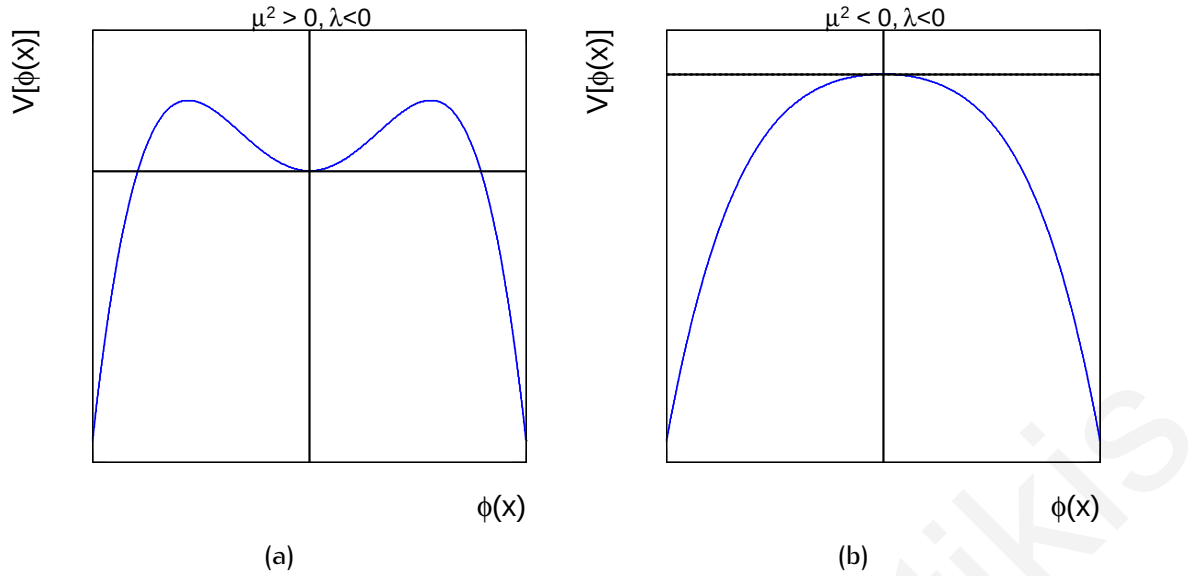

Figure 1.1: The shape of the scalar potential of Eq. (1.2) with $\lambda < 0$, for $\mu^2 > 0$ (a) and $\mu^2 < 0$ (b). For both cases the resultant potential is unbounded from below and it is hence rejected as a possibility.

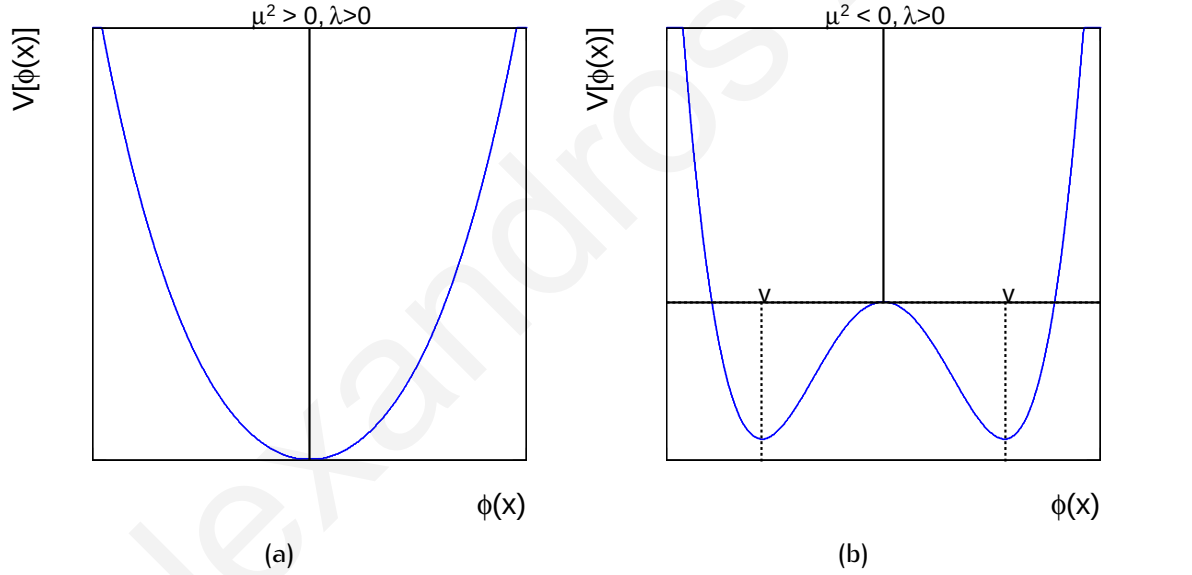

Figure 1.2: The shape of the scalar potential of Eq. (1.2) with $\lambda > 0$, for $\mu^2 > 0$ (a) and $\mu^2 < 0$ (b). In the second case, a continuous set of degenerate vacua exists, each corresponding to a different phase θ, connected through a massless field excitation $\phi_2(x)$.

be an infinite number of degenerate states of minimum energy

$$\phi_0(x) = \frac{v}{\sqrt{2}} e^{i\theta}. \tag{1.5}$$

However, in QFTs, particles are thought of as excitations from a ground state which is the vacuum. Therefore, in order to quantise this theory, a definite choice of vacuum must be made, from which one can perform small fluctuations of the field around its value. Since the potential is symmetric, one can choose any point on the circle of minima as the vacuum of the theory, about which small, stable and approximately harmonic oscillations can occur.

The choice of $\phi(x) = 0$ is obviously rejected, as it is unstable. The alternative option of choosing $\phi_0(x) = \frac{v}{\sqrt{2}} e^{i\theta}$ appears to have the desirable effect, since by choosing a particular solution as the ground state ($\theta = 0$ for example), the symmetry gets spontaneously broken. It is possible to parametrise the complex fields or excitations over the ground state as [1]

$$\phi(x) = \frac{1}{2}[v + \phi_1(x)]\, e^{i\frac{\phi_2(x)}{v}} \tag{1.6}$$

where $\phi_1(x)$ and $\phi_2(x)$ are real fields. The phase corresponds to fluctuations of the field around the valley of the ground state, whereas the modulii are parametrised as the value of the field at the state of minimum energy (v) plus the fluctuation of the field going up the potential hill ($\phi_1(x)$). The field $\phi_2(x)$ must be massless, as it is found at a constant potential and it thus needs no energy to change values around the flat valley. Conversely, field $\phi_1(x)$ is massive, as it can only fluctuate upwards along the potential hill.

Thus, the Lagrangian that describes the massive state $\phi_1(x)$ of mass $m^2_{\phi_1(x)} = -\mu^2$ and the massless state $\phi_2(x)$ takes the form

$$\mathcal{L}_\phi = \frac{1}{2}\partial_\mu\phi_1(x)\,\partial^\mu\phi_1(x) + \frac{1}{2}\left[1 + \frac{\phi_1(x)}{v}\right]\partial_\mu\phi_2(x)\,\partial^\mu\phi_2(x) - V[\phi(x)], \tag{1.7}$$

with the potential $V[\phi(x)]$ written as

$$V[\phi(x)] = V[\phi_0(x)] + \frac{1}{2}m^2_{\phi_1(x)}\phi_1(x) + \lambda v\phi_1(x)\left(\phi_1^2(x) + \phi_2^2(x)\right) + \frac{\lambda}{4}\left(\phi_1^2(x) + \phi_2^2(x)\right)^2. \tag{1.8}$$

Upon inspection of Eq. (1.7), a kinetic term is present for both fields $\phi_1(x)$ and $\phi_2(x)$, while an interaction term between the 2 fields also appears. The potential part of the Lagrangian is even more revealing, where the field $\phi_1(x)$ is clearly related to the quadratic mass term $m^2_{\phi_1(x)} = -\mu^2$, while field $\phi_2(x)$ is massless. The presence of massless excitations associated with the SSB mechanism is a general result, known as the Goldstone theorem [2, 3, 4]. It states that, if a Lagrangian is invariant under a number N of continuous symmetry groups $\mathcal{G}$, then there must exist N massless spin-0 particles (Goldstone bosons).

1.2.2 The Higgs mechanism

The powerful, yet simple Goldstone theorem, can be used to provide the EWK SSB mechanism. This can be done by first writing an $SU(2)_L$ doublet of complex scalar fields [5]

$$\phi(x) = \begin{pmatrix} \phi^{(+)}(x) \\ \phi^{(0)}(x) \end{pmatrix} \tag{1.9}$$

and re-writing the Goldstone Lagrangian of Eq. (1.1) using this doublet structure [1, 6]

$$\mathcal{L}_\phi = (D_\mu\phi(x))^\dagger D^\mu\phi(x) - \mu^2\phi^\dagger(x)\,\phi(x) - \lambda\left(\phi^\dagger(x)\,\phi(x)\right)^2, \tag{1.10}$$

with the parameter choice $\lambda > 0$ and $\mu^2 < 0$. The covariant derivative takes the form [1, 6]

$$D^\mu \phi(x) = \partial^\mu + ig\widetilde{W^\mu} + ig' y_{\phi(x)} B^\mu \tag{1.11}$$

where the scalar field hypercharges are fixed by the electric charge such that

$$y_{\phi(x)} = Q_{\phi(x)} - T_3, \tag{1.12}$$

in order to have correct couplings between the scaler field $\phi(x)$ and the EM field $A^\mu(x)$. This ensures that the photon does not couple to $\phi^{(0)}(x)$ and that $\phi^{(+)}(x)$ has the right charge.

The Lagrangian in Eq. (1.10) remains invariant under $\mathrm{SU}(2)_L \otimes \mathrm{U}(1)_Y$ transformations, with a potential that is very similar to that of the Goldstone model. Therefore, there is an infinite set of degenerate ground states (minima of energy) that satisfy

$$|\langle 0|\phi^{(0)}(x)|0\rangle| = \sqrt{\frac{-\mu^2}{2\lambda}} \equiv \frac{v}{\sqrt{2}}. \tag{1.13}$$

An explicit association of the classical ground state with the quantum vacuum is observed. The Vacuum Expectation Value (VEV), denoted v, is obtained by the electrically neutral field, $\phi^{(0)}(x)$, simply because the electrically charged field $\phi^{(+)}(x)$ cannot have an associated VEV, as it would imply that the vacuum does not conserve electric charge - which of course is not true. Therefore, the neutral scalar field $\phi^{(0)}(x)$ can acquire a VEV, and once a particular ground state is chosen, the $\mathrm{SU}(2)_L \otimes \mathrm{U}(1)_Y$ symmetry is spontaneously broken to the EM subgroup $\mathrm{U}(1)_{\mathrm{QED}}$, which by construction still remains a true symmetry of the vacuum. Therefore, according to the Goldstone theorem, since the Lagrangian in Eq. (1.10) is invariant under 3 phase rotations (an SU(2) symmetry), 3 massless spin-0 particles must exist.

It is possible to parametrise the complex scalar field doublet in Eq. (1.9) in the general form

$$\phi(x) = \exp\{i\frac{\sigma_i}{2}\theta^i(x)\}\frac{1}{\sqrt{2}}\begin{pmatrix} 0 \\ v + H(x) \end{pmatrix}, \tag{1.14}$$

where $\theta^i(x)$ and $H(x)$ represent real fields. Also, due to the $SU(2)_L$ invariance, it is possible to rotate-away the phase dependence $\theta^i(x)$ by adopting the unitary gauge $\theta^i(x) = 0$. Then, in the unitary gauge the kinetic piece of the Lagrangian in Eq. (1.10) becomes [1, 6]

$$\mathcal{L}_\phi^{\text{kinetic}} \xrightarrow{\theta^i(x)=0} (D_\mu \phi(x))^\dagger D^\mu \phi(x) = \frac{1}{2}\partial_\mu H \partial^\mu H + \frac{g^2}{4}(v+H)^2 \left\{ W_\mu^\dagger W^\mu + \frac{1}{2\cos^2\theta_W} Z_\mu Z^\mu \right\}. \tag{1.15}$$

The VEV of the neutral scalar field has generated a quadratic term of the $W^\pm$ and the Z^0 bosons, which now have acquired masses, connected with the relation

$$m_{Z^0}\cos\theta_W = m_{W^\pm} = \frac{1}{2}vg. \tag{1.16}$$

Therefore, while the photon field has remained massless as desired, the H field does interact with the gauge fields W^μ and Z^μ through the cubic and quartic terms involving $2vH$ and H^2, respectively. In this way, the Lagrangian in Eq. (1.10) has provided a way of giving masses to the intermediate carriers of the weak force. The only thing that remains, is to add this Goldstone-like Lagrangian to the $\mathrm{SU}(2)_L \otimes \mathrm{U}(1)_Y$ model. The resultant Lagrangian is invariant under gauge transformations, which guarantees the renormalisability of the associated QFT.

This might appear suspicious at first, since the EWK gauge boson masses are generated without breaking the symmetry. To understand why this happens, one must consider that massive gauge bosons are spin-1 particles with 3 degrees of freedom (polarisations), while massless gauge bosons are spin-1 particles with 2 degrees of freedom. Therefore, massless particles, which travel at the speed of light, have 1 degree of freedom less when compared to massive particles, since they have no rest frame, but instead Lorentz-invariant polarisations; the spin of massless particles can be aligned either parallel or anti-parallel to the particle's momentum. In any arbitrary gauge, other than the unitary gauge, the complete $\mathrm{SU}(2)_L \otimes \mathrm{U}(1)_Y$ including the Goldstone piece, has a total number of bosonic degrees of freedom

$$N_{\text{d.o.f}} = \left(N_{\text{gauge bosons}} \times N_{\text{polarisations}}\right) + N_{\text{Goldstone bosons}} \tag{1.17}$$

$$= (3 \times 2) + 3 = 9 \tag{1.18}$$

where $N_{\text{gauge bosons}} = 3$ refers to the massless $W^\pm$ and Z^0 bosons, $N_{\text{polarisation}} = 2$ is the number of possible polarisations for these bosons, and $N_{\text{Goldstone bosons}} = 3$ is the number of Goldstone bosons predicted by the theory. However, in the unitary gauge, which due to symmetry is equivalent to all arbitrary gauge choices, the spontaneous breaking of the symmetry results into the gauge bosons becoming massive and each acquiring one extra polarisation

$$N_{\text{d.o.f}} = (3 \times 3) + 0 = 9. \tag{1.19}$$

Thus, the EWK gauge bosons have 'eaten' the 3 Goldstone bosons to acquire their extra degree of freedom, without changing the total number of degrees of freedom.

1.2.3 The SM Higgs boson

In the unitary gauge $\theta^i(x) = 0$ and in terms of physical fields, the scalar Lagrangian in Eq. (1.10) may be written as [7]

$$\mathcal{L}_{\text{scalar}} = \frac{1}{4}\lambda v^4 + \mathcal{L}_H + \mathcal{L}_{HG^2} \tag{1.20}$$

where

$$\mathcal{L}_H = \frac{1}{2}\partial_\mu H \partial^\mu H - \frac{1}{2}m_H^2 H^2 - \frac{m_H^2}{2v}H^3 - \frac{m_H^2}{8v^2}H^4 \tag{1.21}$$

and

$$\mathcal{L}_{HG^2} = m_{W^\pm}^2 W_\mu^\dagger W^\mu \left(1 + \frac{2}{v}H + \frac{H^2}{v^2}\right) + \frac{1}{2} m_{Z^0}^2 Z_\mu Z^\mu \left(1 + \frac{2}{v}H + \frac{H^2}{v^2}\right) \tag{1.22}$$

The SM Higgs boson mass is given by the relation

$$m_H = \sqrt{-2\mu^2} = \sqrt{2\lambda}v, \tag{1.23}$$

where of course $\mu^2 < 0$. The Lagrangian in Eq. (1.20) reveals the way in which SM Higgs boson interacts with itself and to the EWK gauge bosons. These interactions, shown in Fig. 1.3, are always proportional to the mass squared of the coupled boson, and are determined by the parameters m_H, $m_{W^\pm}$, m_{Z^0} and the VEV v.

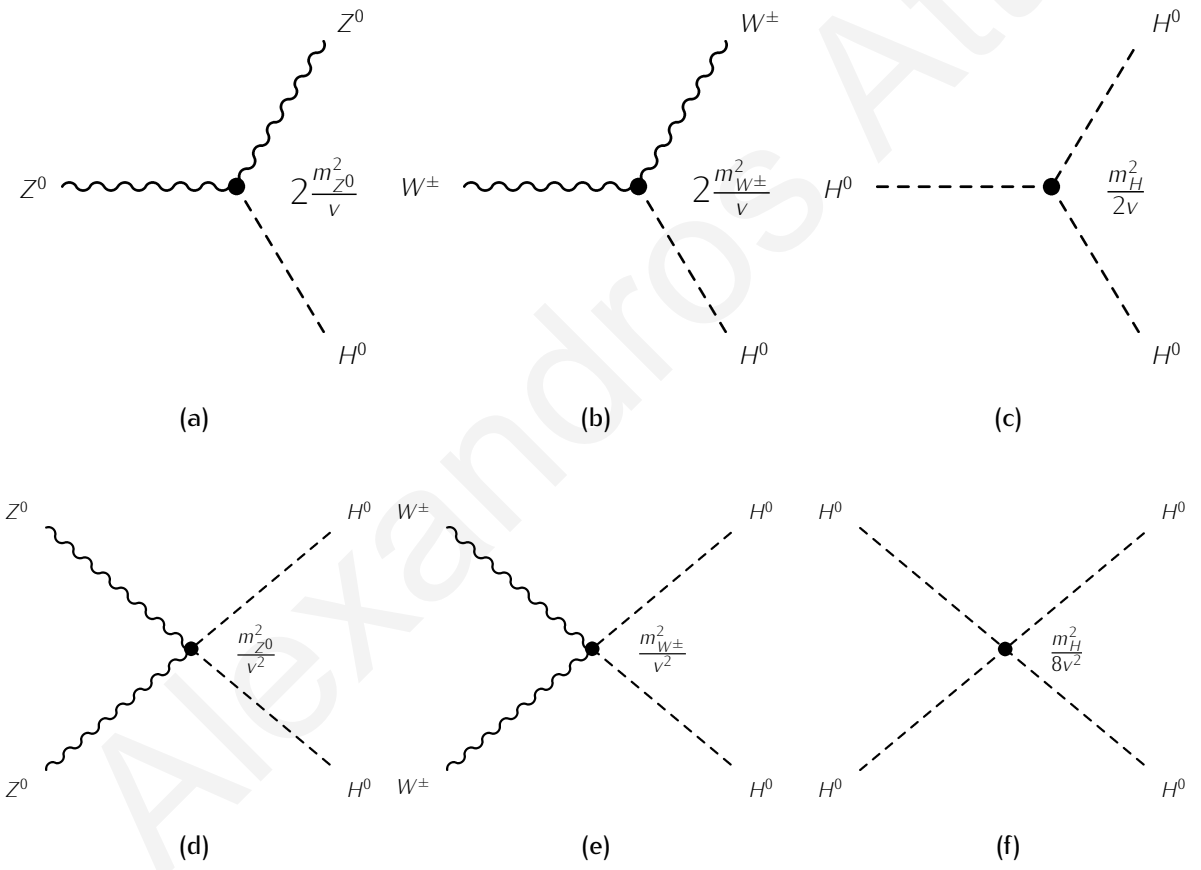

Figure 1.3: Vertices showing the SM Higgs boson trilinear and quadrilinear couplings to the EWK gauge bosons and to itself.

1.2.4 Fermionic mass terms

In a similar way that the addition of a mass term for the EM field in the QED Lagrangian is fobidden because it violates gauge invariance, similarly for the Higgs Lagrangian in Eq. (1.20),

the addition of a fermionic mass term of the form

$$\mathcal{L}_{\text{mass}} = -m\psi(x)\bar{\psi}(x) = -m\left[\psi_L(x)\bar{\psi}_R(x) + \bar{\psi}_R(x)\psi_L(x)\right] \tag{1.24}$$

is not allowed, because it breaks the gauge invariance. The addition of a scalar doublet within the SM however, enables the construction of gauge-invariant fermion-scalar couplings [7]

$$\mathcal{L}_{\text{Yukawa}} = -c_1\left(\bar{u}\,,\,\bar{d}\right)_L\begin{pmatrix}\phi^{(+)}\\ \phi^{(0)}\end{pmatrix}d_R - c_2\left(\bar{u}\,,\,\bar{d}\right)_L\begin{pmatrix}\phi^{(0)*}\\ -\phi^{(-)}\end{pmatrix}u_R - c_3\left(\bar{\nu}_{\text{e}}\,,\,\bar{\text{e}}\right)_L\begin{pmatrix}\phi^{(+)}\\ \phi^{(0)}\end{pmatrix}\text{e}_R + \text{h.c.} \tag{1.25}$$

where the term h.c. involves the $\mathcal{C}$-conjugate scalar field $\phi^c = i\sigma_2\phi^*$. A much simpler form is achieved by adopting the unitary gauge, resulting in

$$\mathcal{L}_{\text{Yukawa}} = -\frac{1}{\sqrt{2}}(v+H)\left\{c_1\bar{d}d + c_2\bar{u}u + c_3\bar{\text{e}}\text{e}\right\} \tag{1.26}$$

with the mass terms identified as

$$m_d = c_1\frac{v}{\sqrt{2}} \quad , \quad m_u = c_2\frac{v}{\sqrt{2}} \quad , \quad m_{\text{e}} = c_3\frac{v}{\sqrt{2}} \tag{1.27}$$

The terms denoted c_i are unknown parameters, which means that the fermion masses are not predicted but are instead arbitrary. Nevertheless, these so-called Yukawa couplings are fixed in terms of the masses, thus revealing a linear coupling of the H to all fermions masses

$$\mathcal{L}_{\text{Yukawa}} = -(v+H)\left\{m_d\bar{d}d + m_u\bar{u}u + m_{\text{e}}\bar{\text{e}}\text{e}\right\}, \tag{1.28}$$

as shown in Fig. 1.4. It is worth noting here that the neutrino cannot acquire mass in an

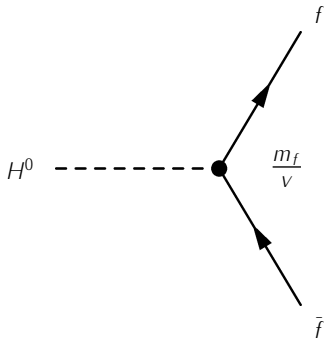

Figure 1.4: SM Higgs boson decay to a fermion-antifermion pair.

analogous way, because right-handed neutrino fields ν_R do not exist within the SM.

Therefore, the introduction of a scalar (Higgs) field which permeates the universe with a non-zero VEV, provides the SSB mechanism and assigns masses to the EWK gauge bosons

and all fermions. The nature of the interaction can be thought to be analogous to that of an object travelling through a fluid, whereby the degree with which the fluid resists motion is proportional to the mass of the object. In this way, all fundamental particles interact with the Higgs field and acquire mass. Of course, although the Higgs field gives mass to all fundamental particles, when these combine into composite particles, hadrons or mesons for example, other sources of mass come into play; the 8 massless gluons, which bind quarks within a proton or a neutron, are quite energetic and also contribute to the total mass through $E = mc^2$.

1.3 Standard Model Higgs boson production and decay

In hadron colliders, if the SM Higgs boson does exist, it can either be directly produced, or be produced in association with other particles. For proton-proton collisions, there are 4 main mechanisms for the production of SM Higgs bosons. The tree-level Feynman diagrams for these production processes are shown in Fig. 1.5, while the corresponding production cross-sections are shown in Fig. 1.6, as a function of the SM Higgs boson.

The gluon-gluon fusion mechanism $gg \rightarrow H^0$, shown in Fig. 1.5 (a), is the dominant production mechanism of the SM Higgs boson. For $m_H < 1$ TeV, the top-quark loop generated gluon-gluon fusion is the dominant production processes at the Large Hadron Collider (LHC). The second most important process is the Vector Boson Fusion (VBF) process $qq \rightarrow qq + W^{\pm}\mathrm{W}^{\mp}/Z^0Z^0 \rightarrow qq + H^0$, shown in Fig. 1.5 (b), which is available in the s-, t- and u-channels. The experimental signature of such process is expected to be 2 hard jets in the forward and backward regions of the detector, along with the SM Higgs boson decay products.

The VBF production is in turn followed in importance by the associated $q\bar{q} \rightarrow W^{\pm}/Z^0 \rightarrow W^{\pm}/Z^0 + H^0$ production process, shown in Fig. 1.5 (c). These are usually referred to as Higgsstrahlung processes, because a virtual $W^{\pm}$ or a Z^0 gauge boson decays to, or emits a SM Higgs boson. Finally, as shown in Fig. 1.5 (d), a SM Higgs boson production in association with top quarks is also possible. In this case, the Higgs boson is radiated off top quarks, through $q\bar{q} \rightarrow t\bar{t}H^0$ or $gg \rightarrow t\bar{t}H^0$, which results in a rather complex event topology, due to the presence of top-quarks which decay promptly to a $W^{\pm}$ boson and b-quark through $t \rightarrow b\mathrm{W}^+$.

Once produced, the SM Higgs boson can decay to any electrically neutral pairs of quarks, leptons and EWK gauge bosons, provided of course that it is kinematically allowed. The dependence of the branching fractions (BR) on the SM Higgs boson mass is shown in Fig. 1.7. Since the SM Higgs boson couples to mass (or mass squared for EWK gauge bosons), the decay channels that dominate a given mass range, involve the heaviest particles the Higgs can decay into. The decay mode to a b-quark pair, through $H^0 \rightarrow b\bar{b}$, is dominating for $m_{H^0} \lesssim 150\,\mathrm{GeV}/c^2$, while the decay mode $H^0 \rightarrow \tau^{\pm}\tau^{\mp}$ is the next most dominant one. At this masss range, the di-tau channel competes with the decay to a gluon-gluon pair, both modes exhibiting similar dependence on the SM Higgs boson mass. The significance of the

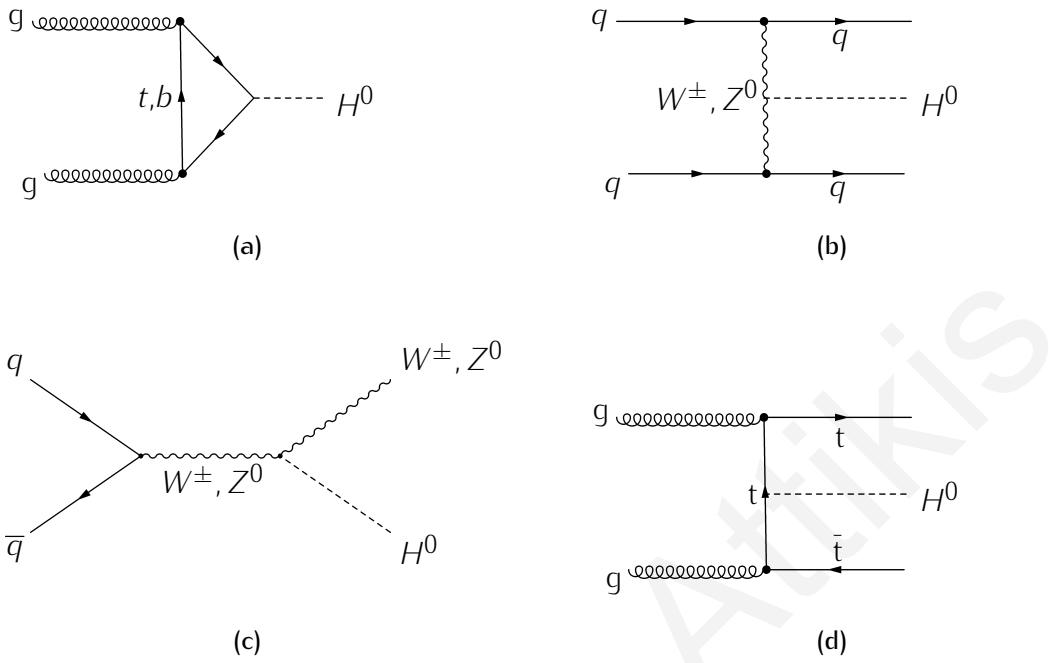

Figure 1.5: Tree-level Feynman diagrams for the SM Higgs boson production through gluon-gluon fusion (a), Vector Boson Fusion (VBF) (b), Higgsstrahlung for $W^{\pm}$ or Z^0 (c), and Higgs boson radiation off top quarks (d).

di-tau channel, however, is intensified by the fact that τ-leptons are relatively easier to distinguish in a collision environment than quark/gluon jets, which are more susceptible to large QCD multi-jet backgrounds. For the same mass spectrum, while the decay to a c-quark pair through $H^0 \to c\bar{c}$ has significant contributions, it is however overshadowed as a discovery channel by the di-photon channel. Even-though it has a very small branching fraction, the decay mode of the SM Higgs boson to a pair of photons $H^0 \to \gamma\gamma$ provides a much cleaner signature. This is due to the unmistakable signature of the 2 photons which, if carefully extracted, they should appear in the data as a clear and sharp peak over the expected background.

For the mass range $150 \lesssim m_{H^0} < 2m_t$ GeV/c^2, the SM Higgs boson decays to a pair of EWK gauge bosons, through $H^0 \to W^{\pm}W^{\mp}$ or $H^0 \to Z^0Z^0$, which are effectively the only available channels. Both decay modes increase rapidly from low values of m_{H^0}, where they are produced off-shell, with the $H^0 \to W^{\pm}W^{\mp}$ mode peaking as soon as the 2 $W^{\pm}$ bosons can be produced on-shell, around $m_{H^0} = m_{W^{\pm}}$. At the exact same point the decay mode $H^0 \to Z^0Z^0$ experiences a sharp dip, as there is enough energy to only produce 1 of the 2 Z^0 bosons on-shell. For $m_{H^0} \gtrsim 2m_{Z^0}$ the 2 decay modes dominate and show flat behaviour over the mass spectrum. This is a region where the so called "golden channel" $H^0 \to Z^0 \to 4\ell$ is increasingly important, due to its high production rate and its clear signature. In the mass range $m_{H^0} \gtrsim 2m_t$ the SM Higgs boson decay to top quark pairs becomes kinematically possible. This decay mode, however, is experimentally challenging to capitulate, due to the complex hadronic nature of the top quark final states.

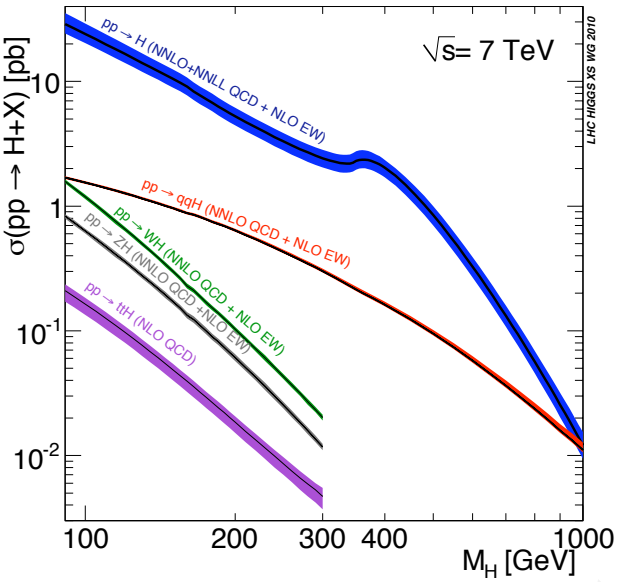

Figure 1.6: The SM model Higgs boson production cross-sections at the LHC, as a function of its mass. Taken from Ref. [8].

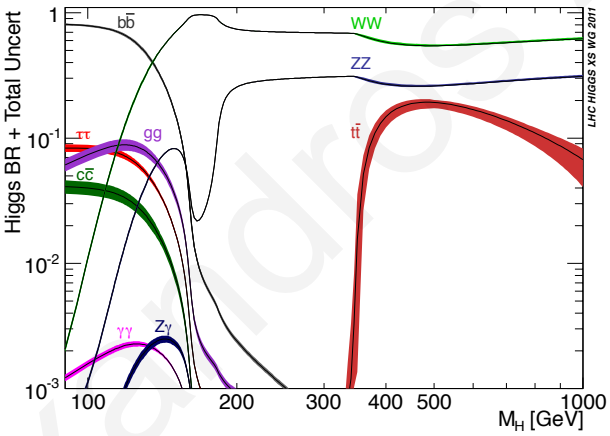

Figure 1.7: The SM model Higgs boson decay branching ratios, as a function of its mass. Taken from Ref. [8].

1.4 Searches for the SM Higgs boson

If the SM Higgs boson does exist, it can only lie within a specific mass range, as specified by various experimental and theoretical observations. Firstly, precision EWK measurements indirectly constrain the SM Higgs boson mass to be less than 158 GeV/c^2 [9]. Most importantly, however, experimental data from the Tevatron, the Large Electron-Positron Collider (LEP) and the LHC experiments provide direct constrains on the SM Higgs boson mass.

In particular, the LEP experiments have placed a lower limit on the SM Higgs boson mass to be $m_H > 114.4$ GeV/c^2 [10], as shown in Fig. 1.8. Recently, the Tevatron experiments have also imposed corresponding limits of $m_H \notin (162 - 166)$ GeV/c^2 [11], as shown in Fig. 1.9. The most recent experimental constraints imposed on the SM Higgs boson mass have been delivered by the LHC experiments, A Toroidal LHC Apparatus (ATLAS) and Compact Muon

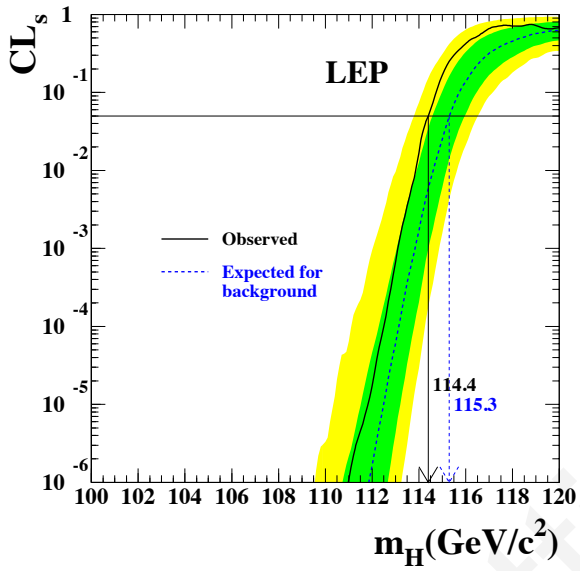

Figure 1.8: Results from the LEP experiments, showing the observed and expected ratio $CL_s(\mu) = CL_{s+b}/CL_{b\text{-only}}$ for the signal+background hypothesis used to search for the SM Higgs boson. The observed curve is used to define the 95% CL lower bound of $m_H > 114.4\,\text{GeV}/c^2$ on the mass of the SM Higgs boson. Taken from Ref. [10].

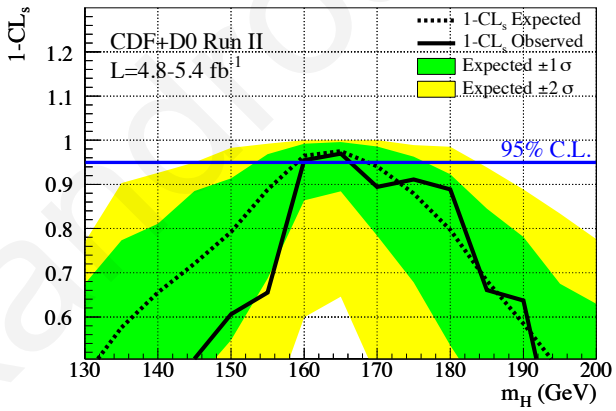

Figure 1.9: Results from the Tevatron experiments, showing the distribution of $1 - CL_s(\mu)$, as a function of the SM Higgs boson mass obtained with the CLs method. The shaded bands indicate the 68% and 95% probability regions in which the log-likelihood ratio is expected to fluctuate, in the absence of signal. Taken from Ref. [11].

Solenoid (CMS). Both experiments have provided their own limits at 95% CL on the SM Higgs boson mass. These results, which are shown in Fig. 1.10, further extend the exclusion range to $m_H \notin (112.7 - 115.5)$, $(131 - 237)$, $(251 - 453)\ \text{GeV}/c^2$ as determined by ATLAS [12], and $m_H \notin (127 - 600)$ as determined by CMS [13].

Even-though the CMS and ATLAS experiments have excluded a significant mass region in which the SM Higgs boson can lie, they have also provided tantalising hints for the presence of a relatively light SM Higgs boson in the data. In particular, and as shown in Fig. 1.11 (a), an excess of events was observed by ATLAS at a SM Higgs boson mass hypothesis close to $126\,\text{GeV}/c^2$. The combined local significance for this mass point was found to be 3.6σ, which

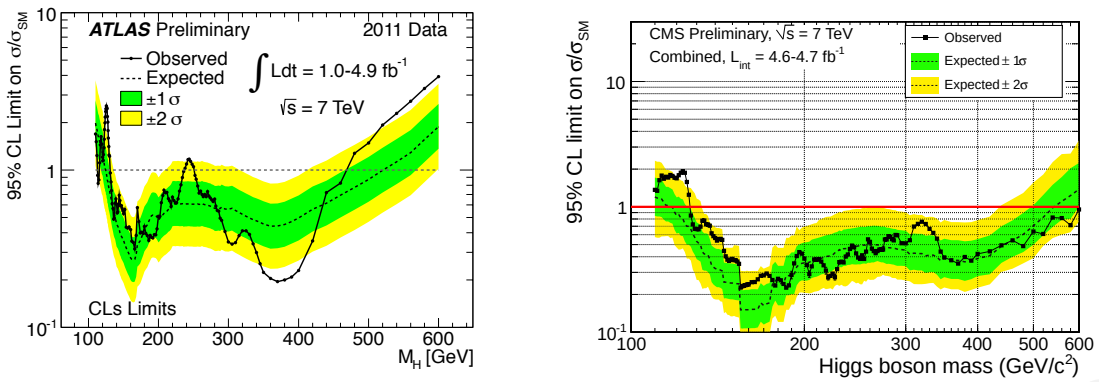

(a) (b)

Figure 1.10: Exclusion limits on the mass of the SM Higgs boson at 95% CL for the mass range $100\,\text{GeV}/c^2 < m_H < 600\,\text{GeV}/c^2$, from the ATLAS (a) and CMS (b) experiments. Taken from Ref. [12] (a) and Ref. [13] (b) .

drops to 2.3σ after taking into account the look-elsewhere effect.[1]. Similar results where also observed by the CMS experiments, where an excess of events above the expected SM background was observed at the low-end of the explored mass range, as shown in Fig. 1.11 (b). The largest excess was observed for a Higgs boson mass hypothesis of $125\,\text{GeV}/c^2$, with a local significane of 2.8σ, while the global significance of an analogous or bigger excess in the whole search range was estimated to be 0.8σ, with the look-elsewhere effect.

Although not conclusive, the experimental hints observed by the ATLAS and CMS experiments are expected to either amplify or go away once more data are added to these studies. Only then can one ascertain the origin of the observed excesses. Nevertheless, it appears that the hunt for the elusive Higgs boson is finally coming to a conclusion, with all outcomes still possible. Within 2012 it is anticipated that the ATLAS and CMS experiments will have acquired enough integrated luminosity to either exclude or confirm the existence of the SM Higgs boson.

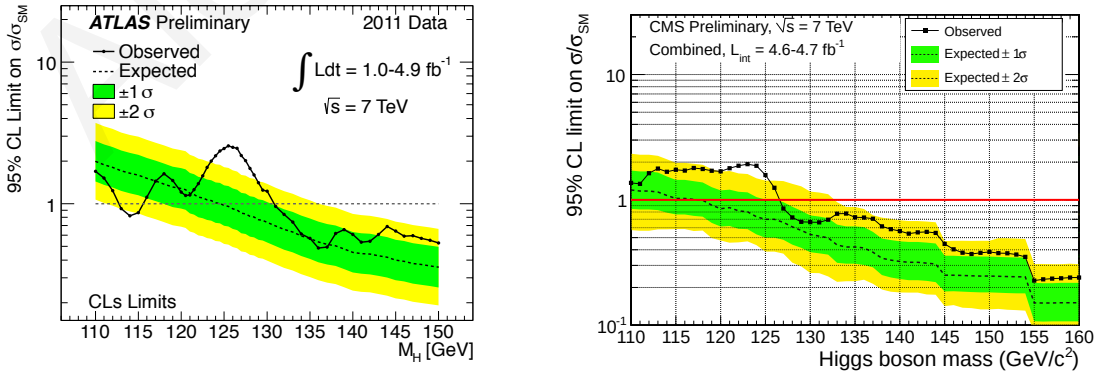

(a) (b)

Figure 1.11: Exclusion limits on the mass of the SM Higgs boson at 95% CL from the ATLAS (a) and CMS (b) experiments, for the mass ranges $110\,\text{GeV}/c^2 < m_H < 150\,\text{GeV}/c^2$ and $100\,\text{GeV}/c^2 < m_H < 160\,\text{GeV}/c^2$, respectively. Taken from Ref. [12] (a) and Ref. [13] (b) .

[1] The global probability of such an excess to occur in the full search range.

1.5 Limitations of the Standard Model

To date, the SM has remarkably survived a wide range of tests with high precision, one of its most recent successes being the direct observation of the top quark at Fermilab Tevatron. Nevertheless, despite the many successes of the model, some very important issues still remain unresolved. Attempts to extend the SM of EWK and Strong interactions to incorporate gravity have to-date been fruitless, due to the fact that no QFT of gravity has been formulated, which supports the conviction that the SM is fundamentally flawed. Furthermore, attempts to unify the EM, Weak and Strong interactions through Grand Unified Theories (GUTs) have also been unsuccessful, due to the fact that the corresponding gauge coupling constants do not converge at the unification energy scale, believed to be around $\Lambda_{GUT} \sim 10^{16}$ GeV, as shown in Fig. 1.12. This unification problem exposes the deficiencies of the SM and reveals the need for new physics at the TeV scale.

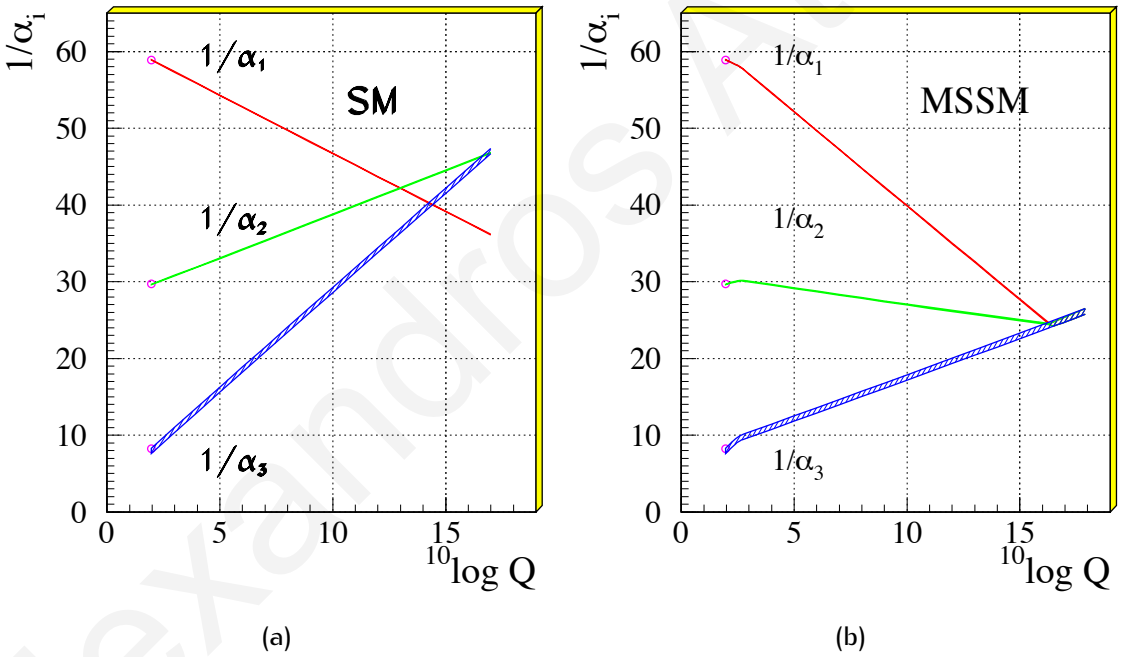

Figure 1.12: Evolution of the inverse of the EM, Weak and Strong coupling constants in the SM (a) and MSSM (b), showing that unification of the forces can only be achieved within the MSSM. The thickness of the lines represents the error in the coupling constants. Taken from Ref. [14].

Following the evidence provided by the Super Kamiokande Collaboration, the massive and flavour-oscillating neutrino is the first experimental evidence for physics Beyond the Standard Model (BSM), since within the SM the neutrino is assumed to be massless. In another mass-related problem, the SM can not explain the large difference between the fermion or vector boson masses. To make things even worse, there are cosmological problems that seem to expose the shortcomings of the SM. The $\mathcal{CPT}$ theorem states that all fundamental interactions must remain invariant under the successive operation of Charge-conjugation ($\mathcal{C}$), Parity-operation ($\mathcal{P}$) and Time-reversal ($\mathcal{T}$). The theorem implies that particles and anti-particles must have exactly the same mass and lifetime, equal and opposite electric

charges and magnetic moments. Thus, the $\mathcal{CPT}$ symmetry suggests that there should have been equal amounts of matter and anti-matter after the Big Bang, contrary to current observations which support the overwhelming predominance of matter over anti-matter in the universe. In addition, there is growing evidence of cosmic inflation; that in its early history the universe expanded rapidly by an enormous factor of at least e^{60}. The SM provides no mechanism through which this cosmic expansion can be explained.

It is also known that ordinary matter, which is comprised of quarks and leptons, contributes only a tiny fraction of $\sim 4\%$ to the matter density of the universe. There is evidence for a different kind of matter that is Weakly interacting and hence non-luminous and non-absorbing, known as Dark Matter, for which the SM offers no explanation. The earliest evidence for this new type of matter came from the observation that various luminous objects such as stars, gas clouds and even entire galaxies, moved faster than expected from the gravitational forces of other nearby visible objects. This form of matter, which is believed to contribute $\sim 23\%$ to the total matter in the universe, may include new elementary particles such as the so called Weakly Interacting Massive Particles (WIMPs). Such particles require an extension of the SM. The remaining $\sim 73\%$ of matter in the universe, as inferred from supernova explosions, is known as Dark Energy and is at the moment wholly mysterious.

Another missing link of the SM is the mechanism through which the fundamental particles and the EWK gauge bosons acquire their masses, which is yet to be firmly established. As already discussed, the gauge-symmetric theories of QED, EWK and QCD, require that all the fundamental particles are massless. However, the EWK field quanta $W^{\pm}$ and Z^0 are known to have masses of $80.399\,\mathrm{GeV}/c^2$ and $91.188\,\mathrm{GeV}/c^2$, respectively [15]. It is commonly believed that the Higgs mechanism is a strong candidate for providing the SSB mechanism, and although recent observations are hinting at its existence, the Higgs boson still remains elusive to direct observation.

Nevertheless, even if the Higgs boson is observed, it still causes problems. The higher-order terms of the perturbative expansion of the quartic Higgs field self-coupling produce quadratic mass divergences, rather than the usual logarithmic divergences, as does the mass of electron in QED, for example. To remedy this hierarchy problem, a cut-off energy $\Lambda_{\text{cut-off}}$, which defines the energy scale up to which the SM is valid, must be introduced to ensure its renormalisability. Even so, for sufficiently high values of $\Lambda_{\text{cut-off}}$, the bare Higgs mass $m_{H^0}^{\text{bare}}$[2] which in generic form can be written as

$$m_{H^0} = m_{H^0}^{\text{bare}} + \delta m_{H^0}, \tag{1.29}$$

and its radiative corrections δm_{H^0}, have to be fine-tuned to up to 16 digits to remove these divergences. This is known as the fine-tuning problem, since the relevant parameter of SM Higgs boson must be adjusted very precisely in order to agree with experimental data. Since the maximum possible value of $\Lambda_{\text{cut-off}}$ depends on the mass of the SM Higgs boson, determining the Higgs boson properties would provide precise limits on the SM and thus

[2] The mass as the scale of probing-distance approaches zero or as the particle's energy approaches infinity.

help in limiting the number of candidate theories to extend it. Since a fine-tuning of 2 digits is already required at $\Lambda_{\text{cut-off}} = 10\,\text{TeV}$, one would expect that the energy scale of $\mathcal{O}(\Lambda_{\text{cut-off}}) = 1\,\text{TeV}$ might by hiding new physics.

In conclusion, the SM is now regarded as a low energy manifestation of a deeper and unknown theory. Not only it is riddled with flaws, it also involves 19 arbitrary parameters, including particle masses and couplings, whose values are chosen to fit the experimentally observed data. Therefore, the need of new physics beyond the SM is evident, but nevertheless, it is certain that the SM will form an integral part of particle physics theories in the future.

Chapter 2

The Minimal Supersymmetric Standard Model

2.1 Introduction

A significant number of arguments were employed in Chapter 1, which indicate that the Standard Model (SM) must be part of a much larger structure. And in fact, the significant problems associated with the Higgs sector suggest that there should be new physics waiting to be explored at an energy scale believed to lie around 1 TeV. In particular, the first-order corrections to the SM Higgs boson mass result in a quadratically divergent term, which arises from SM particle loop corrections. Although many theories have been proposed to remedy or remove completely this problem, like various Supersymmetry (SUSY) [16, 17, 18, 19, 20, 21, 22, 23] extensions of the SM and Technicolor [24, 25, 26][1], perhaps the most favoured extension of the SM that provides crucial fixes to the model is the Minimal Supersymmetric Standard Model (MSSM) [27, 28].

In line with all SUSY models, the MSSM postulates that a symmetry exists between bosons and fermions; Every SM particle has a supersymmetric partner, resulting in more than doubling the number of elementary particles. Since no SUSY particles (also referred to as sparticles) have been experimentally observed to-date, SUSY must be a broken symmetry, in the sense that the superpartners must be much more massive than their SM partners. The benefit of this new particle content is significant, as it protects the Higgs boson mass from the quadratic divergences. The quantum loop-corrections for the Higgs boson mass with sparticles have the ability to cancel out the quadratic divergences encountered in the Higgs self-couplings. Therefore, by extending the SM to include superpartners, this hierarchy problem is solved. Apart from providing a solution to the hierarchy problem, SUSY theories can also accommodate gravity, provided that the supersymmetry is made local. Also, and perhaps as equally important, they can allow the coupling constants of the

[1] Technicolor models conceal Electroweak (EWK) symmetry and generate masses for the EWK gauge bosons $W^{\pm}$ and Z^0 through the dynamics of postulated new gauge interactions. Therefore, no Higgs bosons are expected and, consequently, no loop divergences.

Electromagnetic (EM), Weak and Strong interactions to unite around $\Lambda_{GUT} \sim 10^{16}$ GeV, as it was shown in Fig. 1.12.

To unambiguously prove that SUSY is indeed a symmetry of nature, SUSY particles must be produced and observed in the laboratory. However, the fact that SUSY is broken, results in the sparticles being very heavy, thus requiring a huge amount of energy to create them. To-date the Tevatron has failed to provide evidence of SUSY, and so all hopes of confirming SUSY now solely lie with the Large Hadron Collider (LHC).

In the following, the MSSM Mathematical framework and the 2 Higgs Doublet (HD) model are outlined in Section 2.2. In Section 2.3 the Higgs potential and the mass generation within the MSSM is summarised, and in Section 2.4 the mass spectrum of the MSSM Higgs bosons is given. In Section 2.5 the resultant MSSM Higgs boson production and decay processes are discussed in detail. Finally, the shortcomings of the MSSM are summarised in Section 2.6.

2.2 The two Higgs doublet model

Within the MSSM, the spin-1/2 SM fermions have scalar spin-0 superpartners known as sfermions, where in general each superpartner inherits the name of its SM counterpart, but with the letter "s" appended in front. Thus, the superpartners of electrons are the selectrons, and the two have identical properties, except from mass and spin. Furthermore, in most cases the sparticles also inherit the symbol of their SM counterpart but with a tilde ˜ on top, and are written with a subscript indicating the handedness of the SM partner[2]. So, for example, the selectron is written as $\tilde{e}_L$, and the stop-quark as $\tilde{t}_L$. In similar fashion, for each SM gauge boson and Higgs, γ, $W^{\pm}$,Z^0,H^0, one has to add an extra fermion called gaugino and higgsino. In total, there are 5 classes of sparticles that are the superpartners of the SM particles -squarks, sleptons, gluinos, charginos and neutralinos- each having its own interactions, decays, and subsequent signatures, as described by the MSSM framework. The complete MSSM particle content is tabulated in Table 2.1.

The MSSM, which is discussed in more detail in Refs. [28], [29] and [30] for example, offers a minimal extension of the SM particle content and assumes the SM symmetry group

$$\mathcal{G} = \mathrm{SU}(3)_c \otimes \mathrm{SU}(2)_L \otimes \mathrm{U}(1)_Y . \tag{2.1}$$

Furthermore, within the MSSM a new symmetry of nature is defined to exist, known as $\mathcal{R}$-parity, which serves as a new multiplicatively-conserved quantum number. It is defined as

$$\mathcal{P}_{\mathcal{R}} = (-1)^{2S+3B+L} = (-1)^{3(B-L)+2S} , \tag{2.2}$$

where S is the spin of the particle, B its associated baryon quantum number, and L its lepton

[2] Since sfermions are spin-0 particles, they can have no handedness.

Table 2.1: The MSSM particle content.

Type	Particle	SUSY Particle
Left-handed leptons/sleptons	$\begin{pmatrix} \nu_e \\ e \end{pmatrix}_L, \begin{pmatrix} \nu_\mu \\ \mu \end{pmatrix}_L, \begin{pmatrix} \nu_\tau \\ \tau \end{pmatrix}_L$	$\begin{pmatrix} \tilde{\nu}_e \\ \tilde{e} \end{pmatrix}_L, \begin{pmatrix} \tilde{\nu}_\mu \\ \tilde{\mu} \end{pmatrix}_L, \begin{pmatrix} \tilde{\nu}_\tau \\ \tilde{\tau} \end{pmatrix}_L$
Right-handed leptons/sleptons	e_R, μ_R, τ_R	$\tilde{e}_R, \tilde{\mu}_R, \tilde{\tau}_R$
Left-handed quarks/squarks	$\begin{pmatrix} u \\ d \end{pmatrix}_L, \begin{pmatrix} c \\ s \end{pmatrix}_L, \begin{pmatrix} b \\ t \end{pmatrix}_L$	$\begin{pmatrix} \tilde{u} \\ \tilde{d} \end{pmatrix}_L, \begin{pmatrix} \tilde{c} \\ \tilde{s} \end{pmatrix}_L, \begin{pmatrix} \tilde{b} \\ \tilde{t} \end{pmatrix}_L$
Right-handed quarks/squarks	u_R, c_R, t_R d_R, s_R, b_R	$\tilde{u}_R, \tilde{c}_R, \tilde{t}_R$ $\tilde{d}_R, \tilde{s}_R, \tilde{b}_R$
Vector bosons/charginos	$\gamma, W^\pm, Z^0$	$\tilde{\chi}_a^\pm, a = 1-2$
Scalar bosons/neutralinos	$h^0, H^0, A^0, H^\pm,$	$\tilde{\chi}_a^0, a = 1-4$
Gluons/gluinos	$G_a, a = 1-8$	$\tilde{G}_a, a = 1-8$

quantum number. The need for introducing $\mathcal{R}$-parity arises from the fact that no experimental data exist which support that baryon or lepton quantum number violating processes exist in nature. The strongest constraint for this observation comes from proton decay measurements, which suggest that the proton is stable, with a lifetime of $\tau_{\text{proton}} > 2.1 \times 10^{29}$ years [15]. The fact that baryon and lepton quantum numbers are conserved in all processes, implies that the conditions

$$\Delta L = 0 \tag{2.3}$$

$$\Delta B = 0 \tag{2.4}$$

must be imposed to all MSSM processes, as they are not forbidden by the theory. Therefore, any term that appears in the MSSM Lagrangian must by definition respect this symmetry. As a result, all MSSM particles have $\mathcal{P}_{\mathcal{R}}^{MSSM} = -1$ ($\mathcal{R}$-parity-odd), whilst their SM counterparts must have $\mathcal{P}_{\mathcal{R}}^{SM} = +1$ ($\mathcal{R}$-parity-even).

The $\mathcal{R}$-parity symmetry has important implications on the production of MSSM particles, enumerated below

1. MSSM particles must be pair-produced (i.e. in even numbers) from SM particles.
2. MSSM particles, other than the Lighest Supersymmetric Particle (LSP), must decay into an odd number of LSPs.
3. The LSP, which is the end-product of all MSSM particle decays, must be stable.

From the above, it can be concluded that each interaction vertex must contain an even number of MSSM sparticles, and that no mixing between MSSM and SM particles is allowed. Also, if the LSP is stable and colour/electrically uncharged, it constitutes an excellent candidate for Dark Matter; $\tilde{\chi}_1^0$ would fit that profile as it is the lightest of the 4 neutralinos.

The MSSM introduces 4 new fermionic coordinates θ^1, θ^2, $\bar{\theta}^1$ and $\bar{\theta}^2$, which are additional

to the convectional space-time coordinates $x^\mu = (t, \vec{x})$. In this new 8 dimensional superspace, the matter fields can be represented by chiral superfields, generically denoted as $S = S(x, \theta, \bar{\theta})$. In this way, the left-handed doublets of the leptons and their neutrinos (for each generation) can be written as

$$L_L \equiv L_L(x, \theta, \bar{\theta}) = \begin{pmatrix} \nu_{\ell L}(x, \theta, \bar{\theta}) \\ \ell_L(x, \theta, \bar{\theta}) \end{pmatrix}, \tag{2.5}$$

where as usual the L subscript stands for "left-handed". Similarly, the quarks are denoted

$$Q_L \equiv Q_L(x, \theta, \bar{\theta}) = \begin{pmatrix} U_L(x, \theta, \bar{\theta}) \\ D_L(x, \theta, \bar{\theta}) \end{pmatrix}, \tag{2.6}$$

where U and D represent up- and down-type quarks, respectively. Furthermore, the right-handed lepton singlets, up-type quarks and down-type quarks can be written as

$$L_R \equiv L_R(x, \theta, \bar{\theta}) = \ell_R(x, \theta, \bar{\theta}) \tag{2.7}$$
$$U_R \equiv U_R(x, \theta, \bar{\theta}) \tag{2.8}$$
$$D_R \equiv D_R(x, \theta, \bar{\theta}). \tag{2.9}$$

The gauge bosons of the U(1), SU(2) and SU(3) symmetry groups are represented by gauge vector superfields which take the form

$$V' \equiv V'(x, \theta, \bar{\theta}) \tag{2.10}$$
$$V^a \equiv V^a(x, \theta, \bar{\theta}) \quad , \quad (a = 1, 2, 3) \tag{2.11}$$
$$G_a \equiv G_a(x, \theta, \bar{\theta}) \quad , \quad (a = 1 - 8). \tag{2.12}$$

As in the SM, the generators of the U(1), SU(2) and SU(3) symmetry groups are taken to be Y, σ^a and λ^a; the hypercharge, the 3 Pauli weak-isospin matrices, and the 8 Gell-Mann matrices, respectively. The SU(2) and SU(3) generators, and their properties, are given in Appendix E. Using these definitions, the interaction part of the MSSM Lagrangian can be written as [29]

$$\begin{aligned} \mathcal{L}_{\text{int}}^{MSSM} = \int d^4\theta \Big[& \bar{L}_L \gamma^\mu \left(i\partial_\mu - \frac{g}{2}\sigma_a V_\mu^a - \frac{g'}{2} Y V'_\mu \right) L_L + \bar{L}_R \gamma^\mu \left(i\partial_\mu - \frac{g'}{2} Y V'_\mu \right) L_R \\ & + \bar{Q}_L \gamma^\mu \left(i\partial_\mu - \frac{g_s}{2}\lambda_a G_\mu^a - \frac{g}{2}\sigma_a V^a \mu - \frac{g'}{2} Y V'_\mu \right) Q_L \\ & + \bar{U}_R \gamma^\mu \left(i\partial_\mu - \frac{g_s}{2}\lambda_a G_\mu^a - \frac{g'}{2} Y V'_\mu \right) U_R \\ & + \bar{D}_R \gamma^\mu \left(i\partial_\mu - \frac{g_s}{2}\lambda_a G_\mu^a - \frac{g'}{2} Y V'_\mu \right) D_R \\ & - \frac{1}{4} \left(V^{a\alpha} V_\alpha^a \delta^2(\bar{\theta}) + V'_\alpha V'^\alpha \delta^2(\bar{\theta}) + G^{a\alpha} G_\alpha^a \delta^2(\bar{\theta}) + \text{h.c.} \right) \Big], \end{aligned} \tag{2.13}$$

where the integral is over the fermionic 4-space and the coupling constants g, g', and g_s are the well-known SM couplings for the EM, Weak and Strong interactions, respectively.

In similar fashion to the SM, the massless fields must acquire mass through the Spontaneous Symmetry Breaking (SSB) of the EWK symmetry. However, unlike the SM, where one Higgs boson doublet was required to break this symmetry, in the MSSM two Higgs doublets are required instead. The 2 HD model is the minimal extension of the SM Higgs sector, and it is constructed by the use of 2 Higgs doublets of complex scalar fields with opposite hypercharge

$$H_1 \equiv H_1(x,\theta,\bar{\theta}) = \begin{pmatrix} H_1^1(x,\theta,\bar{\theta}) \\ H_1^2(x,\theta,\bar{\theta}) \end{pmatrix} \quad , \quad Y = -\frac{1}{2} \tag{2.14}$$

$$H_2 \equiv H_2(x,\theta,\bar{\theta}) = \begin{pmatrix} H_2^1(x,\theta,\bar{\theta}) \\ H_2^2(x,\theta,\bar{\theta}) \end{pmatrix} \quad , \quad Y = +\frac{1}{2}, \tag{2.15}$$

where the SU(2) index takes values in the set $\{1,2\}$. These Higgs doublets provide masses to the up- and down-type fermions and introduce a total of $2\times 4 = 8$ degrees of freedom, with 3 of them reserved for the EWK gauge bosons; W^+, $W^-$and Z^0. The remaining 5 degrees of freedom are taken up by 5 Higgs boson states.

In constructing the Higgs part of the Lagrangian, the superpotential must be defined. In its most general form this can be written as [29]

$$W = \mu\epsilon^{ij}H_1^i H_1^j + \epsilon^{ij}\left(fH_1^i L_L^j L_R + f_1 H_1^i Q_L^j D_R + f_2 H_2^i Q_L^j U_R + \text{h.c.}\right), \tag{2.16}$$

where the term denoted μ is a mass parameter for the Higgses and ϵ^{ij} is the anti-symmetric tensor

$$\epsilon^{ij} = \begin{pmatrix} 0 & 1 \\ -1 & 0 \end{pmatrix}. \tag{2.17}$$

It must be noted that the superpotential must be a holomorphic (analytic) function[3] in order to avoid the explicit breaking of SUSY. As a result, although the inclusion of a single doublet H and H^* ($Y = \pm 1$) in Eq. (2.16) could be done in principle, it is nevertheless forbidden to protect the way in which SUSY is broken. An additional incentive for using the 2 HD model is to provide a way to cancel out the chiral anomalies that arise in the 1 HD model.

Using the above identities, the Higgs part of the Lagrangian can be written as [29]

$$\mathcal{L}_{\text{Higgs}}^{MSSM} = \int d^4\theta \left((D_\mu H_1)^\dagger (D^\mu H_1) + (D_\mu H_2)^\dagger (D^\mu H_2) + W\delta^2(\theta) + \bar{W}\delta^2(\bar{\theta}) \right) \tag{2.18}$$

where, as usual, the covariant derivative is denoted D_μ, and W is the Higgs superpotential of Eq. (2.16). The first two terms in Eq. (2.18) yield the couplings between the Higgs field

[3] A function of one or more complex variables that is infinitely differentiable and equal to its own Taylor series.

and the gauge fields.

The fact that SUSY partners have not been experimentally observed, points to the conclusion that they are not mass-degenerate with their SM analogues, and hence SUSY must be a broken symmetry. Although there are several ways to break SUSY, the MSSM is only concerned with the soft-breaking of the symmetry, which preserves logarithmic divergences in the Higgs mass loop corrections. These soft terms include SUSY mass terms for scalar particles and their couplings, and gauginos. Thus, the soft SUSY-breaking Lagrangian takes the form [29]

$$\begin{aligned}\mathcal{L}^{MSSM}_{\text{soft}} &= \int d^4\theta \Big(- m^2_{\ell_L}\bar{\ell}_L\ell_L - m^2_{\nu_\ell}\bar{\nu}_\ell\nu_\ell - m^2_{\ell_R}\bar{\ell}_R\ell_R \\ &\quad -m_1^2 H_1^\dagger H_1 - m_2^2 H_2^\dagger H_2 - m_3^2\epsilon^{ij}\left(H_i^\dagger H_j + \text{h.c.}\right) \\ &\quad +\frac{1}{2}\left(\check{M}V^{\mu a}V^a_\mu + \check{M}'V'^\mu V'_\mu + \text{h.c.}\right)\Big)\delta^4\left(\theta,\bar{\theta}\right). \end{aligned} \tag{2.19}$$

By summing the interaction, Higgs, and soft SUSY-breaking Lagrangians given in Eq. (2.13), (2.18) and (2.19), respectively, the MSSM Lagrangian in superfield formalism is given by

$$\mathcal{L}^{MSSM} = \mathcal{L}^{MSSM}_{\text{int}} + \mathcal{L}^{MSSM}_{\text{Higgs}} + \mathcal{L}^{MSSM}_{\text{soft}}. \tag{2.20}$$

In order to derive the mass terms and couplings of the MSSM Lagrangian in Eq. (2.20), a component field expansion is required. For the Higgs fields in Eq. (2.14), we have [29]

$$\begin{aligned} H_1 \equiv H_1(x,\theta,\bar{\theta}) &= \begin{pmatrix} H_1^1(x,\theta,\bar{\theta}) \\ H_1^2(x,\theta,\bar{\theta}) \end{pmatrix} \\ &= H_1(x) + i\theta\sigma^\mu\bar{\theta}\partial_\mu H_1(x) - \frac{1}{4}\theta\theta\bar{\theta}\bar{\theta}\partial^\mu\partial_\mu H_1(x) \\ &\quad +\sqrt{2}\theta\tilde{H}_1^{(2)}(x) + \frac{i}{\sqrt{2}}\theta\theta\bar{\theta}\bar{\sigma}^\mu\partial_\mu\tilde{H}_1^{(2)}(x) + \theta\theta F_1(x) \end{aligned} \tag{2.21}$$

$$\begin{aligned} H_2 \equiv H_2(x,\theta,\bar{\theta}) &= \begin{pmatrix} H_1^1(x,\theta,\bar{\theta}) \\ H_1^2(x,\theta,\bar{\theta}) \end{pmatrix} \\ &= H_2(x) + i\theta\sigma^\mu\bar{\theta}\partial_\mu H_2(x) - \frac{1}{4}\theta\theta\bar{\theta}\bar{\theta}\partial^\mu\partial_\mu H_2(x) \\ &\quad +\sqrt{2}\theta\tilde{H}_2^{(2)}(x) + \frac{i}{\sqrt{2}}\theta\theta\bar{\theta}\bar{\sigma}^\mu\partial_\mu\tilde{H}_2^{(2)}(x) + \theta\theta F_2(x), \end{aligned} \tag{2.22}$$

where $F_1(x)$ and $F_2(x)$ are auxiliary fields. The terms $\sigma^\mu = (\sigma^0, \vec{\sigma})$ and $\bar{\sigma}^\mu = (\sigma^0, -\vec{\sigma})$ introduce σ^0 which is defined as

$$\sigma^0 = \begin{pmatrix} 1 & 0 \\ 0 & 1 \end{pmatrix}, \tag{2.23}$$

while $\vec{\sigma}$ is composed of the well known Pauli matrices.Also, and as already mentioned, the field terms with the tilde ˜ on top refer to the SUSY partners of the fields. Therefore, $\tilde{H}$ is the Higgsino field, while the superscript (2) refers to the 2-component Weyl spinors. In

this context, the component field expansion for the lepton and quark fields yields similar expressions as in Eq. (2.21) [29].

The component field expansion for the gauge boson fields gives

$$\mathcal{V}^a \equiv \mathcal{V}^a(x,\theta,\bar{\theta}) = -\theta\sigma^\mu\bar{\theta}\mathcal{V}^a_\mu(x) + i\theta\theta\bar{\theta}\bar{\lambda}^a(x) - i\bar{\theta}\bar{\theta}\theta\lambda^a(x) + \frac{1}{2}\theta\theta\bar{\theta}\bar{\theta}D^a(x) \quad (2.24)$$

with λ^a being the 2-component Weyl gaugino fields which are the SUSY partners of the gauge boson fields, while the D-fields are also auxiliary fields. It can be shown that, by applying the Euler-Lagrange equations of motion for the F- and D- fields to the MSSM Lagrangian in Eq. (2.20), the following expression can be obtained [29]

$$F^{j\dagger}_L = -f\epsilon^{ij}H^i_1\tilde{\Phi}_R + \text{h.c.} \quad (2.25)$$
$$F^\dagger_R = -f\epsilon^{ij}H^i_1\tilde{\Phi}^j_L + \text{h.c.} \quad (2.26)$$
$$F^{i\dagger}_1 = -\mu\epsilon^{ij}H^j_2 - f\epsilon^{ij}H^i_1\tilde{\Phi}_L\tilde{\Phi}_R + \text{h.c.} \quad (2.27)$$
$$F^{j\dagger}_2 = -\mu\epsilon^{ij}H^i_1 + \text{h.c.} \quad (2.28)$$
$$D^a = -\frac{g_\mathcal{V}}{2}\left(\tilde{\Phi}^\dagger_L\mathcal{G}^a\Phi_L + \tilde{\Phi}^\dagger_R\mathcal{G}^a\Phi_R + H^\dagger_1\mathcal{G}^aH_1 + H^\dagger_2\mathcal{G}^aH_2 + \text{h.c.}\right), \quad (2.29)$$

where $g_\mathcal{V}$ and $\mathcal{G}^a$ are the coupling constant and symmetry-group generators for the interaction in question. These terms can be used to remove the F- and D-terms from the MSSM Lagrangian, which in component form is written as [29]

$$\begin{aligned}\mathcal{L}^{MSSM}_{\text{int}} = &\left(D^\mu\tilde{L}\right)^\dagger\left(D_\mu\tilde{L}\right) + \left(D^\mu\tilde{R}\right)^\dagger\left(D_\mu\tilde{R}\right)\\ &-i\bar{L}\gamma^\mu D_\mu L - i\bar{R}\gamma^\mu D_\mu R\\ &-g^a_\mathcal{V}\left(\bar{L}\mathcal{G}^a\lambda^a\tilde{L} + \bar{R}\mathcal{G}^a\bar{\lambda}^a\tilde{R} + \text{h.c.}\right)\\ &-g^a_\mathcal{V}\left(\bar{\lambda}^a\gamma^\mu\lambda^b\mathcal{V}^b_\mu + \bar{\lambda}^b\gamma^\mu\lambda^a\mathcal{V}^a_\mu - \bar{\lambda}^b\gamma^\mu\lambda^b\mathcal{V}^a_\mu\right)\\ &-\frac{i}{2}\bar{\lambda}^a\gamma^\mu\partial_\mu\lambda^a - \frac{1}{4}\mathcal{V}^{a\mu\nu}\mathcal{V}^a_{\mu\nu},\end{aligned} \quad (2.30)$$

where D_μ is the covariant derivative and L (R) are the left-handed (right-handed) doublets (singlets) of leptons and quarks, as in the SM. For the complete Lagrangian, summation over the indices a and b and over all particle generations is required.

In a similar manner, by applying component field expansion to the Higgs part of the

MSSM Lagrangian defined in Eq. (2.18), one gets [29]

$$\begin{aligned}
\mathcal{L}_{\text{Higgs}}^{MSSM} &= (D^\mu H_1)^\dagger (D_\mu H_1) + (D^\mu H_2)^\dagger (D_\mu H_2) \\
&\quad -i\bar{\tilde{H}}_1 \gamma^\mu D_\mu \tilde{H}_1 - i\bar{\tilde{H}}_2 \gamma^\mu D_\mu \tilde{H}_2 \\
&\quad + \frac{ig_y^a}{\sqrt{2}} \left(H_1^\dagger \mathcal{G}^a \lambda^a \tilde{H}_1 - \bar{\tilde{H}}_1 \mathcal{G}^a \bar{\lambda}^a H_1 + H_2^\dagger \mathcal{G}^a \lambda^a \tilde{H}_2 - \bar{\tilde{H}}_2 \mathcal{G}^a \bar{\lambda}^a H_2 \right) \\
&\quad - \frac{\mu}{2} \bar{\tilde{H}}_1 \tilde{H}_2 - \frac{\mu}{2} \bar{\tilde{H}}_2 \tilde{H}_1 + \mu \bar{\tilde{H}}_1 \tilde{H}_1 + \mu \bar{\tilde{H}}_2 \tilde{H}_2 \\
&\quad - f \Big(\bar{\tilde{H}}_1 L^1 \tilde{R} + \bar{\tilde{H}}_2 L^1 \tilde{R} - \bar{\tilde{H}}_1 L^2 \tilde{R} + \bar{R} L^1 H_1^2 - \bar{R} L^2 H_1^1 \\
&\quad + \bar{R} \tilde{H}_1^c \tilde{L}^1 + \bar{R} \tilde{H}_2^c \tilde{L}^1 - \bar{R} \tilde{H}_1 \tilde{L}^2 + \text{h.c.} \Big) \\
&\quad - \mu^2 H_1^\dagger H_1 - \mu^2 H_2^\dagger H_2 - \mu f \left(\tilde{H}_2^\dagger \tilde{L} \tilde{R} + \text{h.c.} \right) \\
&\quad - f^2 \Big[\tilde{L}^\dagger \tilde{L} \tilde{R}^\dagger \tilde{R} + H_1^\dagger H_1 \tilde{L}^\dagger \tilde{L} + H_1^\dagger H_1 \tilde{R}^\dagger \tilde{R} + \left(H_1 \tilde{L} \right)^\dagger \left(H_1 \tilde{L} \right) \Big] \\
&\quad - \frac{g^2}{2} \left(\tilde{L}^\dagger \sigma^a \tilde{L} + H_1^\dagger \sigma^a H_1 + H_2^\dagger \sigma^a H_2 \right)^2 \\
&\quad - \frac{g^2}{8} \tan^2 \theta_W \left(\tilde{L}^\dagger \tilde{L} - 2\tilde{R}^\dagger \tilde{R} + H_1^\dagger H_1 - H_2^\dagger H_2 \right)^2 ,
\end{aligned} \tag{2.31}$$

where $g' = g \tan \theta_W$. The terms denoted f are constants, the superscript c implies charge conjugation, while the superscripts 1 and 2 of a field correspond to the upper or lower spinors of the fields ($\mu = 1, 2$ or $\mu = 3, 4$).

Finally, the soft SUSY-breaking MSSM Lagrangian in Eq. (2.32) can also be expressed in component field expansion form to give [29]

$$\begin{aligned}
\mathcal{L}_{\text{soft}}^{MSSM} &= m_L^2 \tilde{L}^\dagger \tilde{L} - m_R^2 \tilde{R}^\dagger \tilde{R} - m_1^2 H_1^\dagger H_1 - m_2^2 H_2^\dagger H_2 + m_3^2 \epsilon^{ij} \left(H_1^i H_2^j + \text{h.c.} \right) \\
&\quad - \frac{1}{2} M \left(\lambda^a \lambda^a + \bar{\lambda}^a \bar{\lambda}^a \right) .
\end{aligned} \tag{2.32}$$

The full MSSM Lagrangian in component field expansion is again given by summing the interaction, Higgs, and soft SUSY-breaking Lagrangians given in Eq. (2.30), (2.31) and (2.32), respectively, as indicated in Eq. (2.20).

2.3 Higgs potential and mass generation

The results shown in Section 2.2 can be used to express the scalar MSSM Higgs potential. It takes the form [29]

$$\begin{aligned}
V_{\text{Higgs}} &= \left(m_1^2 + \mu^2 \right) H_1^\dagger H_1 + \left(m_2^2 + \mu^2 \right) H_2^\dagger H_2 - m_3 \epsilon^{ij} \left(H_1^i H_2^j + \text{h.c.} \right) \\
&\quad + \frac{g^2}{2} \left(H_1^\dagger \sigma^a H_1 + H_2^\dagger \sigma^a H_2 \right)^2 + \frac{g'^2}{8} \left(H_1^\dagger H_1 + H_2^\dagger H_2 \right)^2 .
\end{aligned} \tag{2.33}$$

One may choose the phases of the scalar Higgs fields so that all mass parameters m_i^2 ($i = 1, 2, 3$) are real and that the Vacuum Expectation Values (VEVs) of the Higgs fields are non-negative. Furthermore, and similarly to the SM, as the Higgs fields acquire a VEV and a particular ground state is chosen, the EWK gauge symmetry $\mathrm{SU}(2)_L \otimes \mathrm{U}(1)_Y$ is spontaneously broken to the EM sub-group $\mathrm{U}(1)_{\mathrm{QED}}$, which by construction still remains a true symmetry of the vacuum. This means that the charged components of the Higgs doublets can not develop non-vanishing VEVs, as it would imply that the vacuum does not conserve electric charge - which of course is not true. Therefore, the breaking of the symmetry leads to two expectation values of the vacuum, v_1 and v_2, respectively

$$H_1 = \begin{pmatrix} v_1 \\ 0 \end{pmatrix} \; H_2 = \begin{pmatrix} 0 \\ v_2 \end{pmatrix} \tag{2.34}$$

and the potential in vacuum is given by [29]

$$V_{\mathrm{Higgs}}^{\mathrm{vacuum}} = \left(m_1^2 + \mu^2\right) v_1^2 + \left(m_2^2 + \mu^2\right) v_2^2 - 2m_3^2 v_1 v_2 + \frac{1}{8}\left(g^2 + g'^2\right)\left(v_1^2 - v_2^2\right)^2 . \tag{2.35}$$

From this expression a stability condition arises such that

$$m_1^2 + m_2^2 - 2m_3^2 \geq 0, \tag{2.36}$$

which guarantees that the potential is bounded from below in the direction $v_1 = v_2$. The procedure of minimising the Higgs vacuum potential also yields one of the MSSM free parameters which relates the two VEVs

$$\tan\beta = \frac{v_2}{v_1}, \tag{2.37}$$

and since $v_1, v_2 \geq 0$, it is constrained by the inequality

$$0 \leq \beta \leq \frac{\pi}{2}. \tag{2.38}$$

The Weak gauge boson masses can also be obtained from the Higgs part of the MSSM Lagrangian in Eq. (2.31) by applying the result in Eq. (2.34), to get

$$m_{W^\pm} = \frac{g^2}{2}\left(v_1^2 + v_2^2\right) = \left(\frac{gv}{\sqrt{2}}\right)^2 \tag{2.39}$$

$$m_{Z^0} = \frac{g}{2\cos^2\theta_W}\left(v_1^2 + v_2^2\right) = \frac{1}{2}\left(g^2 + g'^2\right)\left(v_1^2 + v_2^2\right), \tag{2.40}$$

where $v^2 = v_1^2 + v_2^2$. The photon field remains massless, as required.

The masses for the leptons are generated by the Yukawa part of the MSSM superpotential in Eq. (2.16), and can be obtained from the term that couples the left- and right-handed lepton

fields to the Higgs field

$$\begin{aligned} f\epsilon^{ij}\bar{R}L^{i}H_1^{j} + \text{h.c.} &\rightarrow -f_\ell v_1\left(\bar{\ell}\ell_L + \bar{\ell}_L\ell_R\right) \\ &= -f_\ell v_1\bar{\ell}\ell \\ \Rightarrow m_\ell &= f_\ell v_1 . \end{aligned} \tag{2.41}$$

In a similar way, the quark masses can be determined to be $f_q v_1$ and $f_q v_2$ for the up- and down-type quarks, respectively. The neutrino, however, remains massless, as in the SM. The slepton masses are slightly more involved to derive, since they are generated by both the Higgs and soft SUSY-breaking part of the MSSM Lagrangian, which results in the appearance of cross-terms for the left- and right-handed sleptons. It can be shown that the slepton masses can be expressed as [29]

$$m^2_{\tilde{\ell}_1} = m^2_\ell + \frac{1}{2}\left(\left(m^2_L + m^2_R\right) + \sqrt{\left(m^2_L + m^2_R\right) + 4\mu^2 m^2_\ell \tan^2\beta}\right) \tag{2.42}$$

$$m^2_{\tilde{\ell}_2} = m^2_\ell + \frac{1}{2}\left(\left(m^2_L + m^2_R\right) - \sqrt{\left(m^2_L + m^2_R\right) + 4\mu^2 m^2_\ell \tan^2\beta}\right), \tag{2.43}$$

with the degree of left- and right- mixing of the masses unconstrained by theory. If one assumes maximal mixing such that $\tilde{m}^2_\ell = m^2_L = m^2_R$, then

$$\tilde{\ell}_1 = \frac{\tilde{\ell}_L + \tilde{\ell}_R}{\sqrt{2}} \tag{2.44}$$

$$\tilde{\ell}_2 = \frac{\tilde{\ell}_L - \tilde{\ell}_R}{\sqrt{2}} \tag{2.45}$$

while their corresponding masses become

$$m^2_{\tilde{\ell}_1,\tilde{\ell}_2} = \tilde{m}^2 + m^2_\ell \pm |\mu| m_\ell \tan\beta. \tag{2.46}$$

The masses of the squarks can be obtained in similar fashion as for the sleptons.

The MSSM also predicts the existence of SUSY partners for the EWK gauge bosons γ, $W^\pm$, Z^0 and Higgs boson H^0, which are known as bino (photino), wino, zino and 4 higgsinos (2 charged and 2 neutral). These are Weyl fermions that mix with themselves as well as the other gauginos to form charginos and neutralinos. It is these objects that are the observed fermions. In particular, mixing of the bino, zino and neutral higgsino form the neutralinos $\tilde{\chi}^0$, while the winos and charged higgsinos mix to form the charginos $\tilde{\chi}^\pm$.

For the charginos, the mixing between the winos and the charged higgsinos results in 2 physical charginos, $\tilde{\chi}^\pm_1$ and $\tilde{\chi}^\pm_2$, while the mixing between the bino, zino and the neutral higgsinos results in 4 physical neutralinos; $\tilde{\chi}^0_1$, $\tilde{\chi}^0_2$, $\tilde{\chi}^0_2$, $\tilde{\chi}^0_4$.

2.4 The physical MSSM Higgs boson spectrum

Although in the SM one starts by expanding around the Higgs VEVs and identifies the new state as the physical state, in the MSSM the same procedure results in states that do not represent physical mass eigenstates. Instead, the physical eigenstates are obtained by diagonalising the Higgs boson mass-square matrix

$$\mathcal{M}_{ij}^2 = \frac{1}{2}\frac{\partial^2 V_{\text{Higgs}}}{\partial H_i \partial H_j}\bigg|_{\text{min}} \tag{2.47}$$

where the subscript "min" indicates that the evaluation must be performed at the minima of the 2 Higgs doublets, as described in detail in Ref. [29]. Therefore, the Higgs doublets, which provide masses to the up- and down-type fermions, apart from generating masses for the 3 EWK gauge bosons (W^+, W$^-$and Z^0), they also result in 5 physical Higgs boson states; h^0, H^0, A^0, H^+, and H^-.

The pseudoscalar $\mathcal{CP}$-odd A^0 acquires a mass

$$m_{A^0}^2 = -m_3^2(\tan\beta + \cot\beta) = -2\frac{m_3^2}{\sin 2\beta}. \tag{2.48}$$

Using this expression, the $\mathcal{CP}$-even Higgs boson masses can be expressed as

$$m_{h^0}^2 = \frac{1}{2}\left(m_{A^0}^2 + m_{Z^0}^2 - \sqrt{\left(m_{A^0}^2 + m_{Z^0}^2\right)^2 - 4m_{A^0}^2 m_{Z^0}^2 \cos^2 2\beta}\right) \tag{2.49}$$

$$m_{H^0}^2 = \frac{1}{2}\left(m_{A^0}^2 + m_{Z^0}^2 + \sqrt{\left(m_{A^0}^2 + m_{Z^0}^2\right)^2 - 4m_{A^0}^2 m_{Z^0}^2 \cos^2 2\beta}\right), \tag{2.50}$$

where it emerges that the $\mathcal{CP}$-even light and $\mathcal{CP}$-even heavy neutral Higgs boson masses are related to those of the $\mathcal{CP}$-odd neutral Higgs boson A^0, the mass of the EWK gauge boson Z^0 and the angle β of Eq. (2.37).

At tree-level, the charged higgs boson mass is related to the mass of the $\mathcal{CP}$-odd MSSM Higgs bosdon A^0 by the relation

$$\begin{aligned} m_{H^\pm}^2 &= \frac{1}{2}\left(g^2 + 2\frac{m_3^2}{v_1 v_2}\right)\left(v_1^2 + v_2^2\right) \\ \Rightarrow m_{H^\pm}^2 &= m_{A^0}^2 + m_{Z^0}^2, \end{aligned} \tag{2.51}$$

revealing that at least at tree-level, the mass of the charged MSSM Higgs boson is greater than that of the $\mathcal{CP}$-odd A^0. Furthermore, a general observation is that the masses of the 5 physical Higgs bosons are all inter-linked, as shown in Fig. 2.1. This means that only 1 Higgs boson mass is a free parameter and if determined the rest are fixed by it. This is especially important, since, in order to cancel-out the quadratic divergences in the quartic Higgs boson couplings, the masses of the A^0, H^0 and $H^\pm$ must be below ~ 1 TeV, otherwise the Higgs self-couplings become too strong for a perturbative expansion. A detailed review of the latest searches for the charged Higgs boson is given in Section 4.1.

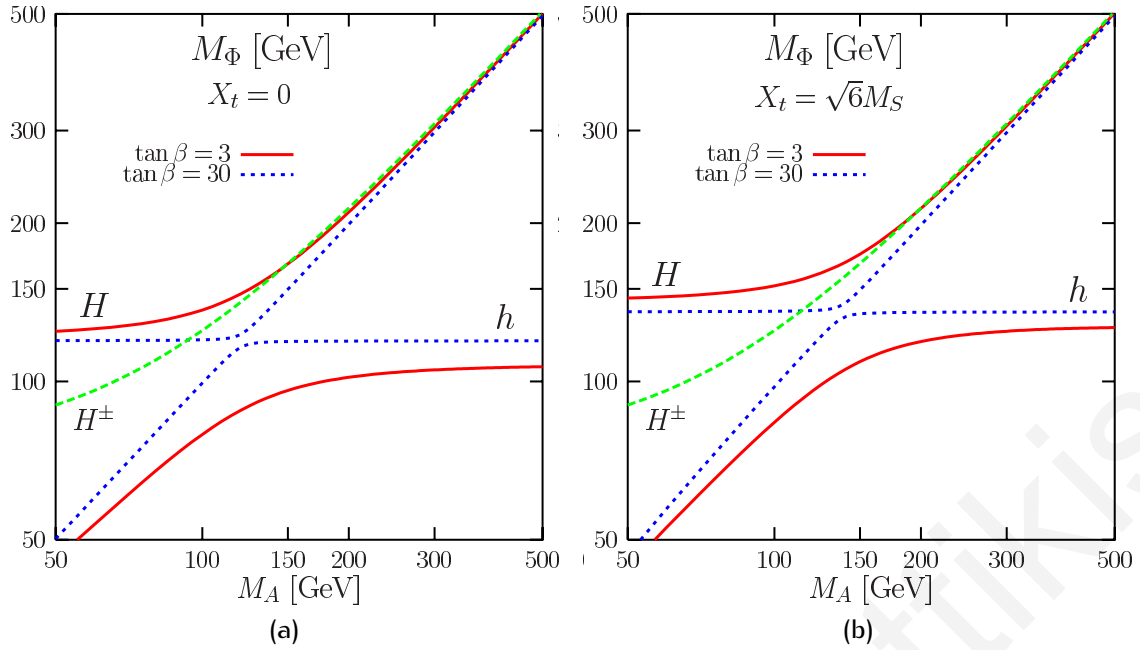

Figure 2.1: The masses of the MSSM Higgs bosons as a function of m_{A^0}, for $\tan\beta = 3$ and $\tan\beta = 30$, in the no mixing $m_h^{\text{no-mix}}$ (a) and maximal mixing m_h^{max} (b) scenarios with $M_{\text{SUSY}} = 2\,\text{TeV}$ and all the other SUSY parameters set to 1 TeV. Taken from Ref. [27].

Apart from Higgs boson mass, the other free parameters is the ratio of the VEVs $\tan\beta$, the μ and its sign, and the mixing angle α which mixes the $\mathcal{CP}$-even neutral Higgs bosons

$$\begin{pmatrix} H^0 \\ h^0 \end{pmatrix} = \begin{pmatrix} \cos\alpha & \sin\alpha \\ -\sin\alpha & \cos\alpha \end{pmatrix} \begin{pmatrix} H_1^1 \\ H_2^2 \end{pmatrix} \tag{2.52}$$

and is given by the expression

$$\cos 2\alpha = -\cos 2\beta \frac{m_{A^0}^2 - m_{Z^0}^2}{m_{H^0}^2 - m_{h^0}^2}. \tag{2.53}$$

2.5 MSSM Higgs boson production and decay

Due to the fact that the $\tan\beta$ and μ parameters are largely unconfined, in order to somewhat restrict the MSSM parameter space, it is common to subject it to some benchmark scenarios [31]. Common examples include the no-mixing and the maximal-mixing benchmark scenarios, denoted $m_h^{\text{no-mix}}$ and m_h^{max}, respectively. The latter, on which the present thesis will largely concentrate on, tunes the MSSM parameters such that the maximum possible lighter $\mathcal{CP}$-even Higgs boson mass m_{h^0} as a function of $\tan\beta$ is obtained. In other words, it maximises the upper bound of the lighter $\mathcal{CP}$-even Higgs-boson mass m_{h^0}. This is achieved by fixing the parameters M_{SUSY} and setting m_{A^0} to its maximal value of $m_{A^0} = 1\,\text{TeV}$. This results in the maximal mixing between the left- and right-handed stop eigenstates. A summary of the selected parameters for the no-mixing $m_h^{\text{no-mix}}$ and maximal-mixing m_h^{max} scenarios is given in Table 2.2. The parameter M_{SUSY} denotes the common soft SUSY-breaking squark

mass of the 3rd generation, $X_t = A_t - \mu \cot\beta$ is the stop mixing parameter, while A_t and A_b are the stop and sbottom trilinear couplings, respectively. The parameter μ is the Higgsino mass parameter, the gluino mass is denoted $m_{\tilde{g}}$, and finally M_2 is the SU(2) gaugino mass parameter.

Table 2.2: The parameters for the no-mixing m_h^{no-mix} and maximal-mixing m_h^{max} scenarios of the MSSM.

Parameter	no-mixing m_h^{no-mix}	maximal-mixing m_h^{max}
M_{SUSY}	2 TeV	1 TeV
X_t	0	$2M_{SUSY}$
μ	+200 GeV	+200 GeV
$m_{\tilde{g}}$	1.6 TeV	$0.8M_{SUSY}$
M_2	200 GeV	+200 GeV
A_t	A_b	A_b

2.5.1 Neutral Higgs bosons

The dominant production modes of the neutral MSSM Higgs bosons h^0, H^0, and A^0 are similar to the SM Higgs boson. More specifically, the most important processes are the gluon-gluon fusion process $gg \to h^0/H^0/A^0$, and Higgs boson radiation off b-quarks $gg \to h^0/H^0/A^0 + b\bar{b}$. Conversely, the analogous contribution for Higgs boson radiation off top-quarks is relatively small. For low $\tan\beta$ values however, the Vector Boson Fusion (VBF) process $qq \to qq + W^{\pm}W^{\mp}/Z^0Z^0 \to qqh^0/H^0$ also contributes in the light Higgs boson h^0 production. The associated production (Higgsstrahlung) processes through $qq \to W^{\pm}/Zz \to H^0/Z^0H^0$ is also comparatively small. The tree-level Feynman diagrams for all aforementioned processes were presented in Fig. 1.5.

The total production cross-sections for the neutral MSSM Higgs bosons h^0, H^0, and A^0, are presented in Fig. 2.2, as a function of the corresponding Higgs mass within the no-mixing scenario m_h^{no-mix} and for the values $\tan\beta = 5$ and $\tan\beta = 30$. A detailed description of the uncertainties in the MSSM Higgs boson production can be found in Refs. [32] and [33]. In both figures, the maximum allowed mass for the light MSSM Higgs boson h^0 is $m_{h^0} \lesssim 130\,\text{GeV}/c^2$, with this number also serving as the lower mass limit for the heavy MSSM Higgs boson H^0. For h^0, the cross-section is an increasing function of its mass m_{h^0}, while for H^0 the opposite effect is observed. A general feature is that gluon-gluon fusion is either competing or dominating the Higgs boson radiation off b-quarks for $\tan\beta = 5$, while the latter clearly dominates for $\tan\beta = 30$.

Once produced, the charged and neutral MSSM Higgs bosons can decay to a wide spectrum of final states, which is heavily influenced by the values assigned to the MSSM parameters $\tan\beta$ and μ. The branching ratios presented in the following were calculated in the m_h^{max} scenario, which fixes the MSSM theory up to the $\tan\beta$ and the mass of one of

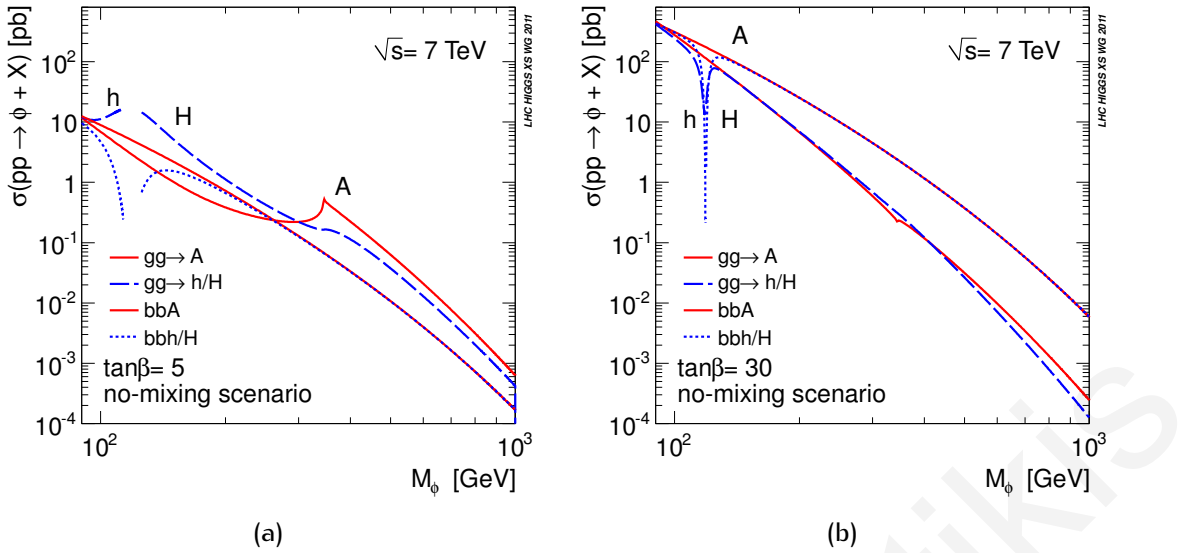

Figure 2.2: The production cross-section for the MSSM Higgs bosons at the LHC and at $\sqrt{s}$=7 TeV , for $\tan\beta = 5$ (a) and $\tan\beta = 30$ (b). The dominant processes are shown only, namely gluon-gluon fusion $gg \to h^0/H^0/A^0$ and Higgs radiation off b-quarks $gg \to h^0/H^0/A^0 + b\bar{b}$. Taken from Ref. [32].

the MSSM Higgs bosons. It must be noted though that the branching fractions of all MSSM Higgs bosons to SUSY particles depends greatly on their masses as well as the μ parameter. Furthermore, since the m_h^{max} scenario is probed here, the masses of the neutralinos $\tilde{\chi}_a^0$ and charginos $\tilde{\chi}_a^{\pm}$ are set to a considerably lower level than 1 TeV. This results in them having a considerable branching ratio over the whole mass-spectrum and $\tan\beta$ parameter-space, for all 5 MSSM Higgs bosons. Conversely, within the m_h^{max} scenario the squark and slepton masses are too large to allow their production in MSSM Higgs boson decays. For comparison purposes, corresponding plots with the benchmark scenario adopted in Ref. [27] are presented in Appendix F.

In Fig. 2.3, the branching ratios for the lighter $\mathcal{CP}$-even MSSM Higgs boson h^0 are shown, as a function of its mass and for $\tan\beta = 3$ and $\tan\beta = 30$. These can be compared to the branching ratio values for the SM Higgs boson, which were presented in Fig. 1.7. The main features of the two diagrams are similar, with the $h^0 \to b\bar{b}$ decay dominating at low masses and the $h^0 \to \tau^{\pm}\tau^{\mp}$ channel being the sub-leading decay process. As a consequence, the discovery channels for the SM Higgs boson and the $\mathcal{CP}$-even MSSM Higgs boson are quite similar. These features persist for the full low-mass spectrum and for both values of $\tan\beta = 3$ and $\tan\beta = 30$. Due to the imposed upper bound of the lighter $\mathcal{CP}$-even Higgs-boson mass $m_{h^0} \lesssim 130\,\mathrm{GeV}/c^2$, the decays to $t\bar{t}$, EWK gauge bosons and SUSY particles is kinematically forbidden.

The branching ratios for the heavier $\mathcal{CP}$-even MSSM Higgs boson H^0 are presented in Fig. 2.4 for $\tan\beta = 3$ and $\tan\beta = 30$, where again similarities can be observed with the values obtained for the SM Higgs boson in Fig. 1.7. In particular, this SM-like behaviour is especially true for the mass spectrum $m_{H^0} < m_t$ and for small $\tan\beta$ values. In this spectrum, the decay modes $H^0 \to b\bar{b}$, $H^0 \to W^{\pm}W^{\mp}$, and $H^0 \to Z^0Z^0$ dominate, while

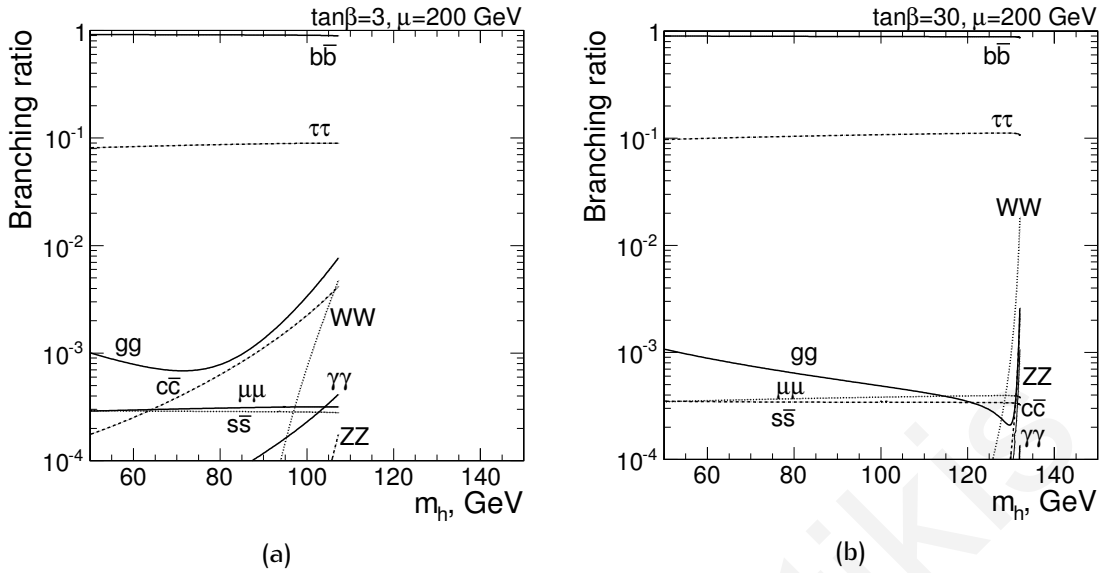

Figure 2.3: The decay branching ratios of the $\mathcal{CP}$-even MSSM Higgs boson h^0 as a function of its mass, for $\tan\beta = 3$ (a) and $\tan\beta = 30$ (b). Taken from Ref. [34].

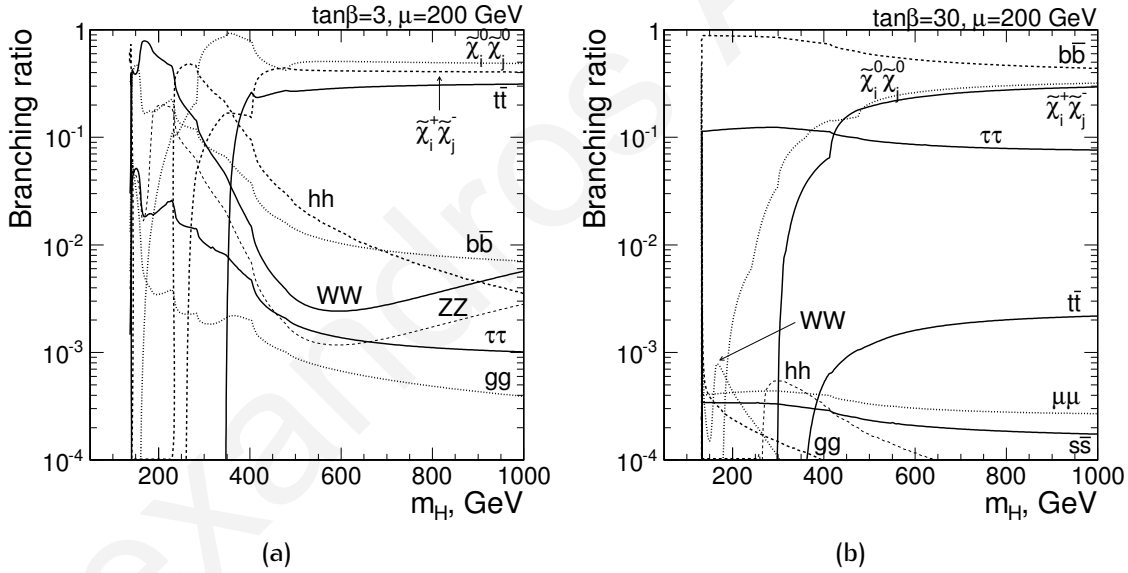

Figure 2.4: The decay branching ratios of the heavier $\mathcal{CP}$-even MSSM Higgs boson H^0 as a function of its mass, for $\tan\beta = 3$ (a) and $\tan\beta = 30$ (b). Taken from Ref. [34].

sizeable contributions from the decays $H^0 \to h^0 h^0$ and $H^0 \to \tau^\pm \tau^\mp$ are also expected. For $m_{H^0} > 300\,\mathrm{GeV}/c^2$ however, the decays $H^0 \to \tilde{\chi}_i^0 \tilde{\chi}_j^0$ and $H^0 \to \tilde{\chi}_i^+ \tilde{\chi}_j^-$ are kinematically allowed and thus take over as the dominant modes. The only decay mode which is able to compete with the 2 aforementioned SUSY modes is the $H^0 \to t\bar{t}$ decay mode, which only becomes kinematically allowed for $m_{H^0} \geq 2m_t \sim 340\,\mathrm{GeV}/c^2$. However, despite a relatively large rate of events from this particular decay mode, the presence of top quarks implies a complex final state with multiple hadronic products. Therefore, the $H^0 \to t\bar{t}$ decay mode can be quite challenging to be used as a discovery signature, mainly due to anticipated large Quantum Chromodynamics (QCD) multi-jet background. The same arguments can be used for the $H^0 \to b\bar{b}$ decay mode, which dominates for large $\tan\beta$ values over the whole mass spectrum, while the decays $H^0 \to \tilde{\chi}_i^0 \tilde{\chi}_j^0$ and $H^0 \to \tilde{\chi}_i^+ \tilde{\chi}_j^-$ are now restricted to a sub-

dominant role. It can be argued that the process $H^0 \to \tau^\pm\tau^\mp$, which is the next dominant decay mode, is the best decay signature for large $\tan\beta$ values. The production of two τ-leptons guarantees the presence of large missing energy and either isolated leptons or τ jets, both constituting distinct signatures in a collision environment. Similar arguments can be used to suggest that the $H^0 \to \mu^\pm\mu^\mp$ decay mode is also a promising discovery channel, although it has a much smaller branching ratio.

In Fig. 2.5, the branching ratios for the $\mathcal{CP}$-odd MSSM Higgs boson A^0 are presented, as a function of its mass for $\tan\beta = 3$ and $\tan\beta = 30$. These branching ratios show similar features as those for the $\mathcal{CP}$-even MSSM Higgs boson H^0, with the exceptions that the $A^0 \to t\bar{t}$ decay mode is slightly enhanced, while the decays to EWK gauge bosons pairs, $A^0 \to W^\pm W^\mp$ and $A^0 \to Z^0Z^0$ are forbidden. This is because the A^0 transforms as a pseudo-scalar, (i.e. γ_5) whereas the $W^\pm$ and Z^0 transform as vectors[4]. Therefore, the decay $A^0 \to W^\pm W^\mp / Z^0Z^0$ violates $\mathcal{CP}$-invariance, while the Higgs sector is $\mathcal{CP}$-even. However, a new decay mode opens up through $A^0 \to h^0Z^0$, which however only contributes significantly for low masses and small values of $\tan\beta$. In general, for low $\tan\beta$ values the $\mathcal{CP}$-odd A^0 prefers to decay through neutralinos, charginos, top-quark and b-quark pairs through $A^0 \to \tilde{\chi}_i^0\tilde{\chi}_j^0$, $A^0 \to \tilde{\chi}_i^+\tilde{\chi}_j^-$, $A^0 \to t\bar{t}$ and $A^0 \to b\bar{b}$, respectively. Larger values of $\tan\beta$ significantly enhance the contribution from the decay $A^0 \to \tau^\pm\tau^\mp$, which appears to be approximately flat for the whole mass spectrum. Thus, this mode can constitute an important discovery signature for this parameter space, since even-though the $A^0 \to b\bar{b}$ is dominating it is susceptible to large QCD multi-jet backgrounds and hence very hard to disentangle.

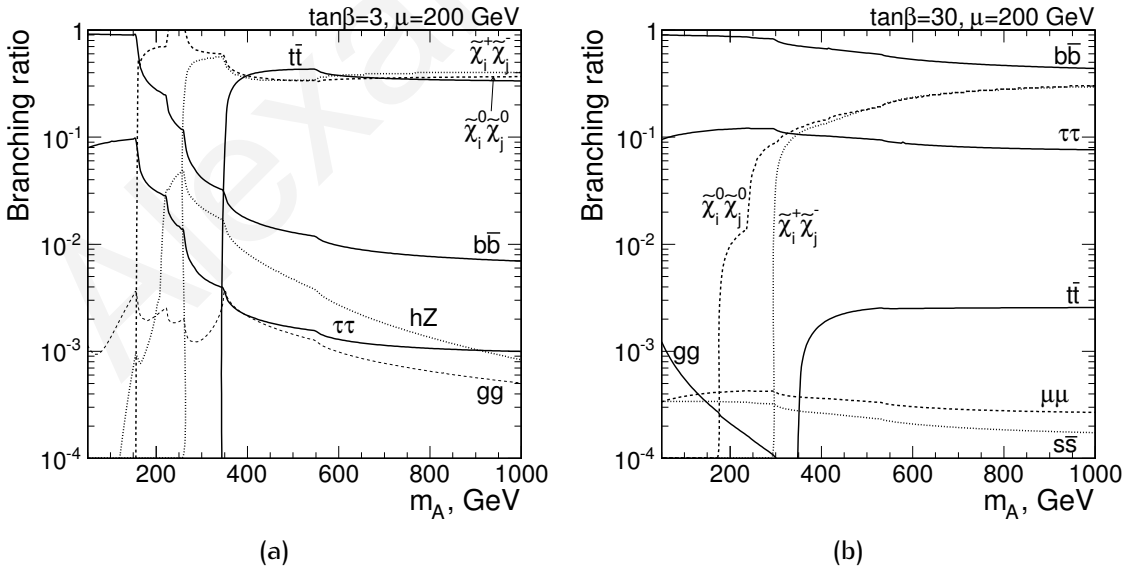

Figure 2.5: The decay branching ratios of the heavier $\mathcal{CP}$-even MSSM Higgs boson A^0, as a function of its mass, for $\tan\beta = 3$ (a) and $\tan\beta = 30$ (b). Taken from Ref. [34].

[4] $\mathcal{CP}(\text{pseudo-scalar}) = -1 \neq \mathcal{CP}(\text{vector}) \cdot \mathcal{CP}(\text{vector}) = 1$.

2.5.2 Charged Higgs bosons

The production mechanisms for the charged MSSM Higgs bosons at the LHC greatly depend on their masses. It is common to distinguish between a "light" and a "heavy" charged MSSM Higgs boson, with the former having a mass "lighter" than the top quark such that $m_{H^\pm} \lesssim m_t - m_b$, while the latter is "heavier" than the top quark with $m_{H^\pm} \gtrsim m_t$. Therefore, the dominant production process for the charged MSSM Higgs boson can be categorised as follows

$$\text{top-quark decay}: \quad t \to bH^\pm + X \qquad m_{H^\pm} \lesssim m_t - m_b \tag{2.54}$$

$$\text{associated production}: \quad pp \to tbH^\pm + X \qquad m_{H^\pm} \gtrsim m_t, \tag{2.55}$$

where Eq. (2.54) is the dominant production for the light charged MSSM Higgs, and Eq. (2.55) for the heavy charged MSSM Higgs.

While light charged MSSM Higgs bosons are effectively produced in direct $t\bar{t}$ production through $q\bar{q} \to t\bar{t}$ or $gg \to t\bar{t}$, heavy charged MSSM Higgs bosons are produced through gluon$-b$ fusion and gluon-gluon fusion with small contributions from $q\bar{q}$ annihilation in the latter case. Typical Feynman diagrams for light and heavy charged MSSM Higgs boson production at the LHC are presented in Fig. 2.6 and Fig. 2.7, respectively. This thesis concentrates on light charged MSSM Higgs bosons, and so henceforth it will be discussed almost exclusively.

(a) (b)

Figure 2.6: Typical Feynman diagrams for the light charged MSSM Higgs boson production at the LHC.

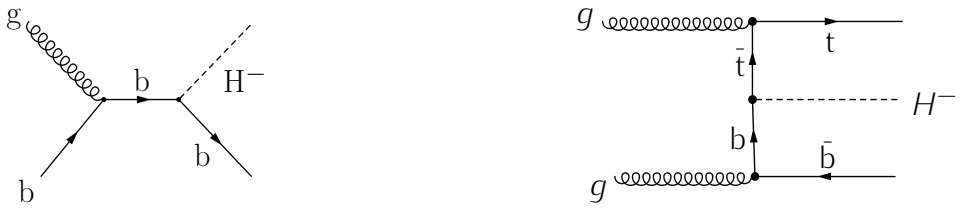

(a) (b)

Figure 2.7: Typical Feynman diagrams for the heavy charged MSSM Higgs boson production at the LHC.

The production cross-section for light charged MSSM Higgs bosons at the LHC is shown in Fig. 2.8 for several $\tan\beta$ values. In Fig. 2.8 (a), the cross-section of having at least one light charged MSSM Higgs boson is shown, whereby the total cross-section of the process $pp \to t\bar{t}$ is multiplied by the branching ratio of the decay of a top-quark to a b-quark and a charged MSSM Higgs boson BR($t \to bH^{\pm}$). In Fig. 2.8 (b) the total cross-section of the process $pp \to t\bar{t} \to bH^{\pm}b\mathrm{W}^{\mp}$ is shown, which is by far the dominant contributing process for small values of BR($t \to bH^{\pm}$).

In both figures, the central cross-section values are shown as a function of the charged MSSM Higgs boson mass and for several $\tan\beta$ values. The shaded bands around the central values represent the theoretical uncertainties in calculating these values, which include the $t\bar{t}$ cross-section from scale variation and 68% Confidence Level (CL) Probability Density Function (PDF) uncertainties, 5% for missing one-loop EWK, 2% for missing two-loop QCD, and b-quark mass-related uncertainties [35]. A significant feature of these cross-section plots is the fact that it appears to be a decreasing function of the light charged MSSM Higgs boson mass $m_{H^{\pm}}$, and greatly depended on the value of the parameter $\tan\beta$.

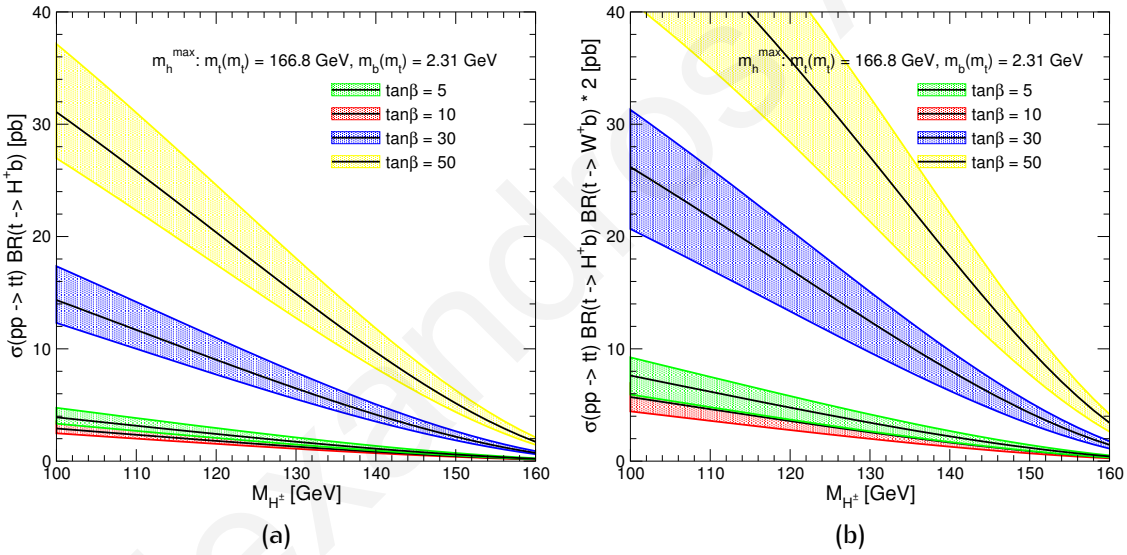

Figure 2.8: The production cross-section for the light charged MSSM Higgs bosons at the LHC and at $\sqrt{s}$=7 TeV for $\tan\beta = 5, 10, 30, 50$. In (a), the cross-section of at least one light charged MSSM Higgs boson being produced in shown, while in (b) the total cross-section of the process $pp \to t\bar{t} \to bH^{\pm}b\mathrm{W}^{\mp}$ is shown. The cross-section of the process $pp \to t\bar{t}$ was taken to be $\sigma_{t\bar{t}} = 164.57$. Taken from Ref. [32].

The branching ratios for the charged MSSM Higgs boson are presented in Fig. 2.9, as a function of its mass for $\tan\beta = 3$ and $\tan\beta = 30$. For the light charged MSSM Higgs boson and small values of $\tan\beta$, decays proceed almost exclusively through the process $H^{\pm} \to \tau^{\pm}\nu_{\tau}$ with a branching ratio BR($H^{\pm} \to \tau^{\pm}\nu_{\tau}$) ≈ 1. The effect is enhanced at larger values of $\tan\beta$, over the whole mass spectrum, due to the fact that the $H^{\pm}$ coupling to $\tau^{\pm}\nu_{\tau}$ depends linearly on $\tan\beta$, while the $H^{\pm}$ coupling to $\bar{t}b$ is proportional to $m_t \cot\beta$.

For the decay modes of the heavy charged MSSM Higgs boson, which switch on for $m_{H^{\pm}} \gtrsim m_t$, contributions from decays to top-quarks and SUSY particles become dominant.

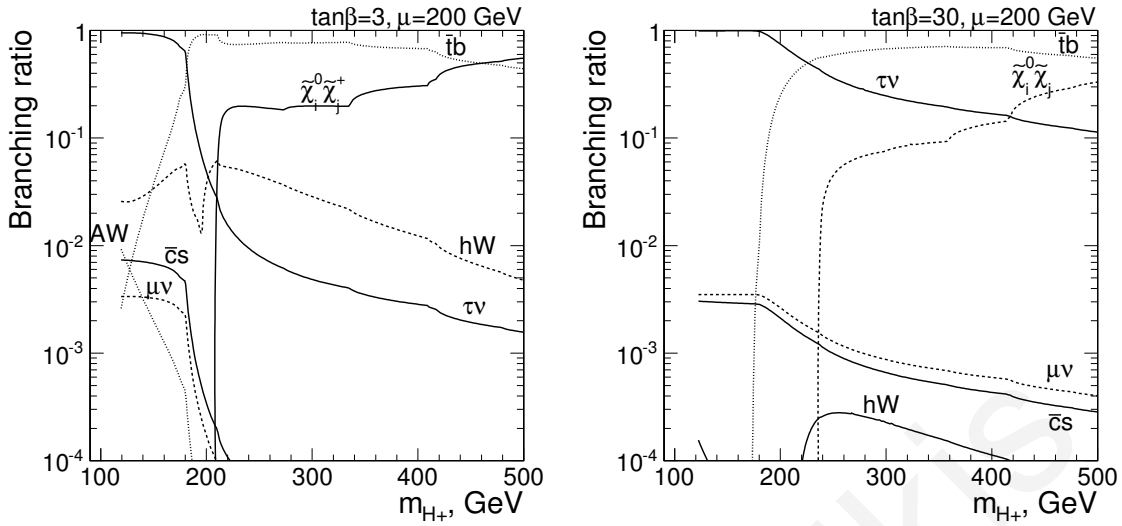

Figure 2.9: The decay branching ratios of the charged MSSM Higgs boson $H^{\pm}$, as a function of its mass, for $\tan\beta = 3$ (a) and $\tan\beta = 30$ (b). Taken from Ref. [34].

For small values of $\tan\beta$, the heavy charged MSSM Higgs boson decays are dominated by the process $H^+ \to \bar{t}b$, while the $H^+ \to \tau^{\pm}\nu_{\tau}$ remains sub-dominant in a narrow mass-window, becoming decreasingly important at even larger mass values. For large values of $\tan\beta$, the heavy charged MSSM Higgs decays are also dominated by the process $H^+ \to \bar{t}b$, while the $H^+ \to \tau^{\pm}\nu_{\tau}$ remains sub-dominant for almost the entire mass spectrum. The branching ratio of $H^+ \to \tilde{\chi}_i^0\tilde{\chi}_j^+$ starts contributing considerably as soon as it becomes kinematically allowed. With all these in mind, it can be concluded that the most promising decay mode for both the light and heavy charged MSSM Higgs bosons is the decay to a τ-lepton through $H^+ \to \tau^{\pm}\nu_{\tau}$. This applies for both small and large values of $\tan\beta$, and is based on the fact that not only is a significantly contributing decay mode, it also guarantees the presence of large missing energy and either isolated leptons or τ jets which can help to significantly suppress the expected large QCD multi-jet background. This however cannot be said for the $H^+ \to \bar{t}b$ decay mode, which despite having being the dominant decay mode in most of the parameter space, it should prove a difficult task to distinguish from QCD multi-jet backgrounds.

2.6 Limitations of the MSSM

Ironically, although the MSSM- and SUSY theories in general - provide crucial remedies to the ill-defined SM, the MSSM nevertheless has its own limitations and shortcomings. Perhaps the most significant of all is the non-inclusion of gravity, which entails that even if experimentally verified at the LHC, the MSSM will still remain an incomplete theory which fails to incorporate all known particles and interactions. Moreover, although experimental data point to the fact that SUSY is in fact a broken symmetry, the currently-available theoretical models do not explain the soft SUSY-breaking terms, neither do they provide an account for the SUSY-breaking mechanism.

Furthermore, if mixing between particle generations and complex phases are allowed within MSSM, these soft SUSY-breaking terms result in $\mathcal{O}(100)$ new parameters that need to be determined. This is especially alarming if one considers that the SM, which has "only" 19 free parameters, is already considered too unrestricted and arbitrary. Its SUSY extensions are thus far from being elegant and deviate from the ultimate desire of converging to a theory of everything, where physical laws can be obtained from symmetry considerations and first principles.

Another serious problem with the MSSM is the so called μ-problem. It refers to the SUSY Higgs mass parameter μ, which appears in the superpotential of Eq. (2.16) in the form $\mu\epsilon^{ij}H_1^iH_2^j$, and in the Higgs potential of Eq. (2.33). In order to ensure that $H_1^iH_2^j$ acquire non-zero VEVs after EWK symmetry breaking, this parameter must be of the order of magnitude of the EWK scale of about 246 GeV[5] and hence orders of magnitude smaller than the Planck scale,[6] which is the natural cut-off scale. Furthermore, the soft SUSY-breaking terms should also be of the same order of magnitude as the EWK scale, which makes one wonder why these scales are so much smaller than the cut-off scale. Therefore, although the soft SUSY-breaking term and the SUSY Higgs mass parameter μ have different physical origins, they must correspond to similar energy scales and just taking it as a lucky coincidence is begging the question. This is known as the naturalness problem.

A $\mathcal{CP}$-violation related problem also arises, due to the fact that to-date no $\mathcal{CP}$-violating processes have been observed experimentally that fall outside the SM. This implies that the MSSM Lagrangian must be fully $\mathcal{CP}$-invariant, or at least minimally violating $\mathcal{CP}$-invariance. Therefore, $\mathcal{CP}$-violating phases in the MSSM must be kept small.

Finally, perhaps the most important missing-link in the MSSM is the absence of experimental data supporting the existence of a Higgs boson. If the Higgs mechanism is in fact the SSB mechanism that breaks the EWK symmetry, it should manifest itself in the form of 5 Higgs bosons which are postulated by the MSSM. In the previous sections, arguments have been set forward to support why τ-leptons should play an essential role in the hunt of MSSM Higgs bosons. This is especially true for the case of charged MSSM Higgs bosons, and therefore understanding the properties of τ-leptons can be crucial in the optimal extraction of the signal from the experimental data.

[5] $v = \left(\sqrt{2}\cdot G_F\right)^{-1/2} \simeq \left(\sqrt{2}\cdot 1.16637\times 10^{-5}\,\text{GeV}^{-2}\right)^{-1/2} = 246\,\text{GeV}$.

[6] The Planck scale is defined as the energy scale, at which the strength of gravity becomes comparable to all other forces, believed to be at $M_{\text{Planck}} \simeq \mathcal{O}\left(10^{19}\,\text{GeV}\right)$.

Chapter 3

The Tools: The LHC and the CMS detector

In order to address the natural drawbacks and unresolved problems of the Standard Model, experimental data from high-energy particle collisions beyond the TeV-scale are required, to indicate which of the seemingly infinite candidate theories are more likely to be correct. There are primarily 2 ways of achieving this; a lepton collider and a hadron collider. Lepton colliders are capable of providing polarised beams with a well defined initial state to the Interaction Point (IP). The resulting collisions between the elementary (point-like) leptons produce particles democratically at a precise centre-of-mass-energy ($\sqrt{s}$) and in relatively clean final states, while momentum conservation facilitates the decay product analysis. Conversely, at hadron colliders the composite nature of hadrons results in a far more intricate collision environment. Unlike leptons, hadrons are complex objects with a high multiplicity of sea/valence quarks and gluons (collectively known as partons), resulting in an a priori-unknown initial state. Each of the partons carries a fraction of the hadron energy and the probability density to find a parton with a given energy fraction is given by the Parton Distribution Function (PDF), a distribution that has to be determined by experiment. Consequently, since the effective energy released in each collision can vary dramatically from zero to $\sqrt{s}$, the kinematics of the events are not fully constrained, meaning that momentum conservation can only be used in the plane transverse to the beam. To make things worse, due to the large coupling strength of the strong force, the expected overwhelming Quantum Chromodynamics (QCD) multi-jet background impedes further the final state reconstruction of the decay products. However, the deciding factor in choosing the type of collider at very high energies is the effect of synchrotron radiation; the phenomenon whereby charged particles emit Electromagnetic (EM) radiation when accelerated radially. The amount of energy loss due to synchrotron radiation (ΔE_{synch}) is dependent on the fourth inverse power of the mass of the accelerated particles (m)

$$-\Delta E_{\text{synch}} \propto \left(\frac{E}{mc^2}\right)^4 \tag{3.1}$$

which means that hadrons, being much heavier than leptons, are more suitable for higher energies in circular colliders. Indicatively, comparing the relative energy loss of a circular collider with electrons ($m_e \approx 0.510998910\,\text{MeV}/c^2$ [15]) and protons ($m_p \approx= 938.272013\,\text{MeV}/c^2$ [15]) one gets

$$\frac{\Delta E_{\text{synch}^e}}{\Delta E_{\text{synch}^p}} = \left(\frac{m_p}{m_e}\right)^4 \sim 10^{13}, \tag{3.2}$$

revealing the enormous difference in energy loss that needs to be compensated by inputting large amounts of Radio Frequency (RF) power. On this account, hadron colliders have the ability to reach much higher energies than their lepton counterparts.

The above-mentioned descriptions indicate that lepton colliders are commonly used as precision measurement tools, as was the case for Large Electron-Positron Collider (LEP), which determined the mass of the $W^{\pm}$ and Z^0 bosons to within one part in a thousand. On the contrary, hadron colliders are more suited for exploring new energy domains and are hence mostly utilised as discovery machines, mainly because of their ability to reach higher and wider-range of energies. This is especially important when it is unclear at what energy-region the new physics might lie, a point well illustrated by the Tevatron with the discovery of the top quark. With all things into consideration, the decision to replace the LEP machine, which operated successfully from 1989 to 2000, with the Large Hadron Collider (LHC) as a tool for probing new physics at the TeV-scale was well justified.

3.1 The CERN accelerator network

The LHC is the world's newest and most powerful tool for High-Energy Physics (HEP) research. Built at the European Organisation for Nuclear Research (CERN), it is located in Geneva, near the Franco-Swiss border (see Fig. 3.1) and at a depth ranging from $50-175\,\text{m}$ underground, mainly to shield against synchrotron radiation and due to the necessity of having very stable beam orbits. It is designed as a two-ring-superconducting-hadron accelerator and collider and installed in the 26.659 km tunnel that used to house the LEP machine. The LHC is designed to collide proton (heavy ion[1]) beams, with a nominal energy of 7 TeV per beam (2.8 TeV per nucleon) and an unprecedented luminosity of $\mathcal{L} = 10^{34}\,\text{cm}^{-2}\,\text{s}^{-1}$ ($\mathcal{L} = 10^{27}\,\text{cm}^{-2}\,\text{s}^{-1}$). The beam energy and design luminosity of the LHC have been chosen specifically to investigate the TeV energy scale, enabling a wide range of potential physics discoveries. With that in mind, 5 experiments were approved for the LHC, 2 of which are general-purpose colliding beam experiments; ATLAS and CMS, located at IP1 and IP5, respectively. The LHC-*b* is a fixed target experiment located at IP8 and is dedicated for *b*-quark physics, whereas ALICE is a heavy ion collision experiment positioned at IP2. In addition to collision experiments, the ToTal Elastic and diffractive cross-section Measurement (TOTEM) experiment is designed to measure the beam luminosity and study diffraction physics in

[1] Lead (Pb) ions.

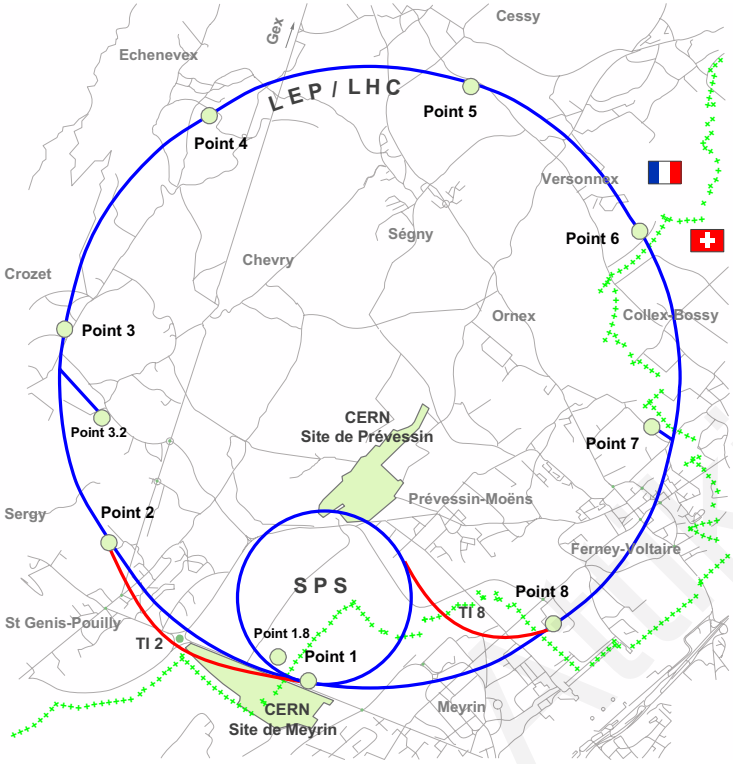

Figure 3.1: Map of CERN sites and the LHC access points, including the location of the 4 IPs that house the ongoing experiments. ATLAS at IP1, ALICE at IP2, CMS at IP5 and LHC-*b* at IP8.

the very forward directions of the CMS experiment. The proton collisions delivered to the IP of each experiment present a factor of ~ 7 increase in energy and ~ 100 in luminosity, compared to the Tevatron at Fermilab which officially ceased operations on the 30^{th} of September 2011. Correspondingly, the heavy ion collision capabilities of the LHC will exceed the energy and luminosity of the previously largest operating machine for heavy ions, the Relativistic Heavy Ion Collider (RHIC) at Brookhaven, by factors of ~ 27 and ~ 3, respectively. The energy density at the IPs of these heavy ion collisions is expected to be large enough for studying quark-gluon plasma, a state of matter believed to have existed in the early moments after the Big Bang where quarks were not bound together by the colour force.

The LHC is complemented by a network of other particle accelerators, sketched in Fig. 3.2. In order to deliver the 7 TeV proton beams for collisions, a series of operations is required to first generate protons, collect them into beams and accelerate them through several energy stages before filling them to the LHC ring, which further accelerates them to their final energies before bringing them to collision at the 4 interaction points. The protons originate from a duoplasmatron ion source, whereby a hot cathode filament emits electrons into a vacuum chamber via thermionic emission. An anode accelerates these electrons and directs them into a hydrogen gas (H_2) chamber, which becomes ionised from the resulting interactions with the free electrons and finally generates protons through the following

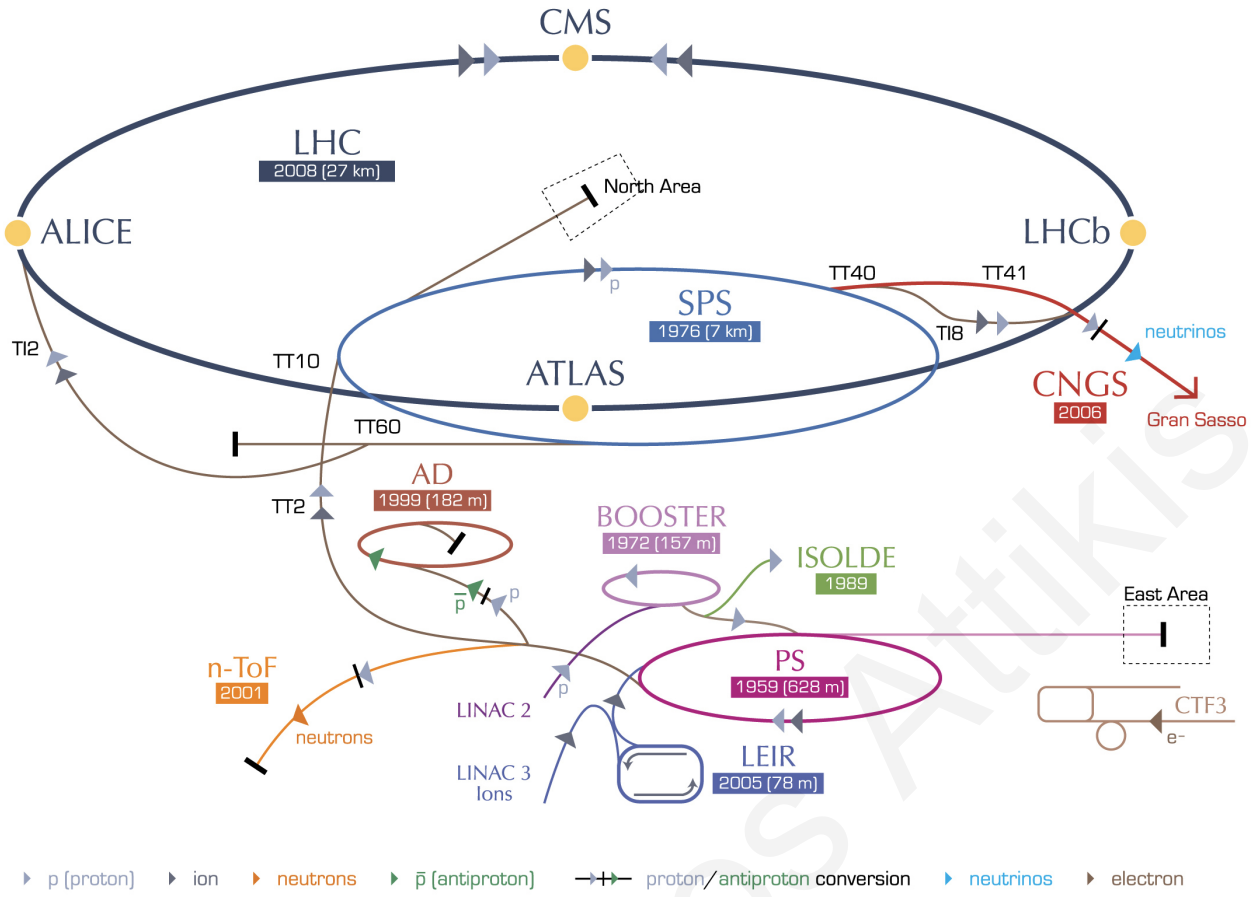

Figure 3.2: A schematic overview of the CERN accelerator network.

processes

$$\begin{aligned} H_2 + e^- &\rightarrow H_2^+ + 2e^- \\ H_2^+ + e^- &\rightarrow H^+ + H + e^- \\ H + e^- &\rightarrow H^+ + 2e^-. \end{aligned}$$

The protons are then collected to a cathode to form a proton beam, which is accelerated in the LINear ACcelerator (LINAC)-2 to an energy of 5 MeV and then transferred to the Proton Synchrotron Booster (PSB). In the PSB, the proton beam is first distributed into 4 rings whereby intensities of $> 10^{13}$ protons per ring are achieved, while the beam is boosted to 1.4 GeV before recombination and transfer to the Proton Synchrotron (PS). The PS accelerates the proton beam to 28 GeV, before injecting it into the Super Proton Synchrotron (SPS). The SPS, which from 1981 to 1984 served as a proton-anti proton collider and led to the discovery of the $W^{\pm}$ and Z^0 bosons by the the UA1 and UA2 experiments, is used to accelerate the proton beam to 450 GeV before injecting 2 counter-rotating beams into the LHC ring. For heavy ion collisions, the ions are provided by a lead (Pb) source and are injected into the Low Energy Ion Ring (LEIR) by LINAC-3, before reaching the PSB from where they follow the same chain as protons.

3.2 The LHC - The Large Hadron Collider

The LHC is divided into 8 arcs and 8 straight sections, as shown in Fig. 3.3, which besides the housing of the experiments serve as utility insertions. The experimental insertions located in octants 2 and 8 include the injection systems for the two beams from the SPS, while octants 3 and 7 contain collimation systems whereby particles with too large momentum dispersion are cleaned up. The 2 independent RF-systems that provide acceleration to each LHC beam are located in octant 4, while the beams are extracted and dumped into large graphite cylinders via fast-pulsed deflecting (kicker) magnets in octant 6.

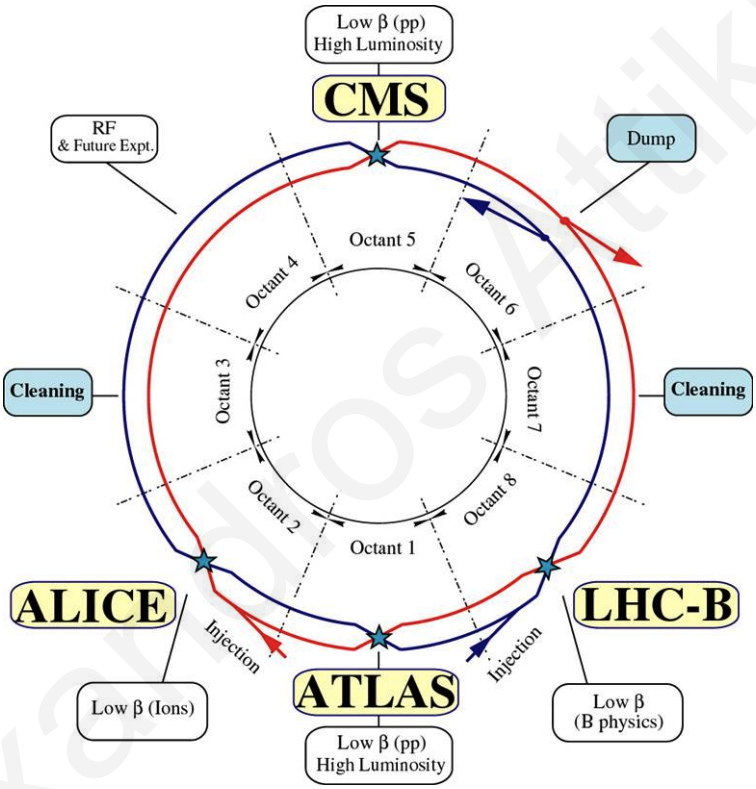

Figure 3.3: Schematic layout of the LHC, showing the separation into octants, with beam-1 rotating clockwise and beam-2 rotating anti-clockwise. Taken from Ref. [36].

Inside the LHC ring, 2 separate proton beams circulate in opposite directions and are accelerated to their nominal energy of 7 TeV by 8 RF-cavities per beam, which operate at 2 MV (accelerating field of 5 MV m^{-1}) and a frequency of 400 MHz. The 2 beams only share the same vacuum pipe right before/after the collisions, through a distance of 126 m in IP2 and IP8, and 140 m in IP1 and IP5. The long common beam pipe implies 34 parasitic collision points close to the region of the IPs and to suppress this effect the beams are separated into orbit bumps and brought to collision at a crossing angle at the IPs. The collision parameters as well as the most important nominal parameters of the LHC are summarised in Table 3.1. Within each beam, the protons are packed into up to 2808 filled bunches (more details in Section 3.2.1). Each bunch contains up to 1.15×10^{11} protons (beam intensity) and is nominally separated by $\Delta t = 25$ ns (or $\Delta x \simeq c\Delta t \simeq 7.5$ m) with the preceding/succeeding bunch, thus forming the so called bunch trains. At peak energy, each bunch is travelling

Table 3.1: Nominal parameters of the LHC ring. Taken from Ref. [37].

Quantity	Value	Unit
Circumference	26.659	km
Nominal beam energy at collision, protons (ions)	7 (2.76)	TeV
Number of magnets	9593	
Number of main dipoles	1232	
Lattice quadrupoles	392	
Lattice sextupoles	688	
Lattice octupoles	168	
Minimum distance between bunches	7.5	m
Design luminosity, protons (ions)	10^{34} (10^{27})	$cm^{-2}\,s^{-1}$
Number of bunches per proton beam	2808	
Number of protons per bunch	1.15×10^{11}	
Total crossing-angle	285	μrad
Proton revolution frequency	11.246	kHz
Number of RF-cavities per beam	8	
Harmonic number	35640	
Events per bunch-crossing	~ 20	
Number of collisions points	4	
Elastic (inelastic) cross-section	40 (60)	mb
Number of elastic (inelastic) collisions per second	400 (600)	MHz

relativistically around the LHC ring, with a Lorentz-factor (γ)

$$\gamma_p = \frac{E_p}{m_p c^2} = \frac{7\,\text{TeV}}{938.272013\,\text{MeV}/c^2 c^2} \simeq 7460 \tag{3.3}$$

and hence at a velocity (β) very close to the speed of light

$$\beta_p = \sqrt{\left(1 - \gamma_p^{-2}\right)} \simeq 0.999999991, \tag{3.4}$$

which translates to revolution frequency $f_{\text{rev}} \simeq 11.246\,\text{kHz}$ or a period of $T_{\text{rev}} \simeq 89\,\mu\text{s}$ to go around the 26.659 km long ring of radius $R_{\text{LHC}} \simeq 4.3\,\text{km}$. In order to keep the beams travelling with momentum p_p in orbit, a series of superconducting dipole magnets is used to provide the required centripetal force

$$F_c = \frac{p_p^2}{m_p R_{\text{LHC}}} \tag{3.5}$$

through the Lorentz-Force

$$F_{Lorentz} = q_p \left(c\vec{\beta}_p \times \vec{B}\right). \tag{3.6}$$

By equating these 2 forces, the magnetic field ($\vec{B}$) strength that has to be supplied normal to the plane of the orbit can be written as

$$B(T) = \frac{p_p(\,\text{TeV})}{0.3 R_{\text{LHC}}(\,\text{km})}. \tag{3.7}$$

Thus, for a proton beam travelling with a momentum of 7 TeV/c, the magnetic field required is about 5.4T. In practise, however, since the LHC ring cannot be completely filled with magnets, the required bending power is provided by about 1232 superconducting dipole magnets, each one able to provide a magnetic field of 8.33T.

3.2.1 Beam stability

To achieve the required magnetic field, a two-in-one design was chosen for the dipole magnets, as illustrated in Fig. 3.4, to provide a uniform vertical dipole field over the width of the beam pipes for the two counter-rotating proton beams. The 2 vacuum chambers

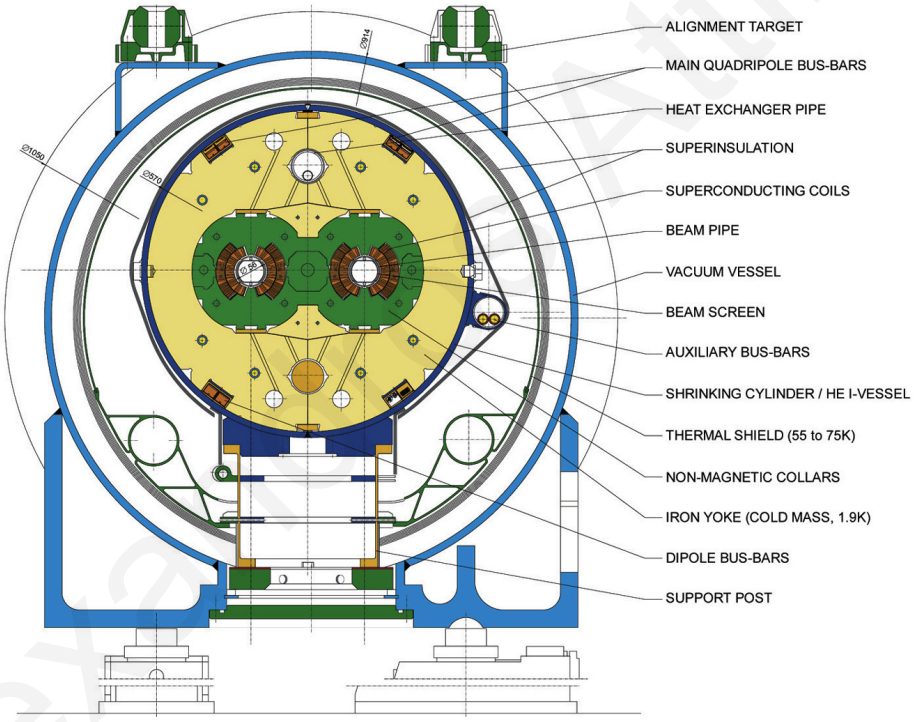

Figure 3.4: Schematic cross-section of the LHC superconducting dipole two-in-one magnet (lengths in mm). Taken from Ref. [36].

which carry the counter-rotating protons are held at a pressure of $\sim$ 100 nPa, are 55 mm in diameter and 194 mm apart. The beam vacuum pressure is imperative in order to avoid collisions with gas molecules, and for this reason close to the IP where collisions take place it is kept at even lower pressures, at $<$ 1 nPa. The beam pipes are surrounded by the superconducting coils and in order to counter the repulsive forces between the cables which tend to "open" the magnet, the conductors are held in place by stainless steel (non-magnetic) collars. These collars are in turn surrounded by an iron (ferromagnetic) return yoke. The aforementioned parts comprise the dipole cold mass and are contained inside a shrinking cylinder/He II vessel. The dipole cold mass is operated at 1.9K in superfluid He II. Thermal insulation is achieved by use of a vacuum vessel and a super-insulating layer. The dipole configuration generates a magnetic field of nominal magnitude 8.33T and is opposite in

direction on each beam, as shown in Fig. 3.5; vertically up in the left-hand beam pipe and vertically down in the right-hand one. In order to reach the nominal field strength of 8.33T,

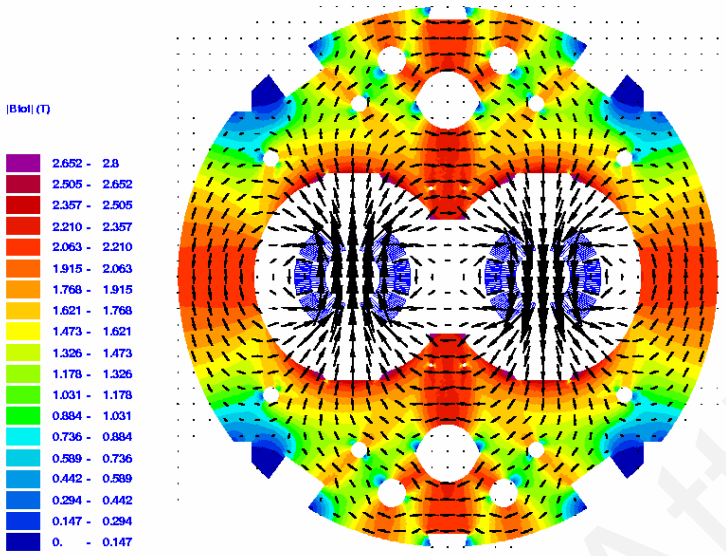

Figure 3.5: Magnetic flux plot, showing the oppositely directed fields for the 2 vacuum tubes of an LHC dipole. Taken from Ref. [37].

necessary for stabilising the 7 TeV beams into orbit, a current of 11.850 kA is required. This is achieved by the use of 80 cables, placed in 2 layers, running to the beam pipe axis and back on the other side. These cables house 36 strands of superconducting wire, each strand housing 6500 superconducting filaments of Niobium-Titanium (NbTi). The main parameters of the LHC dipole magnets are summarised in Table 3.2.

Table 3.2: Main parameters of the LHC dipole cold mass. Taken from Ref. [36].

Quantity	Value	Unit
Injection field (0.45 TeV beam energy)	0.54	T
Current at injection field	763	A
Nominal field (7 TeV beam energy)	8.33	T
Current at nominal field	11.850	kA
Stored energy (both apertures) at nominal field	6.93	MJ
Ultimate field	9	T
Current at ultimate field	12.840	kA
Stored energy (both apertures) at ultimate field	8.11	MJ
Operating temperature	1.9	K
Distance between aperture axes at 1.9K	194	mm
Inner coil diameter at 293K	56	mm
Cold mass length at 293K (active part)	15.18	m
Cold mass diameter at 293K	570	mm
Cold mass overall length with ancillaries	16.5	m
Total mass	$\sim$ 27.5	t

In addition to sustaining the proton beams in orbit, the stabilisation and focussing of the proton bunches is of paramount importance, otherwise the particles might diverge and

be lost. For this purpose, the LHC is equipped with 392 main quadrupole magnets. These magnets provide magnetic fields that are zero in the beam pipe centre but increase linearly away from it, and can thus be used as vertically focussing and horizontally defocussing, or vice-versa. For this reason, the lattice of the LHC machine employs alternate quadrupoles with their poles reversed, so that an alternate focussing and defocussing effect is achieved, the net effect being the focussing in both planes. However, this focusing effect on the proton bunches causes oscillations of the particles around the centre of the beam pipes. The number of oscillations in 1 turn of the machine is known as the betatron tune(Q), whose value is carefully tuned to avoid resonance with the betatron motion (more details in Section 3.2.1). Additionally, within a proton bunch, particles tend to have different energies and hence follow slightly different orbits, which means each requires a different Q-value. The change in focusing with energy is known as the chromaticity and it has an adverse effect on the beam, causing instability and tune spread. To counter this, the LHC utilises sextupole magnets which are designed to provide magnetic fields that are zero in the beam pipe centre but increase quadratically away from it. In particular, there are 2 sextupole families per plane per beam for chromaticity corrections. Moreover, higher magnetic multipoles are also used to assist in beam focussing and to compensate for other interactions that the beams suffer along their orbits, including the EM interactions within the proton bunches, beam interaction with electron clouds from the beam pipe walls and the gravitational force experienced by the protons. Indicatively, a simple calculation reveals that without the gravitational corrections the protons would fall under the force of gravity through a vertical distance $\Delta y = \frac{55\,\text{mm}}{2}$, within a time interval of $\Delta t = \sqrt{2\frac{\Delta y}{g}} \simeq 73\,\text{ms}$ or, multiplying by the revolution frequency (f_{rev}), within ~ 820 laps around the LHC ring.

3.2.2 Beam particle motion

In all modern synchrotrons, as is the LHC, particles are accelerated by RF-cavities that are in synchronisation with both the particle's velocity and the bending field as they increase to their nominal values (hence the name synchrotron). These RF-cavities generate a longitudinal oscillating voltage, which the particles see as an accelerating voltage. The standing waves generated inside the resonating RF-cavity capture the incident beam and contain it in what is known as an RF-bucket. The particles are thus trapped in the RF-voltage and this gives the bunch structure to the beam. Even-though this RF-structure is present only inside the RF-cavities, the RF-buckets can be thought of as virtual positions on the LHC circumference that may or may not contain beam. If the RF-bucket contains a beam, then the beam within the bucket is referred to as a bunch.

Within a given bunch, the protons do not have ideal circular orbits, but instead oscillate in and out of the orbit path in both the horizontal and transverse planes; this is known as betatron motion. In an alternating-gradient quadrupole magnet configuration synchrotron like the LHC, the transverse equation of motion for the particles can be approximated as a pseudo-harmonic oscillator with a path-dependent spring constant. This is described by

Hill's equation

$$\frac{d^2x(s)}{ds^2} + K(s) = 0 \tag{3.8}$$

where $x(s)$ is the position or displacement from the longitudinal coordinate s (in the beam direction) and $K(s)$ is the varying spring constant. The simplest solution reveals that the single particle transverse motion is described by an oscillatory term analogous to the general solution of simple harmonic motion

$$x(s) = A\sqrt{\beta_[(s)x]}\cos\left(\phi(s) + \phi_0\right) \tag{3.9}$$

where A and ϕ_0 are constants connected to the amplitude and phase, respectively, and $\sqrt{\beta_[(s)x]}$ is an s-dependent amplitude that modulates the envelope of the transverse motion. The betatron phase advance (μ) over 1 turn around the LHC ring is defined as the integral of $\beta_[(s)x]$ over the closed path

$$\mu = \oint d\phi(s) = \oint \frac{ds}{\beta_[(s)x]}. \tag{3.10}$$

The betatron tune(Q), defined as $Q = \frac{\mu}{2\pi}$, is the number of betatron oscillations about the closed path of the LHC ring and it is a carefully adjusted parameter to avoid betatron resonance. Moreover, at the neighbourhood of an IP the beam optics of the ring are configured so as to produce a local minimum of the betatron amplitude function, at which point it is designated as $\beta^*(s)$ instead. This transverse betatron motion of the particles evolves with the longitudinal coordinate s forming an ellipse in $\{x(s), dx(s)/ds\}$ phase-space. For an ensemble of Gaussianly-distributed particles in $\{x(s), dx(s)/ds\}$, the transverse emittance (ϵ_x) is defined as the area of the ellipse containing 1 standard deviation

$$\epsilon_x = \pi\frac{\sigma_x}{\beta_x(s)}, \tag{3.11}$$

with a corresponding expression for the other transverse direction, y. The term $\sigma_[\,x]$ is the projection of the ellipse in the x axis and represents the beam size in the direction transverse to the longitudinal coordinate s. Therefore, a particle beam with low transverse emittance is one where the particles are confined to a small distance and have similar momentums, and it can be loosely described as the smallest opening you can squeeze the beam through.

In addition to the transverse oscillations, the particles also oscillate longitudinally under the influence of the RF-cavities. To complement the coordinates used to describe the motion of particles, the longitudinal variables $\{z, \Delta p/p\}$ is added to the aforementioned transverse phase-space $\{x(s), dx(s)/ds, y(s), dy(s)/ds\}$. The variable z describes the distance by which a given particle leads an ideal particle traversing the LHC ring trajectory. The quantity Δp is the particle's momentum error while $\Delta p/p$ is the momentum spread of the beam. The individual particles get in and out of step with the ideal, synchronous phase, for which the increase in momentum per turn from the RF-kick exactly matches the increase in the

bending field. Thus, if a particle is lagging with respect to the synchronous particles, it will arrive later than the RF-kick and will thus see a smaller accelerating voltage. However, since the bending field has now increased according to the exact synchronous particle, the effect will be to launch the asynchronous particle into a smaller orbit. As a consequence, during the next time around the asynchronous particle will now arrive earlier with the exact opposite outcome; experience a larger RF-kick that will launch it into a larger orbit and hence cause it to arrive later next time around. In this way, even though the proton bunch as a whole remains stable while circulating around the LHC ring, the protons themselves undergo longitudinal oscillations, also known as synchrotron oscillations. Therefore, instead of the protons being uniformly distributed around the circumference of the LHC ring, they instead clump around the synchronous particle in a bunch, which is in turn contained in an RF-bucket. Now, in order for the particles to always see the accelerating RF-voltage, the RF-frequency (f_{RF}) must be an integer multiple (h) of the revolution frequency (f_{rev}).

$$f_{RF} = h f_{\text{rev}} \tag{3.12}$$

in which case h is known as the harmonic number and for the LHC machine it has a value of $h_{LHC} = 35640$. Therefore, even though the LHC has the ability to accelerate a beam made up of 35640bunches, the nominal number of occupied buckets is instead 2808. The reason for this is that a number of consecutive buckets are required to not contain a beam, thus forming an abort gap. An abort gap is a measure which is required in the beam-dump process, due to the fact that it takes a short yet significant time to switch on the kicker magnets that divert the beam from the LHC into the dump area.

3.2.3 Beam Luminosity

Once the proton beams have reached nominal energies and have acquired stabilised orbits inside the LHC ring, they are brought to collisions in the 4 IPs at which the detectors are positioned. The reaction rate (R) at these regions, for a given interaction with cross-section σ_{int}, is given by

$$R = \mathcal{L}\sigma_{int} \tag{3.13}$$

where the instantaneous luminosity ($\mathcal{L}$) for 2 oppositely directed beams of relativistic particles with revolution frequency f_{rev} is defined as

$$\mathcal{L} = f_{\text{rev}} \frac{n_1 n_2}{4\pi\sigma_x\sigma_y}. \tag{3.14}$$

In this expression, the terms n_1 and n_2 are the number of protons within a beam bunch. The quantity $4\pi\sigma_x\sigma_y$ can be thought of as the effective cross-section area of the bunched beams, assuming they overlap completely. From Eq. (3.14) it can be deduced that the number of interactions at any instance in time is directly proportional to the intensity of each colliding

beam and the revolution frequency of the bunches, and inversely proportional to the beam size or momentum spread within a bunch. The equation can be recast in terms of transverse emittance and betatron amplitude functions as follows

$$\mathcal{L} = \frac{f_{\text{rev}}}{4} \frac{n_1 n_2}{\sqrt{\epsilon_x \beta_x(s)^* \epsilon_y \beta_y(s)^*}} \tag{3.15}$$

revealing that, while there are no fundamental limits to restrict the peak luminosity, the LHC luminosity is constrained by the machine's ability to sustain highly populated bunches of low transverse emittance, while being able to suppress betatron oscillations of the protons with high precision.

The aforementioned parameters are not constant in time, but instead deteriorate over a physics run. In particular, the intensity and transverse emittance of the circulating beams degrade over time and cause the initial luminosity ($\mathcal{L}_0$) to decay exponentially

$$\mathcal{L}(t) = \mathcal{L}_0 e^{-t/\tau_{\text{nuclear}}}, \tag{3.16}$$

where the initial decay time of the bunchintensity due to beam collisions is expressed as

$$\tau_{\text{nuclear}} = \frac{N_0}{k \mathcal{L}_0 \sigma_{tot}}. \tag{3.17}$$

The term N_0 is the initial beam intensity, k is the number of IPs, and σ_{tot} is the total cross-section of the LHC at a specific centre-of-mass-energy ($\sigma_{tot} \simeq 100\,\text{mb}$ at $\sqrt{s} = 14\,\text{TeV}$). The time required for the initial luminosity to reach $1/e$ of its initial value is given by

$$\tau_{\text{nuclear},1/e} = (\sqrt{e} - 1)\tau_{\text{nuclear}} \tag{3.18}$$

and for a nominal LHC operation this yields $\tau_{\text{nuclear},1/e} \simeq 29h$. Besides the beam losses due to collisions, luminosity lifetime is affected by Touschek Scattering, whereby particle losses within a bunch are due to single particle-particle collisions. In addition to that, slow transverse emittance blow-up caused by the scattering of particles on residual gas in the beam pipes, RF-noise, beam-beam interactions and Intra-Beam Scattering (IBS)[2] can further decrease the luminosity lifetime. By approximating the luminosity decay by an exponential process, the net luminosity lifetime takes the form

$$\frac{1}{\tau_{\mathcal{L}}} = \frac{1}{\tau_{IBS}} + \frac{1}{\tau_{\text{nuclear},1/e}} + \frac{1}{\tau_{\text{rest gas}}}, \tag{3.19}$$

and assuming $\tau_{IBS} \simeq 80h$ and $\tau_{\text{rest gas}} \simeq 100h$ it has a value of $\tau_{\mathcal{L}} \simeq 14.9h$. Therefore, by integrating Eq. (3.16) the luminosity lifetime can be used to estimate the integrated luminosity ($\mathcal{L}_{\text{int}}$), which takes the general form of

$$\mathcal{L}_{\text{int}} = \mathcal{L}_0 \left(1 - e^{-t_{\text{run}}/\tau_{\mathcal{L}}}\right), \tag{3.20}$$

[2]The process where particles within an accelerator beam elastically scatter off each other.

where t_{run} is the total length of the luminosity run. Once the beam losses have reached a level where the luminosity has dropped significantly, the beam is dumped and a new fill cycle begins. The theoretical beam injection time from the SPS into the LHC is 16 m, while the minimum time required for ramping the beam energy from the 450 GeV to 7 TeV is approximately 20 m . The ramping down of the magnets from the nominal 7 TeV back to 450 GeV (in case of beam abort) is 20 m, while the theoretical minimum time interval from the end of a luminosity run and a new beam at top energy (turnaround) is 70 m, although in practise the average turnaround time is 7 h.

3.2.4 Achievements and current status

The construction of the LHC officially completed in 2008, with the ring cold at $1.9K$ and under vacuum. On the 10^{th} of September 2008, the first beams were circulated in the ring. However, almost a week later, on the 19^{th} of September 2008, operations were halted due to a magnet quench[3] incident resulting from a faulty electrical connection between 2 dipole magnets. The development of high resistance ($\sim 220\,n\Omega$) in the electrically faulty joint lead to the explosion of helium gas from the magnet cold mass into the tunnel. This sudden escape of helium lead to a mechanical shock wave that damaged 58 of the dipole magnets. The result of this accident was $\sim$ 14 months of repairs, the decision to drop the centre-of-mass energy to the safer level of $\sqrt{s} = 7$ TeV, and a new LHC Quench Protection System (QPS) for online monitoring and protection against superconducting coils and bus-bars that develop high resistance. On the 20^{th} of November 2009, the first beams were circulated for the first time after the accident and 3 days later the first 900 GeV collisions took place. A week later LHC became the world's highest-energy particle accelerator, by circulating beams of 1.18 TeV each, while on the 20^{th} of December 2009 the first proton-proton collisions at $\sqrt{s} = 2.36$ TeV were achieved in all 4 experiments, dethroning the Tevatron as the most powerful collider. After the 2009 winter shutdown, the re-start of operations in 2010 found the machine operating normally, with a collision energy of $\sqrt{s} = 7$ TeV. The first collisions at 7 TeV were recorded on the 30^{th} of March 2010, one of the first collision candidates shown in Fig. 3.6 (a), and by November 2011 the LHC machine had reached a peak instantaneous luminosity of $\sim 3.5 \times 10^{33} \text{cm}^{-2}\,\text{s}^{-1}$ and recorded an integrated luminosity of $5.22\,\text{fb}^{-1}$, as shown in Fig. 3.6 (b).

On the 13^{th} of February 2012, CERN announced that the LHC will run with a beam energy of 4 TeV for 2012, with the bunch spacing remaining at 50 ns. This decision was accompanied by a strategy to optimise LHC running to deliver the maximum possible amount of data before a long LHC shutdown to prepare for higher energy running. The data target for 2012 is $15\,\text{fb}^{-1}$ for ATLAS and CMS, which, if accomplished, will be 3 times higher than the integrated luminosity recorded in 2011. For the end of 2012 a long technical stop of around 20 months is scheduled, with the LHC restarting close to its full design energy late in 2014

[3] The abrupt termination of a magnet operation that occurs when part of the coil leaves the superconducting state and enters the resistive state.

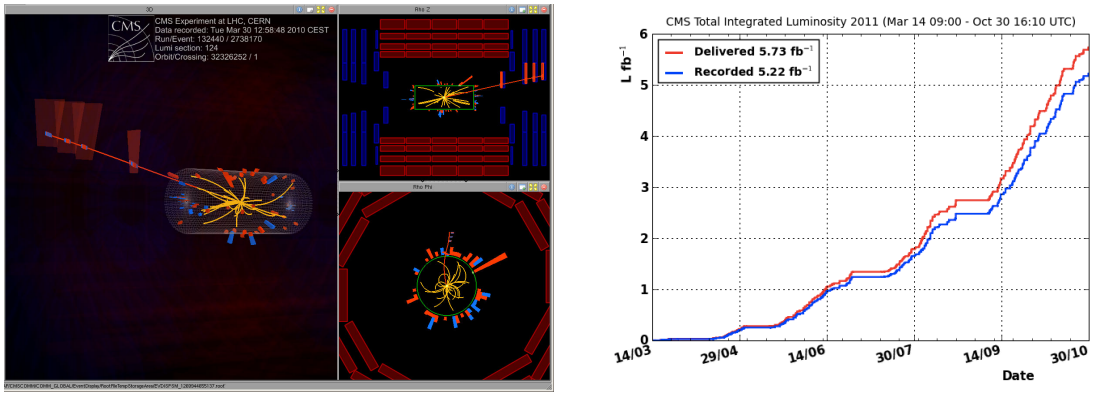

(a) (b)

Figure 3.6: One of the first CMS collision events at $\sqrt{s} = 7$ TeV as visualised by Fireworks [38] on the 30^{th} of March 2010 (a), and a cumulative rolling but not certified plot of integrated luminosity as a function of time delivered to, and recorded by CMS at $\sqrt{s} = 7$ TeV (**right**).

and operating for physics at the new high energy in early 2015.

3.3 CMS - The Compact Muon Solenoid

The Compact Muon Solenoid is one of the 2 general purpose detectors constructed for the LHC and is well documented in Refs. [39], [40], [41] and [42]. It is housed at IP5, at a depth of $\sim$ 100 m underground, close to the French village of Cessy, between the Lake Geneva and the Jura mountains. Its name stems from the fact that it employs a superconducting solenoid coil to generate a magnetic field, which requires less space than the alternative choice of a toroidal magnetic field (as used by ATLAS). One of its main design goals is to enable the study of proton-proton collisions in search for the mechanism responsible for the Electroweak (EWK) symmetry breaking. Furthermore, possible discoveries that could pave the way towards a unified theory, be it in the form of Supersymmetric particles or extra dimensions, were also considered in the design. Within the CMS physics objectives are also the search for $\mathcal{CP}$-violation and the study of quark-gluon plasma through the analysis of heavy ions collisions. Finally, the CMS is capable of studying diffractive physics together with the TOTEM experiment, described in Refs. [43] and [44], which uses detectors close to the beams, up to 400 m upstream the IP5 region, to measure the elastic scattering of protons at the LHC.

However, in order to be able to probe collisions occurring at an unprecedented rate and energy, in search for a wide range of physics objectives, a very careful design of the detector and its subsystems is required. The CMS detector, shown in Figures 3.7, 3.8, and 3.9, is 21.6 m long, has a diameter of 14.6 m and weighs 14500 tons. The LHC-delivered beams are guided to cross each other at the nominal full crossing-angle of 285 μrad at the IP5, located in the centre of the detector. The resulting information arising from the collision debris is recorded by the CMS detector, whose main volume is a multi-layered cylinder, with its subsystems forming concentric layers around the beam pipe. Moving from

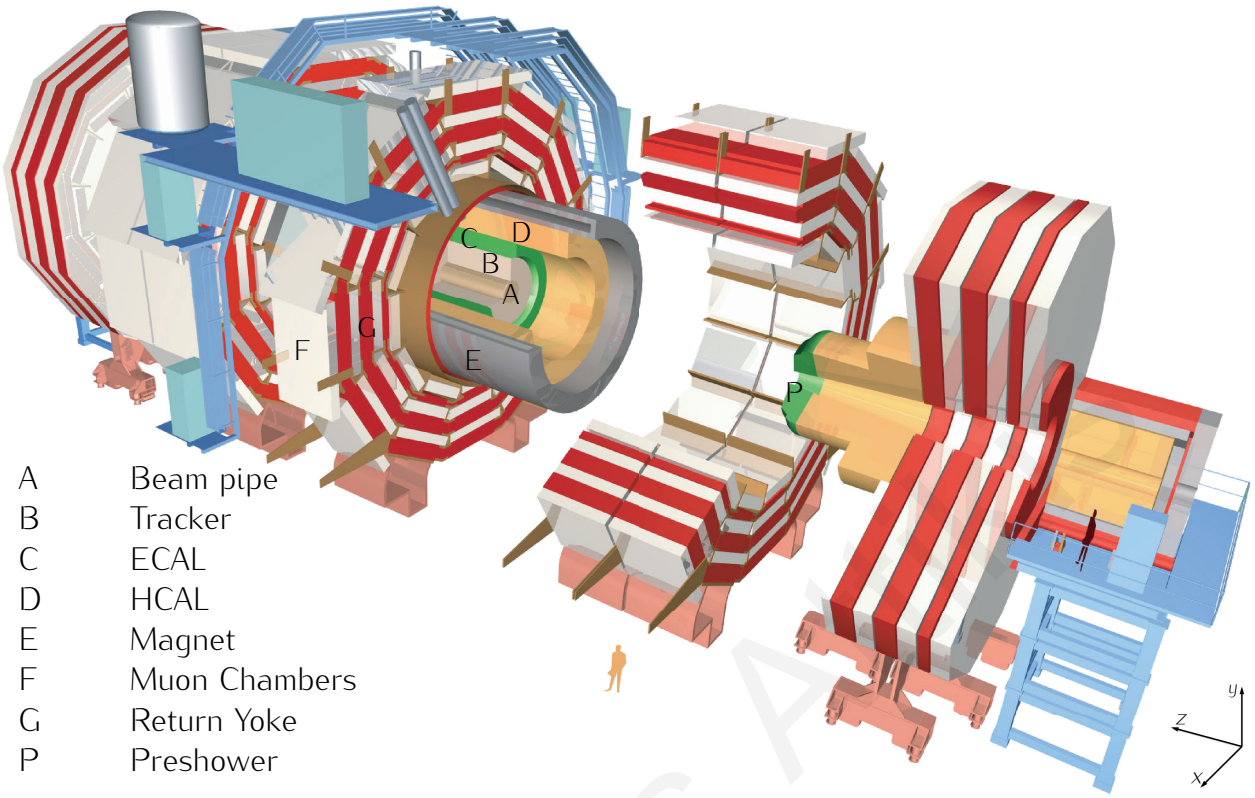

Figure 3.7: Schematic view of the CMS detector, with labels designating its constituent subdetectors.

the IP outwards, the innermost layer is the beam pipe which houses the counter-rotating proton beams at ultra-high vacuum ($< 1\,\mathrm{nPa}$). The beam pipe is surrounded by a high-quality silicon-based tracking system, which consists of silicon pixels and silicon microstrip detectors and is dedicated at recording the tracks of electrically charged particles produced in the collisions. The tracking system is surrounded by the calorimetry system, comprised of the scintillating lead tungstate ($PbWO_4$) crystal Electromagnetic Calorimeter (ECAL) and the brass/scintillator sampling[4] Hadronic Calorimeter (HCAL). The ECAL detector provides energy measurements for electrons (e^-), positrons (e^+) and photons (γ), which produce EMcascade showers within the detector volume through bremsstrahlung[5] and pair-production (or photon conversion)[6]. A Preshower system is installed in front of the ECAL endcap for π^0 rejection, an important measure due to the fact that π^0's can mimic high-energy photons when they decay into two closely-spaced photons that the ECAL picks up together. The HCAL detector is dedicated to measuring the total ionisation energy deposited by the cascade of particles that penetrate the ECAL, and determining the direction of jets of particles that result from the fragmentation of quarks and gluons into hadrons. Correspondingly, the calorimetry system plays an important role in the identification of neutrinos or exotic particles, due to the

[4]A sampling calorimeter is one which samples a fraction of the total energy deposited. The total energy of the incoming particle is thus inferred from the ionisation deposited in the sampling layers, usually by converting it to an electrical signal and digitising it.

[5]The process of energy loss and consequent deceleration of an electron through photon radiation, caused by the presence of a nuclear electric field.

[6]The process by which a high energy photon converts to an electron-positron pair, in the field of a nucleus.

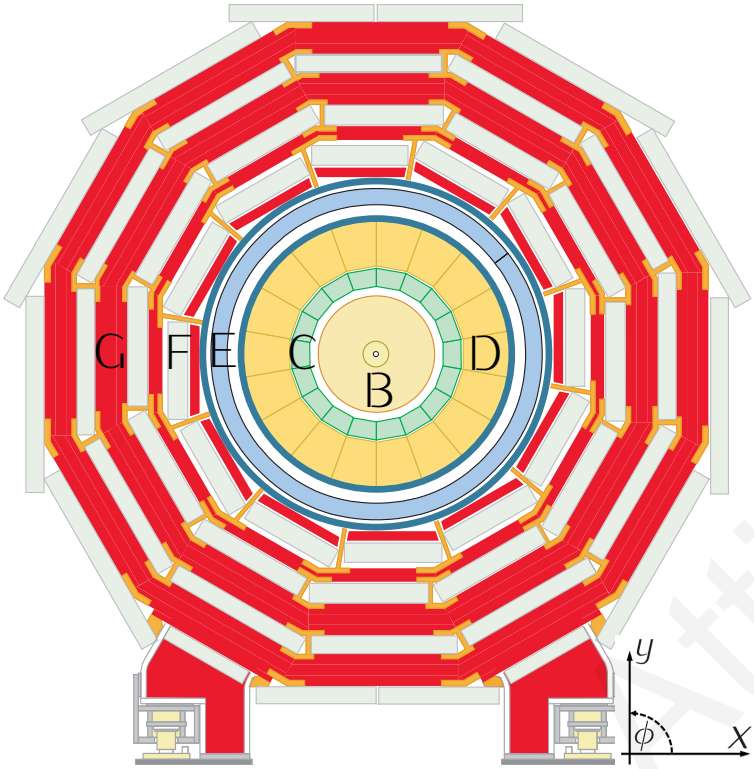

Figure 3.8: Schematic Cross-section view of the CMS detector, showing the azimuthal angle ϕ measured in x-y transverse plane while the z-axis direction is along the anti-clockwise rotating proton beam. The labels definitions are identical to Fig. 3.7.A slice of the cross-section view of the CMS detector can be seen in Fig. 3.9.

fact that these particles escape the detector volume without interacting with the detector material. The apparent transverse energy imbalance observed in the detector is used to infer the presence of such particles and to quantify what is known as the missing transverse energy ($E_{\mathrm{T}}^{\mathrm{miss}}$) of the event.

The beam pipe along with the tracking, ECAL and HCAL detectors are all fitted inside the superconducting coil of the solenoid magnet, 12.9 m long and 5.9 m in diameter, which is aligned in parallel to the beam pipe and is capable of generating a homogeneous magnetic field of $3.8T$ through 2168 turns of a 19.5 kA current-currying wire. The orientation of the solenoid is such that the magnetic field is parallel to the beam line (coming inside/outside of page in Fig. 3.8) and is used to infer the electric charge and momentum of the particles from the curvature of their tracks caused by the Lorentz-Force (Eq. (3.6) on page 44), as shown in Fig. 3.9. As a downside, the presence of the magnetic field causes particles with small momenta to spiral before reaching the first tracking detectors, causing the emission of photons (synchrotron emission) whose energy must be included when determining the particles' momenta.

Outside the solenoid magnet are the muon stations, which are interspersed with the iron return yoke (ferromagnetic) of the solenoid magnet. The muon stations are used to detect muons which, unlike other charged particles, tend to penetrate the main detector volume while only depositing a small fraction of their energy and are hence known as Minimum Ionising Particles (MIPs). The energy and position recorded by the muon detector system is

combined with the information provided by the tracker to provide excellent muon momentum resolution. The main volume of the CMS detector is complemented by endcap discs positioned at both ends of the the barrel structure, hence providing a nearly hermetic detector coverage of the collisions.

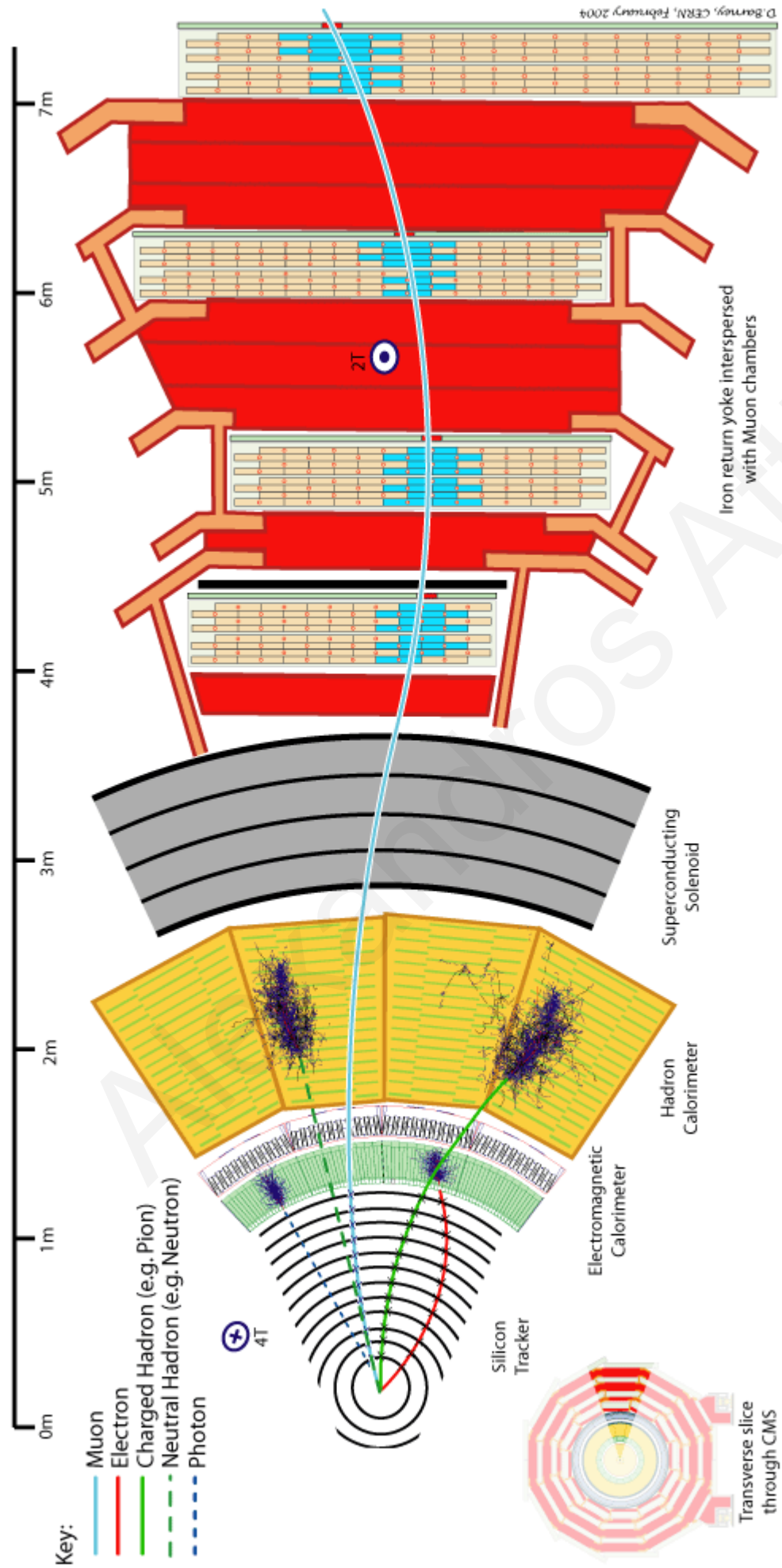

Figure 3.9: Transverse slice through the CMS detector, showing the interaction of eclectically charged and neutral particles with the detector subsystems.

Besides the detection of the flux of particles generated at the IP, the CMS subdetectors must be fast enough to process these signals before the next bunch-crossing, a time interval of 25 ns away. Since the total proton-proton cross-section at $\sqrt{s} = 14$ TeV is roughly 100 mb, at the design luminosity of the LHC there will be approximately $400(600) \times 10^6$ elastic (inelastic) events per second. This high rate of events causes the CMS detector and its subsystems to be constantly irradiated by an immense flux of particles, making the use of radiation-hard detectors a necessity. Moreover, the unprecedented event rate presents a formidable experimental challenge to the online event selection process (trigger) which selects the events to be stored for subsequent analysis, as it must reduce this event rate to a value it can support (triggerbandwidth), at about 100 Hz. Even at this lower rate of event selection made possible by the trigger system, the yearly data volume to be accumulated is of the order of 1 petabyte (10^{15} bytes), raising additional technological challenges for storing these data and making them available for analysis to the thousands of CMS users around the world.

Furthermore, an additional challenge lies in the fact that, at the LHC design luminosity, a mean of ~ 20 inelastic collisions will occur simultaneously during the same bunch-crossing, a term known as pile-up. Under these conditions, a mean of ~ 50 charged particles will be produced per inelastic collision, which implies a flux of ~ 1000 particles emerging from the IP, at every bunch-crossing. This means that the products of a specific interaction could be confused with those of another in the same bunch-crossing, thus impeding the reconstruction of the actual event under study. The effects of pile-up can however be moderated by the use of detectors with high-granularity and good time resolution. The former quality is important for keeping the subdetectors in low occupancy, while the latter can help identify the time-wise collision origin of a specific event. Of course, detectors with high-granularity require a large number of detector electronic channels, which in turn must be in very good synchronisation in order to give the desirable result.

In the following sections, the kinematic definitions for the CMS detector are explained briefly in Section 3.3.1, while the tracking, calorimetry and muon systems are described in Sections 3.3.2, 3.3.3 and 3.3.6, respectively. A description of the trigger and Data Acquisition (DAQ) systems is given in Section 3.3.8, while a brief outline of the CMS computing system is given in Section 3.3.9.

3.3.1 Kinematic definitions

The CMS experiment uses a right-handed coordinate system, with the origin at the IP, the x-axis pointing to the centre of the LHC ring and the y-axis pointing vertically upwards perpendicular to the LHC plane. It then follows that the z-axis, from which the polar angle θ is measured, is oriented to be parallel to the anti-clockwise rotating proton beam, as shown in Fig. 3.7. The azimuthal angle (ϕ) is measured from the positive x-axis in the x-y plane, , as shown in Fig. 3.8, whereas the radius (r) denotes the distance from the z-axis.

However, these set of coordinates are not convenient in relativistic kinematics and hence

the Lorentz-invariant coordinates of pseudorapidity (η) and azimuthal angle (ϕ) are used instead. The pseudorapidity η is a spatial coordinate directly related to the polar angle θ, and is used to quantify the angular direction of a particle relative to the beam-axis (z-axis). It is defined as

$$\eta = -\ln\left(\tan\frac{\theta}{2}\right), \tag{3.21}$$

where θ is the angle between the beam-axis and a particle's momentum vector $\vec{p} = \left(p_x, p_y, p_z\right)$. In term of these momenta, the pseudorapidity can be expressed as

$$\eta = \frac{1}{2}\ln\frac{|\vec{p}|+p_z}{|\vec{p}|-p_z} \tag{3.22}$$

and it is closely related to the rapidity (ω) in relativistic kinematics. In special relativity theory, it is very useful to think of Lorentz Transformations (LTs) as generalised rotations, and this is possible by exploiting the fact that the equation $\gamma^2 - (\beta\gamma)^2 = 1$ can be expressed in terms of hyperbolic functions as

$$\cosh^2\omega - \sinh^2\omega = 1 \tag{3.23}$$

by setting

$$\gamma \equiv \cosh\omega \quad , \quad \beta\gamma \equiv \sinh\omega. \tag{3.24}$$

Therefore, combining the results of Eq. (3.24), the rapidity of an object relative to a given reference frame can be expressed as

$$\omega = \tanh^{-1}\beta \tag{3.25}$$

and by using the hyperbolic identity

$$\tanh^{-1}\beta = \frac{1}{2}\ln\left(\frac{1+\beta}{1-\beta}\right) \tag{3.26}$$

it can be recast in the form

$$\omega = \frac{1}{2}\ln\left(\frac{E+p_z}{E-p_z}\right) \tag{3.27}$$

whereby the substitution $\beta = \frac{p_z}{E}$ has been made with E being the particle's energy. This differs from the definition of rapidity, which uses $|[|\ \vec{p}\ ]$ instead of E. Comparing this last form of rapidity in Eq. (3.27) with the definition of pseudorapidity in Eq. (3.21), one can see that they are indeed closely related. In fact, in the relativistic limit where the particle is travelling close to the speed of light ($E \gg m$), the pseudorapidity in Eq. (3.22) can be

expressed as

$$\eta \simeq \frac{1}{2} \ln \left(\frac{E + p_z}{E - p_z} \right) \equiv \omega \tag{3.28}$$

The pseudorapidity η is thus a Lorentz-invariant spatial quantity which is approximately equal to the rapidity ω for relativistic objects and it can be measured in detectors when the mass and momentum of the particle are unknown. In collider experiments such as CMS, the forward direction refers to regions of the detector that are close to the beam axis (high values of η) while the central direction refers to regions of the detector that are perpendicular to the beam axis (small values of η), as shown in Fig. 3.10 (a). Since the pseudorapidity is

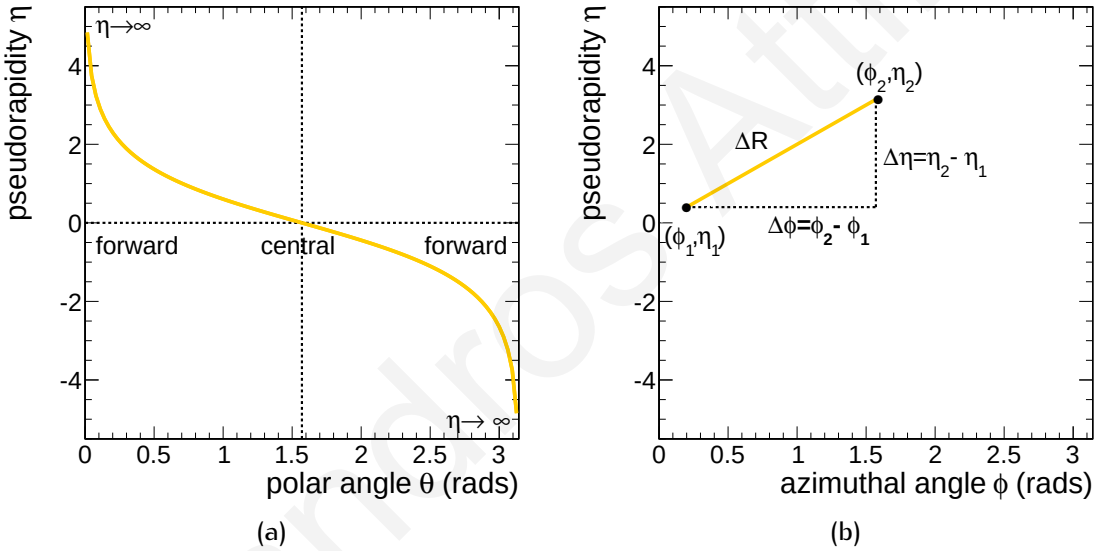

Figure 3.10: Mapping of pseudorapidity η with the polar angle θ (a) and definition of distance in η-ϕ space (b), according to Eq. (3.21) and Eq. (3.29), respectively.

independent of Lorentz boosts along the beam axis, the distance between two objects in η-space is simply the difference of their pseudorapidities ($\Delta\eta = \eta_1 - \eta_2$). Therefore, the radial distance between two objects in η-ϕ plane is given by

$$\Delta R = \sqrt{(\Delta\eta)^2 + (\Delta\phi)^2}, \tag{3.29}$$

as shown in Fig. 3.10 (b).

Finally, it is worth noting that it is possible to define the transverse energy of a particle as the energy deposited in a calorimeter component, corrected for its position as

$$E_T = \frac{E}{\cosh \eta} \tag{3.30}$$

and it is equal to the particle's transverse momentum (p_T) in the relativistic limit ($E \gg m$), and neglecting calorimeter resolution effects.

3.3.2 Tracking system

3.3.2.1 Overview

The innermost part of the CMS detector is the inner tracking system [43, 45, 46, 47, 48], which is 5.8 m long and 2.5 m in diameter. It surrounds the thin beryllium beam pipe which houses the vacuum of the LHC and is centred at the IP5 where the beams are brought to collide. Its task is to provide a robust, efficient and precise measurement of the charge and trajectories of charged particles that emerged from IP5 with transverse momenta above 1 GeV/c and within the pseudorapidity range $|\eta| < 2.5$. Furthermore, the efficient identification of heavy flavours requires that the tracking system is able to determine precisely secondary vertices and impact parameters.

At the LHC design luminosity, an average of 1000 charged particles that originate from more than 20 overlapping proton-proton interactions are produced every 25 ns, and first propagate through the tracker before reaching the next detector layer, the calorimetry system. This leads to a hit rate density of 100 MHz cm^{-2} in the barrel part at a radius of 4 cm, as shown in Table 3.3, which can have dire consequences in terms of detector occupancy

Table 3.3: Expected particle hit rate, fluence and flux in differential radial layers of the CMS tracker barrel part for an integrated luminosity of 500 fb^{-1} ($\approx$ 10 years). Taken from Ref. [43].

Radius (cm)	Hit rate density (MHz cm^{-2})	Fast hadron fluence (cm^{-2})	Charged particle flux (cm^{-2} s^{-1})
4	100	32	10^8
11		4.6	
22	6	1.6	6×10^6
75		0.3	
115	0.3	0.2	3×10^5

and radiation damage to the tracking system. The coloured-scaled CMS tracker diagram in Fig. 3.11 also indicates how the occupancy varies with the radius and pseudorapidity η, for minimum bias events.. Therefore, in order to be able to cope with this enormous particle flux, the tracker system must have high granularity and a fast response to provide a very good position resolution, as well being able to withstand the severe radiation damage for an integrated luminosity of 500 fb^{-1}, that roughly corresponds to 10 years of LHC operations. However, this is contrary to the aim of keeping the amount of tracker material to as little as possible, in order to minimise the amount by which a given particle is perturbed, manifested through multiple scattering, bremsstrahlung, photon conversion and nuclear interactions. Finally, the information provided by the tracking system must be fast enough to be able to contribute to the online selection of events through the High-Level Trigger (HLT) system, which must reduce the event rate from the LHC nominal value of 40 MHz down to 100 Hz, which is the CMS triggerbandwidth.

To fulfil the requirements on granularity, speed and radiation hardness, the CMS tracker is entirely based on silicon technology. It is composed of 1440 pixel and 15148 microstrip

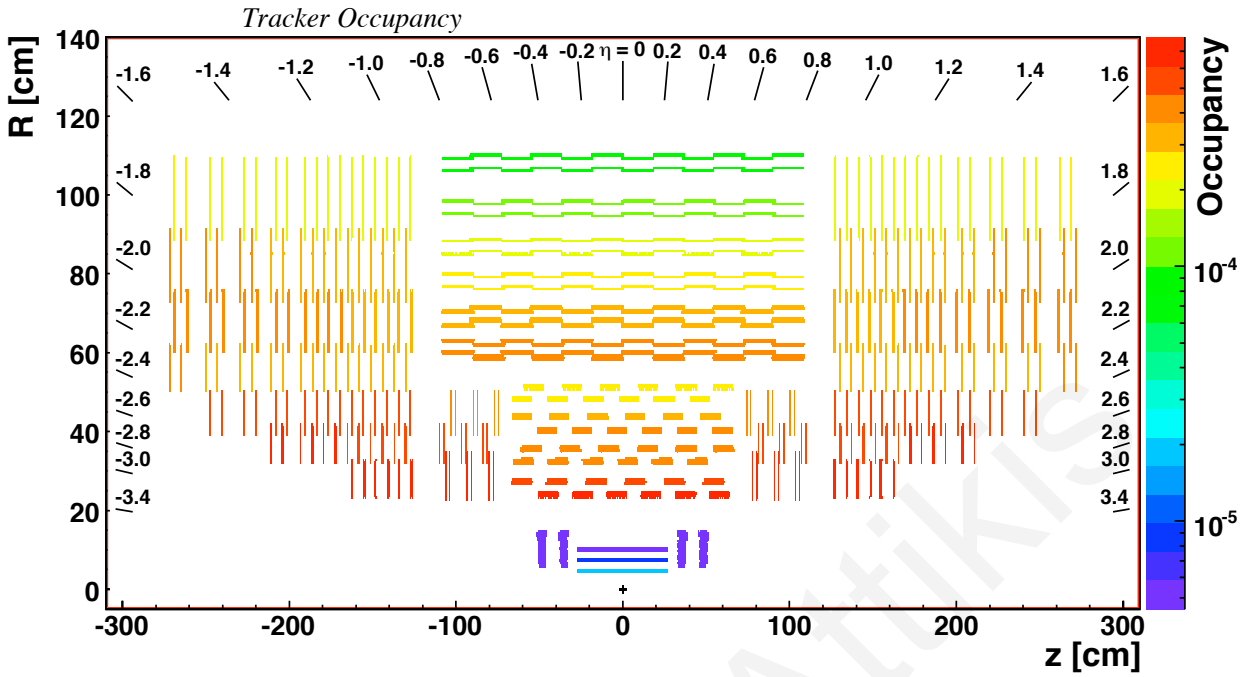

Figure 3.11: Schematic diagram in the *r*-*z* view of the CMS silicon tracker occupancy for minimum-bias events, simulated with superimposed pile-up collisions. Taken from Ref. [49].

detector modules that are arranged in a barrel and endcap configuration, as shown in Fig. 3.12. The barrel part consists of the Barrel Pixel (BPix), the Tracker Inner Barrel (TIB)

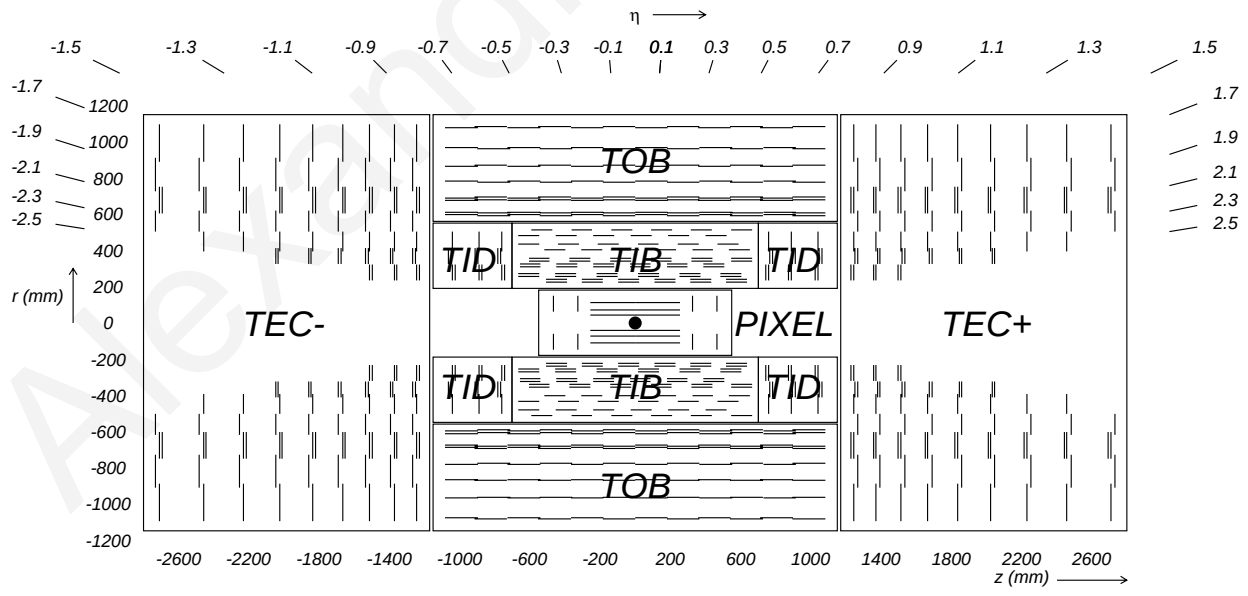

Figure 3.12: Schematic of the CMS silicon tracker, in the *r*-*z* view. Each line represents a detector module, while double lines represent back-to-back modules which deliver stereo hits. Taken from Ref. [50].

and the Tracker Outer Barrel (TOB), and collectively they form 13 concentric layers in total, positioned around the IP5 to provide coverage in the central region. The endcap part consists of the Forward Pixel (FPix), the Tracker Inner Disks (TID) and the Tracker EndCap (TEC) that form 14 disks in total, positioned on each side of the barrels to provide coverage for the

more forward regions, up to a pseudorapidity acceptance of $|\eta| < 2.5$. With a total active silicon area of about 200 m^2, the CMS tracker is the largest silicon tracker built to date. The most important parameters of the CMS tracker subsystems are summarised in Table 3.4 and explained in the following sections.

Table 3.4: Overview of the parameters of the CMS tracker subsystems.

System	Layers (Disks)	r (cm)	z (cm)	Granularity (μm)	Modules	$\sigma_{r-\phi}$ (μm)	σ_z (μm)
BPix	3	4.4 7.3 10.2	[-26.5, +26.5]	100×150	768	15-20 μm	15-20 μm
FPix	(2)	[6,15]	±34.5 ±46.5	100×150	672	15 μm	15 μm
TIB	4	25.5 33.9 41.9 49.8	[-73.0, +73.0]	80, 120	2724	23-35 μm	230 μm
TID	(3)	[23.5-33.5] [32.6-42.6] [37.7-50.2]	±78.8 ±91.8 ±104.7	81, 158	816	varies	varies
TOB	6	60.8 69.2 78.0 86.8 96.5 108.0	[-118.0, +118.0]	122, 183	5208	35-53 μm	530 μm
TEC	(9)	[22.5, 113.5]	[132.3, 266.8] [-266.8, -132.3]	96-188	6400	varies	varies

3.3.2.2 Pixel detector

Due to the high hit rate density at very small radii around the IP5 (Table 3.3), radiation hard detectors with very fine granularity must be used, in order to avoid saturation and keep the occupancy of the CMS tracker at the level of 1% or below. For this reason, the innermost part of the CMS tracker consists of about 66×10^6 pixel detectors, with a pixel unit cell of $100 \times 150\,\mu m^2$ in both the r-ϕ and z coordinates. The pixel detector covers a total area of about $1\,m^2$, and due to the high granularity of the pixels it has an occupancy of only 10^{-4} per pixel at the nominal LHCbunch-crossing frequency.

As shown in Fig. 3.13, the 47923200 pixels in BPix are arranged into 3 barrel layers, each 53.3 cm long and positioned at mean radii of 4.4 cm, 7.3 cm and 10.2 cm around IP5, providing an active area of $0.78\,m^2$. These are complemented by 17971200 pixels in FPix arranged into 2 endcap disks on each side of the barrels, at $z = \pm 34.5$ cm and $z = \pm 46.5$ cm, spanning through a radius range of $6 - 15$ cm and covering an area of $0.28\,m^2$. The barrel layers are composed of modular detector units (modules) placed on carbon fibre supports (ladders). As shown in Fig. 3.14, each ladder includes 8 modules with pixels arranged in quadratic arrays of $n+$ implants on $n-$ substrates, with a thickness of $250\,\mu m^2$. As charged

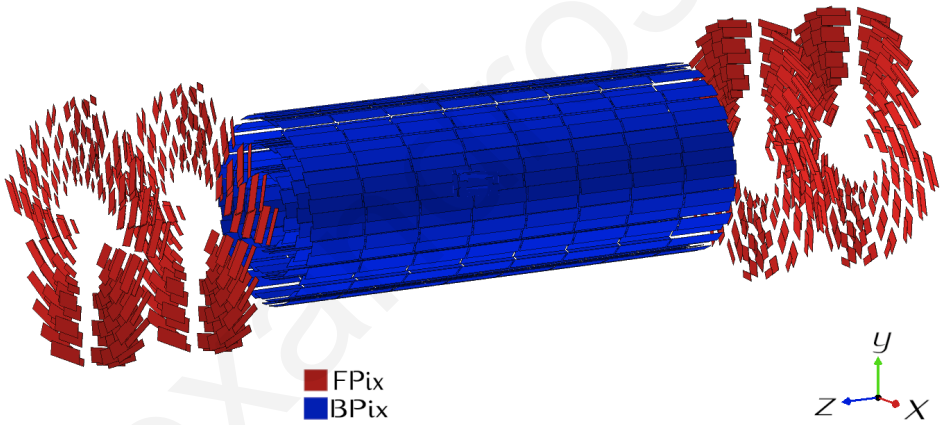

Figure 3.13: Layout of the CMS BPix and FPix detectors, as visualised by Fireworks [38] showing the distinct turbine-like geometry of the endcaps.

particles traverse the depletion region of the junction they eject electrons from the silicon atoms, causing the production of electron-hole pairs. Each pixel uses an electric field to collect these charges on the surface to metal contacts. To read out the detector, a Readout Chip (ROC) is bump-bonded [51] to the pixel modules, which extracts the signal off the top by reading an array of 52×80 pixels. The ROCs, which amount to about 16000, amplify the signals and apply a threshold filter before registering a hit. In the endcaps, the disks are split into half. Each half is comprised of 12 trapezoid-shaped blades which is sandwich of 2 back-to-back panels. Rectangular sensors of 5 sizes are bump-bonded to arrays of ROCs in such a way to form plaquettes. The 672 in total plaquettes are arranged to overlap, so as to provide full coverage for charged particles emerging from the IP5.

To enhance the spatial resolution by analogue signal interpolation, the effect of charge

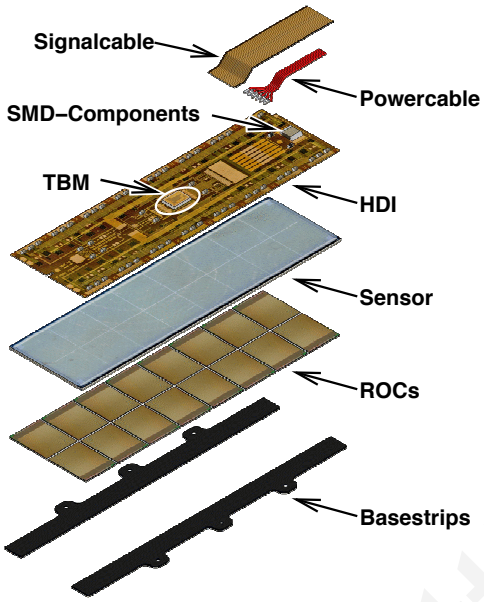

Figure 3.14: A an exploded view of a BPix module.

sharing induced by the Lorentz drift in the 3.8T magnetic field is used. Charge generated by an ionising track traversing the sensor perpendicularly will be spread over 150 μm at the surface in the r-ϕ plane and perpendicular to the magnetic field. Therefore, since in the barrel layers the pixels are perpendicularly oriented to the magnetic field, they are deliberately not tilted. The resolution along the z-axis is determined by the pixel pitch (p)[7] in the central regions (low values of η) and by charge sharing if the tracks hit the sensors at an angle, whereby typically pixel clusters share the charge carriers created in the depletion region. Conversely, in the endcap regions, the orientation of the pixel modules is parallel to the magnetic field. Therefore, the modules are deliberately tilted to about 20° resulting in a turbine-like geometry, which enhances charge sharing between channels due to the Lorentz effect. The spatial resolution of the pixels is about 20 μm for the r-ϕ measurement ($\sigma_{r\text{-}\phi}$) and about 15 μm for the z measurement (σ_z).

The arrangement of the pixel detector into barrel and endcap parts, provides a pseudo-rapidity coverage of $|\eta| < 2.5$, as shown in Fig. 3.15 (a). In the same figure (b) the expected efficiency of a particle registering at least 2 hits within the pixel detector is presented as a function of pseudorapidity, showing a marked fall in the forward region. This drop in hit coverage is due to the fact that in the high η regions the pixel information from the 2 disks has to be combined with the innermost layer of the barrel, which only covers the region up to $|\eta| < 2.2$, leaving the pseudorapidity range $2.2 \leq |\eta| \leq 2.5$ to be solely covered by the endcap disks. In this way the pixel detector provides 3 high precision space points on each charged particle trajectory, enabling the determination of small impact parameter resolution, which is important for good secondary vertex reconstruction for low track multiplicity of b-quark and τ-lepton decays. Moreover, the pixel detector may be used to perform fast track finding, which may be used to set coarse constrains for selecting interesting events

[7] The distance between the strips on a piece of silicon (inter-strip distance).

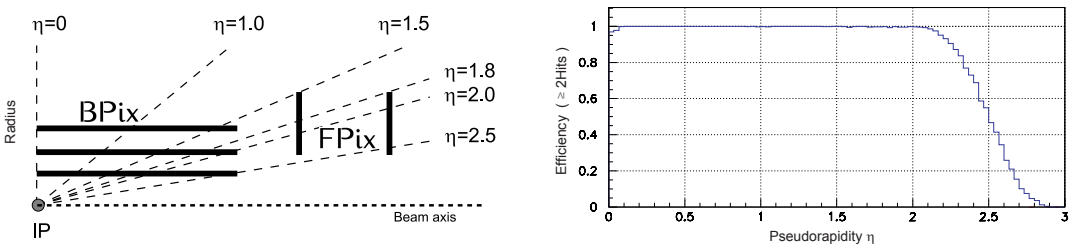

(a) (b)

Figure 3.15: Geometrical layout of the BPix and FPix subsystems (a) and hit coverage of the full pixel detector as a function of pseudorapidity η (b). Taken from Ref. [43].

with the trigger.

3.3.2.3 Strip detector

The tracker silicon strip detector, which surrounds the pixel detector, has a total of 9.3×10^6 silicon microstrips, covering an area of 198 m^2, and is divided into 3 separate subsystems; the Tracker Inner Barrel and Disks (TIB and TID), the Tracker Outer Barrel (TOB), which surrounds the former, and the Tracker EndCap (TEC), which seals off the TOB, as shown in Fig. 3.16. The placement of the barrel and endcap subsystems has been designed such that each

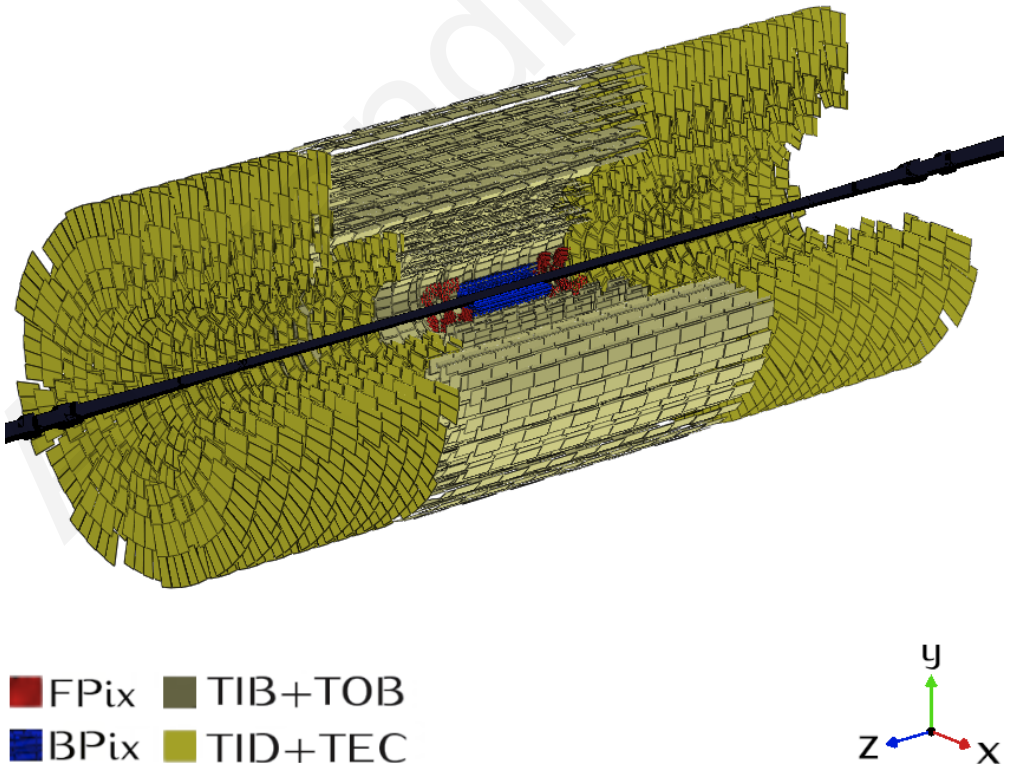

Figure 3.16: Layout of the complete CMS tracker detector, as visualised by Fireworks [38]. Parts of the CMS detector have been cut away for visualisation purposes.

particle must pass through at least 10 sensors, independent of pseudorapidity and, assuming they have high enough transverse momentum, to be within the tracker acceptance. Each

of the subsystems has silicon microstrip modules, designed differently for its place within the detector. The choice to use silicon sensors was based on building a compact, high-resolution, efficient, reliable yet cost-efficient tracker. Analogously to the pixel detector, the silicon microstrip sensors have very fast response, excellent spatial resolution, are radiation-hard and can be operated at nearly room temperature. The aforementioned features make them highly suited for the purpose of detecting the large particle flux emerging from IP5 and through the pixel detector. Furthermore, silicon microstrip detectors operate in similar fashion to the pixels. When a charged particle propagates through the depletion region of the material, the current from the liberated electron-hole pairs can be measured by collecting them to metal contacts through an applied electric field. The small pulse of current, which typically lasts a few nanoseconds, is then amplified by ROCs, thus registering a hit and allowing for the particle's trajectory to be reconstructed.

The layout of CMS microstrip sensors is illustrated in Fig. 3.17 for a r-z quarter slice of the CMS tracker. The TIB consists of 4 concentric layers of silicon microstrip sensors.

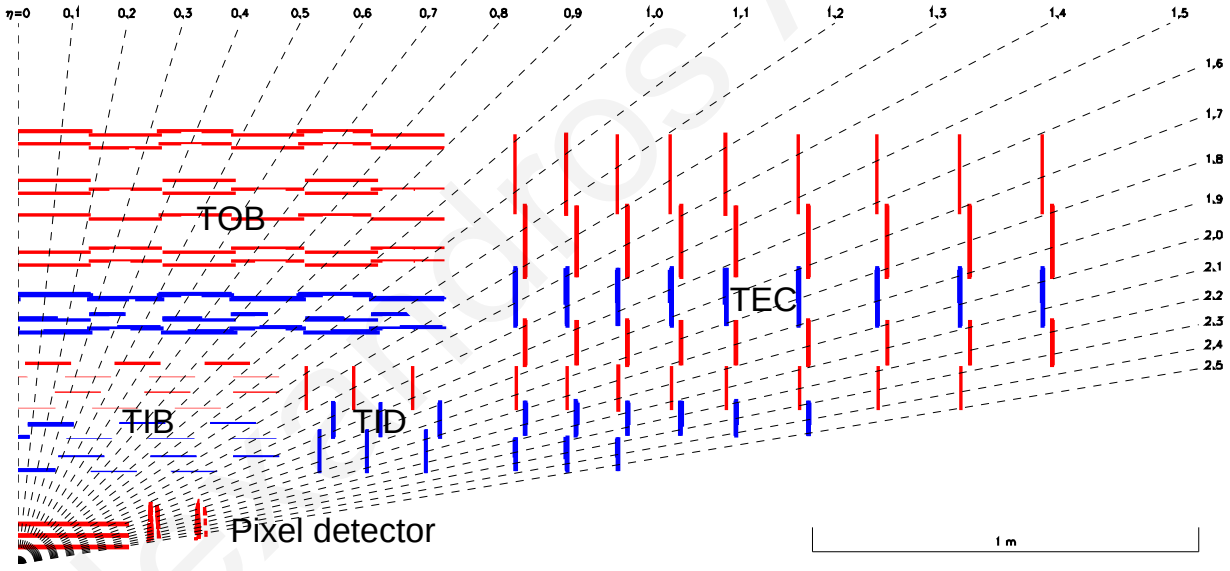

Figure 3.17: Schematic of one-quarter of the CMS silicon tracker, in the r-z view. The red and blue lines correspond to single and double-sided (stereo) sensor modules, respectively. Taken from Ref. [45].

Each side of the barrel is sealed off with the TID endcaps. The TIB layers are 146 cm long and are positioned at mean radii of 25.5 cm, 33.9 cm, 41.9 cm and 49.8 cm around IP5. These are complemented by 3 disks in the TID on each side of the barrels at ±78.8 cm, ±91.8 cm and ±104.7 cm and spanning through a radius range of 23.5−33.5 cm, 32.6−42.6 cm and 37.7 − 50.2 cm, respectively. The combined TIB/TID subsystem, which has its silicon microstrips oriented parallel (radial) to the beam axis in the barrel (disks), delivers up to 4 r-ϕ measurements on a trajectory. The layers are fitted with 320 μm-thick and 12 cm-long microstrips silicon sensors, with a strip pitch in the range of 80 − 120 μm, leading to an occupancy of up to 2-3% per strip at the nominal LHCbunch-crossing frequency. The 2

innermost layers of the TIB, and rings 1 and 2 of the TID are equipped with stereo modules that are coupled back-to-back and rotated at an angle of 100 *m*rad with respect to each other, hence providing measurements in both the r-ϕ and r-z coordinates. The resulting spatial resolution for TIB is about 23-35 μm for the r-ϕ measurement and about 230 μm for the z measurement. For the TID, the resolution varies with the strip pitch, which is typically quoted as $\sigma_p = \frac{p}{\sqrt{12}}$[8] if one assumes that a given particle has struck at the centre of the strip [52]. However, accounting for charge sharing between neighbouring strips due to Lorentz-drifts of electrons in the presence of a strong magnetic field can result in much better resolutions.

Surrounding the TIB is the TOB, consisting of 6 concentric layers, each 236 cm long and positioned at mean radii of 60.8 cm, 69.2 cm, 78.0 cm, 86.2 cm, 96.5 cm and 108.0 cm around IP5. Being further away from the IP5 than the TIB, the relatively lower particle flux (Table 3.3) enables the use of longer strip length and wider pitch. The maximum strip length is 16 cm while the pitch range is 122-183 μm. The increase in strip length relative to the inner barrel is purely for logistical reasons, as the outer barrel has to cover a much larger area than the inner barrel, while also constraining the number of read-out channels. However, the longer strip length implies a relative increase in electronics noise, which is a linear function of strip length. To compensate for the apparent deterioration of the signal-to-noise ration, the silicon sensors in the TOB are much thicker than those in TIB, with a thickness of 500 μm. The expected increase in signal is roughly proportional to the increase in thickness, due to the fact that for a given material of unit area, thickness d, and ionisation energy I_0, the number of electron/holes produced by a traversing ionising particle, with a material differential energy loss $\frac{dE}{dx}$, is given by $\frac{dE}{dx} \cdot \frac{d}{I_0}$. Accordingly, the thickness of the microstrips in the TOB was selected to maintain a signal-to-noise ratio well above 10. Additionally, and in similar fashion to the TIB, the 2 innermost layers of the TOB are equipped with back-to-back stereo modules, rotated at an angle of 100 *m*rad with respect to each other. They provide measurements in both the r-ϕ and r-z coordinates with resolutions 35-53 μm and 530 μm, respectively.

The outer barrel region, is supplemented by the TEC subsystem, which is comprised of 9 endcap disks on each side, thus closing the barrel gaps to form a cylindrical-like tracker volume. Each of the disks carries up to 7 rings of silicon microstrip detectors, with a thickness and pitch range of 320-500 μm and 97-184 μm, respectively. This arrangement of the disks in the TEC provides another 9 r-ϕ measurements per trajectory. To further enhance the performance of the TEC subsystem, the rings 1, 2 and 5 carry stereo microstrip detectors that enable the measurement of the z coordinate (r coordinate) in the the barrel (disks). Similarly to the TID, the achieved single point resolution in TEC varies with the strip pitch.

The above described tracker layout provides a pseudorapidity coverage of $|\eta| < 2.4$ and ensures at least $\approx$ 9 hits in the silicon strip tracker, with at least 4 of them being two-dimensional measurements (stereo). The ultimate acceptance of the tracker ends at $|\eta| \approx .5$.

[8] $\sigma_p = \sqrt{\frac{\int_{-p/2}^{+p/2} (x-0)^2 dx}{\int_{-p/2}^{+p/2} x dx}} = \frac{p}{\sqrt{12}}$.

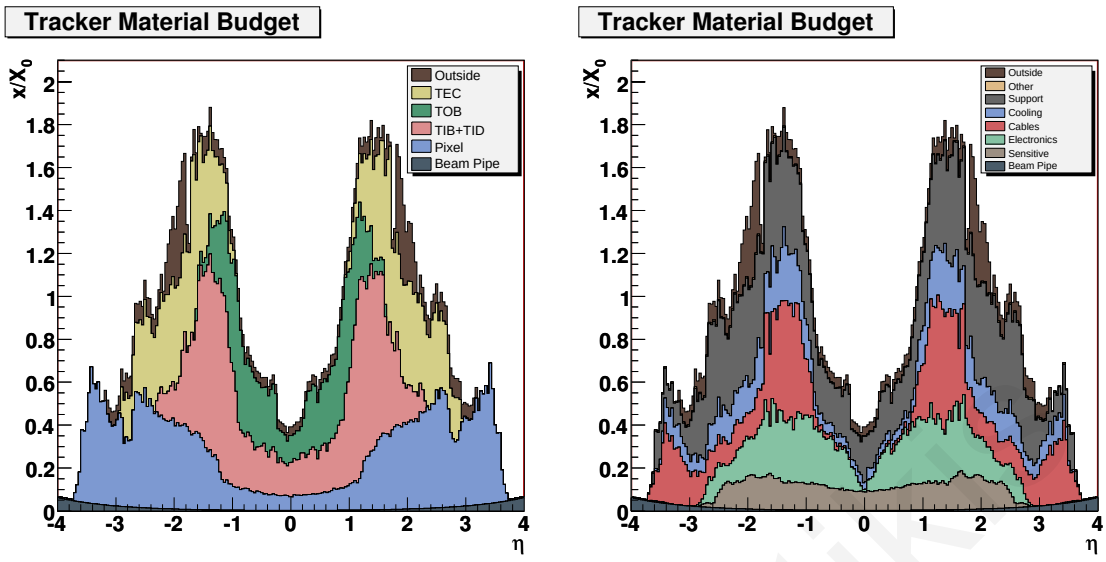

(a) (b)

Figure 3.18: Material budget of the CMS tracker in units of radiation length (X_0), as a function of the pseudorapidity η for the different subdetectors (a) and functionalities (b). Taken from Ref. [43]. The radiation length is the mean distance over which the energy of a high-energy electron drops to $1/e$ by bremsstrahlung. It is also defined as 7/9 of the mean free path for pair production by a high-energy photon, corresponding to a layer thickness of material where pair-production happens with a probability of $P = 1 - e^{-\frac{7}{9}} \approx 54\%$[53, 54].

However, despite the efforts to minimise the amount by which a given particle is perturbed, by carefully selecting the tracker design and material, the tracker does exhibit a small but finite material budget to the incoming particle flux, as shown in Fig. 3.18, before they penetrate the next layer of the CMS detector; the calorimetry system.

3.3.3 Calorimetry system

3.3.3.1 Overview

The tracking system of the CMS detector is surrounded by the calorimetry system [43, 45], whose main goal is to measure the energy and direction of jets of particles forming from quark or gluon hadronisation processes. Additionally, it plays a crucial role in the identification of electrons, photons and muons when the information it provides is combined with that coming from the tracking and muon systems. The calorimetry system also plays a central role in the identification of neutrinos or exotic particles that escape the detector volume undetected, due to their minimal interaction with matter, by measuring the transverse missing energy. It is comprised of the Electromagnetic Calorimeter (ECAL) and the Hadronic Calorimeter (HCAL), which are centred around the IP5 and with both being divided into a barrel part, ECAL Barrel (EB) and HCAL Barrel (HB), and an endcap part, ECAL Endcap (EE) and HCAL Endcap (HE). The ECAL is complemented in the forward regions by the Endcap preShower (ES) system, which is installed in front of the EE and provides additional granularity for measuring electrons and photons, aiming for π^0 rejection. The layout of the CMS calorimetry system

is shown in Fig. 3.19 for a r-z quarter slice of the CMS. As already discussed, the immense

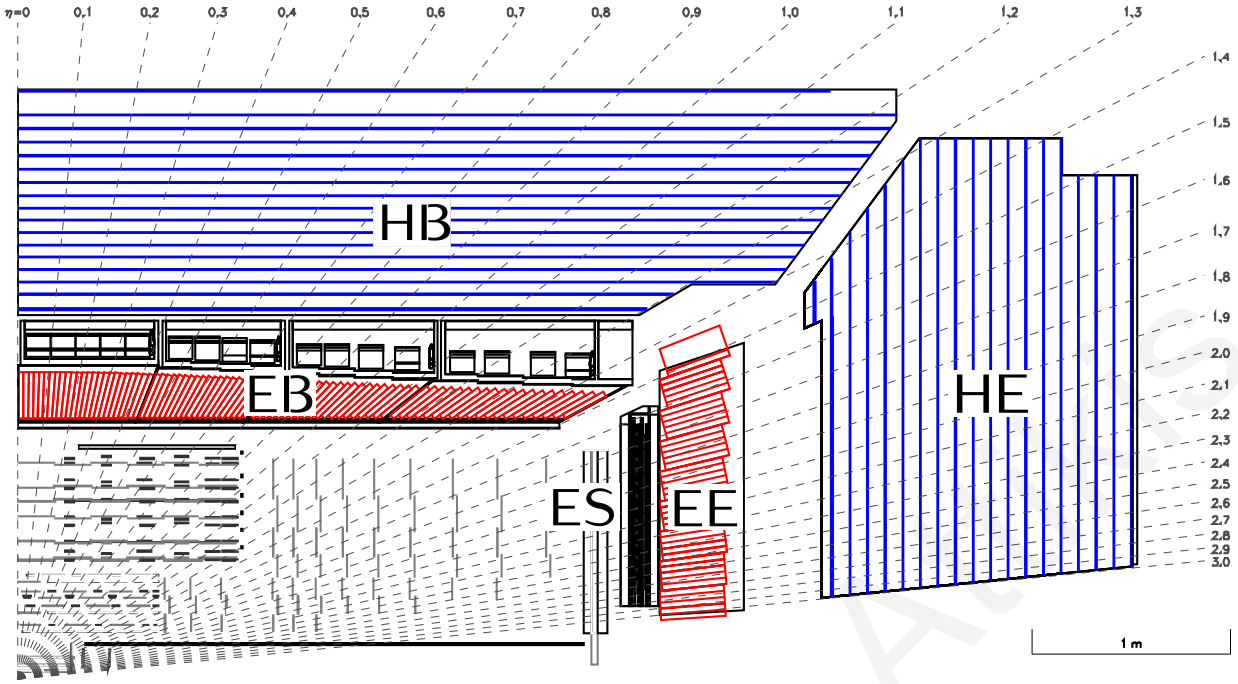

Figure 3.19: Schematic of one-quarter of the CMS calorimetry system, in the r-z view. The barrel and endcap parts of the ECAL and HCAL are shown, in red and blue colour, respectively. The ES system is also shown in black, positioned in front of the EE.

particle flux generated at the IP5 with every LHCbunch-crossing occurring every 25 ns, first propagates through the tracker before reaching the calorimetry system. While the tracking system is designed to perturb the incident particles as little as possible, the calorimetry system aims at doing exactly the opposite; measure the energy and position coordinates of incident particles by total-absorption methods. In this absorption process, incident particles interact with the large detector mass of the calorimetry system and generate secondary particles that in turn generate tertiary particles and so on, giving particle EMcascade showers. In this way, the incident energy appears as excitation or ionisation in the detector medium, which measures the total deposited energy. In the following, the ECAL and HCAL detectors are described in detail in Section 3.3.4 and Section 3.3.5, respectively.

3.3.4 Electromagnetic Calorimeter

The first detector layer encountered by a particle emerging from the tracking system is the ECAL [43, 45, 55, 56], whose task is to identify electrons and photons and also measure their energy and position. The deposition of energy from high-energy electrons and photons in the ECAL proceeds through EMcascade showers [53], which are generated from bremsstrahlung and pair-production, as shown in Fig. 3.22 on page 75. An electron with energy E_0 traversing the detector medium radiates photons through bremsstrahlung which produce e^+e^- pairs through pair-production. This process is repeated with the number of particles (N) increasing exponentially with traversed in the medium (X) as $N = 2^X$ with photons, electrons and

positrons approximately equal in numbers. This process continues until the energy of a particle at a given depth in the medium, parametrised as $E(X) = E_0/2^X$ reaches a critical value E_C, at which the ionisation losses become dominant and take over. The EMcascade shower will reach a maximum of $X_{\max} = \frac{\ln(E_0/E_C)}{\ln 2}$ and then ceases abruptly with the number of particles at the maximum, being equal to $N_{\max} = E_0/E_C$, while the total shower length (L) will be $L \simeq E_0/E_C$. Therefore, the maximum depth reached by an incident particle increases logarithmically with primary energy E_0, to which the number of shower particles and total track-length are proportional. In addition to the longitudinal spread, the EMcascade shower will also spread laterally due to Coulomb scattering by an order of 1 Molière radius unit $R_m = 21\,(X_0/E_C)$, with E_c in MeV.

The aforementioned characteristics dictate that, in order for electromagnetic-shower detectors to measure completely the energy of electrons and photos, they must be built from high-Z materials of small X_0 so as to be able to contain the showers in their active volumes. For this exact reason, the electromagnetic calorimeter of CMS is made of lead tungstate ($PbWO_4$) crystals. It is a hermetic homogeneous calorimeter, as shown in as Fig. 3.20, as well as compact, enabling it to fit within the CMS magnet coil. It is made of 75848 in total $PbWO_4$ crystals, with 61200 of them mounted in the barrel and 14648 found in the endcaps. The ES detector, which is placed in front of the EE crystals, is made of 2 planes of lead followed by silicon sensors, similar to those used in the tracker. Its design was heavily influenced by the postulated Higgs boson decay to 2 photons, as it enables the identification of π^0 decays which can mimic high-energy photons when they decay into 2 closely-spaced lower energy photons that the ECAL crystal calorimeter picks up together.

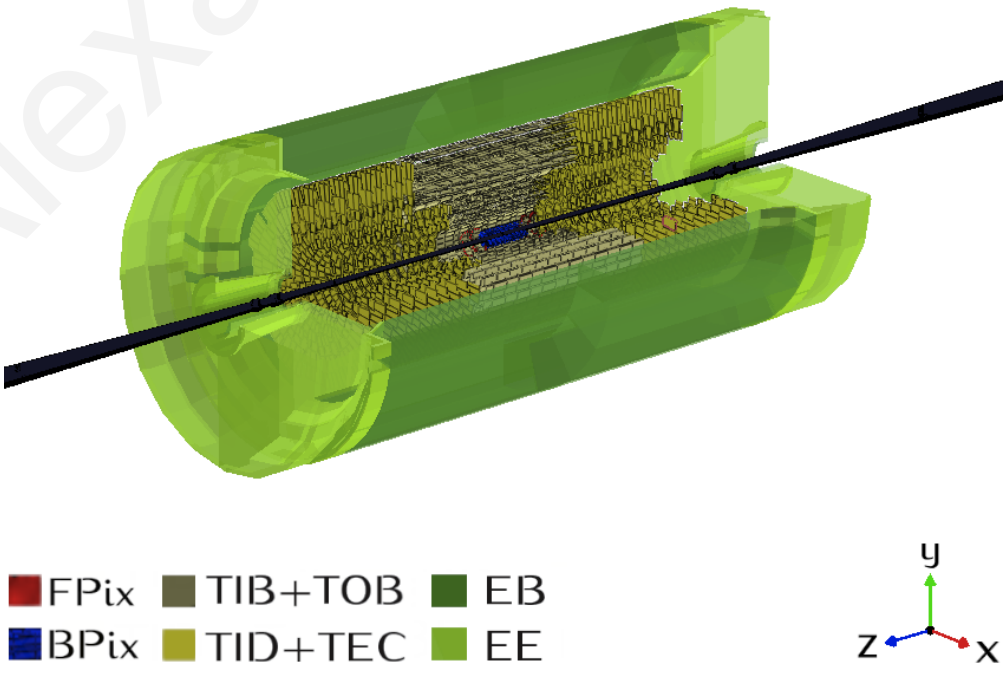

Figure 3.20: Layout of the complete CMS ECAL detector, as visualised by Fireworks [38]. Parts of CMS detector have been cut away for visualisation purposes.

The barrel part of the ECAL covers a crystal-volume of 8.14 m^3, weighting 67.4 t and covering a pseudorapidity range of $|\eta| < 1.479$, with a granularity of $\Delta\eta \times \Delta\phi = 0.0175 \times 0.0175$. The crystals, whose shape slightly varies with pseudorapidity, have a cross-section face of 22×22 mm^2 at the front and 26×26 mm^2 at the back and are oriented in a quasi-projective geometry. The orientation of these 230 mm ($25.8X_0$) long crystals is such that they make an angle of 3° with respect to the vector from IP5, while the centre of their faces is 1.29 m from IP5. The crystals are contained in thin-walled alveolar structures that are called submodules and packed in 2×5 configuration with an intra-submodule and inter-submodule crystal distance of 0.35 mm and 0.5 mm, respectively. Arrays of 4×10 (5×10) submodules are themselves assembled into modules containing 400 (500) crystals, with the array dimensions depending on the pseudorapidity position of the modules. Finally, 4modules are assembled in a supermodule which contains a total of 1700 crystals, as shown in Fig. 3.21 (a). A total of 18supermodules form half of the barrel, each covering 20° in ϕ. The layout of the CMS ECAL crystal modules, supermodules, supercrystals is shown in Fig. 3.21 (b).

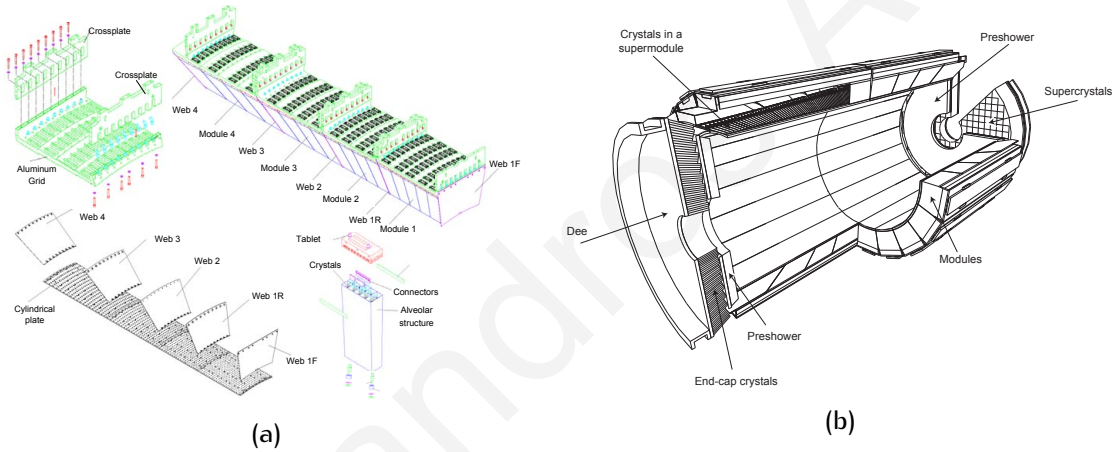

Figure 3.21: Layout of a CMS ECAL showing the crystal modules, supermodules, supercrystals and endcap, with the preshower in front. Taken from Ref. [43].

The endcap part of the CMS ECAL consists of the EE and the ES. The ES, which is placed in front of the EE to prevent false π^0 signals, covers a pseudorapidity range of $1.653 < |\eta| < 2.6$. Besides assisting in the identification of π^0 decays in the endcaps, it also helps in the identification of electrons against MIPs and improves the determination of electrons and photons with its much finer granularity. It is a sampling calorimeter, consisting of 2 lead (Pb) absorbers of length $2X_0$ and $1X_0$ respectively, and 2 planes positioned behind the absorbers equipped with silicon strip sensors similar to those used in the tracker. About 95% of the single incident photons start showering before the second sensor plane. Each silicon sensor measures 63×63 mm^2, providing an active area of 61×61 mm^2, which is divided into 32 strips. The strips, which have a nominal thickness of 320 μm, have a pitch of 1.9 mm. The silicon sensors are arranged in a grid in the endcaps to form a disc 20 cm-thick and 2.5 m-long in circumference, thus covering most of the area of the ECAL EE. The lead absorbers are used to initiate EMcascade showers from electrons and photons which the silicon sensors detect and measure, providing 2 measurements and hence allowing to determine the particle's position.

The position sensitive silicon sensors are used to measure the spatial energy distribution of the EMcascade showers. This information can be used to determine whether the high-energy photon candidates observed in the crystal ECAL are genuine or originating from π^0 decays by extrapolating their paths back to the centre of the collision. By combining the information regarding the hit position in the ES and the energy deposited there, with the information from the crystal EE, the distinction can be made between individual high-energy photons or lower energy photon pairs. The EE covers a crystal-volume of 2.90 m^3, weighting 24.0 t and covering a pseudorapidity range of $1.479 < |\eta| < 3.0$. The endcaps contain the crystals in 5×5 arrays within an alveolar structure known as SuperCrystal (SC). Each endcap is divided into 2 exact halves, thus forming 2 Dees, each containing 3662 crystals. The EE crystals, which are 220 mm ($24.7X_0$) long and are identically shaped, have a cross-section face of $28.62 \times 28.62\,mm^2$ at the front and $30 \times 30\,mm^2$ at the back. Their orientation is such so that they point at a focus of 1300 mm beyond IP5, thus making an angle of $2 - 8°$ with respect to the vector from IP5, while the centre of their faces is 3.154 m from IP5. The CMS ECAL subsystems are summarised in Table 3.5.

Table 3.5: Overview of the CMS ECAL subsystems.

System	η-coverage	Active Medium	Radiation length
EB	$\|\eta\| < 1.479$	61200 $PbWO_4$ crystals	$25.8X_0$
EE	$1.479 < \|\eta\| < 3.0$	14648 $PbWO_4$ crystals	$24.7X_0$
ES	$1.653 < \|\eta\| < 2.6$	silicon strips	$3X_0$

The use of high density crystals, with short radiation length and small Molière radius, allows for a fast and radiation resistant calorimeter with fine granularity, all attributes that are of a paramount imporantece in the LHC environment. When high-energy electrons or photons traverse a CMS ECAL crystal, the resulting EMcascade showers of electrons, positrons and photons interact electromagnetically with the atoms of the crystals. These interactions cause excitation of the crystal atoms, with electrons being excited to higher orbitals. Once these electrons fall back to their ground states they emit photons of energies corresponding to the energy level difference between ground and excited states. For $PbWO_4$ crystals, these photons provide a wide spectrum of frequencies in the visible, with a broad peak around 420 – 430 nm corresponding to blue-green scintillation light. This scintillation light is totally internally reflected inside the crystal walls and collected at the back face of the crystal by Avalanche Photo-Diodes (APDs) and Vacuum Photo-Triodes (VPTs) in the EB and EE, respectively. The APD photodetectors, which are made of semiconducting silicon, collect the electrons produced when a scintillation photon strikes a silicon atom with a strong electric field applied to its ends. In their journey, these accelerated electrons cause more electrons to be knocked off and so on, causing an avalanche effect, whose end result is an exponential increase in their numbers. In this way, APDs produce high currents in a short time interval before amplifying and digitising the information, all necessary steps due to the low light output of the crystals. The scintillation decay time is comparable to the LHCbunch-crossing time interval of 25 ns, while the number of photoelectrons produced at

18°C is 4.5 MeV^{-1}. Unlike the barrel, VPTs are employed in the endcaps, mainly because of the radiation damage being much greater in this region. A VPT contains three electrodes within a vacuum. Analogously to the APD, electrons are released when the scintillation light strikes atoms in the first electrode. A potential difference applied between the electrodes accelerates the electrons into the second electrode (anode), producing several more electrons. These electrons are then accelerated to the third electrode (dynode), generating a second bundle of electrons. The end result is analogous to that of APDs, with a large current being produced by a finite amount of scintillation. However, the scintillation light yield depends strongly on temperature, which requires the temperature of the crystals to be mounted within ±0.1°C with a dedicated cooling system. The characteristics of the CMS ECAL crystals used in EE and EB are summarised in Table 3.6.

Table 3.6: Summary of the CMS ECAL $PbWO_4$ crystal characteristics.

Quantity	Value	Unit
Front (back) cross-section in EB	22 × 22 (26 × 26)	mm^2
Front (back) cross-section in EE	28.62 × 28.62 (30 × 30)	mm^2
Length EB (EE)	230 (220)	mm
Radiation lengths EB (EE)	25.8 (24.7)	X_0
Density	8.28	g cm^{-3}
Refractive index n at peak wavelength	2.29	
Scintillation decay time (80%)	25	ns
Photoelectrons produced at 18°	4.5	MeV^{-1}
Molière radius (R_m)	0.89	cm
Emission spectrum maximum	420 – 430	nm
Light output loss at 18°	2.1	%°C^{-1}

3.3.5 Hadronic Calorimeter

The second detector layer encountered by a particle emerging from the tracking system is the HCAL [43, 45, 57], whose task is to measure the energy and direction of jets arising from hadronisation processes of quarks and gluons. The deposition of energy from strongly interacting particles in the HCAL proceeds through hadronic cascade showers [53, 54] which are generated from the elastic and inelastic interactions of these hadrons with the calorimeter material. The interactions that take place between the incident particles and the nucleons of the calorimeter material produce several secondary hadrons, the majority of which are π and K mesons, neutrons and protons. If the secondary particles have enough energy they themselves will undergo inelastic collisions, producing tertiary hadrons and so forth, as shown in Fig. 3.22, with the cascade process repeated until the hadron energies are so small that they are either absorbed in a nuclear process or are stopped by ionisation energy loss. These hadroniccascade showers develop spatially with a scale that depends on the nuclear absorption or interaction length ($\lambda = \frac{1}{n\sigma_{\text{inelastic}}}$), which is the mean distance travelled before an inelastic collision of cross-section $\sigma_{\text{inelastic}}$ occurs in a material with a number density n.

Compared with the values of the radiation length X_0 of high-Z materials, the size of hadronic showers is large, which correspondingly means hadron calorimeters must be also large to completely contain the hadroniccascade showers. However, apart from energy losses due to particles leaking out longitudinally or laterally and the presence of MIPs and neutrinos which deposit little or no energy in the active calorimeter medium , hadronic sampling calorimeters have losses due to additional reasons. The inelastic collisions of shower particles induce nuclear excitations, fission and spallation[9] in the nuclei of the absorber material, which produces other protons, neutrons, nuclear fragments and low-energy photons. Therefore, unlike EMcascade showers where the incident energy appears eventually in the form of ionisation, in hadroncascade showers about 30% of the incident energy is lost in these processes and does not give an observable signal. One way of retrieving part of this energy is by using ^{238}U as the calorimeter material, as the energy released by fast neutron and photon fission can compensate some of the missing energy; hence the name compensating calorimeters.

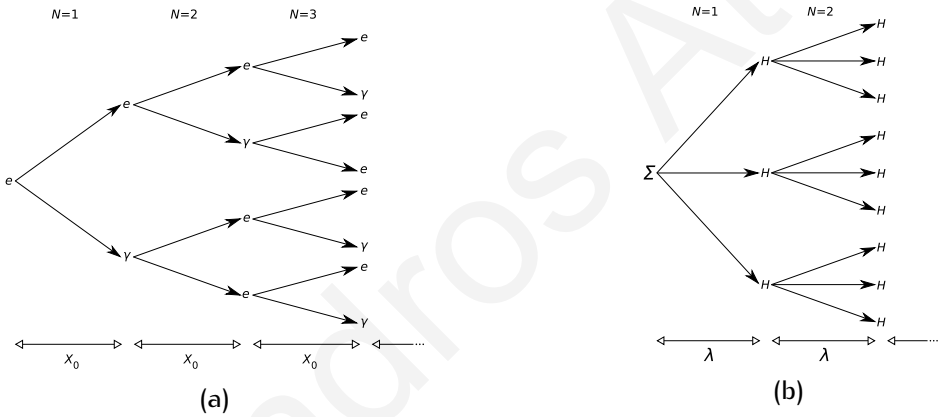

Figure 3.22: Schematic diagram of the development of simple electromagnetic (a) and hadronic (b) showers. Taken from Ref. [58].

The aforementioned characteristics dictate that, in order for hadronic-shower detectors to measure completely the energy of hadrons, they must be built from high-density (ρ) materials, so as to be able to contain the showers in their active volumes ($\lambda \propto 1/\rho$). For this reason as well as its non-magnetic properties, the main absorber material chosen for the hadronic calorimeter of CMS is brass, whose main properties can be seen in Table 3.7. Similar to the tracker and ECAL detectors, the HCAL is divided into a barrel and endcap parts, HCAL Barrel (HB) and HCAL Endcap (HE), with both contained within the CMS magnet solenoid. The HCAL is positioned behind the tracker and ECAL detectors as seen from IP5 (Fig. 3.24), and it is radially restricted to be between the outer extent of the ECAL (1.77 m) and the inner extent of the magnetic coil (2.95 m). Consequently, the amount of material that can be used to absorb the incident particle energy is constrained accordingly. For this reason, the HCAL Outer (HO) is placed outside of the magnetic solenoid, acting as an outer hadron calorimeter or a tail catcher. In the forward regions it is complemented by the HCAL Forward (HF) calorimeters, positioned at a distance of 11.2 m from the IP5 and outside the

[9] A nuclear reaction in which many particles are ejected from an atomic nucleus by incident particles of sufficiently high energy.

Table 3.7: The physical properties of the HB and HE absorber material.

Quantity	Value	Unit
Composition	70%	Cu
	30%	Zn
Density	8.53	g cm^{-3}
Radiation Length (X_0)	1.49	cm
Interaction Length (λ)	16.42	cm

muon chamber. The layout of the CMS HCAL system is shown in Fig. 3.23 for a r-z quarter slice of the CMS.

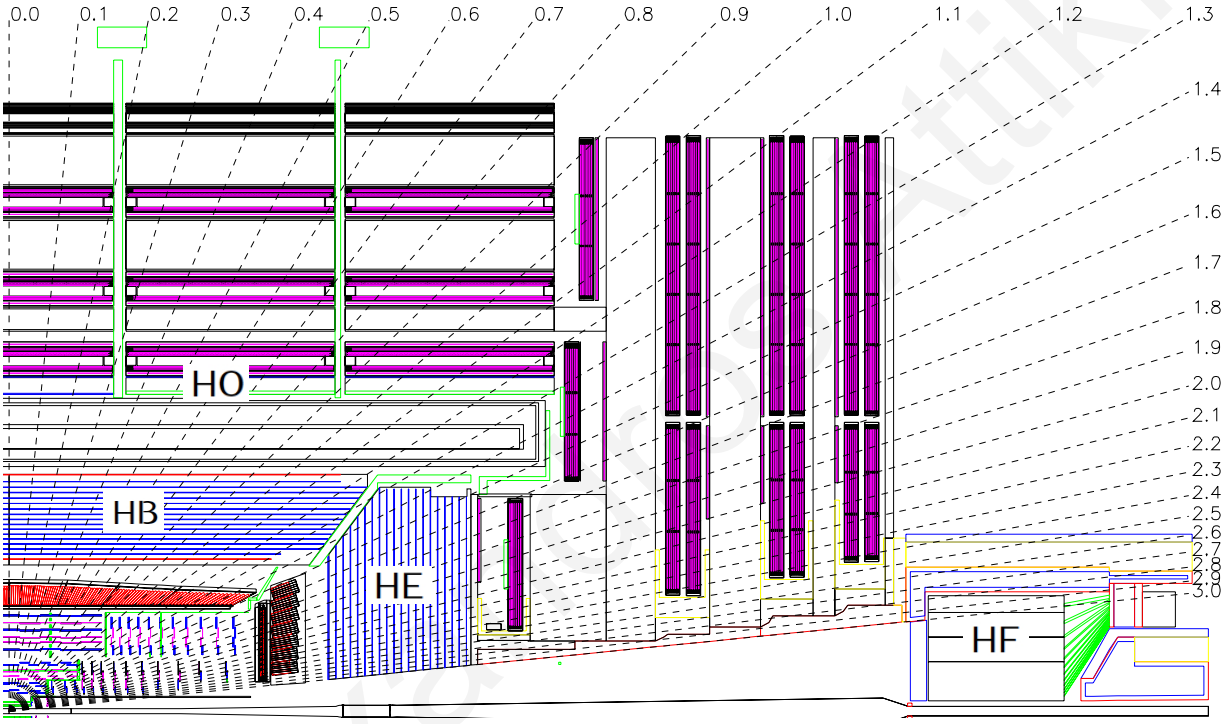

Figure 3.23: Schematic of one-quarter of the CMS HCAL system, in the r-z view, showing the locations of HB, HE, HO and HF. Taken from Ref. [43].

The barrel part of the HCAL is a sampling calorimeter, covering a pseudorapidity range $|\eta| < 1.3$. It consists of 36 in total identical 20° wedges which form 2 half barrels, constructed of flat brass absorber plates aligned parallel to the beam axis. Each wedge, which is segmented into 4 ϕ-sectors, has its innermost and outermost plates made of stainless steel, to provide the necessary structural strength. A total of 14 brass plates are sandwiched between the stainless steel plates. The first layer is a 40 mm-thick stainless steel plate, followed by 50.5 mm-thick brass plates 1 – 8. These are followed by 56.5 mm-thick brass plates 9 – 14, which are finally closed by a 75 mm-thick stainless steel plate. There are 17 plastic scintillator tiles interspersed between the stainless steel and brass material. The first scintillator layer is immediately after the ECAL and it is 9 mm-thick, much thicker than the nominal scintillator tile thickness of 3.7 mm, to sample low energy showering particles from support material between the ECAL and HCAL. An identical scintillator tile is also positioned

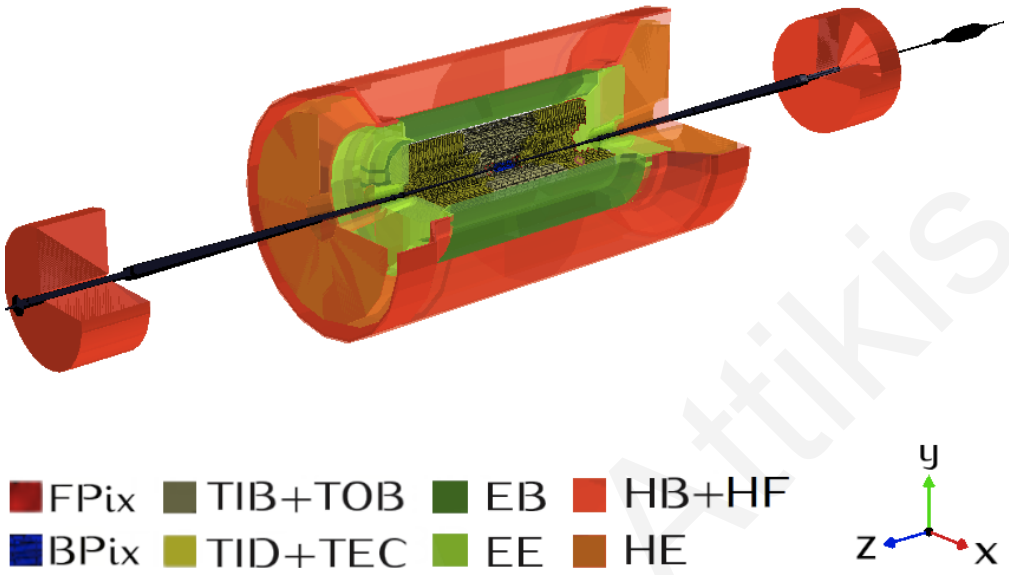

Figure 3.24: Layout of the complete CMS HCAL detector, as visualised by Fireworks [38]. Parts of the CMS detector have been cut away for visualisation purposes.

after the last stainless steel plate. The exact plate configuration is summarised in Table 3.8. The staggered wedge geometry provides a total absorber thickness of 5.82λ at $|\eta| = 0$, which increases with polar angle θ as $1/\sin\theta$, resulting in 10.6λ at $|\eta| < 1.3$. Each scintillator tile is segmented to provide a granularity of $\Delta\eta \times \Delta\phi = 0.087 \times 0.087$ and it is instrumented with a WaveLength-Shifting (WLS) fibre. As the hadroniccascade showers develop due to brass absorber material, particles pass through the alternating scintillator layers, causing them to emit photons in the blue-violet spectrum. The gaps between tiles are filled with a reflective paint to ensure that light produced in each tile does not escape into neighbouring ones. The WLS fibres are used to absorb this light and their wavelength to the green region of the spectrum, while clear optic fibres then carry the green light away to readout boxes located within the HCAL volume. Before they are saved, the optical signals are amplified and digitised by Hybrid Photo-Diode (HPD) photosensors, which use the photoelectric effect to convert light to an electric signal and a silicon diode target to amplify it.

The endcap part of the CMS HCAL is the hermetic HE which covers the very active pseudorapidity range $1.3 < |\eta| < 3.0$, a region occupied by about 34% of the particles produced in an LHCbunch-crossing. Therefore, the HE is required to be radiation resistant and have enough granularity to cope with the high flux of particles. Furthermore, as the HE sits at the end of the $3.8T$ solenoid magnet, it has to be made of non-magnetic materials while also being thick enough to present an adequate number of interaction lengths to fully contain hadroniccascade showers. Similarly to HB, the material chosen for these tasks was brass. The absorber design is such as to minimise crack between HB and HE, and its resolution is

Table 3.8: The staggered configuration of material in an HB wedge.

Layer	Material	Thickness (mm)
0	plastic scintillator	9 mm
	stainless steel	40 mm
1 – 8	plastic scintillator	3.7 mm
	brass absorber	50.5 mm
9 – 14	plastic scintillator	3.7 mm
	brass absorber	56.5 mm
15+16	plastic scintillator	3.7 mm
	stainless steel	75 mm
	plastic scintillator	9 mm

limited by parton fragmentation, pile-up and magnetic effects [59, 60]. The HE is divided into 18 20° ϕ-sectors, in a geometry that matches the barrel part of the hadron calorimeter. The absorbers are composed entirely of 79 mm-thick brass plates with 9 mm gaps to accommodate 19 3.7 mm-thick scintillators. These provide a granularity of $\Delta\eta \times \Delta\phi = 0.087 \times 0.087$ for $1.3 < |\eta| < 1.6$, thus matching the HB, which however deteriorates to $\Delta\eta \times \Delta\phi \approx 0.17 \times 0.17$ for $1.6 < |\eta| < 3.0$. The total length of the HE is about 10λ.

The outer part of the CMS HCAL is the HO which is located outside of the solenoid magnet. It covers the central region of pseudorapidity range $|\eta| < 1.26$, a region in which the stopping power of the EB and HB does not provide sufficient containment of the hadroniccascade showers. The HO thus utilises the additional absorber thickness of $1.4/\sin\theta\lambda$ to identify these later showers. The size and position of scintillator tiles in the HO approximately match the HB layers, providing a similar granularity of $\Delta\eta \times \Delta\phi \approx 0.087 \times 0.087$. The HO consists of 5, each 2.54 m wide along the z-axis and each having 12 identical ϕ-sectors. The central ring (ring 0) consists of 2 scintillator layers which are 10 mm thick, at a radial distance of 3850 mm and 4097 mm from the IP5. The rest of the rings ($\pm 2, \pm 1$) only have 1 layer of scintillator tiles, at a radial distance of 4097 mm. The scintillation light produced by hadroniccascade showers within the CMS detector that reach the HO calorimeter is collected by WLS fibres and transported to photodetectors with clear fibres, in similar fashion as in HB. The additional thickness provided by the HO increases the total depth of the CMS calorimeter system to a minimum of 11λ for the pseudorapidity range $|\eta| < 1.26$.

The very forward location of the HFs, results in an unprecedented average energy deposited of 760 GeV per LHCbunch-crossing, with a pronounced maximum at the highest rapidities. Compared to the rest of the detectors which receive about 100 GeV, this is a significant difference. The radiation-wise hostile environment that the HFs are exposed to was the primary factor when considering their design, aiming for a lifetime corresponding to 10 years of LHC operations. The HF calorimeters are symmetrically positioned 11.2 m away from the IP5 and centred around the beam pipe. Each HF is essentially a cylindrical steel structure of outer radius 1.3 m, covering a pseudorapidity range of $3.0 < |\eta| < 5.2$. Each of this cylindrical structures is divided into 18 20° ϕ-wedges, composed of 5 mm-thick steel absorber plates, with quartz fibres embedded into dedicated grooves. The full depth

of the absorber is 1.65 m, which corresponds to about 10λ. The quartz fibres, which were chosen as the active medium of the calorimeter, primarily due to their radiation hardness, run parallel to the beam line and are bundled in such a way as to provide a granularity of $\Delta\eta \times \Delta\phi = 0.175 \times 0.175$. They are used to generate Cherenkov light emitted by particles traversing the active medium, with energy above the Cherenkov threshold , thereby rendering the calorimeter more sensitive to the electromagnetic component of cascade showers. In order to enhance the ability to distinguish between electromagnetic and hadroniccascade showers, the HF employs 2 set of quartz fibres which are read out separately. Half of the quartz fibres run over the full width of the steel absorber, while the other half start at a depth of 0.22 m from the face of the calorimeter. In this way, electromagnetic showers can be distinguished from hadroniccascade showers, due to the fact that the former deposit a large fraction of their energy in the first 0.22 m, while the latter produce nearly equal signal on average over the 2 segments. The light produced in the quartz fibres is directed via lightguides into a shielded area where it is detected by Photomultiplier Tubes (PMTs). The CMS HCAL subsystems are summarised in Table 3.9.

Table 3.9: Overview of the CMS HCAL subsystems.

System	η-coverage	Active Medium	Radiation length
HB	$\lvert\eta\rvert < 1.3$	plastic scintillators	$5.82 - 10.6\lambda$
HE	$1.3 < \lvert\eta\rvert < 3.0$	plastic scintillators	$\sim 10\lambda$
HO	$\lvert\eta\rvert < 1.26$	plastic scintillators	$\geq 11\lambda$[10]
HF	$3.0 < \lvert\eta\rvert < 5.2$	quartz fibres	$\sim 10\lambda$

3.3.6 Muon system

The muon system of the CMS detector [43, 45, 61] is the last detector layer encountered by a particle emerging from the IP5, whose task is three-fold; to identify muons passing through the detector material, to measure their momentum, and to trigger events based on their presence. The muon momentum resolution and triggering capabilities are made possible by the presence of the strong solenoid magnet and its flux return yoke, which not only provides the required bending Lorentz force but also absorbs hadrons that escape the calorimetry system. Due to the fact that muons are MIPs, unlike most particles they can punch-through the detector material preceding the muon system whose total thickness is shown in Fig. 3.25, and the several metres of iron in the return yoke without interacting. Therefore, muon chambers are placed as the last detector layer, since muons are the only particles likely to register a signal there.

The solenoid magnet shape led to the natural decision to design a muon system with a closed cylindrical shape, with a Muon Barrel (MB) and two Muon Endcaps (MEs) that close it, as shown in Tools:Muon-3D-View. The deposition of energy and the subsequent

[10] Including the radiation length provided by HB.

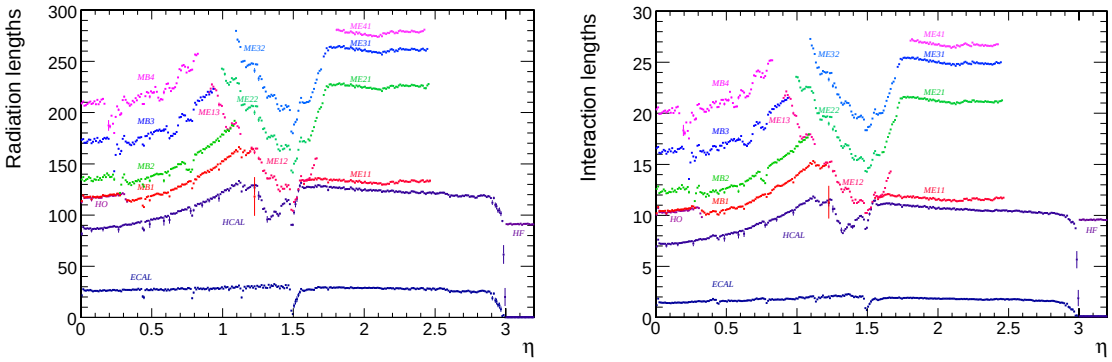

Figure 3.25: Material thickness in radiation lengths X_0 (a) and interaction lengths λ (b) at various depths of the CMS detector, as a function of pseudorapidity η. Taken from Ref. [62].

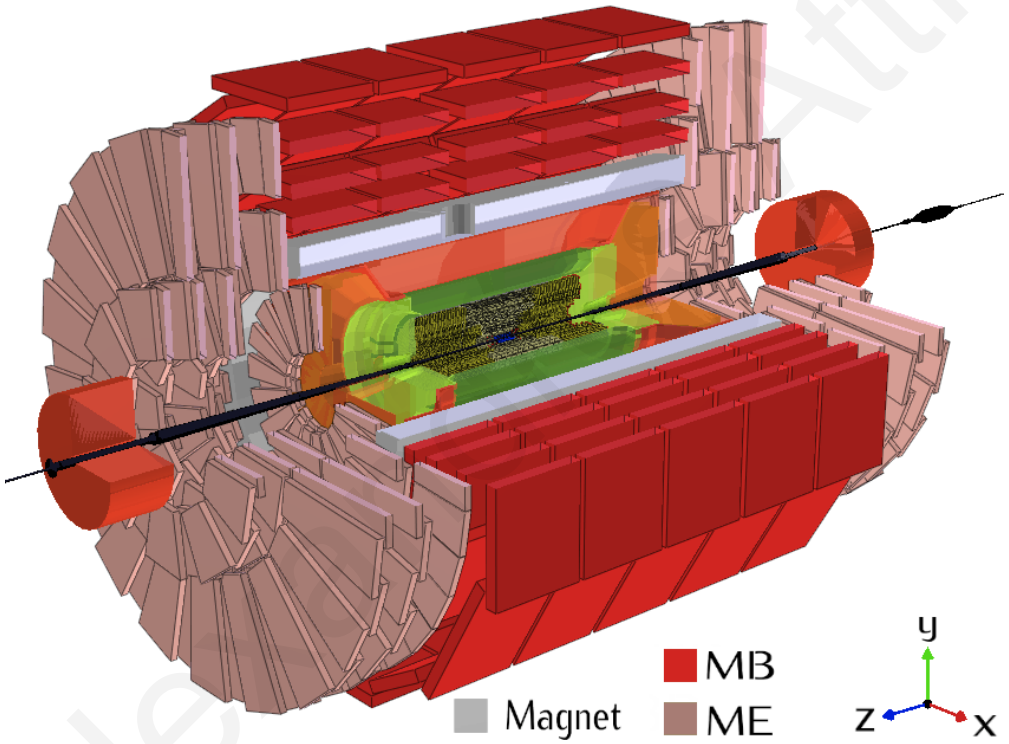

Figure 3.26: Layout of the complete CMS muon detector, as visualised by Fireworks [38]. Parts of the CMS detector have been cut away for visualisation purposes.

detection of muons in the CMS muon system proceeds through the ionisation of an active gas volume and the collection of the resulting ions. The CMS muon system employs 3 different types of gaseous particle detectors for muon identification; Drift Tubes (DTs), Cathode Strip Chambers (CSCs) and Resistive Plate Chambers (RPCs). The DTs measure muon position in the barrel part of the detector, where the neutron-induced background and muon rates are small, while the 3.8T magnetic field is uniform and mostly contained in the iron return yoke. The CSCs are used in the endcaps, where the magnetic field is uneven and particle rates are high, while the RPCs are used in both the barrel and endcaps to provide fast decisions for the muon trigger system. The layout of the muon system is shown in Fig. 3.27 for a r-z quarter slice of the CMS.

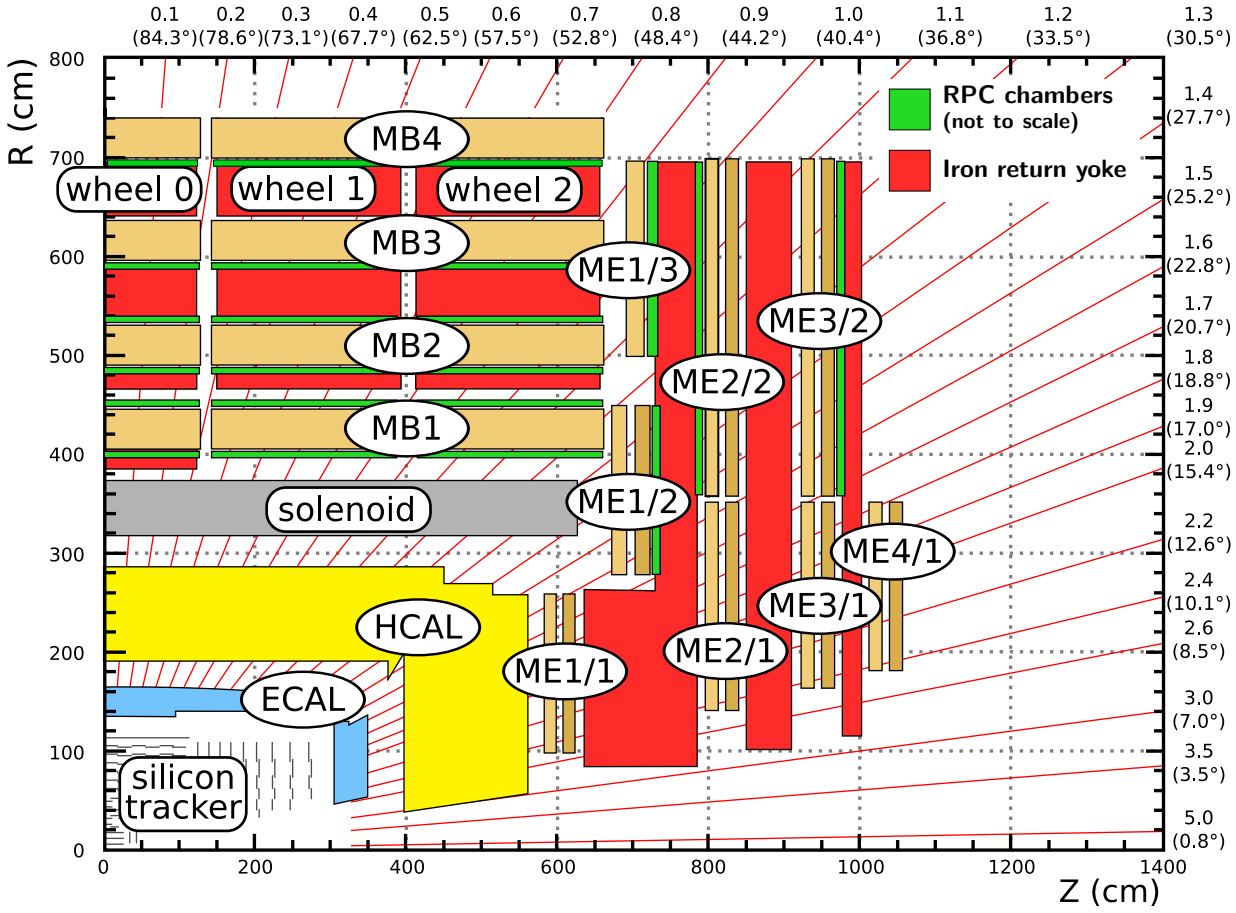

Figure 3.27: Schematic of one-quarter of the CMS muon system, in the r-z view, showing the locations of DTs, CSCs and RPCs in the barrel and endcap regions. Taken from Ref. [63].

The barrel DTs of the CMS muon system, cover the pseudorapidity range $|\eta| < 1.2$ and are organised into 4 concentric cylindrical stations (MB1-MB4), which are interspersed with the iron return yoke layers and house 250 in total chambers. Each muon station consists of 5 wheels, each divided into 12 30° ϕ-sectors. The 3 innermost stations (MB1,MB2 and MB3) have 60 drift chambers each, while the outermost station (MB4) has 70, resulting in about 172000 sensitive wires. A DT chamber is made of 3(or 2) SuperLayers (SLs), as shown in Fig. 3.28, which are the smallest independent units of the design and are each comprised of 4 consecutive layers of rectangular DT cells. The DT cells are offset by a half-cell width with respect to their neighbour to ensure that no dead spots are present. Within a given DT chamber, the 2 outer SLs are oriented parallel to the beam axis ($SL_{r\text{-}\phi}$) to provide measurements of muon tracks in the magnetic bending plane (r-ϕ), while the inner SL is orthogonal to the beam axis to provide z-position measurements ($SL_{r\text{-}z}$). Therefore, a muon emerging from the IP5 passes through a ϕ-measuring SL, then a z-measuring SL followed by another ϕ-measuring SL. The $SL_{r\text{-}z}$ layer is absent in the fourth station (MB4), which therefore provides no z-position measurement. When a muon traverses a DT cell, whose main properties are shown in Table 3.10, it ionises the active Ar/CO_2 gas volume inside and the resulting electrons are collected to the 2.4 m-long anode wire to which they drift due to the presence of a strong electric field. The dimensions of a DT cell are $42 \times 13\,mm^2$, as shown in Fig. 3.29, which means the maximum path that the electrons have to drift is about

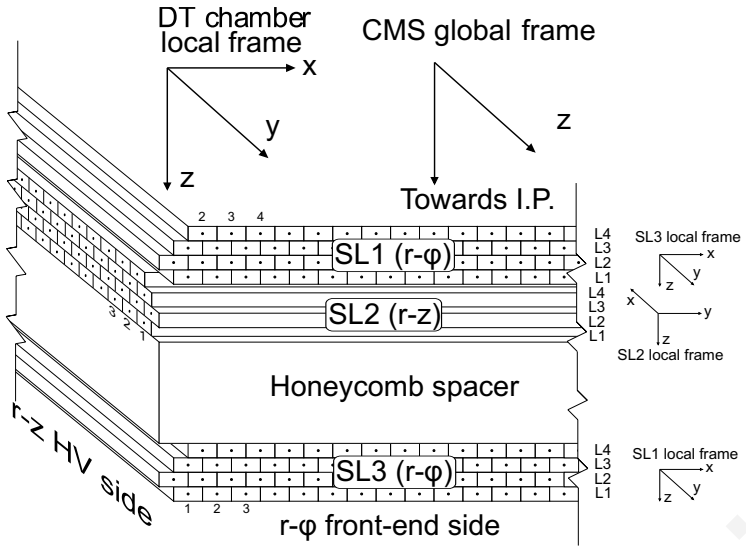

Figure 3.28: The layout of a DT chamber inside a muon barrel station. Taken from Ref. [64].

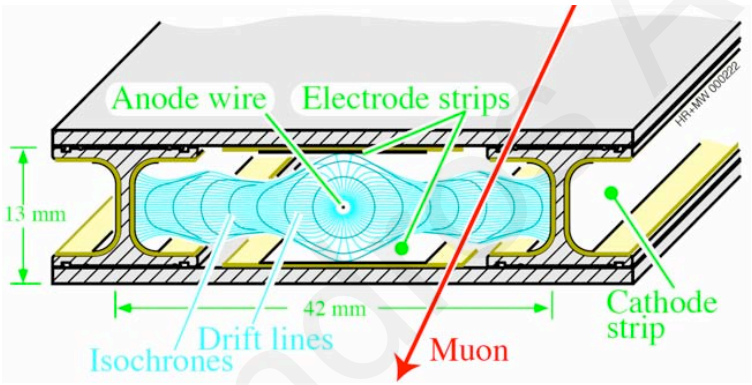

Figure 3.29: Schematic view of a DT cell. The drift lines of the electrons are shown, along with isochrone lines which connect places from which it takes the same time to drift to the anode. In the presence of a strong magnetic field these lines become distorted. The presence of electrodes is necessary to optimise the drift lines. Taken from Ref. [43].

Table 3.10: The properties of a DT cell of the CMS muon system.

Quantity	Value	Unit
Composition	85%	Ar
	15%	CO_2
Gas gain	10^5	
Anode voltage	+3.6	kV
Cathode voltage	−1.2	kV
Electrode voltage	+1.7	kV
Dead time	150	ns

21 mm, corresponding to a drift time of about 380 ns. This value, which is determined by the size of the cell, the electric field and the gas mixture, is small enough to ensure a low occupancy of the DT cells which are large enough to limit the number of active channels to an affordable value. By registering where along the anode wire the ionised electrons

hit and by calculating the muon drift distance, the DTs give two coordinates for the muon position with a single wire resolution of about 100 μm for the r-ϕ measurement.

As every other CMS detector located in the more forward regions, the endcap part of the CMS muon system experiences large background levels and high muon rates. However, unlike the rest of the CMS forward detector systems, the muon endcaps are not enclosed inside the magnet solenoid and hence are exposed to a large magnetic field that is non-uniform. Thus, due to the high particle flux and large magnetic field strength, the use of DTs in the forward regions is not suitable as the drift path of electrons becomes too long. Consequently, the CMS ME is equipped with 468 radiation resistant, fine segmented CSCs with fast response time that cover the pseudorapidity range $0.9 < |\eta| < 2.4$. In each endcap, the CSCs are organised into 4 stations of chambers (ME1-ME4), in order of increasing distance from the IP5. These chambers are mounted on the disks enclosing the CMS solenoid magnet and are oriented perpendicularly to the beam axis and interspersed with the iron return yoke plates. Each disk has 2 concentric rings around the beam axis where the CSCs are placed, except for ME1, which has 3. The CSC chambers have a trapezoidal shape, as shown in Fig. 3.30 (a) and cover 10° or 20° in the azimuthal angle ϕ. They are MultiWire Proportional Chambers (MWPCs),

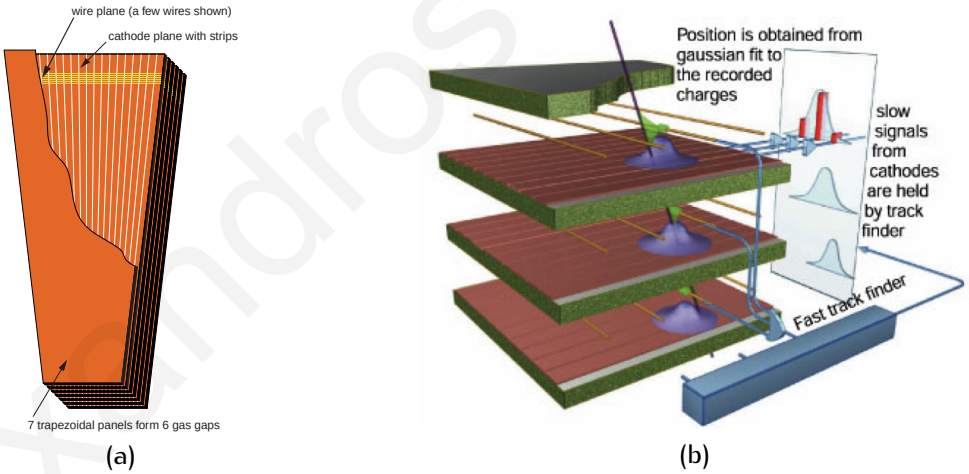

Figure 3.30: Schematic view of a CSC chamber of the CMS muon system (a) and illustration of the principle of obtaining a precise localisation of an avalanche along a wire in a CSC (b). Taken from Ref. [43] (a) and Ref. [65] (b) .

comprised of 6 anode wires interleaved with 7 cathode panels that form 6 gas gaps. They operate on the principle that if an electric field is established in a gas, the electrons released when a charged particle ionises the gas volume will drift to the anode wire. With a high enough field strength, drifting electrons gain enough energy to cause secondary ionisation and so forth, leading to an avalanche of secondary electrons which can be collected as a pulse at the anode. In the CSC trapezoidal geometry, the anode wires are arranged in a plane between a common pair of cathode strips, each wire acting as a standalone detector. Since the cathode strips and anode wires are perpendicular to each other, 2 position coordinates are obtained for each passing particle traversing the active gas volume. The anode wires run azimuthally and measure a muon's radial coordinate, while strips that are machined in the cathode panels run at constant azimuthal angle ϕ, thus providing the azimuthal angle

measurement by a Gaussian fit to the charge induced in the strips as shown in Fig. 3.30 (b). In total, the CSC chambers are comprised of about 2×10^6 wires, with an active gas volume of $> 50\,m^3$ and a sensitive area of $5000\,m^2$, resulting in 220000 (180000) cathode (anode) read-out channels. The off-line spatial resolution provided by the CSCs is about $75 - 150\,\mu m$ for the r-ϕ measurement. Moreover, besides being able to accurately identify muons, the closely spaced wires make the CSCs fast detectors suitable for triggering.

In both the barrel and endcap sections of the CMS muon system, RPCs are employed as a dedicated muon trigger, while also contributing to the muon identification and reconstruction alongside DTs and CSCs. In MB, the 480 RPCs are sorted in 6 layers, 2 in each of the first 2 stations (MB1-MB2), and 1 in each of the last 2 stations (MB3-MB4) covering the pseudorapidity range $|\eta| < 1.2$. In ME, 432 RPCs are found in 1 plane in each of the first 3 stations (ME1-ME3), covering the pseudorapidity range $0.9 < |\eta| < 1.6$. At a later stage, the endcap regions will be equipped with an additional layer that will increase the RPC coverage in the endcaps to $0.9 < |\eta| < 2.1$. Thus, there are 6 RPC layers in the central region, and 3 RPC layers in the forward region. The RPCs are fast gaseous detectors with a coarse spatial resolution and a precise time measurement, whose main properties are shown in Table 3.11. They consist of 2 parallel plates, an anode and a cathode as shown in Fig. 3.31, both made

Table 3.11: The main properties of an RPC used in the CMS muon system.

Quantity	Value	Unit
Gas Composition	90%	Freon $C_2H_2F_4$
	5%	Isobutane C_4H_{10}
Gas gap width	2	mm
Gas gaps	2	
bakelite thickness	2	mm
Operating voltage	8.5-9.0	kV

of bakelite, a plastic material of very high resistivity. These double-gap plates, which are

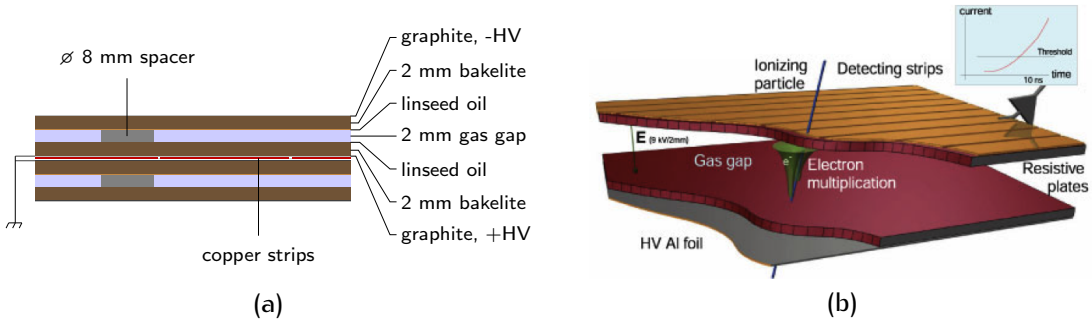

Figure 3.31: Schematic view of a double-gap RPC chamber of the CMS muon system (a), and diagram illustrating the operation principle (b). Taken from Ref. [63] (a) and Ref. [65] (b) .

coated with graphite to make electrodes, are separated by a gas volume that is ionised when a muon passes through the chamber, and the resulting electrons are accelerated in an electric field to create an avalanche of electrons. These electrons are collected by external aluminium strips instead of the electrodes, which are transparent to the electrons.

The geometry of the RPC strips is primarily decided by the need to trigger on the muon transverse momentum. Each of the 912 in total RPC chambers contains a plane of strips, which are rectangularly segmented in the barrel and oriented parallel to the bream axis, whereas the endcaps are equipped with trapezoidal shaped strips providing a granularity of $\Delta\eta \times \Delta\phi \approx 0.1 \times 0.1$. Overall, the RPCs provide a spatial resolution of about 1 cm and a time resolution of $\lesssim 3$ ns, a time interval much shorter that the LHCbunch-crossing period of 25 ns.

To conclude, the CMS muon subsystems, which are summarised in Table 3.12, provide 4 measurement points via the DT and CSC detectors, except for a gap at $|\eta| \approx 1.4$, where only 3 measurement points are provided. In addition, the RPC subsystem provides 6 measurements in the barrel region and 3 in the endcaps, enabling a relatively good muon momentum estimation even without the use of the tracking system. Furthermore, the excellent time resolution provided by the RPC subsystem provides an unambiguous identification of the relevant LHCbunch-crossing to which a muon track is associated, even at the high rates and large backgrounds expected at nominal LHC operations, constituting the CMS muon system as fully adequate for the muon trigger system purposes. All the muon subsystems -DTs,CSCs and RPCs- contribute to the CMS trigger sytem, which is described in Section 3.3.8.

Table 3.12: Overview of the CMS muon subsystems. Gas mixtures are subject to change during commissioning and operation periods.

System	η-coverage	Active Medium
DTs	$\lvert\eta\rvert < 1.2$	Gas volume (85% Ar, 15% CO_2)
CSCs	$0.9 < \lvert\eta\rvert < 2.4$	Gas volume (30%Ar, 50%CO_2, 20%CF_4)
RPCs	$\lvert\eta\rvert < 1.6$	Gas volume (95.5% $C_2H_2F_4$, 4.5% C_4H_{10})

3.3.7 Expected subdetector performance

The CMS muon system provides good muon identification and momentum resolution over a wide range of momenta and pseudorapidities, as shown in Fig. 3.32. As also indicated in the same figure, good charged-particle momentum resolution is provided from the inner tracker, while the overall performance is enhanced significantly at high p_T by combining information from the muon and the tracking systems. Furthermore, good dimuon mass resolution is achieved of about 1% at 100 GeV, while the charge of muons with $p < 1$ TeV is also unambiguously determined.

The performance of the CMS tracking system is summarised in Figures 3.33 and 3.34, whereby the expected resolution of transverse momentum, transverse impact parameter and longitudinal impact parameter for single muons of transverse momenta of 1, 10 and 100 GeV are presented, as a function of pseudorapidity η. For momentum tracks at around 100 GeV, where multiple scattering in the tracker material is significant (20 – 30% in resolution), a transverse momentum resolution of about 1 – 2% is achieved in the central regions of

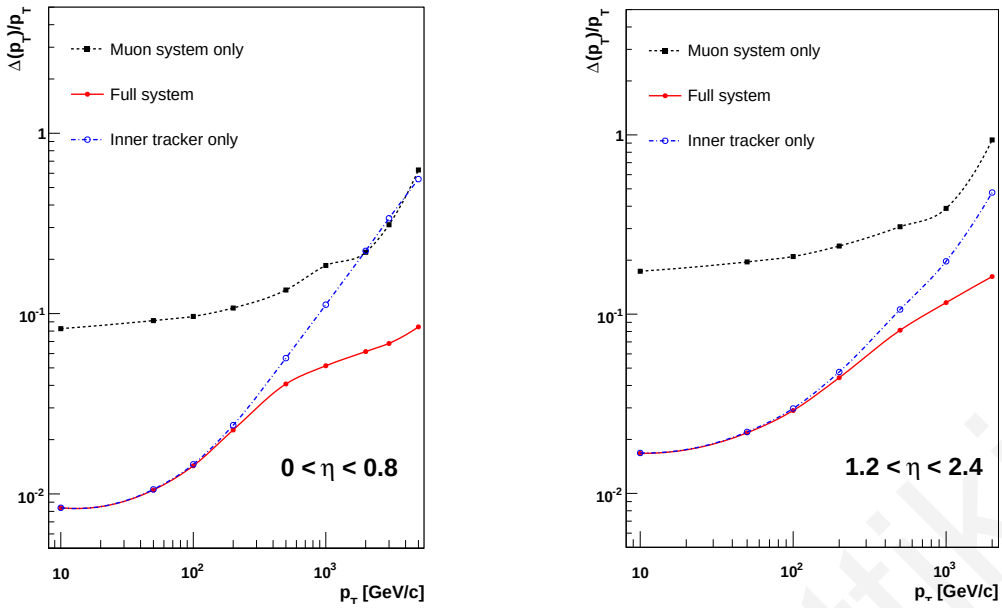

Figure 3.32: Expected muon transverse momentum resolution as a function of the transverse momentum (p_T), for the pseudorapidity acceptance $|\eta| < 0.8$ (a) and $1.2 < |\eta| < 2.4$ (b), using the muon system only, the inner tracking only, and both. Taken from Ref. [43].

$|\eta| \approx 1.6$. The transverse impact parameter resolution, shown in Fig. 3.34 (a) as a function of pseudorapidity η, reaches the 10 μm-level for high p_T tracks. This resolution performance is dominated by the resolution of the first pixel hit, while at lower momenta it is degraded by multiple scattering. A similar behaviour is exhibited for the longitudinal impact parameter resolution, shown in Fig. 3.34 (b), with however a stronger dependence on the pseudorapidity η.

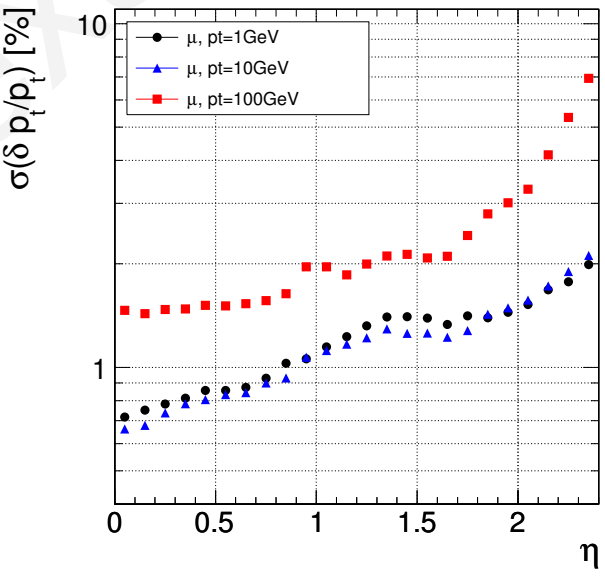

Figure 3.33: Expected Transverse momentum resolution for single muons with transverse momenta of 1, 10 and 100 GeV, using the tracking system. Taken from Ref. [43].

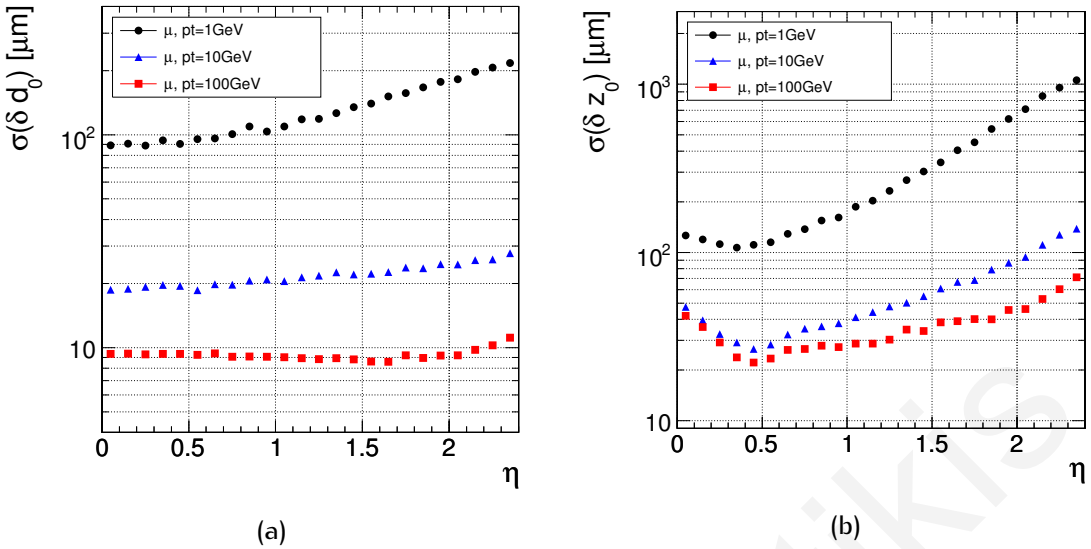

Figure 3.34: Resolution of the transverse (a) and longitudinal (b) impact parameter, for single muons with transverse momenta of 1, 10 and 100 GeV. Taken from Ref. [43].

The ECAL system with its crystal technology ensures an excellent EM energy resolution, good diphoton and dielectron mass resolution of about 1% at 100 GeV. Additionally, it has a wide geometric coverage and can provide strong π^0 rejection, while also efficiently enabling the isolation of photons and leptons, even at high luminosities. The ECAL energy resolution, as measured from electron test beams is shown in Fig. 3.35, and can be parametrised as follows[11] [43]

$$\frac{\sigma_E}{E} = \frac{S}{\sqrt{E}} \oplus \frac{N}{E} \oplus C, \tag{3.31}$$

where the energy (E) is in GeV. The term $S = 2.8\%\,\text{GeV}^{1/2}$ is a stochastic term attributed to fuctuations in the lateral shower containment and in the energy released in the Preshower system. The term denoted $N = 12\%\,\text{GeV}$ is noise, caused by the electronics, the digitization and pile-up, while the term $C = 0.3\%$ is a constant term that arises due to intercalibration errors, energy leaks from the back of the crystals and due to the light collection being non-uniform. The values of these terms were determined through fits to the test beam results.

For the HCAL, the resolution is described as

$$\frac{\sigma_E}{E} = \frac{S'}{\sqrt{E}} \oplus C', \tag{3.32}$$

with $S' = 90\%\,\text{GeV}^{1/2}$ and $C' = 4.5\%$ for the HB, HO and HE. The corresponding resolution for the the HF is also given by Eq. (3.32), with $S' = 172\%\,\text{GeV}^{1/2}$ and $C' = 9\%$. However, as most particles start showering in the ECAL, the response and resolution of the CMS calorimeter system depends on both the ECAL and the HCAL. It is thus more useful to refer to the energy resolution achieved by combining measurements from both the ECAL and HCAL. This can be

[11] $a \oplus b = \sqrt{a^2 + b^2}$.

written as [66]

$$\frac{\sigma_E}{E} = \frac{S''}{\sqrt{E}} \oplus C'', \tag{3.33}$$

with $S'' = 84.7 \pm 1.6\,\mathrm{GeV}^{1/2}$ and $C'' = 7.4 \pm 0.8\%$ [67]. The energy resolution in the endcaps is similar to that in the barrel. The large hermetic geometric coverage and the fine lateral

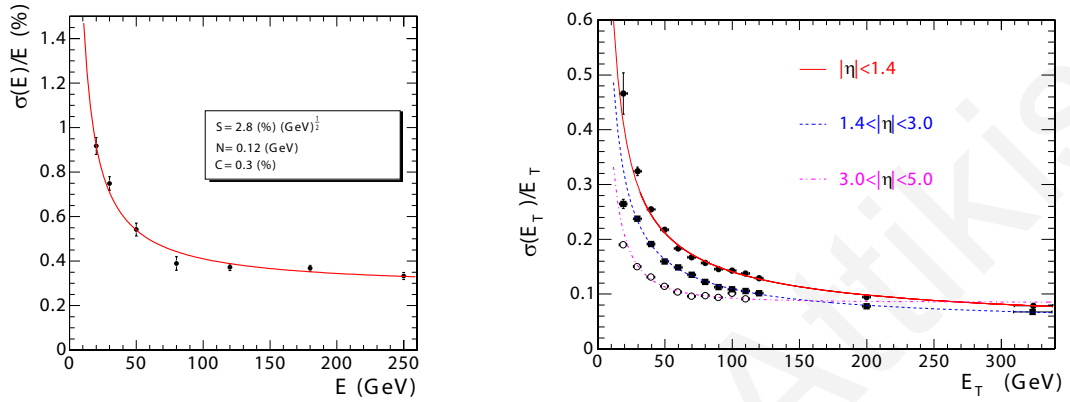

Figure 3.35: ECAL energy resolution as a function of electron energy, as measured from test beams (a). The energy was measured in an array of 3×3 crystals, with an electron impacting the central crystal. In (b), the jet transverse-energy resolution, as a function of the jet transverse energy for the barrel, endcap and very forward regions, $|\eta| < 1.4$, $1.4 < |\eta| < 3.0$ and $3.0 < |\eta| < 5.0$, respectively. The jets were reconstructed with an iterative cone algorithm with cone radius $\Delta R = 0.5$. Taken from Ref. [43].

segmentation of the HCAL also provide good $E_{\mathrm{T}}^{\mathrm{miss}}$ and di-jet-mass resolution.

3.3.8 Trigger and data acquisition

The 2 counter-rotating proton beams are focused to cross each other in the centre of the CMS detector every 25 ns at the LHC design operation, which corresponds to a bunch crossing frequency of 40 MHz. At the design luminosity of $10^{34}\mathrm{cm}^{-2}\,\mathrm{s}^{-1}$ for proton-proton collisions, this corresponds to an average of $\sim$ 20 simultaneous interactions per event, which results in a total event rate of $\sim$ 1 GHz. As shown in Table 3.1 on page 44, about less than half of these interactions are just elastic collisions, with protons scattering diffractively off each other to a very forward direction. Such events will be analysed by the TOTEM experiment, which is also located at IP5, to provide measurements for the total proton-proton cross section and for studying elastic and diffractive scattering. On the other hand, the CMS experiment was designed to investigate inelastic collisions, whereby the protons collide head-on providing more energy localisation in a point-like state and thus making it available for conversion to new particles. However, the CMS detector cannot possibly record every inelastic collision that takes place at IP5, but instead it has to decide which events are interesting enough to store and which can be discarded. For this reason, CMS employs a trigger system Ref. [43, 45, 68, 69], that is able to select only interesting events

as defined by the CMS Collaboration, while achieving a drastic event rate reduction. This task is accomplished in 2 steps; the Level-1 (L1) Trigger and High-Level Trigger (HLT).

The L1 Trigger is hardware-based and consists of custom-designed and largely programmable electronics capable of analysing every LHCbunch-crossing. Its design is such as to support an output rate limit of 100 kHz, although in practise this is limited to $\sim$ 30 kHz, so as to provide a safety factor of three. Therefore, it has the capability of achieving a rate reduction of the order of $\sim 10^4$, from the LHC design interaction rate of $\sim$ 1 GHz down to the maximum output rate of 100 kHz. The L1 Trigger decision is based on coarsely segmented data originating from the the CMS calorimeter and muon systems, while the L1 Trigger latency, which is the time interval between a given bunch-crossing and the distribution of a L1 Trigger decision to the front-end detector electronics, is about 3.2 μs. During this time the high-resolution data of all the subdetectors is stored in pipelined memories in the front-end electronics. The L1 Trigger, whose architecture is schematically shown in Fig. 3.36, is comprised of the L1 Calorimeter Trigger (CT), the L1 Muon Trigger (MT) and the L1 Global Trigger (GT), with the 2 former being composed of 3 hierarchical components; Local, Regional and Global. The Local Triggers, which are also called the Trigger Primitive

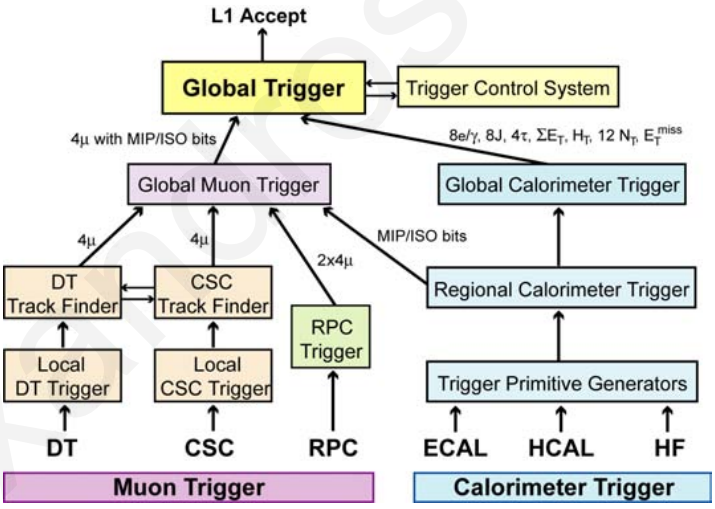

Figure 3.36: Schematic diagram of the CMS L1 Trigger architecture. Taken from Ref. [43].

Generators (TPGs), use information provided by calorimeter Trigger Tower (TT) in the form of energy deposits, and from the muon system in the form of hit patterns or track segments. The Regional Triggers combine this information and employ pattern logic to create a list of trigger objects, such as electron and muon candidates, which is sorted in terms of energy (or momentum) and quality expressing the level of confidence in the L1 parameter measurements. The Global Calorimeter and Muon Triggers determine the best candidate trigger objects across the entire CMS detector and transfer them to the GT, which sits at the top of the CMS L1 hierarchy and makes the final decision of rejecting an event or forwarding it to the HLT for further processing. Apart from algorithm calculations, this decision also depends on the Trigger Control System (TCS), which provides information on the readiness of all the subdetectors and the DAQ system. Finally, the Timing, Trigger and Control (TTC) system

communicates the Level-1 Accept (L1A) decision to all the CMS subdetectors. An overview of the CMS L1 Trigger is shown in Table 3.13.

Table 3.13: Overview of the CMS L1 Trigger.

Quantity	Value	Unit
Input rate	~ 1	GHz
Output rate (Safe)	100 (~ 30)	kHz
Rate reduction factor	$\sim 10^4$	
Latency	3.2	μs

3.3.8.1 Calorimeter trigger

The first step in the L1 CT is the TPG, which uses calorimeter TT to sum up the transverse energies in ECAL crystals or HCAL read-out towers and assign the correct bunch-crossing number. In total the CMS calorimeter trigger has 4176 towers, with 2448 found in the barrel, 1584 in the endcaps and 144 in the forwards calorimeters, as shown in Fig. 3.37. These TTs, which have a 1 : 1 correspondence between ECAL andHCAL, are segmented to provide a granularity of $\Delta\eta \times \Delta\phi = 0.087 \times 0.087$ for the region $|\eta| < 1.74$, beyond which the TTs are larger. For most of the CMS ECAL, a 5×5 array of $PbWO_4$ crystals is mapped into TTs. The TPGs, whose electronics are integrated with the calorimeter read-out, are transmitted to

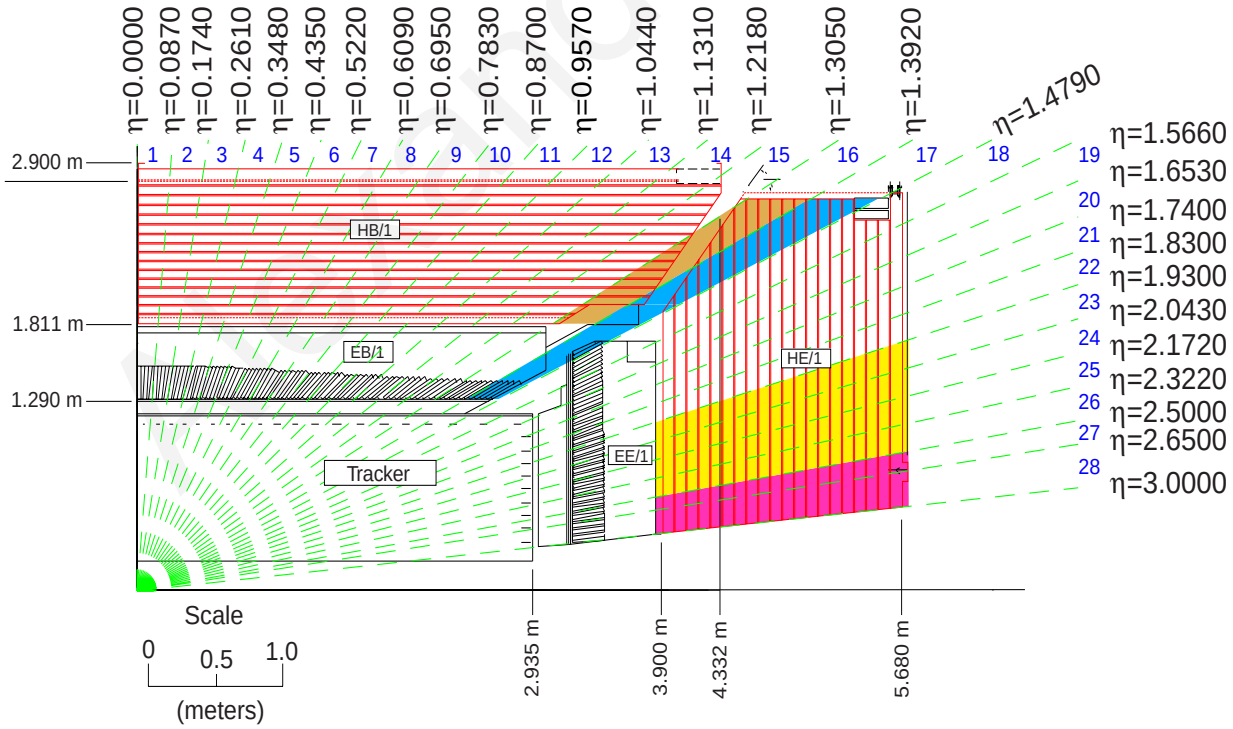

Figure 3.37: Schematic of one-quarter of the CMS L1 Calorimeter TTs, in the r-z view. The filled coloured areas indicate Calorimeter TTs, which have dimensions $\Delta\eta \times \Delta\phi = 0.087 \times 0.087$ for $|\eta| < 1.74$, beyond which the become larger. Taken from Ref. [68].

the Regional Calorimeter Trigger (RCT) through high-speed serial links. The RCTs determine

regional trigger object candidates such as transverse energy sums per calorimeter region, excluding the HF, to determine τ-veto bits on jets for $|\eta| < 3.0$. It also determines trigger object candidates, such as electrons/photons ($e^{\pm}$, γ), through a dedicated algorithm whose overview is shown in Fig. 3.38. The algorithm uses a 3×3 TT sliding window technique and is applied across the entire ECAL region to determine the tower with the largest energy deposit, called the central hit TT. The $e^{\pm}/\gamma$ candidate E_T is then determined by summing the E_T in the hit tower, with the maximum E_T tower of its 4 broad-side neighbours. Isolated

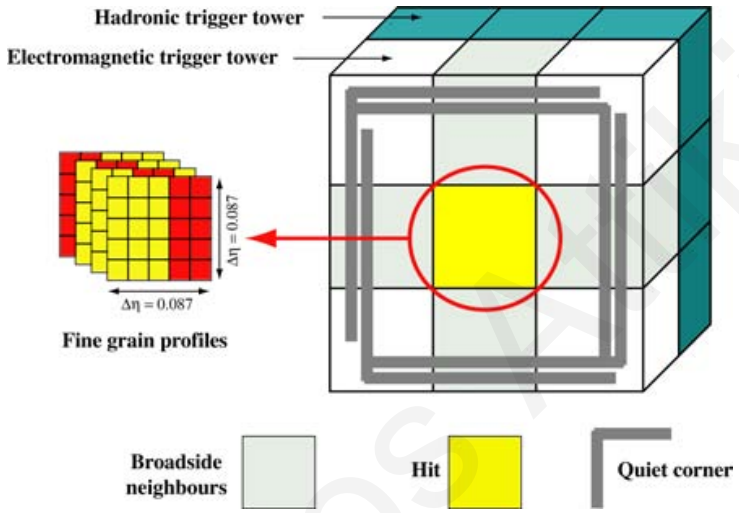

Figure 3.38: Overview of the CMS L1 Calorimeter Trigger electron/photon algorithm. Taken from Ref. [43].

and non-isolated $e^{\pm}/\gamma$ candidates within $|\eta| < 2.5$ are also separetely determined, based on the lateral extension of cascade showers and the ratio of deposited energies in the hadronic and EM sections. Thus, a non-isolated $e^{\pm}/\gamma$ candidate is one that passes these 2 shower profile vetoes. Isolated $e^{\pm}/\gamma$ candidates require passing of 2 additional vetoes, the first of which is based on passing the cascade shower profile constrain on all 8 nearest neighbours. The second additional veto is based on there being at least 1 quiet corner made of 4 groups of 5 EM towers surrounding the hit tower. In total, 4 isolated and for non-isolated $e^{\pm}/\gamma$ candidates per region are selected. In addition, RCTs calculate muon information related to their isolation and their compatibility with MIPs, providing muon Isolation (ISO) and MIP bits, respectively. A muon is considered isolated if the energy deposit in the relevant calorimeter region from which it emerges is below a predefined theshold. The last step performed by the RCT is to determine the highest-ranking trigger object candidates and feed them to the Global Calorimeter Trigger (GCT). All calorimeter trigger object candidates are collected from the entire CMS detector to the GCT, which determines jets, the total transverse energy ($\sum E_T$) and missing transverse energy (E_T^{miss}), jet multiplicity and the scalar transverse energy sum of all jets above a given threshold (H_T). The jets are found with a 4-stage clustering technique, whereby they are classified as τ jets if none of the corresponding RCT regions have a τ-veto bit set. The classification relies on the fact that τ jets are narrower than ordinary quark/gluon jets. After sorting all trigger object candidates, up to 8 jets and 4

τ jets are forwarded to the GT, along with the magnitude and direction of E_T^{miss}, twelve jet multiplicities (N_T) for different programmable E_T thresholds and optionally $\eta - \phi$ regions, the total transverse energy ($\sum E_T$) and the scalar transverse energy sum of all jets above a given threshold (H_T). The 4 isolated and 4 non-isolated $e^{\pm}/\gamma$ candidates, which are received from the RCT, are also forwarded to the Global Muon Trigger (GMT).

3.3.8.2 Muon trigger

The DTs, CSCs and RPCs of the muon system provide information to the L1 Muon trigger, which covers the pseudorapidity range $|\eta| < 2.1$, with plans for extending it to $|\eta| < 2.4$. The DT chambers in the barrel, provide local trigger information in the form of track segments in the azimuthal angle ϕ-projection and hit patterns in the pseudorapidity η-projection. The CSCs, which are located in the endcaps, deliver 3-dimensional track segments while both the DTs and CSCs help in identifying the bunch-crossing associated to the event under investigation. Additionally, the DT and CSC Track Finders are responsible for completing tracks and assigning physical parameters to them, and together they comprise the Regional Muon Trigger (RCT). The RPC trigger chambers, which are located both in the barrel and the endcaps, also play an important role in delivering their own track candidates with excellent time resolution. All this information is delivered to the GMT which combines it to obtain an improved momentum resolution and efficiency, relative to the stand-alone systems.

The DT local trigger is comprised of the Bunch and Track Identifiers (BTIs), the Track Correlators (TRACOs), the Trigger Servers (TSs) and the Sector Collectors (SCs), as shown in Fig. 3.39. The BTIs use signals caused by the passage of a muon to generate a trigger at a

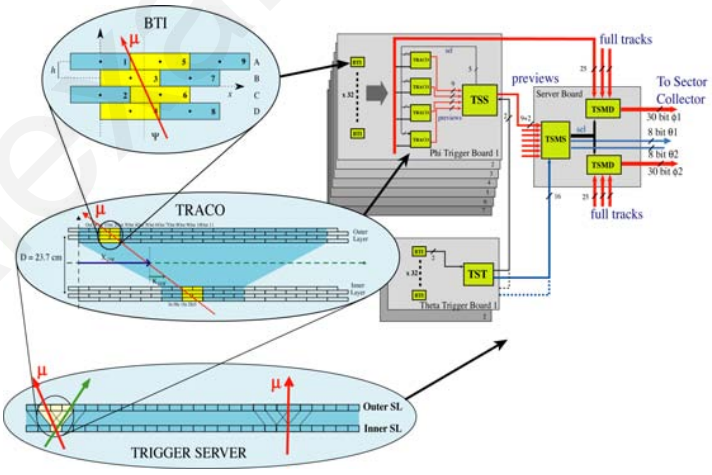

Figure 3.39: Overview of the CMS L1 DT Local Trigger. Taken from Ref. [43].

fixed time, while searching for coincident and aligned hits inside the 4 layers of staggered DTs in each SL. By associating hits a spatial resolution better than 1.4 mm and an angular resolution better than 60 μrad is achieved. The TRACOs attempt to correlate track segments found in the 2 outer SLs of a DT chamber, that are oriented parallel to the beam axis ($SL_{r-\phi}$) and provide measurements of muon tracks in the magnetic bending plane (r-ϕ), to enhance

the angular resolution and produce a quality hierarchy. The TSs have 2 components, one for the transverse projection and one for the longitudinal projection, with the former processing the TRACO output and the latter using directly the BTI output. The trigger and the read-out data from all sectors of the CMS are sent to the SCs, where information including the position, transverse momentum and track quality is coded and transmitted to the Drift Tube Trigger Track Finder (DTTF), which is the DT Regional Trigger and delivers up to 4 muons to the GMT.

The CSC local trigger operation is illustrated in Fig. 3.40. The Local Charged Tracks (LCTs) are muon track segments consisting of information on position, angle and bunch-crossing time which are determined separately with anode and cathode. These are then correlated in time and in the number of layers hit, and by requiring at least 4 layer hits a spatial resolution of 0.15 strip widths is achieved, with the strip width varying in the range 1.5 – 8 mm. The track segments from the anode and cathode are combined to obtain 3-dimensional LCTs, which are characterised by a high-precision ϕ-coordinate in the bending plane, a rough η-value and the bunch-crossing number. Finally, the best 2 LCTs from each CSC chamber are forwarded to the CSC Track Finder (CSCTF), which is the Regional CSC Trigger and joins segments to complete tracks.

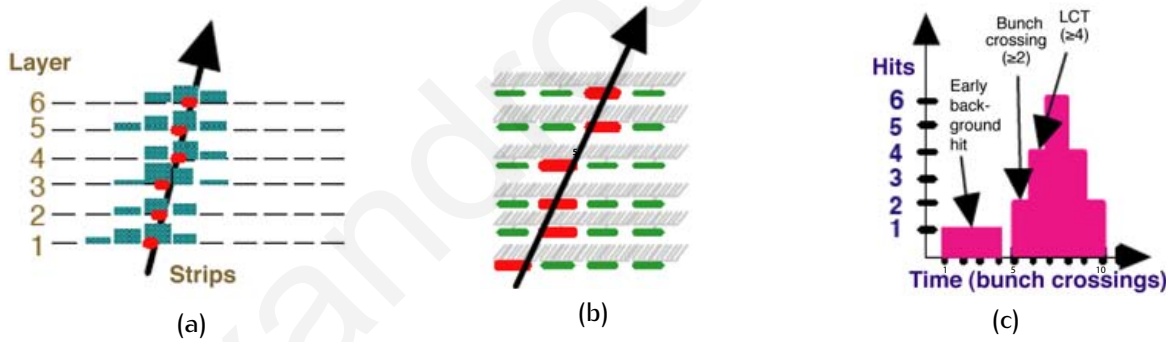

Figure 3.40: Overview of the CMS L1 CSC Local Trigger, with the cathode LCT formation from strips (a) and wire group hits (b) and bunch brossing assignment (c). Taken from Ref. [43].

Unlike the DTs and CSCs, the RPCs are dedicated trigger detectors. They are mounted on DTs in the barrel and on CSCs in the forward regions to provide a time resolution of $\lesssim$ 3 ns, thus ensuring bunch-crossing identification without ambiguity. Additionally, they also measure the azimuthal coordinate ϕ at several points along a muon's track thus providing the transverse momentum. The RPC trigger uses the timing and position coincidence of hits in several layers. The Pattern Comparator Trigger (PACT) compares strip signals in all 4 muon stations in MB or ME with predefined patterns to asign the transverse momentum and charge of the muon candidates. A necessary condition is the establishment of a mimimum of 3 time-wise coincident hits in 4 planes. Spatially-wise, the PACT requirement on the minimum number of hits depends on the muon transverse momentum and pseudorapidity η-value. The RPC trigger also uses information from the HO to reduce rates and suppress backgrounds, and to enhance low quality RPC triggers. Finally, the RPC muon candidates are sorted separately in the barrel and forwards regions, with the best 4 from each being

sent to the GMT.

All the information that is forwarded to the GMT from the 3 muon subsystems is used to improve muon trigger efficiency, to reduce trigger rates and suppress background. For each bunch-crossing, the GMT receives up to 4 muon candidates from the DTs, 4 muon candidates from the CSCs, 4 muon candidates from the barrel RPCs and 4 muon candidates from the endcap RPCs. The candidate information includes the muon transverse momentum, the charge, η and ϕ coordinates and a quality code. Additionally, the GMT also has ISO and MIP bits that are supplied from the GCT. Furthermore, the spatial information is used in attempts to match DT and CSC candidates with RPC candidates in the barrel and endcap regions, and, if succesful, the kinematic parameters are merged. Finally, the muons are sorted by transverse momentum and quality to deliver 4 final candidates to the GT.

3.3.8.3 Global trigger

The ultimate decision of accepting or rejecting an event is provided by the GT and is based on trigger objects provided to it by the GCT and GMT. These trigger objects consist of candidate-particle which include isolated and non-isolated $e^{\pm}/\gamma$ candidates, muons, central and forward hadronic jets and τ jets. Additionally, global quantities are also available for consideration, including missing transverse energy (E_T^{miss}), the scalar sum of the tranvserse energies of jets about a given threshold (H_T) and twelve jet multiplicities (N_T) which can be threshold-dependent. The particle and jet candidates are ranked and sorted according to their p_T (or E_T), $\eta - \phi$-coordinates and quality, with up to 4 objects of a given type being available. For muons, the additional information relating to the ISO and MIP bits is also available.

The GT employs 5 steps; input, logic, decision, distribution and reado-out. The first step is the input of objects from the appropriate GCT and GMT sources. These objects are processed in the logic step, where the Global Trigger Logic (GTL) algorithm applies p_T (or E_T) and numeric thresholds on each of them, while more complex location or quality-related calculations are also possible. The results of these calculations are sent to the Final Decision Logic (FDL) in the form of 1 bit per algorithm for the final L1Adecision, which is consequently distributed to all the CMS subsystems. The last step is executed by the Global Trigger Front-End (GTFE) board, which collects the GT data, appends the event time received from the LHC machine and sends them to the DAQ for reado-out.

3.3.8.4 High-Level Trigger and Data Acquisition

By processing fast trigger information coming from the CMS calorimeter and muon systems and only selecting events with interesting signatures, the CMS L1 Trigger is able to analyse all LHCbunch-crossings and forward information for further filtering at a maximum rate of 100 kHz. With a mean event size of 1 MB of zero-suppressed data in the CMS read-out systems, this rate corresponds to a data flow of about 100 GBs^{-1} fed by the L1 Trigger to the

DAQ system. The DAQ system must thus be able to sustain these rates and is responsible for providing enough computing power for the HLT, which is a software-based filter system that is sometimes divided into Level-2 (L2), Level-2.5 (L2.5) and Level-3 (L3) Triggers, based on the type of data the algorithm utilises. The HLT's task is to provide a further event rate reduction of the order of $\sim 10^3$, reducing the incoming L1 Trigger input of 100 kHz to a rate of events of about 100 Hz, which will be recorded for offline processing and analysis. In order for the HLT algorithms to achieve the required rate reduction of $\sim 10^3$, a computing power corresponding to $\mathcal{O}(1000)$ processing nodes is required. An overview of the CMS HLT parameters is shown in Table 3.14. During LHC operations, the HLT algorithms evolve greatly with time and experience and are hence not described here. Similarly, the trigger thresholds and trigger pre-scales are optimised for the better utilisation of the DAQ and HLT systems.

Table 3.14: Overview of the CMS HLT Trigger.

Quantity	Value	Unit
Input rate	100	kHz
Output rate	100 Hz	Hz
Rate reduction factor	$\sim 10^3$	
Latency	$\lesssim 1$	s

To achieve the required rate reduction, all events that pass the L1 Trigger are sent to a computer farm known as the Event Filter, located in a dedicated room on the surface of the CMS cavern, not far away from the CMS detector. The Event Filter uses access to the full read-out data from the CMS detector to perform physics selections using faster versions of the offline recostruction software, in order to filter events and reduce the output rate to the required one within a time interval ranging from 40 ms – 1 s. The various subdetector Front-End Systems (FESs) store data continuously in 40 MHz pipelined buffers, and upon the arrival of a L1A decision via the TTC system, the full detector data are extracted and pushed to the DAQ system by the Front-End Drivers (FEDs). The Event Builder assembles the data from all FEDs into a single complete event and transmits it to a Filter Unit (FU) in the Event Filter for further processing. Upon running offline-quality reconstruction modules and filters, the Event Filter selects the events destined for storage and distributes Data Quality Monitoring (DQM) information which is dedicated for checking the quality of CMS event data. Finally, the Event Filter routes selected events to a local storage at the CMS site depending on the trigger configuration and from there it transfers them to a mass storage located at the CERN data centre at the Meyrin site. This stored data is reconstructed offline and shared with universities and institutes via the Worldwide LHC Computing Grid (WLCG) project, which is a collaboration between LHC experiments, computing centres and middleware providers.

3.3.9 Computing

3.3.9.1 Data formats

The CMS offline computing system supports the storage, transfer and manipulation of the recorded data by accepting real-time detector data from the DAQ system at the CMS site. However, the large statistics datasets and fine granularity of the CMS experiment result in an unprecedented volume of data which has to by highly flexible, allowing access to all users performing any kind of analysis. For this reason the majority of data storage and processing resources available to CMS lies in a distributed computing model which is based on Grid middleware with services managed by the WLCG project. The design of the CMS computing system involves a modular design of loosely coupled components with well defined interfaces.

The central concept of the CMS data model is the Event, which provides access to data recorded from a single triggered bunch, or data derived from it. Besides the inclusion of raw digitised data, reconstruction products or HLT objects for real or simulated crossings, the Event contains provenance information, thus allowing users to unambiguously determined how a specific event was produced. The Events, which are stored as ROOT [70] files, have provenance information which includes condition/calibration setups used in the data production and software configuration.

Within the CMS experiment, the process of data reduction and analysis takes place in several steps involving different computing centres, with several event formats with differing levels of detail and precision available. The RAW type of data events typically occupy 1.5 MB per event and contain the full detector information, including the trigger decision and other metadata, and is accepted into the offline system of up to 300 Hz for proton-proton collisions. They are permanently stored as they comprise the top level data formats from which all other format can be extracted. For simualted data, the RAW events include Monte-Carlo (MC) truth information, increasing their typical size to 1.5 MB per event. For organisation purposes the RAW data are classified into Primary Datasets (PDs) based upon trigger signature.

By applying several levels of pattern recognition and compression algorithms to the RAW data the Reconstructed (RECO) data are produced, which contain high-level physics objects and the full record of the reconstructed hits and clusters used to produce them. The algorithms involved in this production rely on cross-detector information to filter and correct the digitised RAW data, find clusters and tracks, produce primary and secondary vertices and perform particle identification. RECO events occupy less space than RAW events, with a typical value of 0.5 MB per event.

The wide range of physics analyses is conducted through the use of the Analysis Object Data (AOD) event format, which requires about 100 kB per event thus enabling the storate of very large samples in many computing centres. The AOD events are produced by filtering on RECO data and contain the parameters of high-level physics objects and additional information that could enable kinematical refitting.

3.3.9.2 Computing centres

The CMS computing system relies on computing resources from collaborating universities and institutes all around the world. It is based on a Tiered structure with a single Tier-0 centre at CERN, a few Tier-1 centres at national computing facilities and several Tier-2 centres at individual institutes, as shown in Fig. 3.41.

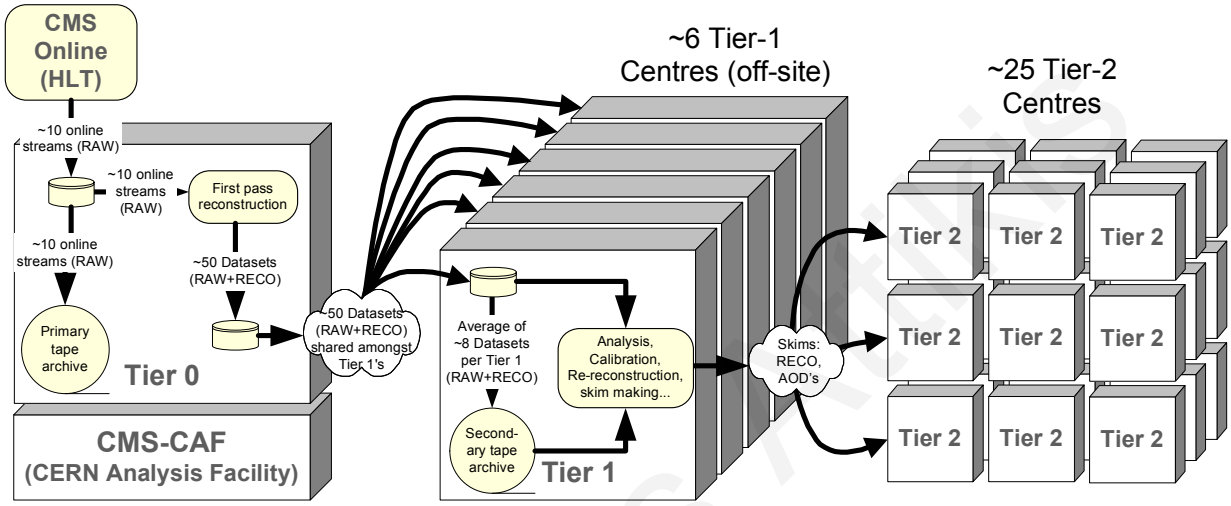

Figure 3.41: Schematic diagram of the data-flow between CMS computing centres. Taken from Ref. [43].

The Tier-0 centre, which is located at CERN, receives RAW data from the online system and stores them permanently, while also providing RECO datasets by performing prompt reconstruction. In parallel, it exports a copy of RAW and RECO data to Tier-1 centres, but it is not accessible for analysis use. The Tier-1 centres, which include the CERN computing centre, are located around the world and provide reliable delivery of data-intensive processing services. Each centre provides a large computing power, a mass storage system and very high speed international links. Their primary functions include the long-term storage of RAW data, the store and transfer of simulated and RECO/AOD data to Tier-2, the carry out second-pass reconstructions and the provision of rapid access to very large data samples for skimming and data-intensive analysis. The Tier-2 centres, which are hosted at CMS institutes, provide to CMS users access to data samples transferred from Tier-1 centres. They are mostly intended for final-stage analysis over a reduced dataset, offline calibration and alighment tasks and MC productions and their transfer to Tier-1 centres.

The integration of the CMS computing resources is achieved through Grid middleware which presents a standard interface to storage and computing facilities at each WLCG. The Grid allows for remote job submission and handling through CMS Remote Analysis Builder (CRAB). For a generic CMS user, CRAB is a dedicated tool for workflow management of jobs and allows the submition of jobs to remote computing elements with access to CMS data, while all infrastructure complexities remain hidden. In this way any kind of analysis can be performed from anywhere in the world as easily as accessing local data.

Chapter 4

Search for light charged Higgs bosons

4.1 Introduction

As established in Chapter 2, the Minimal Supersymmetric Standard Model (MSSM) contains two Higgs doublets, in order to preserve supersymmetry [16, 17, 18, 19, 20, 21, 22, 23], which implies the existence of five physical Higgs states: the $\mathcal{CP}$-even h^0 and H^0, the $\mathcal{CP}$-odd A^0, and the electrically charged H^+ and H^- states [27, 71]. At lowest-order, the MSSM Higgs boson sector is defined by the gauge couplings, the ratio of the two Higgs vacuum expectation values $\tan\beta$, and the mass of the $\mathcal{CP}$-odd Higgs boson A^0.

Within the Standard Model (SM), top quarks decay promptly to a $W^\pm$ boson and a b-quark through $t \to b\mathrm{W}^+$ and its charge-conjugate $\bar{t} \to \bar{b}\mathrm{W}^-$. Because of lepton universality, the branching ratio of $W^\pm$ bosons to leptons $\mathrm{BR}(W^\pm \to \ell^\pm \nu_\ell)$ is evenly distributed among the 3 lepton flavours ($\ell^\pm = \mathrm{e}^\pm, \mu^\pm, \tau^\pm$). However, within the MSSM and if the charged MSSM Higgs boson has a mass such that $m_{H^\pm} \lesssim m_t - m_b$, top-quarks can also decay to a light charged MSSM Higgs boson and a b-quark, via $t \to bH^+$, and via the charge-conjugate process $\bar{t} \to \bar{b}H^-$. This opens the possibility to search for such particles in the $t\bar{t} \to bW^\pm bH^\mp$ and $t\bar{t} \to bH^\pm bH^\mp$ processes.

As already discussed in Section 2.5.2, for values of $\tan\beta > 5$ the light charged MSSM Higgs boson preferentially decays to a τ-lepton and a neutrino through $H^\pm \to \tau^\pm \nu_\tau$, with $\mathrm{BR}(H^\pm \to \tau^\pm \nu_\tau) \approx 1$. Therefore, in deriving experimental limits, it is common to assume that the $H^\pm \to \tau^\pm \nu_\tau$ decay occurs exclusively, with $\mathrm{BR}(H^\pm \to \tau^\pm \nu_\tau) = 1$. The fact that the light charged MSSM Higgs boson preferentially decays to a τ-lepton, not adhering to the lepton universality of the $W^\pm$ boson, implies that should it exist, the prediction of the τ-lepton yield in the decay products of SM $t\bar{t}$ pairs must be altered. The Large Electron-Positron Collider (LEP) experiments have imposed a lower limit that the mass of the charged MSSM Higgs boson can be to $\sim 80\,\mathrm{GeV}$ [72], as shown in Fig. 4.1 (a). Also, the current upper limit on the branching ratio $\mathrm{BR}(t \to bH^\pm)$ is set by the Collider Detector at Fermilab (CDF) [73] and DØ [74] experiments at the Tevatron, which place it at $\mathrm{BR}(t \to bH^\pm) \leq 0.2$ for the mass range $80\,\mathrm{GeV}/c^2 < m_{H^\pm} < 155\,\mathrm{GeV}/c^2$ and assuming $\mathrm{BR}(H^\pm \to \tau^\pm \nu_\tau) = 1$, as shown

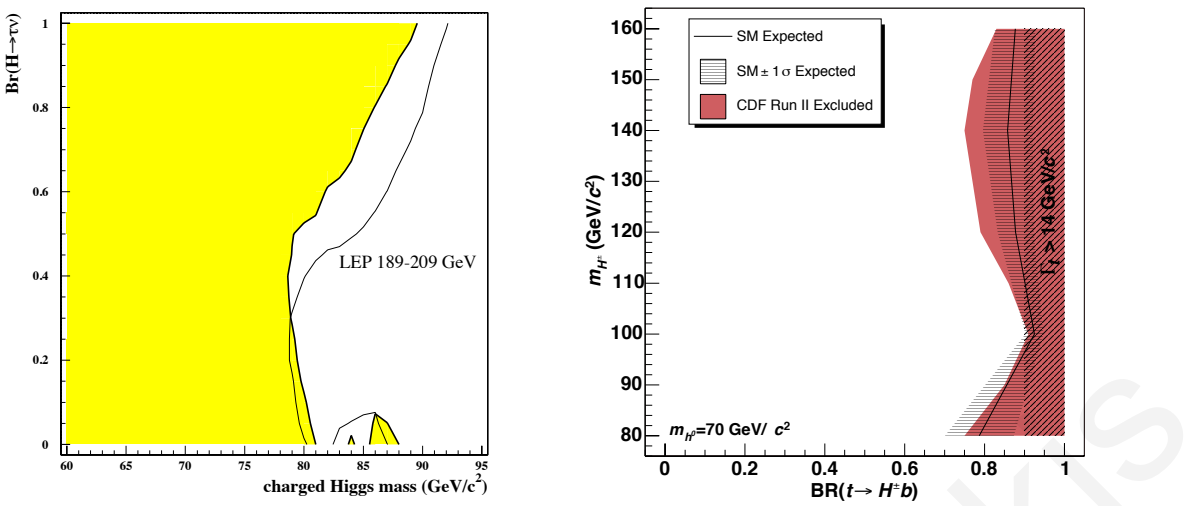

(a) (b)

Figure 4.1: The 95% CL bounds on $m_{H^\pm}$, as a function of the branching ratio BR($H^\pm \to \tau^\pm \nu_\tau$), as obtained by combining the data collected by the four LEP experiments (a) and the Tevatron CDF experiment (b). Taken from Ref. [72] (a) and Ref. [73] (b) .

in Fig. 4.1 (b) and Fig. 4.2 (a), respectively. In Fig. 4.2 (b), the corresponding excluded region of the $(\tan\beta, m_{H^\pm})$ parameter space, for the MSSM m_h^{max} scenario is presented, as determined by the Tevatron DØ experiment. Even more recently, the A Toroidal LHC

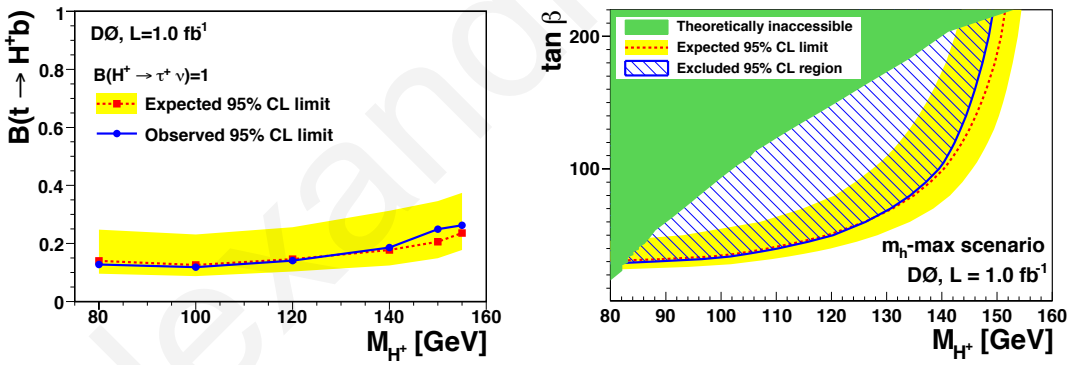

(a) (b)

Figure 4.2: The 95% CL upper limit on BR($t \to bH^\pm$) (a) and the corresponding excluded region of the $(\tan\beta, m_{H^\pm})$ parameter space (b) in the MSSM for the m_h^{max} scenario, as determined by the Tevatron DØ experiment. Taken from Ref. [74].

Apparatus (ATLAS) experiment at the Large Hadron Collider (LHC) has set the upper limit on the BR($t \to bH^\pm$) between 5 – 1% for charged Higgs boson masses in the mass range $90\,\text{GeV}/c^2 < m_{H^\pm} < 160\,\text{GeV}/c^2$ and assuming BR($H^\pm \to \tau^\pm \nu_\tau$) = 1 [75], as shown in Fig. 4.3.

The dominant process of production of top quarks at the LHC is through $pp \to t\bar{t}$ production, and thus the search for a light charged MSSM Higgs boson is carried out in decay products of top quark pairs, $t\bar{t} \to bH^\pm b\mathrm{W}^\mp$ and $t\bar{t} \to bH^\pm bH^\mp$, with the $H^\pm \to \tau^\pm \nu_\tau$ decay. In total, there are 4 main final states for the dominant $t\bar{t} \to bH^\pm b\mathrm{W}^\mp$ process:

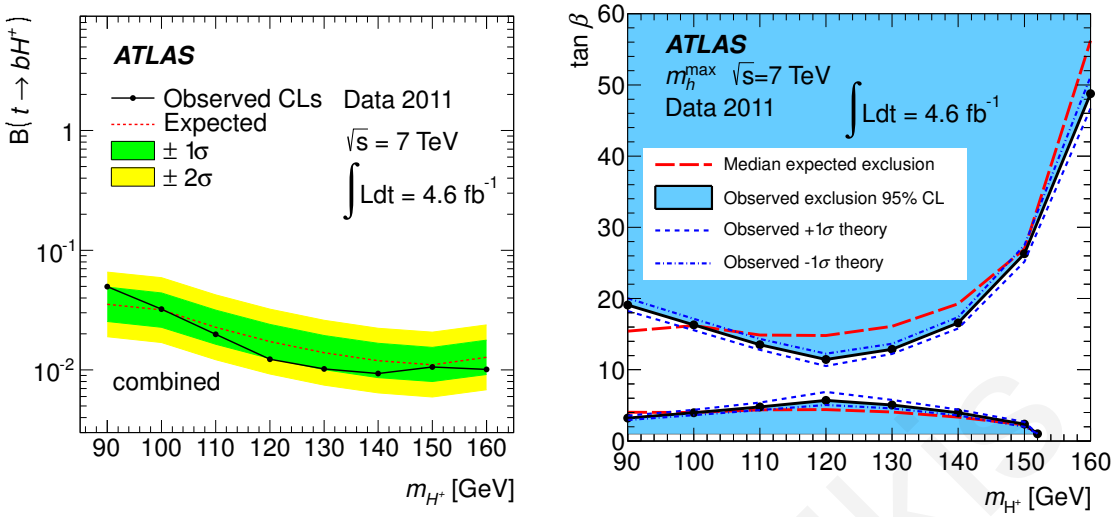

Figure 4.3: The 95% CL upper limit on BR($t \to bH^{\pm}$) (a) and the corresponding excluded region of the ($\tan\beta$, $m_{H^{\pm}}$) parameter space (b) in the MSSM for the $m_{\mathrm{h}}^{\mathrm{max}}$ scenario, as determined by the LHC ATLAS experiment. Taken from Ref. [75].

1. the semi-leptonic final state; an isolated lepton is observed from the associated top decay and a τ jet is observed from the $H^{\pm} \to \tau^{\pm}\nu_{\tau}$ decay,

2. another semi-leptonic final state; an isolated electron or muon is observed from both the $H^{\pm} \to \tau^{\pm}\nu_{\tau} \to \ell^{\pm}\nu_{\ell}\nu_{\tau}\nu_{\tau}$ decay, while the associated top quark decays hadronically through $W^{\pm} \to \mathrm{q\bar{q}'}$.

3. the di-lepton final state; an isolated electron or muon is observed from both the $H^{\pm} \to \tau^{\pm}\nu_{\tau} \to \ell^{\pm}\nu_{\ell}\nu_{\tau}\nu_{\tau}$ decay, and the decay of the associated top quark,

4. the fully hadronic final state; a τ jet is observed from the $H^{\pm} \to \tau^{\pm}\nu_{\tau}$ decay and the associated top quark decays hadronically through $W^{\pm} \to \mathrm{q\bar{q}'}$.

The present study, which is a continuation of the work documented in Refs. [76] and [77], is concerned with the search for a light charged MSSM Higgs boson in the fully hadronic final state. The analysis is based on an integrated luminosity of $2.3\,\mathrm{fb}^{-1}$ of data recorded with the Compact Muon Solenoid (CMS) detector in 2011, with an instantaneous luminosity of up to $5 \times 10^{33}\mathrm{cm}^{-2}\,\mathrm{s}^{-1}$. The events were selected by employing a single τ jet + $E_{\mathrm{T}}^{\mathrm{miss}}$ trigger, while the offline event selection was comprised of a well identified and isolated τ jet, large missing transverse energy ($E_{\mathrm{T}}^{\mathrm{miss}}$), multiple jets with at least one of them required to originate from the hadronisation of a b-quark (b-jet or b-tagged jet), and the requirement that the τ jet and $E_{\mathrm{T}}^{\mathrm{miss}}$ object were separated in transverse plane by an angle $\Delta\phi(\tau\text{ jet}, E_{\mathrm{T}}^{\mathrm{miss}})$ which was less than a chosen threshold. To further improve the event selection, the τ-helicity correlations were exploited by setting a lower bound on the fraction of the τ-jet energy carried by the leading charged particle ($R_{\tau} = p^{\text{Ldg. Trk.}}/p^{\text{visible }\tau}$).

After all signal selection requirements, the signal extraction was achieved by fitting the light charged MSSM Higgs boson transverse mass, reconstructed from the selected τ jet

and the $E_{\mathrm{T}}^{\mathrm{miss}}$ objects, $m_{\mathrm{T}}(\tau\text{ jet}, E_{\mathrm{T}}^{\mathrm{miss}})$. The event selection was performed for 3 options of the cut in the azimuthal angle; without $\Delta\phi(\tau\text{ jet}, E_{\mathrm{T}}^{\mathrm{miss}})$ cut, $\Delta\phi(\tau\text{ jet}, E_{\mathrm{T}}^{\mathrm{miss}}) < 160°$ and $\Delta\phi(\tau\text{ jet}, E_{\mathrm{T}}^{\mathrm{miss}}) < 130°$ with only the $\Delta\phi(\tau\text{ jet}, E_{\mathrm{T}}^{\mathrm{miss}}) < 160°$ options being finally used to extract the observed and expected upper limits on the $\mathrm{BR}(t \to bH^{\pm})$. Corresponding limits in the $(\tan\beta, m_{H^{\pm}})$ and the $(\tan\beta, m_{A^0})$ parameter space were also extracted for the MSSM $m_{\mathrm{h}}^{\mathrm{max}}$ scenario (see Table 2.2). A combined analysis was also conducted, which included 3 of the 4 aforementioned final states, and is documented in Refs. [78] and [79].

In the following sections, the signal process and its signatures are discussed in Section 4.2. The events samples used, comprised of collision and simulated data samples, are presented in Section 4.3. A detailed description of the triggers employed for collecting the data and their associated efficiency measurements is provided in Section 4.4. The reconstruction and identification of physics objects are discussed in Section 4.5, while the full set of signal selection requirements are summarised in Section 4.5.9. The various corrections applied to the simulated samples are described in Section 4.6, while the systematic uncertainties of simulations are discussed in Section 4.7. In Section 4.8, the measurements of Quantum Chromodynamics (QCD) multi-jet backgrounds and Electroweak (EWK) backgrounds with and without genuine τ jets are presented. The event yields and systematic uncertainties from the signal selection and background measurements are summarised in Section 4.9. Finally, observed and expected model-independent upper limits on $\mathrm{BR}(t \to bH^{\pm})$ are presented in Section 4.10, together with an exclusion region in the $(\tan\beta, m_{H^{\pm}})$ and the $(\tan\beta, m_{A^0})$ parameter space of the MSSM $m_{\mathrm{h}}^{\mathrm{max}}$ scenario.

4.2 Signatures of light charged Higgs bosons

The dominant production process for light charged MSSM Higgs bosons at the LHC is through $pp \to t\bar{t}$. The $t\bar{t} \to bH^{\pm}bW^{\mp}$ and $t\bar{t} \to bH^{\pm}bH^{\mp}$ processes, which contribute about 87% to the total production, are shown in Fig. 4.4 and Fig. 4.5, respectively, for the fully hadronic final state. The contribution from the $t\bar{t} \to bH^{\pm}bH^{\mp}$ process is relatively small for $\mathrm{BR}(t \to bH^{\pm}) \lesssim 10\,\%$ [77], as it can be seen in Fig. 4.6.

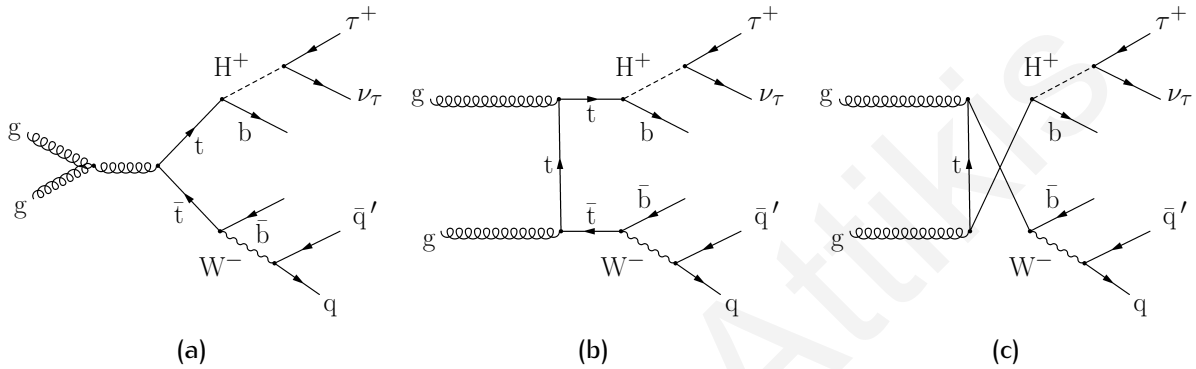

Figure 4.4: The dominant Feynman diagrams (~ 87%) for the $t\bar{t} \to bH^{\pm}bW^{\mp}$ signal production at the LHC; gluon-gluon fusion through the s-channel (a), t-channel (b) and u-channel (c). The diagrams were created with feynMF [80]

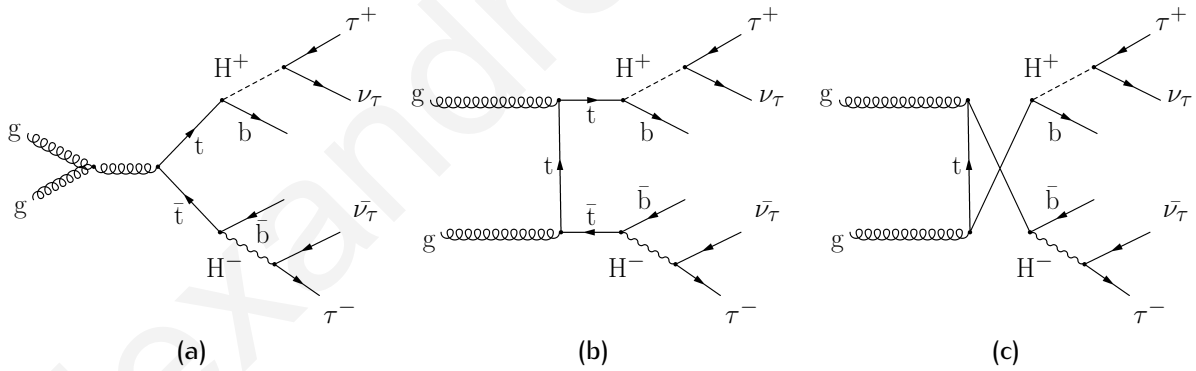

Figure 4.5: The dominant Feynman diagrams (~ 87%) for the $t\bar{t} \to bH^{\pm}bH^{\mp}$ signal production at the LHC; gluon-gluon fusion through the s-channel (a), t-channel (b) and u-channel (c). The diagrams were created with feynMF [80]

The main characteristics of the fully hadronic final state is the presence of large $E_{\mathrm{T}}^{\mathrm{miss}}$, which originates primarily from the presence of neutrinos produced in the $H^{\pm} \to \tau^{\pm}\nu_{\tau}$ decay and the subsequent decay of the τ-lepton to hadrons $\tau^{\pm} \to \text{hadrons} + \nu_{\tau}$. Semi-leptonic b-quark decays are also expected to contribute to the $E_{\mathrm{T}}^{\mathrm{miss}}$, as are detector-related effects, such as Jet Energy Scale (JES) and jet resolution effects which can cause the presence of fake $E_{\mathrm{T}}^{\mathrm{miss}}$. The presence of 2 b-quarks in the final state provides significant discriminating handle in extracting the signal from the background, due to the unique properties of b-quarks and B-hadrons which are discussed in detail in Section 4.2.2. Finally, another key feature of the final state topology is the presence of a τ jet, which can be discriminated from hadronic jets by the use of several unique features, as discussed next.

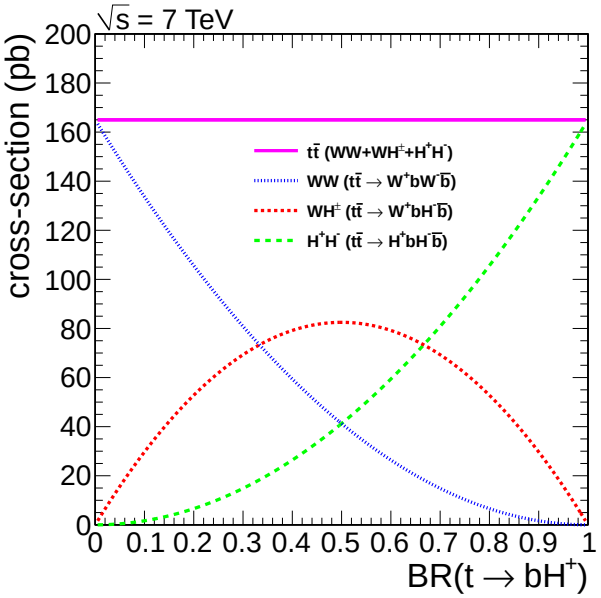

Figure 4.6: Cross-section of $t\bar{t}$ events expected at $\sqrt{s} = 7$ TeV as a function of BR($t \to bH^{\pm}$). Expectations are shown separately for the $W^{\mp}H^{\pm}$, $H^{\pm}H^{\mp}$, and $W^{\pm}W^{\mp}$ contributions.

4.2.1 Properties of τ-leptons and τ jets

The τ-lepton decays to hadrons with a total branching ratio of about 64%, with the majority of these decays involving only 1 charged particle (hadronic 1-prong decays), as shown in Table 4.1. The hadronic 1-prong and 3-prong decay modes present 48.1% and 14.6% of all τ-lepton decays, respectively. The fraction of decay modes with K^0's is only 2%. The simplest τ-lepton decay mode, $\tau^+ \to \pi^+ \bar{\nu}_\tau$, presents 24.1% of all 1-prong hadronic decay modes. The 1-prong decay modes containing π^0's proceed through the $\rho^{\pm}(770)$ and $a_1^{\pm}(1260)$ resonances, and also result in more energetic leading charged particle in the $H^+ \to \tau^+ \nu_\tau$ decays than in the $W^+ \to \tau^+ \nu_\tau$ decays, due to τ helicity correlations [82, 83] which are discussed further in Section 4.2.1.1.

Thus, τ jets are characterised by low charged-track multiplicity, unlike QCD jets or b-jets which can involve a large number of charged tracks in their decay products. Furthermore, τ jets are known to produce localised energy deposits in the Electromagnetic Calorimeter (ECAL) due to π^0's, which are amply produced in τ-lepton decays and which decay to photon pairs through $\pi^0 \to \gamma\gamma$. Moreover, the showering process of charged hadrons in τ jets can start already in the ECAL, in which case the so called Electromagnetic (EM) energy fraction contributes significantly to the total energy deposited by the jet. What's more, the EM energy originating from τ jet is typically contained within a narrow signal cone around the leading track direction, due to the boost effect of the τ-lepton. This containment becomes increasingly important the heavier the τ-lepton mother particle is; for example a light charged MSSM Higgs boson with mass much greater than the $W^{\pm}$ boson, is expected to produce a narrower τ jet through $H^{\pm} \to \tau^{\pm} \nu_\tau$ than its counterpart through $W^{\pm} \to \tau^{\pm} \nu_\tau$. Hadronic jets in QCD multi-jet events comprise perhaps the most dangerous background for τ jets, due to the mere fact that the cross-section of such processes overwhelmingly exceeds

Table 4.1: Branching ratios for τ-lepton decays [81]. The term $h^{\pm}$ stands for the mesons $\pi^{\pm}$ or $K^{\pm}$.

Process	$\Gamma_i/\Gamma_{\text{total}}$(%)	$\sum_i \Gamma_i/\Gamma_{\text{total}}$(%)
leptonic	–	35.9
$\tau^- \to e^- \bar{\nu}_e \nu_\tau$	17.9	–
$\tau^- \to \mu^- \bar{\nu}_\mu \nu_\tau$	17.4	–
hadronic 1-prong (excl. K^0's)	–	48.1
$\tau^- \to h^- \nu_\tau$	11.6	–
$\tau^- \to \rho^- \nu_\tau \to h^- \pi^0 \nu_\tau$	26.0	–
$\tau^- \to a_1^- \nu_\tau \to h^- \pi^0 \pi^0 \nu_\tau$	9.3	–
$\tau \to h^- \nu_\tau + \geq 3\pi^0$	1.3	–
hadronic 3-prong (excl. K^0's)	–	14.6
$\tau^- \to a_1^- \nu_\tau \to h^- h^+ h^- \nu_\tau$	9.7	–
$\tau^- \to h^- h^+ h^- \nu_\tau + \geq 1\pi^0$	5.2	–
hadronic 5-prong (excl. K^0's)	–	0.1
$\tau^- \to h^- h^+ h^- h^+ h^- \nu_\tau + \geq 0\pi^0$	0.1	–
hadronic with K^0's	–	2.0
$\tau^- \to K_S^0 + X$	0.9	–
$\tau^- \to K_L^0 + X$	1.1	–

the cross-section of other candidate EWK backgrounds processes, such as $t\bar{t}$ and W + jets.

4.2.1.1 τ-polarisation and helicity correlations

The $t\bar{t}$, W + jets and single-top backgrounds contain genuine τ-leptons from $W^{\pm}$ boson decays. Although the W+jets background can efficiently be suppressed by requiring jets and b-jets present in a collision event, the $t\bar{t}$ and single-top backgrounds are largely irreducible. However, the τ helicity correlations can be used to suppress these backgrounds, as proposed in Refs. [82] and [84]. The method relies on the fact that, since the charged MSSM Higgs boson is a scalar particle ($J_{H^{\pm}} = 0$) and since only left-handed (right-handed) neutrinos (anti-neutrinos) exist in nature, the τ-lepton in the $H^+ \to \tau^+ \nu_\tau$ decay is produced left-handed, as shown in Fig. 4.7.

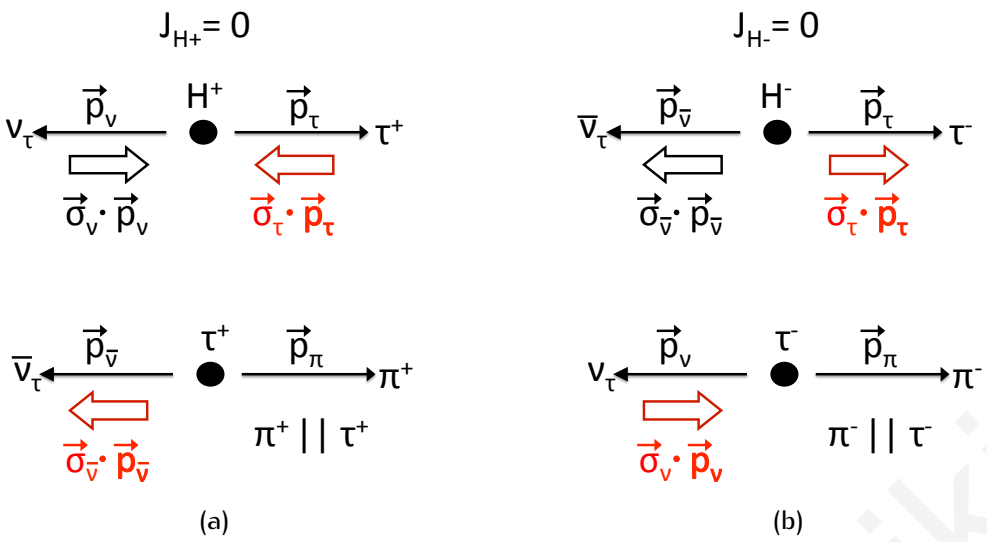

Figure 4.7: Schematic diagram showing the simplest case of helicity correlations of τ-leptons in $H^+ \to \tau^+\nu_\tau$ (a) and $H^- \to \tau^-\bar{\nu}_\tau$ (b), for the $\tau^+ \to \pi^+\bar{\nu}_\tau$ and $\tau^- \to \pi^-\nu_\tau$ decay modes, respectively.

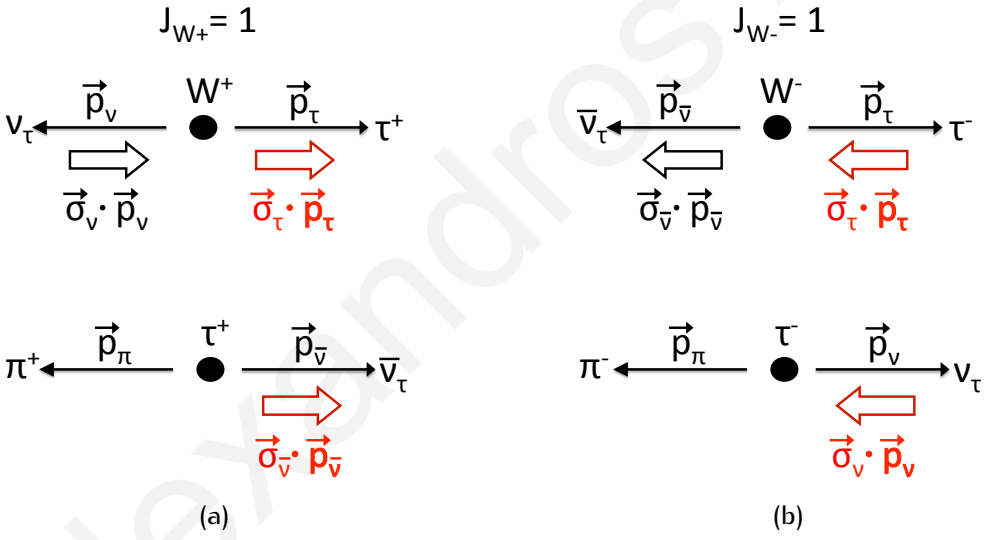

Figure 4.8: Schematic diagram showing the simplest case of helicity correlations of τ-leptons in $W^+ \to \tau^+\nu_\tau$ (a) and $W^- \to \tau^-\bar{\nu}_\tau$ (b), for the $\tau^+ \to \pi^+\bar{\nu}_\tau$ and $\tau^- \to \pi^-\nu_\tau$ decay modes, respectively.

On the contrary, in the $W^+ \to \tau^+\nu_\tau$ decay, the τ-lepton emerges right-handed due to the vector nature of the $W^\pm$ boson ($J_{W^\pm} = 1$), as shown in Fig. 4.8.

More specifically, the differential decay width distributions of τ-leptons decaying to a pion $\pi^\pm$ or a vector meson $v = \rho^\pm, a_1^\pm$ are given by [82]

$$\frac{1}{\Gamma_\pi}\frac{d\Gamma_\pi}{d\cos\theta} = \tfrac{1}{2}(1 + P_\tau \cos\theta) \qquad \tau^\pm \to \pi^\pm\nu_\tau \tag{4.1}$$

$$\frac{1}{\Gamma_v}\frac{d\Gamma_{v,\,L}}{d\cos\theta} = \frac{\frac{1}{2}m_\tau^2}{m_\tau^2+2m_v^2}(1 + P_\tau \cos\theta) \qquad \tau^\pm \to v^\pm\nu_\tau \tag{4.2}$$

$$\frac{1}{\Gamma_v}\frac{d\Gamma_{v,\,T}}{d\cos\theta} = \frac{\frac{1}{2}m_v^2}{m_\tau^2+2m_v^2}(1 - P_\tau \cos\theta) \qquad \tau^\pm \to v^\pm\nu_\tau, \tag{4.3}$$

where L and T denote the longitudinal and transverse polarisation states of the vector mesons v, respectively. The term θ is the angle between the $\pi^{\pm}$ direction and the τ-lepton line-of-flight, in the τ-lepton's rest frame. The term $P_{\tau} = \pm 1$ is taken to be positive for the τ-lepton originating from the charged MSSM Higgs boson decays, and negative for the τ-lepton originating from the $W^{\pm}$ decays [82]

$$P_{\tau}^{H^{\pm}} = +1 \tag{4.4}$$
$$P_{\tau}^{W^{\pm}} = -1. \tag{4.5}$$

The fraction x of the τ-lepton's momentum in the lab frame, carried by its meson decay product, is related in each case to the angle θ in the collinear approximation via [82]

$$x = \frac{1}{2}(1 + \cos\theta) + \frac{m_{\pi,v}^2}{m_{\tau}^2}(1 - \cos\theta). \tag{4.6}$$

Since the only measurable quantity is the momentum of the visible products of the τ-lepton, one can express the energy of the τ jet as [82]

$$p^{\tau\text{ jet}} = x \cdot p^{\tau\text{-lepton}}. \tag{4.7}$$

From Eq. (4.1) and (4.2), it is evident that τ polarisation-effects result in harder τ jets in charged MSSM Higgs boson decays, compared to those originating from $W^{\pm}$ gauge boson decays, for the $\pi^{\pm}$ and the longitudinal (L) vector meson contributions. Conversely, for the transverse (T) vector meson case in Eq. (4.3) the situation is reversed. The effect of this oppositely contributing effects is the dilution of the polarisation effect, by as much as 50% for $\rho^{\pm}$, and much almost entirely for the $\alpha_1^{\pm}$ contribution.

These two polarisations can however be distinguished, by exploiting the fact that the transverse vector meson decays ($\rho_T^{\pm}$ and $\alpha_{1,T}^{\pm}$) favour even sharing of momentum among the decay pions, as shown in Fig. 4.9. Conversely, longitudinal vector meson decays ($\rho_L^{\pm}$ and $\alpha_{1,L}^{\pm}$) favour uneven sharing; i.e. decays in which the charged pion carries either very little or the majority of the vector meson momentum. Thus, the fraction of the visible τ jet momentum carried by the charged prong, defined as

$$R = \frac{p^{\pi^{\pm}}}{p_{\text{visible}}^{\tau\text{-lepton}}}, \tag{4.8}$$

can be used to disentagle to some extend the polarisations. For example, the requirement $R \gtrsim 0.8$ results in retaining $\sim 50\%$ of the $\rho_L^{\pm}$ along with the pion, but very little of the transverse contributions $\rho_T^{\pm}$. Therefore, the $R \gtrsim 0.8$ requirement not only can discriminate between $H^{\pm} \to \tau^{\pm}\nu_{\tau}$ and $W^{\pm} \to \tau^{\pm}\nu_{\tau}$ decays, it can also be used to suppress fake τ jet backgrounds, like QCD multi-jet. A similar gain can be obtained in principle by exploiting the instances where the charged pion carries very little of the τ jet energy, by requiring $R \lesssim 0.2$ for example.

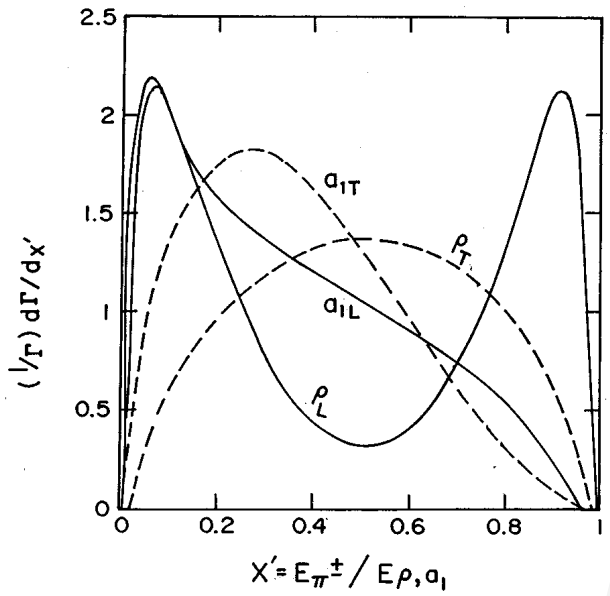

Figure 4.9: Differential decay widths for the $\rho^{\pm}_{L,\ T} \to \pi^{\pm}\pi^0$ and $\alpha^{\pm}_{1,L,\ T} \to \pi^{\pm}\pi^0\pi^0$, as a function of the energy fraction x. The distributions are broken down to longitudinal L and transverse T contributions. Taken from Ref. [82].

Transiting from theory to experiment, instead of the $\pi^{\pm}$ and visible τ-lepton momentums, the leading charged particle ($p^{\text{Ldg. Trk.}}$) and τ jet momentums are used

$$R_\tau = \frac{p^{\text{Ldg. Trk.}}}{p^{\tau\text{ jet}}}. \tag{4.9}$$

However, in a real collision environment, trigger requirements on $p^{\text{Ldg. Trk.}}$ and the limited jet energy resolution of the calorimeter used to measure the quantities in Eq. (4.9) might spoil significantly or entirely the discriminating power of the R_τ variable. Firstly, the use of $R_\tau \lesssim 0.2$ is in general not possible due to the fact tha τ-lepton triggers are designed to include hard requirements on the p_{T} of the leading track. Therefore, pragmatically only the $R \gtrsim 0.8$ requirement should be available for use in a collision environmnent. Even in this case however, the limited jet energy resolution of the detector may result in the washing-out of its discriminating power. Despite that, since the mass of the light charged MSSM Higgs boson lies in the range $m_{W^\pm} \lesssim m_{H^\pm} \lesssim m_t$, the R_τ variable can be used with varying success, depending on the value of $m_{H^\pm}$. In particular, for values such that $m_{H^\pm} > m_{W^\pm}$ the additional boost-effect received by the τ-lepton in the $H^\pm \to \tau^\pm\nu_\tau$ decays is expected to enhance the discriminating power of the R_τ variable, with the effect becoming increasingly important for even larger values of $m_{H^\pm}$.

It is also worth mentioning that, provided that neutral pions can be efficiently reconstructed, a discriminating variable based on the even/uneven momentum distribution between the charged and neutral pions can also be constructed [82]. In particular, the quantity $\Delta p_T = |p_T^{\pi^\pm} - p_T^{\pi^0}|$ is expected to be large for τ-leptons originating from $H^\pm \to \tau^\pm\nu_\tau$ and small for $W^\pm \to \tau^\pm\nu_\tau$ decays. It retains most of the $\rho^\pm_L$ and $\alpha^\pm_{1,L}$ contributions along with the π, as it includes both $R_\tau \simeq 1$ and $R_\tau \simeq 0$ regions. However, for the latter case which

implies a soft charged track along the direction of a hard calorimetric energy deposit, the strong magnetic field inside the detector could result in significantly deflecting this track away from the τ jet cone. As a consequence, the efficiency with which such soft tracks can be succesfully reconstructed as part of the τ jet energy is expected to be quite small.

To conclude, the phenomena of τ-polarisation and the different intrinsic spin properties of the $W^{\pm}$ and $H^{\pm}$ bosons can be exploited to suppress the irreducible $t\bar{t}$ background, by setting a lower bound on the polarisation variable R_{τ}. This can be achieved by requiring that the leading charged particle carries a large fraction ($\sim 70-80\%$) of the visible τ-lepton energy.

4.2.2 Properties of b-quarks and b-jets

The presence of 2 b-quarks in the final state, provides an additional discriminating handle in extracting the signal from the background. The b-jets are different from other hadronic jets, such as lighter quark flavour (u, d, s) jets or gluon jets, because they contain B-hadrons. These contain at least one b-quark, accompanied by light-partner quarks, such a d-, u- or s-quarks, and are thus comparably heavy ($m_b \sim 4.8\,\text{GeV}/c^2$). Since the b-quark, which is the weak-doublet partner of the top-quark, is lighter than the top-quark, the decays of B-hadrons occur via generation-changing processes, through the Cabibbo-Kobayashi-Maskawa (CKM) matrix. Thus, the ground states of B-hadrons decay via the Weak interaction into light-partner quarks, and such decays are normally described by the spectator model; the b-quark decays as if it were free, while the accompanying quark just spectates.

The dominant decay mode is the spectator decay, whereby the b-quark interacts Weakly via $b \to cW^{*-}$ and the virtual W^- decays either into a lepton-neutrino pair (semi-leptonic b-quark decays) or into a pair of quarks (hadronic decays), which then hadronise. The decays in which the spectator quark combines with one of the quarks from the virtual $W^{\pm}$ decay, to form one of the final state hadrons are colour-suppressed[1], by a factor $\sim 1/9$ [15]. The transitions $b \to u$ are also strongly suppressed by a factor $|\mathrm{V}_{ub}/\mathrm{V}_{cb}|^2 \sim (0.1)^2$ relative to $b \to c$ transitions [15]. This gives way to rarer decay modes, such as the loop-induced $b \to s$ decays, whose rates are comparable to the CKM-suppressed $b \to u$ processes.

The aforementioned properties of B-hadrons, result in them having a comparably much longer life-time of typically $\tau_{\text{B-hadrons}} \sim 1.5\,\text{ps}$, thus enabling them to travel a distance

$$L = \beta\gamma c\tau \tag{4.10}$$

before decaying within the CMS tracker, as measured in the laboratory frame. Thus, B-hadrons have an average decay length of about $L \sim 480\,\mu\text{m}$, depending on the boost-effect received from the decay of the heavy top quark, and their decay products result in a reconstructable secondary vertex and a non-zero impact parameter (d), as shown in Fig. 4.10. Therefore, a jet originating from a b-quark can be characterised by the presence of tracks displaced with respect to the primary vertex, caused by the decay of heavy B-hadrons. The impact parameter of a given track, is defined as the distance of closest approach, extrapolated from the secondary vertex to the Interaction Point (IP), and takes the form

$$\mathrm{d}^{\text{track}} = L\sin\delta = \beta\gamma c\tau\sin\delta, \tag{4.11}$$

where δ is the polar angle between the direction of the track and the direction of the parent particle. In general, tracks produced at the secondary vertex will be characterised with a large transverse impact parameter

$$\mathrm{d}_{xy}^{\text{track}} = \mathrm{d}^{\text{track}}\sin\theta = \gamma c\tau\sin\delta\sin\theta, \tag{4.12}$$

[1] In order for this to happen the colours of the 2 quarks must match to give a colour-less state.

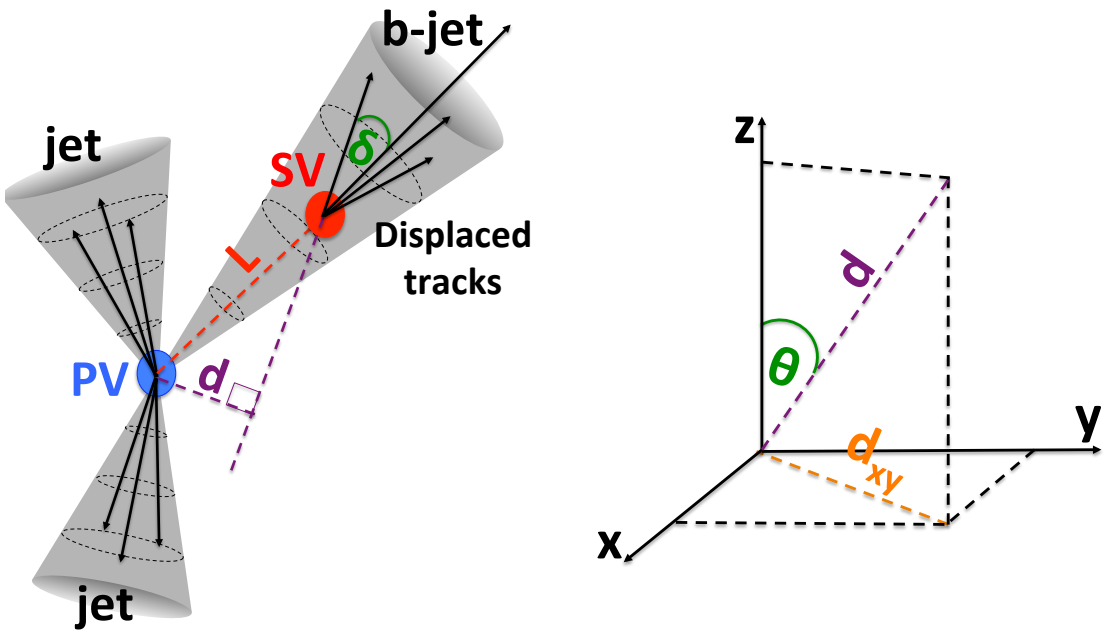

Figure 4.10: Schematic diagram of a b-jet, whereby tracks are reconstructed in a jet with some of them originating from a secondary vertex, denoted SV. The B-hadron, which is produced at the primary vertex, denoted PV, travels a through a distance L_{xy} to before decaying itself to produce a secondary vertex with displaced tracks.

where θ is the polar angle between the track direction and the CMS beam axis (z-axis). Thus, the transverse impact parameter is just the projection of the impact parameter in the transverse plane, as shown in Fig. 4.10.

In the instance where a B-hadron decays to C-hadrons, which also have a long enough life-time to be reconstructable, the B-hadron decay signature might include a reconstructable tertiary vertex. Moreover, a significant feature of b-jets is the fact that they produce a decay chain to lighter quark flavours, and hence tend to have a high number of charged particles (on average $\sim$ 5 charged particles per decay). Such decays are mediated by virtual $W^{\pm}$ bosons, which can also decay to electrons or muons via $W^{\pm} \to e^{\pm}\nu_e$ and $W^{\pm} \to \mu^{\pm}\nu_{\mu}$, with branching ratios BR($W^{\pm} \to e^{\pm}\nu_e$) $\simeq$ 10% and BR($W^{\pm} \to \mu^{\pm}\nu_{\mu}$) $\simeq$ 10%, respectively. This results in $\sim$ 20% of the b-jets having electrons or muons in the final state; the so-called semi-leptonic b-quark decays. The chance of leptonic decay within a b-jet results in another key unique feature of being able to find non-isolated leptons within the jet cone. Nevertheless, processes involving light flavoured jets, as well as gluon jets, constitute a significant background to b-jets, as they have a good chance of mimicking them. However, the most difficult background is constituted by the c-jets, since, having similar properties as b-jets, they can also produce secondary vertices and can thus easily fake b-jets.

4.3 Event samples

4.3.1 Collision data and integrated luminosity

The certification of the quality of the CMS data consists of a multi-step procedure, ranging from online data-taking to the offline reprocessing of data. It is based on both visual inspection of data distributions from Data Quality Monitoring (DQM) shifters, as well as their algorithmic tests against references. The Run Registry (RR) [85] is responsible for creating official good-run list files, which are used as input in the selection of the data for physics analyses. During CMS data-taking periods, the recorded data are monitored by a data quality procedure that ensures their accurate certification. The online DQM is synchronous to the data production and recording. The offline DQM is performed as soon as the full set of event data of a given run has been processed at Tier-0 level. The sign-off step involves the review of the data by detector and software subsystem experts. The completed step involves the freezing of the certification information in the RR, and the official good run list file in Java Script Object Notation (JSON) format is produced and distributed to the CMS community for analysis.

For the present analysis, the certified data collected with the CMS detector during Run2011A in the early 2011 data-taking period was used, corresponding to an integrated luminosity of $2.3\,\text{fb}^{-1}$, with a maximum instantaneous luminosity of $5 \times 10^{33}\text{cm}^{-2}\,\text{s}^{-1}$ reached during that period. The May10 and Aug05 re-reconstructed data and the prompt reconstructed data not covered by the re-reconstructions were used, for which the JSON certification files are tabulated in Table 4.2. The data were processed with the official CMSSW_4_2_8_patch2 [86] software, while the global tag GR_R_42_V20 [87] was used in the processing. Special clean-up selections were applied on all the data samples used, as shown in Table 4.3, to remove beam-scrapping events [88][2]. This was achieved by requiring that, if there are more than 10 tracks (N^{Trks}) in the event, at least 25% of them were required to be high-purity tracks ($N^{\text{Trks}}_{\text{high-purity}}$). In the unlikely occurrence of less than 10 tracks being present, the event is accepted anyway. Events with significant noise in the hadronic calorimeter were also rejected. The aforementioned selections are commonly used for all CMS data analyses.

Table 4.2: The JSON certification files used in this analysis.

RECO	JSON file
May10 re-RECO	Cert_160404 – 163869_7TeV_May10ReReco_Collisions11_JSON _v3.txt
Aug05 re-RECO	Cert_170249 – 172619_7TeV_ReReco5Aug_Collisions11_JSON_v2.txt
prompt RECO	Cert_160404 – 173692_7TeV_PromptReco_Collisions11_JSON.txt

For the investigation of the signal events relevant to the present analysis and for the

[2] Events where beam-gas interactions produce a spray of particles close to the beam.

Table 4.3: Breakdown of the clean-up selections that were applied on all data samles used.

	Selection	Description
1	Beam-scrapping veto	For $N^{\text{Trks}} \geq 10$: $\frac{N^{\text{Trks}}_{\text{high-purity}}}{N^{\text{Trks}}} \geq 0.25$ For $N^{\text{Trks}} < 10$: Accept anyway
2	HCAL noise veto	Reject events with significant noisy HB/HE noise

QCD multi-jet data-driven measurement, a dedicated unprescaled[3] single τ jet + $E_{\text{T}}^{\text{miss}}$ trigger was used, which is discussed in detail in Section 4.4.1. Due to gradual increases in the LHC luminosity towards the design value of $10^{34}\text{cm}^{-2}\,\text{s}^{-1}$, the thresholds of this trigger increased over time in order to keep the rate within the 5 Hz trigger bandwidth, as allocated from the CMS collaboration to all analyses. The specific triggers along with their corresponding certified runs and integrated luminosities are shown in Table 4.4. The run regions with

Table 4.4: Collision data processed for the signal selection and QCD multi-jet data-driven background measurement. The triggers were unprescaled in all run periods.

Dataset	Runs	$\mathcal{L}$ (fb^{-1})
/Tau/Run2011A-May10ReReco-v1/AOD		
HLT_IsoPFTau35_Trk20_MET45	160431–163869	0.22
/Tau/Run2011A-PromptReco-v4/AOD		
HLT_IsoPFTau35_Trk20_MET45	165088–165633	0.14
HLT_IsoPFTau35_Trk20_MET60	165970–167913	0.82
/Tau/Run2011A-05Aug2011-v1/AOD		
HLT_IsoPFTau35_Trk20_MET60	170722–172619	0.40
/Tau/Run2011A-PromptReco-v6/AOD		
HLT_IsoPFTau35_Trk20_MET60	172620–173198	0.44
HLT_MediumIsoPFTau35_Trk20_MET60	173236–173692	0.27
Total integrated luminosity		2.27

different High-Level Trigger (HLT) $E_{\text{T}}^{\text{miss}}$ thresholds, 45 GeV and 60 GeV, were combined by requiring offline that HLT $E_{\text{T}}^{\text{miss}} > 60$ GeV.

A single μ trigger was employed in the EWK + $t\bar{t}$ background data-driven measurement, whereby the trigger muon was replaced with a tau with the τ-embedding method. Additionally, the same trigger was employed for the efficiency determination of the $E_{\text{T}}^{\text{miss}}$- part of the signal trigger which is described in detail in Section 4.4.2.2. The single μ triggers along with their corresponding certified runs and integrated luminosities are shown in Table 4.5. For the purpose of determining the $E_{\text{T}}^{\text{miss}}$- part of the signal trigger efficiency, additional datasets were used selected with prescaled single τ jet trigger, as shown in Table 4.6.

For the efficiency measurement of the τ-part of the signal trigger, which is discussed

[3] A prescaled trigger with factor n will only record 1-in-n events that satisfy the trigger requirements.

Table 4.5: Collision data processed for the EWK + $t\bar{t}$ data-driven background measurement, and for determining the efficiency of the $E_{\mathrm{T}}^{\mathrm{miss}}$- part of the signal trigger. The triggers were unprescaled in all run periods.

Dataset	Runs	$\mathcal{L}$ (fb^{-1})
/SingleMu/Run2011A-May10ReReco-v1/AOD		
HLT_Mu20	160431–163261	0.046
HLT_Mu24	163270–163869	0.16
/SingleMu/Run2011A-PromptReco-v4/AOD		
HLT_Mu30	165088–166150	0.23
HLT_Mu40	166161–167913	0.72
/SingleMu/Run2011A-05Aug2011-v1/AOD		
HLT_Mu40	170722–172619	0.40
/SingleMu/Run2011A-PromptReco-v6/AOD		
HLT_Mu40	172620–173198	0.44
HLT_Mu40_eta2p1	173236–173692	0.27
Total integrated luminosity		2.27

Table 4.6: Collision data processed for the $E_{\mathrm{T}}^{\mathrm{miss}}$ trigger efficiency measurement. Triggers were prescaled in all run periods.

Dataset	Runs	$\mathcal{L}$ (fb^{-1})
/Tau/Run2011A-PromptReco-v4/AOD		
HLT_IsoPFTau35_Trk20 (prescaled)	165970–167913	0.82
/Tau/Run2011A-05Aug2011-v1/AOD		
HLT_IsoPFTau35_Trk20 (prescaled)	170722–172619	0.40
/Tau/Run2011A-PromptReco-v6/AOD		
HLT_IsoPFTau35_Trk20 (prescaled)	172620–173198	0.44
HLT_MediumIsoPFTau35_Trk20 (prescaled)	173236–173692	0.27
Total integrated luminosity		1.93

in detail in Section 4.4.2.1, datasets with single isolated μ trigger were used as shown in Table 4.7.

4.3.2 Simulated samples

The official Summer11 Monte-Carlo (MC) production of simulated samples was used in this analysis. The centre-of-mass energy for proton-proton collisions was set to 7 TeV, while the detector response was simulated in detail using the GEANT4 [89] package. The samples were processed with CMSSW_4_2_8_patch2 [86] with the global tag START42_V13. The simulated samples were normalised by their cross-section to the total integrated luminosity of the collision data, unless stated otherwise. Furthermore, in all the simulated MC samples, pile-up interactions were taken into account by including additional interactions per bunch

Table 4.7: Collision data processed for determining the efficiency of the τ-part of the signal trigger. The triggers were unprescaled in the early run periods, and prescaled in later run periods as shown below.

Dataset	Runs	$\mathcal{L}$ (fb^{-1})
/SingleMu/Run2011A-Tau-May10ReReco-v1/RAW-RECO		
HLT_IsoMu17	160431–163869	0.22
/SingleMu/Run2011A-Tau-PromptSkim-v4/RAW-RECO		
HLT_IsoMu17	165088–165633	0.97
HLT_IsoMu17 (prescaled)	165970–167913	
/SingleMu/Run2011A-Tau-PromptSkim-v6/RAW-RECO		
HLT_IsoMu17 (prescaled)	172620–173198	0.41
HLT_IsoMu20 (prescaled)	173236–173692	0.27
Total integrated luminosity		1.87

crossing.

The inclusion of pile-up interactions in simulated samples is paramount in achieving accurate agreement between collision and simulated data. At the LHC design luminosity, a mean of ~ 20 inelastic collisions occur simultaneously during the same bunch crossing, meaning that the products of a specific interaction are likely to be confused with those of another in the same bunch crossing. This can affect the ability to reconstruct the event under study, with pile-up effects manifested in losses of events due to isolation criteria in lepton identification, discrepancies in the p_T distributions of jets due to the increased particle multiplicities and p_T, and complications arising from additional vertices. The number of pile-up interactions was taken from a distribution which was flat up to 10 interactions, and Poisson with a mean of 20 interactions, values that were chosen to reasonably match the LHC luminosity profile.

Apart from pile-up interactions, the Underlying Event (UE) activity at the LHC environment was also addressed in the simulated samples. In hadron-hadron scatterings, the UE is defined as any hadronic activity in addition to the hadronisation of partons that are involved in the hard parton-parton scattering process, and to the QCD Initial State Radiation (ISR) and Final State Radiation (FSR). Therefore, UE activity is connected with the hadronisation of partonic constituents that have undergone Multiple Parton Interactions (MPI), as well as to beam-beam remnants, concentrated along the beam direction. Failing to account for the UE activity can result in poor agreement between collision and simulated data due to similar effects as in the case of pile-up interactions. For this reason, the PYTHIA6 [90] Tune Z2 [91] for parton showering was used in the generation of all MC background samples, which resulted from a detailed study in the measurement of the UE activity at the LHC [92] and incorporates fine-tuning of the PYTHIA6 generator parameters related to colour re-connection and parton showering.

The signal simulated events in the processes $t\bar{t} \to bH^{\pm}bW^{\mp}$ and $t\bar{t} \to bH^{\pm}bH^{\mp}$ with

$H^{\pm} \to \tau^{\pm}\nu_{\tau}$ were generated with the PYTHIA6 event generator, as shown in Table 4.8. The dedicated package TAUOLA [93] was used to simulate the τ-leptons decays. Due to the fact that $H^{\pm}$ is a scalar boson while $W^{\pm}$ is a vector boson, the use of the TAUOLA package is essential to take account of the τ polarisation effects, which are important in discriminating the τ-leptons originating from the signal and those from the EWK backgrounds. The number of signal events was calculated based on the $t\bar{t}$ cross-section of $\sigma_{t\bar{t}} = 165\,\text{pb}$ [8] and taking $\text{BR}(t \to bH^{\pm})$ =0.05, and normalising the yield to the total integrated luminosity of the collision data, unless stated otherwise. The signal samples were mainly used in estimating the signal contamination to control samples, in optimising the final state selection criteria and in estimating the signal efficiencies to the various triggers.

The QCD multi-jet samples, shown in Table 4.9, were generated with PYTHIA6 with the Tune Z2 [91] for parton showering. The samples were produced in bins of $\hat{p}_{\text{T}}$, starting from 30 GeV/c up to 470 GeV/c, where the variable $\hat{p}_{\text{T}}$ is the transverse momentum of the outgoing partons in a $2 \to 2$ process, in the centre-of-mass frame, relative to the axis defined along the trajectory of the incoming partons. The cross-section values of the QCD $\hat{p}_{\text{T}}$-binned samples were calculated in Leading Order (LO). The QCD samples were only used in the development of the QCD multi-jet background measurement methods, but not for the final results which where obtained using data-driven techniques. An additional muon-enriched QCD sample with $\hat{p}_{\text{T}} > 20\,\text{GeV}/c$ was used as a background for the EWK + $t\bar{t}$ background measurement, with the requirement $p_{\text{T}}^{\mu} > 15\,\text{GeV}/c$, ensuring that muons at generator level had transverse momenta exceeding 15 GeV/c.

The di-boson (WW, WZ, ZZ) samples, shown in Table 4.10, were also generated with PYTHIA6 employing the Tune Z2 [91] for parton showering, while the dedicated package TAUOLA was used to simulate the τ-leptons decays. All relevant cross-sections used were calculated to Next-to-Leading Order (NLO). These samples were used in the EWK+$t\bar{t}$ genuine τ background measurement with the τ-embedding method, and for the EWK + $t\bar{t}$ fake tau background measurements.

The $t\bar{t}$ + jets, W + jets, and Drell-Yan ($Z^0/\gamma^* \to \ell\ell$) backgrounds, which are shown in Table 4.11, were all generated with the MADGRAPH [94] event generator and were subsequently processed with PYTHIA6 generator using the Tune Z2 [91]. Similarly to the di-boson samples, these samples were used in the EWK + $t\bar{t}$ genuine tau background measurement with the τ-embedding method and for the EWK + $t\bar{t}$ fake tau background measurements. The $t\bar{t}$ + jets production cross-section was determined to Next-to-Next-to-Leading Logarithm (NNLL), while for W + jets and Drell-Yan to Next-to-Next-to-Leading Order (NNLO).

The single-top backgrounds in the s-channel, t-channel, and tW-channel were generated with the POWHEG [95, 96, 97, 98, 99] event generator and were subsequently processed with PYTHIA6 employing the Tune Z2 [91]. Along with the di-boson, $t\bar{t}$ + jets, W + jets, and Drell-Yan samples, the single-top simulated samples were used in the EWK + $t\bar{t}$ genuine tau background measurement with the τ-embedding method and for the EWK + $t\bar{t}$ fake tau background measurements. Their cross-sections were determined to NNLL or NNLO, as

indicated in Table 4.12.

Table 4.8: Simulated signal samples for the process $t\bar{t} \to bH^{\pm}bW^{\mp}$ and $t\bar{t} \to bH^{\pm}bH^{\mp}$ with $H^{\pm} \to \tau^{\pm}\nu_{\tau}$, generated with PYTHIA6 +TAUOLA. The example cross-section values shown were calculated using branching ratios calculated with FeynHiggs [100], using $\tan\beta = 20$ and $\mu = 200\,\text{GeV}$ while the $t\bar{t}$ cross-section was taken to be $\sigma_{t\bar{t}} = 165\,\text{pb}$ [8]. Below `X` is shorthand notation for `Summer11-PU_S4_START42_V11-v1`.

Process	$m_{H^{\pm}}$	$\sigma \times \text{BR}$ (pb)	Events	Dataset name (AODSIM data tier)
$t\bar{t} \to bH^{\pm}bW^{\mp}$, $H^{\pm} \to \tau^{\pm}\nu_{\tau}$	$80\,\text{GeV}/c^2$	N/A†	218 050	`/TTToHplusBWB_M-80_7TeV-pythia6-tauola/X`
$t\bar{t} \to bH^{\pm}bW^{\mp}$, $H^{\pm} \to \tau^{\pm}\nu_{\tau}$	$90\,\text{GeV}/c^2$	16.19	218 050	`/TTToHplusBWB_M-90_7TeV-pythia6-tauola/X`
$t\bar{t} \to bH^{\pm}bW^{\mp}$, $H^{\pm} \to \tau^{\pm}\nu_{\tau}$	$100\,\text{GeV}/c^2$	13.82	218 200	`/TTToHplusBWB_M-100_7TeV-pythia6-tauola/X`
$t\bar{t} \to bH^{\pm}bW^{\mp}$, $H^{\pm} \to \tau^{\pm}\nu_{\tau}$	$120\,\text{GeV}/c^2$	8.77	218 400	`/TTToHplusBWB_M-120_7TeV-pythia6-tauola/X`
$t\bar{t} \to bH^{\pm}bW^{\mp}$, $H^{\pm} \to \tau^{\pm}\nu_{\tau}$	$140\,\text{GeV}/c^2$	4.07	218 400	`/TTToHplusBWB_M-140_7TeV-pythia6-tauola/X`
$t\bar{t} \to bH^{\pm}bW^{\mp}$, $H^{\pm} \to \tau^{\pm}\nu_{\tau}$	$150\,\text{GeV}/c^2$	2.16	219 000	`/TTToHplusBWB_M-150_7TeV-pythia6-tauola/X`
$t\bar{t} \to bH^{\pm}bW^{\mp}$, $H^{\pm} \to \tau^{\pm}\nu_{\tau}$	$155\,\text{GeV}/c^2$	1.38	219 000	`/TTToHplusBWB_M-155_7TeV-pythia6-tauola/X`
$t\bar{t} \to bH^{\pm}bW^{\mp}$, $H^{\pm} \to \tau^{\pm}\nu_{\tau}$	$160\,\text{GeV}/c^2$	0.74	218 400	`/TTToHplusBWB_M-160_7TeV-pythia6-tauola/X`
$t\bar{t} \to bH^{\pm}bH^{\mp}$, $H^{\pm} \to \tau^{\pm}\nu_{\tau}$	$80\,\text{GeV}/c^2$	N/A†	218 400	`/TTToHplusBHminusB_M-80_7TeV-pythia6-tauola/X`
$t\bar{t} \to bH^{\pm}bH^{\mp}$, $H^{\pm} \to \tau^{\pm}\nu_{\tau}$	$90\,\text{GeV}/c^2$	N/A†	219 000	`/TTToHplusBHminusB_M-90_7TeV-pythia6-tauola/X`
$t\bar{t} \to bH^{\pm}bH^{\mp}$, $H^{\pm} \to \tau^{\pm}\nu_{\tau}$	$100\,\text{GeV}/c^2$	0.32	218 800	`/TTToHplusBHminusB_M-100_7TeV-pythia6-tauola/X`
$t\bar{t} \to bH^{\pm}bH^{\mp}$, $H^{\pm} \to \tau^{\pm}\nu_{\tau}$	$120\,\text{GeV}/c^2$	0.12	218 800	`/TTToHplusBHminusB_M-120_7TeV-pythia6-tauola/X`
$t\bar{t} \to bH^{\pm}bH^{\mp}$, $H^{\pm} \to \tau^{\pm}\nu_{\tau}$	$140\,\text{GeV}/c^2$	0.026	218 800	`/TTToHplusBHminusB_M-140_7TeV-pythia6-tauola/X`
$t\bar{t} \to bH^{\pm}bH^{\mp}$, $H^{\pm} \to \tau^{\pm}\nu_{\tau}$	$150\,\text{GeV}/c^2$	0.0071	218 800	`/TTToHplusBHminusB_M-150_7TeV-pythia6-tauola/X`
$t\bar{t} \to bH^{\pm}bH^{\mp}$, $H^{\pm} \to \tau^{\pm}\nu_{\tau}$	$155\,\text{GeV}/c^2$	0.0029	217 400	`/TTToHplusBHminusB_M-155_7TeV-pythia6-tauola/X`
$t\bar{t} \to bH^{\pm}bH^{\mp}$, $H^{\pm} \to \tau^{\pm}\nu_{\tau}$	$160\,\text{GeV}/c^2$	0.00083	220 000	`/TTToHplusBHminusB_M-160_7TeV-pythia6-tauola/X`

† Not Available: FeynHiggs could not provide cross-sections for the specific $H^{\pm}$ mass point.

Table 4.9: Simulated QCD background samples, generated with PYTHIA6, Tune Z2 [91]. All cross-section values were calculated to LO. Below `X` is shorthand notation for `Summer11-PU_S4_START42_V11-v1`.

Process	$\sigma \times$ BR (pb)	Events	Dataset name (AODSIM data tier)
QCD $30 < \hat{p}_T < 50$ GeV/c	5.31×10^7	6 583 068	`/QCD_Pt_30to50_TuneZ2_7TeV_pythia6/X`
QCD $50 < \hat{p}_T < 80$ GeV/c	6.36×10^6	6 600 000	`/QCD_Pt_50to80_TuneZ2_7TeV_pythia6/X`
QCD $80 < \hat{p}_T < 120$ GeV/c	7.84×10^5	6 589 956	`/QCD_Pt_80to120_TuneZ2_7TeV_pythia6/X`
QCD $120 < \hat{p}_T < 170$ GeV/c	1.15×10^5	6 127 528	`/QCD_Pt_120to170_TuneZ2_7TeV_pythia6/X`
QCD $170 < \hat{p}_T < 300$ GeV/c	2.43×10^4	6 220 160	`/QCD_Pt_170to300_TuneZ2_7TeV_pythia6/X`
QCD $300 < \hat{p}_T < 470$ GeV/c	1.17×10^3	6 432 669	`/QCD_Pt_300to470_TuneZ2_7TeV_pythia6/X`
QCD $\hat{p}_T > 20$ GeV/c (μ-enriched)	8.48×10^4	25 080 241	`/QCD_Pt-20_MuEnrichedPt-15_TuneZ2_7TeV-pythia6/X`

Table 4.10: Simulated di-boson (WW, WZ, ZZ) background samples, generated with PYTHIA6 +TAUOLA, Tune Z2 [91]. The relevant cross-section values were all calculated to NLO. Below `X` is shorthand notation for `Summer11-PU_S4_START42_V11-v1`.

Process	$\sigma \times$ BR (pb)	Events	Dataset name (AODSIM data tier)
WW	43.0	4 225 916	`/WW_TuneZ2_7TeV-pythia6-tauola/X`
WZ	18.2	4 265 243	`/WZ_TuneZ2_7TeV-pythia6-tauola/X`
ZZ	5.9	4 187 885	`/ZZ_TuneZ2_7TeV-pythia6-tauola/X`

Table 4.11: Simulated $t\bar{t}$+jets, W+jets and Drell-Yan background samples, generated with MADGRAPH +PYTHIA6 +TAUOLA, Tune Z2 [91]. The $t\bar{t}$+jets cross-section was calculated to NNLL [101], while the cross-sections for the W + jets and $Z^0/\gamma^* \to \ell\ell$ sample were calculated to NNLO. Below `X` is shorthand notation for `Summer11-PU_S4_START42_V11-v1`.

Process	$\sigma \times$ BR (pb)	Events	Dataset name (AODSIM data tier)
$t\bar{t}$ + jets	165	3 701 947	`/TTJets_TuneZ2_7TeV-madgraph-tauola/X`
W + jets	31314	81 352 581	`/WJetsToLNu_TuneZ2_7TeV-madgraph-tauola/X`
$Z^0/\gamma^* \to \ell\ell$	3048	33 576 416	`/DYJetsToLL_TuneZ2_M-50_7TeV-madgraph-tauola/X`

Table 4.12: Simulated single-top background samples, generated with POWHEG +PYTHIA6 +TAUOLA, Tune Z2 [91]. The t-channel cross-sections were calculated to NNLO [102], the tW-channel to NNLL [103], and the s-channel to NNLL [104]. Below `X` is shorthand notation for `Summer11-PU_S4_START42_V11-v1`.

Process	$\sigma \times$ BR (pb)	Events	Dataset name (AODSIM data tier)
t, t-channel	41.92	3 900 171	`/T_TuneZ2_t-channel_7TeV-powheg-tauola/X`
$\bar{t}$, t-channel	22.65	1 944 826	`/Tbar_TuneZ2_t-channel_7TeV-powheg-tauola/X`
t, tW-channel	7.87	809 984	`/T_TuneZ2_tW-channel-DR_7TeV-powheg-tauola/X`
$\bar{t}$, tW-channel	7.87	814 390	`/Tbar_TuneZ2_tW-channel-DR_7TeV-powheg-tauola/X`
t, s-channel	3.19	259 971	`/T_TuneZ2_s-channel_7TeV-powheg-tauola/X`
$\bar{t}$, s-channel	1.44	137 980	`/Tbar_TuneZ2_s-channel_7TeV-powheg-tauola/X`

4.4 Trigger

The experimental signature of events with a light charged Higgs boson are characterised by an energetic τ jet and significant missing transverse energy originating from the $H^{\pm}$ and τ-lepton decays, 2 b-jets from the top quark decays and 2 hadronic jets originating from the hadronically-decaying $W^{\pm}$ boson. In the fully hadronic final state topology, the absence of EWK products translates to the fact that QCD multi-jet events dominate, which can only be significantly suppressed by employing a dedicated trigger with features that are not present in QCD processes, like $E_{\mathrm{T}}^{\mathrm{miss}}$ and leptons. In the following, the single τ jet + $E_{\mathrm{T}}^{\mathrm{miss}}$ trigger is described in Section 4.4.1, while the methodology employed for trigger efficiency measurements and the corresponding results are described in Section 4.4.2.

4.4.1 Signal trigger description

Because of the topology of the charged Higgs boson production, the signal event may be triggered using any combination of the single τ jet, multiple jets, or missing transverse energy. The use of a dedicated multi-jet trigger requiring the presence of four central calorimeter jets with one of which matched to an isolated Particle Flow (PF) τ jet as used in Ref. [105] was considered and consequently rejected, on the the grounds that the hadronic jet thresholds were too high, which would result in low signal efficiencies. In particular, the HLT_QuadJet40_PFTau40 and HLT_QuadJet45_PFTau45 triggers that were used in Ref. [105], would suppress a great proportion of the signal events due to the fact that the signal final state is very sensitive to hadronic jet and τ jet E_{T} thresholds. The effect becomes increasingly profound for charged Higgs masses closer to the mass of the top quark, where the phase-space of the b-quark from the decay $t \to bH^{\pm}$ becomes more and more limited. Therefore, the alternative approach of combining a τ jet and missing transverse energy into a single τ jet + $E_{\mathrm{T}}^{\mathrm{miss}}$ trigger was employed for the selection of signal events, which besides significantly restraining the QCD multi-jet dominance it also constrained the trigger rates within the allocated CMS trigger bandwidth. The definitions for the trigger menus used in the 2011 data-taking period are summarised in Table 4.13.

Table 4.13: Single triggers with their HLT paths and corresponding L1 seeds, their design luminosities and their corresponding run ranges. The last three triggers are prescaled control triggers for measuring the trigger efficiency. In the run period 160431–167913 the $E_{\mathrm{T}}^{\mathrm{miss}}$ reconstruction at HLT excluded the HF, while in the runs 170722–173198 the HF was included. The triggers where $E_{\mathrm{T}}^{\mathrm{miss}}$ reconstruction included the HF are marked below with †. The L1_Jet52_Central seed is equivalent to L1_SingleTauJet52 OR L1_SingleJet52 seeds, while the L1_SingleJet52_Central seed is equal to L1_SingleTauJet52 AND L1_SingleJet52. The L1_SingleJet52_Central seed used in the control triggers was supposed to be equal to L1_SingleTauJet52 OR L1_SingleJet68, i.e. same as in the main trigger, but due to a mistake in the L1 menu it is instead equal to the L1_SingleTauJet52 AND L1_SingleJet52 seeds. However, since the L1_SingleTauJet52 AND L1_SingleJet52 is a subset of L1_SingleTauJet52 OR L1_SingleJet52, this does not make the events unusable, only the size of the collected event sample is lower. Finally, the difference between HLT IsoPFTau and HLT MediumIsoPFTau is that the former is tighter, containing both tracker and ECAL isolation, while the MediumIsoPFTau menu contains the tracker isolation only.

L1 seed	HLT path	Design luminosity ($\mathrm{cm}^{-2}\,\mathrm{s}^{-1}$)	Run range
L1_SingleTauJet52 OR L1_SingleJet68	HLT_IsoPFTau35_Trk20_MET45	1×10^{33}	160431–165633
L1_SingleTauJet52 OR L1_SingleJet68	HLT_IsoPFTau35_Trk20_MET60	2×10^{33}	165970–167913
L1_Jet52_Central_ETM30	HLT_IsoPFTau35_Trk20_MET60†	2×10^{33}	170722–173198
L1_Jet52_Central_ETM30	HLT_MediumIsoPFTau35_Trk20_MET60†	3×10^{33}	173236–173692
L1_SingleTauJet52 OR L1_SingleJet68	HLT_IsoPFTau35_Trk20 (prescaled)	1×10^{33}	165970–167913
L1_SingleJet52_Central	HLT_IsoPFTau35_Trk20 (prescaled)	2×10^{33}	170722–173198
L1_SingleJet52_Central	HLT_MediumIsoPFTau35_Trk20 (prescaled)	3×10^{33}	173236–173692

At the L1 Trigger, the single τ jet+$E_{\mathrm{T}}^{\mathrm{miss}}$ trigger is solely based on calorimeter information. At this level, only L1 jets with $|\eta|< 3.0$ are considered. The L1 calorimeter jet algorithm scans the $\eta - \phi$ space within a sliding window of 3×3 trigger regions, each region comprised of 4×4 Trigger Towers (TTs) which are represented by little squares in Fig. 4.11. The jet

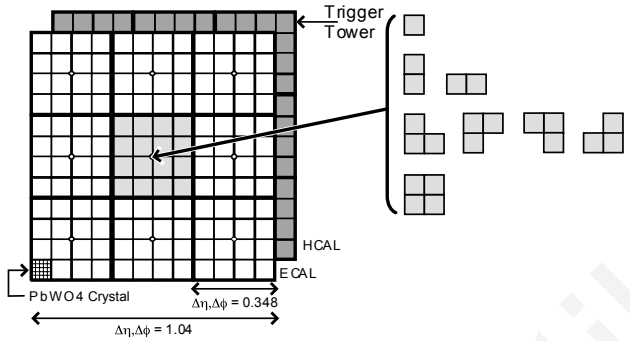

Figure 4.11: Visualisation of hadronic jet and τ jet L1 trigger algorithms. A square depicts a calorimeter TT while an array of 4×4 TTs enclosed by thick black lines represent trigger regions. The jet algorithm sliding window spans 3×3 trigger regions, thus forming a 12×12 TT configuration. See also Fig. 3.37 on page 90. Taken from Ref. [50].

algorithm analyses the E_{T} deposition in them, and a L1 jet is found if the E_{T} deposition in the central trigger region of the sliding window exceeds a given E_{T} threshold, and is also higher than any of the 8 surrounding trigger regions.

A dedicated τ-Veto pattern search is carried out by examining the energy deposition in the TTs separately for each trigger region of the sliding window. The TTs are considered active if their ECAL and Hadronic Calorimeter (HCAL) energy deposits exceed a given threshold. If the active TTs in a given trigger region do not match any of the allowed patterns shown in Fig. 4.11, they are assigned a τ-Veto bit. If none of the τ-Veto bits of the trigger regions in the sliding window are set, then the L1 jet is labelled as a L1 τ jet, thus exploiting the narrowness of the energy deposition of τ jets.

Furthermore, τ-isolation requires that the jet's energy be contained within 2 square Regional Calorimeter Trigger (RCT) regions, each one spanning 4×4 TTs. Events with at least one jet passing the L1 τ-Veto, τ-isolation and an E_{T} threshold of 52 GeV (L1_SingleTauJet52) are fed to the HLT. For the $1 \times 10^{33}\mathrm{cm}^{-2}\,\mathrm{s}^{-1}$, and up to the $2 \times 10^{33}\mathrm{cm}^{-2}\,\mathrm{s}^{-1}$ menu, in order to counter the drop in the efficiency of L1 τ-Veto and τ-isolation at high E_{T}, events with at least 1 jet failing either of these requirements were also passed on to the HLT, provided their E_{T} was 68 GeV or greater (L1_SingleJet68).

Additionally, in order to increase the L1 efficiency, central jets not passing the L1 τ-isolation requirement are also included, but with higher E_{T} threshold. A summary of the L1 seed jet trigger requirements is presented in Table 4.14. During the 2011 data-taking period the LHC instantaneous luminosity increased, and consequently the trigger menus had to be tightened accordingly. For the $2 \times 10^{33}\mathrm{cm}^{-2}\,\mathrm{s}^{-1}$ menu, the chosen L1 requirements included a central jet of 52 GeV and missing transverse energy of at least 30 GeV (L1_Jet52 AND L1_ETM30). The $E_{\mathrm{T}}^{\mathrm{miss}}$ requirement was introduced at L1 (L1_ETM30) to keep the trigger rates under con-

Table 4.14: Summary of the L1 seed jet trigger requirements.

Requirement	L1_SingleTauJet52	L1_SingleJet68
Minimum E_T corrected (uncorrected)	52 (32) GeV	68 (40) GeV
Maximum $\|\eta\|$	3.0	3.0
τ-isolation	yes	no
τ-Veto	yes	no

trol and had no significant decrease in the overall L1 +HLT efficiency for the signal events. After introducing the L1 E_T^{miss} (L1 _ETM) in the single τ jet + E_T^{miss} trigger, the L1 _ETM was dominating the L1 rate, which allowed the jet threshold to remain at low levels.

All events successfully passing the L1 selection were analysed in more detail at HLT. More specifically, at Level-2 (L2), a calorimeter jet was reconstructed and it was required to match the L1 object, and have an associated E_T equal or greater than 35 GeV. At Level-2.5 (L2.5), a fixed cone PF tau was reconstructed and matched to the L2 jet. Finally, at Level-3 (L3) isolation criteria were applied to charged hadron and photon candidates. More

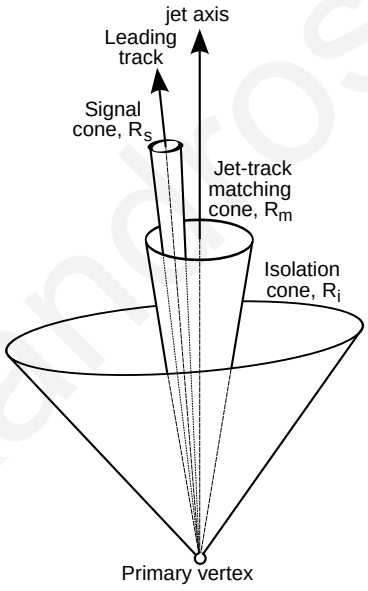

Figure 4.12: Sketch of the basic principle of τ-jet identification at L3.

specifically, the direction of the τ jet was defined by the axis of the calorimeter jet, as shown in Fig. 4.12. The track-finding algorithm first reconstructs all charged track candidates and then the interaction vertices from these tracks. Track candidates in a matching cone R_m around the jet direction and above a threshold p_T are considered in the search for the signal tracks. The leading signal track is defined as the track with the highest p_T while the vertex from which it originates is the signal vertex. Around the leading track a cone in $\eta - \phi$ space is created with an opening angle R_s and any track from the signal vertex lying within this narrow signal cone is assumed to come from the τ-lepton decay. Charged hadrons and photon candidates with transverse momentum above a given p_T threshold x are then searched for inside an isolation cone of opening angle R_i. If no such candidates are found

in the isolation cone, excluding the ones already found in the R_s cone, the τ-jet isolation criteria are fulfilled. This can be expressed by an isolation variable P_{iso}, which for charged hadron candidates may be written as

$$P^{h}_{iso} = \sum_{R_i - R_s}^{p_T > x\,GeV/c} = 0. \tag{4.13}$$

and for photon candidates as

$$P^{\gamma}_{iso} = \sum_{R_i - R_s}^{E_T > x\,GeV} = 0, \tag{4.14}$$

The cone sizes were set to R_s =0.15, R_m =0.2 and R_i =0.5 for the signal, matching and isolation cones, respectively. A p_T cut of 35 GeV/c was applied on the τ jet object, while the leading charged candidate of the τ jet was required to have a p_T equal or greater than 20 GeV/c.

Several changes in both the E_T^{miss} and τ jet parts of the HLT path were introduced to address the issue of high trigger rates as the luminosity increased throughout 2011. In the τ-part, the EM isolation was removed for the 3×10^{33}cm^{-2} s^{-1} menu as it was found to be affected by pile-up, and the resulting HLT_MediumIsoPFTau35_Trk20_MET60 trigger path was found to be more robust. In the E_T^{miss}- part of the trigger, a threshold increase was required from the 45 GeV used for 5×10^{32}cm^{-2} s^{-1} menu to 60 GeV for the 1×10^{33}cm^{-2} s^{-1} menu. An analytic breakdown of the trigger selection used for the data collected in 2011 is presented in Table 4.15.

Table 4.15: Breakdown of the signal trigger requirements. The HF was excluded in L2 MET calculation for runs $\leq$ 167913, and included for runs $\geq$ 170722.

Level	Description	Note
L1	τ jet $E_T > 52$ GeV OR L1 central jet $E_T > 68$ GeV	runs $\leq$ 167913
L1	τ jet or central jet $E_T > 52$ GeV AND L1 $E_T^{miss} > 30$ GeV	runs $\geq$ 170722
L2	$E_T^{miss} > 45$ GeV for events passing L1_SingleTau	runs $\leq$ 165633
L2	$E_T^{miss} > 60$ GeV for events passing L1_SingleTau	runs $\geq$ 165970
L2	Jet with opening angle R=0.2 matches L1 τ jet object	$E_T > 35$ GeV, $\lvert\eta\rvert < 3$
L2.5	Fixed cone PF τ jet matches L2 jet	$p_T > 35$ GeV/c, $\lvert\eta\rvert < 2.5$
L2.5	Leading track found	$p_T > 20$ GeV/c
L3	Tight isolation: $P^{h}_{iso} = \sum_{R_i - R_s}^{p_T > 1.0\,GeV/c} = 0 + P^{\gamma}_{iso} = \sum_{R_i - R_s}^{E_T > 1.5\,GeV} = 0$	runs $\leq$ 173198
L3	Medium isolation: $P^{h}_{iso} = \sum_{R_i - R_s}^{p_T > 1.0\,GeV/c} = 0$	runs $\geq$ 173236

4.4.2 Signal trigger efficiency measurement

One of the most critical elements in many collider physics analysis is the accurate and reliable measurement of the trigger efficiency, especially for analyses which aim in measuring the cross-section of a given process. The reliance on trigger efficiency predictions from MC simulations can produce large systematic errors due to imperfections in modelling both the data and the detector response, so trigger efficiencies are ideally measured directly from the data. The problem then becomes one of identifying the desired particle types in data, with a small or subtracted fake rate. In this analysis, the efficiencies for the τ-part and $E_{\mathrm{T}}^{\mathrm{miss}}$- part of the single τ jet + $E_{\mathrm{T}}^{\mathrm{miss}}$ trigger were measured separately from data.

4.4.2.1 τ-part trigger efficiency

A well established data-driven approach in measuring particle efficiencies is the so called Tag-and-Probe method. The Tag-and-Probe method utilises a known mass resonance, such as Z^0, to select particles of a specific type and probe the efficiency with which a particular selection is successful in identifying them. In general, the tag is an object that passes a set of very tight selection criteria designed to isolate the required particle type, and consequently the fake rate for passing the tag selection criteria is normally quite small. Conversely, the probe is a generic set of the desired particle type with much looser selection criteria. The probe is thus selected by pairing it with a tag object, such that the invariant mass of the combination is consistent with the mass of the resonance under consideration. The definition of the probe object depends on the specifics of the selection criterion being examined. The probe efficiency is then measured by counting the number of probe particles that pass the desired selection criteria as

$$\varepsilon = \frac{N_{\mathrm{probes}}^{\mathrm{pass}}}{N_{\mathrm{probes}}} \tag{4.15}$$

where $N_{\mathrm{probes}}^{\mathrm{pass}}$ is the number of probes passing the desirable selection and N_{probes} is the total number of probes counted using the resonance. It is possible that a probe object will also pass the tag selection criteria. In this case it will appear in both the tag and the probe lists and produce a double pairing in the same event, in which case the definition in Eq. (4.15) must account for the double pairing.

The Tag-and-Probe method was employed for the purpose of measuring the τ-part efficiency of the single τ jet + $E_{\mathrm{T}}^{\mathrm{miss}}$ trigger. Drell-Yan events with 2 τ-leptons in the final state ($Z^0/\gamma^* \rightarrow \tau^{\pm}\tau^{\mp}$) were selected, where one τ-lepton decays to a μ (tag) and the other decays hadronically (probe), in a selection similar to offline τ-jet identification efficiency studies [106]. The datasets were selected using a single isolated μ trigger, with the required muon trigger thresholds for the different runs shown in Table 4.16. The events were required to have exactly 1 reconstructed muon [107], that is identified as a Global-muon and a Tracker-muon and successfully passed the GlobalMuonPromptTight muon identification. The latter requires that the reconstructed muon has a normalised chi-squared value

Table 4.16: Muon triggers used for the τ-part efficiency measurement of the single τ jet + $E_{\mathrm{T}}^{\mathrm{miss}}$ trigger, with their corresponding run range and their offline p_{T} thresholds.

Run range	Muon trigger	Offline muon p_{T} threshold
160404–165633	HLT_IsoMu17	$p_{\mathrm{T}} > 17\,\mathrm{GeV}/c$
165970–167913	HLT_IsoMu17 (prescaled)	$p_{\mathrm{T}} > 17\,\mathrm{GeV}/c$
170722–172619	HLT_IsoMu17 (prescaled)	$p_{\mathrm{T}} > 17\,\mathrm{GeV}/c$
173236–173692	HLT_IsoMu20 (prescaled)	$p_{\mathrm{T}} > 20\,\mathrm{GeV}/c$

of χ^2/n.d.o.f < 10 and at least 1 hit in the muon stations. Furthermore, at least 11 hits were required in the tracker, at least 1 hit in pixel tracker, at least 2 segments matched to the Global-muon and its transverse impact parameter with respect to the beam-spot to satisfy $\mathrm{d}_{xy}^{\text{beam-spot}} < 0.02\,\mathrm{cm}$. In addition, the reconstructed muon had kinematic requirements such that $p_{\mathrm{T}} > 17$ or $20\,\mathrm{GeV}/c$, depending on the trigger used, and $|\eta| < 2.1$, while its relative PF[4] isolation, defined as

$$P_{\text{rel. iso}}^{\text{PF}} = (\sum p_{\mathrm{T}}^{\text{charged hadron}} + \sum E_{\mathrm{T}}^{\text{photon}} + \sum E_{\mathrm{T}}^{\text{neutral hadron}})/p_{\mathrm{T}}^{\mu} \tag{4.16}$$

was required to satisfy $P_{\text{rel. iso}}^{\text{PF}} < 0.1$. Moreover, events in which a second reconstructed Global-muon was found with $p_{\mathrm{T}} > 15\,\mathrm{GeV}/c$, $|\eta| < 2.4$ and $P_{\text{rel. iso}}^{\text{PF}} < 0.15$ were rejected. The events were required to have exactly one τ jet identified with the same criteria as those used in the signal selection, described in Section 4.5.3. The selected muon and the τ jet were required to have opposite charges, and to be separated in $\eta - \phi$ space by $\Delta R(\mu, \tau\text{ jet}) > 0.7$. The transverse mass reconstructed from the muon and the $E_{\mathrm{T}}^{\mathrm{miss}}$ objects was required to be $m_{\mathrm{T}}\left(\mu, E_{\mathrm{T}}^{\mathrm{miss}}\right) < 40\,\mathrm{GeV}/c^2$ in order to reject background from W + jets events. The visible mass calculated from the muon and the τ jet objects was required to be $m_{\mathrm{vis}}\,(\mu, \tau\text{ jet}) < 80\,\mathrm{GeV}/c^2$ in order to reject background from $Z^0/\gamma^* \to \mu^{\pm}\mu^{\mp}$ events, where a muon could be misidentified as τ jet in the offline τ-jet identification. Despite the fact that the againstMuonTight discriminator is employed in τ-jet reconstruction, aiming at the rejection of muons faking τ jets, still some badly reconstructed muons do pass the requirements. Such $Z^0/\gamma^* \to \mu^{\pm}\mu^{\mp}$ events, which can fake genuine $Z^0/\gamma^* \to \tau^{\pm}\tau^{\mp}$ events whereby one τ-lepton has decayed to a μ, have a narrow peak around $m_{\mathrm{vis}}\,(\mu, \tau\text{ jet}) \simeq 90\,\mathrm{GeV}/c^2$. By setting an upper limit on $m_{\mathrm{vis}}\,(\mu, \tau\text{ jet})$, a large fraction of these events is rejected, resulting in a relatively pure and statistically-rich $Z^0/\gamma^* \to \tau^{\pm}\tau^{\mp}$ events sample. The complete set of requirements imposed on the muon are summarised in Table 4.17.

The efficiency of the τ-part of the single τ jet + $E_{\mathrm{T}}^{\mathrm{miss}}$ trigger was then defined as the probability of the existence of τ objects at each trigger level within a certain distance in $\eta - \phi$ space ΔR with respect to the probe τ jet. The L1 τ objects were taken from the L1 extra object collection in the event. The HLT τ objects were reconstructed with the OpenHLT software from the RAW data, and the selections in the trigger path were applied successively. The probe τ jet was considered to pass a given trigger level if there was a trigger object

[4] The PF algorithm is described in Section 4.5.1

Table 4.17: Identification criteria for the reconstructed muon, which assumes the role of the tag object in the Tag-and-Probe method employed to measure the τ-part trigger efficiency from the data.

	Selection	Description
1	$p_{\mathrm{T}} > 17, 20\,\mathrm{GeV}/c$	Transverse momentum acceptance
2	$\lvert\eta\rvert < 2.1$	Pseudorapidity acceptance
3	$P^{\mathrm{PF}}_{\mathrm{rel.\ iso}} < 0.10$	Relative PF isolation
	Common muon identification selections	
4	Is Global-muon	Outside-in track fit approach (muon → tracker)
5	Is Tracker-muon	Inside-out track fit approach (tracker → muon)
6	Is GlobalMuonPromptTight	χ^2/n.d.o.f < 10 and $\mathrm{N}^{\mathrm{hits}}_{\mathrm{muon}} \geq 1$
7	$\mathrm{N}^{\mathrm{hits}}_{\mathrm{tracker}} \geq 11$	At least 11 hits in the tracker
8	$\mathrm{N}^{\mathrm{hits}}_{\mathrm{pixel}} \geq 1$	At least 1 hit in pixel tracker
9	$\mathrm{N}^{\mathrm{matched}}_{\mathrm{segments}} \geq 2$	At least 2 muon segments matched to Global-muon
10	$\mathrm{d}^{\mathrm{beam\text{-}spot}}_{xy} < 0.02\,\mathrm{cm}$	Transverse impact parameter
	Secondary muon event-rejection requirements	
1	$p_{\mathrm{T}} > 15\,\mathrm{GeV}/c$	Transverse momentum acceptance
2	$\lvert\eta\rvert < 2.4$	Pseudorapidity acceptance
3	Is Global-muon	Outside-in track fit approach (muon → tracker)
4	$P^{\mathrm{PF}}_{\mathrm{rel.\ iso}} < 0.15$	Relative PF isolation

of that level within $\Delta R(\tau_{\mathrm{offline}}, \tau_{\mathrm{trigger}}) < 0.5, 0.2, 0.3$ for L1, L2, and L2.5/L3, respectively. The definition of the overall L1+HLT efficiency was given by

$$\varepsilon_{\mathrm{L1+HLT}} = \frac{N^{\mathrm{pass}}_{\mathrm{probes}}}{N^{\mathrm{pass}}_{\mathrm{probes}} + N^{\mathrm{fail}}_{\mathrm{probes}}}, \tag{4.17}$$

with the probes being selected with the offline τ-jet selection. Thus, $N^{\mathrm{pass}}_{\mathrm{probes}}$ denotes the number of selected offline probes matching to the L1, L2, L2.5, and L3 τ objects. Conversely, the term $N^{\mathrm{fail}}_{\mathrm{probes}}$ denotes the selected offline probes that failed to match all the aforementioned trigger objects. The efficiencies for the 3 L1+HLT combinations in the Run2011A data, namely L1_SingleTauJet52 OR L1_SingleJet68 with HLT_IsoPFTau35_Trk20, L1_Jet52_Central with HLT_IsoPFTau35_Trk20 and L1_Jet52_Central with HLT_MediumIsoPFTau35_Trk20, were measured separately with the data in the corresponding run regions. The overall L1+HLT efficiencies as a function of offline τ-jet p_{T} for the 3 L1+HLT triggers are shown in Fig. 4.13. As an illustration, a fit with a function

$$f(p_{\mathrm{T}}) = \frac{p_0}{2} \times \left[1 + \mathrm{erf}\left(\frac{\sqrt{p_{\mathrm{T}}} - \sqrt{p_1}}{\sqrt{2}p_2}\right)\right] \tag{4.18}$$

was made to the efficiency values. The differences in the efficiencies in data and simulations

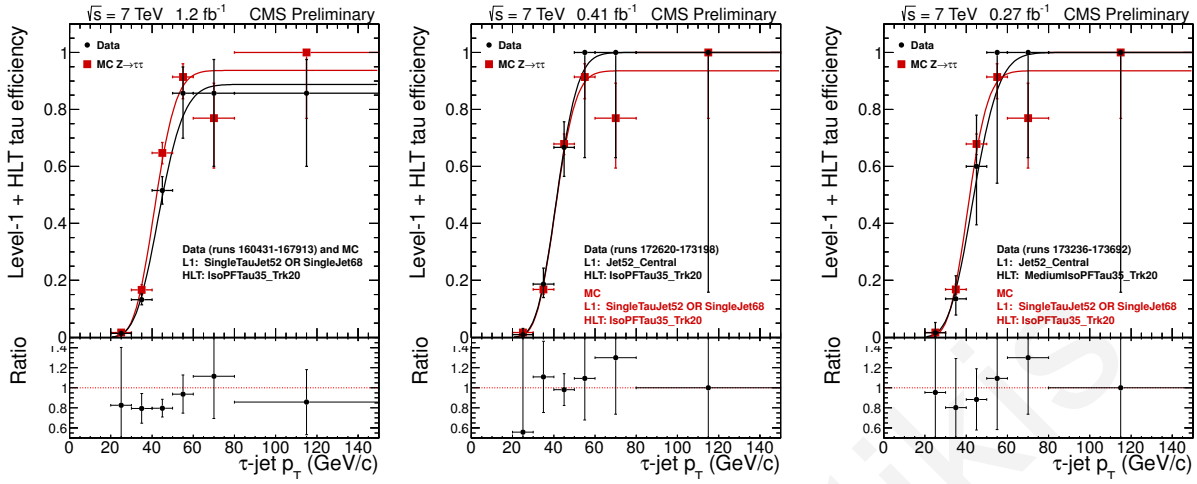

Figure 4.13: Overall L1+HLT efficiencies of the 3 tau trigger configurations in the Run2011A data set. The τ-jet p_T threshold in the signal event selection was 40 GeV/c. For comparison with simulations, the trigger configuration in simulations was set to the one in Summer11 samples and is the same in all 3 plots. Therefore, an agreement between data and simulations is expected only in plot (a). The discrepancies are taken into account with scale factors defined as the ratio of data and simulations, as discussed in Section 4.6.2.

were taken into account with scale factors applied to simulations. The scale factors are discussed further in Section 4.6.2.

4.4.2.2 E_T^{miss}-part trigger efficiency

The efficiency of E_T^{miss}- part of the single τ jet+E_T^{miss} trigger was measured with uncorrected calo E_T^{miss}, which was assumed to be a good approximation of the E_T^{miss} reconstructed at HLT (HLT E_T^{miss}). In the first part of Run2011A, the HF was excluded from the HLT E_T^{miss}, while in the latter part the HF was included in the HLT E_T^{miss}, as shown in Table 4.13. This change in HLT E_T^{miss} reconstruction also coincided with the addition of L1 E_T^{miss} to the L1 seed of the single τ jet + E_T^{miss} trigger. The efficiencies of the E_T^{miss}- part of the signal triggers were therefore measured separately for the 2 run periods. In the first part, offline uncorrected calo E_T^{miss} with HF excluded was used, while in the second part offline uncorrected calo E_T^{miss} with HF included was used. In Summer11 simulation, the HF was excluded from the HLT E_T^{miss} reconstruction, as was the case for the first part of the Run2011A data.

The first step in determining the efficiency of the E_T^{miss}- part of the single τ jet + E_T^{miss} trigger was to establish whether the uncorrected calo E_T^{miss} is a good approximation of the HLT E_T^{miss}. This was achieved by using data collected with a prescaled single τ jet trigger, which is the τ-part of the single τ jet + E_T^{miss} trigger described in Section 4.4.1. The events were required to pass this prescaled single τ jet trigger, to have 3 PF jets, of which one was identified as a b-jet, and no isolated electrons or muons. The hadronic jets and b-tagging selections, as well as the veto of isolated leptons, were the same as those

used in the signal selection, described in Sections 4.5.5, 4.5.7 and 4.5.4, respectively. With these events the efficiencies of HLT $E_T^{miss} > 60\,GeV$ and calo $E_T^{miss} > 60\,GeV$ cuts were measured as a function of uncorrected PF E_T^{miss} for the 2 run periods, as shown in Fig. 4.14. The HLT $E_T^{miss} > 60\,GeV$ cut was simply applied by requiring that the events triggered by the prescaled single τ jet trigger also passed the single τ jet + E_T^{miss} trigger. The HLT $E_T^{miss} > 60\,GeV$ and calo $E_T^{miss} > 60\,GeV$ efficiencies are shown to agree within the statistical uncertainties, which were estimated using the Clopper-Pearson method[108, 109], confirming that the uncorrected calo E_T^{miss} is indeed a good approximation of HLT E_T^{miss}.

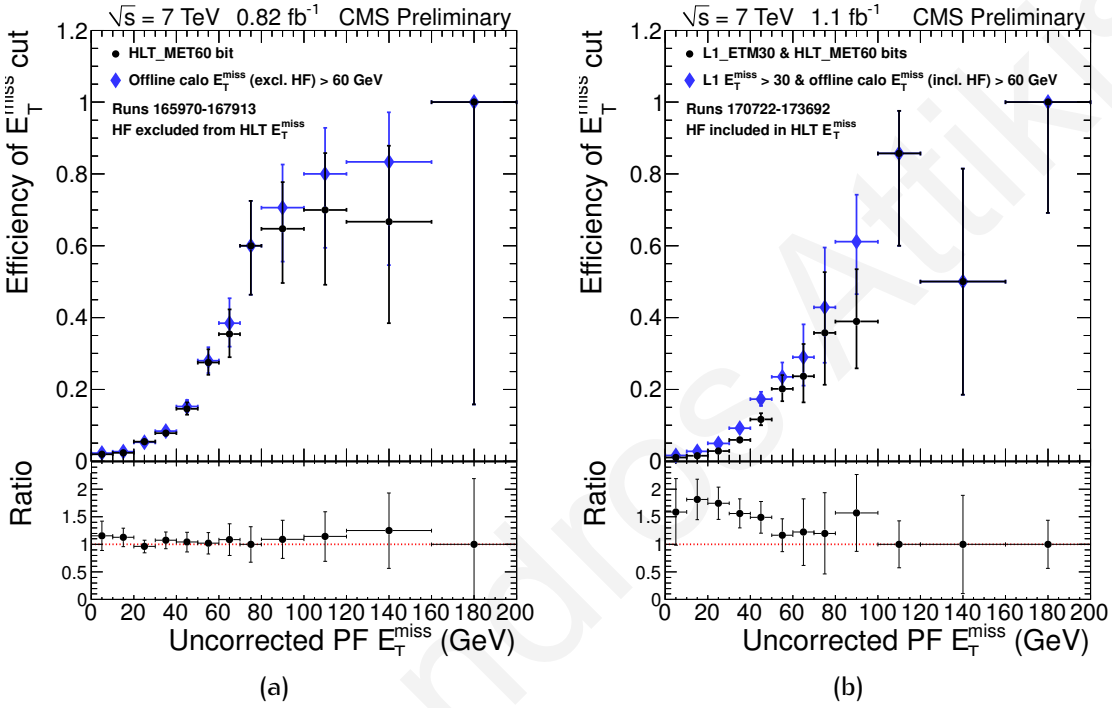

Figure 4.14: Comparison of efficiencies of HLT $E_T^{miss} > 60\,GeV$ and offline calo $E_T^{miss} > 60\,GeV$ requirements as a function of uncorrected PF E_T^{miss}. In the data in (a) [(b)], the HF was excluded [included] from the offline calo E_T^{miss} reconstruction to reflect the configuration of the HLT E_T^{miss} reconstruction in the data. In the signal event selection the uncorrected PF E_T^{miss} was required to be $E_T^{miss} > 50\,GeV$.

After establishing that the uncorrected calo E_T^{miss} is a good approximation of HLT E_T^{miss}, the next step was to use it to determine the efficiency of the E_T^{miss}- part of the single τ jet + E_T^{miss} trigger. This was done using events with signal-like topologies, triggered with the single μ triggers of HLT_Mu20, HLT_Mu24, HLT_Mu30, HLT_Mu40 or HLT_Mu40_eta2p1, depending on which was the lowest unprescaled trigger in the corresponding run. The mapping between run numbers and the required trigger path is shown in Table 4.5 on page 114. In the simulated MC samples used, the events were triggered with HLT_Mu20. The events were required to have exactly 1 good muon with the full requirements tabulated in Table 4.18. To emulate the absence of the τ jet, the muon was required to be isolated based on criteria, that closely matched the Hadron plus Strips (HPS)[5] byTightIsolation isolation criteria as used for the τ-jet identification in the signal selection. The key idea was not to

[5]The HPS algorithm is described in Section 4.5.3.

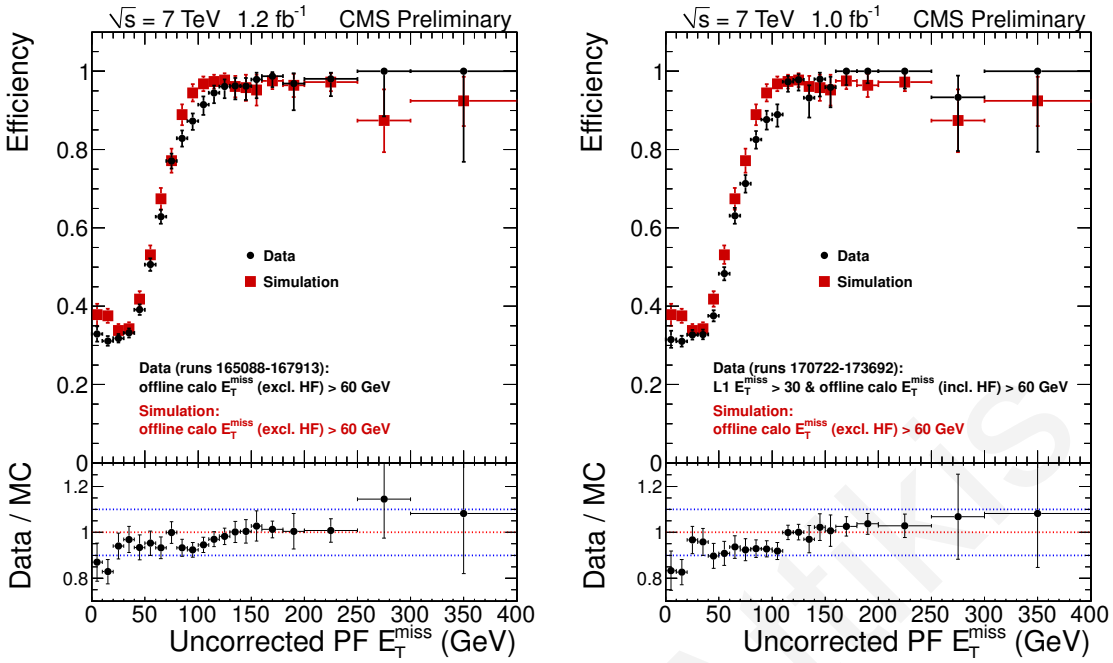

Figure 4.15: Efficiencies of the calo $E_T^{miss} > 60\,GeV$ requirement for data (dots) and simulated samples (filled squares). In the data in (a) [(b)], the HF was excluded [included] from the offline calo E_T^{miss} reconstruction to reflect the configuration in HLT E_T^{miss} reconstruction in the data. For the simulations the HF was excluded from the offline calo E_T^{miss} reconstruction as it was excluded from the HLT E_T^{miss} in the Summer11 samples. In the signal event selection the uncorrected PF E_T^{miss} was required to be $E_T^{miss} > 50\,GeV$.

over-clean the cone around the muon where the tau reconstruction, tau constituent finding and tau isolation were performed. This goal was achieved by introducing a signal cone of opening angle R_s, and an isolation cone of opening angle R_i, around the muon, giving an isolation annulus of $0.1 < \Delta R < 0.4$ around the muon to be considered for the isolation. In this way, possible biases originating from the use of a muon, instead of a τ jet, in the final state for the E_T^{miss}- part efficiency determination were eliminated. Events with more than one muon passing the selections in Table 4.18 were also rejected, while events with additional isolated electrons or muons were rejected with criteria identical to those used in the signal selection, described in Section 4.5.4. The events were required to have at least 3 PF jets, identified as described in Section 4.5.5, with at least 1 of them being successfully b-tagged, as described in Section 4.5.7. In addition, the selected jets were required to be separated from the selected muon with $\Delta R(\mu, \text{jet}) > 0.1$. This is imporant to avoiding double counting, since within PF most muons can give rise to a PF jet. Thus, unless a dedicated cleaning is performed, when using reconstructed muons and PF jets, it is common practise to reject these muon-jets by the aforementioned ΔR requirement.

The measured efficiencies are shown in Fig. 4.15, as a function of the uncorrected PF E_T^{miss}. The efficiency of the simulated samples is a combination of the efficiencies of the QCD multi-jet, $t\bar{t}$ and W + jets background samples, weighted by their cross sections. The efficiencies for data and simulations agree within 10% in the uncorrected PF $E_T^{miss} > 50\,GeV$ region. This uncertainty was included in the systematic uncertainties of simulated samples

Table 4.18: Identification criteria for the reconstructed muon in events triggered with single μ triggers, for the purpose of determining the efficiency of the $E_{\mathrm{T}}^{\mathrm{miss}}$- part of the single τ jet + $E_{\mathrm{T}}^{\mathrm{miss}}$ trigger.

	Selection	Description
1	$p_{\mathrm{T}} > 40\,\mathrm{GeV}/c$	Transverse momentum acceptance
2	$\lvert\eta\rvert < 2.1$	Pseudorapidity acceptance
	Common muon identification selections	
3	Is Global-muon	Outside-in track fit approach (muon → tracker)
4	Is Tracker-muon	Inside-out track fit approach (tracker → muon)
5	Is GlobalMuonPromptTight	χ^2/n.d.o.f < 10 and $\mathrm{N}_{\mathrm{muon}}^{\mathrm{hits}} \geq 1$
6	$\mathrm{N}_{\mathrm{tracker}}^{\mathrm{hits}} \geq 11$	At least 11 hits in the tracker
7	$\mathrm{N}_{\mathrm{pixel}}^{\mathrm{hits}} \geq 1$	At least 1 hit in pixel tracker
8	$\mathrm{N}_{\mathrm{segments}}^{\mathrm{matched}} \geq 2$	At least 2 muon segments matched to Global-muon
9	$\mathrm{d}_{xy}^{\text{beam-spot}}$ <0.02 cm	Transverse impact parameter less than 0.02 cm
	HPS byTightIsolation-like criteria: charged hadrons	
10	$\mathrm{P}_{\mathrm{iso}}^{h} = \sum_{\mathrm{R}_i-\mathrm{R}_s}^{p_{\mathrm{T}}>0.5\,\mathrm{GeV}/c} = 0$	Isolation in annulus formed by R_i =0.4 and R_s =0.1
11	$\mathrm{N}_{\mathrm{tracker}}^{\mathrm{hits}} \geq 3$	At least 3 hits in the tracker by charged hadron
12	χ^2/n.d.o.f < 100	Goodness of track fit for charged hadron
13	$\mathrm{d}_{xy}^{\mathrm{PV}} < 0.03\,\mathrm{cm}$	Transverse impact parameter for charged hadron
14	$\mathrm{d}_{z}^{\mathrm{PV}} < 0.2\,\mathrm{cm}$	Longitudinal impact parameter for charged hadron
	HPS byTightIsolation-like criteria: photons	
15	$\mathrm{P}_{\mathrm{iso}}^{\gamma} = \sum_{\mathrm{R}_i-\mathrm{R}_s}^{E_{\mathrm{T}}>0.5\,\mathrm{GeV}} = 0$	Isolation in annulus formed by R_i =0.4 and R_s =0.1

for the $E_{\mathrm{T}}^{\mathrm{miss}}$- part of the trigger. The distributions of the uncorrected PF $E_{\mathrm{T}}^{\mathrm{miss}}$ are presented in Fig. 4.16, showing a reasonable agreement between data and simulations, before and after applying the calo $E_{\mathrm{T}}^{\mathrm{miss}} > 60\,\mathrm{GeV}$ cut.

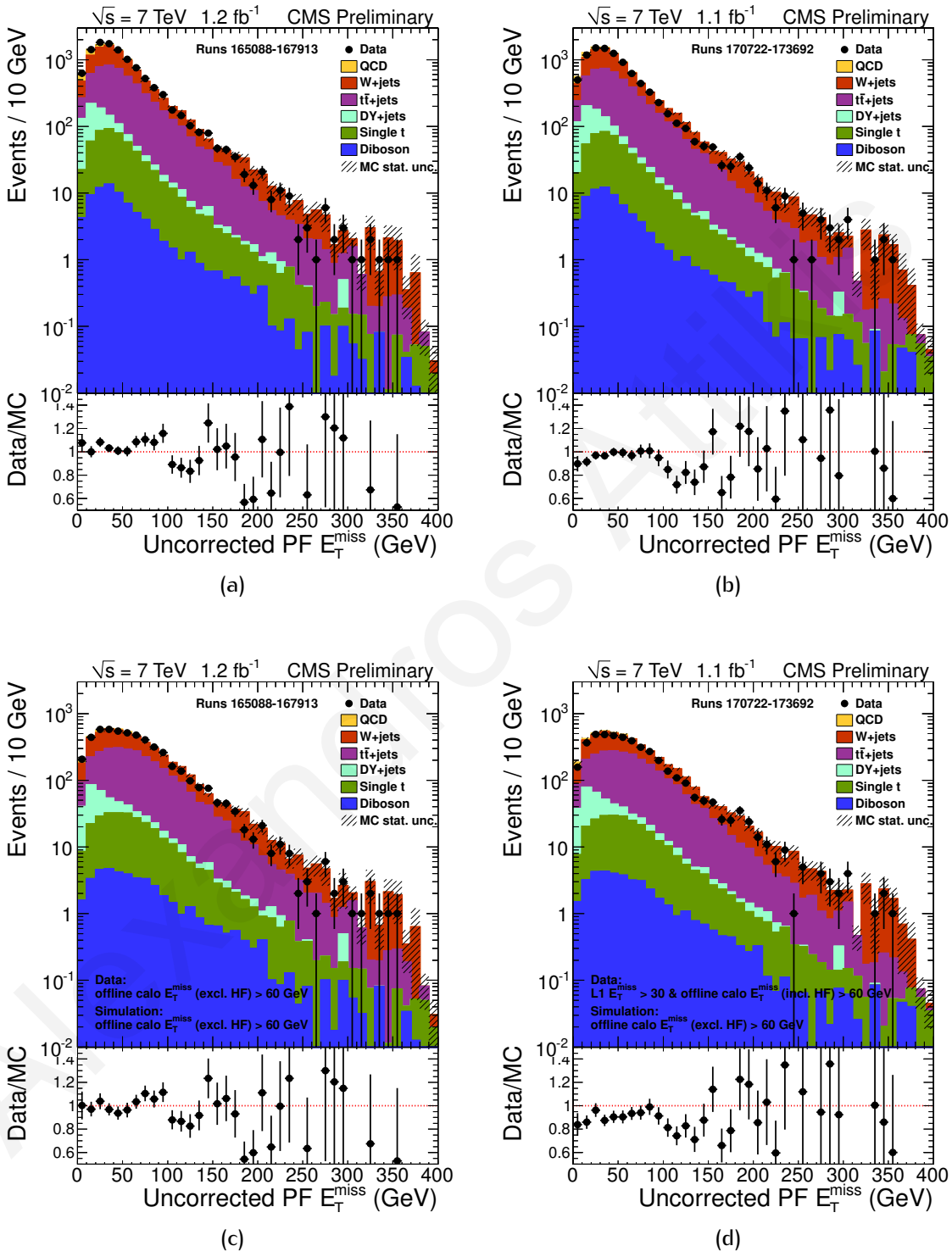

Figure 4.16: Distributions of the uncorrected PF $E_{\mathrm{T}}^{\mathrm{miss}}$ after the $\mu+ \geq 3$ jets(≥ 1 b tag) selection (a) and (b) and after the additional cut in calo $E_{\mathrm{T}}^{\mathrm{miss}}$ (c) and (d). The distributions in (a) and (c) [(b) and (d)] are from runs 165088 – 167913 [170722 – 173692], where the HF was excluded [included] from the HLT $E_{\mathrm{T}}^{\mathrm{miss}}$ reconstruction. For simulation, different pile-up re-weighting factors, described in Section 4.6.1, were used corresponding to the run period.

4.5 Object reconstruction and identification

The following sections describe the consecutive event selection steps taken for the signal analysis. For all the steps, the event selection was tested with the simulated backgrounds, providing a comparison between data and simulation results. The QCD multi-jet background was simulated with a LO event generator, but after the τ-jet object selection it was found that the LO treatment could not describe the data sufficiently well, while there was also significant deficiency of MC statistics in certain regions of phase-space. For this reason, and considering that the analysis relied on data-driven measurements in describing the QCD multi-jet processes, the simulated MC QCD multi-jet background is not shown in any of the figures. Comparison of distributions with data and data-driven QCD multi-jet and EWK+$t\bar{t}$ genuine τ backgrounds are presented in Section 4.9.

4.5.1 Particle Flow Reconstruction

In this analysis, the object reconstruction and identification relied heavily[6] objects on the CMS Particle Flow (PF) reconstruction technique [110, 111, 112], which combines information from all CMS subdetectors, to define a unique event description, in the form of mutually exclusive particles. Therefore, all stable particles in the event -including electrons, muons, photons, charged hadrons and neutral hadrons - are known as PF candidates, and are reconstructed by employing all CMS subdetectors in order to obtain the optimal determination of their direction, energy and type. The ultimate goal of the PF algorithm is to identify as many particles as possible, at the lowest possible energy and momentum threshold. In order to achieve this, dedicated tracking and calorimeter clustering techniques are used to efficiently identify PF candidates while keeping the fake rate to a low level.

The CMS detector is well suited for the PF technique, due to the fact that it combines a superior tracking system with a strong $3.8T$ magnetic field, provided by a superconducting solenoid coil. The aforementioned characteristics enable the efficient reconstruction of charged-particle tracks with $p_T > 150\,\text{MeV}/c$ and $|\eta| < 2.6$, with adequately small fake rates. This is especially important considering the fact that most stable particles produced in proton-proton collisions have relative low p_T; for example, in a quark/gluon jet of $p_T < 100\,\text{GeV}/c$, the average p_T carried by the stable constituents is of the order of a few GeV. The reconstruction of particles within the PF algorithm is primarily achieved by the use of the charged-particle tracks and calorimeter clusters, which comprise the fundamental "elemenets" of the technique. These elements are topologically linked into "blocks" by a dedicated link algorithm, which are subsequently identified as particles.

[6] Only the electron/muon veto part of the analysis was not based on PF reconstruction.

4.5.1.1 Iterative tracking algorithm

An iterative-tracking strategy is adopted in CMS, aiming for high efficiency and low fake rate, in which at first tracks are seeded and reconstructed with very tight criteria. Although it results in moderate tracking efficiency, it also yields a very low fake rate. The tracker hits that are unambiguously assigned are removed from the list and the iteration is repeated with progressively looser track seeding criteria. As a result, the tracking efficiency is increased, while the track removal procedure ensures that the fake rate is strongly suppressed due to a reduced number of combinatorics. Characteristically, for tracks from within a thin cylinder around the beam axis, the first 3 iterations result in an efficiency of 99.5% for isolated muons within the tracker acceptance, and $> 90\%$ for charged hadrons in jets.

The constraints of the fourth and fifth iterations also involve the the relaxing on the origin vertex of the tracks. This allows for the reconstruction of tracks originating from photon conversions and nuclear interactions in the tracker material, as well as long-lived particles such as, K_s^0 and Λ's. The CMS iterative-tracking strategy enables the reconstruction of tracks with ≥ 3 hits, $p_T \geq 150\,\text{MeV}/c$, and an origin vertex as much as 50 cm away from the beam axis. The fake rate is constrained to about a few per cent.

4.5.1.2 Calorimeter clustering algorithm

The detection and measurement of stable neutral particles, such as photons and neutral hadrons, is achieved by the calorimeter clustering algorithm. The same algorithm is also responsible for separating neutral particles from charged hadrons in energy deposits, and the reconstruction of electrons. These electrons incorporate all the accompanying bremsstrahlung photons, that are produced as electrons traverse the tracker material inside the strong magnetic field. Furthermore, low-quality or high-p_T tracks of charged hadrons are also measured.

The clustering is performed separately for each subdetector, namely the ECAL Barrel (EB), ECAL Endcap (EE), HCAL Barrel (HB), HCAL Endcap (HE), and the 2 Endcap preShower (ES) layers. In the HF each cell give rises to 1 cluster. The clustering procedure involves 3 steps, whereby at first "cluster seeds" are identified as local calorimeter cell maxima, which register energies above a given threshold. These seeds are used to create "topological clusters", by collecting nearby cells whose energy exceeds the predefined threshold. These nearby cells must have at least 1 side in common with a cell already in the cluster.

4.5.1.3 Link algorithm - from elements to blocks

Through the aforementioned iterative tracking and calorimeter clustering procedures, it is expected that a given particle will give rise to several PF elements in the CMS subdetectors. For example, a candidate particle might produce a charged-particle track, calorimeter clusters and a muon track in the muon system.

In order to connect together these elements, a dedicated link algorithm is required, so that each particle can be fully reconstructed. Furthermore, the algorithm must take care of avoiding double counting from the different subdetectors. The CMS PF link algorithm achieves this, by provisionally linking all pairs of elements, and assigning distance-variable which quantifies the quality of the link. Elements that are either directly or indirectly linked are used to create "blocks" of elements; typically containing $1-3$ elements.

The linking between a charged-particle track and a calorimeter deposit starts-off by extrapolating the track, from its last measurement hit in the tracking system to the 2 layers of the ES, the ECAL, and the HCAL. The extrapolation distance within a detector is chosen to be the maximum of a typical longitudinal EM shower profile for the ECAL, and 1 interaction length (λ) for the HCAL, as it is typical for a hadronic shower. The link is established provided that the extrapolation point is within the cluster boundaries. The link distance is defined as the distance in $\eta-\phi$ plane, between the extrapolated track and cluster positions.

In the case of electrons, the link between a track and ECAL must also incorporate all bremsstrahlung photons emitted by the electrons. To establish a link with ECAL bremsstrahlung clusters, tangents to an electron track are extrapolated to the ECAL, from the intersection points between the track and each of the track layers. If the extrapolated tangent position is within the boundaries of a cluster a link is established and a distance in $\eta-\phi$ is assigned.

For a link between 2 calorimeter clusters to be established, ECAL and HCAL for example, the cluster position in the more granular of the 2 calorimeters (ECAL) must be within the cluster envelope of the less granular one (HCAL). If succsesful, a link distance in $\eta-\phi$ is assigned, thus quantifying the quality of the link.

Finally, in the case of muons, a link between a charged-particle track and a muon track in the muon system is established when a global fit between the 2 tracks returns a χ^2 above a given threshold. Such muons, that are formed with an outside-in approach (muon system $\rightarrow$ tracker system) are known as Global-muons. Muons formed with Tracker-muon an inside-out approached (tracker system $\rightarrow$ muon system) are known as Tracker-muons. If for a given muon track several such Global-muons can be fit using several tracker tracks, the one with the smallest link distance is retained. The link distance in this case is defined by the χ^2 of the fit, with the smallest value representing the shortest link distance.

4.5.1.4 Reconstruction and identification

The PF algorithm is responsible for the reconstruction and identification of particles, using the block of elements. For each block of elements, the PF algorithm employs dedicated and predefined criteria to first reconstruct and identify PF muons and then PF electrons. Tighter criteria are applied to the remaining tracks, by requiring that the measured p_T must be smaller than the relative calorimetric energy resolution expected for charged hadrons. Through a dedicated procedure, PF charged hadrons are created, whose momentum and energy are taken directly from the track momentum, under the charged-pion hypothesis. If

the calibrated energy of the closest ECAL and HCAL clusters, linked to a track (or tracks), is much larger than the total associated charged-particle momentum, it can give rise to a PF photon and possibly to a PF neutral hadron. More specifically, if the excess is larger than the total ECAL energy, a PF photon is created with that ECAL energy, and a PF neutral hadron is also created using the excess energy. In cases where, for various reasons, ECAL and HCAL clusters are not linked to any track or are disabled, PF photons and neutral hadrons are created, respectively.

The resultant list of reconstructed PF particles provides a global description of a given event. The list of individual PF candidates particles is then used, as if it originated from a MC event generator, to construct higher level objects such as jets, missing transverse energy $E_{\mathrm{T}}^{\mathrm{miss}}$, τ jets, b-jets, as well as isolation deposits for leptons.

4.5.2 Primary vertices

After the special clean-up selections that were applied to the data, as described in Section 4.3.1, the precise determination of the collision points in proton-proton interactions was achieved via a primary vertex reconstruction. This is especially important when multiple collisions in the same bunch-crossing are non-negligible, requiring the determination of the number of vertices and the assignment of tracks to different collisions. Within CMSSW_4_2_8_patch2 [86] which was used for this analysis, the primary vertices were reconstructed with the Deterministic Annealing method [113], whereby the vertex finding and vertex fitting took place in two steps.

As a first step, selected tracks were grouped into clusters based on the z-coordinate of their point of closest approach to the beam line. As a second step, a 3-dimensional vertex fit was performed with the tracks in each cluster, using the full track information. Since multiple vertices are possible, they were sorted according to the sum of the square of transverse momenta of the tracks in the track cluster

$$p_{\mathrm{T}}^{\mathrm{PV}} = \sum_{i}^{\mathrm{tracks}} p_{\mathrm{T},\,i}^{2}, \tag{4.19}$$

where the sum runs over all tracks associated to the vertex. Such a vertex can be valid, fake, or invalid. A valid vertex is one which has been obtained from a vertex fit of tracks, and all data is meaningful. A fake vertex, which is considered valid, is a vertex which was not made out of a proper fit with tracks and still has a position and error, but its χ^2 and number of degrees of freedom (n.d.o.f.) are null. An invalid vertex on the other hand has no meaningful data.

In this analysis, the vertex with the largest $p_{\mathrm{T}}^{\mathrm{PV}}$ was selected as the primary vertex. Furthermore, the vertex was required to not be fake, have more than 4 n.d.o.f., have a maximum distance of 2 cm from the origin (0, 0, 0), in the $x-y$ plane, and a z-coordinate that should be less than 24 cm. A summary of the primary vertex requirements is presented in Table 4.19.

The distribution of primary vertices passing the aforementioned requirements is shown in Fig. 4.17 after trigger and pile-up re-weighting for the simulated samples. It is worth mentioning that the primary vertex selection in this analysis had no implications on the jet clustering, τ-jet identification or $E_{\mathrm{T}}^{\mathrm{miss}}$ calculation. For the Run2011A data, which was used in this analysis, the primary vertex requirements were applied for the sole reason of ensuring that the data did have a primary vertex that was well defined, but otherwise the analysis was independent of this selection.

Table 4.19: Breakdown of the primary vertex selection criteria.

	Selection	Description
1	largest $p_{\mathrm{T}}^{\mathrm{PV}}$	Select the vertex with the largest associated $p_{\mathrm{T}}^{\mathrm{PV}} = \sum_{i}^{\mathrm{tracks}} p_{\mathrm{T},\,i}^{2}$
2	Is NotFake	The primary vertex is not fake
3	n.d.o.f. > 4	The primary vertex has more than 4 degrees of freedom
4	$\lvert\rho\rvert = \sqrt{x^2 + y^2} < 2\,\mathrm{cm}$	Maximum distance from the origin (0, 0, 0) in the $x - y$ plane
5	$\lvert z\rvert < 24\,\mathrm{cm}$	The primary vertex z-coordinate should be less than 24 cm

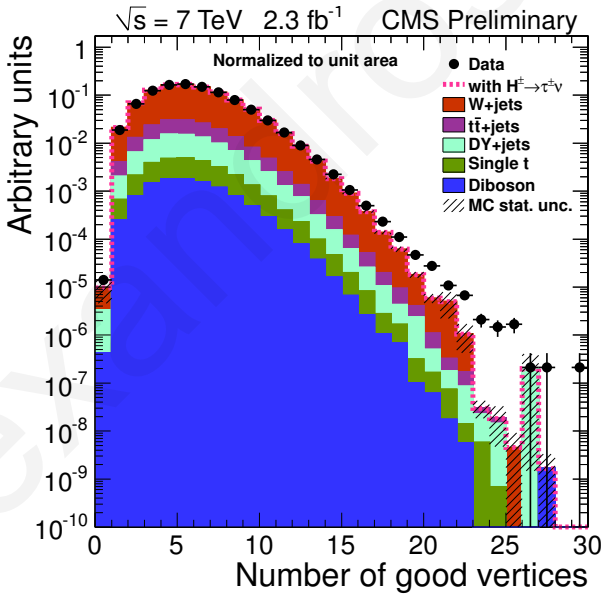

Figure 4.17: Distribution of the number of good reconstructed primary vertices, after triggering and pile-up re-weighting for the simulated samples. The data and total EWK simulations were normalised to unit area.

4.5.3 τ jet selection with the HPS τ-jet identification algorithm

In this analysis, the τ jets were reconstructed with the Hadron plus Strips (HPS) algorithm which employs a decay mode finding technique, and was originally designed for the $Z^0H^0 \to \tau^{\pm}\tau^{\mp}$ analysis, as described in Ref. [114]. An account of its performace, as determined using a data sample of $36\,\mathrm{pb}^{-1}$ recorded by the CMS detector, can be found in Ref. [115].

Traditionally, τ-jet identification algorithms apply narrowerness and isolation requirements to jets in order to discriminate genuine τ jets from quark/gluon jets. In this approach, a signal cone around the jet axis or the jet leading track is formed which is supposed to include all signal tracks originating from the jet. An isolation cone is also formed around the signal cone, thus definining an annulus to be used in isolation requirements for the signal cone constituents. This method is susceptible to mis-measuring the τ jet's energy, due to the fact besides the actual τ-lepton decay products, the signal cone is likely to envelope additional particles originating from UE activity. As a result the τ jet energy is overestimated, an effect which becomes increasingly enhanced with pile-up events, which are an increasing function of the instantaneous luminosity.

Traditional τ-jet identification algorithms are also vulnerable to isolation-related problems, since it is possible that a narrow hadronic jets falls into the signal cone. In such cases, these additional constituents,which are falsely regarded as signal, will not be used in evaluating the isolation of the τ jet. This effect is demonstrated in Fig. 4.18, in which the fake τ jet candidate appears to be less isolated in using the decay mode approach due to the fact that no isolation cone is required.

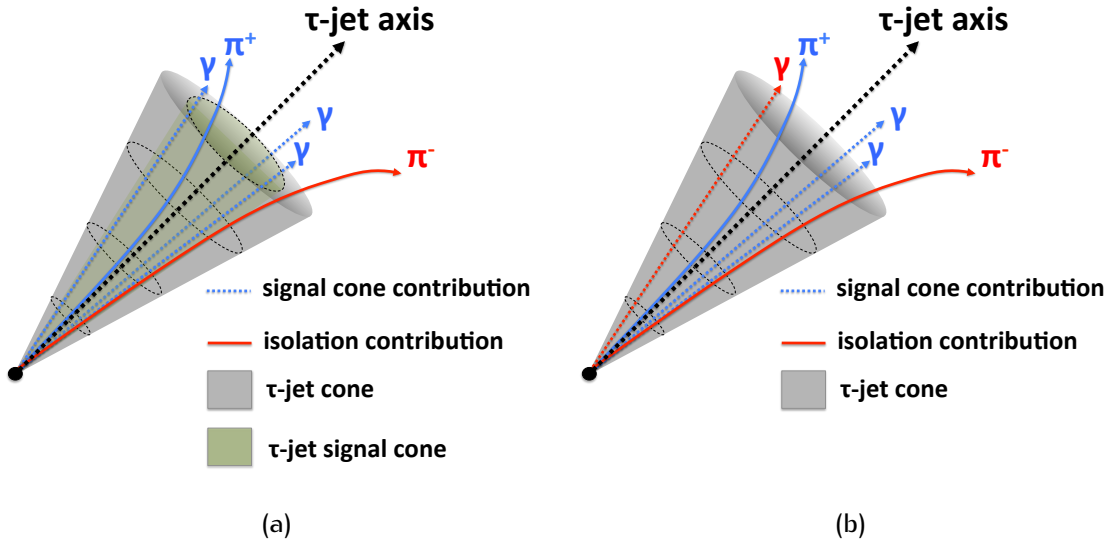

Figure 4.18: Illustration of the improved performance offered by the HPS τ-jet identification algorithm for the $\tau^+ \to \rho^+ \nu_\tau \to \pi^+ \pi^0 \nu_\tau$ decay, by employing a decay mode reconstruction.

The 2 aforementioned problems are addressed in the HPS τ-jet identification method, by utilising the reconstruction of the actual decay mode. This is achieved by individually reconstructing the $\rho^\pm(770)$ and $\alpha_1^\pm(770)$ resonances, through which the τ-lepton decays proceed. This allows for the isolation sums to be calculated by using only particles that are not associated with the actual τ-lepton decay mode, thus optimising the separation between signal and isolation constituents. Consequently, an improved performance is provided for accurately determining the τ jet's energy, and rejecting unwanted background.

The HPS τ-jet identification algorithm [114] is based on charged hadrons and neutral EM objects (photons), which are provided by the CMS PF reconstruction. It starts the reconstruc-

Table 4.20: Hadronic decay modes for τ-leptons that are looked for in the HPS τ-jet identification decay mode reconstruction, through decayModeFinding.

Process	$\Gamma_i/\Gamma_{\text{total}}(\%)$	$\sum_i \Gamma_i/\Gamma_{\text{total}}(\%)$
hadronic 1-prong	–	48.4
$\tau^- \to h^- \nu_\tau$	11.6	–
$\tau^- \to \rho^- \nu_\tau \to h^- \pi^0 \nu_\tau$	26.0	–
$\tau^- \to a_1^- \nu_\tau \to h^- \pi^0 \pi^0 \nu_\tau$	10.8	–
hadronic 3-prong	–	14.6
$\tau^- \to a_1^- \nu_\tau \to h^- h^+ h^- \nu_\tau$	9.8	–
$\tau^- \to h^- h^+ h^- \pi^0 \nu_\tau$	4.8	–
Total	–	63.0
Other hadronic modes	–	1.7

tion of τ jets from a PF jet, and looks for τ-lepton decay products produced in the hadronic decay modes tabulated in Table 4.20. The possible broadening of calorimeter signatures by photon conversions through $\gamma \to e^+e^-$ is countered by reconstructing photons in "strip" objects, that are bulit from EM particles. The strip reconstruction starts by taking the most energetic EM particle as the centre of the strip. Other neighboring EM particles are then searched for in a $\Delta\eta \times \Delta\phi = 0.05 \times 0.20$ window, around the strip centre. If the search is succesfull, the most energetic of the EM particles is associated with the strip and the strip centre position is recalculated to match the sum of 4-vectors of all PF particles associated with the strip. The next most energetic EM particle is then searched for within the same $\Delta\eta \times \Delta\phi$ window around the new strip centre. This procedure is repeated until no further particles can be associated with the strip. The 4-momentums obtained from charged hadrons and strips are reconstructed according the τ-lepton decay modes in Table 4.20, and are required to be compatible with the masses of intermediate $\rho^\pm$ and $a_1^\pm$ meson resonances.

Furthermore, the narrowness of the jet is employed as a background rejection criterion, by requiring that the cone of the hadronic τ-lepton is smaller than $\Delta R = 2.8/p_{\text{T}}^{\tau\text{ jet}}$, where $p_{\text{T}}^{\tau\text{ jet}}$ is evaluated by summing the 4-vectors of reconstructed charged hadrons and strips. However, a maximum and minimum allowed values are imposed of $\Delta R^{\text{max}} = 0.1$ and $\Delta R^{\text{min}} = 0.05$, respectively. Finally, the hypothetical visible τ-lepton momentum $p^{\tau\text{-lepton}}$ is required to match in η-ϕ that of the seeding PF jet, within $\Delta R(p^{\tau\text{-lepton}}, \text{PF jet}) = 0.1$. In the case where more than one decay modes are succesfully reconstructed, the decay mode which is most isolated is selected; that is, the one which has the lowest E_{T} sum of not-associated jet constituents. This ensures that only one HPS τ-jet is identified per PF jet.

In this analysis, the identification of τ jets was comprised of 2 selection steps, which first involved the selection of a τ jet candidate, and the subsequent requirement that this candidate successfully passes more stringent τ-jet identification criteria. Such division enabled the ability to factorise out the τ-jet identification part, needed for the measurement of the QCD multi-jet background. The τ jet candidate selection and τ-jet identification are described in detail in the Section 4.5.3.1 and Section 4.5.3.2, respectively.

4.5.3.1 τ-jet candidate selection

A collection of τ objects matched to the single τ jet + $E_{\mathrm{T}}^{\mathrm{miss}}$ trigger were first taken as the input for the τ jet candidate selection and required to be within $\Delta R < 0.4$ from the HLT τ object which had fired the trigger. In order for a τ object to be considered as a τ jet candidate it had to satisfy the selections tabulated in Table 4.21. Firstly, the τ

Table 4.21: Breakdown of the τ jet candidate selection criteria.

	Selection	Description
1	decayModeFinding	τ jet decay mode was successfully reconstructed
2	$p_{\mathrm{T}} > 40\,\mathrm{GeV}/c$	Transverse momentum acceptance
3	$\lvert\eta\rvert < 2.1$	Pseudorapidity acceptance
4	$p_{\mathrm{T}}^{\mathrm{Ldg.\ Trk.}} > 20\,\mathrm{GeV}/c$	Threshold for the leading electrically charged particle
5	againstElectronMedium	Rejection of electrons faking τ jets
6	againstMuonTight	Rejection of muons faking τ jets
7	ECAL fiducial volume cuts	τ jet is not in known η cracks or gaps

object was required to have a decay mode that was successfully reconstructed with the HPS algorithm as one of the predefined allowed decay modes, shown in Table 4.20. If the decay mode requirement is successfully met, additional requirements are imposed on the p_{T} and η of the τ object which have thresholds of $p_{\mathrm{T}} > 40\,\mathrm{GeV}/c$ and $\lvert\eta\rvert < 2.1$[7] respectively.

Furthermore, the leading electrically charged particle of the τ object must have transverse momentum of at least $20\,\mathrm{GeV}/c$, while the τ object must not lie within the ECAL fiducial volume cuts that describe regions between the barrel and endcap parts and regions in η between ECAL superclusters, as shown in Table 4.22. This was necessary due to the fact that, although the ECAL has been built to be as hermetic as possible, it is a known effect that a small amount of electrons may escape through the cracks between the modules and the gap in between the barrel and endcap detectors to the HCAL.

Table 4.22: ECAL fiducial volume cuts that describe regions between the barrel and endcaps and regions in η between ECAL superclusters.

	Selection	Description
1	$\lvert\eta\rvert < 0.018$	ECAL cracks
2	$\lvert\eta\rvert > 0.423$ & $\lvert\eta\rvert < 0.461$	ECAL cracks
3	$\lvert\eta\rvert > 0.770$ & $\lvert\eta\rvert < 0.806$	ECAL cracks
4	$\lvert\eta\rvert > 1.127$ & $\lvert\eta\rvert < 1.163$	ECAL cracks
5	$\lvert\eta\rvert > 1.460$ & $\lvert\eta\rvert < 1.558$	ECAL gaps

Additionally, the τ objects were required to pass the againstElectronMedium discrim-

[7] In accordance with the τ-embedding method, which employed a single μ trigger covering $\lvert\eta\rvert < 2.1$.

inator, designed for the rejection of electrons faking τ jets, by requiring that the leading charged candidate of the τ jet candidate is not indentified as a PF electron and that the τ jet candidate direction is incompatible with the ECAL crack and supermodules boundaries; i.e. not within $1.4442 < |\eta| < 1.566$.

Finally, the τ object was also subjected to the againstMuonTight discriminator, designed for the rejection of muons faking τ jets. This requires that the τ jet candidate leading track is not matched to a Global-muon[8] or Tracker-muon[9]. It also performs additional checks for calorimeter compatibility with 1-prong decay.

4.5.3.2 τ-jet identification

All the τ jet candidates were taken as input for the τ-jet identification procedure, which is summarised in Table 4.23. The most important τ-jet identification method is the isolation of the τ-jet contents. The isolation of the τ jet candidates was done with the HPS tight working point, known as byTightIsolation discriminator [106], which requires that no charged hadrons (photons) must be present in the isolation regions of the τ jet candidates with p_T (E_T) greater than 0.5 GeV/c.

Upon passing the isolation requirements, the number of charged particles identified in the decay mode were counted. Events with only 1 charged particle were selected, thus limiting the τ-jet identification procedure to only the subset of 1-prong τ-lepton hadronic decays. The inclusion of 3-prong τ-lepton hadronic decays proved to increase too much the yield of QCD multi-jet events, and was hence discarded as an option. Apart from requiring that the total electric charge of τ jet must be 1, the final requirement for a successful τ-jet identification was a cut on the τ polarisation variable $R_\tau = \frac{p^{\text{Ldg. Trk.}}}{p^{\tau\text{ jet}}} > 0.7$.

The τ jet candidates passing all τ-jet identification criteria were considered to be identified τ jets. Finally, events were required to have exactly one identified τ jet present, meaning that a veto was placed on the event if more than one identified τ jets were found. Because of the tight isolation criteria and hence a low identification efficiency for genuine τ jets, events with two identified τ jets were below the 1% level of all events even for the $t\bar{t} \to H^\pm H^\mp$ final state.

The p_T and η distributions of the τ jets are shown in Fig. 4.19 after τ-jet identification with the HPS method and excluding the byTightIsolation requirement, where it can be seen that QCD multi-jet events dominate the event sample. Fig. 4.20 shows the distribution of the R_τ variable, after τ-jet identification using the HPS method. The peak at $R_\tau \sim 1$ due to the $\tau^\pm \to \pi^\pm \nu_\tau$ decay is clearly visible. Based on the R_τ distribution, it can be seen that selecting events with large R_τ values suppresses the background from events with genuine τ-leptons from $W^\pm \to \tau^\pm \nu_\tau$ decays.

[8] Muons that are seeded from the CMS muon chambers and are then linked to tracks found in the tracking system form Global-muons.

[9] A Tracker-muon is a tracker track extrapolated to the muon system with at least one muon segment compatible with the extrapolated track.

Table 4.23: Breakdown of the τ-jet identification selection criteria.

	Selection	Description
1	$P^{h}_{iso} = \sum_{R_i-R_s}^{p_T>0.5\,GeV/c} = 0$	no PF charged candidates with $p_T > 0.5\,GeV/c$
2	$P^{\gamma}_{iso} = \sum_{R_i-R_s}^{E_T>0.5\,GeV} = 0$	no PF photon candidates with $E_T > 0.5\,GeV$
3	1-prong	number of charged particles in signal cone
4	$Q_{\tau\ jet} = \pm 1$	total electric charge of τ jet must be 1
5	$R_\tau = \frac{p^{Ldg.\ Trk.}}{p^{\tau\ jet}} > 0.7$	τ polarisation variable
6	secondary τ jet veto	require the presence of exactly 1 such τ jet

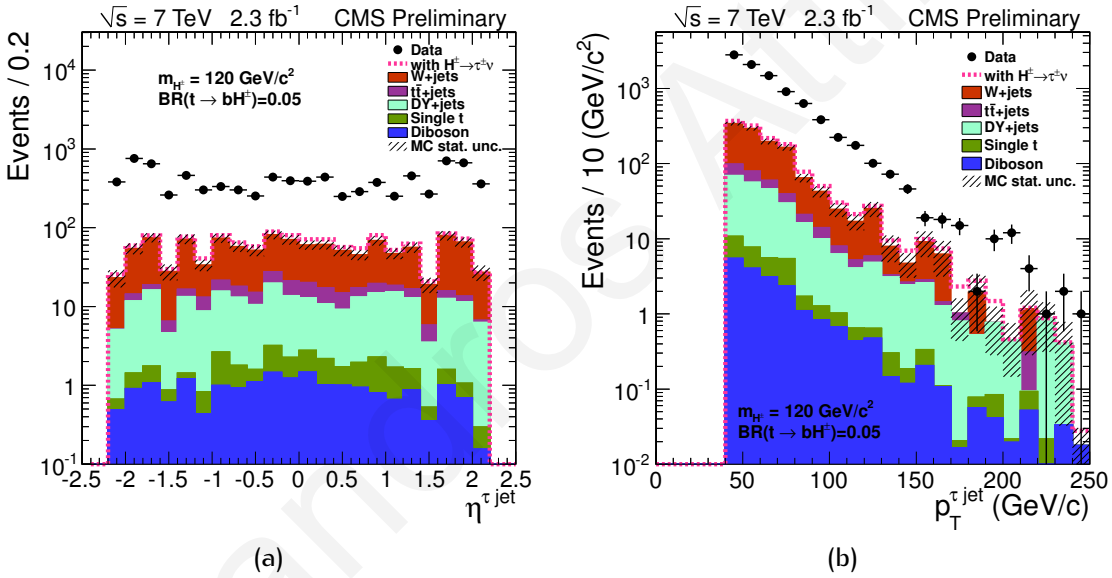

Figure 4.19: Distribution of p_T (a) and η (b) for the selected τ jet, after the τ-jet identification selection. The expected event yield in the presence of the $t \to bH^{\pm}$, $H^{\pm} \to \tau^{\pm}\nu_\tau$ decays is shown as the dashed red line for $m_{H^{\pm}} = 120\,GeV/c^2$ and assuming $BR(t \to bH^{\pm}) = 0.05$ and $BR(H^{\pm} \to \tau^{\pm}\nu_\tau) = 1$. The contribution from simulated QCD multi-jet events is not shown.

4.5.4 Electrons and muons

4.5.4.1 Electron veto

Events with isolated electrons or muons were excluded from the signal analysis, to improve the discriminating power of the transverse mass reconstructed from the selected τ jet and the E_T^{miss} for the separation of the signal from the residual backgrounds. The presence of leptonic $W^{\pm}$ decays from the associated top quark ($\bar{t} \to \bar{b}W^{\pm}$, $W^{\pm} \to \ell\nu_\ell$) would lead to the smearing of the high edge of the transverse mass distribution in the $t\bar{t}$ and W + jets events. Veto on isolated electrons and muons is also required to ensure orthogonality with the semi-leptonic and fully-leptonic final states of $t\bar{t} \to H^{\pm}W^{\mp}$ production, the results from which were used to yield a combined analysis results.

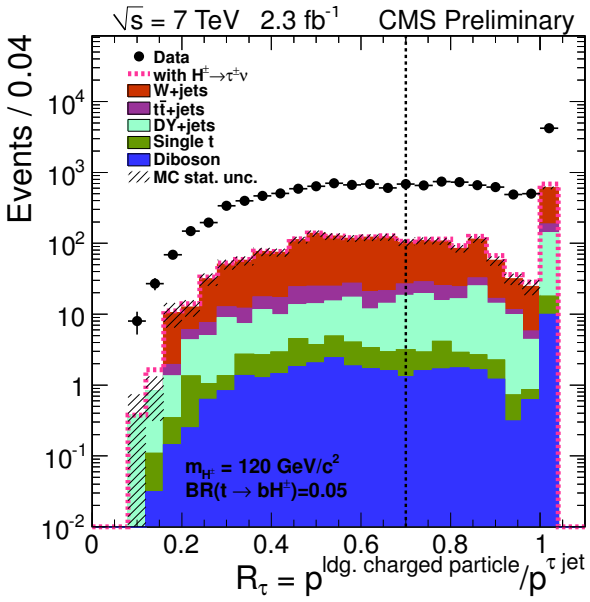

Figure 4.20: Distribution of $R_\tau = \frac{p^{\text{Ldg. Trk.}}}{p^{\tau\text{ jet}}}$ after τ-jet identification. The expected event yield in the presence of the $t \to bH^\pm$, $H^\pm \to \tau^\pm\nu_\tau$ decays is shown as the dashed red line for $m_{H^\pm} = 120\,\text{GeV}/c^2$ and assuming $\text{BR}(t \to bH^\pm) = 0.05$ and $\text{BR}(H^\pm \to \tau^\pm\nu_\tau) = 1$. The contribution from simulated QCD multi-jet events is not shown.

The electrons, reconstructed with the Gaussian Sum Filter (GSF) method,[10] were used as candidates for electron identification and subsequent veto. The GSF is an extended Kalman filter tracking technique, which takes into account the effect of the interaction of the tracker material with a particle on its trajectory. In this way, at each layer of material the window to look for the next track hit is re-estimated based on Bethe-Heitler energy loss formula[11] approximated by a sum of Gaussians. The resulting GSF fit on candidate hits has track parameters varying with distance from the vertex.

The electron identification was performed with a simple cut-based method, which relies on variables quantifying the shape of the shower caused by an electron candidate in the calorimeter, and on track-cluster matching requirements. Electron and photon showers deposit their energy in several crystals in the ECAL, with $\sim 94\%$ of the incident energy of a single electron or photon contained in 3×3 crystals, and $\sim 97\%$ in 5×5 crystals. Summing the energy measured in such fixed arrays gives the best performance for unconverted photons, or for electrons in test beams. The presence of material in front of the calorimeter results in bremsstrahlung and photon conversion, while electrons radiating in the tracker material in the presence of a strong magnetic field spread energy reaching the calorimeter in ϕ. The spread energy is clustered by building a cluster of clusters -a supercluster- which is extended in ϕ. The transition region between the ECAL barrel and endcap was excluded by removing the range $1.442 < |\eta_{sc}| < 1.566$, where η_{sc} is the pseudorapidity of the supercluster.

The identification of electrons is summarised in Table 4.24. Firstly, all electrons with

[10] As recommended by the CMS E/gamma-POG.
[11] Evaluates the energy loss by electrons traversing absorbers of heavy nuclei through collision and radiation.

Table 4.24: Breakdown of the selection criteria for isolated electron identification and subsequent veto.

	Selection	Description
1	$p_T > 15\,\text{GeV}/c$	Transverse momentum acceptance
2	$\lvert\eta\rvert < 2.5$	Pseudorapidity acceptance
3	GSF track found	Electron track found reconstructed with GSF technique
4	$1.442 < \lvert\eta_{sc}\rvert < 1.566$	ECAL fiducial cut on electron supercluster η coordinate
		SimpleEleId95relIso
5	$P_{\text{rel. iso}}^{\Delta R<0.3} \leq 0.15$	Subdetector-based relative isolation of the electron
6	$N_{\text{lost}}^{\text{Trk. hits}} \leq 2$	Maximum number of missing tracker hits
7	$d_{r\text{-}\phi} \geq 0.02$	Minimum distance between conversion tracks
8	$\lvert\Delta\cot(\theta)\rvert \geq 0.02$	Minimum $\Delta\cot\theta$ between conversion tracks at vertex
9	$\text{d}_{xy}^{\text{beam-spot}} \leq 0.04$	Maximum value of transverse impact parameter
10	$\Delta R(e,\mu) \geq 0.1$	Minimum distance between electron and Global/Tracker-muon

$p_T > 15\,\text{GeV}/c$ and $\lvert\eta\rvert < 2.5$ were considered as candidates to be vetoed. Furthermore, the electrons were required to have a valid GSF track and their superclusters to not lie within a fiducial volume cut of $1.442 < \lvert\eta_{sc}\rvert < 1.566$. A simple cut-based identification was employed, and more specifically the SimpleEleId95relIso working point. This has a 95% efficiency for electrons averaged over the full p_T spectrum. It applies relative isolation based on subdetector information from the tracker, ECAL, and HCAL by summing the energies in a cone of $\Delta R < 0.3$ around the electron candidate

$$P_{\text{rel. iso}}^{\Delta R<0.3} = \left(\sum_{\Delta R<0.3} p_{\text{T,iso}}^{\text{tracker}} + \sum_{\Delta R<0.3} p_{\text{T,iso}}^{\text{ECAL}} + \sum_{\Delta R<0.3} p_{\text{T,iso}}^{\text{HCAL}} \right) / p_{\text{T}}^{e} < 0.15. \tag{4.20}$$

This cut-based electron identification also includes a photon conversion rejection, whereby electrons originating from the process $\gamma \rightarrow e^+e^-$ were not considered. The details and parameter values of this method can be found in Ref. [116], Specifically, electrons with more than 2 lost hits in the tracker ($N_{\text{lost}}^{\text{Trk. hits}}$), or with a distance between them and their closest opposite sign track less than 0.02 ($\lvert\Delta\cot\theta\rvert < 0.2$), were not considered. Similarly, electrons with a distance between them and their closest opposite sign track in r-ϕ plane less than 0.02 ($d_{r\text{-}\phi} < 0.02$) were also not considered.

Additionally, the transverse impact parameter with respect to the beam-spot, applied on the GSF track of the electron candidate, was required to be $\text{d}_{xy}^{\text{beam-spot}} \leq 0.04$. $\text{d}_{xy}^{\text{beam-spot}} > 0.04$. Events with electrons found to lie within $\Delta R < 0.1$ of a muon identified both as Global/Tracker-muon and whose number of hits in the inner tracker was greater than 10, were not considered for veto . Fig. 4.21 shows the p_T and η distributions of the identified electrons, for the signal with $m_{H^\pm} = 120\,\text{GeV}/c^2$ superimposed on the total simulated back-

ground excluding the QCD multi-jet background and for the data, after τ-jet identification.

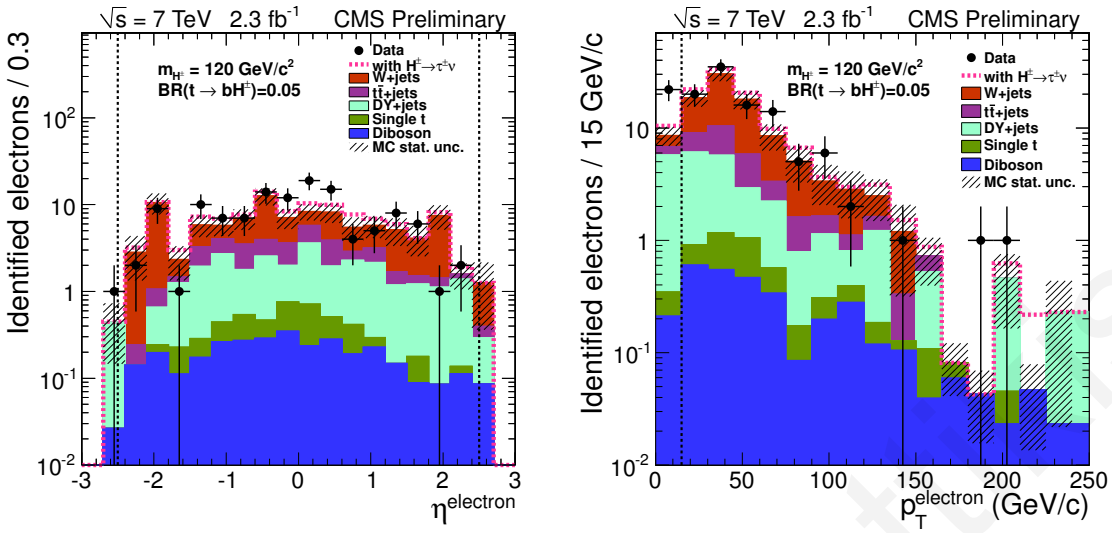

(a) (b)

Figure 4.21: Distribution of η (a) and p_T with $|\eta| < 2.4$ (b) for the identified electrons, after τ-jet identification. The expected event yield in the presence of the $t \to bH^{\pm}$, $H^{\pm} \to \tau^{\pm}\nu_{\tau}$ decays is shown as the dashed red line for $m_{H^{\pm}} = 120\,\text{GeV}/c^2$ and assuming $\text{BR}(t \to bH^{\pm}) = 0.05$ and $\text{BR}(H^{\pm} \to \tau^{\pm}\nu_{\tau}) = 1$. The contribution from simulated QCD multi-jet events is not shown.

4.5.4.2 Muon veto

The muon identification selections are summarised in Table 4.25 and their reconstruction is described in detail in Ref. [107]. Firstly, all muons with $p_T > 15\,\text{GeV}/c$ and $|\eta| < 2.5$ were considered as candidates to be vetoed. Isolation-wise, the muons were required to be isolated inside the tracker and calorimeters, by demanding that the relative isolation variable based on subdetector information has a value

$$P^{\Delta R<0.3}_{\text{rel. iso}} = \Big(\sum_{\Delta R<0.3} p^{\text{tracker}}_{\text{T,iso}} + \sum_{\Delta R<0.3} p^{\text{ECAL}}_{\text{T,iso}} + \sum_{\Delta R<0.3} p^{\text{HCAL}}_{\text{T,iso}}\Big)/p^{\mu}_{\text{T}} \leq 0.15. \quad (4.21)$$

The isolation sums were calculated by summing the p_T values of the tracks and the E_T values of the ECAL cells and the HCAL cells, around the muon track in the isolation cone of $\Delta R < 0.3$. Tracks with $p_T > 1$ GeV/c were used in the isolation sum. Furthermore, the muons were required to be identified as a Global-muon and a Tracker-muon, and to successfully pass the GlobalMuonPromptTight muon identification. The GlobalMuonPromptTight requirement imposes the condition that the muon has a normalised chi-squared value of $\chi^2/\text{n.d.o.f.} < 10$ and at least 1 hit in the muon stations. Moreover, at least 11 hits are required in the tracker ($N^{\text{hits}}_{\text{tracker}} \geq 11$), at least 1 hit in pixel tracker ($N^{\text{hits}}_{\text{pixel}} \geq 1$), at least 2 segments matched to the Global-muon ($N^{\text{matched}}_{\text{segments}} \geq 2$) and the muon transverse impact parameter with respect to the beam-spot to satisfy $|d^{\text{beam-spot}}_{xy}| < 0.02\,\text{cm}$. Fig. 4.22 shows the p_T and η distributions of the

Table 4.25: Breakdown of the selection criteria for isolated muon identification and subsequent veto selection criteria.

	Selection	Description
1	$p_T > 15\,\text{GeV}/c$	Transverse momentum acceptance
2	$\lvert\eta\rvert < 2.5$	Pseudorapidity acceptance
3	$P^{\Delta R<0.3}_{\text{rel. iso}} \leq 0.15$	Subdetector-based relative isolation of the muon
	Common muon identification selections	
4	Is Global-muon	Outside-in track fit approach (muon → tracker)
5	Is Tracker-muon	Inside-out track fit approach (tracker → muon)
6	Is GlobalMuonPromptTight	χ^2/n.d.o.f. < 10 and $N^{\text{hits}}_{\text{muon}} \geq 1$
7	$N^{\text{hits}}_{\text{tracker}} \geq 11$	At least 11 hits in the tracker
8	$N^{\text{hits}}_{\text{pixel}} \geq 1$	At least 1 hit in pixel tracker
9	$N^{\text{matched}}_{\text{segments}} \geq 2$	At least 2 muon segments matched to Global-muon
10	$\lvert d^{\text{beam-spot}}_{xy}\rvert < 0.02\,\text{cm}$	Transverse impact parameter

selected muons for the data and the signal with $m_{H^\pm} = 120$ GeV/c^2 superimposed on the total $t\bar{t}$,EWK and the rest of the simulated backgrounds, after τ-jet identification and electron veto.

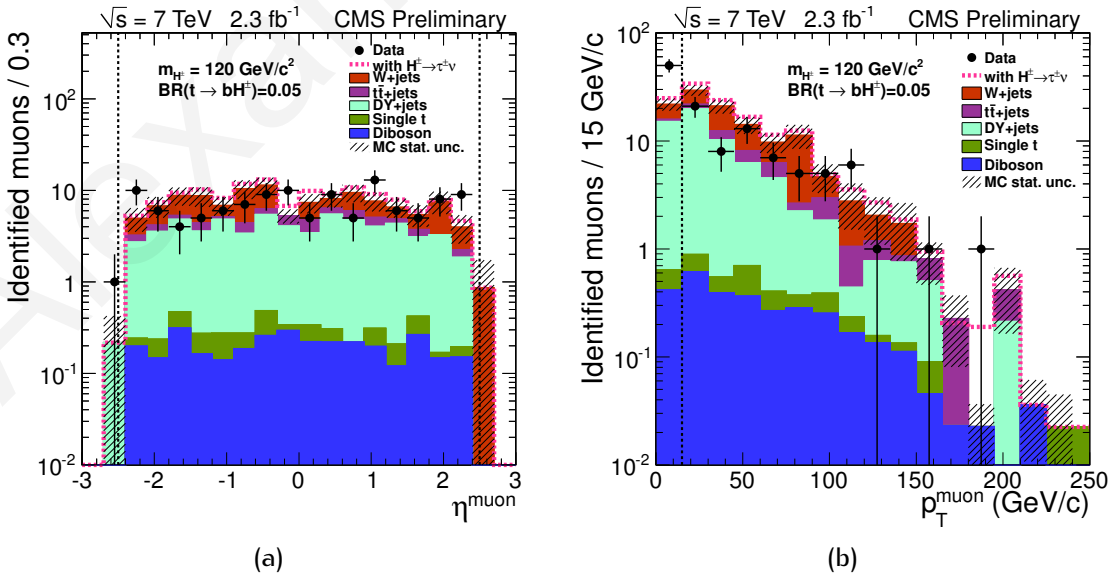

Figure 4.22: Distribution of η (a) and p_T with $\lvert\eta\rvert < 2.4$ (b) for the identified muons, after τ-jet identification. The expected event yield in the presence of the $t \to bH^\pm$, $H^\pm \to \tau^\pm\nu_\tau$ decays is shown as the dashed red line for $m_{H^\pm} = 120\,\text{GeV}/c^2$ and assuming $\text{BR}(t \to bH^\pm) = 0.05$ and $\text{BR}(H^\pm \to \tau^\pm\nu_\tau) = 1$. The contribution from simulated QCD multi-jet events is not shown.

4.5.5 Hadronic jet selection

The PF algorithm was used to reconstruct particles contributing to jets from energy deposits in the ECAL and HCAL systems, along with particles reconstructed in the tracker and muon systems. From these PF objects, jets were reconstructed by clustering all particles reconstructed by the PF event reconstruction [111] with the anti-k_T algorithm [117] with distance parameter of R=0.5. The jets were corrected with L1FastJet, L2Relative, L3Absolute, and L2L3Residual jet energy scale corrections [118].

The L1FastJet correction addresses issues related with spurious energy contributions to reconstructed hadronic jets, known as offset. These include electronics noise in the CMS calorimeters, energy from additional proton-proton interactions within the same bunch crossing, and energy integrated by the read-out electronics from preceding and subsequent bunch crossings.

The L2Relative jet corrections remove the pseudorapidity (η) dependence of the jet energy response. This is achieved with dijet balancing methods, which were used for the derivation of the relative jet corrections from collision data.

The L3Absolute jet energy calibrations were performed with γ +jet events, to set the absolute jet energy scale as a function of the transverse momentum. The calibration procedure exploited the balance in the transverse plane between the photon and the recoiling jet, given the good energy resolution expected for the ECAL which allows a good calibration precision.

The L2L3Residual corrections, were necessary as it was observed that data appeared to have higher relative response than the MC predictions, for $|\eta| \gtrsim 1.5$ which is rougly the region between the endcap and the forward calorimeters. This means that the default jet energy corrections, which are derived from MC truth are systematically over-correcting the jets in the data, in this pseudorapidity region. For this reason, a data-driven residual correction was applied to the data only, on top of the already L2L3 corrected jets. This simple correction factor affects mostly jets beyond $|\eta| \simeq 1.5$, with typical values of the order of $2-3\%$, with the exception of the region $2.5 < |\eta| < 3.0$ where it reaches the value of 10%. For $|\eta| \lesssim 1.5$ this residual correction is $\simeq 1$.

The PF jet identification criteria are summarised in Table 4.27. The collection of jets was cleaned from the selected τ jet with the cut $\Delta R(\text{jet}, \tau\text{ jet}) > 0.5$. The jets were required to have corrected $p_T > 30\,\text{GeV}/c$ and $|\eta| < 2.4$, and to pass the loose jet identification working point. The loose PF jet identification requirements, summarised in Table 4.26, require that the number of particles in the jet were required to be greater than one ($N_{\text{jet}}^{\text{particles}} > 1$), the fraction of charged EM energy compared to jet energy to be less than 99% (EMFraction $<$ 99%), the fraction of neutral hadronic energy compared to jet energy to be less than 99% (NHFraction $<$ 99%) and the fraction of neutral EM energy compared to jet energy to also be less than 99% (NEMFraction $<$ 99%). Additionally, a non-zero fraction of charged hadron energy compared to the jet energy within $|\eta^{\text{jet}}| < 2.4$ is also required (CHFraction > 0), while

the PF jets were also required to have at least 1 charged particle track within $|\eta^{\text{jet}}|< 2.4$ ($N_{\text{jet}}^{\text{Ch. Trk.}} \geq 1$). The minimum number of jets required to satisfy all the aforementioned criteria was set to 3 ($N_{\text{jets}} \geq 3$). The distributions of the p_{T} and the η of the selected PF jets,

Table 4.26: Breakdown of the PF jet loose identification selection criteria.

	Selection	Description
1	$N_{\text{jet}}^{\text{particles}} > 1$	Number of particles in the jet be greater than one
2	EMFraction $< 99\%$	Fraction of charged EM energy less than 99%
3	NHFraction $< 99\%$	Fraction of neutral hadronic energy less than 99%
4	NEMFraction $< 99\%$	Fraction of neutral EM energy less than 99%
5	CHFraction > 0	Non-zero fraction of charged hadron energy within $\|\eta^{\text{jet}}\|< 2.4$
6	$N_{\text{jet}}^{\text{Ch. Trk.}} \geq 1$	At least one charged particle track in the jets within $\|\eta^{\text{jet}}\|< 2.4$

Table 4.27: Breakdown of the hadronic jet identification selection criteria.

	Selection	Description
1	$p_{\text{T}} > 30\,\text{GeV}/c$	Transverse momentum acceptance
2	$\|\eta\|< 2.4$	Pseudorapidity acceptance
3	$\Delta R(\text{jet}, \tau\text{ jet}) > 0.5$	Minimum distance in $\eta - \phi$ between PF jet and τ jet
4	PF loose jet-ID	Pass the PF loose jet identification summarised in Table 4.26.
5	$N_{\text{jets}} \geq 3$	Minimum number of hadronic jets satisfying all criteria

and the number of selected PF jets are shown in Fig. 4.23 after τ-jet identification and the isolated lepton veto.

4.5.6 Missing transverse energy ($E_{\text{T}}^{\text{miss}}$)

The $E_{\text{T}}^{\text{miss}}$ object is related to the momentum imbalance of all reconstructed objects in an event, in the plane perpendicular to the beam axis. In proton colliders, the z-component of the proton's momentum cannot be used in momentum conservation calculations because a significant momentum is carried by the proton remnants down the beam pipe, while the momentum transfer of the collision is also impossible to extract from the final state products. Conversely, the colliding proton beams are balanced in the plane transverse to the beam motion during proton-proton collisions. Therefore, such imbalance can only be caused by the production of particles such as neutrinos, which rarely interact with matter and thus escape the detector volume undetected, or by jet resolution/mis-mearurement effects or by the presence of Minimum Ionising Particles (MIPs), such as muons, which deposit only a small fraction of their energy in the detector.

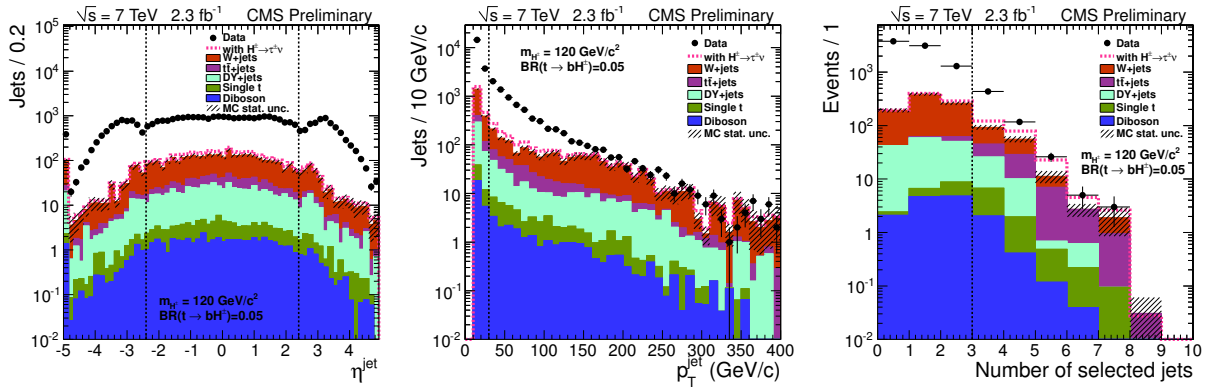

(a) (b) (c)

Figure 4.23: Distribution of η (a) and p_T with $|\eta| < 2.4$ (b) for hadronic jets, and the number of selected jets (c) with $p_T > 30\,\text{GeV}$ and $|\eta| < 2.4$, after τ jet identification and lepton veto. The expected event yield in the presence of the $t \to bH^\pm$, $H^\pm \to \tau^\pm \nu_\tau$ decays is shown as the dashed red line for $m_{H^\pm} = 120\,\text{GeV}/c^2$ and assuming $\text{BR}(t \to bH^\pm) = 0.05$ and $\text{BR}(H^\pm \to \tau^\pm \nu_\tau) = 1$. The contribution from simulated QCD multi-jet events is not shown.

It is therefore straightforward to determine the E_T^{miss} after the PF event reconstruction in CMS, as it merely consists of forming the transverse momentum vector sum over all reconstructed PF particles in the event, and then taking the opposite of this azimuthal momentum two-vector, with the missing transverse energy being the modulus of this vector. The true E_T^{miss} is derived in a similar manner in MC simulations, with all visible generated particles or, equivalently, with all invisible generated particles, like neutrinos and neutralinos. Therefore, E_T^{miss} is used to infer the existence of invisible particles and to estimate their transverse momenta, while it is also often used to identify top quarks and τ-leptons as these particles decay to neutrinos. In the present analysis, the uncorrected PF E_T^{miss} was used, reconstructed as the negative vector sum of the momentum of all reconstructed PF particles in the transverse plane

$$\text{PF}\,E_T^{miss} = -\sum_{i}^{\text{PF particles}} \vec{E}_{T,\,i}. \tag{4.22}$$

In fact, it would be more precise to speak of missing transverse momentum rather than missing transverse energy, but the latter term will be adopted in this analysis rather than the former for historical and aesthetic reasons. Furthermore, due to the fact that PF E_T^{miss} is computed from all reconstructed PF particles, it is noteworthy to point out that it can be computed before any other level objects are reconstructed in the event. The uncorrected PF E_T^{miss} distribution after τ jet identification, vetoes of isolated leptons, and hadronic jet selection, excluding the τ-jet isolation and R_τ selections, is shown in Fig. 4.24. A lower bound of $E_T^{miss} > 50\,\text{GeV}$ was set for the selection of signal events.

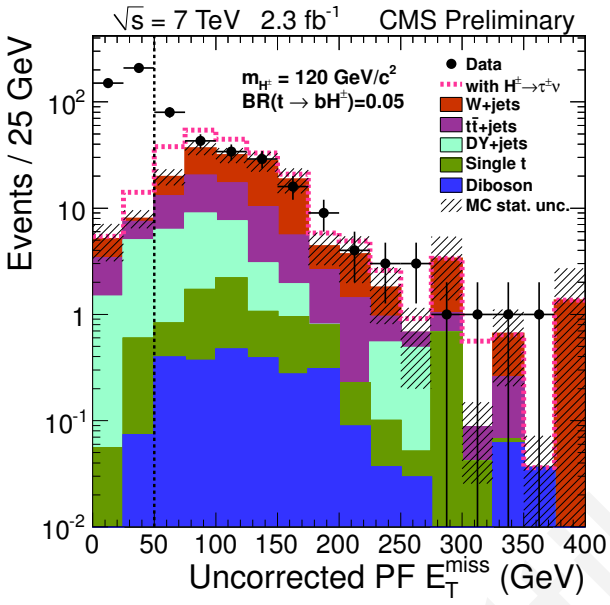

Figure 4.24: Distribution of uncorrected PF $E_{\mathrm{T}}^{\mathrm{miss}}$, after τ jet identification, lepton veto and hadronic jets requirements. The expected event yield in the presence of the $t \to bH^{\pm}$, $H^{\pm} \to \tau^{\pm}\nu_{\tau}$ decays is shown as the dashed red line for $m_{H^{\pm}} = 120\,\mathrm{GeV}/c^2$ and assuming $\mathrm{BR}(t \to bH^{\pm}) = 0.05$ and $\mathrm{BR}(H^{\pm} \to \tau^{\pm}\nu_{\tau}) = 1$. The contribution from simulated QCD multi-jet events is not shown.

4.5.7 b-tagging of hadronic jets

The b-tagging was performed on the hadronic jets, selected as described in Section 4.5.5, with a robust track-counting method known as Track Counting High Efficiency (TCHE) [119] algorithm. This b-tagging algorithm was designed to maximise the efficiency of finding genuine b-jets and relies on tracks with large impact parameters to tag hadronic jets as originating from b-quark decays.

All tracks have been ordered in decreasing Impact Parameter Significance (SIP)-value, the discriminating variable for the TCHE b-tagging algorithm is the value of S_{IP} of the 2^{nd} SIP-ordered track. In this analysis this discriminator was set to $S_{IP}^{2^{nd}\mathrm{Trk.}} > 1.7$, meaning that all the selected hadronic jets whose 2^{nd} SIP-ordered track had a SIP value exceeding 1.7, were taken to be genuine b-jets. The choice of the threshold corresponds to the loose working point [119], which provides a mis-tag rate in terms of the acceptance of light flavour jets of 10%, as estimated from QCD MC simulations for jets with p_{T} of about 80 GeV.

Table 4.28: Breakdown of the b-jet identification selection criteria.

	Selection	Description
1	$p_{\mathrm{T}} > 30\,\mathrm{GeV}/c$	Transverse momentum acceptance
2	$\lvert\eta\rvert < 2.4$	Pseudorapidity acceptance
3	$S_{IP}^{2^{nd}\mathrm{Trk.}} > 1.7$	Track Counting High Efficiency b-tagging algorithm requirement
4	$N_{\text{b-jets}} \geq 1$	Minimum number of b-jets satisfying all criteria

Apart from the b-tagging algorithm, the b-jets where required to have $p_T > 30\,\text{GeV}/c$ and be within the pseudorapidity acceptance of $|\eta| < 2.4$. At least 1 such b-jet satisfying all the aforementioned criteria was required to be present in the event. The full b-tagging selection for the signal events is summarised in Table 4.28. The distributions of the p_T and the η, and the number of b-tagged jets are shown in Fig. 4.25 after τ-jet identification, lepton veto, E_T^{miss} cut and the requirement of at least 3 hadronic jets. The events were required to have at least 1 b-tagged jet present. For simulated events a scaling factor, defined in Section 4.6.3, was applied to each event.

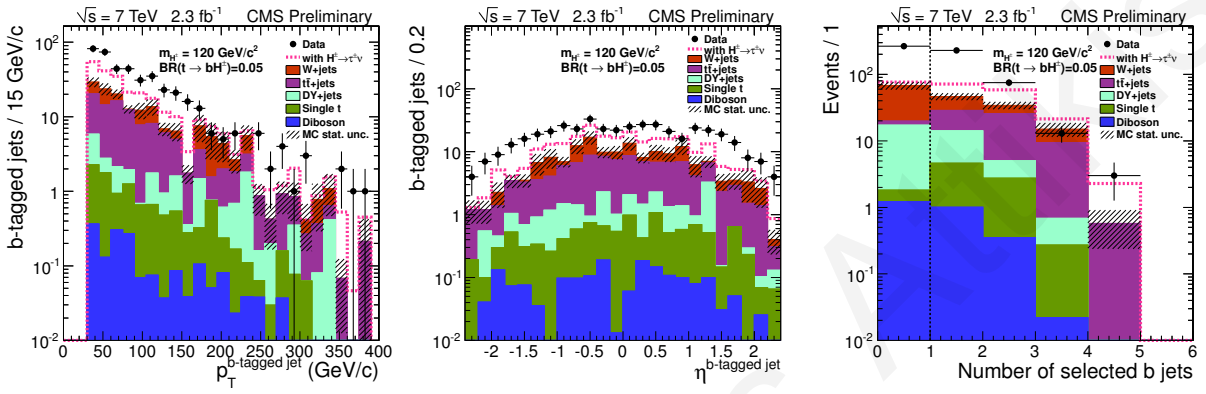

(a) (b) (c)

Figure 4.25: Distribution of p_T (a) and η (b) for b-tagged jets, and the number of selected b-jets (c) with $p_T > 30\,\text{GeV}$ and $|\eta| < 2.4$ after τ-jet identification, lepton veto, E_T^{miss} cut and requirement of at least 3 hadronic jets. The expected event yield in the presence of the $t \to bH^\pm$, $H^\pm \to \tau^\pm \nu_\tau$ decays is shown as the dashed red line for $m_{H^\pm} = 120\,\text{GeV}/c^2$ and assuming $\text{BR}(t \to bH^\pm) = 0.05$ and $\text{BR}(H^\pm \to \tau^\pm \nu_\tau) = 1$. The contribution from simulated QCD multi-jet events is not shown. The b-tagging scale factor is applied.

4.5.8 Transverse mass and $\Delta\phi$ distribution

In the case of a single heavy particle of mass m, produced in association with visible particles, and which decays to 2 particles, one of which being invisible, the invariant mass

$$m = \sqrt{(E_1 + E_2)^2 + (\vec{p}_1 + \vec{p}_2)^2} \quad (4.23)$$

$$= \sqrt{m_1^2 + m_2^2 + 2\,(E_1 E_2 - |p_1||p_2|\cos\Delta\phi)} \quad (4.24)$$

of the single heavy mother particle is impossible to be reconstructed due to the unavailable information related to the z-component of the invisible particle's momentum. Although the invariant mass of the mother particle cannot be reconstructed, it can however be constrained with the quantity known as transverse mass defined as

$$m_T = \sqrt{\left(E_{T,1} + E_{T,2}\right)^2 + \left(\vec{p}_{T,1} + \vec{p}_{T,2}\right)^2} \quad (4.25)$$

$$\simeq \sqrt{2E_{T,1}E_{T,2}\,(1 - \cos\Delta\phi)}, \quad (4.26)$$

where the mass terms have vanished by assuming that the masses of the 2 particles are approximately zero ($m_1 \approx 0$, $m_2 \approx 0$), which is equivalent with assuming that both particles approach the relativistic limit ($E_1 \gg m_1$, $E_2 \gg m_2$). The transverse mass distribution is thus constrained to lie in the range $0 \leq m_T \leq m$, a modulo smearing over the intrinsic width of the mother particle resonance. The end-points of the m_T distribution, which possesses a Jacobian peak at $m_T = m$, are unchanged by the transverse motion of the the mother particle.

The Jacobian peak can be employed as a powerful discriminating variable in the separation of SM background processes and charged Higgs boson production processes, especially in the case when the charged Higgs boson is much heavier than the $W^{\pm}$ boson, whereby the $t\bar{t}$ irreducible background can be greatly suppressed by distinguishing $W^{\pm}$ mediated decays from charged Higgs mediated decays. For the present work, the light charged Higgs boson transverse mass was calculated from the selected τ jet and the E_T^{miss} objects as

$$m_T \simeq \sqrt{2E_T^{\tau\ jet} E_T^{miss} (1 - \cos\Delta\phi)} \tag{4.27}$$

where $\Delta\phi$ is the angle between the selected τ jet and the E_T^{miss} objects in the transverse plane. In order to reduce W + jets and EWK+$t\bar{t}$ genuine τ backgrounds events and thus maximise the signal sensitivity, the discriminating power of the transverse mass distribution was exploited. As shown in Fig. 4.26 (a), a significant portion of these backgrounds can be rejected by a simple cut on the m_T variable. However, instead of a simple counting experiment as done in a previous version of the present analysis [77], the transverse mass shape was used in a binned maximum likelihood fit to extract a possible signal. For this implementation, the transverse mass shapes of the different contributing processes were determined directly from data in control-region events, which were required pass the similar requirements as for the signal selection, as discussed in Section 4.9.1.

Fig. 4.26 shows the m_T and $\Delta\phi$ distributions of the selected events for the signal with $m_{H^{\pm}} = 120\,\text{GeV}/c^2$ superimposed on simulated backgrounds and for the data, after τ-jet identification, lepton veto, E_T^{miss} cut, requirement of at least 3 hadronic jets and b-tagging. Apart from the smearing of the m_T shape, which is mainly caused by detector resolution effects, the expected Jacobian peak of the transverse mass distribution from the signal and EWK+$t\bar{t}$ genuine τ backgrounds is further spoiled by the fact that the τ-lepton energy information is incomplete. Since the τ-lepton decays to hadrons and an associated neutrino, the neutrino carries away some of the τ-lepton's energy which is not recovered by the τ-jet reconstruction.

Another observation that could be made is the fact that QCD multi-jet background, presented in Fig. 4.26 as the difference of the data and the simulated backgrounds, is enhanced at large $\Delta\phi$ values, while the signal and EWK+$t\bar{t}$ genuine τ backgrounds are concentrated at low $\Delta\phi$ values. This behaviour is expected, since neutrinos present in events containing genuine τ-leptons are likely to be produced co-linearly with the τ-lepton, since both are produced boosted by the heavy mother particle, which can be either a $W^{\pm}$ or a $H^{\pm}$ bo-

son. In the QCD multi-jet case, the $\Delta\phi$ distribution can be understood by the fact that, at LO, 2 back-to-back jets are produced which are separated in the ϕ-plane by an angle π. The $E_{\mathrm{T}}^{\mathrm{miss}}$ in the event is caused by the mis-measurement of one of the jets, and points in the same (opposite) direction as the direction of the under-measured (over-measured) jet. The majority of the events either have a very small angle ($\Delta\phi \to 0$) or a very large angle ($\Delta\phi \to \pi$) between the falsely identified as τ jet hadronic jet and the $E_{\mathrm{T}}^{\mathrm{miss}}$, depending on which of the mis-measured jets was identified as a τ jet and which not.

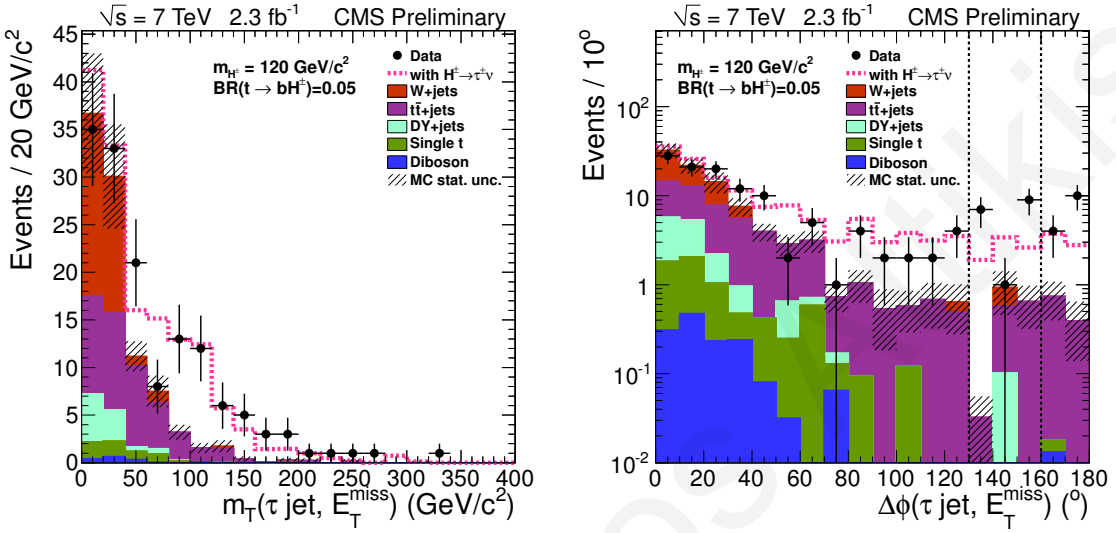

Figure 4.26: Distribution of m_{T} (a) and $\Delta\phi$ (b) for the selected events. The expected event yield in the presence of the $t \to bH^{\pm}$, $H^{\pm} \to \tau^{\pm}\nu_{\tau}$ decays is shown as the dashed red line for $m_{H^{\pm}} = 120\,\mathrm{GeV}/c^2$ and assuming $\mathrm{BR}(t \to bH^{\pm}) = 0.05$ and $\mathrm{BR}(H^{\pm} \to \tau^{\pm}\nu_{\tau}) = 1$. The contribution from simulated QCD multi-jet events is not shown.

4.5.9 Signal selection summary and results

The complete event selection steps taken for the signal analysis are summarised in Table 4.29. In Table 4.30, the number of selected events for the signal in the $t\bar{t} \to bW^{\pm}bH^{\mp}$ process is shown for $m_{H^{\pm}} = 80 - 160\,\mathrm{GeV}/c^2$, an integrated luminosity of $2.3\,\mathrm{fb}^{-1}$ and assuming $\mathrm{BR}(t \to bH^{\pm}) = 0.05$ and $\mathrm{BR}(H^{\pm} \to \tau^{\pm}\nu_{\tau}) = 1$. The corresponding number of events for the signal in the $t\bar{t} \to bH^{\pm}bH^{\mp}$ process are shown in Table 4.31. The contribution of the $t\bar{t} \to bH^{\pm}bH^{\mp}$ production process to the total number of signal events surviving the full selection requirements, ranges from $\sim 5\% - 1\%$ ($m_{H^{\pm}} = 80 - 160\,\mathrm{GeV}/c^2$) for the assumed branching ratio of $\mathrm{BR}(t \to bH^{\pm}) = 0.05$ and $\mathrm{BR}(H^{\pm} \to \tau^{\pm}\nu_{\tau}) = 1$. The signal rates decrease only slightly after the application of the $\Delta\phi\left(\tau\text{ jet}, E_{\mathrm{T}}^{\mathrm{miss}}\right)$ cuts.

Table 4.29: Summary of the event selection steps taken for the signal analysis.

	Selection	Description
1	Data clean-up	Remove beam-scrapping events
2	single τ jet + $E_{\mathrm{T}}^{\mathrm{miss}}$ trigger	Selection of signal-like events using dedicated triggers
3	Good primary vertex	Selection of good-quality primary vertex
4	τ jet selection	τ jet candidate and τ-jet identification selection
5	Isolated lepton veto	Veto on the presence of isolated electrons/muons
6	hadronic jets selection	Selection of at least 3 PF jets
7	$E_{\mathrm{T}}^{\mathrm{miss}}$ requirement	Require the presence of $E_{\mathrm{T}}^{\mathrm{miss}}$ of at least 50 GeV
8	b-jets selection	Selection of at least 1 TCHE b-tagged jets
9	$\Delta\phi\left(\tau \text{ jet}, E_{\mathrm{T}}^{\mathrm{miss}}\right)$ option	No $\Delta\phi$ cut, $\Delta\phi < 160°$, $\Delta\phi < 130°$

Table 4.30: Number of selected events as a function of selection cuts for the signal from $t\bar{t} \to bW^{\pm}bH^{\mp}$ with $m_{H^{\pm}} = 80$, 90, 100, 120, 140, 150, 155 and 160 GeV/c^2. The samples were normalised to the integrated luminosity of 2.3 fb^{-1} with BR($t \to bH^{\pm}$) = 0.05 and BR($H^{\pm} \to \tau^{\pm}\nu_{\tau}$) = 1.

$m_{H^{\pm}}$ (GeV/c^2)	80	90	100	120	140	150	155	160
Trigger	2322	2466	2599	2963	3538	3860	4049	4217
One identified τ jet	73	93	101	134	162	191	214	214
Trigger scale factor	74	95	101	134	164	193	218	216
Electron veto	66	84	89	118	146	173	191	196
Muon veto	55	70	75	103	127	154	167	173
≥ 3 hadronic jets	41	50	47	67	73	87	86	89
$E_{\mathrm{T}}^{\mathrm{miss}} > 50$ GeV	34	41	39	61	66	80	82	85
≥ 1 b-tagged jets	32 ± 3	38 ± 4	36 ± 3	54 ± 4	62 ± 5	69 ± 5	69 ± 5	74 ± 5
$\Delta\phi\left(\tau \text{ jet}, E_{\mathrm{T}}^{\mathrm{miss}}\right) < 160°$	31 ± 3	37 ± 3	34 ± 3	49 ± 4	56 ± 4	64 ± 5	64 ± 5	67 ± 5
$\Delta\phi\left(\tau \text{ jet}, E_{\mathrm{T}}^{\mathrm{miss}}\right) < 130°$	28 ± 3	33 ± 3	33 ± 3	43 ± 4	47 ± 4	53 ± 4	53 ± 4	55 ± 4

Table 4.31: Number of selected events as a function of selection cuts for the signal from $t\bar{t} \to bH^{\pm}bH^{\mp}$ with $m_{H^{\pm}} = 80$, 90, 100, 120, 140, 150, 155 and 160 GeV/c^2. The samples were normalised to the integrated luminosity of 2.3 fb^{-1} with BR($t \to bH^{\pm}$) = 0.05 and BR($H^{\pm} \to \tau^{\pm}\nu_{\tau}$) = 1.

$m_{H^{\pm}}$ (GeV/c^2)	80	90	100	120	140	150	155	160
Trigger	80	85	91	107	132	150	158	167
One identified τ jet	5.4	5.8	7.1	9.3	11	13	13	14
Trigger scale factor	5.4	5.8	7.1	9.4	11	13	14	14
Electron veto	5.1	5.5	6.7	8.6	10	12	12	13
Muon veto	4.7	5.0	6.1	7.9	9.5	11	11	12
≥ 3 hadronic jets	2.5	2.5	3.1	3.5	3.0	2.1	1.7	1.5
MET > 50 GeV	2.3	2.3	2.8	3.3	2.9	2.0	1.7	1.5
≥ 1 b-tagged jets	2.1 ± 0.1	2.1 ± 0.1	2.7 ± 0.1	2.9 ± 0.2	2.4 ± 0.1	1.5 ± 0.1	1.1 ± 0.1	0.90 ± 0.08
$\Delta\phi(\tau \text{ jet}, E_{\mathrm{T}}^{\mathrm{miss}}) < 160°$	1.8 ± 0.1	1.7 ± 0.1	2.2 ± 0.1	2.2 ± 0.1	1.9 ± 0.1	1.3 ± 0.1	0.86 ± 0.09	0.78 ± 0.08
$\Delta\phi(\tau \text{ jet}, E_{\mathrm{T}}^{\mathrm{miss}}) < 130°$	1.4 ± 0.1	1.3 ± 0.1	1.7 ± 0.1	1.4 ± 0.1	1.3 ± 0.1	0.93 ± 0.09	0.63 ± 0.07	0.66 ± 0.08

The standalone selection efficiencies for the signal processes $t\bar{t} \to bW^{\pm}bH^{\mp}$ and $t\bar{t} \to bH^{\pm}bH^{\mp}$ are presented in Fig. 4.27, as a function of the light charged Higgs boson mass ($m_{H^{\mp}}$) in the $t \to bH^{\pm}$ process. The standalone efficiencies of signal triggers and of the τ-jet identification show an increase as a function of $m_{H^{\pm}}$, mainly due to the presence of more energetic τ-lepton and neutrinos in the event, as a result of a heavier light charged Higgs boson. Another feature observed is that the trigger efficiency for the $t\bar{t} \to bH^{\pm}bH^{\mp}$ production process is overall higher than that for $t\bar{t} \to bW^{\pm}bH^{\mp}$. This is understood by the fact that, since the τ-jet isolation employed in the trigger is very tight, it is very rare that two τ jets are found in a given event. However, having two genuine τ-leptons within the event doubles the probability for having exactly one identified τ jet in it, with one τ jet identified and the second one failing to pass the online identification.

As anticipated, the isolated lepton veto standalone efficiency appears to have no dependence on $m_{H^{\pm}}$. Conversely, the signal efficiency is shown to depend significantly on the requirement of at least 3 hadronic jets, with a significant decrease observed for $m_{H^{\pm}} > 100\,\text{GeV}/c^2$. This behaviour was expected due to the decreasing phase-space available to the b-jet produced in association with the light charged Higgs boson, as the mass of the latter increases. Therefore, at high light charged Higgs masses, the b-jet from the $t \to bH^{\pm}$ decay is produced softer, which results in a larger probability of it failing the jet selection requirement of $p_{\text{T}} > 30\,\text{GeV}/c$. This effect is understandably significantly larger for the signal process $t\bar{t} \to bH^{\pm}bH^{\mp}$, where both b-jets are deprived of a significant portion of their phase-space at larger $m_{H^{\mp}}$ values. The standalone $E_{\text{T}}^{\text{miss}}$ requirement appears to have a little dependence on $m_{H^{\mp}}$, with higher efficiencies shown for larger light charged Higgs masses, an effect which is understood to be related to the fact that products of the $H^{\pm} \to \tau^{\pm}\nu_{\tau}$ decay are more boosted at higher values of $m_{H^{\pm}}$. The standalone b-tagging efficiency exhibits a flat behaviour as a function of $m_{H^{\pm}}$ for the $t\bar{t} \to bW^{\pm}bH^{\mp}$ production processes, while a mild decrease in efficiency is observed for the $t\bar{t} \to bH^{\pm}bH^{\mp}$ processes for the same reason as that attributed to the hadronic jets selection decrease in efficiency. Finally, the $\Delta\phi\left(\tau\text{ jet}, E_{\text{T}}^{\text{miss}}\right) < 160^{\circ}$ cut seems to affect democratically the signal efficiency for all mass points considered.

The combined selection efficiencies for the signal processes $t\bar{t} \to bW^{\pm}bH^{\mp}$ and $t\bar{t} \to bH^{\pm}bH^{\mp}$ are presented in Fig. 4.28, as a function of the light charged Higgs boson mass ($m_{H^{\mp}}$) in the $t \to bH^{\pm}$ process. For the $t\bar{t} \to bW^{\pm}bH^{\mp}$ process, which contributes the vast majority of signal events to the signal event yield, The combined signal selection efficiency increases from $\sim 8.9 \times 10^{-4}$ at $m_{H^{\pm}} = 80\,\text{GeV}/c^2$ to $\sim 2.1 \times 10^{-3}$ at $m_{H^{\pm}} = 160\,\text{GeV}/c^2$ for the $t\bar{t} \to bH^{\pm}b\text{W}^{\mp}$ process, after the b-tagging requirement. Conversely, the opposite behaviour is exhibited by the $t\bar{t} \to bH^{\pm}bH^{\mp}$ process, which has a sharp fall in the total selection efficiency for $m_{H^{\pm}} > 120\,\text{GeV}/c^2$ after the hadronic jets selection requirement, due to the loss of soft b-jets. This effect is amplified by the b-tagging requirement, which with the loss of the soft b-jet subsequently has as smaller efficiency of succesfully tagging a b-jet from the selected hadronic jets. The combined signal selection efficiency for the $t\bar{t} \to bH^{\pm}bH^{\mp}$ process after the b-tagging requirement thus decreases from $\sim 2.3 \times 10^{-3}$ at $m_{H^{\pm}} = 80\,\text{GeV}/c^2$

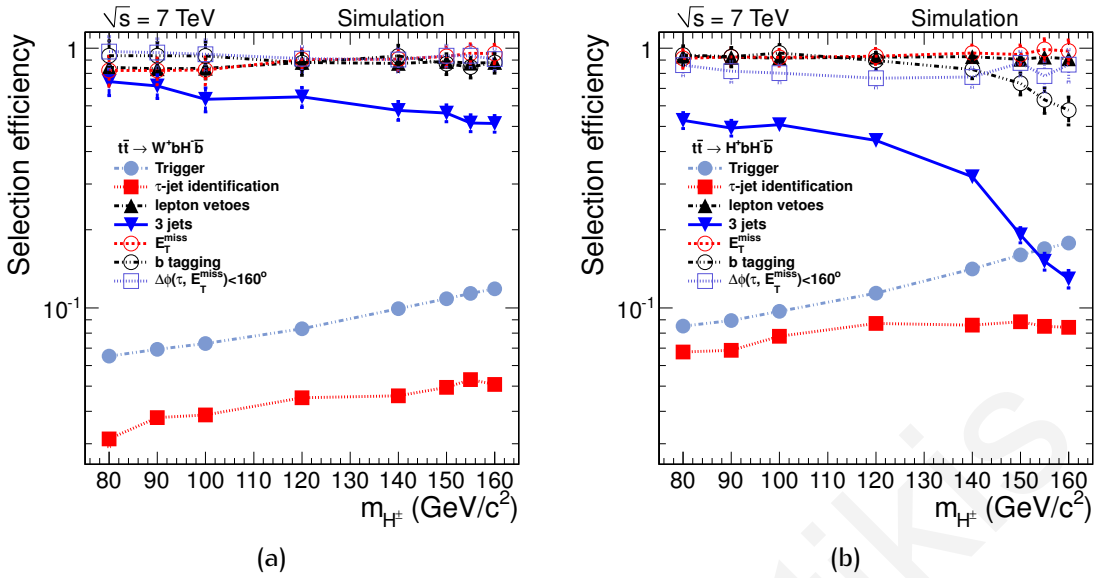

Figure 4.27: Standalone signal selection efficiencies for the processes $t\bar{t} \to bW^{\pm}bH^{\mp}$ (a) and $t\bar{t} \to bH^{\pm}bH^{\mp}$ (b) for the trigger (dash-double-dotted line), τ-jet identification (dotted line), lepton vetoes (dash-dotted line), requirement of at least 3 hadronic jets (solid line), $E_{\mathrm{T}}^{\mathrm{miss}}$ cut (dashed line), b-tagging (dash-triple-dotted line) and $\Delta\phi\left(\tau \text{ jet}, E_{\mathrm{T}}^{\mathrm{miss}}\right) < 160°$ (fine-dotted line) cut, as a function of the light charged Higgs boson mass ($m_{H^{\mp}}$) in the $t \to bH^{\pm}$ process.

to $\sim 9.0 \times 10^{-4}$ at $m_{H^{\pm}} = 160\,\mathrm{GeV}/c^2$

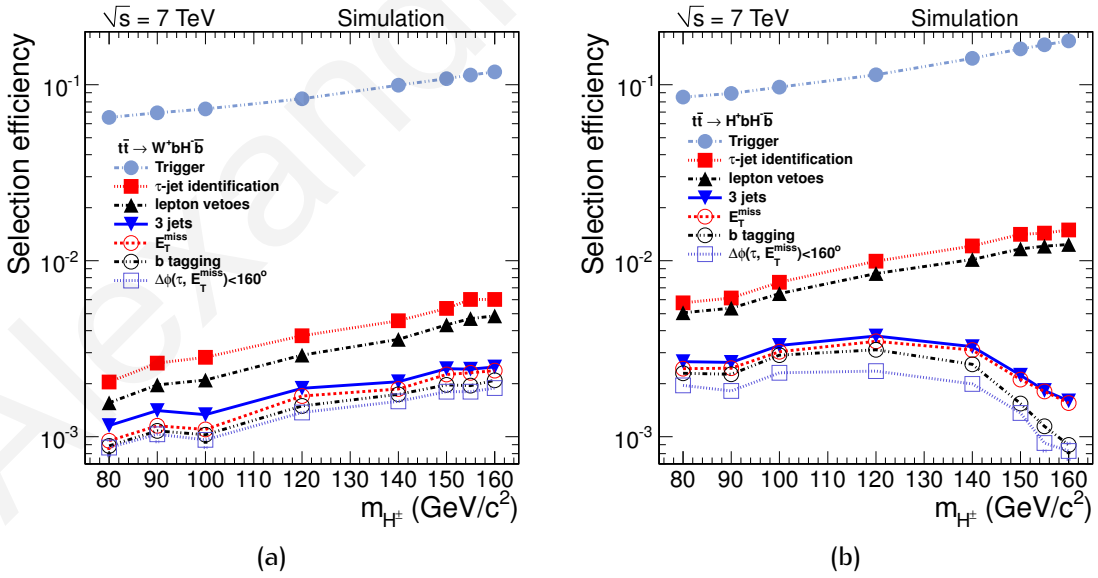

Figure 4.28: Combined signal selection efficiencies for the processes $t\bar{t} \to bW^{\pm}bH^{\mp}$ (a) and $t\bar{t} \to bH^{\pm}bH^{\mp}$ (b) for the trigger (dash-double-dotted line), τ-jet identification (dotted line), lepton vetoes (dash-dotted line), requirement of at least 3 hadronic jets (solid line), $E_{\mathrm{T}}^{\mathrm{miss}}$ cut (dashed line), b-tagging (dash-triple-dotted line) and $\Delta\phi\left(\tau \text{ jet}, E_{\mathrm{T}}^{\mathrm{miss}}\right) < 160°$ cut (fine-dotted line), as a function of the light charged Higgs boson mass ($m_{H^{\mp}}$) in the $t \to bH^{\pm}$ process.

Fig. 4.29 shows the event yields after each selection step up to the number of selected jets for the signal at $m_{H^{\pm}} = 120\,\mathrm{GeV}/c^2$ and for the simulated backgrounds. The branching

ratio for $t \to bH^{\pm}$ was set to BR($t \to bH^{\pm}$) = 0.05, while that of the light charged Higgs boson to τ-leptons was set to BR($H^{\pm} \to \tau^{\pm}\nu_{\tau}$) = 1. The event yields after the requirement of at least 3 PF hadronic jets are shown in Section 4.9.1 with event yields from the data-driven background measurements.

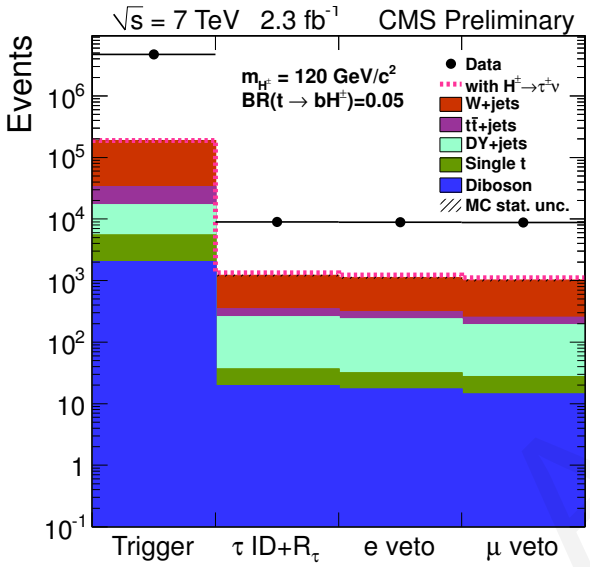

Figure 4.29: Distribution of events yields for the signal and backgrounds after every selection step from the simulations up to the jet selection. The expected event yield in the presence of the $t \to bH^{\pm}$, $H^{\pm} \to \tau^{\pm}\nu_{\tau}$ decays is shown as the dashed red line for $m_{H^{\pm}} = 120\,\text{GeV}/c^2$ and assuming BR($t \to bH^{\pm}$) = 0.05 and BR($H^{\pm} \to \tau^{\pm}\nu_{\tau}$) = 1. The contribution from simulated QCD multi-jet events is not shown.

4.6 Data/simulation corrections

Certain imperfections in the modelling of data by simulations were corrected as described in the following subsections. The corrections were applied only to simulated samples, i.e. signal samples and the samples used in EWK + $t\bar{t}$ fake tau background measurement. These corrections do not affect the results of QCD multi-jet and EWK + $t\bar{t}$ background measurements, as those were directly measured from data with dedicated data-driven techniques.

4.6.1 pile-up re-weighting

The term pile-up is used to describe the additional interactions that occur in each beam-crossing because the instantaneous bunch-by-bunch collision luminosity is very high. These interactions are additional to the hard-scatter interaction that has caused the event to fire the trigger, and their number depends on the intensity of the proton beams and on the time interval between proton bunches. Given that the total inelastic cross section at LHC is $\sim 60\,\text{mb}$, assuming an instantaneous luminosity of the order of $\sim 60\,\text{mb}^{-1}$, there will be one interaction per bunch-crossing, whereas on average by the end of 2011 there were ~ 15 interactions per bunch-crossing, while for 2012 it is anticipated that this number will be as high as ~ 30 interactions per bunch-crossing. These pile-up interactions can be separated into contributions from in-time and out-of-time pile-up interactions, where the former refers to the interactions that occur in the bunch-crossing that fires the trigger while the latter to the interactions that occur in bunch-crossings earlier or later than the in-time interaction. The in-time pile-up for the early part of 2011 data-taking period was about 6. Depending on the integration time of the different CMS detector elements, such interactions can leave energy/tracks in the detector. In general terms, the tracking system is only sensitive to in-time pile-up, the calorimetry system is sensitive to out-of-time pile-up, while the muon system is sensitive to out-of-time pile-up.

The aforementioned facts imply that one needs to account for the in- and out-of-time pile-up interactions in simulated samples. However, the average number of simultaneous pile-up interactions differ between simulation in which the pile-up is fixed and data, in which pile-up changes as a function of instantaneous luminosity. Generically, the re-weighting of MC samples is often done by assigning weights to a MC event such that the observed distribution of some variable in MC matches the observed distribution of the same variable in a data sample. One can also re-weight using the MC truth information to match some assumed truth in the data. With pile-up re-weighting, these options are all available. Although the Deterministic Annealing method [113] for primary vertex reconstruction was shown to be efficient and well-behaved up to the levels of pile-up experienced in 2011, the final distribution for the number of reconstructed primary vertices (pile-up) is still sensitive to the details of the primary vertex reconstruction and to the UE in data and simulated samples. Additionally, there is the potentially larger effect that the distribution for the number of reconstructed vertices can be biased by the offline event selection criteria and even by the trigger. In order

to factorise these effects, instead of re-weighting the simulated samples by the number of reconstructed primary vertices, the number of pile-up interactions is instead re-weighted from the MC simulation truth. The target pile-up distribution for data is derived by using the per-bunch-crossing-per-luminosity section instantaneous luminosity from the luminosity database, together with the total proton-proton inelastic cross-section, to generate an expected pile-up distribution, correctly weighted by the per-bunch-crossing-per-luminosity section integrated luminosity over the entire data-taking period.

As mentioned already in Section 4.3.2, the Summer11 MC production of simulated samples had been generated with a flat distribution from $1-10$ convoluted with a Poisson-like tail for the number of pile-up interactions, which was meant to roughly cover, though not exactly match, the conditions expected for the 2011 data-taking period. The distribution for the number of interactions per bunch-crossing in the simulation samples was chosen in advance to simulate a desired luminosity profile. Therefore, the re-weighting of pile-up interactions was necessary to match the data luminosity distributions. To achieve this, the simulated samples were re-weighted by the true number of interactions in a bunch-crossing with the 3D Re-weighting method [120, 121], a method which employs a 3-dimensional matrix of in- and out-of-time pile-up to calculate weights for the true distributions. In this way, the re-weighting is done with the true numbers of interactions in the 0 in-time and in the ± 1 out-of-time bunch-crossings, whereby the -1 out-of-time interactions are early and $+1$ out-of-time interactions are late. Given that for the Summer11 simulated samples the MC information on how many interactions are in each in- and out-of-time bunch-crossing is available, an event weight can be generated based on these 3 quantities that will give a better description of any out-of-time energy. This is possible because the true distribution for the data is also calculable, given the known instantaneous luminosity for each event together with the total proton-proton inelastic cross-section, enabling the generation of an expected pile-up distribution, correctly weighted by the per-bunch-crossing-per-luminosity section integrated luminosity over the entire data-taking period. The true input distribution is sampled sequentially for data and MC separately, yielding a distribution of instantaneous luminosities. What is needed is a cumulative probability distribution that this input profile will populate in the space describing the number of in- and out-of-time interactions. The weights are based on the probability that the input luminosity will generate a triplet $[N_{-1}][N_0][N_{+1}]$, where the indices refer to the number of interactions in bunch-crossing -1, 0, $+1$. The probability matrices are calculated analytically by using the input distributions to generate the distributions of the mean number of interactions, and then evaluating the Poisson probability for each triplet of interaction multiplicities. The normalised entries in each bin of the input histograms are used as the weight when accumulating probabilities in the data and MC matrices. Once the probability distributions have been calculated, the MC histogram is divided cell-by-cell by the data histogram in order to generate a 3-dimensional weight array. Every time this is done, the weight matrix, the data and MC matrices are saved for a future run.

Table 4.32: Trigger scale factors, obtained from the τ-part of the trigger turn-on curves and used for simulated samples that employed the single τ jet + $E_{\mathrm{T}}^{\mathrm{miss}}$ trigger. The run periods have been combined by weighted average of the integrated luminosity of the run periods with the total integrated luminosity of 2.3 fb^{-1} .

τ-jet p_{T} range	τ-part trigger scale factor
$40 - 50$	0.940 ± 0.067
$50 - 60$	1.05 ± 0.10
$60 - 80$	1.14 ± 0.22
> 80	0.92 ± 0.18

4.6.2 Trigger scale factors

The differences in the trigger efficiencies between data and simulations were taken into account with scale factors. The efficiency differences due to slightly different trigger configurations in data and simulations are implicitly included in the scale factors. For the τ-part of the single τ jet + $E_{\mathrm{T}}^{\mathrm{miss}}$ trigger, the scale factors were calculated and applied in τ-jet p_{T} bins. The scale factors were calculated separately for the run periods 160431 – 167913, 170722 – 173198, 173236 – 176023 where the trigger definitions in data were slightly different, and combined as an integrated luminosity weighted average. The scale factors, defined as the ratio of the efficiencies from data and simulations

$$\mathrm{Ratio} = \frac{\varepsilon_{\mathrm{trigger}}^{\mathrm{data}}}{\varepsilon_{\mathrm{trigger}}^{\mathrm{MC}}}, \tag{4.28}$$

are shown in Fig. 4.13 on page 129 separately for the three run periods. The averaged scale factors are shown in Table 4.32 as a function of τ-jet p_{T}. For the $E_{\mathrm{T}}^{\mathrm{miss}}$- part of the single τ jet + $E_{\mathrm{T}}^{\mathrm{miss}}$ trigger, the efficiencies in data and simulations are in agreement within 10%, as was shown in Fig. 4.15 on page 131. The efficiency in simulations was not corrected with a scale factor, but instead a 10% uncertainty was added in quadrature to the uncertainty from the τ-part.

4.6.3 B-tagging scale factor

The b-tagging efficiency as measured from data differs from the one obtained from simulated samples [119]. This effect can be taken into account by using tagging and mis-tagging scale factors, f_{tag} and $f_{\mathrm{mis\text{-}tag}}$ respectively, defined as

$$f_{\mathrm{tag}}(p_{\mathrm{T}}) = \frac{\varepsilon_{\mathrm{tag}}^{\mathrm{data}}(p_{\mathrm{T}})}{\varepsilon_{\mathrm{tag}}^{MC}(p_{\mathrm{T}})} \tag{4.29}$$

$$f_{\mathrm{mis\text{-}tag}}(p_{\mathrm{T}}) = \frac{\varepsilon_{\mathrm{mistag}}^{\mathrm{data}}(p_{\mathrm{T}})}{\varepsilon_{\mathrm{mistag}}^{MC}(p_{\mathrm{T}})} \tag{4.30}$$

where $\varepsilon_{\mathrm{tag}}$ and $\varepsilon_{\mathrm{mistag}}$ are the b-tagging and mistag efficiencies per jet. Indicatively, the rates for b-jet tagging and b-jet mis-tagging, associated with the TCHE b-tagging algorithm's loose

working point, were found to be $\sim 76\%$ and 12.8%, respectively, for jets with p_{T} between 50 and 80 GeV/c [119]. The probability P that an event passes the b-tagging selection is

$$\mathrm{P} = \prod_{i=1}^{N_{\text{b-flavour jets}}^{\text{tagged}}} \varepsilon_{\text{tag},i} \prod_{j=1}^{N_{\text{b-flavour jets}}^{\text{not tagged}}} (1-\varepsilon_{\text{tag},j}) \prod_{k=1}^{N_{\text{light flavour jets}}^{\text{tagged}}} \varepsilon_{\text{mistag},k} \prod_{l=1}^{N_{\text{light flavour jets}}^{\text{not tagged}}} (1-\varepsilon_{\text{mistag},l}), \tag{4.31}$$

where $N_{\text{b-flavour jets}}^{\text{tagged}}$ is the number of b-flavour jets that were b-tagged, $N_{\text{b-flavour jets}}^{\text{not tagged}}$ is the number of b-flavour jets that were not tagged, $N_{\text{light flavour jets}}^{\text{tagged}}$ is the number of light-flavour jets that were falsely b-tagged and $N_{\text{light flavour jets}}^{\text{not tagged}}$ the number of light-flavour jets that were not falsely b-tagged. For simulation samples, the scaling factors f_{tag} and f_{mistag} are used for b-jets, and light quark/gluon jets, respectively. Here the c-quark is taken as a light quark. The event weight w which must be applied to simulated events due to the inclusion of the b-tagging scaling factors is defined as

$$w = \frac{\mathrm{P}^{\text{data}}}{\mathrm{P}^{MC}} \tag{4.32}$$

$$= \prod_{i=1}^{N_{\text{b-flavour jets}}^{\text{tagged}}} f_{\text{tag},i} \prod_{j=1}^{N_{\text{b-flavour jets}}^{\text{not tagged}}} \left(\frac{1-f_{\text{tag},j}\varepsilon_{\text{tag},j}^{\text{MC}}}{1-\varepsilon_{\text{tag},j}^{\text{MC}}} \right) \times \prod_{k=1}^{N_{\text{light flavour jets}}^{\text{tagged}}} f_{\text{mistag},k} \prod_{l=1}^{N_{\text{light flavour jets}}^{\text{not tagged}}} \left(\frac{1-f_{\text{mistag},l}\varepsilon_{\text{mistag},l}^{\text{MC}}}{1-\varepsilon_{\text{mistag},l}^{\text{MC}}} \right), \tag{4.33}$$

where N denotes the number of jets tagged or not tagged as b-jets out of the selected jets. The data-to-simulation scale factors and b-tagging/mistag efficiencies were taken from Ref. [119], in which the b-tagging efficiencies were measured using events enriched with jets from semi-muonic b-hadron decays, while the mistag rates were measured in an inclusive jet sample. Gluon jets and jets, for which the flavour matching failed, were taken to be jets of light flavour.

4.7 Systematic uncertainties for simulated samples

The evaluation of the systematic uncertainties for the simulated samples, which includes the signal and EWK fake taus, are described in the following subsections. The systematic uncertainties from the data-driven background measurements are described in Section 4.8.1.3 and in Section 4.8.2.5 for the QCD multi-jet and the EWK + $t\bar{t}$ genuine tau backgrounds, respectively. The values of systematic uncertainties are summarised in Section 4.9.

4.7.1 Trigger

The uncertainties of the trigger scale factors were estimated from the uncertainties of the trigger efficiency measurement from data and simulation in bins of τ-jet p_{T}. The trigger scale factors were applied to the signal and to the EWK fake tau background which relies on simulations, by taking into account the τ-jet p_{T} spectrum. The scale factors of different bins are assumed to be uncorrelated, and to have Gaussian uncertainties. By denoting N_i the number of MC events, f_i and Δf_i the scale factor and its associated uncertainty in the τ-jet p_{T} bin i, both of which are shown in Table 4.32 on page 163, through the application of error propagation the total relative uncertainty becomes

$$\frac{\Delta\left(\sum_{i}^{\tau\text{-jet } p_{\mathrm{T}} \text{ bins}} N_i f_i\right)}{\sum_{i}^{\tau\text{-jet } p_{\mathrm{T}} \text{ bins}} N_i f_i} = \frac{\sqrt{\sum_{i}^{\tau\text{-jet } p_{\mathrm{T}} \text{ bins}} (N_i \Delta f_i)^2}}{\sum_{i}^{\tau\text{-jet } p_{\mathrm{T}} \text{ bins}} N_i f_i}. \tag{4.34}$$

4.7.2 τ-jet identification

A 6% uncertainty [115] on the τ-jet identification was taken for the signal selection. The τ-jet identification efficiency and its associated uncertainty was measured by employing a Tag-and-Probe method in a $Z^0 \to \tau\tau \to \mu\tau$ data sample with the τ-lepton decaying hadronically, by using a global fit to the invariant mass of all $Z^0 \to \tau\tau$ decay channels and constraining the yield to the measured combined $Z^0 \to \mu\mu, ee$ cross-section. For the EWK fake tau measurement an uncertainty of 15% was taken for the mis-identification of a τ jet [115], which describes the probability for quark/gluon jets or electrons to be mis-identified as τ jets. The τ-jet mis-identification rate and its associated uncertainty was determined by the use of QCD-type gluon-enriched samples, Z^0- and $W^{\pm}$-type quark-enriched samples, and muon-enriched QCD samples. The τ-jet mis-identification rate as a function of the jet p_{T} was determined in all the samples and the uncertainty was assigned according to the data-to-simulation uncertainty.

4.7.3 Jet and $E_{\mathrm{T}}^{\mathrm{miss}}$ energy scale

The uncertainty due to the JES was calculated by fluctuating the jet energies and propagating the fluctuations to the $E_{\mathrm{T}}^{\mathrm{miss}}$ object calculation. The τ-jet energy was varied by $\pm 3\%$. The jet energies were variated with an asymmetric factor for the uncertainty taken from a look-up table in the global tag START42_V13 depending on jet p_{T} and η [122]. The same sign was taken for the τ jet and jet energy scale fluctuation. To fluctuate the $E_{\mathrm{T}}^{\mathrm{miss}}$ scale, the $E_{\mathrm{T}}^{\mathrm{miss}}$ object calculation was divided into a clustered component and an un-clustered energy component. The clustered $E_{\mathrm{T}}^{\mathrm{miss}}$ component was obtained from the already scaled jets, while the un-clustered $E_{\mathrm{T}}^{\mathrm{miss}}$ was determined by subtracting the non-varied jets from the $E_{\mathrm{T}}^{\mathrm{miss}}$ object. A scale uncertainty of $\pm 10\%$ was added for the un-clustered energy part of $E_{\mathrm{T}}^{\mathrm{miss}}$ [123].

The JES and the uncertainty on the un-clustered energy were fluctuated independently, and after the selection the number of events were counted and the transverse mass shapes $m_{\mathrm{T}}(\tau\text{ jet}, E_{\mathrm{T}}^{\mathrm{miss}})$ were recorded, as constructed from the τ jet and the $E_{\mathrm{T}}^{\mathrm{miss}}$ objects. The maximum deviation in the number of counted events and the transverse mass $m_{\mathrm{T}}(\tau\text{ jet}, E_{\mathrm{T}}^{\mathrm{miss}})$ shapes were recorded. The maximum deviation in the number of counted events with respect to the nominal number of events after the selection was selected as the overall uncertainty on the jet and $E_{\mathrm{T}}^{\mathrm{miss}}$ energy scale. The transverse mass shapes from the variations with largest positive and negative deviations were selected for the shape uncertainties from JES.

4.7.4 Lepton vetoes

For the uncertainty on the veto on isolated electrons and isolated muons, the uncertainty was calculated as

$$\left(\frac{N_{\text{electron veto}}^{\text{not passed}}}{N_{\text{electron veto}}^{\text{passed}}} \times \Delta_{\text{electron ID}} \right)^2 + \left(\frac{N_{\text{muon veto}}^{\text{not passed}}}{N_{\text{muon veto}}^{\text{passed}}} \times \Delta_{\text{muon ID}} \right)^2 \tag{4.35}$$

where N corresponds to the counted number of events failing or passing the isolated electron and muon veto selection, $\Delta_{\text{electron ID}}$ was taken to be 2%, and $\Delta_{\text{muon ID}}$ was taken to be 1%.

4.7.5 B-tagging

The uncertainty of b-tagging was obtained from the uncertainty of the b-tagging/mis-tagging scale factors. Error propagation was applied to Eq. (4.33) by assuming f_{tag} and f_{mistag} are

uncorrelated. The relative systematic uncertainty used was

$$\left(\frac{\Delta w}{w}\right)^2 = \left(\frac{N^{\text{tagged}}_{\text{b-flavor jets}}}{f_{\text{tag}}} - \sum_{i=1}^{N^{\text{not tagged}}_{\text{b-flavor jets}}} \frac{\varepsilon^{\text{MC}}_{\text{tag},i}(p_{\text{T}})}{1 - f_{\text{tag}}\varepsilon^{\text{MC}}_{\text{tag},i}(p_{\text{T}})}\right)^2 \left(\Delta f_{\text{tag}}\right)^2 + \left(\frac{N^{\text{tagged}}_{\text{light flavor jets}}}{f_{\text{mistag}}} - \sum_{j=1}^{N^{\text{not tagged}}_{\text{light flavor jets}}} \frac{\varepsilon^{\text{MC}}_{\text{mistag},j}(p_{\text{T}})}{1 - f_{\text{mistag}}\varepsilon^{\text{MC}}_{\text{mistag},j}(p_{\text{T}})}\right)^2 \left(\Delta f_{\text{mistag}}\right)^2, \quad (4.36)$$

where Δf_{tag} and Δf_{mistag} are according to Ref. [119] 0.05 and 0.11, respectively. It should be noted that the terms with tagged/non tagged jets are anti-correlated. The systematic uncertainty was calculated separately for each event passing the b-tagging selection. The combined uncertainty for a given dataset was obtained by properly weighting the systematic uncertainty obtained for each event.

4.7.6 Cross-section

The theoretical uncertainty of the production cross-section has mainly two sources, the uncertainty of the Parton Distribution Functions (PDFs) and the scale uncertainty. These uncertainties have been estimated by the LHC cross-section working group to be +7.0%−9.6% for the $t\bar{t}$ background [124]. The uncertainty of 4% was taken for the cross-section of the $Z^0/\gamma^* \to \ell\ell$ and WW, WZ, and ZZ backgrounds. For the W+jets, an approximate uncertainty of 7% was taken for the cross-section.

4.7.7 Luminosity

The luminosity uncertainty was taken to be 2.2% [125], a marked improvement over the previous 4.4% [126] uncertainty. The old method for luminosity determination relied on the HF detector, which was designed to be used as a luminometer through its response to the incoming flux of particles which can be used to determine the instantaneous luminosity. Studies of the 2011 data from the CMS HF luminosity system, revealed however 3 distinct problems. Firstly the HF response was a non-linear function of the instantaneous luminosity, secondly the HF was subject to afterglow effects whereby energy from a given bunch-crossing created a small response in subsequent bunch-crossings, and thirdly a slow drift in the calibration constant was observed. Although correction factors were introduced to address these issues, the complications in the measurement and the resulting increase in the luminosity uncertainty lead to the decision of devising a luminosity measurement based on a Pixel Cluster Counting (PCC) method.

It is known that the number of interactions per bunch-crossing scales Poissonianly with the instantaneous luminosity. Each interaction leaves a certain amount of energy in each subdetector, but with the large number of independent channels ($\sim 66 \times 10^6$) the occupancy

is expected to be lowest in the tracker. It thus appears natural to define a physical quantity purely based on tracker quantities to monitor the luminosity. The CMS PCC offline luminosity measurement, starts with the determination of the pixel cluster cross-section (σ_{pixel}) determined in a Van der Meer (vdM) scan by sweeping beams transversely across each other. While σ_{pixel} is not an interaction cross-section in the usual sense, it can however be treated as such for the purpose of luminosity measurements. Having established a value for σ_{pixel}, the luminosity for a given luminosity section is determined by counting the number of pixel clusters per zero-bias trigger (N_{cluster} >), whereby the only requirement is that proton bunches from each beam pass through one another. The overall systematic uncertainty of the integrated PCC luminosity for 2011 was obtained by adding all contributing components in quadrature, with the dominant contributors originating from scan-to-scan variations (1.5%), whereby subsequent vdM scans lead to slightly different results, and afterglow effects (1%).

4.8 Measurement of backgrounds

The main backgrounds for the fully hadronic channel are the QCD multi-jet production and the $t\bar{t}$ and W + jets events. Smaller backgrounds from single-top production, di-boson production (WW, WZ, ZZ) and Drell-Yan ($Z^0/\gamma^* \rightarrow \ell\ell$) events were also taken into account. The potential background from Supersymmetry (SUSY) cascade decays was studied in [77], and was found to be negligible for the mass range investigated. The QCD multi-jet background was measured from data with a factorisation method with events passing the signal trigger as QCD multi-jet events strongly dominate at this level of selection. The background from $t\bar{t}$, W+jets, and single top production with genuine τ jets was measured from data with muonic multi-jet events, transforming the muon to a simulated τ jet with the τ-embedding method. The remaining backgrounds without genuine τ jets excluding the QCD multi-jet yield were estimated from simulation.

The main backgrounds are QCD multi-jet events, EWK + $t\bar{t}$ events with genuine taus, and EWK + $t\bar{t}$ fake tau events with electron, muon or hadronic jets being mis-identified as τ jets. The EWK processes include W + jets, single-top (s-, t- and tW-channels), Drell-Yan ($Z^0/\gamma^* \rightarrow \ell\ell$) and di-boson (WW, WZ, ZZ) production. The QCD multi-jet and EWK+$t\bar{t}$ genuine τ backgrounds were measured from data as described in Sections 4.8.1 and 4.8.2, respectively. The EWK+$t\bar{t}$ fake τ background, described in detail in Section 4.8.3, was found to be small and was therefore estimated from simulations.

4.8.1 QCD multi-jet background

At high-energy hadron colliders, such as the LHC, events containing multiple jets in the final state are ample and provide an ideal testing ground for the theory of QCD. In Leading Order Perturbative Quantum Chromodynamics (*p*QCD), jet production in proton-proton collisions occurs when two incoming partons interact via the strong force to produce two final-state partons. The elementary processes that contribute to the final state are $qq \rightarrow qq$, qg $\rightarrow$ qg, $gg \rightarrow gg$, $gg \rightarrow qq$. It is probable that the final state particles will subsequently lose energy through the emission of other quarks or gluons, in a process commonly referred to as Parton Shower (PS). These parton shower products undergo hadronisation and form hadronic jets, resulting in a final state with multi-jets as shown in Figures 4.30 and 4.31. Such events with 3 or more jets in the final state originate from hard-gluon radiation and other higher-order QCD processes. Within this framework, the energy of hadronic jets is related to the energy of the produced outgoing partons, with the jet transverse momentum p_T, jet azimuthal angle ϕ and jet rapidity ω being strongly correlated with those of the final-state partons.

Apart from constituting an important probe in testing the robustness of the QCD theoretical framework, QCD multi-jet events are often an important background in searches for new particles and new interactions at high energies. In particular, systematic uncertainties that contribute to multi-jet cross-section measurements can significantly limit the performance

of search analyses. In this light, studies on QCD multi-jet backgrounds are significant in $t\bar{t}$ and SUSY analyses, mainly due to jets faking electrons in the e + jets final state and muons in hadronic jets from heavy flavours in the μ + jets final state. For this reason, several data-driven methods have been developed in CMS to estimate the QCD multi-jet background contribution in the signal regions, including fake-rate application methods [127], extrapolation methods with relative isolation [128] and the kinematical variable α_T [129], and fits to discriminating variables with template fit methods [127]. Most relevantly with the present analysis, QCD multi-jet background is important in the τ + jets final state, especially when the τ-lepton decays hadronically. Despite the fact that genuine τ jets can be effectively discriminated from hadronic quark/gluon jets through various of their distinct characteristics, including lower track multiplicity, isolation in the tracking and calorimetry systems and narrower calorimeter clusters, the large and poorly known cross-section of QCD multi-jet processes means that it is crucial to be able to control and accurately measure such backgrounds. In this study, a data-driven method based on factorisation and shape analysis is presented for measuring the number of QCD multi-jet events in the signal region.

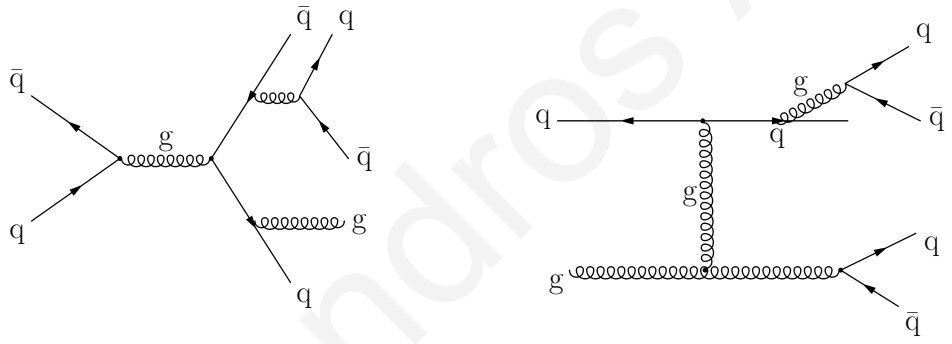

Figure 4.30: Representative Feynman diagrams for QCD multi-jet production, through $qq \to qq$ (a) and $qg \to qg$ (b). The diagrams were created with feynMF [80].

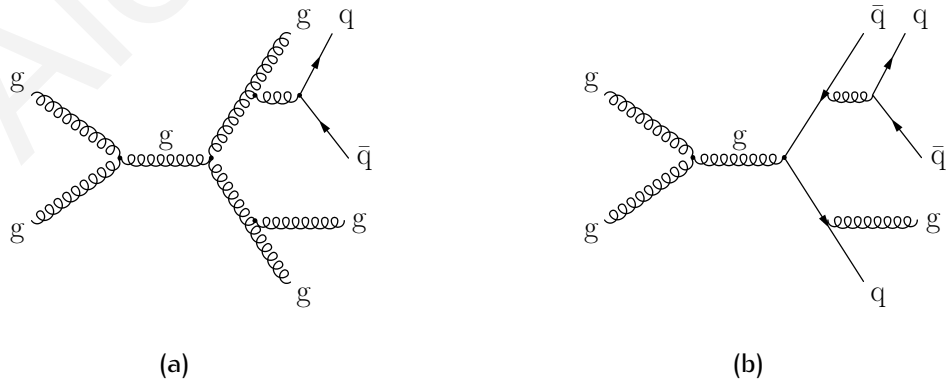

Figure 4.31: Representative Feynman diagrams for QCD multi-jet production, through $gg \to gg$ (a) and $gg \to qq$ (b). The diagrams were created with feynMF [80].

For the measurement of QCD multi-jet backgrounds discussed in this section, exactly the same cuts as those applied in the signal analysis described in Section 4.5 were either

applied or factorised out of the cut-flow. The factorisation was conducted within p_T bins of τ jet candidates, to account for the fact that the probability of a quark/gluon jet to pass the τ-jet isolation criteria as well as the R_τ selection was found to be depended on the jet p_T. An additional incentive, directly related to this, was to minimise the correlation between the E_T^{miss} and τ-jet identification. This is demonstrated in Fig. 4.32, whereby the PF E_T^{miss} and the τ-jet p_T distributions are shown, before and after τ-jet isolation. The PF E_T^{miss} distribution, shown in Fig. 4.32 (a), appears to be correlated with the τ-jet isolation selection, resulting in the enhancement of its tail.

The physics interpretation of this behaviour, is that the composition of the data sample is changed, as it results in rejecting a large portion of QCD multi-jet events (no genuine τ-leptons or E_T^{miss}) and thus enhancing the relative contribution of EWK processes (contain genuine τ-leptons and E_T^{miss}). As a result and as anticipated, this change in composition is manifested by an increase in the tail of the E_T^{miss} distribution. Another effect of applying the τ-jet isolation requirement, is that the p_T spectrum of the now identified τ jets is also affected, as shown in Fig. 4.32 (b). This has a direct impact on the number QCD multi-jet events, due to the fact that τ jet fake-rate is a function of the jet p_T.

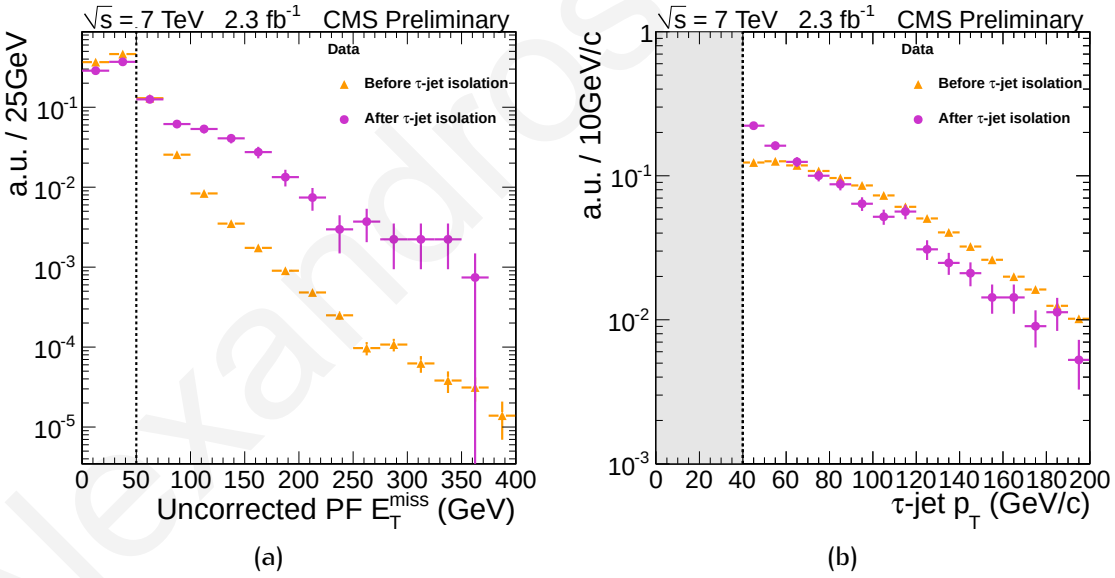

Figure 4.32: Distribution of PF E_T^{miss} (a) and τ-jet p_T (b), normalised to unit area, before and after applying full τ-jet isolation, after the *basic-selections* 1 – 6 in the cut-flow procedure. The latter is explained in detail in Section 4.8.1.1.

Nevertheless, the τ-jet identification-E_T^{miss} correlation was found to be reduced to a negligible level within a given τ-jet candidate p_T bin. The position in the cut-flow at which the factorisation was conducted, was chosen such that the QCD multi-jet background was found to be the dominant contributing process in all τ-jet candidate p_T bins. This data-driven method enabled a qualitative and quantitative measurement of the contribution of QCD multi-jet background processes to the signal region. With a similar technique, the QCD multi-jet transverse mass shape after all selections was extracted from the data using two similar methods.

In the following sections, the strategy employed in acquiring the data-driven estimate for the QCD multi-jet background is described in Section 4.8.1.1, while the results and associated systematic uncertainties are presented in Section 4.8.1.2 and Section 4.8.1.3, respectively. The techniques used in extracting the corresponding transverse mass shapes are described in Section 4.8.1.4 followed by the description of the results and the systematic uncertainties associated with these measurements. Finally, a thorough study on the possible effects that the presence of a possible signal in the data might have on the QCD multi-jet background estimate and transverse mass shape determination are presented in Section 4.8.1.6.

4.8.1.1 Strategy of measurement

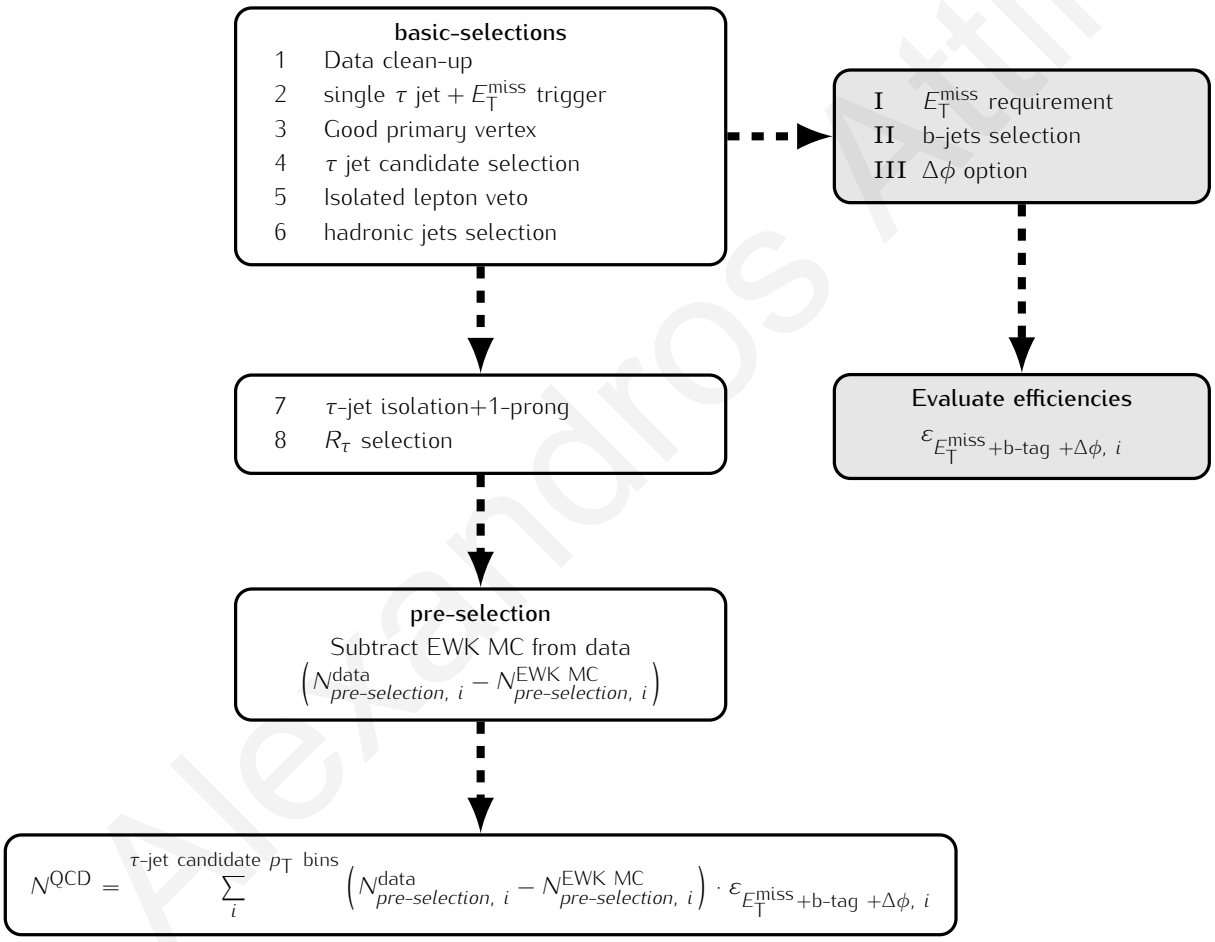

Figure 4.33: Schematic overview of the QCD multi-jet background measurement. The selections I+II+III, shown in the shaded block, were factorised out of the cut-flow after the *basic-selections* 1 – 6. The individual selections are described in detail in Section 4.5.

The cut-flow used in the QCD multi-jet background measurement is shown in Fig. 4.33, which involves all the signal selection requirements, as described in Section 4.5. The selection range 1 – 6 will henceforth be referred to as *basic-selections*. At this exact point the $E_{\mathrm{T}}^{\mathrm{miss}}$, b-tagging and $\Delta\phi\left(\tau \text{ jet candidate}, E_{\mathrm{T}}^{\mathrm{miss}}\right)$ ($\Delta\phi$ for short) selections, henceforth referred to as selections I+II+III, were collectively factorised out of the cut flow in τ-jet candidate p_{T} bins. The point where the factorisation was conducted was chosen such that there was

minimum correlation between selections, while also ensuring that the selected data sample was composed almost exclusively by QCD multi-jet events.

The τ-jet isolation, which is particularly effective in suppressing QCD multi-jet events by a factor of about $\sim 100 - 500$ [115] depending on the isolation working point selected, was applied as late as possible in the cut-flow in order to maximise the QCD multi-jet composition of the preceding *basic-selections* sample. The selection range $1 - 8$ excluding selections I+II+III will be hereafter referred to as the *pre-selection*. For quick reference, the categorisation of the selection cuts is summarised in Table 4.33.

Table 4.33: Summary of the cut-flow categorisation used in QCD multi-jet background measurement.

Cut-flow	Selections
basic-selections	$1 - 6$
pre-selection	$1 - 6, 7 + 8$
$E_{\mathrm{T}}^{\mathrm{miss}}$+b-tag $+\Delta\phi$	I+II+III

From the above described cut-flow and the factorisation steps employed, the measurement for the number of QCD multi-jet events expected in the signal region can be expressed as

$$N^{\mathrm{QCD}} = \sum_{i}^{\tau\text{-jet candidate } p_{\mathrm{T}} \text{ bins}} \left(N^{\mathrm{data}}_{\textit{pre-selection},\ i} - N^{\mathrm{EWK\ MC}}_{\textit{pre-selection},\ i} \right) \cdot \varepsilon_{E_{\mathrm{T}}^{\mathrm{miss}}\text{+b-tag }+\Delta\phi,\ i} \tag{4.37}$$

where the term $N^{\mathrm{sample}}_{\text{after cut } X,\ i}$ is defined as the number of counted events after a given selection X of the cut-flow using a given sample, be it data or EWK MC. The expression EWK MC refers to all simulated background samples available for this study, namely di-boson (WW, WZ, ZZ), $t\bar{t}$ + jets, W + jets, Drell-Yan ($Z^0/\gamma^* \rightarrow \ell\ell$) and single-top as shown in Tables 4.10, 4.11 and 4.12. It follows that by subtracting the number of EWK MC events from the number of data events yields the number of QCD multi-jet events. The term $\varepsilon_{E_{\mathrm{T}}^{\mathrm{miss}}\text{+b-tag }+\Delta\phi,\ i}$ is defined as the combined $E_{\mathrm{T}}^{\mathrm{miss}}$, b-tagging and $\Delta\phi$ efficiency. The index i denotes the τ-jet candidate p_{T} bin for which the measured quantities were determined. The chosen p_{T} bin widths were 10 GeV/c up to 80 GeV/c, then 80−100 GeV/c, 100−120 GeV/c, 120−150 GeV/c, and $>$ 150 GeV/c. The choice of bin-width was made based on the need to have a sufficient number of events in each bin, while also keeping correlations between variables to a minimum level. It should be emphasised that the QCD multi-jet MC samples were not used in the derivation of the results, although they were used in preliminary studies in which the measurement strategy was developed.

The p_{T} distribution of the τ jet candidates after the *basic-selections* is shown in Fig. 4.34 (a), confirming that the QCD multi-jet background dominates all other backgrounds over the whole τ-jet candidate p_{T} range. In order to quantify the fraction of QCD multi-jet events

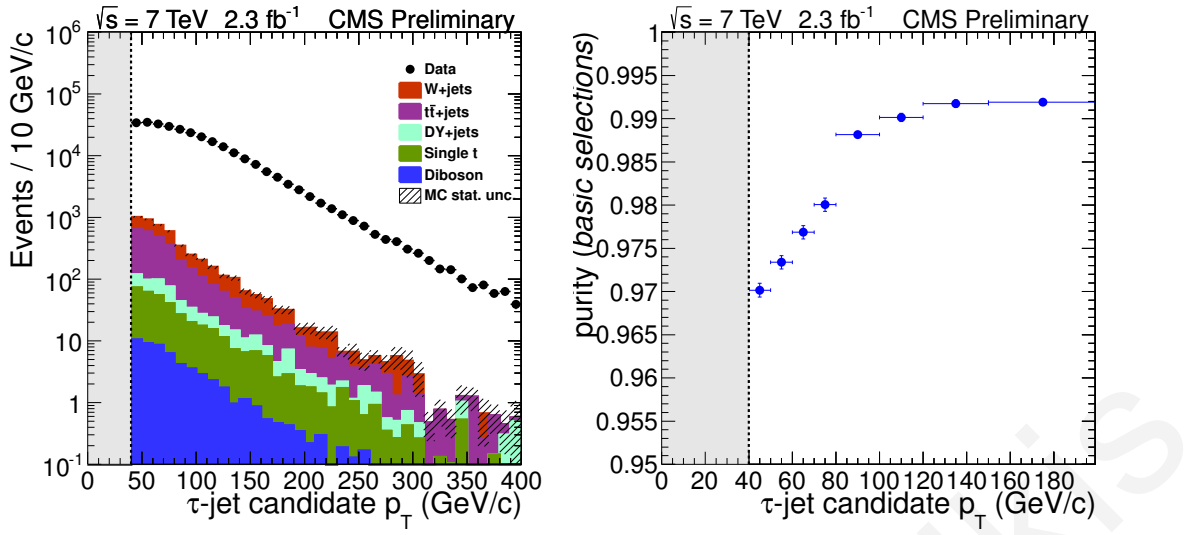

Figure 4.34: Distribution of p_T for the τ jet candidates (a) and QCD multi-jetpurity (b) in τ-jet candidates p_T bins after the *basic-selections*. The contribution from simulated QCD multi-jet events, which is assumed to fill the empty area between data and simulation points, is not shown. The last τ-jet candidates p_T bin corresponds to $p_T > 150\,\text{GeV}/c$.

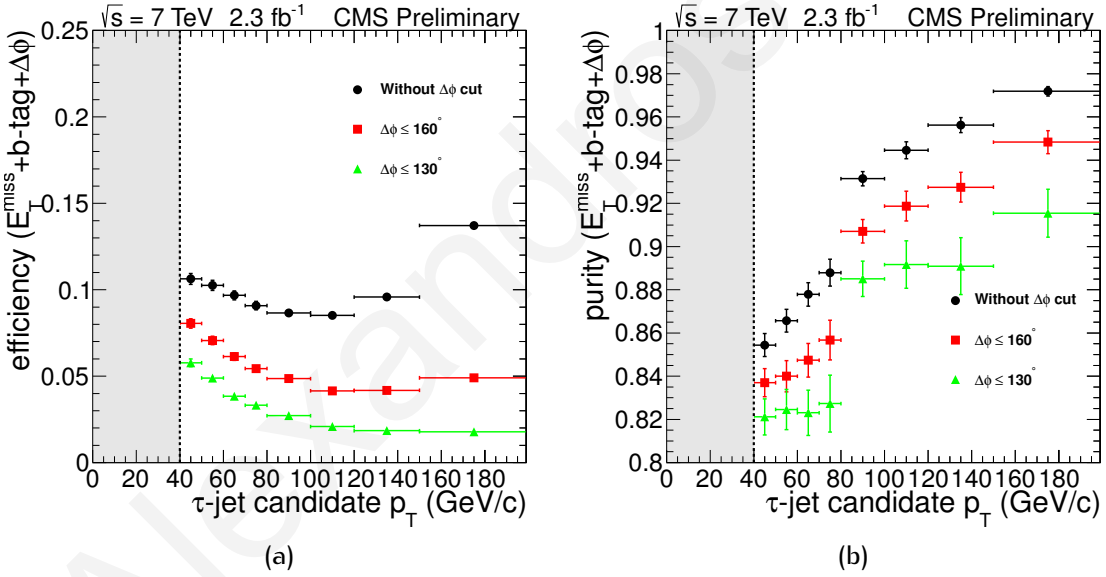

Figure 4.35: Efficiency (a) and QCD multi-jetpurity (b) of the E_T^{miss}+b-tag $+\Delta\phi\left(\tau \text{ jet candidate}, E_T^{\text{miss}}\right)$ collective cut in p_T bins of τ jet candidates ($\varepsilon_{E_T^{\text{miss}}+\text{b-tag}\ +\Delta\phi,\ i}$). The last τ-jet candidate p_T bin corresponds to $p_T > 150\,\text{GeV}/c$.

in the selected data sample at a specific position X of the cut-flow, the term $f_{X,\ i}$ was defined

$$f_{X,\ i} = \frac{N^{\text{data}}_{\text{after cut } X,\ i} - N^{\text{EWK MC}}_{\text{after cut } X,\ i}}{N^{\text{data}}_{\text{after cut } X,\ i}} \tag{4.38}$$

for the τ-jet candidate p_T bin i and will henceforth be referred to as the QCD multi-jetpurity of the sample. In Fig. 4.34 (b), the explicit values of the QCD multi-jetpurity in τ-jet candidate p_T bins are shown, with the sample purity varying in the individual bins of τ-jet candidate p_T. The apparent mild p_T dependence is linear up to $\sim 100\,\text{GeV}/c$, beyond which a purity-

plateau is reached. In a similar manner, the efficiency of a given selection X was generically quantified as

$$\varepsilon_{X,\,i} = \frac{N^{\text{data}}_{\text{after cut }X,\,i} - N^{\text{EWK MC}}_{\text{after cut }X,\,i}}{N^{\text{data}}_{\text{before cut }X,\,i} - N^{\text{EWK MC}}_{\text{before cut }X,\,i}} \tag{4.39}$$

for a given τ-jet candidate p_{T} bin i. With this definition, the combined $E_{\text{T}}^{\text{miss}}$+b-tag $+\Delta\phi$ efficiency was defined as

$$\varepsilon_{E_{\text{T}}^{\text{miss}}\text{+b-tag }+\Delta\phi,\,i} = \frac{N^{\text{data}}_{\textit{basic-selections}+\text{I}+\text{II}+\text{III},\,i} - N^{\text{EWK MC}}_{\textit{basic-selections}+\text{I}+\text{II}+\text{III},\,i}}{N^{\text{data}}_{\textit{basic-selections},\,i} - N^{\text{EWK MC}}_{\textit{basic-selections},\,i}} \tag{4.40}$$

for the p_{T} bin i of the τ jet candidates. These efficiencies and their corresponding QCD multi-jetpurities were found to depend on the τ-jet candidate p_{T} and on the $\Delta\phi$ option, as can be seen in Fig. 4.35.

4.8.1.2 Results

The QCD multi-jet background estimates, as measured from data in τ-jet candidate p_{T} bins with Eq. (4.37) are graphically shown in Fig. 4.36, where the differential (a) and total (b) contributions from each τ-jet candidate p_{T} bin are presented. The estimate on the number of QCD multi-jet events expected in the signal region, denoted as N^{QCD}, and its associated statistical and systematic uncertainties are summarised in Table 4.34 and were found to be $42 \pm 3 \pm 1$ when no $\Delta\phi$ cut was applied, $26 \pm 2 \pm 1$ for $\Delta\phi < 160°$ and $17.0 \pm 1.2 \pm 0.7$ for $\Delta\phi < 130°$, for an integrated luminosity of $2.3\,\text{fb}^{-1}$. The fraction of QCD multi-jet events of the selected data sample estimated with Eq. (4.38) was evaluated to be $97\% - 99\%$ and $82 - 92\%$ after *basic-selections* and after $E_{\text{T}}^{\text{miss}} + \text{b-tag} + \Delta\phi < 160°$. An analytic breakdown of the N^{QCD} estimate for $\Delta\phi < 160°$ is presented in Table 4.35, while a detailed description of the associated uncertainties is given in Section 4.8.1.3.

Table 4.34: Summary of the number of events expected from QCD multi-jet processes in the signal region, as extracted with a dedicated data-driven method and for 3 $\Delta\phi$ options.

$\Delta\phi\left(\tau\text{ jet candidate}, E_{\text{T}}^{\text{miss}}\right)$	Events	Stat. Error	Syst. Error	Stat.⊕Syst. Error
Without $\Delta\phi$ cut	42	±3	±1	±2
$\Delta\phi < 160°$	26	±2	±1	±2
$\Delta\phi < 130°$	17.0	±1.2	±0.7	±1.4

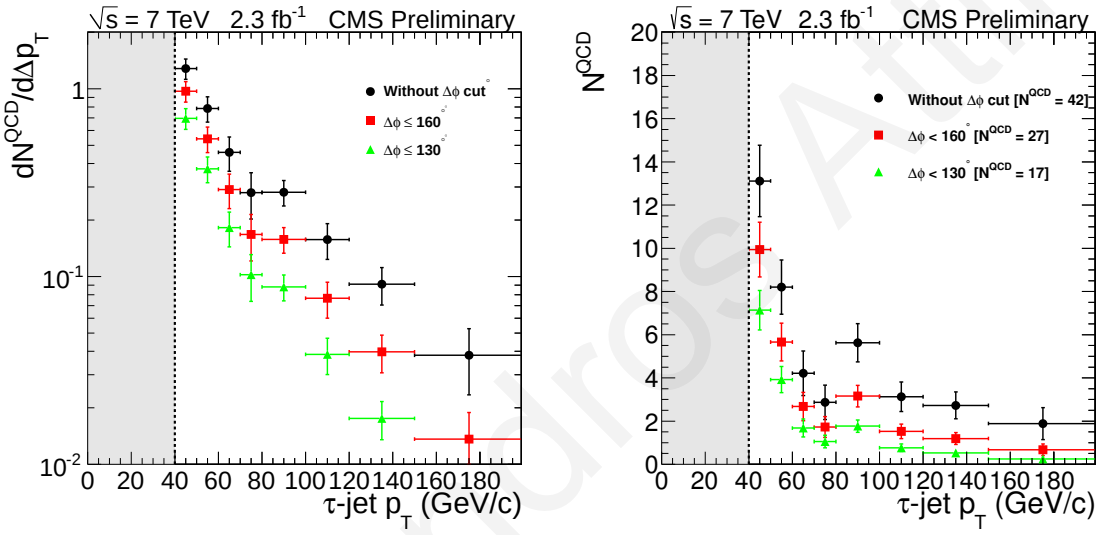

Figure 4.36: The differential (a) and total (b) contribution from each τ-jet candidate p_T bin in the predicted number of QCD multi-jet events in the signal region, for 3 $\Delta\phi\left(\tau \text{ jet candidate}, E_T^{miss}\right)$ options: without $\Delta\phi$ cut, $\Delta\phi < 160°$ and $\Delta\phi < 130°$. The combined systematic and statistical uncertainties are also shown. The chosen p_T bin widths, denoted Δp_T, are shown explicitly in Table 4.35.The last τ-jet candidate p_T bin corresponds to $p_T > 150\,\text{GeV}/c$.

Table 4.35: Analytic breakdown of the QCD multi-jet event yield estimate in the signal region, denoted as N^{QCD} and obtained using Eq. (4.37). The number of data and EWK MC events after *pre-selections*, and the efficiencies of the $E_{\mathrm{T}}^{\mathrm{miss}} + \text{b-tag} + \Delta\phi < 160°$ collective cut are shown explicitly in τ-jet candidate p_{T} bins. The numbers correspond to an integrated luminosity of $2.3\,\mathrm{fb}^{-1}$.

p_{T} (GeV/c)	$40-50$	$50-60$	$60-70$	$70-80$
p_{T} bin width Δp_{T} (GeV/c)	10	10	10	10
$N^{\mathrm{data}}_{\textit{pre-selection, i}}$	167 ± 13	110 ± 10	72 ± 8	51 ± 7
$N^{\mathrm{EWK\ MC}}_{\textit{pre-selection, i}}$	42 ± 7	29 ± 5	27 ± 6	19 ± 5
$\varepsilon_{E_{\mathrm{T}}^{\mathrm{miss}}+\text{b-tag}+\Delta\phi,\ i}$	0.081 ± 0.003	0.071 ± 0.002	0.062 ± 0.002	0.055 ± 0.002
N^{QCD}	10 ± 1	5.8 ± 0.9	2.8 ± 0.6	1.8 ± 0.5

p_{T} (GeV/c)	$80-100$	$100-120$	$120-150$	>150
p_{T} bin width Δp_{T} (GeV/c)	20	20	30	60
$N^{\mathrm{data}}_{\textit{pre-selection, i}}$	82 ± 9	48 ± 7	35 ± 6	20 ± 5
$N^{\mathrm{EWK\ MC}}_{\textit{pre-selection, i}}$	17 ± 4	11 ± 4	6 ± 3	6 ± 3
$\varepsilon_{E_{\mathrm{T}}^{\mathrm{miss}}+\text{b-tag}+\Delta\phi,\ i}$	0.049 ± 0.001	0.042 ± 0.001	0.042 ± 0.001	0.049 ± 0.001
N^{QCD}	3.2 ± 0.5	1.5 ± 0.3	1.2 ± 0.3	0.7 ± 0.3

4.8.1.3 Systematic uncertainties

The uncertainty associated with the number of QCD multi-jet events expected in the signal region, denoted N^{QCD}, was obtained by applying error propagation to Eq. (4.37)

$$\Delta^2_{N^{\text{QCD}}} = \sum_{i}^{\tau\text{-jet candidate } p_{\text{T}} \text{ bins}} \Big[\Big(\Delta^2_{N^{\text{data}}_{\text{pre-selection},\ i}} + \Delta^2_{N^{\text{EWK MC}}_{\text{pre-selection},\ i}} \Big) \times \varepsilon^2_{E_{\text{T}}^{\text{miss}}\text{+b-tag }+\Delta\phi,\ i} + \Big(N^{\text{data}}_{\text{pre-selection},\ i} - N^{\text{EWK MC}}_{\text{pre-selection},\ i} \Big)^2 \times \Delta^2_{\varepsilon_{E_{\text{T}}^{\text{miss}}\text{+b-tag }+\Delta\phi,\ i}} \Big] \tag{4.41}$$

where

$$\Delta_{N^{\text{data}}_{\text{pre-selection},\ i}} = \sqrt{N^{\text{data}}_{\text{pre-selection},\ i}} \tag{4.42}$$

is the Poissonian uncertainty associated to the number of events observed in the data. The combined absolute uncertainty associated to the number of EWK MC events after selection X of the cut-flow and for the τ-jet candidate p_{T} bin i, $\Delta^2_{N^{\text{EWK MC}}_{\text{after cut } X,\ i}}$, was defined to be attributed to a systematic and a statistical term, denoted $\Delta^2_{N^{\text{EWK MC}}_{\text{after cut } X,\ i},\ \text{Syst.}}$ and $\Delta^2_{N^{\text{EWK MC}}_{\text{after cut } X,\ i},\ \text{Stat.}}$, respectively, as follows

$$\Delta^2_{N^{\text{EWK MC}}_{\text{after cut } X,\ i}} = \Delta^2_{N^{\text{EWK MC}}_{\text{after cut } X,\ i},\ \text{Stat.}} + \Delta^2_{N^{\text{EWK MC}}_{\text{after cut } X,\ i},\ \text{Syst.}}. \tag{4.43}$$

The EWK MC statistical uncertainty was defined as

$$\Delta^2_{N^{\text{EWK MC}}_{\text{after cut } X,\ i},\ \text{Stat.}} = \sum_{k}^{\text{EWK MC samples}} \left(w_k \sqrt{N^{\text{EWK MC GEN}}_{\text{after cut } X,\ ik}} \right)^2, \tag{4.44}$$

where w_k is the MC weight factor for EWK sample k and $N^{\text{EWK MC GEN}}$ is the number of MC generated (un-weighted) EWK events. The systematic uncertainty was considered by adopting a conservative 20% uncertainty on the number of MC EWK events

$$\Delta^2_{N^{\text{EWK MC}}_{\text{after cut } X,\ i},\ \text{Syst.}} = \sum_{k}^{\text{EWK MC samples}} \left(0.2 N^{\text{EWK MC}}_{\text{after cut } X,\ ik} \right)^2. \tag{4.45}$$

The decision was based on the fact that, by far the dominant sources of systematic uncertainty were found to be the JES, the trigger scale factors and the $t\bar{t}$ cross-sections uncertainty. Adding them in quadrature, resulted in a systematic uncertainty of $\sim 17\%$. It was thus decided to adopt the conservative 20% uncertainty on the number of MC EWK events. Therefore, with Eq. (4.43), Eq. (4.44) and Eq. (4.45), the total uncertainty introduced by the reliance on EWK MC can be expressed as

$$\Delta^2_{N^{\text{EWK MC}}_{\text{after cut } X,\ i}} = \sum_{k}^{\text{EWK MC samples}} \left[\left(w_k \sqrt{N^{\text{EWK MC GEN}}_{\text{after cut } X,\ ik}} \right)^2 + \left(0.2 N^{\text{EWK MC}}_{\text{after cut } X,\ ik} \right)^2 \right] \tag{4.46}$$

for the τ-jet candidate p_{T} bin i. With Eq. (4.46) the combined absolute uncertainty associated to the general efficiency term $\varepsilon_{X,\,i}$, defined in Eq. (4.39), is given by

$$\begin{aligned}\Delta^2_{\varepsilon_{X,\,i}} &= \frac{1}{\left(N^{\text{data}}_{\text{before cut X},\,i} - N^{\text{EWK MC}}_{\text{before cut X},\,i}\right)^2}\left[\Delta^2_{N^{\text{data}}_{\text{after cut }X,\,i}} + \Delta^2_{N^{\text{EWK MC}}_{\text{after cut }X,\,i}}\right] \\ &= \frac{1}{\left(N^{\text{data}}_{\text{before cut X},\,i} - N^{\text{EWK MC}}_{\text{before cut X},\,i}\right)^2}\left[N^{\text{data}}_{\text{after cut }X,\,i} + \sum_{k}^{\text{EWK MC samples}}\left[\left(w_k\sqrt{N^{\text{EWK MC GEN}}_{\text{after cut }X,\,ik}}\right)^2\right.\right. \\ &\quad \left.\left. + \left(0.2N^{\text{EWK MC}}_{\text{after cut }X,\,ik}\right)^2\right]\right]. \end{aligned} \tag{4.47}$$

A breakdown of the absolute uncertainty associated with the predicted number of QCD multi-jet events in the signal, $\Delta^2_{N^{\text{QCD}}}$, can be seen in Fig. 4.37. The dominant source of uncertainty in the QCD multi-jet background determination is the statistical uncertainty of the data sample in the two main contributing τ-jet candidate p_{T} bins; $40-50$ and $50-60\,\text{GeV}/c$.

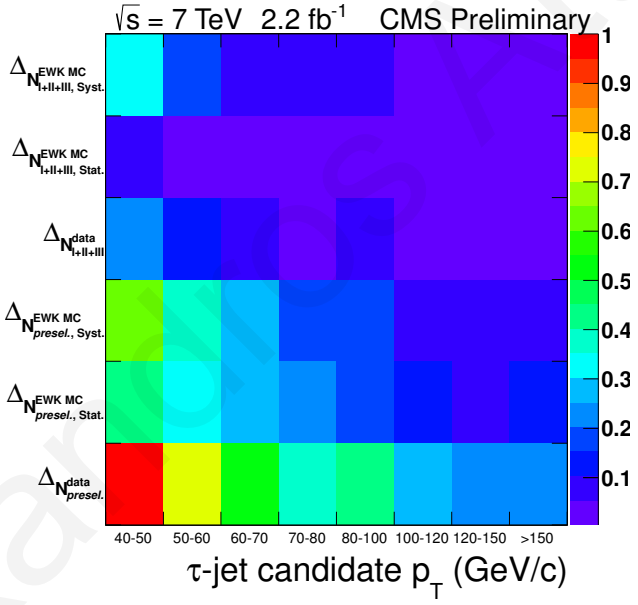

Figure 4.37: Analytic breakdown of the contributors to the absolute uncertainty, $\Delta^2_{N^{\text{QCD}}}$, for the predicted number of QCD multi-jet events in the signal region N^{QCD}.

4.8.1.4 Transverse mass shape extraction

In order to extract the transverse mass shape for the QCD multi-jet background, two similar yet distinct data-driven methods were developed; one that employs MC information to correct for the QCD multi-jetpurity of the data sample used, and one that instead employs anti-isolated τ jet candidates to enhance the QCD multi-jetpurity, henceforth referred to as *Purity-Corrected* and *Anti-Isolation* methods, respectively. For both methods, the main strategy was to extract the QCD multi-jet transverse mass shape after all the signal selection requirements, as described in Section 4.5, while constraining systematic and statistical uncertainties. The resulting shape was then normalised to the event yield of the QCD multi-jet background estimate, N^{QCD}, which was obtained as described in Section 4.8.1.1. The dominant source of

uncertainty for both methods was found to be the statistical uncertainty of the data sample in the two main contributing τ-jet candidate p_T bins; $40-50$ and $50-60\,\text{GeV}/c$. As a consequence, both methods were found to have comparable uncertainties. With this into consideration, the *Purity-Corrected* method was preferred over the *Anti-Isolation* method due to the fact that, unlike the latter, the former has no dependence on the purity of the selected QCD multi-jet sample. Therefore, the *Purity-Corrected* method was chosen to obtain the QCD multi-jet transverse mass shape for this analysis, while the *Anti-Isolation* method was used to validate the results of the former.

***Purity-Corrected* method** The main ingredient in this method is the transverse mass reconstructed from the τ jet candidate and E_T^{miss} objects, after *basic-selections*+I+III and in τ-jet candidate p_T bins. The τ-jet identification step was factorised out of the cut-flow, whereas the b-tagging selection step was found to have a negligible effect on the transverse mass shape, as shown in Fig. 4.38, and was hence left out of the procedure to enhance the QCD multi-jetpurity of the data sample. The relevant efficiency of the b-tagging selection

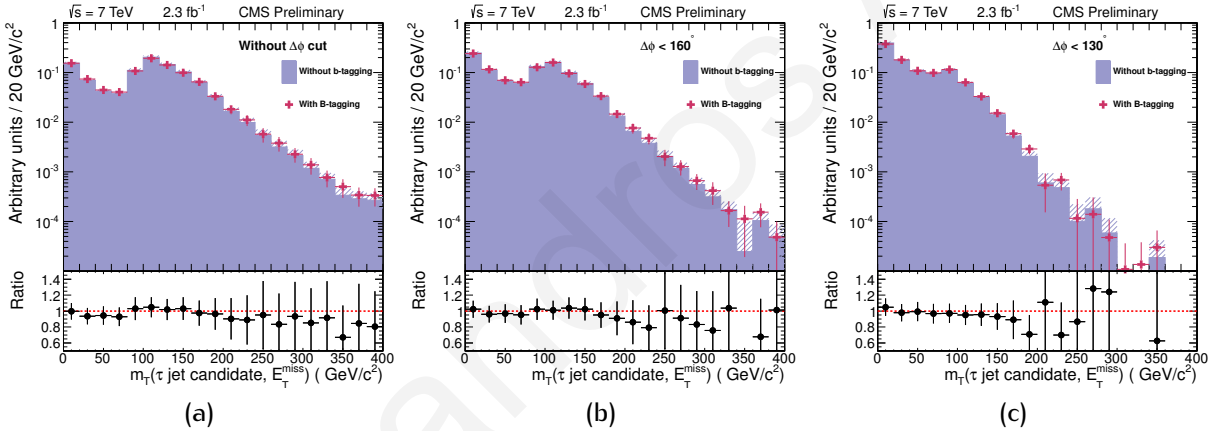

Figure 4.38: The QCD multi-jet transverse mass shapes, normalised to unit area, as extracted with the *Purity-Corrected* method. The shaded histograms (cross-shaped markers) represent the shape with (without) the b-tagging cut applied. The shapes were extracted for 3 $\Delta\phi\left(\tau \text{ jet candidate}, E_T^{miss}\right)$ options: without $\Delta\phi$ cut (a), $\Delta\phi < 160°$ (b) and $\Delta\phi < 130°$ (c).

is defined as

$$\varepsilon_{\text{b-tag},\ i} = \frac{N^{\text{data}}_{\textit{basic-selections}+\text{I}+\text{II}+\text{III},\ i} - N^{\text{data}}_{\textit{basic-selections}+\text{I}+\text{II}+\text{III},\ i}}{N^{\text{data}}_{\textit{basic-selections}+\text{I}+\text{III},\ i} - N^{\text{data}}_{\textit{basic-selections}+\text{I}+\text{III},\ i}} \tag{4.48}$$

for the τ-jet candidate p_T bin i, and is shown in Fig. 4.39. The dependency of the b-tagging efficiency on the p_T of the τ jet candidates is understood to arise from the correlation between jet energies in QCD multi-jet events. For example, to first approximation, in QCD di-jet events the harder the τ jet candidates is, the harder its recoil jet will be. This in conjunction with the fact that the b-tagging fake rate is an increasing function of jet p_T [119], can be used to understand the shape of the b-tagging efficiency plot.

A schematic overview of the QCD multi-jet transverse mass shape extraction through the

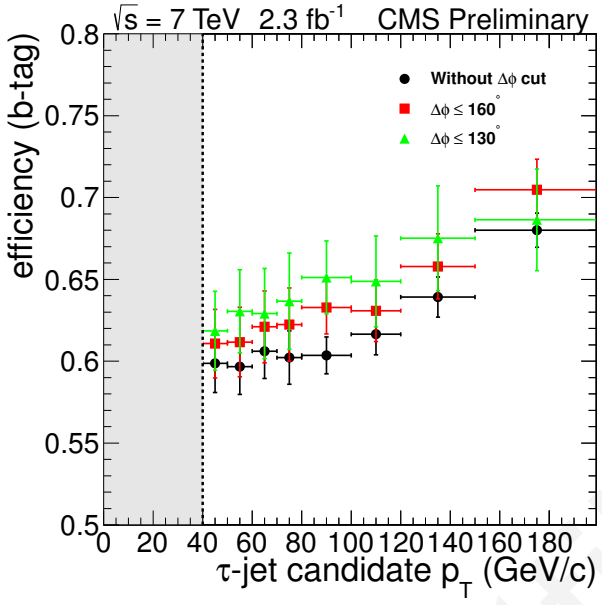

Figure 4.39: Efficiency of b-tagging in p_T bins of τ jet candidates, $\varepsilon_{\text{b-tag},\,i}$, as defined in Eq. (4.48) and as measured from data. The last τ-jet candidate p_T bin corresponds to $p_T > 150\,\text{GeV}/c$.

Purity-Corrected method can be seen in Fig. 4.40. After subtracting the EWK MC from the data-extracted transverse mass distributions, the purity-corrected QCD multi-jet transverse mass shapes were then weighted according to the efficiency of passing the τ-jet identification step, defined as

$$\varepsilon_{\tau\text{-jet ID},\,i} = \frac{N^{\text{data}}_{\textit{basic-selections+7+8},\,i} - N^{\text{EWK MC}}_{\textit{basic-selections+7+8},\,i}}{N^{\text{data}}_{\textit{basic-selections},\,i} - N^{\text{EWK MC}}_{\textit{basic-selections},\,i}} \tag{4.49}$$

for the τ-jet candidate p_T bin i. The τ-jet identification efficiencies and the corresponding QCD multi-jetpurities of the data samples used are shown in Fig. 4.41. In this way, the number of events in bin j of the transverse mass shape is given by

$$N_{ij} = \left(N^{\text{data}}_{\textit{basic-selections+I+III},\,ij} - N^{\text{EWK MC}}_{\textit{basic-selections+I+III},\,ij}\right) \times \varepsilon_{\tau\text{-jet ID},\,i} \tag{4.50}$$

where again the index i denotes the τ-jet candidate p_T bin under consideration. Summing over all contributing τ-jet candidate p_T bins yields the total number of events in bin j of the QCD multi-jet transverse mass shape

$$N_j = \sum_{i}^{\tau\text{-jet candidate } p_T \text{ bins}} \left(N^{\text{data}}_{\textit{basic-selections+I+III},\,ij} - N^{\text{EWK MC}}_{\textit{basic-selections+I+III},\,ij}\right) \times \varepsilon_{\tau\text{-jet ID},\,i}. \tag{4.51}$$

The final step to extract the QCD multi-jet transverse mass shape was to normalise the area of this distribution to the QCD multi-jet background estimate event yield, N^{QCD}, as determined from Eq. (4.37)

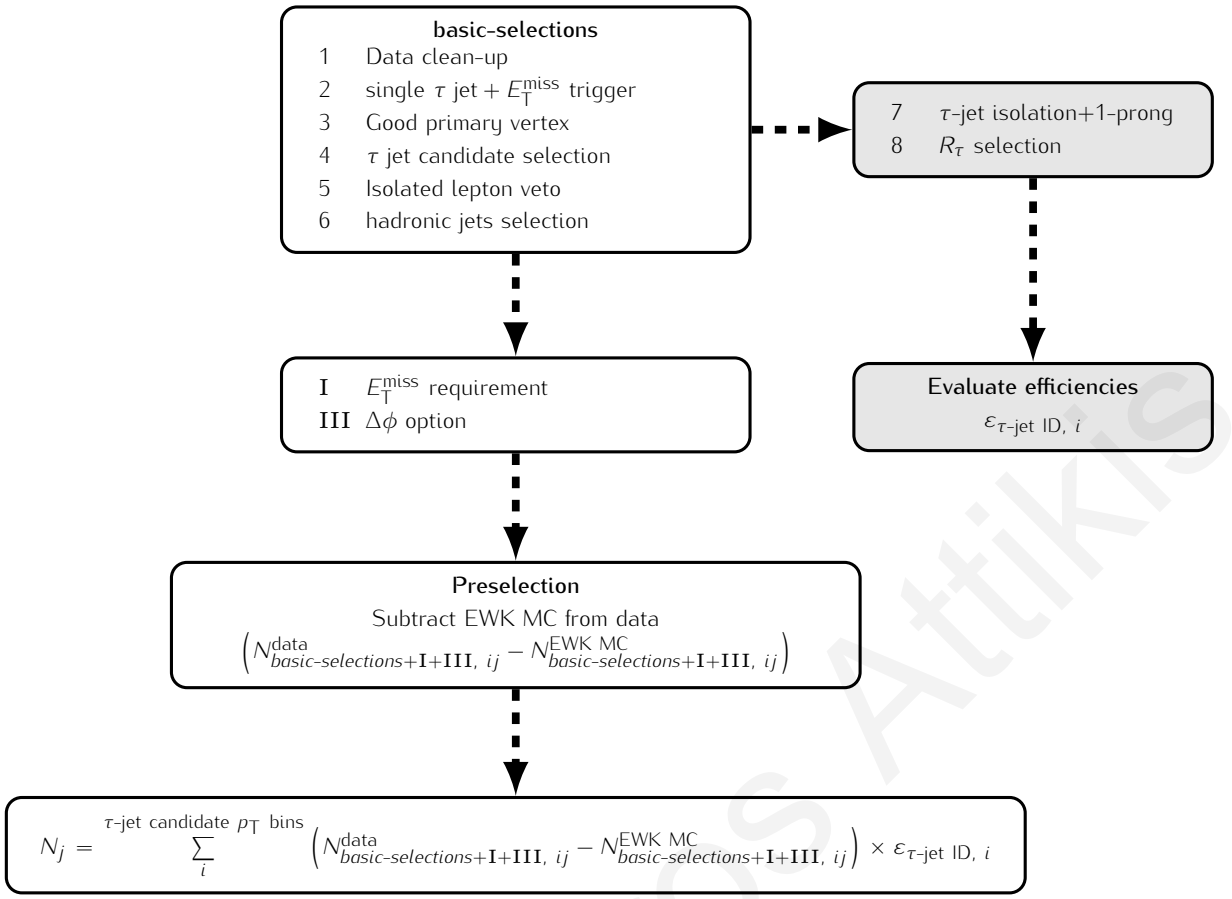

Figure 4.40: Schematic overview of the QCD multi-jet transverse mass shape extraction, using the *Purity-Corrected* method. The selections 7+8, shown in the shaded block, were factorised out of the cut-flow after the *basic-selections* $1-6$. The b-tagging selection was shown to have a negligible effect on the transverse mass shapes and was consequently omitted. The individual selections are described in detail in Section 4.5.

Method results and uncertainties The transverse mass shapes obtained with the *Purity-Corrected* method, for the individual τ-jet candidate p_T bins and for all 3 $\Delta\phi$ options are shown in Figs. 4.42, 4.43, and 4.44 for the without $\Delta\phi$ cut option, Figs. 4.45, 4.46, and 4.47 for the $\Delta\phi < 160°$ option, and Figs. 4.48, 4.49, and 4.50 for the $\Delta\phi < 130°$ option. The absolute uncertainty for the extracted QCD multi-jet transverse mass shape was estimated by applying error propagation to Eq. (4.51)

$$\Delta^2_{N_j} = \sum_i^{\tau\text{-jet candidate } p_T \text{ bins}} \Big[\left(\Delta^2_{N^{data}_{basic\text{-}selections+I+III,\, ij}} + \Delta^2_{N^{EWK\ MC}_{basic\text{-}selections+I+III,\, ij}} \right) \times \varepsilon_{\tau\text{-jet ID},\, i} + \Delta^2_{\varepsilon_{\tau\text{-jet ID},\, i}} \times \left(N^{data}_{basic\text{-}selections+I+III,\, ij} - N^{EWK\ MC}_{basic\text{-}selections+I+III,\, ij} \right) \Big], \tag{4.52}$$

where

$$\Delta_{N^{data}_{basic\text{-}selections+I+III,\, ij}} = \sqrt{N^{data}_{basic\text{-}selections+I+III,\, ij}} \tag{4.53}$$

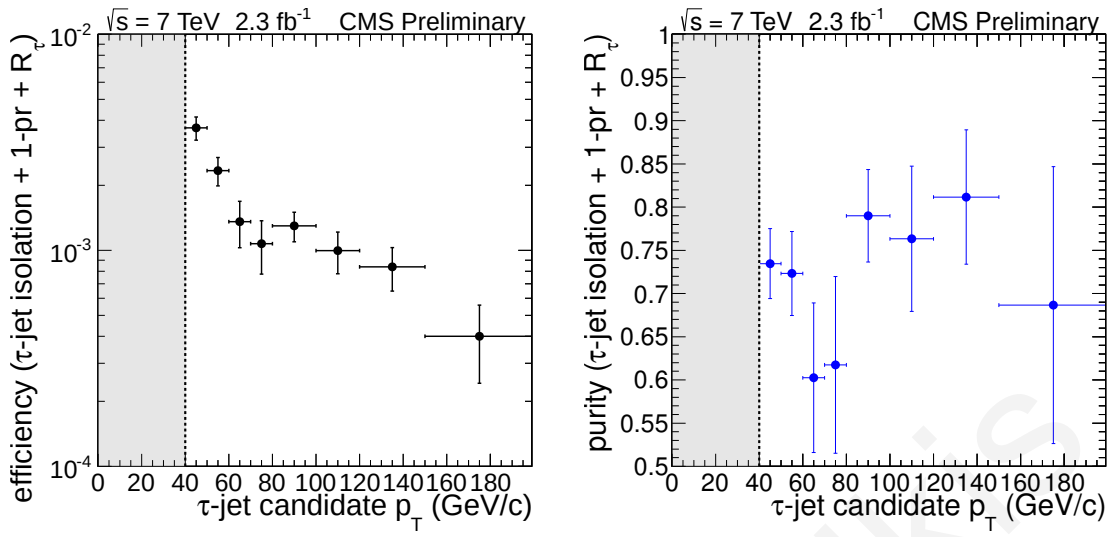

Figure 4.41: Efficiency (a) and QCD multi-jetpurity (b) of τ-jet identification in p_T bins of τ jet candidates ($\varepsilon_{\tau\text{-jet ID},\ i}$), as measured from data. The last τ-jet candidate p_T bin corresponds to $p_T > 150\,\text{GeV}/c$.

is the Poissonian uncertainty of the number of data events associated with τ-jet candidate p_T bin i and transverse mass bin j. With Eq. (4.46), the total uncertainty introduced by the reliance on EWK MC events is given by

$$\begin{aligned}\Delta^2_{N^{\text{EWK MC}}_{\text{basic-selections+I+III},\ ij}} &= \Delta^2_{\text{MC Stat.},\ ij} + \Delta^2_{\text{MC Syst.},\ ij} \\ &= \sum_{k}^{\text{EWK MC samples}} \left[\left(w_k \sqrt{N^{\text{EWK MC GEN}}_{\text{basic-selections+I+III},\ ij}} \right)^2 + \left(0.2 N^{\text{EWK MC GEN}}_{\text{basic-selections+I+III},\ ij} \right)^2 \right]\end{aligned} \tag{4.54}$$

whereas with Eq. (4.47) the absolute uncertainty of the term $\varepsilon_{\tau\text{-jet ID},\ i}$ can be expressed as

$$\begin{aligned}\Delta^2_{\varepsilon_{\tau\text{-jet ID},\ i}} = \frac{1}{\left(N^{\text{data}}_{\text{basic-selections},\ i} - N^{\text{EWK MC}}_{\text{basic-selections},\ i} \right)^2} \Bigg[& N^{\text{data}}_{\text{basic-selections+7+8},\ i} \\ & + \sum_{k}^{\text{EWK MC samples}} \left[\left(w_k \sqrt{N^{\text{EWK MC GEN}}_{\text{basic-selections +6+7},\ ik}} \right)^2 \right. \\ & \left. + \left(0.2 N^{\text{EWK MC}}_{\text{basic-selections +6+7},\ ik} \right)^2 \right] \Bigg]\end{aligned} \tag{4.55}$$

A breakdown of the absolute statistical uncertainty originating from data (a) and EWK MC (b) are presented in Fig. 4.51, for the individual transverse mass bins. One can easily notice the common feature appearing over most τ-jet candidate p_T bins, whereby the bulk of the statistics lie in two p_T bins, providing a two-bump structure for all transverse mass shapes. The first bump is related to the first bin, while the second bump, which was first described in Section 4.5.8, primarily originates from mis-measured back-to-back jets, and appears to shift to higher transverse mass values with increasing τ-jet candidate p_T. The origin of this shift is understood to be caused by the extension of the phase-space available due to the more energetic τ jet candidates, allowing the reach of higher values of the transverse mass

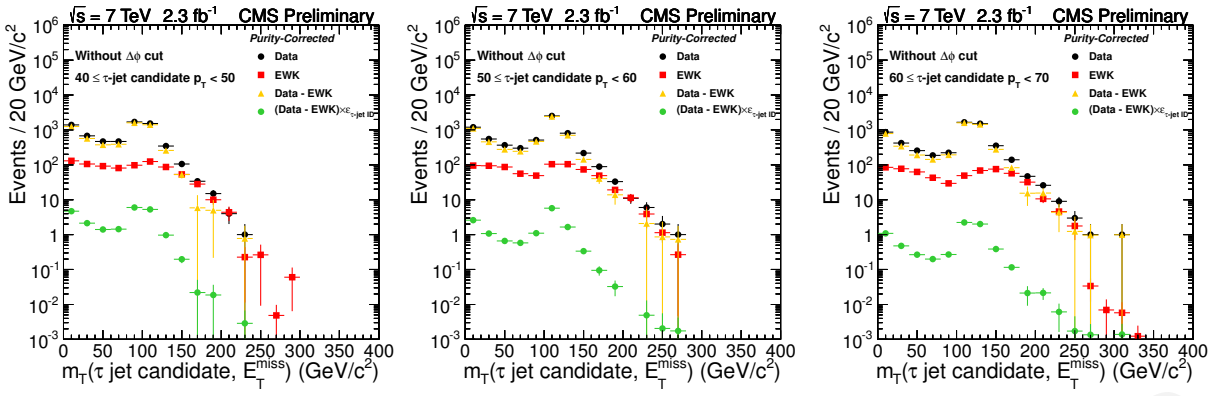

Figure 4.42: Transverse mass distributions after *basic-selections*+I+III for the τ-jet candidate p_T bin range $40-50\,\text{GeV}/c$ (a), $50-60\,\text{GeV}/c$ (b) and $60-70\,\text{GeV}/c$ (c) as extracted with the *Purity-Corrected* method and without the $\Delta\phi$ option.

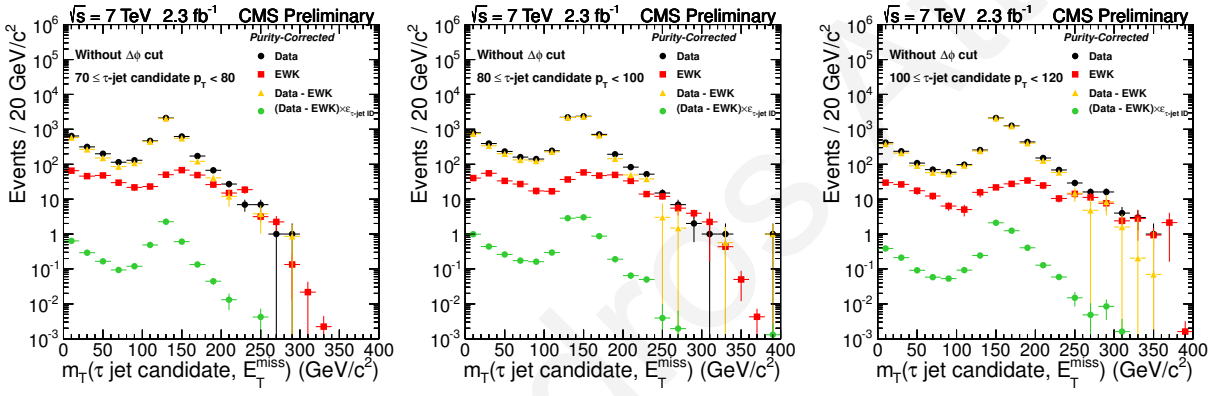

Figure 4.43: Transverse mass distributions after *basic-selections*+I+III for the τ-jet candidate p_T bin range $70-80\,\text{GeV}/c$ (a), $80-100\,\text{GeV}/c$ (b) and $100-120\,\text{GeV}/c$ (c), as extracted with the *Purity-Corrected* method and without the $\Delta\phi$ option.

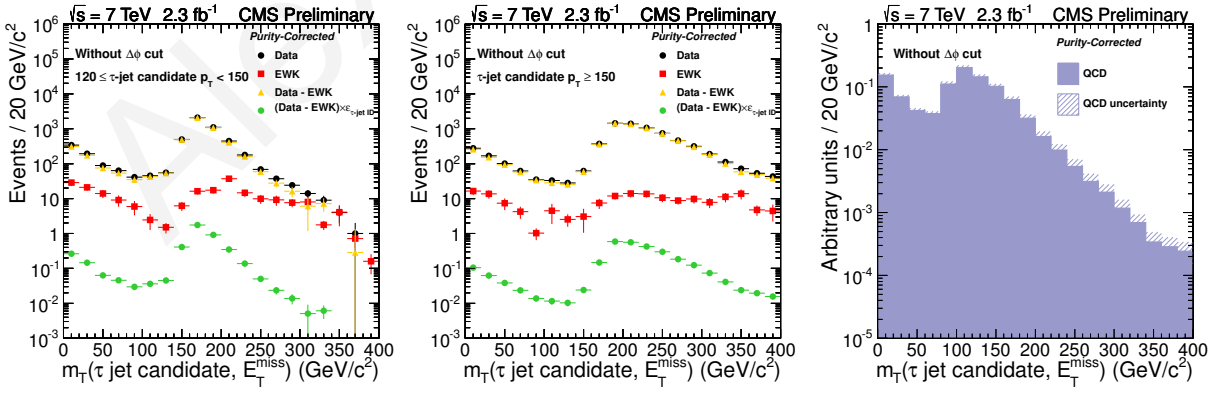

Figure 4.44: Transverse mass distributions after *basic-selections*+I+III for the τ-jet candidate p_T bin range $120-150\,\text{GeV}/c$ (a) and $>150\,\text{GeV}/c$ (b), as extracted with the *Purity-Corrected* method and without the $\Delta\phi$ option. The QCD multi-jet transverse mass shape derived using Eq. (4.51) and normalised to unit area is also shown (c).

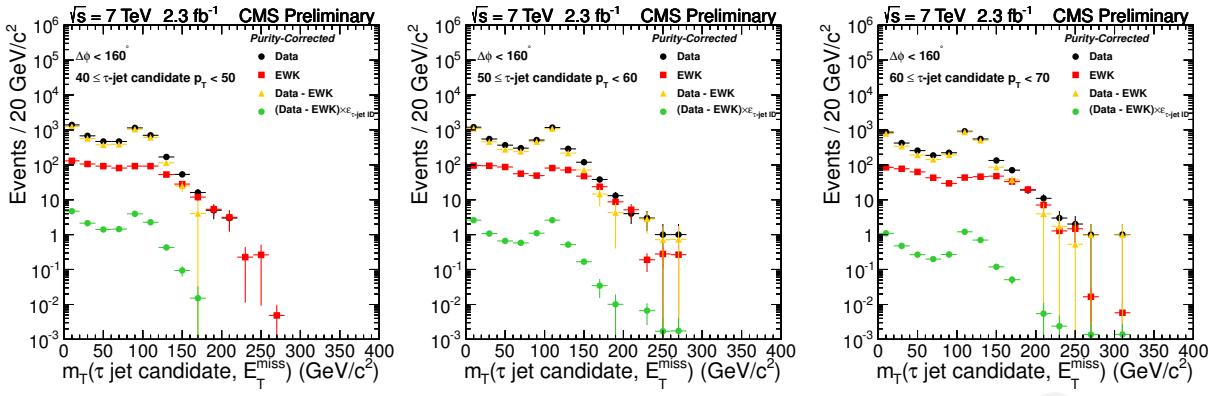

Figure 4.45: Transverse mass distributions after *basic-selections*+I+III for the τ-jet candidate p_T bin range $40-50\,\text{GeV}/c$ (a), $50-60\,\text{GeV}/c$ (b) and $60-70\,\text{GeV}/c$ (c) as extracted with the *Purity-Corrected* method for the $\Delta\phi < 160°$ option.

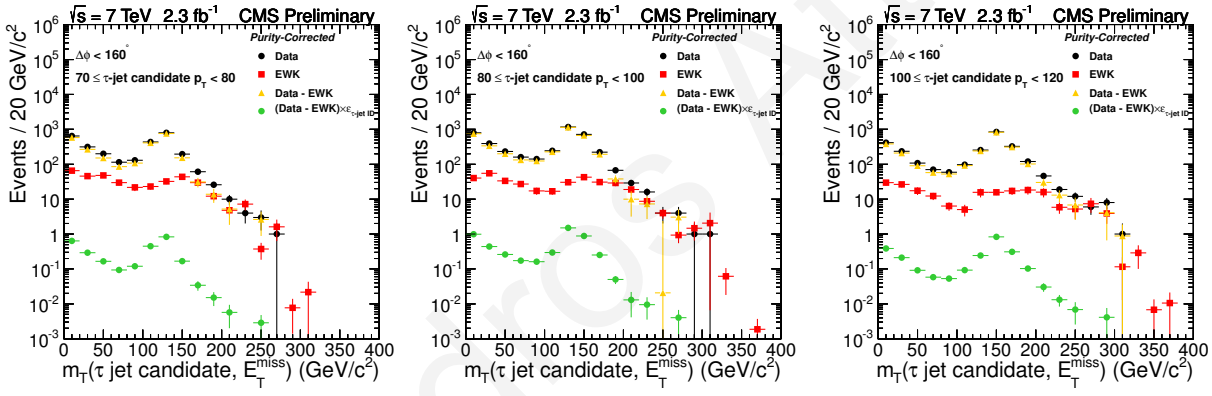

Figure 4.46: Transverse mass distributions after *basic-selections*+I+III for the τ-jet candidate p_T bin range $70-80\,\text{GeV}/c$ (a), $80-100\,\text{GeV}/c$ (b) and $100-120\,\text{GeV}/c$ (c), as extracted with the *Purity-Corrected* method and for the $\Delta\phi < 160°$ option.

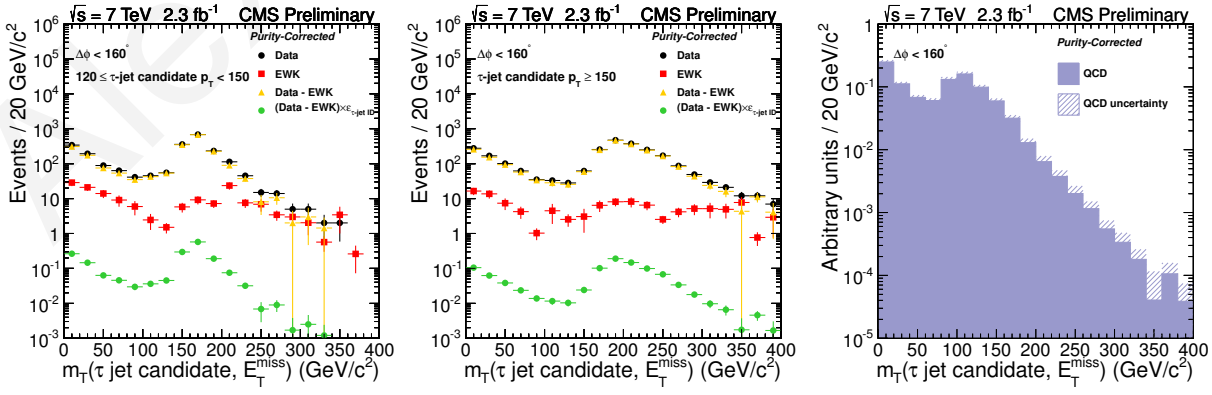

Figure 4.47: Transverse mass distributions after *basic-selections*+I+III for the τ-jet candidate p_T bin range $120-150\,\text{GeV}/c$ (a) and $> 150\,\text{GeV}/c$ (b), as extracted with the *Purity-Corrected* method and for the $\Delta\phi < 160°$ option. The QCD multi-jet transverse mass shape derived using Eq. (4.51) and normalised to unit area is also shown (c).

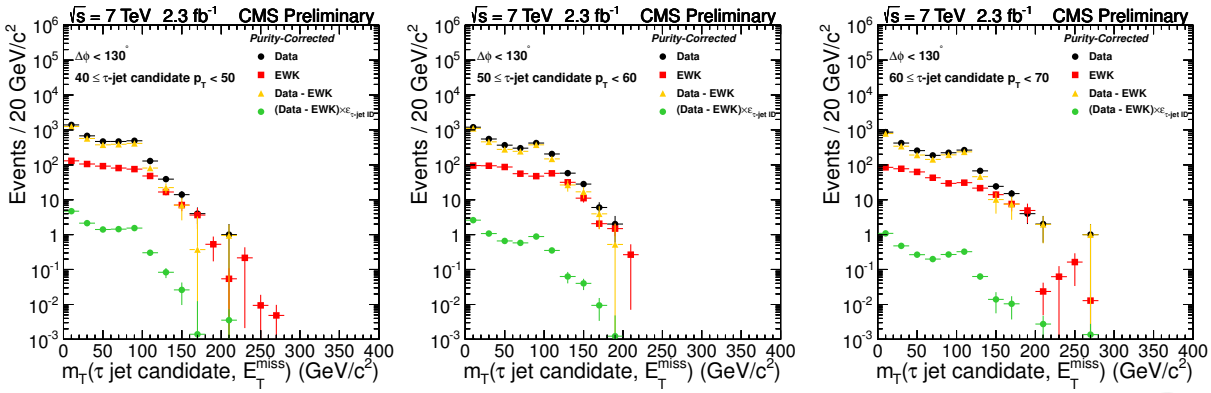

Figure 4.48: Transverse mass distributions after *basic-selections*+I+III for the τ-jet candidate p_T bin range $40-50\,\text{GeV}/c$ (a), $50-60\,\text{GeV}/c$ (b) and $60-70\,\text{GeV}/c$ (c) as extracted with the *Purity-Corrected* method for the $\Delta\phi < 130°$ option.

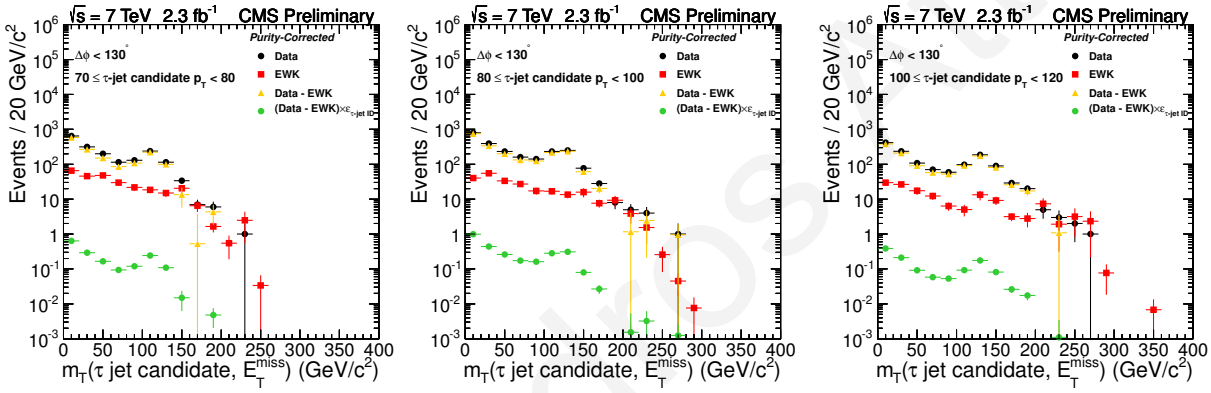

Figure 4.49: Transverse mass distributions after *basic-selections*+I+III for the τ-jet candidate p_T bin range $70-80\,\text{GeV}/c$ (a), $80-100\,\text{GeV}/c$ (b) and $100-120\,\text{GeV}/c$ (c), as extracted with the *Purity-Corrected* method and for the $\Delta\phi < 130°$ option.

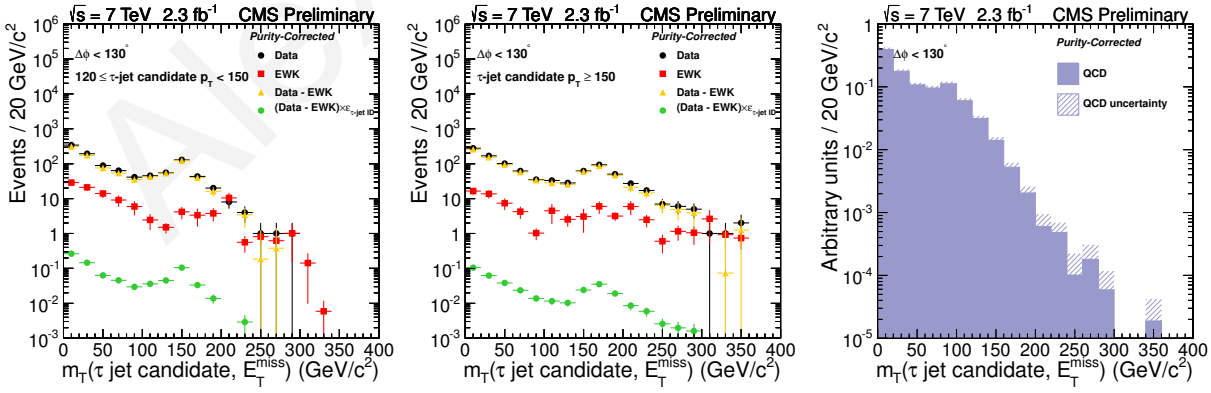

Figure 4.50: Transverse mass distributions after *basic-selections*+I+III for the τ-jet candidate p_T bin range $120-150\,\text{GeV}/c$ (a) and $> 150\,\text{GeV}/c$ (b), as extracted with the *Purity-Corrected* method and for the $\Delta\phi < 130°$ option. The QCD multi-jet transverse mass shape derived using Eq. (4.51) and normalised to unit area is also shown (c).

(Eq. (4.25) on page 152). In Fig. 4.51 (c) the absolute systematic uncertainties arising from the reliance on EWK MC are also presented. Another prominent feature is the fact that the dominant source of uncertainty in extracting the QCD multi-jet transverse mass shape is the statistical uncertainty of the data sample in the first two τ-jet candidate p_{T} bins; $40-50$ and $50-60\,\mathrm{GeV}/c$.

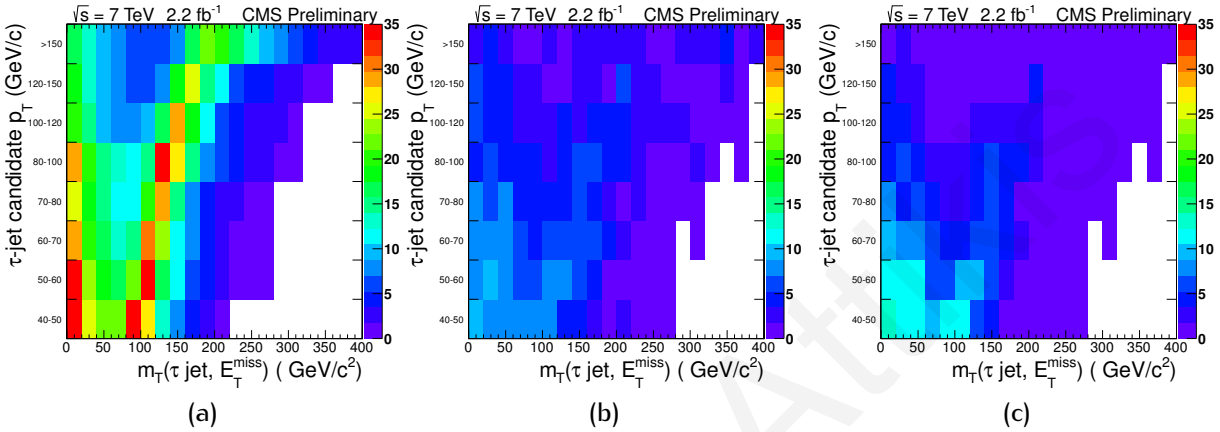

Figure 4.51: Analytic breakdown of the absolute statistical uncertainty from data (a) and EWK MC (b), for the individual bins of the QCD multi-jet transverse mass shape, as extracted with the *Purity-Corrected* method. The analogous absolute systematic uncertainties for the EWK MC are also shown (c).

***Anti-Isolation* method** A schematic overview of the QCD multi-jet transverse mass shape extraction through the *Anti-Isolation* method can be seen in Fig. 4.52. The concept of the *Anti-Isolation* method is almost identical to that of the *Purity-Corrected* method, with the exception that the transverse mass is reconstructed with anti-isolated τ jet candidates; τ jet candidates that fail the isolation requirement. The selection of anti-isolated τ jet candidates enhances somewhat the QCD multi-jet purity of the data sample when compared to the case where this selection is not applied, as shown in Fig. 4.53, which diminishes the need to rely on simulated samples to correct for EWK contamination in the extracted transverse mass shapes. In this method, the QCD multi-jetpurity of the data sample, ranged from $\sim 86\%-92\%$ for the hardest of the 3 $\Delta\phi$ options with $\Delta\phi < 130^{\circ}$, while for the softest of the 3 options, whereby no $\Delta\phi$ cut was applied, the purity ranged from $\sim 89\%-97\%$. The level of QCD multi-jetpurity of the control sample is much more important in the *Anti-Isolation* method than the *Purity-Corrected* method, due to the fact that no MC information is used to correct for the contamination of the data sample from EWK events. Therefore, the presence of such events can bias the transverse mass shapes extracted from the control sample, leading to systematic effects and to minimise these effects the QCD multi-jetpurity must be as high as possible.

In this method, the expression for the total number of events in bin j of the QCD multi-jet

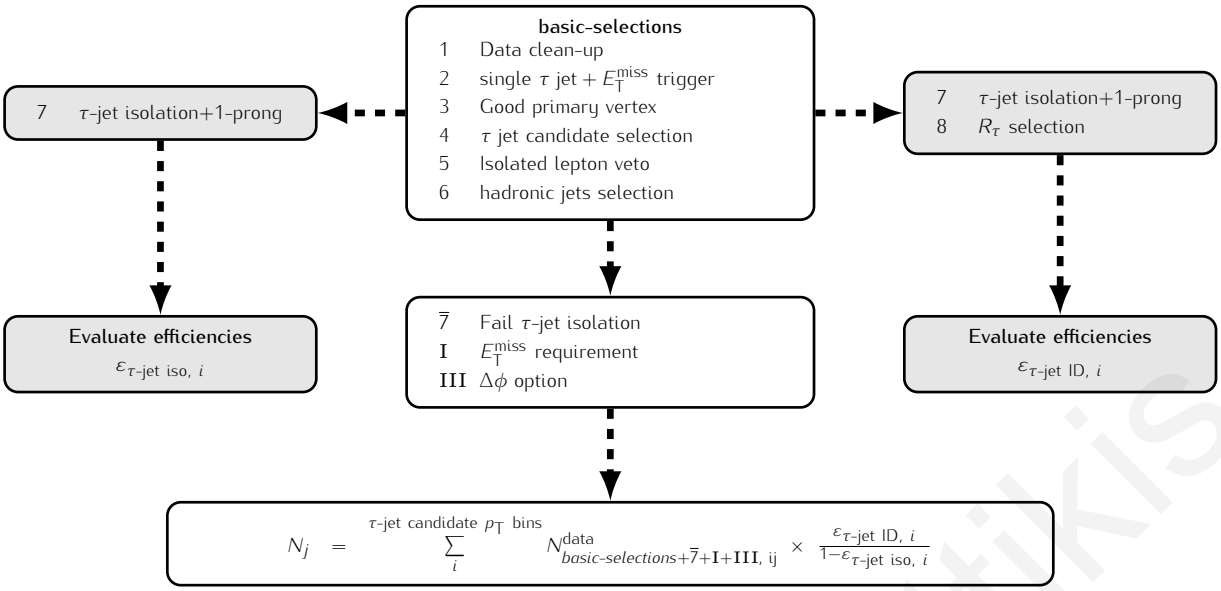

Figure 4.52: Schematic overview of the QCD multi-jet transverse mass shape extraction, using the *Purity-Corrected* method. The selections 7+8, shown in the shaded block, were factorised out of the cut-flow after the *basic-selections* 1 – 6. The b-tagging selection was shown to have a negligible effect on the transverse mass shapes and was consequently omitted. The individual selections are described in detail in Section 4.5.

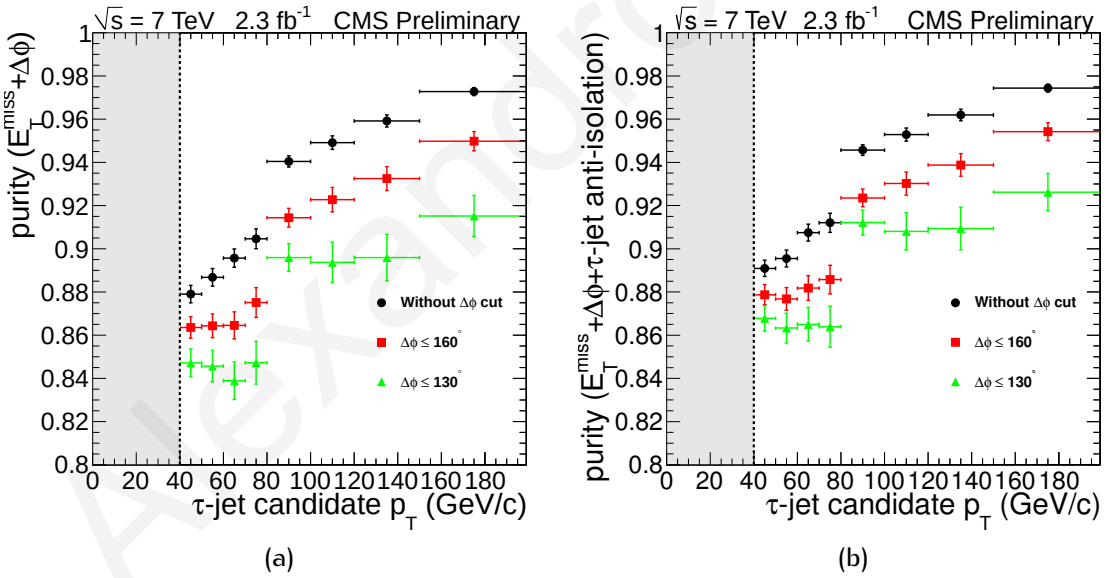

Figure 4.53: QCD multi-jetpurity after *basic-selections*, E_T^{miss} and $\Delta\phi$ cut (*basic-selections*+I+III) (a) and after *basic-selections*, anti-isolation, E_T^{miss}, and $\Delta\phi$ cuts (*basic-selections*+$\bar{7}$+I+III) (b) in p_T bins of τ jet candidates (b). The last τ-jet candidate p_T bin corresponds to $p_T > 150\,\text{GeV}/c$.

transverse mass becomes

$$N_j = \sum_i^{\tau\text{-jet candidate } p_T \text{ bins}} N^{data}_{basic\text{-}selections+\bar{7}+I+III,\ ij} \times \frac{\varepsilon_{\tau\text{-jet ID, } i}}{1-\varepsilon_{\tau\text{-jet iso, } i}} \tag{4.56}$$

for the τ-jet candidate p_T bin i, where the factor $\varepsilon_{\tau\text{-jet iso, } i}$ in the denominator describes the

efficiency of passing the τ-jet isolation requirement, defined as

$$\varepsilon_{\tau\text{-jet iso},\ i} = \frac{N^{\text{data}}_{\textit{basic-selections+7},\ i} - N^{\text{EWK MC}}_{\textit{basic-selections+7},\ i}}{N^{\text{data}}_{\textit{basic-selections},\ i} - N^{\text{EWK MC}}_{\textit{basic-selections},\ i}} \tag{4.57}$$

and is required to reverse the anti-isolation selection. In this way, the QCD multi-jet transverse mass distribution with the *Anti-Isolation* methods is obtained by adding together the individual transverse mass shapes obtained in p_{T} bins of anti-isolated τ jet candidates, each weighted with the factor of $\varepsilon_{\tau\text{-jet ID},\ i}$ to account for factorising the τ-jet identification step, and the factor $\left(1 - \varepsilon_{\tau\text{-jet iso},\ i}\right)^{-1}$ to account for the use of anti-isolated τ jet candidates. In a similar fashion to the *Purity-Corrected* methods, the final step in extracting the QCD multi-jet transverse mass shape was to normalise the area of this distribution to the QCD multi-jet background estimate event yield, N^{QCD}, as determined from Eq. (4.37).

Method results and uncertainties The transverse mass shapes obtained with the *Anti-Isolation* method, for the individual τ-jet candidate p_{T} bins and for all 3 $\Delta\phi$ options are shown in Figs. 4.54, 4.55, and 4.56 for the without $\Delta\phi$ cut option, Figs. 4.57, 4.58, and 4.59 for the $\Delta\phi < 160°$ option, and Figs. 4.60, 4.61, and 4.62 for the $\Delta\phi < 130°$ option. Unlike the *Purity-Corrected* method, the uncertainty in the *Anti-Isolation* extracted shapes has smaller contributions from the reliance on MC information. To avoid correlation complications between the terms $\varepsilon_{\tau\text{-jet iso},\ i}$ and $\varepsilon_{\tau\text{-jet ID},\ i}$, the latter term can be re-expressed as

$$\begin{aligned} \varepsilon_{\tau\text{-jet ID},\ i} &= \varepsilon_{\tau\text{-jet iso},\ i} \times \varepsilon_{R_\tau,\ i} \\ &= \frac{N^{\text{data}}_{\textit{basic-selections+7+8},\ i} - N^{\text{EWK MC}}_{\textit{basic-selections+7+8},\ i}}{N^{\text{data}}_{\textit{basic-selections},\ i} - N^{\text{EWK MC}}_{\textit{basic-selections},\ i}} \end{aligned} \tag{4.58}$$

with

$$\varepsilon_{R_\tau,\ i} = \frac{N^{\text{data}}_{\textit{basic-selections+7+8},\ i} - N^{\text{EWK MC}}_{\textit{basic-selections+7+8},\ i}}{N^{\text{data}}_{\textit{basic-selections+7},\ i} - N^{\text{EWK MC}}_{\textit{basic-selections+7},\ i}} \tag{4.59}$$

and

$$\varepsilon_{\tau\text{-jet iso},\ i} = \frac{N^{\text{data}}_{\textit{basic-selections+7},\ i} - N^{\text{EWK MC}}_{\textit{basic-selections+7},\ i}}{N^{\text{data}}_{\textit{basic-selections},\ i} - N^{\text{EWK MC}}_{\textit{basic-selections},\ i}} \tag{4.60}$$

The $\varepsilon_{\tau\text{-jet iso},\ i}$ and $\varepsilon_{R_\tau,\ i}$ efficiencies as a function of τ jet candidate p_{T} are shown in Figures 4.41 and 4.63, respectively, accompanied by the corresponding QCD multi-jetpurity plots.

Then, Eq. (4.56) can be re-written as

$$N_j = \sum_{i}^{\tau\text{-jet candidate } p_{\text{T}} \text{ bins}} N^{\text{data}}_{\textit{basic-selections+}\overline{7}\textit{+I+III},\ \text{ij}} \times \frac{\varepsilon_{\tau\text{-jet iso},\ i} \times \varepsilon_{R_\tau,\ i}}{1 - \varepsilon_{\tau\text{-jet iso},\ i}} \tag{4.61}$$

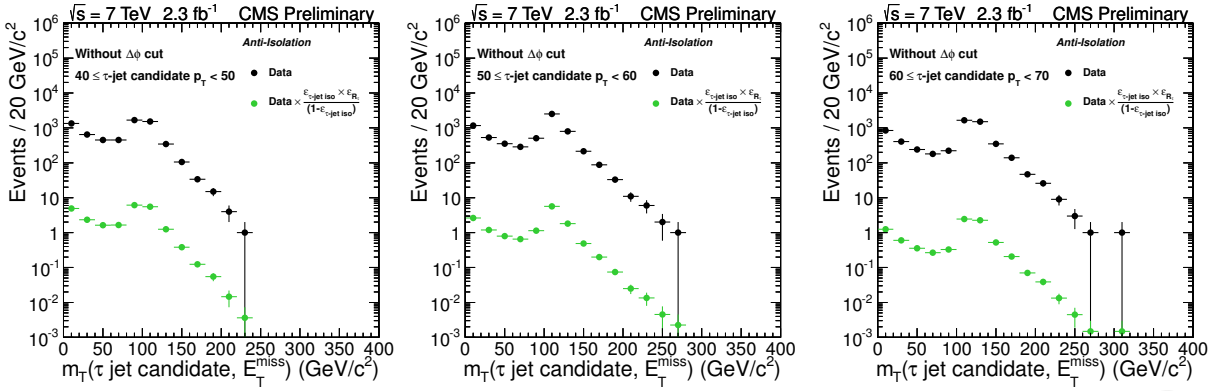

Figure 4.54: Transverse mass distributions after *basic-selections*+$\bar{7}$+I+III for the τ-jet candidate p_T bin range $40-50\,\text{GeV}/c$ (a), $50-60\,\text{GeV}/c$ (b) and $60-70\,\text{GeV}/c$ (c) as extracted with the *Anti-Isolation* method and without the $\Delta\phi$ option.

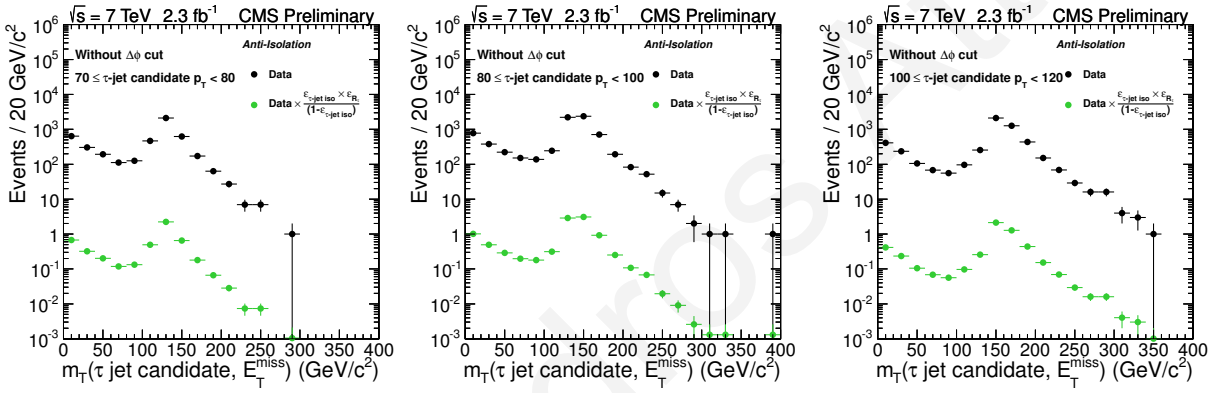

Figure 4.55: Transverse mass distributions after *basic-selections*+$\bar{7}$+I+III for the τ-jet candidate p_T bin range $70-80\,\text{GeV}/c$ (a), $80-100\,\text{GeV}/c$ (b) and $100-120\,\text{GeV}/c$ (c), as extracted with the *Anti-Isolation* method and without the $\Delta\phi$ option.

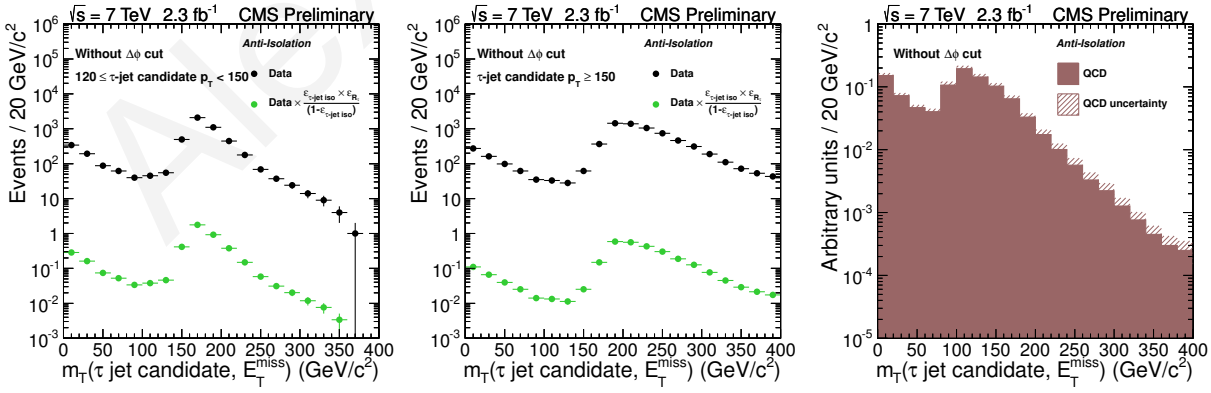

Figure 4.56: Transverse mass distributions after *basic-selections*+$\bar{7}$+I+III for the τ-jet candidate p_T bin range $120-150\,\text{GeV}/c$ (a) and $>150\,\text{GeV}/c$ (b), as extracted with the *Anti-Isolation* method and without the $\Delta\phi$ option. The QCD multi-jet transverse mass shape derived using Eq. (4.56) and normalised to unit area is also shown (c).

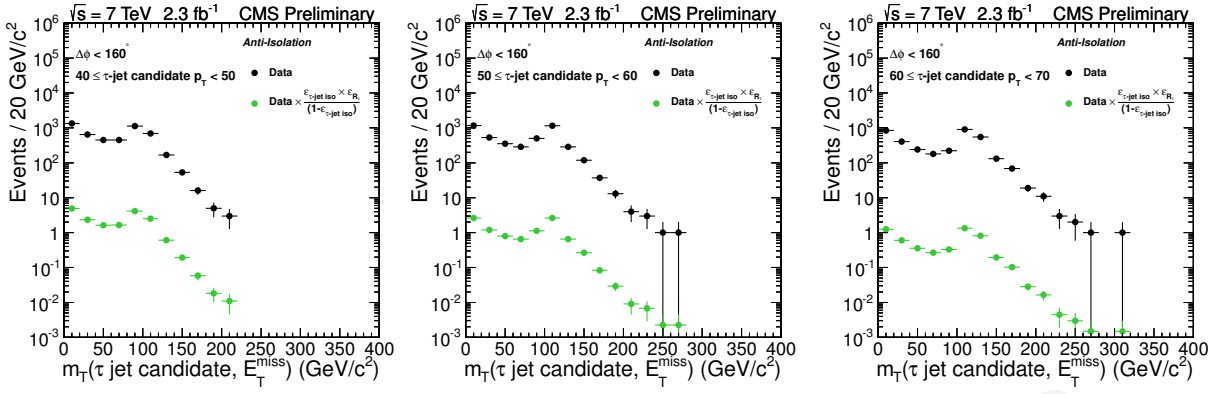

Figure 4.57: Transverse mass distributions after *basic-selections*+$\bar{7}$+I+III for the τ-jet candidate p_T bin range $40-50\,\text{GeV}/c$ (a), $50-60\,\text{GeV}/c$ (b) and $60-70\,\text{GeV}/c$ (c) as extracted with the *Anti-Isolation* method for the $\Delta\phi < 160°$ option.

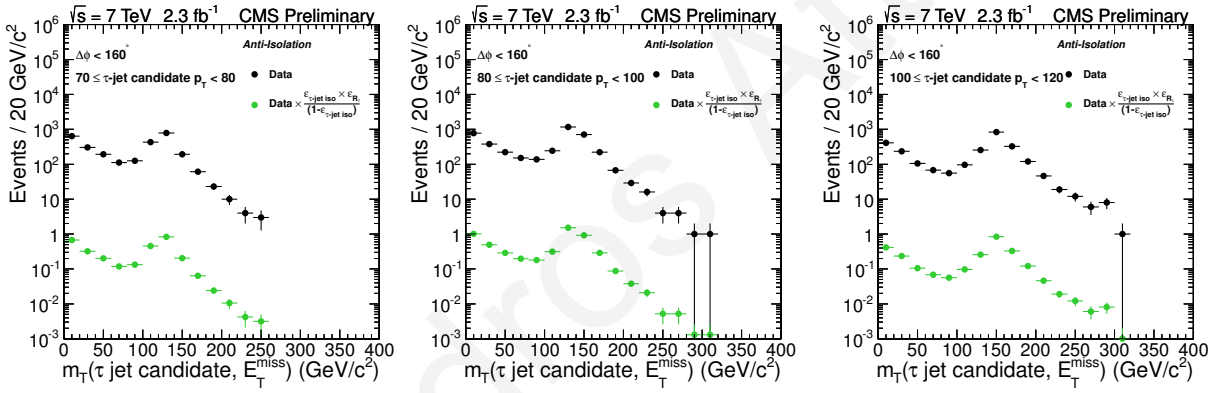

Figure 4.58: Transverse mass distributions after *basic-selections*+$\bar{7}$+I+III for the τ-jet candidate p_T bin range $70-80\,\text{GeV}/c$ (a), $80-100\,\text{GeV}/c$ (b) and $100-120\,\text{GeV}/c$ (c), as extracted with the *Anti-Isolation* method and for the $\Delta\phi < 160°$ option.

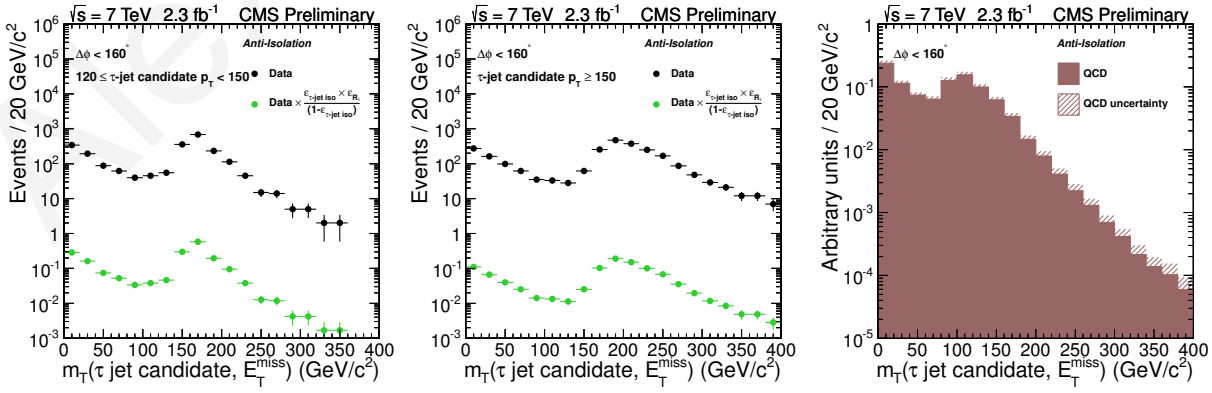

Figure 4.59: Transverse mass distributions after *basic-selections*+$\bar{7}$+I+III for the τ-jet candidate p_T bin range $120-150\,\text{GeV}/c$ (a) and $> 150\,\text{GeV}/c$ (b), as extracted with the *Anti-Isolation* method and for the $\Delta\phi < 160°$ option. The QCD multi-jet transverse mass shape derived using Eq. (4.56) and normalised to unit area is also shown (c).

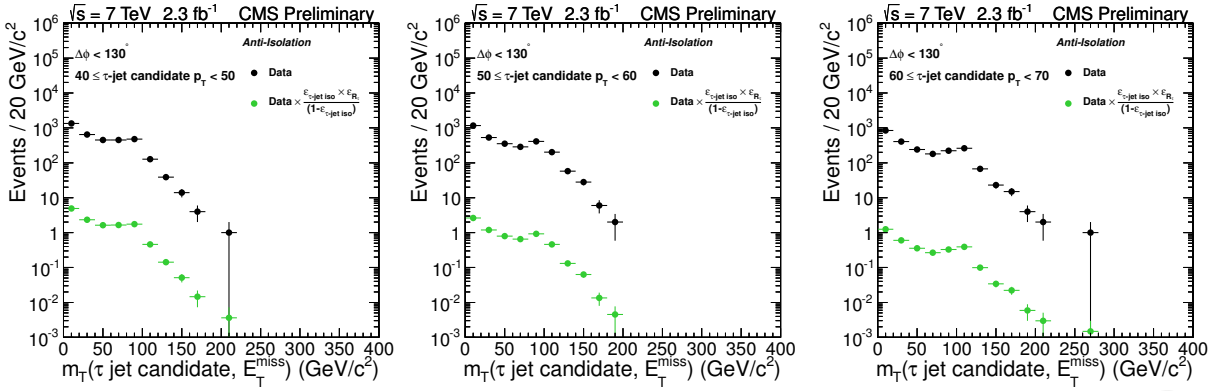

Figure 4.60: Transverse mass distributions after *basic-selections*+$\bar{7}$+I+III for the τ-jet candidate p_T bin range $40-50\,\text{GeV}/c$ (a), $50-60\,\text{GeV}/c$ (b) and $60-70\,\text{GeV}/c$ (c) as extracted with the *Anti-Isolation* method for the $\Delta\phi < 130°$ option.

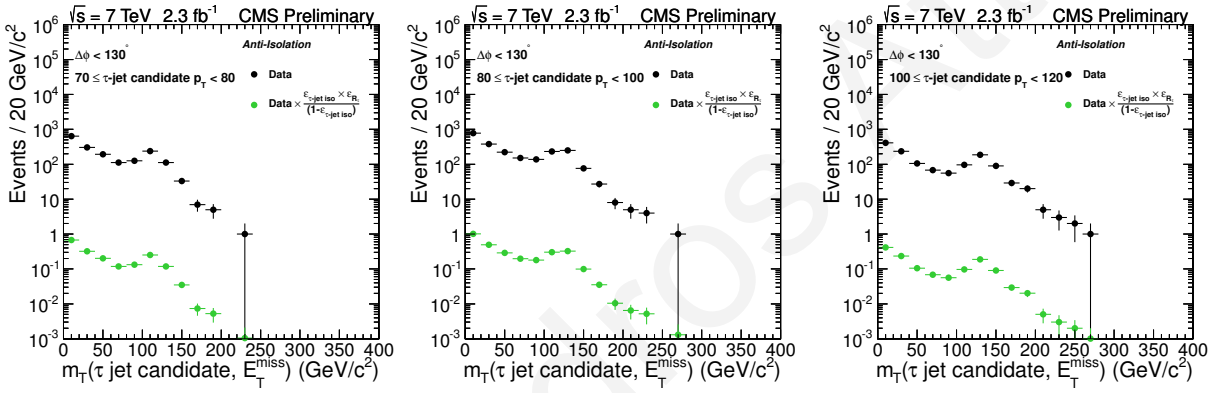

Figure 4.61: Transverse mass distributions after *basic-selections*+$\bar{7}$+I+III for the τ-jet candidate p_T bin range $70-80\,\text{GeV}/c$ (a), $80-100\,\text{GeV}/c$ (b) and $100-120\,\text{GeV}/c$ (c), as extracted with the *Anti-Isolation* method and for the $\Delta\phi < 130°$ option.

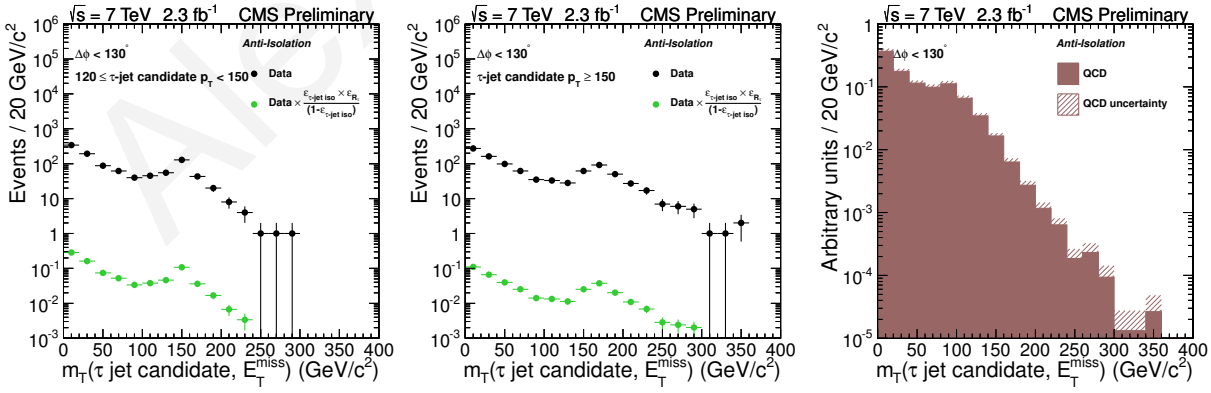

Figure 4.62: Transverse mass distributions after *basic-selections*+$\bar{7}$+I+III for the τ-jet candidate p_T bin range $120-150\,\text{GeV}/c$ (a) and $> 150\,\text{GeV}/c$ (b), as extracted with the *Anti-Isolation* method and for the $\Delta\phi < 130°$ option. The QCD multi-jet transverse mass shape derived using Eq. (4.56) and normalised to unit area is also shown (c).

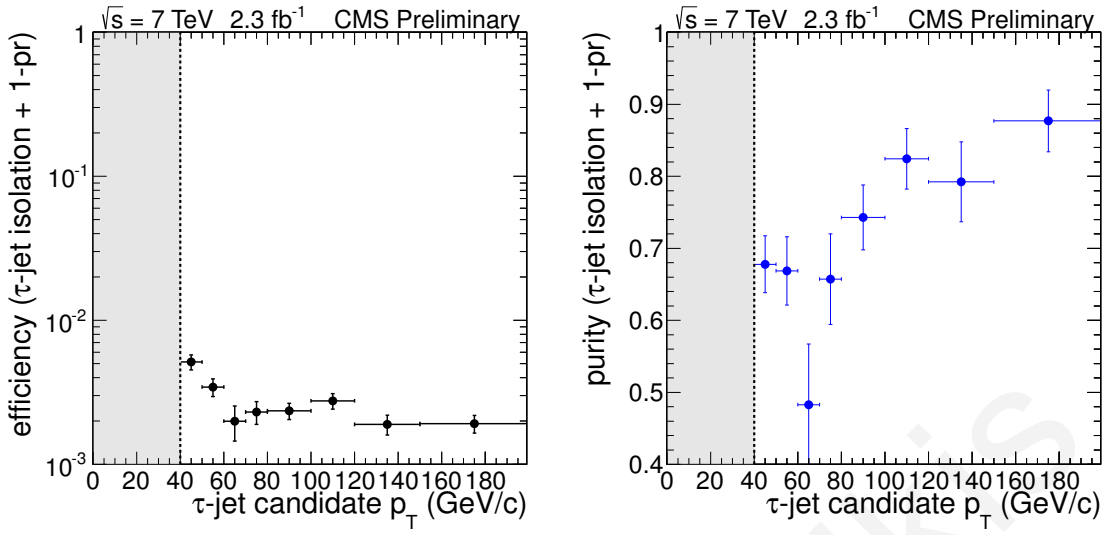

Figure 4.63: Efficiency of τ-jet isolation in p_T bins of τ jet candidates, $\varepsilon_{\tau\text{-jet iso, } i}$, as measured from data (a). QCD multi-jetpurity after *basic-selections* and τ-jet isolation cuts in p_T bins of τ jet candidates (b). The last τ-jet candidate p_T bin corresponds to $p_T > 150\,\text{GeV}/c$.

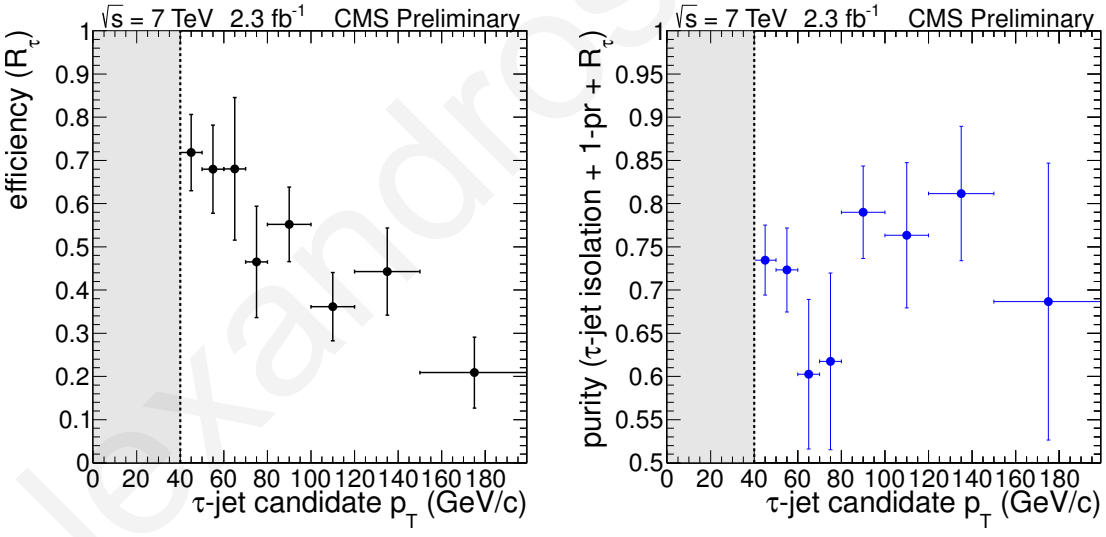

Figure 4.64: Efficiency (a) of and QCD multi-jetpurity (b) of the R_τ cut in p_T bins of τ jets, $\varepsilon_{R_\tau,\ i}$, as measured from data. The purity of the sample is exactly the same as in determination of the τ-jet identification in Fig. 4.41 but is also shown here for practical reasons.

and its associated absolute uncertainty is given by error propagation as

$$\Delta_{N_j} = \sum_{i}^{\tau\text{-jet candidate } p_T \text{ bins}} \left\{ N_j^2 \left[\frac{1}{N^{\text{data}}_{\textit{basic-selections}+\overline{7}+\text{I}+\text{III, ij}}} + \left(\frac{\Delta_{\varepsilon_{\tau\text{-jet iso, } i}}}{\varepsilon_{\tau\text{-jet iso, } i}\left(1-\varepsilon_{\tau\text{-jet iso, } i}\right)} \right)^2 \right] + \left(\frac{\Delta^2_{\varepsilon_{R_\tau,\ i}}}{\varepsilon_{R_\tau,\ i}} \right)^2 \right\}, \tag{4.62}$$

where the uncertainty associated with the efficiency term $\varepsilon_{R_\tau,\ i}$ is given by Eq. (4.47) as

$$\Delta^2_{\varepsilon_{R_\tau,\ i}} = \frac{1}{\left(N^{\text{data}}_{\text{basic-selections+7},\ i} - N^{\text{EWK MC}}_{\text{basic-selections+7},\ i}\right)^2}\Bigg[N^{\text{data}}_{\text{basic-selections+7+8},\ i} + \sum_{k}^{\text{EWK MC samples}}\Bigg[\left(w_k\sqrt{N^{\text{EWK MC GEN}}_{\text{basic-selections +6+7},\ ik}}\right)^2 + \left(0.2N^{\text{EWK MC}}_{\text{basic-selections +6+7},\ ik}\right)^2\Bigg]\Bigg] \tag{4.63}$$

and similarly the uncertainty associated with the efficiency term $\varepsilon_{\tau\text{-jet iso},\ i}$ is given by Eq. (4.47) as

$$\Delta^2_{\varepsilon_{\tau\text{-jet iso},\ i}} = \frac{1}{\left(N^{\text{data}}_{\text{basic-selections},\ i} - N^{\text{EWK MC}}_{\text{basic-selections},\ i}\right)^2}\Bigg[N^{\text{data}}_{\text{basic-selections+7},\ i} + \sum_{k}^{\text{EWK MC samples}}\Bigg[\left(w_k\sqrt{N^{\text{EWK MC GEN}}_{\text{basic-selections +6},\ ik}}\right)^2 + \left(0.2N^{\text{EWK MC}}_{\text{basic-selections +6},\ ik}\right)^2\Bigg]\Bigg] \tag{4.64}$$

The QCD multi-jet transverse mass shapes, as extracted with the *Anti-Isolation* method, are compared to those extracted with the *Purity-Corrected* method without the $\Delta\phi$ cut, for $\Delta\phi < 160°$ and for $\Delta\phi < 130°$ in Fig. 4.65 (a), Fig. 4.65 (b), and Fig. 4.66, respectively. For all 3 $\Delta\phi\left(\tau\text{ jet candidate}, E_{\text{T}}^{\text{miss}}\right)$ options, good agreement is shown between the two methods, especially for the softest of the 3 $\Delta\phi\left(\tau\text{ jet candidate}, E_{\text{T}}^{\text{miss}}\right)$ options, which was anticipated due to the higher QCD multi-jetpurity of the control sample used for the *Anti-Isolation* method.

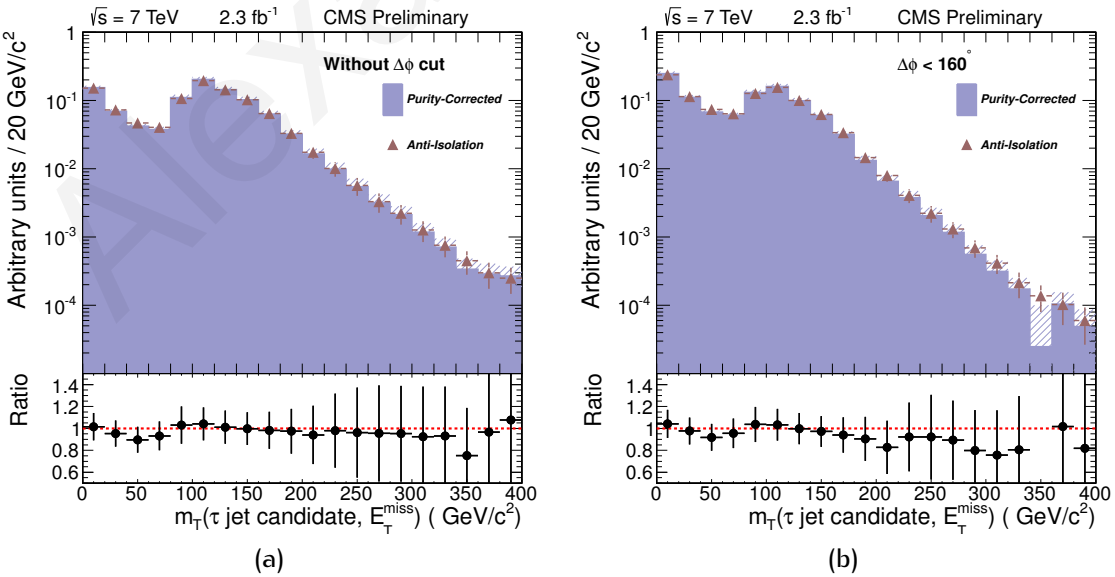

Figure 4.65: Comparison between the QCD multi-jet transverse mass shapes as extracted with the *Purity-Corrected* (filled area) and *Anti-Isolation* (triangle markers) methods, normalised to unit area, without the $\Delta\phi$ cut (a) and for $\Delta\phi < 160°$ (b).

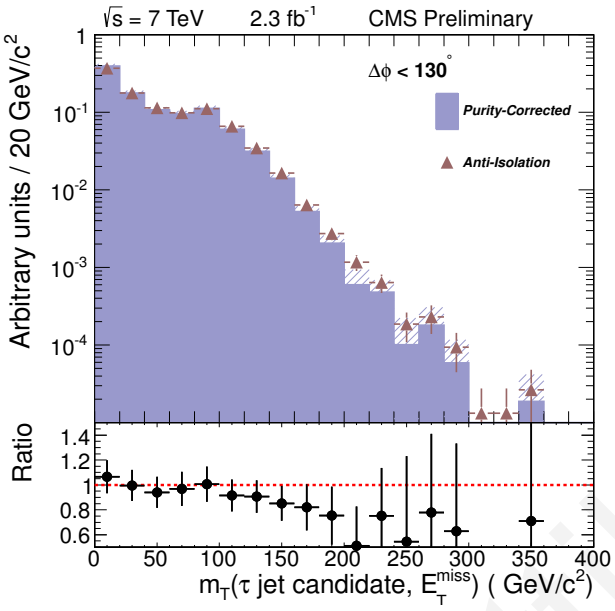

Figure 4.66: Comparison between the QCD multi-jet transverse mass shapes as extracted with the *Purity-Corrected* (filled area) and *Anti-Isolation* (triangle markers) methods, normalised to unit area, for $\Delta\phi < 130°$.

4.8.1.5 Stability of QCD multi-jet estimate under τ jet candidate p_T bin variation

In order to suppress the correlation between τ-jet identification and E_T^{miss}, the data sample was divided into slices of τ-jet candidate p_T. To understand why this was done, the consequence of not performing the measurement in τ-jet candidate p_T slices must be considered. If the τ-jet identification-E_T^{miss} correlation is not minimised, or ignored all-together, in obtaining an estimate for the expected QCD multi-jet event yield, it should result in the underestimation or overestimation of the event yield. Conversely, if the measurement is conducted by employing enough τ-jet candidate p_T slices, the τ-jet identification-E_T^{miss} correlation can be suppressed to a negligible level. In order to conclusively decide whether the employed τ-jet candidate p_T binning scheme is fine enough to suppress this correlation, one can re-evaluate the results using a finer binning scheme, and check whether the QCD multi-jet estimate changes. Provided the correlation is suppressed in both binning schemes under consideration, one expects to obtain the same QCD multi-jet estimate, whereas, in the case where the τ-jet identification-E_T^{miss} correlation persist, the results should differ.

Therefore, in order to assess the stability of the QCD multi-jet prediction (N^{QCD}), as evaluated with Eq. (4.37), an investigation was conducted to examine the impact of selecting a different τ-jet candidate p_T binning scheme. In particular, the effect of selecting a finer binning for the factorisation procedure was investigated, by sub-dividing each τ-jet candidate p_T bin of the default binning scheme into 2 bins, except for the overflow bin. Therefore, the whole QCD multi-jet prediction procedure was redone, with the chosen p_T bin-widths being 5 GeV/c up to 80 GeV/c, then 80 – 90 GeV/c, 90 – 100 GeV/c, 100 – 110 GeV/c, 110 – 120 GeV/c, 120 – 135 GeV/c, 135 – 150 GeV/c, and $>$ 150 GeV/c.

Using the aforementioned fine bin selection, the combined E_T^{miss}, b-tagging and $\Delta\phi$ effi-

ciencies $\varepsilon_{E_T^{miss}+b\text{-tag}+\Delta\phi,\ i}$ for all τ-jet candidate p_T bins were re-evaluated, using Eq. (4.40). These were in turn used to calculate a new QCD multi-jet prediction, according to Eq. (4.37). The results without the $\Delta\phi$ cut, for $\Delta\phi < 160°$ and for $\Delta\phi < 130°$ are shown in Fig. 4.67 (a), Fig. 4.67 (b), and Fig. 4.68, respectively.

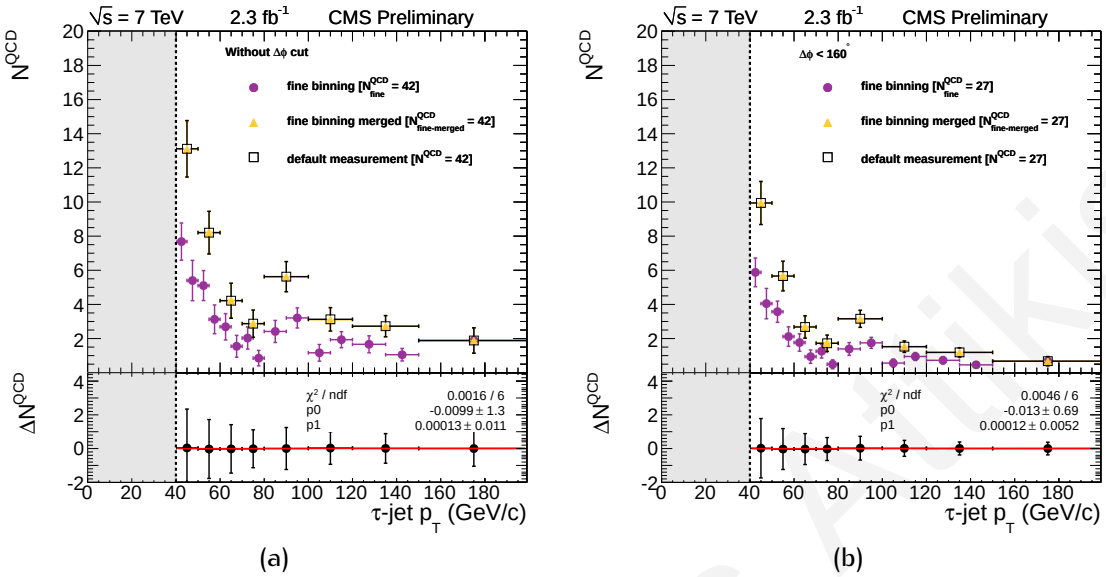

Figure 4.67: The total contribution from each τ-jet candidate p_T bin in the predicted number of QCD multi-jet events, without the $\Delta\phi$ cut (a) and for $\Delta\phi < 160°$ (b), using a finer binning scheme (N_{fine}^{QCD}). These results were consequently merged to the default binning scheme to get $N_{fine-merged}^{QCD}$, thus enabling a direct compariron with the default QCD multi-jet prediction, denoted as N^{QCD}. The combined systematic and statistical uncertainties are shown for both cases. The last τ-jet candidate p_T bin corresponds to $p_T > 150\,GeV/c$.

The results from the finer binning scheme, denoted N_{fine}^{QCD} were consequently merged to the default binning scheme, denoted $N_{fine-merged}^{QCD}$, in order to allow a direct comparison with the default results, denoted N^{QCD}. This was achieved by evaluating the difference of the two predictions, defined as

$$\Delta N^{QCD} = N^{QCD} - N_{fine-merged}^{QCD}. \tag{4.65}$$

A first-order polynomial was fitted through these results, showing that for all 3 $\Delta\phi$ options, the fitted polynomial is compatible with $\Delta N^{QCD} = 0$. In all cases, the resulting slope of the fitted polynomial is negligibly small and within error compatible with zero. The aforementioned results provide firm proof that the QCD multi-jet event yield N^{QCD}, is stable with respect to the choice of τ-jet candidate p_T bin selection to a remarkable extend, for all 3 $\Delta\phi\left(\tau \text{ jet candidate}, E_T^{miss}\right)$ options.

To conclude, the QCD multi-jet event yield N^{QCD} was re-evaluated user a finer binnining scheme, in order to test the stability of the measurement and to ensure that the τ-jet identification-E_T^{miss} correlation is adequately suppressed under the chosen binning scheme. The resulting test proved that the default τ-jet candidate p_T binning scheme is sufficient to reduce correlation to a negligible level.

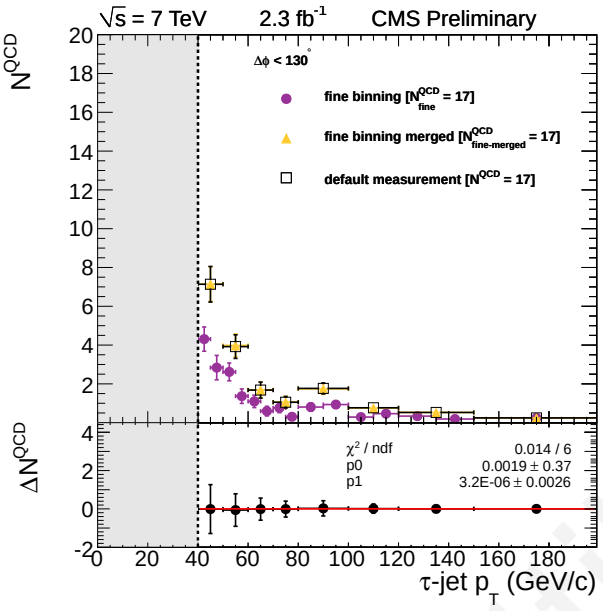

Figure 4.68: The total contribution from each τ-jet candidate p_{T} bin in the predicted number of QCD multi-jet events, for $\Delta\phi < 130°$, using a finer binning scheme ($N^{\mathrm{QCD}}_{\mathrm{fine}}$). These results were consequently merged to the default binning scheme to get $N^{\mathrm{QCD}}_{\mathrm{fine\text{-}merged}}$, thus enabling a direct compariron with the default QCD multi-jet prediction, denoted as N^{QCD}. The combined systematic and statistical uncertainties are shown for both cases. The last τ-jet candidate p_{T} bin corresponds to $p_{\mathrm{T}} > 150\,\mathrm{GeV}/c$.

4.8.1.6 Signal contamination investigation

An investigation was conducted to examine the implications that the presence of a signal in the data might have on the QCD multi-jet background estimate. From the definition of the QCD multi-jet background estimates N^{QCD} in Eq. (4.37), it is apparent that if a signal is present in the data the QCD multi-jet estimate can be affected through both the $\varepsilon_{E_{\mathrm{T}}^{\mathrm{miss}}+\text{b-tag}+\Delta\phi,\ i}$ and $N^{\mathrm{data}}_{\mathit{pre\text{-}selection}}$ terms. Moreover, since the QCD multi-jet transverse mass shapes extracted with both methods are normalised according to this N^{QCD} estimate, the possible signal contamination can have a two-pronged effect. Additionally, the transverse mass shapes could be susceptible to systematic effects in the presence of a signal in the data if the τ-jet identification efficiencies, $\varepsilon_{\tau\text{-jet ID}}$, defined in Eq. (4.49), are in-homogeneously affected within the τ-jet candidate p_{T} bins.

For this reason, all the relevant quantities were re-evaluated in the presence of a signal for all 3 $\Delta\phi\left(\tau\text{ jet candidate}, E_{\mathrm{T}}^{\mathrm{miss}}\right)$ options and for two H^{+} mass points; $80\,\mathrm{GeV}/c^2$ and $160\,\mathrm{GeV}/c^2$. The mass points were chosen to represent the best ($m_{H^{\pm}} = 80\,\mathrm{GeV}/c^2$) and worst ($m_{H^{\pm}} = 160\,\mathrm{GeV}/c^2$) case scenarios, since the event selection efficiency for the signal process is strongly mass dependent, as already shown in Figures 4.27 and 4.28. The branching ratio for the top quark decay to $H^{\pm}$ was taken to be $\mathrm{BR}(t \to bH^{\pm}) = 0.03$ for both relevant mass points. This number was chosen based on updated exclusion results obtained by the semi-leptonic and di-lepton final state parts of this study [78] for the $80\,\mathrm{GeV}/c^2$ mass point, and from published ATLAS results [130] for the $160\,\mathrm{GeV}/c^2$ mass point.

In Figures 4.69, 4.70, and 4.71 the combined $E_{\mathrm{T}}^{\mathrm{miss}}$+b-tag $+\Delta\phi$ efficiency values, defined in Eq. (4.40), are compared to the default values used in the QCD multi-jet measurement in which the assumption was made that no signal is present, without the $\Delta\phi$ cut, for $\Delta\phi < 160°$ and for $\Delta\phi < 130°$, respectively. The ratio between the two efficiencies, defined as

$$\text{Ratio} \quad = \quad \frac{\varepsilon_{E_{\mathrm{T}}^{\mathrm{miss}}\text{+b-tag }+\Delta\phi,\ i}}{\varepsilon^{m_{H^{\pm}}=X\ \mathrm{GeV}/c^2}_{E_{\mathrm{T}}^{\mathrm{miss}}\text{+b-tag }+\Delta\phi,\ i}} \tag{4.66}$$

is also shown with a first-order polynomial fitted through the points, where the term $\varepsilon^{m_{H^{\pm}}=X\ \mathrm{GeV}/c^2}_{E_{\mathrm{T}}^{\mathrm{miss}}\text{+b-tag }+\Delta\phi,\ i}$ refers to the $E_{\mathrm{T}}^{\mathrm{miss}}$+b-tag $+\Delta\phi$ efficiency in the presence of a signal of mass $X\ \mathrm{GeV}/c^2$. For both mass points and all 3 $\Delta\phi$ (τ jet candidate, $E_{\mathrm{T}}^{\mathrm{miss}}$) options, the fitted polynomial is compatible with Ratio = 1, while the slope of the fit in all cases is negligibly small and within error compatible with zero.

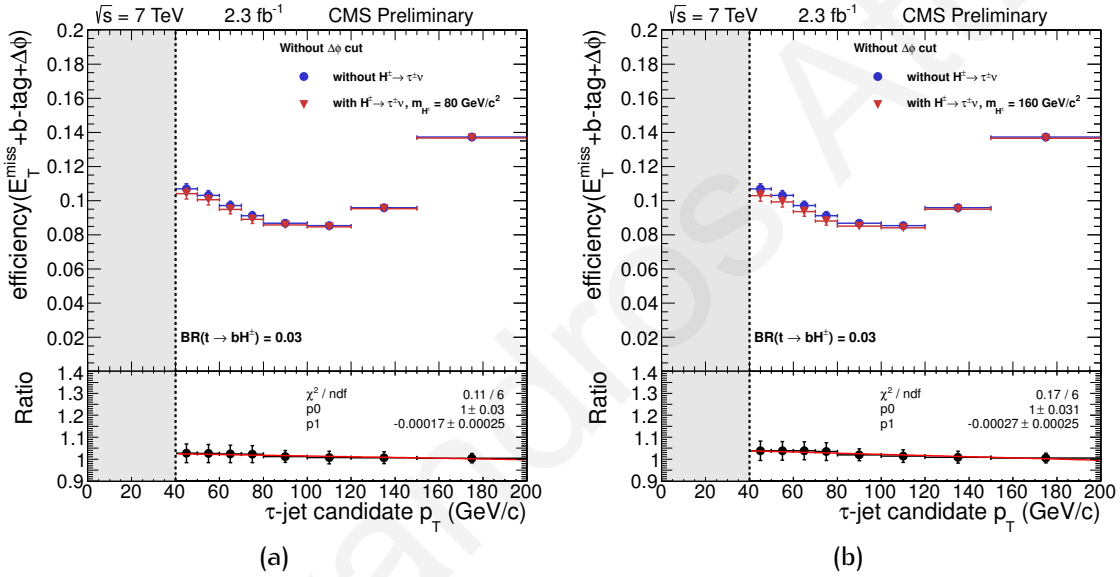

Figure 4.69: Efficiency of the $E_{\mathrm{T}}^{\mathrm{miss}}$+b-tag $+\Delta\phi$ collective cut in p_{T} bins of τ jet candidates, $\varepsilon_{E_{\mathrm{T}}^{\mathrm{miss}}\text{+b-tag }+\Delta\phi,\ i}$, for $m_{H^{\pm}} = 80\ \mathrm{GeV}/c^2$ (a) and $m_{H^{\pm}} = 160\ \mathrm{GeV}/c^2$ (b), without the $\Delta\phi$ cut. The last τ-jet candidate p_{T} bin corresponds to $p_{\mathrm{T}} > 150\ \mathrm{GeV}/c$. For the signal hypothesis, the $t\bar{t}$ cross section was decreased by the BR($t \to bH^{\pm}$).

The QCD multi-jet background estimate, N^{QCD}, was also re-evaluated in the presence of the signal and compared to the default values used in the QCD multi-jet measurement in which no signal is assumed to be present. The predictions for the estimate N^{QCD} for each τ jet candidate p_{T} bin, in the case where a signal is present, are shown in Fig. 4.72. Below these values the difference between the two predictions is also shown as ΔN^{QCD}, defined as

$$\Delta N^{\mathrm{QCD}} \quad = \quad N^{\mathrm{QCD}} - N^{\mathrm{QCD}}_{m_{H^{\pm}}=X\ \mathrm{GeV}/c^2} \tag{4.67}$$

where $N^{\mathrm{QCD}}_{m_{H^{\pm}}=X\ \mathrm{GeV}/c^2}$ refers to the prediction of the number of QCD multi-jet events after all selections in the presence of a signal of mass $X\ \mathrm{GeV}/c^2$. A line was added at $\Delta N^{\mathrm{QCD}} = 0$ to show that for all τ jet candidate p_{T} bins considered, the results obtained with and without the presence of signal are within error consistent between them. In particular, for $m_{H^{\pm}} =$

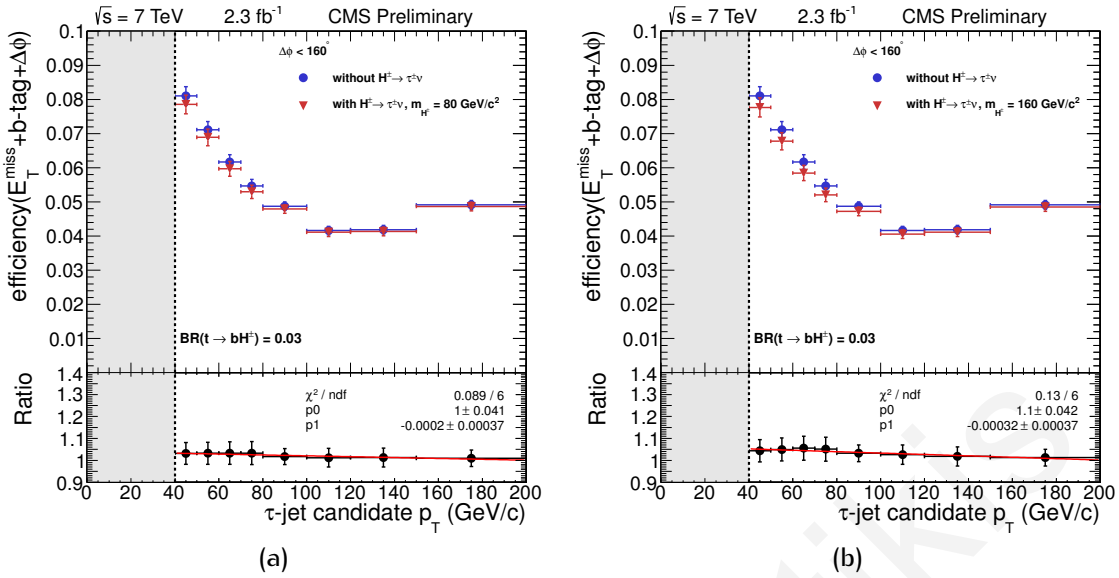

Figure 4.70: Efficiency of the $E_{\mathrm{T}}^{\mathrm{miss}}$+b-tag $+\Delta\phi$ collective cut in p_{T} bins of τ jet candidates, $\varepsilon_{E_{\mathrm{T}}^{\mathrm{miss}}+\text{b-tag}+\Delta\phi,\ i}$, for $m_{H^{\pm}} = 80\,\mathrm{GeV}/c^2$ (a) and $m_{H^{\pm}} = 160\,\mathrm{GeV}/c^2$ (b), for the $\Delta\phi < 160°$ option. The last τ-jet candidate p_{T} bin corresponds to $p_{\mathrm{T}} > 150\,\mathrm{GeV}/c$.

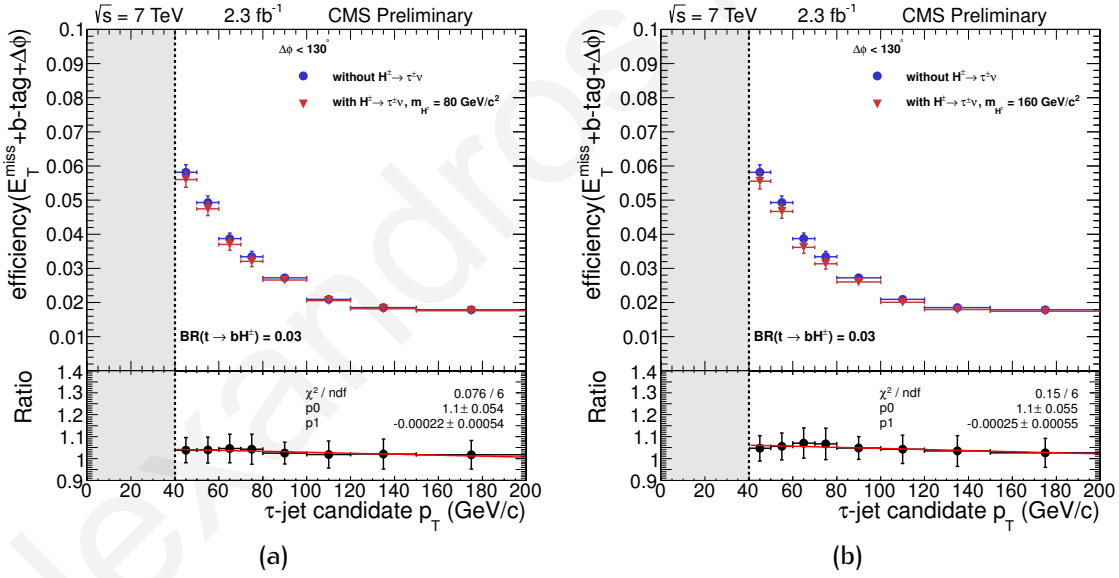

Figure 4.71: Efficiency of the $E_{\mathrm{T}}^{\mathrm{miss}}$+b-tag $+\Delta\phi$ collective cut in p_{T} bins of τ jet candidates, $\varepsilon_{E_{\mathrm{T}}^{\mathrm{miss}}+\text{b-tag}+\Delta\phi,\ i}$, for $m_{H^{\pm}} = 80\,\mathrm{GeV}/c^2$ (a) and $m_{H^{\pm}} = 160\,\mathrm{GeV}/c^2$ (b), for the $\Delta\phi < 130°$ option. The last τ-jet candidate p_{T} bin corresponds to $p_{\mathrm{T}} > 150\,\mathrm{GeV}/c$. For the signal hypothesis, the $t\bar{t}$ cross section was decreased by the BR($t \to bH^{\pm}$).

$80\,\mathrm{GeV}/c^2$ the estimate for N^{QCD} was found to be 40 ± 3 without the $\Delta\phi$ cut applied, 25 ± 2 for $\Delta\phi < 160°$, and 16 ± 1 for $\Delta\phi < 130°$ for an integrated luminosity of $2.3\,\mathrm{fb}^{-1}$. The analogous results for $m_{H^{\pm}} = 160\,\mathrm{GeV}/c^2$ were found to be 37 ± 3 without the $\Delta\phi$ cut applied, 23 ± 2 for $\Delta\phi < 160°$, and 15 ± 1 for $\Delta\phi < 130°$. These numbers are all within $\sim 1\sigma$ from the default QCD multi-jet background estimates given in Section 4.8.1.2, when summing the errors in quadrature.

Finally, the τ-jet identification and R_τ efficiencies that were used in extracting the QCD multi-jet transverse mass shape were re-evaluated in the presence of a signal. Their values

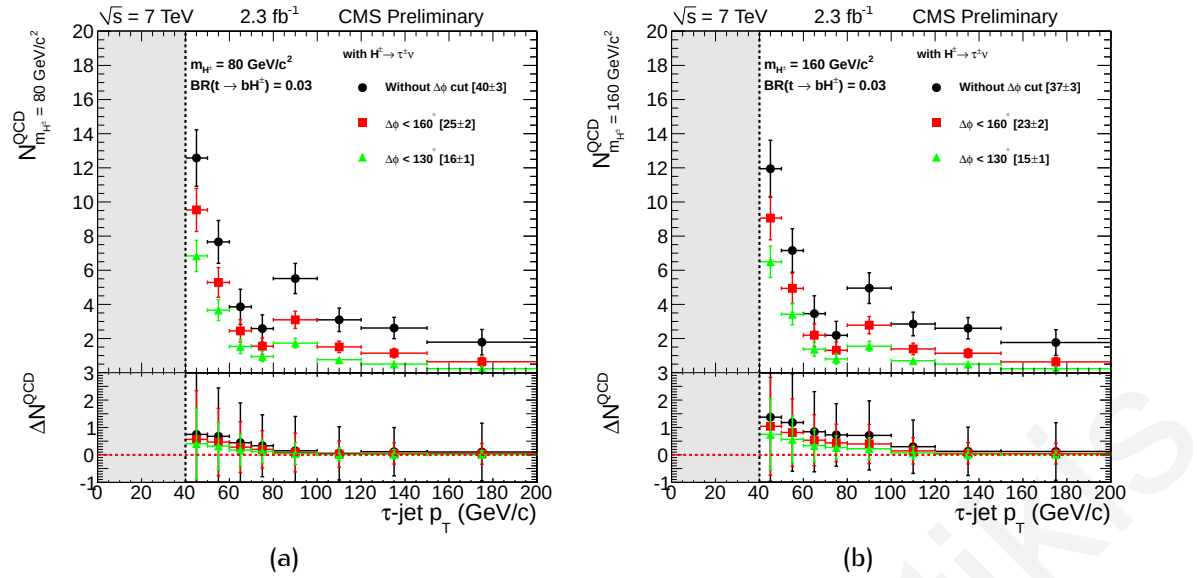

Figure 4.72: Total contribution from each τ jet candidate p_T bin in the predicted number of QCD multi-jet events after all selections and in the presence of a 80 GeV/c^2 (a) and 160 GeV/c^2 (b) signal, for 3 $\Delta\phi\left(\tau \text{ jet candidate}, E_T^{\text{miss}}\right)$ options; without $\Delta\phi$ cut, $\Delta\phi < 160°$ and $\Delta\phi < 130°$. The combined systematic and statistical uncertainties are also shown. The last τ-jet candidate p_T bin corresponds to $p_T > 150$ GeV/c. For the signal hypothesis, the $t\bar{t}$ cross section was decreased by the BR($t \to bH^{\pm}$).

are compared in Fig. 4.73 to the default results obtained under the assumption that no signal is present in the data samples used. The comparison is performed for two signal mass points; $m_{H^{\pm}} = 80$ GeV/c^2 (a) and $m_{H^{\pm}} = 160$ GeV/c^2 (b). The ratio between the two values, defined as

$$\text{Ratio} = \frac{\varepsilon_{\tau\text{-jet ID, } i}}{\varepsilon^{m_{H^{\pm}}=X\text{ GeV}/c^2}_{\tau\text{-jet ID, } i}} \tag{4.68}$$

is also shown with a first-order polynomial fitted through the points, where the term $\varepsilon^{m_{H^{\pm}}=X\text{ GeV}/c^2}_{\tau\text{-jet ID, } i}$ refers to the τ-jet identification efficiency in the presence of a signal of mass X GeV/c^2. For both mass points the slope of the fitted polynomial is negligibly small and within error is compatible with zero. Given that the QCD multi-jet transverse mass distribution is normalised to the QCD multi-jet prediction, N^{QCD}), the necessary condition to ensure that this shape is not affected by the presence of a signal is not the absolute values of the terms $\varepsilon_{\tau\text{-jet ID, } i}$, but instead that all $\varepsilon_{\tau\text{-jet ID, } i}$ values are affected democratically by the presence of a signal. This condition is indeed satisfied by the fact that the polynomial fit slope is within error compatible with a flat curve, which supports the claim that the QCD multi-jet transverse mass shape is stable to the presence of a signal. In this context, the question of whether the ratio-curves are or are not centred at Ratio=1 is therefore irrelevant.

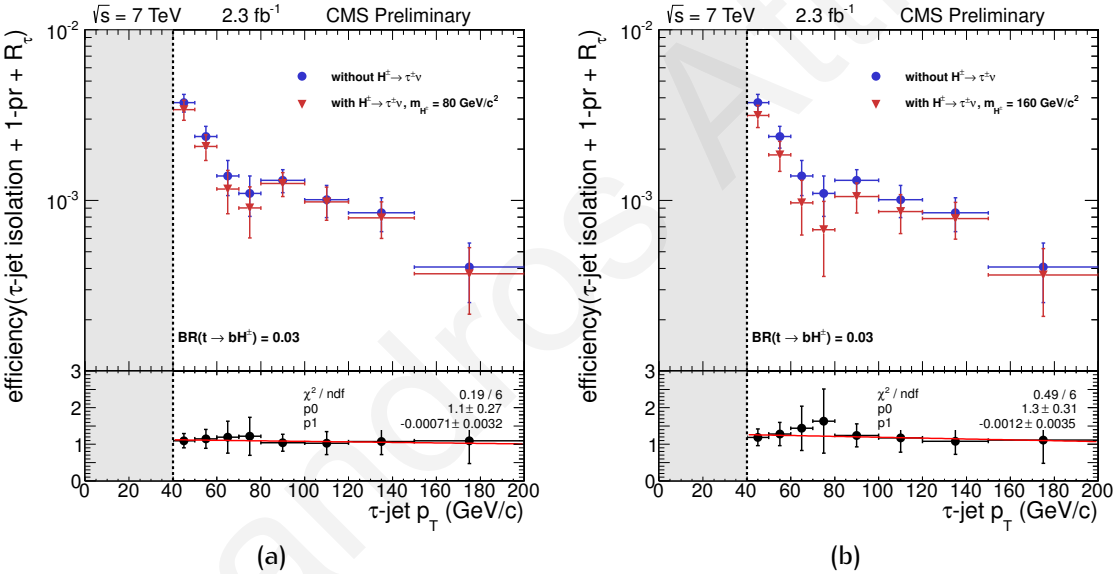

Figure 4.73: Efficiency of τ-jet identification in p_T bins of τ jet candidates $\varepsilon_{\tau\text{-jet ID},\,i}$ as measured from data and assuming the presence of signal of mass $m_{H^\pm} = 80\,\text{GeV}/c^2$ (a) and $m_{H^\pm} = 160\,\text{GeV}/c^2$ (b). The last τ-jet candidate p_T bin corresponds to $p_T > 150\,\text{GeV}/c$. For the signal hypothesis, the $t\bar{t}$ cross section was decreased by the BR($t \to bH^\pm$).

4.8.2 EWK+$t\bar{t}$ genuine τ background

The EWK+$t\bar{t}$ genuine τ background consists of all background processes other than QCD multi-jet which have genuine τ-leptons within the acceptance, either decaying hadronically ($\tau^{\pm} \to$ hadrons ν_τ) or leptonically, to an electron ($\tau^{\pm} \to e^{\pm}\nu_e\nu_\tau$) or a muon ($\tau^{\pm} \to \mu^{\pm}\nu_\mu\nu_\tau$) which are subsequently mis-identified as τ jets. This background was estimated from collision data with μ + jets events and the τ-embedding method [76, 131, 132], yielding an estimate on the background expected from events with genuine τ-leptons mainly originating from W + jets and $t\bar{t}$ processes, but also with smaller contributions from $Z^0/\gamma^* \to \ell\ell$, single-top and di-boson processes, shown in Figs. 4.74, 4.75, 4.76, 4.77, 4.78, 4.79, and 4.80, respectively. With the same method, the transverse mass shape for the EWK+$t\bar{t}$ genuine τ background, reconstructed from the τ jet and the $E_{\mathrm{T}}^{\mathrm{miss}}$ objects $m_{\mathrm{T}}(\tau\,\mathrm{jet}, E_{\mathrm{T}}^{\mathrm{miss}})$, was also extracted. In particular, the measurement method is based on the selection of a control sample with $W^{\pm} \to \mu^{\pm}\nu_\mu$ decays, whereby the muon is removed from the event and replaced with a simulated and reconstructed τ-lepton decay of identical momentum. After the embedding of the τ-lepton in the event, the $E_{\mathrm{T}}^{\mathrm{miss}}$ is subsequently recalculated. The embedding is done at the PF level, with the subsequent embedded events subjected to all the signal selection requirements, as described in Section 4.5. Therefore, the τ-embedding method also includes the cases when the generator-level τ-lepton, that is within the selected acceptance, decays to an electron or a muon ($\tau^{\pm} \to \ell^{\pm}\nu_\ell\nu_\tau$), which is then mis-identified as a τ jet. However, due to the muon selection involved in the procedure, the τ-embedding method can only be applied to the component of the EWK+$t\bar{t}$ genuine τ background containing genuine τ-leptons with $p_{\mathrm{T}} > 40\,\mathrm{GeV}/c$, $|\eta| < 2.1$ (see Tables 4.21 and 4.23 for τ-jet selection requirements). Moreover, the EWK + $t\bar{t}$ background with an electron, muon, or a hadronic jet mis-identified as a τ jet, or with a genuine τ outside the acceptance, is not included in this EWK+$t\bar{t}$ genuine τ background measurement, but was instead determined from simulations as described in Section 4.8.3. The details of the method are discussed in Refs. [76, 133, 77, 78, 134].

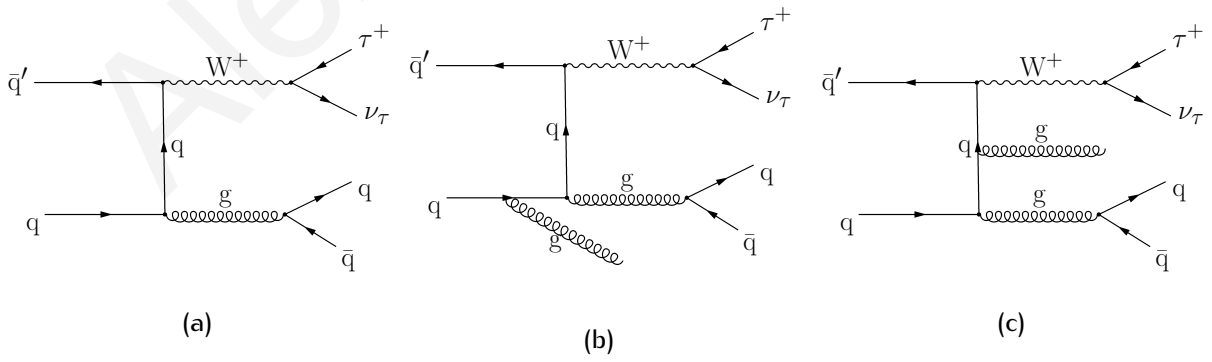

Figure 4.74: Representative Feynman diagrams for W + jets production at the LHC; NLO production (a) and NNLO production with ISR (b) and (c). The diagrams were created with feynMF [80].

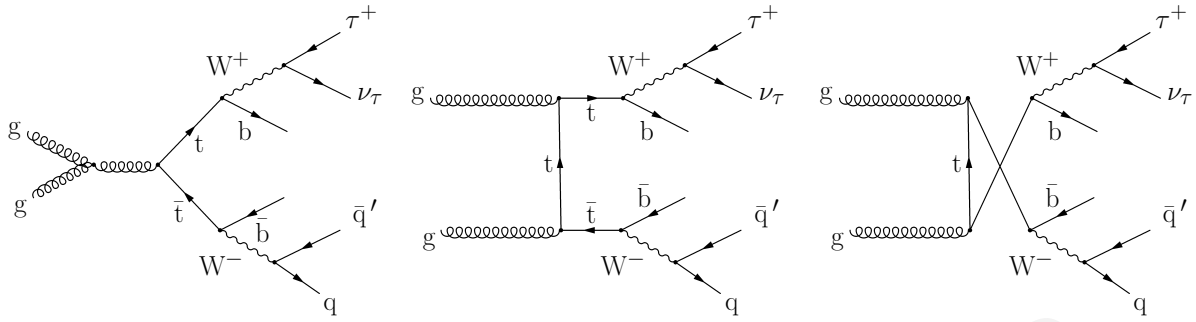

Figure 4.75: Dominant Feynman diagrams (∼ 87%) for $t\bar{t} \to bW^{\pm}bW^{\mp}$ production at the LHC for the fully hadronic final state; gluon fusion through the s-channel (a), t-channel (b) and u-channel (c). The diagrams were created with feynMF [80].

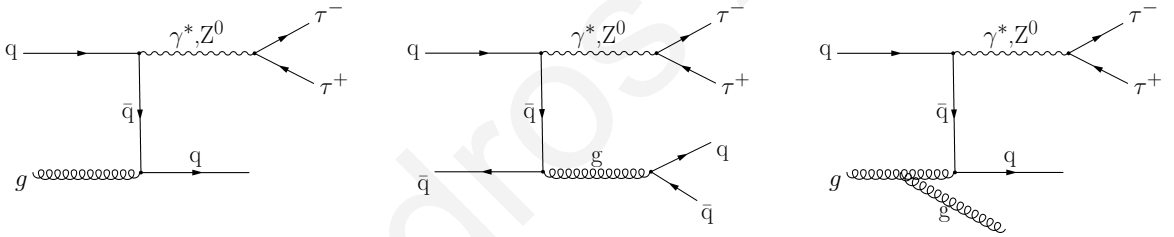

Figure 4.76: Representative Feynman diagrams for Drell-Yan production at the LHC; NLO production (a), NNLO production (b), and NNLO production with ISR (c). The diagrams were created with feynMF [80].

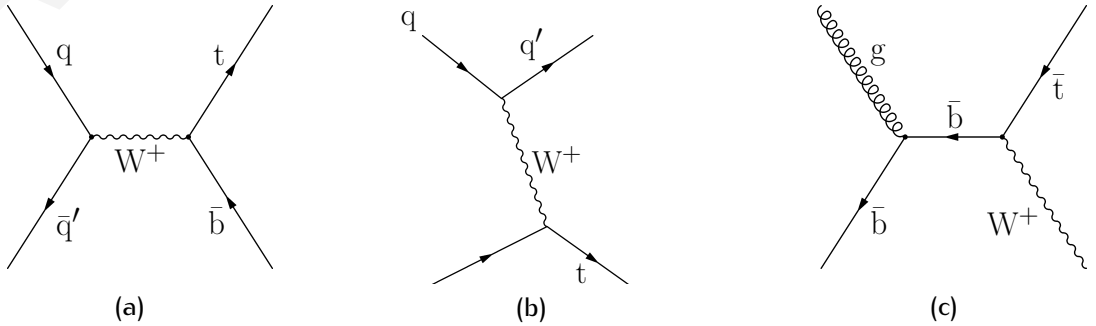

Figure 4.77: Representative Feynman diagrams for single-top (s-, t- and tW-channels) production at the LHC; s-channel (a), t-channel (b) and tW-channel (c). The diagrams were created with feynMF [80].

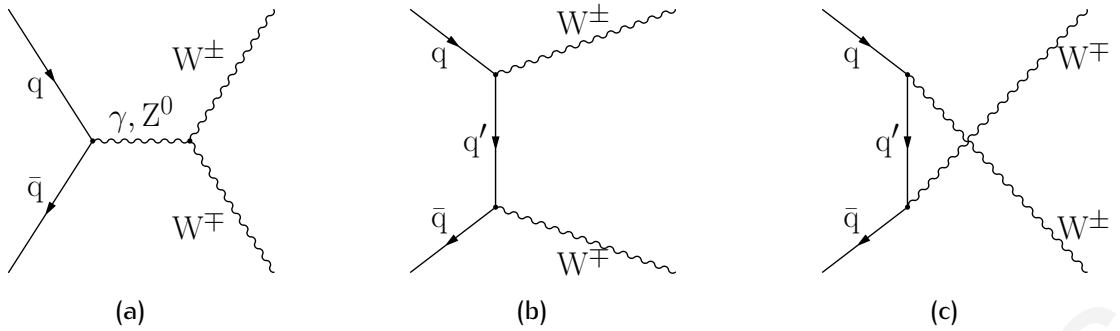

Figure 4.78: Leading Order Feynman diagrams for di-boson ($W^{\pm}W^{\mp}$) production at the LHC; s-channel (a), t-channel (b) and u-channel (c). The diagrams were created with feynMF [80].

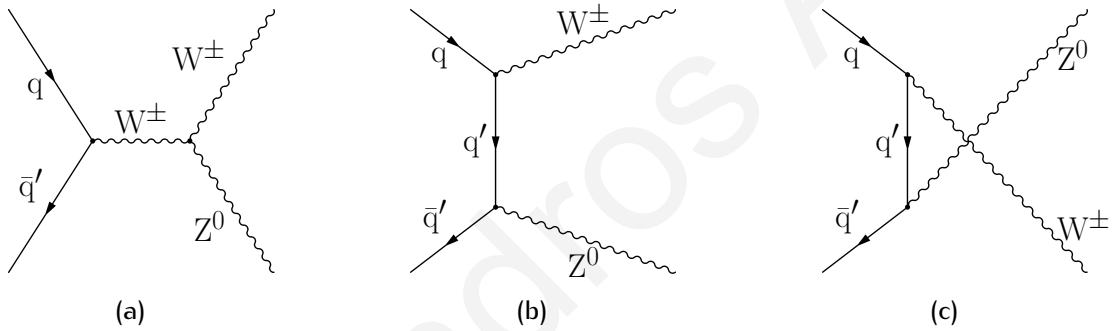

Figure 4.79: Leading Order Feynman diagrams for di-boson (WZ) production at the LHC; s-channel (a), t-channel (b) and u-channel (c). The diagrams were created with feynMF [80].

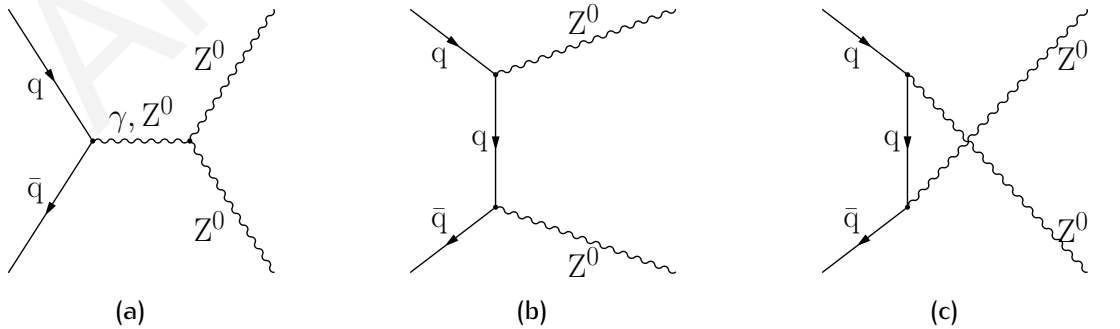

Figure 4.80: Leading Order Feynman diagrams for di-boson (ZZ) production at the LHC; t-channel (b) and u-channel (c). The s-channel (a) is forbidden in the SM due to the fact that $SU(2)_L$ algebra does not generate any neutral vertex with only photons and Z^0 bosons, as discussed in Section D.3. The diagrams were created with feynMF [80].

4.8.2.1 Method description

Control sample event selection The clean-up selections for collision data were the same as in Table 4.3 on page 113, and the primary vertex was selected as described in Section 4.5.2 on page 137. The events were triggered with HLT_Mu20, HLT_Mu24, HLT_Mu30, HLT_Mu40, or HLT_Mu40_eta2p1 depending which one was the lowest unprescaled trigger in the corresponding run. The mapping between run numbers and the required trigger path is shown in Table 4.5. In simulated samples the events were triggered with HLT_Mu20.

The events were required to have exactly one good muon, with the muon selections being identical to those of the efficiency measurement of the $E_{\mathrm{T}}^{\mathrm{miss}}$- part of the single τ jet + $E_{\mathrm{T}}^{\mathrm{miss}}$ trigger, as shown in Table 4.18 on page 132, with a τ jet-like isolation requirement instead of a default muon isolation. The motivation behind the preference of the former rather than the latter isolation, is to ensure that $W^{\pm} \to \mu^{\pm}\nu_{\mu}$ events that would be accepted by a τ-jet reconstruction and isolation are not rejected with the more tight muon isolation requirement. Events with more than one muon passing these selections were rejected, while events with additional isolated electrons or muons were also rejected with the criteria shown in Table 4.24 on page 145 and Table 4.25 on page 147, respectively. Furthermore, the selected events were required to have at least 3 PF jets identified with the selections shown in Table 4.27 on page 149. The only difference was that the selected PF jets were required to be separated from the selected muon with $\Delta R(\mu, \mathrm{jet}) > 0.1$, instead of $\Delta R(\tau, \mathrm{jet}) > 0.5$, as recommended by the CMS TOP group for all μ + jets analyses [135]. The PF jets selection was re-done after the τ-embedding with the default $\Delta R(\tau, \mathrm{jet}) > 0.5$ requirement, while the remaining signal selection requirements were also applied after the muon replacement and the embedding of the τ-lepton in the event, as discussed later on in this section. The pre-selection and subsequent complete selection requirements in obtaining the control sample are summarised in Table 4.36.

Table 4.36: Summary of all event selection steps taken in the τ-embedding method.

	Selection	Description
1	Data clean-up	Remove beam-scrapping events
2	single μ trigger	Selection of signal-like events using dedicated triggers
3	Good primary vertex	Selection of good-quality primary vertex
4	Good muon selection	Select muon with HPSbyTightIsolation-like criteria
5	Isolated lepton veto	Veto on the presence of isolated electrons/muons
6	hadronic jets selection	Selection of at least 3 PF jets, $\Delta R(\mu, \mathrm{jet}) > 0.1$
7	τ-embedding	Perform τ-embedding to get hybrid event
8	Signal selections	Apply signal selection requirements (Table 4.29)

The aforementioned selection structure was chosen such that the events for the τ-embedding were selected with a minimum set of requirements, the physics motivation being that the bulk of the signal selection requirements would be applied after the τ-embedding to

Table 4.37: Number of pre-selected events for the μ + jets control sample, for data and MC and and integrated luminosity of 2.3 fb^{-1} . The MC sample composition is also shown. The quoted uncertainties are statistical.

Sample	Events	Composition
Data	33930 ± 184	–
Simulations total	34560 ± 256	–
W + jets	19685 ± 180	$57.0 \pm 0.7\%$
$t\bar{t}$	8831 ± 41	$25.6 \pm 0.2\%$
$Z^0/\gamma^* \to \ell\ell$	2640 ± 31	$7.6 \pm 0.1\%$
QCD multi-jet	2035 ± 174	$5.9 \pm 0.5\%$
single-top	1017.8 ± 6.7	$2.95 \pm 0.03\%$
di-boson	350.2 ± 3.6	$1.01 \pm 0.01\%$

a final state almost identical to the signal selection, thus minimising any biases introduced by the absence of the τ jet. To emulate the presence of a τ jet, the selected muon was required to be isolated based on requirements that closely matched the HPS byTightIsolation criteria used for the τ-jet identification in the signal selection, as already discussed in Section 4.4.2.2. The motive behind this selection was not to over-clean the cone around the muon where the tau reconstruction, tau constituent finding and tau isolation were performed. In this context, a signal and isolation cones were constructed around the muon with opening angles R_s and R_i, respectively, providing an isolation annulus of $0.1 < \Delta R < 0.4$ around the muon. In this way, possible biases originating from the use of a muon instead of an isolated τ jet in the final state topology and kinematics were eliminated. The composition of the pre-selected control sample, as determined from simulation, is shown in Table 4.37.

Tau embedding and signal selections The τ-embedding technique was applied to the control sample to replace the selected muon with a simulated τ-lepton. The removal of the muon from the event and the subsequent overlay of a simulated τ-lepton resulted in a very realistic hybrid event, which provided a pragmatic description of the full event, while automatically taking into account detector effects and running conditions. The advantage of using this method is thus that the whole event, except for the τ jet, is taken directly from data, including the UE, pile-up, $E_{\mathrm{T}}^{\mathrm{miss}}$, b-jets and hadronic jets, all of which are used in the final event selection for the signal analysis.

The first step in the embedding procedure was the generation of a τ-lepton having the same momentum as that of the selected muon. The energy of the τ-lepton was scaled such that its was set to the world average value 1.7769 GeV/c^2 [136], whith the τ-lepton being decayed with the TAUOLA package under the assumption that the τ-lepton is produced from a decay of a $W^{\pm}$ boson. This assumption is valid for all the samples used, except for the Drell-Yan, as discussed in Section 4.8.2.2. The τ-lepton was allowed to decay to all final states in order to account for contributions from the leptonic τ-lepton decays, $\tau^{\pm} \to \ell^{\pm}\nu_{\ell}\nu_{\tau}$. The detector response to the τ-lepton decay was then simulated in detail using the GEANT4 package [89], and further reconstructed with the PF algorithm up to the list of PF candidate

objects.

The selected muon was removed from the original event by removing the PF muon from the list of reconstructed PF candidate objects which was found to be a distance $\Delta R < 0.001$ from the selected muon. The τ-embedding was achieved by merging the list of reconstructed PF candidate objects from the τ-lepton simulation with the corresponding list of the original event, where the PF candidate object matching to the selected muon has been removed. After the muon removal and the embedding of the simulated τ-lepton in the list of PF candidate objects, the rest of the PF reconstruction was ran, with the merged list of PF candidate objects used as input.

With the successful embedding of the simulated τ-lepton in the event, all the signal selection requirements as described in Section 4.5 were applied, with the only difference being that the PF jets, τ jets, and $E_{\mathrm{T}}^{\mathrm{miss}}$ objects were taken from the PF reconstruction of the embedded event, rather than the original event. The vetoes on isolated electrons and muons were already applied within the $\mu+\geq 3$ jets control sample selection. In this way, a signal-like selection was performed on the hybrid event, with the only significant difference being the trigger used in selecting the data sample, and of course the presence of an embedded τ jet instead of a genuine one.

After the aforementioned steps, the last major step in acquiring an estimate for the number of EWK+$t\bar{t}$ genuine τ background events in the signal region, is the correct normalisation of the control data sample, which is discussed next. The complete τ-embedding procedure used for the EWK+$t\bar{t}$ genuine τ background measurement is shown schematically in Fig. 4.81.

Normalisation Although the τ-embedding method exploits lepton universality to extract an estimate for the expected EWK+$t\bar{t}$ genuine τ background, several normalisation factors must be accounted for, including the efficiency of the single μ trigger used in obtaining the control data sample, the efficiency of the single τ jet + $E_{\mathrm{T}}^{\mathrm{miss}}$ trigger that should have been used instead, and a factor accounting for the leak of $W^{\pm} \to \tau^{\pm}\nu_{\tau} \to \mu^{\pm}\nu_{\mu}\nu_{\tau}\nu_{\tau}$ events in the control region, which can result in an overestimate of the specific background; μ + jets events from the control sample that originate from τ jets events, whereby the τ-lepton has decayed to a muon.

The branching ratio of $W^{\pm}$ decaying to muons ($W^{\pm} \to \mu^{\pm}\nu_{\mu}$), can be assumed to be equal to that of a $W^{\pm}$ decaying to τ-leptons ($W^{\pm} \to \tau^{\pm}\nu_{\tau}$) due to the lepton universality. By denoting the number of embedded events passing the signal selection in τ-jet p_{T} bin i with $N_{\mathrm{sel},\,i}^{\mathrm{EWK}+t\bar{t}\;\tau}$, the estimate for the number of the EWK+$t\bar{t}$ genuine τ events becomes

$$N^{\mathrm{EWK}+t\bar{t}\;\tau} = (1 - f_{W^{\pm}\to\tau^{\pm}\nu_{\tau}\to\mu^{\pm}\nu_{\mu}\nu_{\tau}\nu_{\tau}}) \times \frac{1}{\epsilon_{\mathrm{sel}}^{\mu}} \times \sum_{i}^{\tau\text{-jet } p_{\mathrm{T}} \text{ bins}} N_{\mathrm{sel},\,i}^{\mathrm{EWK}+t\bar{t}\;\tau} \epsilon_{\mathrm{trg},\,i}^{\tau}. \tag{4.69}$$

The term $\epsilon_{\mathrm{trg},\,i}^{\tau}$ describes the τ-part of the single τ jet + $E_{\mathrm{T}}^{\mathrm{miss}}$ trigger efficiency, in bins of τ jet p_{T} indexed i, with the binning described in Section 4.4.2.1. The muon trigger and offline selection efficiency term, denoted $\epsilon_{\mathrm{sel}}^{\mu}$, was measured with the Tag-and-Probe method

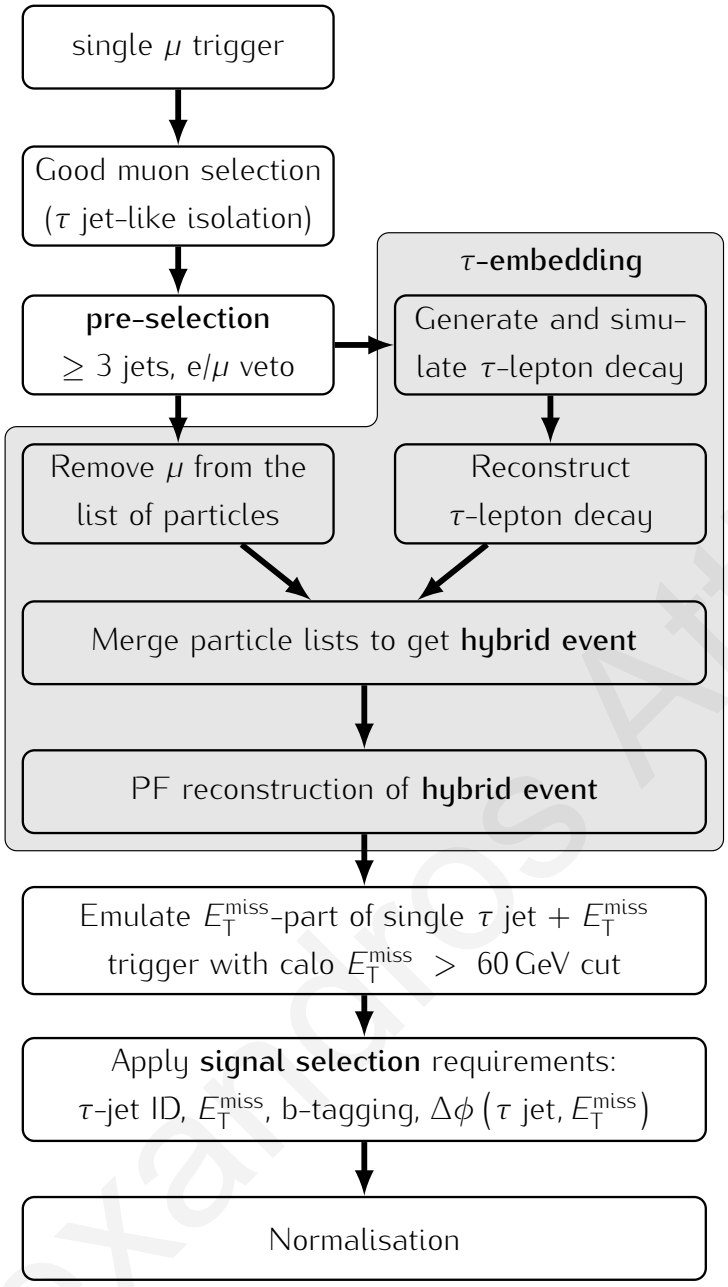

Figure 4.81: Schematic overview of the EWK+$t\bar{t}$ genuine τ background measurement.

as described in Section 4.8.2.2, and is necessary to decouple the use of the single μ trigger and muon offline selection from the measurement. The leakage of $W^{\pm} \to \tau^{\pm}\nu_{\tau} \to \mu^{\pm}\nu_{\mu}\nu_{\tau}\nu_{\tau}$ events in the control region is accounted for by subtracting the fraction $f_{W^{\pm}\to\tau^{\pm}\nu_{\tau}\to\mu^{\pm}\nu_{\mu}\nu_{\tau}\nu_{\tau}}$ from the selected events, and is discussed further in Section 4.8.2.2.

single τ jet + $E_{\mathrm{T}}^{\mathrm{miss}}$ trigger efficiency The τ-part of the single τ jet + $E_{\mathrm{T}}^{\mathrm{miss}}$ trigger was taken into account by weighting the events in τ-jet p_{T} bins with the measured efficiency of the τ-part, described in Section 4.4.2.1. The efficiencies were measured separately for the 3 run periods which had slightly different trigger configurations, with the weights and their corresponding uncertainties taken from Fig. 4.13 on page 129.

For the $E_{\mathrm{T}}^{\mathrm{miss}}$- part it was assumed that calo $E_{\mathrm{T}}^{\mathrm{miss}}$ is good enough approximation of HLT

$E_{\mathrm{T}}^{\mathrm{miss}}$, as discussed in Section 4.4.2.2, and that the contribution from the selected muon to the calorimeter towers and to the calo $E_{\mathrm{T}}^{\mathrm{miss}}$ is negligible. Therefore, a vector sum of the calo $E_{\mathrm{T}}^{\mathrm{miss}}$ objects from the original event and from the simulated τ-lepton decay part is a reasonable approximation of the true calo $E_{\mathrm{T}}^{\mathrm{miss}}$ of the embedded event. The $E_{\mathrm{T}}^{\mathrm{miss}}$- part of the trigger is taken into account by requiring that this vector sum passes the calo $E_{\mathrm{T}}^{\mathrm{miss}} > 60\,\mathrm{GeV}$. The difference in the efficiencies of HLT $E_{\mathrm{T}}^{\mathrm{miss}}$ and offline calo $E_{\mathrm{T}}^{\mathrm{miss}}$ cuts in the bin $40-50\,\mathrm{GeV}$ of the plot in Fig. 4.14 (b) was not corrected for, due to the fact that a requirement of $E_{\mathrm{T}}^{\mathrm{miss}} > 50\,\mathrm{GeV}$ in the signal selection was found to remove any bias.

Averaging over multiple embedding processing rounds The event yields extracted with the τ-embedding procedure were found to depend greatly on the random number generator seeds. In particular, by repeating the embedding procedure multiple times with different random number generator seeds, the event yields of data and simulation samples having only tens of simulated events fluctuated significantly, meaning that the EWK+$t\bar{t}$ genuine τ background event yield was not stable. However, after investigation it was concluded that no systematic source was associated to this effect, which was understood to appear due to statistical fluctuations of the procedure. In order to increase the statistical accuracy of the method, especially for the $m_{\mathrm{T}}(\tau\text{ jet}, E_{\mathrm{T}}^{\mathrm{miss}})$ shapes, the embedding procedure was conducted 10 times for each sample. The resulting event yields, which were assumed to be independent, were estimated with the mean of the 10 trials

$$M = \frac{\sum_{i}^{\mathrm{trials}} N_i}{N_{\mathrm{trials}}}, \tag{4.70}$$

where M is the mean, N_i is the event yield from trial i, and N_{trials} is the total number of trials. The statistical uncertainty of M was calculated with error propagation as

$$\sigma_M^2 = \sum_{i}^{\mathrm{trials}} \left(\frac{\sigma_i}{N}\right)^2 \tag{4.71}$$

$$\tag{4.72}$$

where σ_i is the statistical uncertainty of event yield N_i.

Residual background from di-tau events Further scrutiny of the τ-embedding procedure also revealed that the method underestimated the yield of di-tau events, mainly from Drell-Yan and $W^{\pm}\mathrm{W}^{\mp}$ events. The discrepancy was found to originate from the difference in the veto of events with a second muon in the $\mu+\geq 3$ jets event selection and in the veto of events with a second τ jet in the signal event selection. For example, consider the $Z^0 \to \mu^{\pm}\mu^{\mp}$ and $Z^0 \to \tau^{\pm}\tau^{\mp}$ events, where the effect is the largest. A $Z^0 \to \tau^{\pm}\tau^{\mp}$ event is selected in the signal analysis if one of the τ-leptons passes the τ-jet identification requirement and the other is not, due to the secondary τ jet veto, as summarised in Table 4.23 on page 143. With the τ-embedding method, the original events are from $Z^0 \to \mu^{\pm}\mu^{\mp}$ processes, which

are transformed to the unphysical $Z^0 \to \tau^{\pm}\mu^{\mp}$hybrid event with the τ-embedding method.

Such $Z^0 \to \mu^{\pm}\mu^{\mp}$ events are selected if one of the muons passes the corresponding muon requirements for τ-embedding and the other muon is not selected by the isolated muon veto selections. Since the efficiency of the isolated muon veto, which is applied before the τ-embedding procedure, is expected to be high for prompt muons, these $Z^0 \to \mu^{\pm}\mu^{\mp}$ events are more suppressed than the $Z^0 \to \tau^{\pm}\tau^{\mp}$ events which the embedding procedure is aiming to estimate, thus biasing the normalisation. Therefore more di-muon events are rejected by the secondary muon veto than di-tau events are rejected by the secondary τ jet veto. Of course, the second muon in $Z^0 \to \mu^{\pm}\mu^{\mp}$ events is not always rejected by the isolated muon veto requirement due to acceptance reasons and limited efficiency, which somewhat mitigates the effect. The discrepancy was found to be smaller than 10% of the total EWK+$t\bar{t}$ genuine τ event yield, and was taken into account by the use of simulations. For both $Z^0/\gamma^* \to \ell\ell$ and $W^{\pm}\mathrm{W}^{\mp}$ simulated samples, a residual number of background events, denoted $N_i^{\text{residual MC}}$, was defined as the difference of normal simulated $N_i^{\text{normal MC}}$ and embedded simulated events $N_i^{\text{embedded MC}}$

$$N_i^{\text{residual MC}} = N_i^{\text{normal MC}} - N_i^{\text{embedded MC}}, \tag{4.73}$$

where the index i denotes the simulated sample in question, Drell-Yan and $W^{\pm}\mathrm{W}^{\mp}$. The normal simulated events were required to have a genuine τ-lepton with $p_{\mathrm{T}} > 40\,\mathrm{GeV}/c$ and $|\eta| < 2.1$, 3 PF jets, and no isolated electrons nor muons in order to cover the same phase-space as the embedded events.

4.8.2.2 Measurements for normalisation

Muon trigger and identification efficiency The muon selection efficiency was measured from Drell-Yan $Z^0/\gamma^* \to \mu^{\pm}\mu^{\mp}$ events with the Tag-and-Probe method [137]. An identified and isolated muon passing a single muon trigger was taken as the tag, and a Tracker-muon with $p_{\mathrm{T}} > 40\,\mathrm{GeV}/c$ as the probe. The probe muons were required to pass the selections described in Section 4.8.2.1 without the isolation requirement. The isolation of the muon was not considered to be a part of the muon identification efficiency, as the events rejected with the muon isolation would be rejected with the isolation of the embedded τ-lepton, and this rejection is accounted for in the efficiency of the τ-jet isolation. The efficiencies were measured separately for each run period and were subsequently combined to an integrated luminosity weighted average. The integrated luminosity of the run periods with the HLT_Mu40 and HLT_Mu40_eta2p1 was used in the weighted average for the efficiency measured with HLT_Mu40 trigger. A combined efficiency of

$$\epsilon_{\text{sel}}^{\mu} = 0.882 \pm 0.005 \tag{4.74}$$

was obtained, with the quoted uncertainty attributed to the statistical error.

Table 4.38: The fraction of selected $W^{\pm} \to \mu^{\pm}\nu_{\mu}$ and $W^{\pm} \to \tau^{\pm}\nu_{\tau} \to \mu^{\pm}\nu_{\mu}\nu_{\tau}\nu_{\tau}$ events in simulated W + jets, $t\bar{t}$, and single-top samples. The combination was done by weighting the datasets with their cross-sections.

Sample	$W^{\pm} \to \mu^{\pm}\nu_{\mu}$	$W^{\pm} \to \tau^{\pm}\nu_{\tau} \to \mu^{\pm}\nu_{\mu}\nu_{\tau}\nu_{\tau}$	Other
W + jets	96.5%	3.5%	0.05%
$t\bar{t}$	95.3%	4.5%	0.2%
Single top	92.1%	3.5%	4.6%
Combined	95.9%	3.8%	0.3%

Correction for events with a τ-lepton decaying to a muon The control sample of μ + jets events can be contaminated from events whereby a τ-lepton decays in-flight to a muon through $W^{\pm} \to \tau^{\pm}\nu_{\tau} \to \mu^{\pm}\nu_{\mu}\nu_{\tau}\nu_{\tau}$. Including such events in the control sample can lead to overestimating the EWK+$t\bar{t}$ genuine τ background event yield. In order to account for the $W^{\pm} \to \tau^{\pm}\nu_{\tau} \to \mu^{\pm}\nu_{\mu}\nu_{\tau}\nu_{\tau}$ contamination, their contribution was estimated with simulations. The fractions of such events from simulated W + jets, $t\bar{t}$, and single-top samples are shown in Table 4.38. The cross-section weighted average of the fraction of $W^{\pm} \to \mu^{\pm}\nu_{\mu}$ events was $f_{W^{\pm}\to\mu^{\pm}\nu_{\mu}} = 0.959$, and the corresponding fraction of $W^{\pm} \to \tau^{\pm}\nu_{\tau} \to \mu^{\pm}\nu_{\mu}\nu_{\tau}\nu_{\tau}$ events was found to be $f_{W^{\pm}\to\tau^{\pm}\nu_{\tau}\to\mu^{\pm}\nu_{\mu}\nu_{\tau}\nu_{\tau}} = 0.038$. The uncertainty of the latter was taken to be the maximum difference between the average and the individual values, yielding

$$f_{W^{\pm}\to\tau^{\pm}\nu_{\tau}\to\mu^{\pm}\nu_{\mu}\nu_{\tau}\nu_{\tau}} = 0.038 \pm 0.006. \tag{4.75}$$

4.8.2.3 Validation

The validation of the method was conducted by first validating the τ-embedding procedure, through a comparison of the selection efficiencies and distributions of key quantities between embedded simulation and normal simulation samples. In order to compare only the embedding procedure itself, the single τ jet + $E_{\mathrm{T}}^{\mathrm{miss}}$ trigger was not applied on the normal simulated events, and the corresponding normalisation was also not applied on the embedded simulated events. The application of single τ jet + $E_{\mathrm{T}}^{\mathrm{miss}}$ trigger was validated by repeating the comparison between embedded simulation and normal simulation, but with single τ jet + $E_{\mathrm{T}}^{\mathrm{miss}}$ trigger applied on the normal simulated events, and the corresponding normalisation applied on the embedded simulated events. The embedding procedure on data was validated by comparing embedded data to embedded simulations. Finally, the embedded data with the residual $Z^0/\gamma^* \to \ell\ell$ and $W^{\pm}W^{\mp}$ backgrounds taken from simulation was also compared to normal simulation. In all the considered validation procedures, good agreement was observed for all selection steps, providing concrete evidence that the τ-embedding method provides accurate results.

Table 4.39: The EWK+$t\bar{t}$ genuine τ event yield after the pre-selections and the signal selection requirements, as described in Section 4.8.2.1, for an integrated luminosity of 2.3 fb^{-1} for the 3 $\Delta\phi$ (τ jet, $E_{\mathrm{T}}^{\mathrm{miss}}$) cut options. The quoted uncertainties are statistical.

$\Delta\phi(\tau$ jet, $E_{\mathrm{T}}^{\mathrm{miss}})$ option	EWK + $t\bar{t}$ prediction	Embedded data	Residual Drell-Yan	Residual $W^{\pm}W^{\mp}$
Without $\Delta\phi(\tau$ jet, $E_{\mathrm{T}}^{\mathrm{miss}})$ cut	87.0 ± 3.4	79.7 ± 2.7	6.9 ± 2.0	0.35 ± 0.23
$\Delta\phi(\tau$ jet, $E_{\mathrm{T}}^{\mathrm{miss}}) < 160°$	85.8 ± 3.3	78.4 ± 2.6	7.0 ± 2.0	0.35 ± 0.23
$\Delta\phi(\tau$ jet, $E_{\mathrm{T}}^{\mathrm{miss}}) < 130°$	84.2 ± 3.3	76.9 ± 2.6	6.9 ± 2.0	0.36 ± 0.23

4.8.2.4 Results

The event counts from the τ-embedding, after all signal selection requirements and for the 3 $\Delta\phi(\tau$ jet, $E_{\mathrm{T}}^{\mathrm{miss}})$ cut options are shown in Table 4.39. The transverse mass $m_{\mathrm{T}}(\tau$ jet, $E_{\mathrm{T}}^{\mathrm{miss}})$ distributions are shown in Fig. 4.82 for the 3 $\Delta\phi(\tau$ jet, $E_{\mathrm{T}}^{\mathrm{miss}})$ options without the residual Drell-Yan and $W^{\pm}W^{\mp}$ background contributions.

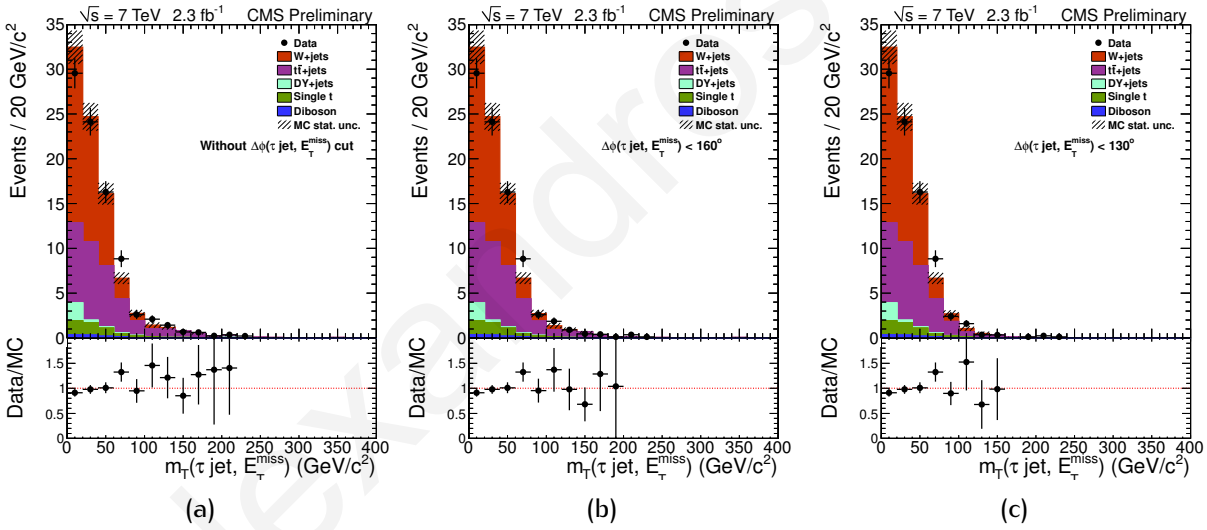

Figure 4.82: Distribution of the transverse mass reconstructed from the τ jet and PF $E_{\mathrm{T}}^{\mathrm{miss}}$ after the signal selection requirements, for 3 $\Delta\phi\left(\tau\text{ jet candidate}, E_{\mathrm{T}}^{\mathrm{miss}}\right)$ options: without $\Delta\phi$ cut (a), $\Delta\phi < 160°$ (b) and $\Delta\phi < 130°$ (c) for embedded data and embedded simulations. The residual Drell-Yan and $W^{\pm}W^{\mp}$ from simulation are not included.

4.8.2.5 Systematic uncertainties

Systematic uncertainties for embedded samples The uncertainty on the single τ jet+$E_{\mathrm{T}}^{\mathrm{miss}}$ trigger efficiency was estimated from the efficiency uncertainties in τ-jet p_{T} bins shown in Fig. 4.13 by taking into account the number of events after the signal selection in each bin. The formula for the total relative uncertainty of the trigger, $\delta\epsilon^{\tau}_{\mathrm{trg}} = \frac{\Delta\epsilon^{\tau}_{\mathrm{trg}}}{\epsilon^{\tau}_{\mathrm{trg}}}$, is similar to Eq. (4.34)

for the trigger scale factor uncertainty, with an additional sum over the run periods

$$\delta^2\epsilon^{\tau}_{\text{trg}} = \frac{\sum_{j}^{\text{Run periods}} \sum_{i}^{\tau\text{-jet } p_{\text{T}} \text{ bins}} \left(N_{ij}\Delta\epsilon^{\tau}_{\text{trg, }ij}\right)^2}{\sum_{j}^{\text{Run periods}} \sum_{i}^{\tau\text{-jet } p_{\text{T}} \text{ bins}} N_{ij}\epsilon^{\tau}_{\text{trg, }ij}}, \tag{4.76}$$

where N_{ij} is the number of events and $\epsilon^{\tau}_{\text{trg, }ij}$ is the single τ jet + $E_{\text{T}}^{\text{miss}}$ trigger efficiency in the τ-jet p_{T} bin i in the run period j. The uncertainty in τ-jet identification, described in Section 4.7.2, was included.

The uncertainty due to the τ-jet energy scale was calculated by fluctuating the τ-jet energies by $\pm 3\%$, as discussed in detail in Section 4.7.3, and propagating the variation to the $E_{\text{T}}^{\text{miss}}$. The number of events and the transverse mass $m_{\text{T}}(\tau\text{ jet}, E_{\text{T}}^{\text{miss}})$ distributions were recorded after the selection. The maximum variation in the event yield was taken as the systematic uncertainty. The transverse mass distributions from the $\pm$JES variations are compared to the baseline distribution in Fig. 4.83. The uncertainty related to the muon

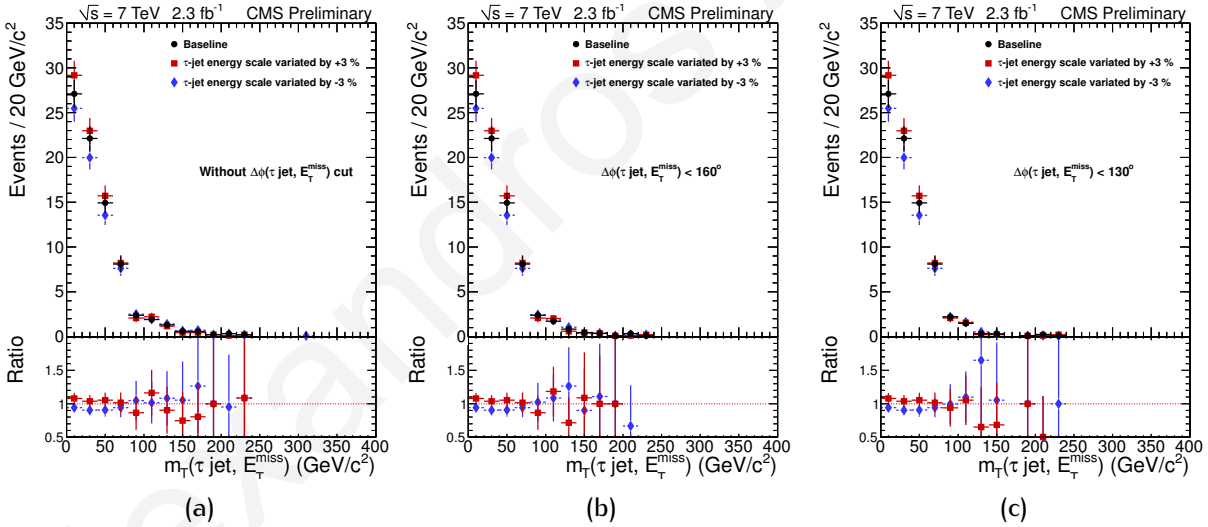

Figure 4.83: Distribution of the transverse mass $m_{\text{T}}(\tau\text{ jet}, E_{\text{T}}^{\text{miss}})$ from the τ-jet energy scale variation after the signal selection requirements, for 3 $\Delta\phi\left(\tau\text{ jet candidate}, E_{\text{T}}^{\text{miss}}\right)$ options: without $\Delta\phi$ cut (a), $\Delta\phi < 160°$ (b) and $\Delta\phi < 130°$ (c). The black dots show the baseline distribution, shown in Fig. 4.82, the red squares the +3% variation, and the blue diamonds the −3% variation. The residual Drell-Yan and $W^{\pm}W^{\mp}$ from simulation are not included.

trigger and identification efficiency was taken to be the statistical error in determining the combined efficiency $\epsilon^{\mu}_{\text{sel}}$ in Eq. (4.74), which was found to be 0.5%. For the fraction of the $W^{\pm} \to \tau^{\pm}\nu_{\tau} \to \mu^{\pm}\nu_{\mu}\nu_{\tau}\nu_{\tau}$ events, the associated uncertainty was taken to be the statistical error in determining $f_{W^{\pm}\to\tau^{\pm}\nu_{\tau}\to\mu^{\pm}\nu_{\mu}\nu_{\tau}\nu_{\tau}}$ in Eq. (4.75), which was found to be 0.7%.

The contamination from QCD multi-jet events after the application of the signal selection requirements was estimated as follows. The normalised number of simulated QCD multi-jet events after τ-jet identification, denoted by $N^{\text{EWK}+t\bar{t}\ \tau}_{\mu\text{-sel}+\tau\text{ id,QCD}}$ was approximately 2. The efficiency of the QCD multi-jet events passing $E_{\text{T}}^{\text{miss}}$ and b-tagging selections, denoted as $\epsilon^{\text{QCD}}_{E_{\text{T}}^{\text{miss}}+\text{b-tag }+\!+\Delta\phi'}$

Table 4.40: Number of embedded simulated EWK + $t\bar{t}$ and signal events, and the fraction of signal events after the b-tagging step in the signal selection for the no-signal hypothesis, and for the signal hypotheses with branching fraction BR($t \to bH^{\pm}$) = 0.03 for the mass range $m_{H^{\pm}} = 80\,\text{GeV}/c^2 - 160\,\text{GeV}/c^2$. The normalisation described in Section 4.8.2.1 was applied. For the signal hypothesis, the $t\bar{t}$ cross section was decreased by the BR($t \to bH^{\pm}$).

Signal Hypothesis	EWK+$t\bar{t}$ events	Signal events	Fraction of signal events
No signal	82.4 ± 2.7	–	–
$m_{H^{\pm}} = 80\,\text{GeV}/c^2$	80.5 ± 2.7	1.03 ± 0.13	$1.26 \pm 0.17\,\%$
$m_{H^{\pm}} = 90\,\text{GeV}/c^2$	80.5 ± 2.7	1.19 ± 0.14	$1.45 \pm 0.18\,\%$
$m_{H^{\pm}} = 100\,\text{GeV}/c^2$	80.5 ± 2.7	1.10 ± 0.13	$1.35 \pm 0.17\,\%$
$m_{H^{\pm}} = 120\,\text{GeV}/c^2$	80.5 ± 2.7	1.22 ± 0.14	$1.49 \pm 0.18\,\%$
$m_{H^{\pm}} = 140\,\text{GeV}/c^2$	80.5 ± 2.7	0.96 ± 0.12	$1.18 \pm 0.16\,\%$
$m_{H^{\pm}} = 150\,\text{GeV}/c^2$	80.5 ± 2.7	1.14 ± 0.14	$1.39 \pm 0.17\,\%$
$m_{H^{\pm}} = 155\,\text{GeV}/c^2$	80.5 ± 2.7	1.14 ± 0.13	$1.40 \pm 0.17\,\%$
$m_{H^{\pm}} = 160\,\text{GeV}/c^2$	80.5 ± 2.7	0.98 ± 0.12	$1.20 \pm 0.16\,\%$

was estimated in the QCD multi-jet background measurement in Section 4.8.1. The estimate for the maximum number of QCD multi-jet events passing both the muon selection and the signal selection then becomes

$$N^{\text{EWK}+t\bar{t}\ \tau}_{\text{signal sel, QCD}} \approx \epsilon^{\text{QCD}}_{E_{\text{T}}^{\text{miss}}+\text{b-tag}\ +\Delta\phi} \times N^{\text{EWK}+t\bar{t}\ \tau}_{\mu\text{-sel}+\tau\ \text{id,QCD}} = 0.11 \times 1.2 = 0.22, \tag{4.77}$$

where a conservative value is obtained by choosing the largest average value of $\epsilon^{\text{QCD}}_{E_{\text{T}}^{\text{miss}}+\text{b-tag}\ +\Delta\phi'}$ out of the 3 $\Delta\phi$ options. Comparing this estimate with the total number of embedded simulated events passing the signal selection, the contamination from QCD multi-jet events was determined to be less than 0.3% and was thus included as a systematic uncertainty to the measurement.

There is also the possibility of the control sample being contaminated from signal events, whereby a muon is generated from the $H^{\pm} \to \tau^{\pm}\nu_{\tau} \to \mu^{\pm}\nu_{\tau}\nu_{\mu}$ decay or the associated $W^{\pm} \to \mu^{\pm}\nu_{\mu}$ decay. The amount of signal events in the embedded sample, after applying the rest of the signal selections, was estimated with simulation. The number of normalised embedded simulated EWK + $t\bar{t}$ and signal events after the b-tagging step in the signal selection are shown in Table 4.40. The branching ratio BR($t \to bH^{\pm}$) was taken to be 0.03, which is also the value used in the analogous contamination study for the QCD multi-jet data-driven measurement in Section 4.8.1.6. The largest fraction of signal events in the mass range $m_{H^{\pm}} = 80\,\text{GeV}/c^2 - 160\,\text{GeV}/c^2$ was found to be $\sim$ 1.6%, and with this under consideration the signal contamination effects were therefore neglected.

The relative systematic uncertainty $\delta N^{\text{EWK}+t\bar{t}\ \tau} = \Delta N^{\text{EWK}+t\bar{t}\ \tau}/N^{\text{EWK}+t\bar{t}\ \tau}$ on the estimate

Table 4.41: Systematic uncertainties of the EWK+$t\bar{t}$ genuine τ background measurement.

Symbol	Description	Uncertainty
$\delta\epsilon^{\tau}_{\text{trg}}$	single τ jet + $E_{\text{T}}^{\text{miss}}$ trigger efficiency	11%
$\delta\epsilon^{\tau}_{\text{id}}$	τ-jet identification	6.0%
$\delta\epsilon^{\tau}_{\text{JES}}$	τ-jet energy scale	6.6%
$\delta N^{\text{EWK}+t\bar{t}\ \tau}_{\text{sel}}$	Control sample stat. uncertainty	3.4%
$\frac{\Delta f_{W^{\pm}\to\tau^{\pm}\nu_{\tau}\to\mu^{\pm}\nu_{\mu}\nu_{\tau}\nu_{\tau}}}{1-f_{W^{\pm}\to\tau^{\pm}\nu_{\tau}\to\mu^{\pm}\nu_{\mu}\nu_{\tau}\nu_{\tau}}}$	Fraction of $W^{\pm}\to\tau^{\pm}\nu_{\tau}\to\mu^{\pm}\nu_{\mu}\nu_{\tau}\nu_{\tau}$ events	0.7%
f_{QCD}	Contamination from QCD multi-jet events	0.3%
$\delta\epsilon^{\mu}_{\text{sel}}$	Muon trigger and identification	0.5%
$\delta N^{\text{EWK}+t\bar{t}\ \tau}$	Combined relative systematic uncertainty	14.6%

for the number of the EWK+$t\bar{t}$ genuine τ events, defined in Eq. (4.69), is then calculated as

$$\begin{aligned}\delta^2 N^{\text{EWK}+t\bar{t}\ \tau} &= \delta^2\epsilon^{\tau}_{\text{trg}} + \delta^2\epsilon^{\tau}_{\text{id}} + \delta^2\epsilon^{\tau}_{\text{JES}} + \delta^2 N^{\text{EWK}+t\bar{t}\ \tau}_{\text{sel}} + \left[\frac{\Delta f_{W^{\pm}\to\tau^{\pm}\nu_{\tau}\to\mu^{\pm}\nu_{\mu}\nu_{\tau}\nu_{\tau}}}{1-f_{W^{\pm}\to\tau^{\pm}\nu_{\tau}\to\mu^{\pm}\nu_{\mu}\nu_{\tau}\nu_{\tau}}}\right]^2 \\ &\quad + f^2_{\text{QCD}} + \delta^2\epsilon^{\mu}_{\text{sel}}\end{aligned} \tag{4.78}$$

where $\delta^2 N^{\text{EWK}+t\bar{t}\ \tau}_{\text{sel}}$ is the statistical uncertainty of the control sample. The values of the systematic uncertainties are summarised in Table 4.41.

Systematic uncertainties for residual di-tau samples The number of residual events was defined in Eq. (4.73) and the corresponding systematic uncertainties were propagated from both $N_i^{\text{normal MC}}$ and $N_i^{\text{embedded MC}}$.

The absolute uncertainty on the trigger was taken as the quadratic sum of the absolute uncertainties from normal and embedded simulation, because for normal simulation the source of the uncertainty is the scale factor, while for embedded simulation the source is the trigger efficiency measured from data. For normal simulation the uncertainty was estimated as described in Section 4.7.1, and for embedded simulation as described in Section 4.8.2.5. For τ-jet identification uncertainty the value from Section 4.7.2 was used.

The uncertainty on jet, τ-jet and $E_{\text{T}}^{\text{miss}}$ energy scales was estimated with the variation technique described in Section 4.7.3. The formula in Eq. (4.73) was applied for each variation case, and the maximum deviation of $N_i^{\text{residual MC}}$ from the nominal value was taken as the overall uncertainty. The uncertainty on pile-up was estimated in a similar method by variating the mean of the target pile-up distributions. The absolute uncertainties on the lepton vetoes and b-jet mis-identification were taken from normal simulation as $N_i^{\text{normal MC}} > N_i^{\text{embedded MC}}$. The cross-section and luminosity uncertainties were taken from Sections 4.7.6 and 4.7.7, since any change in the cross-section or luminosity values would translate to a multiplication of both $N_i^{\text{normal MC}}$ and $N_i^{\text{embedded MC}}$ with the same factor.

Table 4.42: Breakdown of the number of events for the EWK+$t\bar{t}$ fake τ background into contributions from different processes, as estimated from simulations for an integrated luminosity of 2.3 fb^{-1} . This component of the EWK + $t\bar{t}$ backgrounds includes contributions from events whereby an electron, muon, or hadronic jet is mis-identified as the τ jet or the genuine τ is outside the acceptance. The increase in the event rate for W + jets after b-tagging is caused by the b-tagging scale factor applied on a sample with very low surviving events.

Process	$t\bar{t}$	W + jets	$Z^0/\gamma^* \to \ell\ell$	single-top	di-boson
One identified τ jet	15.2 ± 1.8	207 ± 19	19.0 ± 2.8	2.58 ± 0.36	2.67 ± 0.31
Isolated electron veto	8.9 ± 1.3	152 ± 16	15.9 ± 2.6	1.63 ± 0.29	1.89 ± 0.26
Isolated muon veto	5.8 ± 1.0	107 ± 14	5.8 ± 1.5	1.30 ± 0.26	1.38 ± 0.23
≥ 3 hadronic jets	4.35 ± 0.88	3.7 ± 2.4	0.66 ± 0.63	0.48 ± 0.15	0.08 ± 0.05
$E_{\mathrm{T}}^{\mathrm{miss}} > 50$ GeV	3.30 ± 0.77	3.7 ± 2.4	0.04 ± 0.04	0.32 ± 0.13	0.08 ± 0.05
≥ 1 b-tagged jets	2.80 ± 0.69	4.2 ± 3.0	< 0.04	0.17 ± 0.08	0.005 ± 0.004
$\Delta\phi(\tau \text{ jet}, E_{\mathrm{T}}^{\mathrm{miss}}) < 160°$	2.11 ± 0.59	4.2 ± 3.0		0.16 ± 0.08	0.004 ± 0.004
$\Delta\phi(\tau \text{ jet}, E_{\mathrm{T}}^{\mathrm{miss}}) < 130°$	1.79 ± 0.54	4.2 ± 3.0		0.16 ± 0.08	< 0.004

4.8.3 EWK+$t\bar{t}$ fake τ background

After the QCD multi-jet background and EWK+$t\bar{t}$ genuine τ background have been measured, the only background that remained to be determined was the EWK + $t\bar{t}$ background with an electron, muon, or hadronic jet mis-identified as the τ jet or with a genuine τ outside the acceptance. This EWK + $t\bar{t}$ fake τ background was found to be small compared to the other backgrounds and therefore it was estimated with simulation instead of a data-driven method. The estimation was done by performing the signal analysis summarised in Section 4.5 and by matching generator particle information to the selected τ-jet direction. Electrons, muons, and τ's with $p_{\mathrm{T}} > 10$ GeV/c were considered for the matching. If a simulated electron, muon, or τ was found within $\Delta R < 0.1$ of the selected τ jet, a match was considered to be found. If multiple matches were found for the selected τ jet, the τ jet was first checked to match with an electron, then with a muon, and finally with a τ and the first match was taken as the originator of the selected τ jet. If a match was found with both a τ jet and an electron or a muon, i.e. a leptonic τ decay had occurred, the event was rejected, since the leptonic τ decays are counted in the EWK + $t\bar{t}$ background with genuine taus. If no match was found, the selected τ jet was assumed to come from a hadronic jet.

Table 4.42 shows the events for the EWK+$t\bar{t}$ background with fake τ's as a function of the selection cuts. The contribution from $t\bar{t}$ and W + jets events for the fake τ background after the b-tagging was found to be 2.8 ± 0.7 and 4.2 ± 3.0 events, respectively, for an integrated luminosity of 2.3 fb^{-1} . The contribution from $Z^0/\gamma^* \to \ell\ell$, single-top and di-boson events was found to be negligible. The trigger scale factors were taken into account in these numbers, as were the b-tagging scale factors, which can have values greater than one, thus enhancing the number of events passing the b-tagging with respect to the number of events passing the $E_{\mathrm{T}}^{\mathrm{miss}}$ cut.

Table 4.43: Summary of the number of events for the EWK+$t\bar{t}$ fake τ background, as estimated from simulations for an integrated luminosity of 2.3 fb^{-1} and for 3 $\Delta\phi\left(\tau \text{ jet}, E_{\mathrm{T}}^{\mathrm{miss}}\right)$ options: without $\Delta\phi$ cut, $\Delta\phi < 160°$ and $\Delta\phi < 130°$. The quoted event yield (error) was obtained by adding (adding in quadrature) the results from the individual samples shown in Table 4.42 and rounding up to the nearest integer event.

Process	EWK+$t\bar{t}$ fake τ event yield
One identified τ jet	246 ± 208
Isolated electron veto	180 ± 153
Isolated muon veto	121 ± 107
≥ 3 hadronic jets	9 ± 6
$E_{\mathrm{T}}^{\mathrm{miss}} > 50$ GeV	7 ± 5
≥ 1 b-tagged jets	7 ± 5
$\Delta\phi(\tau \text{ jet}, E_{\mathrm{T}}^{\mathrm{miss}}) < 160°$	6 ± 5
$\Delta\phi(\tau \text{ jet}, E_{\mathrm{T}}^{\mathrm{miss}}) < 130°$	6 ± 5

4.9 Summary of results

4.9.1 Data-driven distributions

The data-driven measurements of QCD multi-jet and EWK+$t\bar{t}$ genuine τ processes allowed for key kinematical distributions to be extracted from the data. These distributions of measured backrounds are compared in this section with the distributions from the data for a set of key variables, including hadronic jet-multiplicity, $E_{\mathrm{T}}^{\mathrm{miss}}$, number of b-jets, $\Delta\phi\left(\tau \text{ jet}, E_{\mathrm{T}}^{\mathrm{miss}}\right)$, $m_{\mathrm{T}}(\tau \text{ jet}, E_{\mathrm{T}}^{\mathrm{miss}})$, and the evolution of surviving events through the cut-flow. However, the control sample pre-selection in the EWK+$t\bar{t}$ genuine τ background measurement restricts this procedure to only be possible after the hadronic jets selection step of the complete cut-flow presented in Table 4.29 on page 155. All the following plots are shown at or after this step of the selection.

Fig. 4.84 shows the distributions of number of selected hadronic jets in the event. The first two bins, which are the two most abundant bins, were found to show good agreement between observed and expected events and to be within statistical uncertainty. For the $E_{\mathrm{T}}^{\mathrm{miss}}$ distribution, shown in Fig. 4.85, the number of observed and expected events was found to agree within statistical uncertainty over the full $E_{\mathrm{T}}^{\mathrm{miss}}$ spectrum. It is noteworthy pointing out here the transitional region around 90 GeV, where the EWK background replaces the QCD multi-jet background as the dominant process. Also evident is the fact that, as expected, a large fraction of the QCD multi-jet events is rejected with the $E_{\mathrm{T}}^{\mathrm{miss}} > 50$ GeV cut.

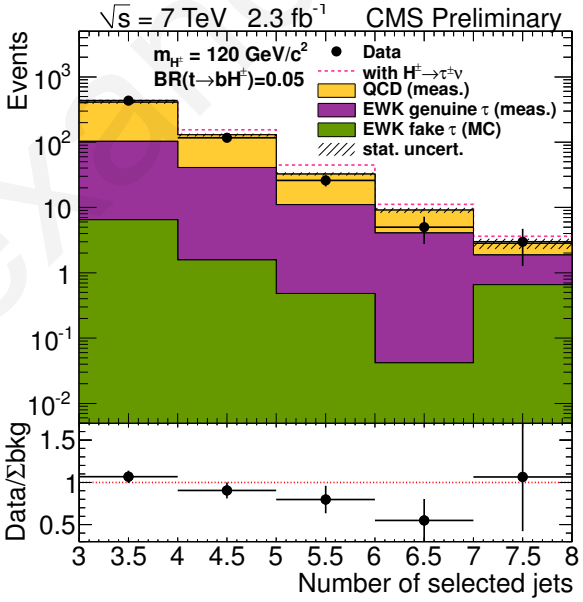

Figure 4.84: Distributions of the number of selected jets for the data and measured backgrounds after τ-jet identification, lepton veto, and requirement of 3 hadronic jets. The expected event yield in the presence of the $t \to bH^{\pm}$, $H^{\pm} \to \tau^{\pm}\nu_{\tau}$ decays is shown as the dashed red line for $m_{H^{\pm}} = 120\,\mathrm{GeV}/c^2$ and assuming $\mathrm{BR}(t \to bH^{\pm}) = 0.05$ and $\mathrm{BR}(H^{\pm} \to \tau^{\pm}\nu_{\tau}) = 1$.

After requiring the presence of at least 1 b-tagged jet in a given event, a slight excess of

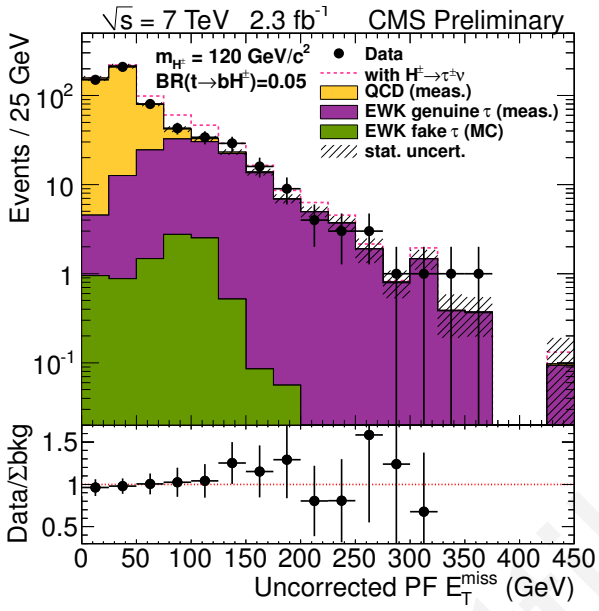

Figure 4.85: Distributions of $E_{\mathrm{T}}^{\mathrm{miss}}$ for the data and measured backgrounds after τ-jet identification, lepton veto, and requirement of 3 hadronic jets. The expected event yield in the presence of the $t \to bH^{\pm}$, $H^{\pm} \to \tau^{\pm}\nu_{\tau}$ decays is shown as the dashed red line for $m_{H^{\pm}} = 120\,\mathrm{GeV}/c^2$ and assuming $\mathrm{BR}(t \to bH^{\pm}) = 0.05$ and $\mathrm{BR}(H^{\pm} \to \tau^{\pm}\nu_{\tau}) = 1$.

observed events was found over the expectation in events that contained exactly 1 b-tagged jet, as can be seen in Fig. 4.86. The origin for this slight excess is not yet understood, but the rest of the spectrum appears to show good agreement between observed and expected number of events, with the two being within statistical uncertainty.

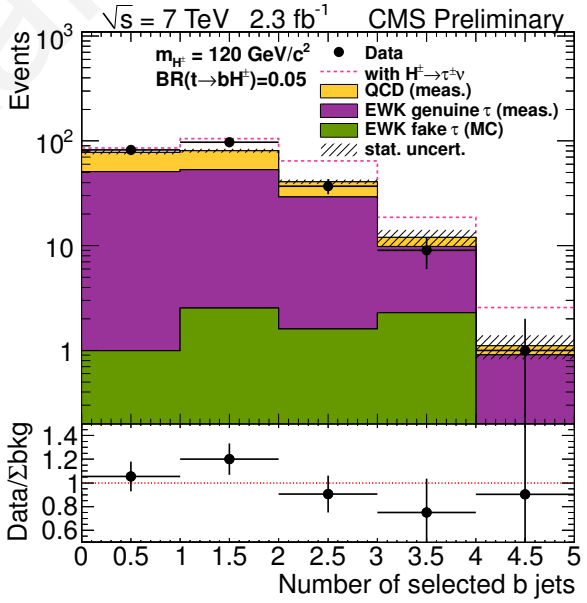

Figure 4.86: Distributions of the number of selected b-jets for the data and measured backgrounds after τ-jet identification, lepton veto, requirement of 3 hadronic jets, and $E_{\mathrm{T}}^{\mathrm{miss}}$ cut. The expected event yield in the presence of the $t \to bH^{\pm}$, $H^{\pm} \to \tau^{\pm}\nu_{\tau}$ decays is shown as the dashed red line for $m_{H^{\pm}} = 120\,\mathrm{GeV}/c^2$ and assuming $\mathrm{BR}(t \to bH^{\pm}) = 0.05$ and $\mathrm{BR}(H^{\pm} \to \tau^{\pm}\nu_{\tau}) = 1$.

Finally, Fig. 4.87 shows the distribution of $\Delta\phi\left(\tau\text{ jet}, E_{\mathrm{T}}^{\mathrm{miss}}\right)$, where a distinct separation between QCD multi-jet and EWK processes is clearly visible. The slight excess from the selection of b-tagged jets is transferred to the $\Delta\phi\left(\tau\text{ jet}, E_{\mathrm{T}}^{\mathrm{miss}}\right)$ distribution. As already discussed in Section 4.5.8, in QCD multi-jet events the $\Delta\phi\left(\tau\text{ jet}, E_{\mathrm{T}}^{\mathrm{miss}}\right)$ distribution structure can be understood by the fact that at LO, two back-to-back jets are produced which are separated in the ϕ-plane by an angle π. The subsequent $E_{\mathrm{T}}^{\mathrm{miss}}$ in the event, which in QCD multi-jet processes is mainly caused by jet resolution/mis-mearurement effects, is primarily caused by the mis-measurement of one of the jets. The $E_{\mathrm{T}}^{\mathrm{miss}}$ vector thus points in the same (opposite) direction as the direction of the under-measured (over-measured) jet. As a consequence, the majority of the events either have a very small angle ($\Delta\phi \to 0$) or a very large angle ($\Delta\phi \to \pi$) between the falsely identified as τ jet hadronic jet and the fake $E_{\mathrm{T}}^{\mathrm{miss}}$, depending on which of the mis-measured jets was identified as a τ jet. The resulting $\Delta\phi\left(\tau\text{ jet}, E_{\mathrm{T}}^{\mathrm{miss}}\right)$ distribution structure provides a powerful handle in controlling the contribution of the QCD multi-jet background in the signal region, by requiring that the τ jet and $E_{\mathrm{T}}^{\mathrm{miss}}$ object are not anti-parallel in the ϕ-plane. For EWK events with the presence of a boosted τ-lepton, the τ's subsequent decay is always connected with the production of a neutrino, which contributes significantly to the $E_{\mathrm{T}}^{\mathrm{miss}}$. In the cases when the τ-lepton is produced boosted, as is the case for $t\bar{t}$ events for example, the neutrino and the rest of the τ-lepton decay products will be co-linear and thus the angle between the reconstructed τ jet and $E_{\mathrm{T}}^{\mathrm{miss}}$ are expected to be small. However, effects such as semi-leptonic b-quark decays and jet mis-measurements can have a smearing effect on the expected $\Delta\phi\left(\tau\text{ jet}, E_{\mathrm{T}}^{\mathrm{miss}}\right)$ distribution which results in the EWK background structure shown in Fig. 4.87.

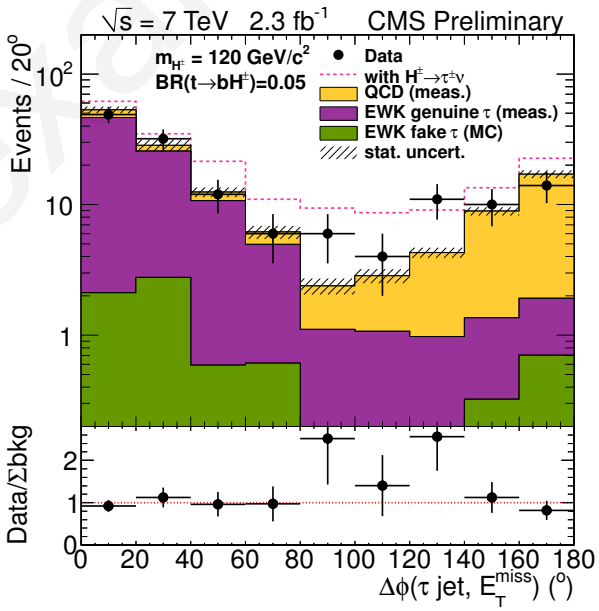

Figure 4.87: Distributions of the $\Delta\phi\left(\tau\text{ jet}, E_{\mathrm{T}}^{\mathrm{miss}}\right)$ for the data and measured backgrounds after τ-jet identification, lepton veto, requirement of 3 hadronic jets, $E_{\mathrm{T}}^{\mathrm{miss}}$ cut and requirement of at least one b-tagged jet. The expected event yield in the presence of the $t \to bH^{\pm}$, $H^{\pm} \to \tau^{\pm}\nu_{\tau}$ decays is shown as the dashed red line for $m_{H^{\pm}} = 120\,\mathrm{GeV}/c^2$ and assuming $\mathrm{BR}(t \to bH^{\pm}) = 0.05$ and $\mathrm{BR}(H^{\pm} \to \tau^{\pm}\nu_{\tau}) = 1$.

The expected and observed event yields after each selection step of the cut-flow are shown in Fig. 4.88, starting from the hadronic jets selection. Approached as a counting experiment, the observation was found to agree with the expectation, within the total uncertainty. The evolution of the background composition and the interplay between the QCD multi-jet and the EWK+$t\bar{t}$ genuine τ backrounds is clearly visible. The fraction of QCD multi-jet events in the selected sample is significantly suppressed with the $E_{\mathrm{T}}^{\mathrm{miss}} > 50\,\mathrm{GeV}$ selection, which was also found to be controllable with the choice of the $\Delta\phi\left(\tau\text{ jet}, E_{\mathrm{T}}^{\mathrm{miss}}\right)$ cut.

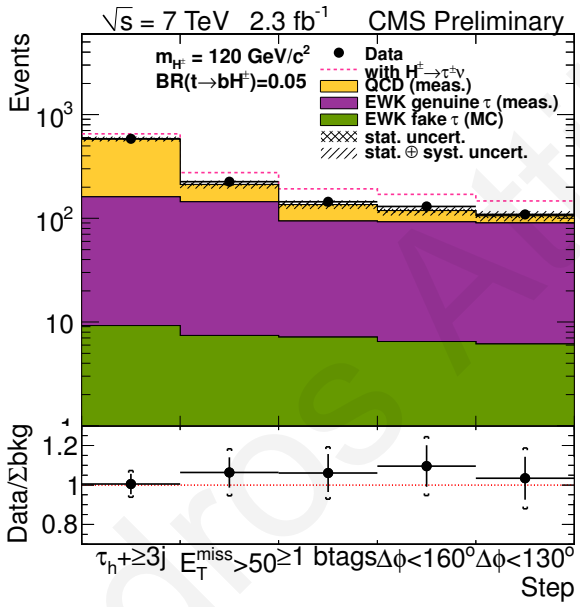

Figure 4.88: The number of observed and expected events after every selection step from the simulations starting from the hadronic jet selection. The expected event yield in the presence of the $t \to bH^{\pm}$, $H^{\pm} \to \tau^{\pm}\nu_{\tau}$ decays is shown as the dashed red line for $m_{H^{\pm}} = 120\,\mathrm{GeV}/c^2$ and assuming $\mathrm{BR}(t \to bH^{\pm}) = 0.05$ and $\mathrm{BR}(H^{\pm} \to \tau^{\pm}\nu_{\tau}) = 1$. The yield from the QCD multi-jet and EWK+$t\bar{t}$ genuine τ backgrounds shown was obtained from the data-driven background measurements. The agreement of the number of expected and observed events within total uncertainty (stat. $\oplus$ syst. $\oplus$ lumi) is shown with brackets.

4.9.2 Event yields

Table 4.44 shows a summary of the event yields and their associated statistical and systematic uncertainties for all relevant processes for 3 $\Delta\phi\left(\tau\text{ jet}, E_{\mathrm{T}}^{\mathrm{miss}}\right)$ options: without $\Delta\phi\left(\tau\text{ jet}, E_{\mathrm{T}}^{\mathrm{miss}}\right)$ cut, for $\Delta\phi\left(\tau\text{ jet}, E_{\mathrm{T}}^{\mathrm{miss}}\right) < 160°$ and for $\Delta\phi\left(\tau\text{ jet}, E_{\mathrm{T}}^{\mathrm{miss}}\right) < 130°$. The main feauture for all 3 cases is the slight excess of observed events in the data over the events expected from the SM, which is expressed as

$$N_{\mathrm{Events}}^{\mathrm{SM}} = N_{\mathrm{Events}}^{\mathrm{QCD\ multi\text{-}jet}} + N_{\mathrm{Events}}^{\mathrm{EWK}+t\bar{t}\ \tau} + N_{\mathrm{Events}}^{Z^0/\gamma^* \to \tau^{\pm}\tau^{\mp}} + N_{\mathrm{Events}}^{\mathrm{W}^{\pm}\mathrm{W}^{\mp} \to \tau^{\pm}\nu_{\tau}\tau^{\mp}\nu_{\tau}} \tag{4.79}$$

(4.80)

where the term $N_{\text{Events}}^{\text{EWK}+t\bar{t}\ \tau}$ includes contributions from both EWK+$t\bar{t}$ genuine τ and EWK+$t\bar{t}$ fake τ backgrounds. Another common feature is that the observed and expected number of events are well within the 1σ range. A signal-candidate event, surviving all signal selection requirements is shown in Fig. 4.89, as reconstructed by Fireworks [38], the official CMS event-display for event visualisation. Additional such pictures can be found in Appendix I.

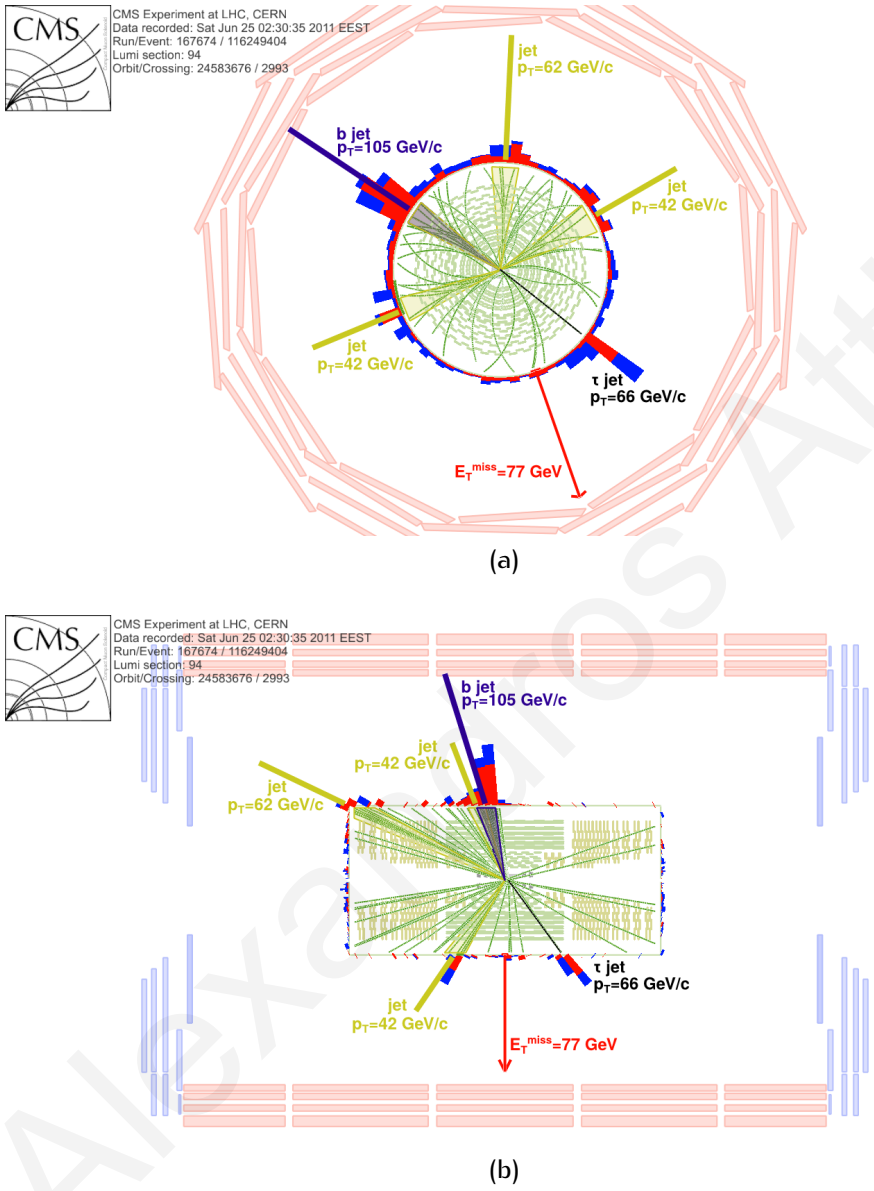

Figure 4.89: Signal-candidate event, surviving all signal selection requirements in the r-ϕ (a) and r-z (b) views, as reconstructed by Fireworks [38], the official CMS event-display for event visualisation. Only tracks with $p_{\text{T}} > 1\,\text{GeV}/c$ are displayed. The HPS τ jet is represented by the black dotted-line, $E_{\text{T}}^{\text{miss}}$ by the red arrow, the hadronic jets with golden cones and the b-jets with dark-blue cones. The ECAL and HCAL energy deposits are represented in red and blue, respectively. The invariant mass of the 2 hadronic jets in the upper hemisphere, with $p_{\text{T}} = 62\,\text{GeV}/c$ and $p_{\text{T}} = 42\,\text{GeV}$, was found to be consistent with a $W^{\pm}$ boson ($m_{\text{jet-jet}} = 80.7\,\text{GeV}/c^2$), while including the b-jet of $p_{\text{T}} = 105\,\text{GeV}/c$ into the calculation gives an invariant mass consistent with a top-quark decay ($m_{\text{jet-jet-b-jet}} = 195\,\text{GeV}/c^2$). Finally, the transverse mass value was calculated to be $m_{\text{T}}(\tau\text{ jet}, E_{\text{T}}^{\text{miss}}) = 40\,\text{GeV}/c^2$. The aforementioned facts, and the event topology, indicate that this signal-candidate event has all the right characteristics of a $t\bar{t}$-like event.

Table 4.44: Summary of the event yield for the signal hypothesis with mass point $m_{H^\pm} = 120\,\text{GeV}/c^2$ and $\text{BR}(t \to bH^\pm) = 0.05$, for the background measurements, and for the data collected at an integrated luminosity of $2.3\,\text{fb}^{-1}$. The luminosity uncertainty is included in the systematic uncertainties. The results are shown for 3 $\Delta\phi\left(\tau\text{ jet}, E_\text{T}^\text{miss}\right)$ options and are in the form Events±Stat.±Syst.

Process	Without $\Delta\phi$ cut	$\Delta\phi < 160°$	$\Delta\phi < 130°$
QCD multi-jet	$42 \pm 3 \pm 1$	$26 \pm 2 \pm 1$	$17.0 \pm 1.2 \pm 0.7$
EWK+$t\bar{t}$ genuine τ	$80 \pm 3 \pm 11$	$78 \pm 3 \pm 11$	$77 \pm 3 \pm 11$
$Z^0/\gamma^* \to \tau^\pm\tau^\mp$ [a]	$6.9 \pm 2.0 \pm 2.2$	$7.0 \pm 2.0 \pm 2.1$	$6.9 \pm 2.0 \pm 2.2$
$\text{W}^\pm\text{W}^\mp \to \tau^\pm\nu_\tau\tau^\mp\nu_\tau$ [a]	$0.35 \pm 0.23 \pm 0.10$	$0.35 \pm 0.23 \pm 0.09$	$0.36 \pm 0.23 \pm 0.09$
EWK+$t\bar{t}$ fake τ	$7 \pm 4 \pm 2$	$6 \pm 3 \pm 1$	$6 \pm 4 \pm 2$
$H^\pm H^\mp + H^\pm\text{W}^\mp$	$57 \pm 4\,^{+8}_{-9}$	$51 \pm 4 \pm 8$	$45 \pm 4 \pm 7$
Expected from SM	$136 \pm 7 \pm 14$	$119 \pm 5 \pm 12$	$107 \pm 6 \pm 14$
Observed in data	144	130	113

[a] The $Z^0/\gamma^* \to \tau^\pm\tau^\mp$ and $\text{W}^\pm\text{W}^\mp \to \tau^\pm\nu_\tau\tau^\mp\nu_\tau$ backgrounds are the residual EWK+$t\bar{t}$ genuine τ backgrounds which are not included in the dedicated data-driven measurement, due to different selection efficiencies of second μ and τ jet for veto and as explained in Section 4.8.2.1.

The transverse mass $m_\text{T}(\tau\text{ jet}, E_\text{T}^\text{miss})$ distributions for the 3 $\Delta\phi\left(\tau\text{ jet}, E_\text{T}^\text{miss}\right)$ options are shown in Figures 4.90, 4.91, and 4.92, without $\Delta\phi\left(\tau\text{ jet}, E_\text{T}^\text{miss}\right)$ cut, for $\Delta\phi\left(\tau\text{ jet}, E_\text{T}^\text{miss}\right) < 160°$ and for $\Delta\phi\left(\tau\text{ jet}, E_\text{T}^\text{miss}\right) < 130°$, respectively. The QCD multi-jet and EWK+$t\bar{t}$ genuine τ backgrounds shapes were determined from the data with dedicated data-driven techniques, while the corresponding transverse mass shape for the EWK+$t\bar{t}$ fake τ background with electrons, muons, or hadronic jets being mis-identified as τ jets was estimated from simulations. Good agreement between the number of observed and expected events was found for the bulk part covered by the region $m_\text{T}(\tau\text{ jet}, E_\text{T}^\text{miss}) < 80\,\text{GeV}/c^2$ of the distribution. The statistical uncertainty of the selected samples was found to dominate the total uncertainty. A common feature that appears for all 3 $\Delta\phi\left(\tau\text{ jet}, E_\text{T}^\text{miss}\right)$ options is the slight excess of observed events in the region of $80\,\text{GeV}/c^2 < m_\text{T}(\tau\text{ jet}, E_\text{T}^\text{miss}) < 100\,\text{GeV}/c^2$. This excess, which is of the order of $\sim 1.5\sigma$ is not yet understood and is thus still under further investigation. Nevertheless, the transverse mass shapes extracted from the data appear to accurately describe the corresponding distribution as observed in the data, and to be in agreement within the total uncertainties for the vast majority of the transverse mass spectrum. The extend of the transverse mass peak-structure in the region of $m_\text{T}(\tau\text{ jet}, E_\text{T}^\text{miss}) \simeq 100\,\text{GeV}$, which as already discussed in Sections 4.5.8 and 4.9.1 is primarily attributed to QCD multi-jet events with mis-measured back-to-back jets, is demonstrated to be effectively controlled by the $\Delta\phi\left(\tau\text{ jet}, E_\text{T}^\text{miss}\right)$ cut option. However, the anomalous excess observed in the region $m_\text{T}(\tau\text{ jet}, E_\text{T}^\text{miss}) \approx 100\,\text{GeV}$ appears to persist for all $\Delta\phi\left(\tau\text{ jet}, E_\text{T}^\text{miss}\right)$ cut options, an observation which seems to suggest that these events are not from QCD multi-jet processes. Nevertheless, no conclusions can be made on this excess which at the moment can only be interpreted as a statistical fluctuation. The incorporation of additional data in future anal-

yses is anticipated to provide more conclusive evidence on the origin of this small excess.

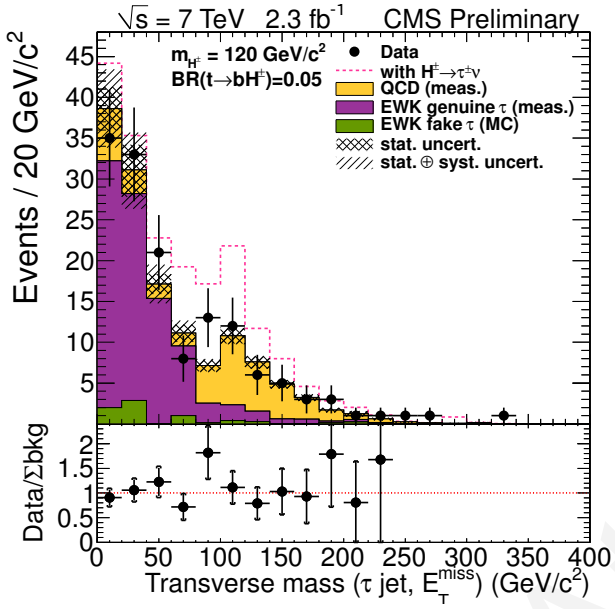

Figure 4.90: The tranverse mass $m_{\mathrm{T}}(\tau\text{ jet}, E_{\mathrm{T}}^{\mathrm{miss}})$ for the data and measured backgrounds for the selection $\Delta\phi\left(\tau\text{ jet}, E_{\mathrm{T}}^{\mathrm{miss}}\right) < 160°$. The expected event yield in the presence of the $t \to bH^{\pm}$, $H^{\pm} \to \tau^{\pm}\nu_{\tau}$ decays is shown as the dashed red line for $m_{H^{\pm}} = 120\,\mathrm{GeV}/c^2$ and assuming $\mathrm{BR}(t \to bH^{\pm}) = 0.05$ and $\mathrm{BR}(H^{\pm} \to \tau^{\pm}\nu_{\tau}) = 1$. The agreement of the number of expected and observed events within total uncertainty (stat. ⊕ syst. ⊕ lumi) is shown with brackets.

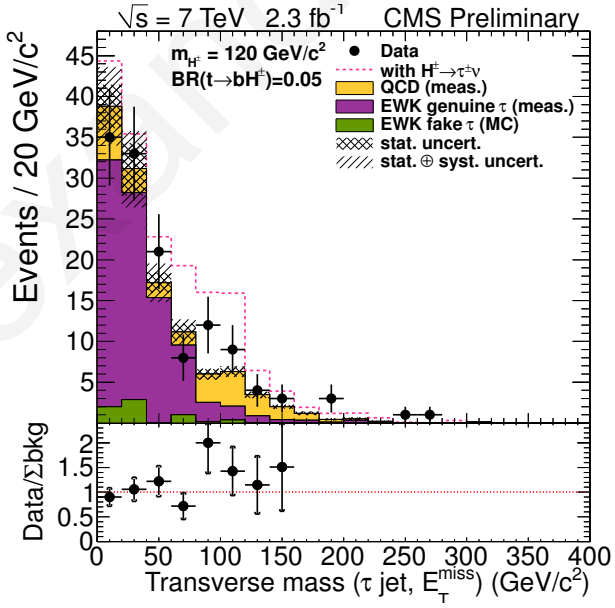

Figure 4.91: The tranverse mass $m_{\mathrm{T}}(\tau\text{ jet}, E_{\mathrm{T}}^{\mathrm{miss}})$ for the data and measured backgrounds for the selection $\Delta\phi\left(\tau\text{ jet}, E_{\mathrm{T}}^{\mathrm{miss}}\right) < 160°$. The expected event yield in the presence of the $t \to bH^{\pm}$, $H^{\pm} \to \tau^{\pm}\nu_{\tau}$ decays is shown as the dashed red line for $m_{H^{\pm}} = 120\,\mathrm{GeV}/c^2$ and assuming $\mathrm{BR}(t \to bH^{\pm}) = 0.05$ and $\mathrm{BR}(H^{\pm} \to \tau^{\pm}\nu_{\tau}) = 1$. The agreement of the number of expected and observed events within total uncertainty (stat. ⊕ syst. ⊕ lumi) is shown with brackets.

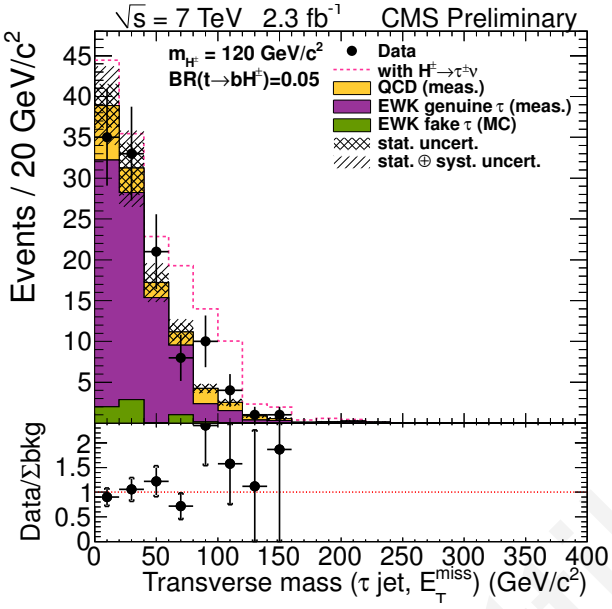

Figure 4.92: The tranverse mass $m_{\mathrm{T}}(\tau\text{ jet}, E_{\mathrm{T}}^{\mathrm{miss}})$ for the data and measured backgrounds for the selection $\Delta\phi\left(\tau\text{ jet}, E_{\mathrm{T}}^{\mathrm{miss}}\right) < 130°$. The expected event yield in the presence of the $t \to bH^{\pm}$, $H^{\pm} \to \tau^{\pm}\nu_{\tau}$ decays is shown as the dashed red line for $m_{H^{\pm}} = 120\,\mathrm{GeV}/c^2$ and assuming $\mathrm{BR}(t \to bH^{\pm}) = 0.05$ and $\mathrm{BR}(H^{\pm} \to \tau^{\pm}\nu_{\tau}) = 1$. The agreement of the number of expected and observed events within total uncertainty (stat. $\oplus$ syst. $\oplus$ lumi) is shown with brackets.

4.9.3 Systematic uncertainties

The evaluation of the systematic uncertainties were discussed in Section 4.7 for the simulations, in Section 4.8.1.3 for the QCD multi-jet background, and in Section 4.8.2.5 for the EWK+$t\bar{t}$ genuine τ background. The values of the systematic uncertainties are summarised in Table 4.45 for the $\Delta\phi\left(\tau\text{ jet}, E_{\mathrm{T}}^{\mathrm{miss}}\right) < 160°$ cut option.

Table 4.45: Breakdown of the systematic uncertainties, quoted in %, for the backgrounds and the signal from $t\bar{t} \to bH^{\pm}bH^{\mp}$ ($H^{\pm}H^{\mp}$) and $t\bar{t} \to bW^{\pm}bH^{\mp}$ ($W^{\mp}H^{\pm}$) processes at $m_{H^{\pm}} = 80\,\text{GeV}/c^2 - 160\,\text{GeV}/c^2$ for the $\Delta\phi < 160°$ option. The $Z^0/\gamma^* \to \ell\ell$ and di-boson backgrounds are negligible after the signal selection requirements, as discussed in Table 4.42, and are thus omitted from the table. For the single-top background the only significant contribution is from the tW-channel, while the s-channel and t-channel contribution is negligible.

Source	$H^{\pm}H^{\mp}$	$W^{\mp}H^{\pm}$	QCD multi-jet	EWK+$t\bar{t}$ genuine τ			EWK+$t\bar{t}$ fake τ		
				Emb. data	$Z^0/\gamma^* \to \tau^{\pm}\tau^{\mp}$	$W^{\pm}W^{\mp} \to \tau^{\pm}\nu_{\tau}\tau^{\mp}\nu_{\tau}$	$t\bar{t}$	tW	W+jets
single τ jet + $E_{\text{T}}^{\text{miss}}$ trigger [a]	12-13	13	-	11	12	11	12	11	14
τ-jet id (excl. R_{τ})	6.0	6.0	-	6.0	6.0	6.0	-	-	-
jet, $\ell \to \tau$ mis-id	-	-	-	-	-	-	15	15	15
JES+$E_{\text{T}}^{\text{miss}}$ +R_{τ}	4.7-14	9.0-18	-	6.6	26	23	8.1	2.4	<10
isolated lepton veto	0.3-0.5	0.5-0.7	-	-	0.9	1.2	0.9	0.6	0.3
b-tagging	1.1-2.1	1.0-1.7	-	-	-	-	1.4	1.6	-
jet→b mis-id	-	-	-	-	2.0	2.6	-	-	4.8
QCD statistical	-	-	6.5	-	-	-	-	-	-
QCD systematic	-	-	3.8	-	-	-	-	-	-
EWK+$t\bar{t}$ τ statistical	-	-	-	3.4	-	-	-	-	-
f_{QCD}	-	-	-	0.3	-	-	-	-	-
$f_{W^{\pm}\to\tau^{\pm}\nu_{\tau}\to\mu^{\pm}\nu_{\mu}\nu_{\tau}\nu_{\tau}}$	-	-	-	0.7	0.1	0.1	-	-	-
muon selections, $\epsilon_{\text{sel}}^{\mu}$	-	-	-	0.5	0.1	0.1	-	-	-
pile-up	0.3-4.2	0.6-5.2	-	-	7.6	3.9	7.1	15	10
MC stat	6.2-11	7.0-10	-	-	29	66	28	49	71
cross-section	$^{+7.0}_{-9.6}$	$^{+7.0}_{-9.6}$	-	-	-	-	$^{+7.0}_{-9.6}$	8.0	5.0
luminosity	2.2	2.2	-	-	2.2	2.2	2.2	2.2	2.2

[a] τ-part of trigger added in quadrature to the $E_{\text{T}}^{\text{miss}}$- part of trigger, which is taken to be 10%.

4.10 Exclusion limits from fits to the reconstructed transverse mass shape

In order to quantify the level of incompatibility of observed experimental data with a signal+background hypothesis, it is common practise to express a given belief as a Confidence Level (CL) [138, 139, 140]. The commonly accepted convention is to require a 95% CL for the exclusion of a signal, even-though the probabilistic interpretation of such a statement as the chance of being correct can be subjective. In this section, the procedure with which the expected and observed 95% CL limits are set on the branching ratio BR($t \to bH^{\pm}$) are explained in detail, using the results summarised in Section 4.9 and the systematic uncertainties discussed in Section 4.7. Firstly, the LHC-recommended procedure in obtaining exclusion limits are discussed in generic form in Section 4.10.1, while in Section 4.10.2 the procedure adopted in the analysis is described in detail, before the results and their interpretation are presented in Section 4.10.2.3.

4.10.1 Exclusion limits: the modified frequentist method

The official LHC guideline for constructing exclusion limits for SM Higgs boson searches is based on the modified frequentist method, often referred to as CL, as documented in Ref. [141]. The limit calculation method is defined by the choice of the test-statistic (q_{μ}) and the way that nuisance parameters (θ)[12] are treated in its construction. The event yields for a given signal+background hypothesis will hereafter be generically denoted as s, while the corresponding symbol for backgrounds will take the generic form of b. These are used to express the event yield in one or multiple bins, while the null results of the signal+background hypothesis will be expressed in terms of a given signal strength modifier, denoted μ, which is taken to change the signal cross-section by a scale μ. The predictions of both s and b event yields are subject to multiple uncertainties, which are all incorporated to the signal and background event yields by introducing a nuisance parameter vector space, such that $s \equiv s(\vec{\theta})$ and $b \equiv b(\vec{\theta})$. In this way, the signal and background events yields become functions of the nuisance parameters. The systematic uncertainties are taken to be 100% correlated or uncorrelated, while systematic errors that are partially correlated are either broken down to sub-components that are 100% correlated or uncorrelated. Alternatively, they are declared to be either 100% or uncorrelated, with the choice being based on what is appropriate or more conservative. The aforementioned approach ensures that all constraints can be included in the likelihood functions in a clean factorised form.

[12] Any parameter which, although of no immediate interest, must be accounted for in the analysis of those parameters which are of interest.

4.10.1.1 Systematic uncertainty probability distribution function

The systematic error Probability Density Functions (PDFs), denoted $\rho\left(\theta|\tilde{\theta}\right)$, reflect the degree of belief on what the true value of the nuisance parameters is, with $\tilde{\theta}$ being the default nuisance parameter value. These systematic error PDFs can have various forms, depending on the nuisance parameter under consideration and the manner with which one chooses to treat it, and include flat priors, Gaussian PDFs (or truncated Gaussian PDFs) to describe uncertainties on parameters that can be both positive and negative (or only positive) and log-normal PDFs. The latter are expressed as

$$\rho\left(\theta|\tilde{\theta}\right) = \frac{1}{\sqrt{2\pi}\ln\kappa}\exp\left(-\frac{\left[\ln\left(\theta/\tilde{\theta}\right)\right]^2}{2\left(\ln\kappa^2\right)}\right)\frac{1}{\theta}, \tag{4.81}$$

where the term κ incorporates the relative systematic uncertainty (δ) associated with the best estimate of $\tilde{\theta}$, such that

$$\kappa = 1 + \delta. \tag{4.82}$$

Example log-normal distributions are presented in Fig. 4.93, for the case of typical systematic uncertainties (9% and 15%) and for the extreme case of overwhelmingly large systematic uncertainties (200%).

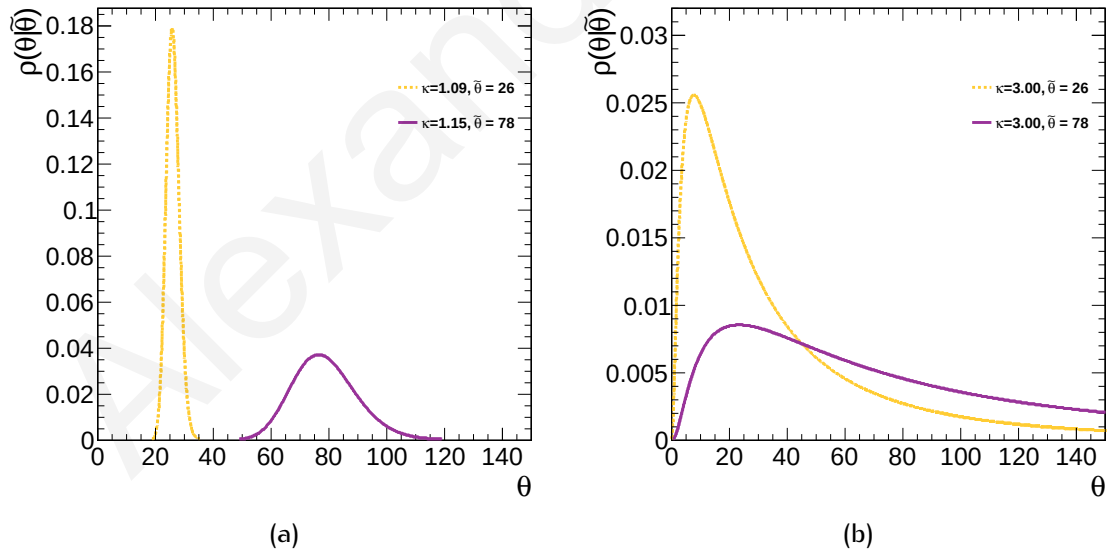

Figure 4.93: Example log-normal distributions with typical (a) and 200% (b) systematic uncertainties.

From Eq. (4.81), by writing $\ln\left(\theta/\tilde{\theta}\right) = \ln\theta - \ln\tilde{\theta}$, it is evident that the log-normal distribution is just a Gaussian with mean $\ln\tilde{\theta}$ and variance $\sigma^2 = (\ln\kappa)^2$. Therefore, the log-normal PDF is simply a Gaussian distribution in the x-axis log-scale, which assigns equal probabilities for the nuisance parameter θ to be a factor κ^n larger (or smaller) than the best estimate $\tilde{\theta}$. In the limiting case where the relative systematic uncertainty approaches zero,

the log-normal distribution becomes a Gaussian[13]

$$\lim_{\delta\to 0}\rho\left(\theta\right) \;=\; \frac{1}{\sqrt{2\pi}\delta}\exp\left(-\frac{\left(\theta-\tilde{\theta}\right)^2}{2\delta^2}\right)\frac{1}{\theta} \tag{4.83}$$

with mean $\tilde{\theta}$ and variance $\sigma^2 = \delta^2$, as it can be seen in Fig. 4.93 (a). Conversely, the log-normal distribution's connection to the Gaussian becomes increasingly inappropriate for higher values of δ, as shown in Fig. 4.93 (b). In general, the log-normal distribution differs from the Gaussian distribution in a variety of ways. Most importantly, the former has larger tails than the latter, which implies that an excess of events will be treated more conservatively in the case where background uncertainties are treated with log-normal distributions rather than Gaussian. Also, the low-end tail of a log-normal distribution terminates at zero, thus forbidding negative θ values, unlike the Gaussian case which requires to be truncated to remove such unphysical θ values.

It is convenient to reinterpret the systematic uncertainty PDFs $\rho\left(\theta|\tilde{\theta}\right)$ as posteriors of some real or imaginary measurements, thus decoupling the need for Bayesian a priori information, and allow a purely frequentist approach to the issue. In this conceptual step, the systematic uncertainty PDFs can be re-formulated using Bayes' theorem as

$$\rho\left(\theta|\tilde{\theta}\right) \sim p\left(\tilde{\theta}|\theta\right)\cdot\pi_\theta\left(\theta\right) \tag{4.84}$$

where the functions $\pi_\theta\left(\theta\right)$ are hyper-priors of the hypothetical real or imaginary measurements. By choosing flat hyper-prior functions, the mapping of Bayesian posterior PDFs $\rho\left(\theta|\tilde{\theta}\right)$ to frequentist auxiliary measurements PDFs $p\left(\tilde{\theta}|\theta\right)$, allows one to represent all systematic uncertainties in the frequentist context. In this way, a systematic uncertainty PDF is expressed as the posterior $\rho\left(\theta|\tilde{\theta}\right)$ constructed from a fictional auxiliary measurement, whose systematic PDF is $p(\tilde{\theta}|\theta)$. The latter can be used to constrain the main measurement and to construct sampling distributions of the test-statistic in pure frequentist calculations.

4.10.1.2 Calculating observed limits

For a given experimental observation with a set of observed events N_i^{obs} in bin i of the shape considered, a likelihood function is constructed of the form

$$\mathcal{L}(\text{data}|\mu,\vec{\theta}) = \prod_i^{\text{All bins}}\frac{\left[\mu s(\vec{\theta}_i)+b_i(\vec{\theta})\right]^{N_i^{\text{obs}}}}{N_i^{\text{obs}}!}\;e^{-\left[\mu s(\vec{\theta}_i)+b_i(\vec{\theta})\right]}\cdot p\left(\tilde{\vec{\theta}}|\vec{\theta}\right). \tag{4.85}$$

This expression quantifies the probability that a given set of data, which are Poissonianly distributed, will be observed for the specified parameters μ, $s(\vec{\theta})$ and $b(\vec{\theta})$. The Poisson product describes the combined probability that, in each of the bins indexed i, which has

[13] Using the identity $\ln(1+x) = \sum_{n=1}^{\infty}\frac{(-1)^{n+1}}{n}x^n$ for $|x|\leq 1$, it follows that $\lim_{x\to 0}\ln(1+x)\approx x$.

Poisson mean of $\mu s(\vec{\theta}_i) + b_i(\vec{\theta})$, an event yield of N_i^{obs} will be observed. The signal strength modifier μ is a parameter that can be used to adjust the event yield expected from a given signal+background hypothesis, while the term $\vec{\theta}$ represents the full set of nuisance parameters.

In order to assess the degree of compatibility between a given set of data and the signal+background hypothesis for a given trial signal strength modifier (μ), and the background-only hypothesis with zero signal ($\mu = 0$), the construction of a test-statistic is required. The chosen test-statistic is based on the profile likelihood ratio

$$\tilde{q}_\mu \quad = \quad -2\ln(\mathcal{Q}) \tag{4.86}$$

where

$$\mathcal{Q} \quad = \quad \frac{\mathcal{L}(\text{data}|\mu, \hat{\vec{\theta}}_\mu)}{\mathcal{L}(\text{data}|\hat{\mu}, \hat{\vec{\theta}})} \quad , \quad 0 \leq \hat{\mu} \leq \mu. \tag{4.87}$$

The term $\hat{\vec{\theta}}_\mu$ refers to the nuisance parameter vector that maximises the likelihood $\mathcal{L}(\text{data}|\mu, \vec{\theta}_\mu)$ for a given trial value of the signal strength modifier μ and for a given set of experimentally observed data or generated toy MC pseudo-data. The pair of parameter estimators $\hat{\mu}$ and $\hat{\vec{\theta}}$ correspond to the parameters that yield the global maximum of the likelihood, for any of the allowed signal strength modifier μ in the range $0 \leq \hat{\mu} \leq \mu$.

The constraints imposed on the allowed values that $\hat{\mu}$ can take, ensure that the unphysical cases where the signal is assigned negative rate is forbidden ($\hat{\mu} \geq 0$ constraint) while also guaranteeing that a one-sided confidence interval will be obtained that is not detached from zero ($\hat{\mu} \geq \mu$ constraint). In other words, any upward fluctuations of the data or toy MC pseudo-data, such that $\hat{\mu} \geq \mu$, are not considered as evidence against the signal+background hypothesis of a signal being present with a trial signal strength modifier μ.

Having defined the test-statistic $\tilde{q}_\mu$ in Eq. (4.86), what is required for the calculation of an observed limit on the signal strength modifier μ is to evaluate 3 key variables; the observed test-statistic value $\tilde{q}_\mu^{\text{obs}}$, which is unique for a given trial value of μ, and the nuisance parameter vectors $\hat{\vec{\theta}}_\mu^{\text{obs}}$ and $\hat{\vec{\theta}}_{\mu=0}^{\text{obs}}$ that best describe the observed data, for the signal+background hypothesis and background-only hypothesis, respectively. These 2 vectors are determined by maximising the likelihoods in Eq. (4.85)

$$\hat{\vec{\theta}}_\mu^{\text{obs}} \quad \equiv \quad \frac{d\mathcal{L}(\text{data}|\mu, \vec{\theta})}{d\vec{\theta}} = 0, \tag{4.88}$$

$$\hat{\vec{\theta}}_{\mu=0}^{\text{obs}} \quad \equiv \quad \frac{d\mathcal{L}(\text{data}|\mu = 0, \vec{\theta})}{d\vec{\theta}} = 0. \tag{4.89}$$

Once the values of the test-statistic $\tilde{q}_\mu$, and the nuisance parameter vectors $\hat{\vec{\theta}}_\mu^{\text{obs}}$ and $\hat{\vec{\theta}}_{\mu=0}^{\text{obs}}$ are determined, the next step is to generate toy MC pseudo-data in order to construct the PDFs of the test-statistic $\tilde{q}_\mu$ for the signal+background hypothesis and background-only

hypothesis, denoted $f(\tilde{q}_\mu|\mu, \hat{\vec{\theta}}^{\text{obs}}_\mu)$ and $f(\tilde{q}_\mu|\mu = 0, \hat{\vec{\theta}}^{\text{obs}}_{\mu=0})$, respectively. Example test-statistic PDF distributions are shown in Fig. 4.94.

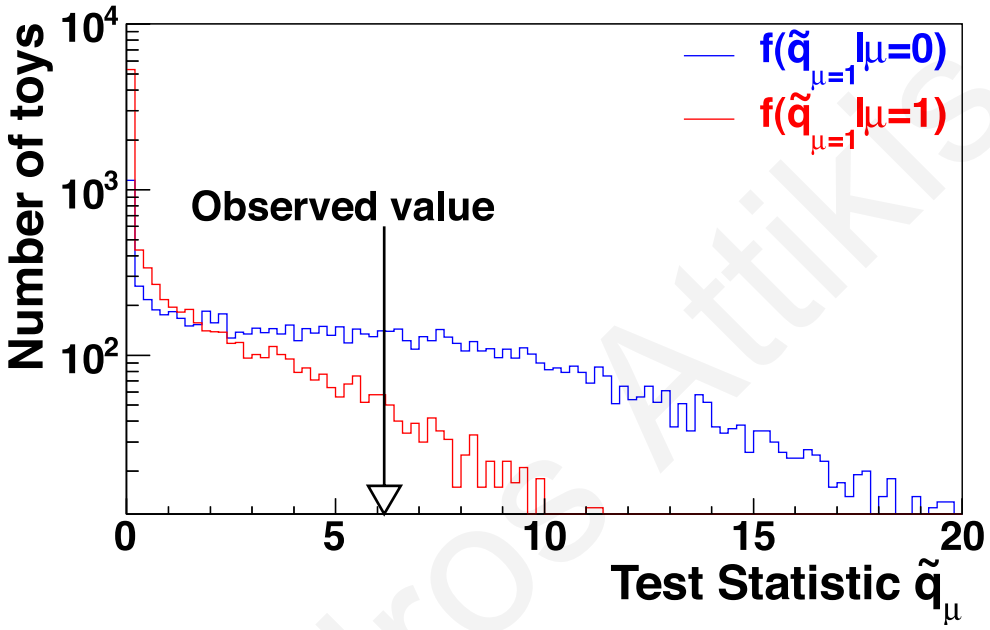

Figure 4.94: Example test-statistic distributions for ensembles of toy MC pseudo-data, generated for a signal+background hypothesis and a background-only hypothesis. The experimentally observed value of the test-statistic is also indicated. Taken from Ref. [141].

In order to generate the toy MC pseudo-data, the vectors $\hat{\vec{\theta}}^{\text{obs}}_\mu$ and $\hat{\vec{\theta}}^{\text{obs}}_{\mu=0}$ remain fixed to the maximum likelihood estimates, as determined by fitting the observed data, although they are allowed to vary for fitting purposes. What is varied in this process is the number of observed toy MC pseudo-data (N^{toy}) which replaces the number of experimental data (N^{obs}), and is generated by sampling from a Poisson distribution with mean $= \mu s(\hat{\vec{\theta}}^{\text{obs}}_\mu) + b(\hat{\vec{\theta}}^{\text{obs}}_{\mu=0})$ and mean $= b(\hat{\vec{\theta}}^{\text{obs}}_{\mu=0})$, for the signal+background hypothesis and background-only hypothesis, respectively. Each set of toy MC pseudo-data thus has a different value for N^{toy} , since this number is sampled from a Poisson distribution of different mean, given that the signal and background events yields are functions of the nuisance parameter values. In this way, the likelihoods are constructed using events yields that account for fluctuations from systematic uncertainties sources and for possible statistical fluctuations of the data.

The PDF distributions $f(\tilde{q}_\mu|\mu, \hat{\vec{\theta}}^{\text{obs}}_\mu)$ and $f(\tilde{q}_\mu|\mu = 0, \hat{\vec{\theta}}^{\text{obs}}_{\mu=0})$ are used to quantify the p-values associated with the signal+background hypothesis and background-only hypothesis,

denoted p_μ and $p_{\mu=0}$, respectively

$$\begin{aligned} p_\mu &= P(\tilde{q}_\mu \geq \tilde{q}_\mu^{\text{obs}} | \text{signal+background}) = \text{CL}_{s+b} \\ \Rightarrow \text{CL}_{s+b} &= \int_{\tilde{q}_\mu^{\text{obs}}}^{\infty} f(\tilde{q}_\mu | \mu, \vec{\hat{\theta}}_\mu^{\text{obs}}) d\tilde{q}_\mu, \end{aligned} \tag{4.90}$$

$$\begin{aligned} 1 - p_{\mu=0} &= P(\tilde{q}_\mu \geq \tilde{q}_\mu^{\text{obs}} | \text{background-only}) = \text{CL}_{b\text{-only}} \\ \Rightarrow \text{CL}_{b\text{-only}} &= \int_{\tilde{q}_\mu^{\text{obs}}}^{\infty} f(\tilde{q}_\mu | \mu = 0, \vec{\hat{\theta}}_{\mu=0}^{\text{obs}}) d\tilde{q}_\mu, \end{aligned} \tag{4.91}$$

The term CL_{s+b} describes the probability that a test-statistic with a value greater or equal to the one evaluated from data $\tilde{q}_\mu^{\text{obs}}$ will be observed under the signal+background hypothesis; that is, how compatible is the test-statistic value of $\tilde{q}_\mu^{\text{obs}}$ with the signal+background hypothesis. Similarly, the term $\text{CL}_{b\text{-only}}$ describes the probability that the observed value of $\tilde{q}_\mu^{\text{obs}}$ is compatible with a background-only hypothesis. By calculating the ratio of these two probabilities as

$$\text{CL}_s(\mu) = \frac{\text{CL}_{s+b}}{\text{CL}_{b\text{-only}}} \tag{4.92}$$

one has the final ingredient for quantifying the probability that a given signal+background hypothesis, with a certain trial signal strength modifier μ, is compatible with the observed data. In particular, the resultant value of $\text{CL}_s(\mu)$ is compared with the parameter α, which takes a custom pre-defined value. The latter defines the CL that the signal+background hypothesis will be tested with, through the relation

$$\text{CL} = (1 - \alpha)\,. \tag{4.93}$$

The signal+background hypothesis is then said to be excluded with a $(1-\alpha)$ $\text{CL}_s(\mu)$ CL, if for the given trial signal strength modifier μ one finds that $\text{CL}_s(\mu) \leq \alpha$. It is noteworthy to mention that this method provides conservative limits, with the actual CL of the exclusions normally being higher than $(1-\alpha)$. So, for example, in the choice of $\alpha = 0.05$, if $\text{CL}_s(\mu) = \alpha$ the signal+background hypothesis is set to be excluded with a 95% CL upper limit on the signal strength modifier μ, and is denoted as $\mu^{95\%\text{CL}}$. In the case where $\text{CL}_s(\mu) > \alpha$ the whole procedure is repeated, each time with an appropriately adjusted trial signal strength modifier μ until the desirable convergence is achieved.

4.10.1.3 Calculating expected limits

The expected exclusion limits for a given trial signal strength modifier μ, are obtained with an algorithm that is almost identical to that used for extracting the observed limits. The procedure starts with the generation of a large set of toy MC pseudo-data, under the assumption of a background-only hypothesis ($\mu = 0$), to obtain a set of event yields N^{toy}

(which replaces N^{obs}) from a Poisson distribution of the form

$$p(N_i^{toy}; \lambda) = \frac{\lambda^{N_i^{toy}} e^{-\lambda}}{N_i^{toy}!} \tag{4.94}$$

where

$$\lambda = \sum_{j}^{\text{all backgrounds}} b_j(\vec{\theta}). \tag{4.95}$$

These toy MC pseudo-data are treated as if they were in fact real experimental data and are used in calculating the test-statistics $\tilde{q}_\mu$ as described in Section 4.10.1.2 with

$$\mathcal{Q} = \frac{\mathcal{L}(\text{pseudo-data}|\mu, \hat{\vec{\theta}}_\mu)}{\mathcal{L}(\text{pseudo-data}|\hat{\mu}, \hat{\vec{\theta}})} \quad , \quad 0 \leq \hat{\mu} \leq \mu. \tag{4.96}$$

The p-values, p_μ and $p_{\mu=0}$, are also evaluated using dedicated toy MC pseudo-data for the signal+background hypothesis (μ) and for the background-only hypothesis ($\mu = 0$). Once the p-values are determined, the value of $CL_s(\mu)$ is compared to the parameter α to determine whether the requirement $CL_s(\mu) \leq \alpha$ is met. The procedure is repeated by adjusting the trial value of the signal strength modifier μ until $CL_s(\mu) = \alpha$ and a corresponding $\mu^{95\%CL}$ is obtained. By repeating this iteration several times, a distribution of $\mu^{95\%CL}$ can be obtained, which can be converted to a PDF distribution and consequently into a CDF (see Fig. 4.95 for Gaussian examples of such distributions). The CDF distribution is then used to finally obtain the expected limit on the signal strength modifier μ, by simply reading off the $\mu^{95\%CL}$ which corresponds to the CDF quantile at 0.5. Similarly, the $\pm 1\sigma$ (68%) and $\pm 2\sigma$ (95%) bands of this expected median are obtained by reading off the CDF quantile at 0.16 and 0.84, and 0.025 and 0.975, respectively, as illustrated in Fig. 4.95 (b).

4.10.2 Upper limits on the branching ratio $t \to bH^{\pm}$

4.10.2.1 Test-statistic used and method employed

In this analysis, upper limits were imposed on the branching ratio $BR(H^{\pm} \to \tau^{\pm}\nu_\tau)$ by fitting the transverse mass shapes $m_T(\tau \text{ jet}, E_T^{miss})$, as determined from all the signal and background processes, to the one reconstructed from the experimental data. To calculate an upper limit for the excess of the events with the expected contributions from the SM, a modified frequentist method (CLs [142, 143, 144]) was performed using the Limits and Signifcance (LandS) software [145], with a 95% CL being used. The transverse mass distribution $m_T(\tau \text{ jet}, E_T^{miss})$ reconstructed from the data, along with those extracted for the signal and background events, shown in Figures 4.90, 4.91, and 4.92, were taken into account, which define the event yield from each relevant process for a given transverse mass bin i. The data-cards used for running LandS, which present the sources of systematic uncertainties

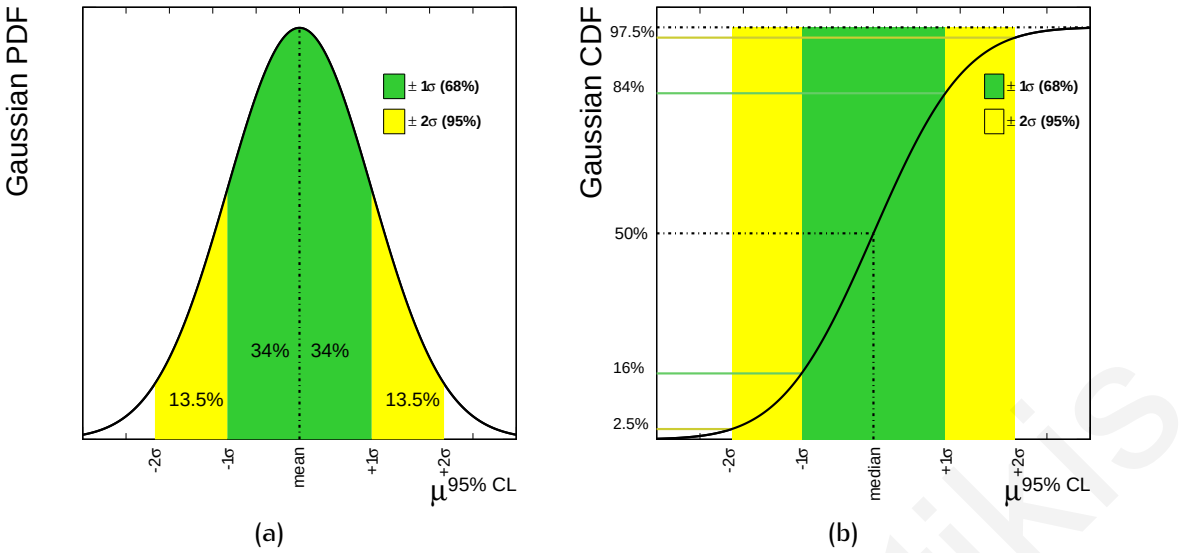

Figure 4.95: Example PDF (a) and CDF (b) distributions of a Gaussianly distributed $\mu^{95\%\text{CL}}$, showing the $\pm 1\sigma$ and $\pm 2\sigma$ bands, which correspond to an area coverage of 68% and 95%, respectively.

and their associated κ-values are shown in Appendix H.

The methodology adopted in obtaining the observed and expected upper limits on the branching ratio $\text{BR}(H^\pm \to \tau^\pm \nu_\tau)$, is similar to the one described in Section 4.10.1, with the exception that a slightly different test-statistic was used instead, and in particular a LEP-type $\text{CL}_s(\mu)$ test-statistic. The signal+background hypothesis under investigation dictates that the complete expression for the total expected event yield must be written in the form

$$\mu s(\vec{\theta}) + b(\vec{\theta}) \equiv s(\mu, \vec{\theta}) + b(\mu, \vec{\theta}) \tag{4.97}$$

$$= \mu^2 \cdot N_{H^\pm H^\mp}(\vec{\theta}) + 2\mu \cdot (1-\mu) \cdot N_{H^\pm \text{W}^\mp}(\vec{\theta}) + (1-\mu)^2 \cdot N_{W^\pm \text{W}^\mp}(\vec{\theta}) + \sum_{i}^{\text{all backgrounds}} b_i(\mu, \vec{\theta}), \tag{4.98}$$

where the terms $N_{H^\pm H^\mp}(\vec{\theta})$, $N_{H^\pm \text{W}^\mp}(\vec{\theta})$ and $N_{W^\pm \text{W}^\mp}(\vec{\theta})$ are the MC signal event yields before multiplying by $\text{BR}(H^\pm \to \tau^\pm \nu_\tau)$. The last term, which incorporates the contribution from all backgrounds, includes a contribution from the EWK+$t\bar{t}$ fake τ backgrounds in $t\bar{t}$ processes that is dependent on the signal strength modifier μ

$$\sum_{i=0}^{\text{all backgrounds}} b_i(\mu, \vec{\theta}) = \sum_{i=1}^{\text{all backgrounds}} b_i(\vec{\theta}) + (1-\mu)^2 \cdot N_{t\bar{t}}^{\text{EWK+}t\bar{t}\text{ fake }\tau}(\vec{\theta}). \tag{4.99}$$

The signal event yields after all signal selection requirements and as a function of the signal strength modifier $\mu = \text{BR}(t \to bH^\pm)$ are graphically illustrated in Figures 4.96 and 4.97, separately for the $t\bar{t} \to bH^\pm b\text{W}^\mp$ and $t\bar{t} \to bH^\pm bH^\mp$ processes and for the mass points $m_{H^\pm} = 80, 120, 140$ and $160\,\text{GeV}/c^2$. The SM $t\bar{t}$ event yield from the process $t\bar{t} \to bW^\pm b\text{W}^\mp$ and the corresponding total MSSM $t\bar{t}$ event yield are also shown. For $\mu > 0$, the $t\bar{t}$ event

yield from MSSM exceeds the one expected from the SM, a feature which was anticipated due to the fact that in the MSSM the light charged Higgs boson decays exclusively to a τ-lepton.

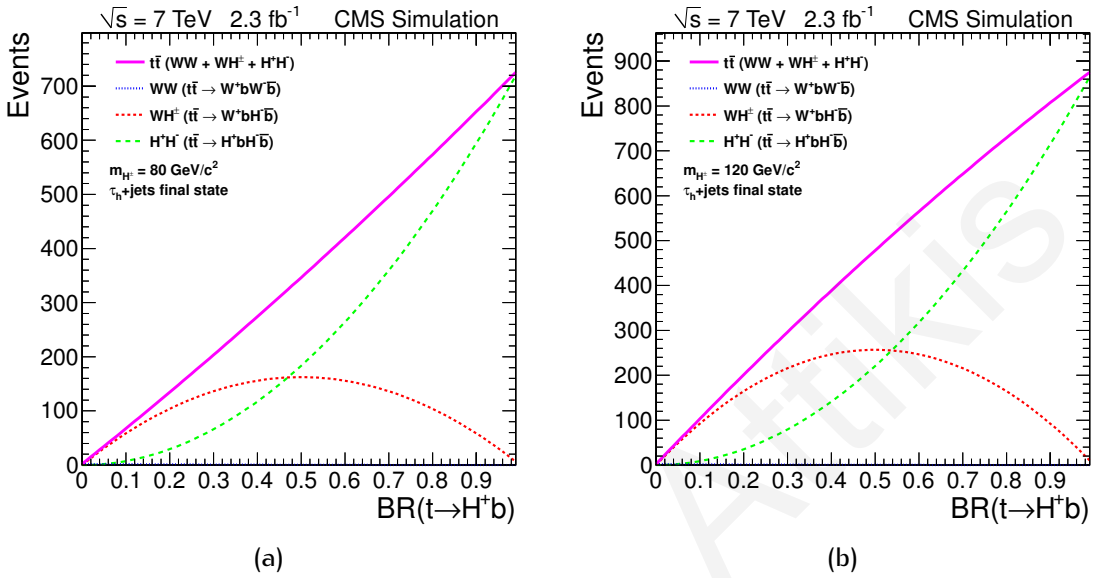

Figure 4.96: The expected number of $t\bar{t}$ events after the full event selection for $m_{H^\pm} = 80\,\text{GeV}/c^2$ (a) and $m_{H^\pm} = 120\,\text{GeV}/c^2$ (b), as a function of $\mu = \text{BR}(t \to bH^\pm)$. Expectations are shown separately for the $\text{W}^\mp H^\pm$, $H^\pm H^\mp$, and $W^\pm\text{W}^\mp$ contributions.

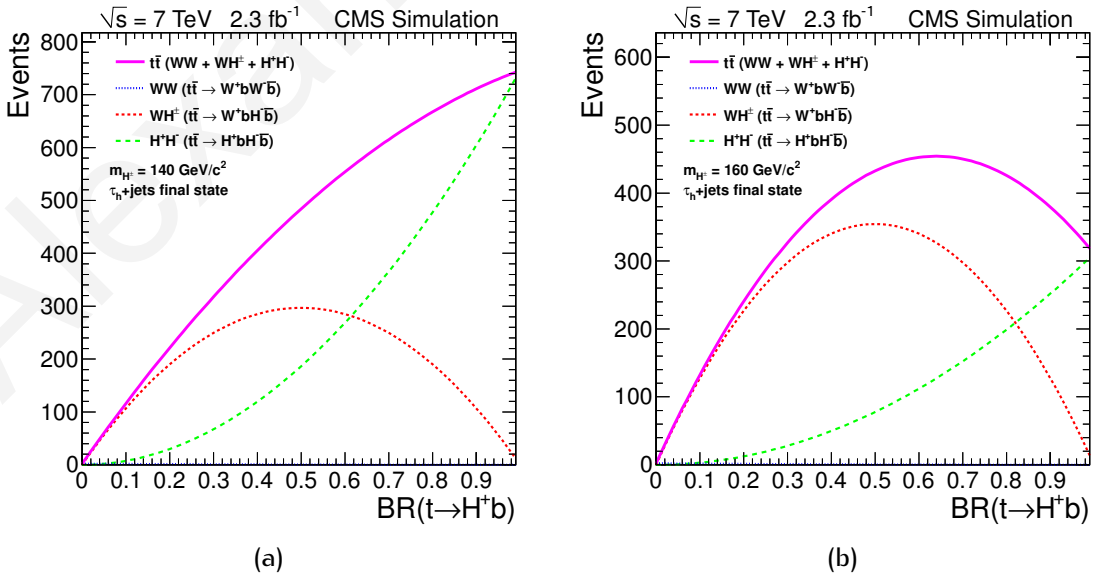

Figure 4.97: The expected number of $t\bar{t}$ events after the full event selection for $m_{H^\pm} = 140\,\text{GeV}/c^2$ (a) and $m_{H^\pm} = 160\,\text{GeV}/c^2$ (b), as a function of $\mu = \text{BR}(t \to bH^\pm)$. Expectations are shown separately for the $\text{W}^\mp H^\pm$, $H^\pm H^\mp$, and $W^\pm\text{W}^\mp$ contributions.

With the expression for the total expected event yield in Eq. (4.97), the likelihood function

defined Eq. (4.85) now takes the form

$$\mathcal{L}(\text{data}|\mu,\vec{\theta}) \;=\; \prod_{i}^{\text{All } m_{\text{T}} \text{ bins}} \frac{\left[s_i(\mu,\vec{\theta}) + \sum_{j=0}^{\text{all backgrounds}} b_{ij}(\mu,\vec{\theta})\right]^{N_i^{\text{obs}}}}{N_i^{\text{obs}}!}\; e^{-\left[s_i(\mu,\vec{\theta}) + \sum_{j=0}^{\text{all backgrounds}} b_{ij}(\mu,\vec{\theta})\right]}, \tag{4.100}$$

where $\mu = \text{BR}(H^{\pm} \to \tau^{\pm}\nu_{\tau})$ and $\vec{\theta}$ is a vector that includes the full set of nuisance parameters. It should be noted that, unlike in Eq. (4.87), the signal strength modifier μ was not constrained in Eq. (4.100) but instead allowed to float freely. In principle however, one could employ simple physics arguments to impose the constrain $0 \leq \mu \leq 1$ to Eq. (4.100).

The predictions of both $\mu s(\vec{\theta})$ and $b(\vec{\theta})$ were subject to the uncertainties summarised in Table 4.45, which were all accounted for by expressing these event yields as functions of the nuisance parameter vector. The full set of nuisance parameters were sampled from a Gaussian distribution with a mean $\tilde{\theta} = 0$ and a unit standard deviation $\sigma_{\tilde{\theta}} = 1$

$$p(\theta; \tilde{\theta} = 0, \sigma_{\tilde{\theta}} = 1) = \frac{1}{\sqrt{2\pi}} e^{-\frac{\theta^2}{2}}. \tag{4.101}$$

Therefore, the signal and background events yields in Eq. (4.98), were modified for a given transverse mass bin i according to the table of systematic errors in Table 4.45, using the relation

$$N_{x,\,i}^{\text{log-normal}} \;=\; N_{x,\,i} \prod_{j}^{\text{All systematics}} \kappa_{ij}^{\theta_{ij}}, \tag{4.102}$$

where the term $\kappa_{ij} = 1 + \delta_{ij}$ defines the relative uncertainty from the systematics source j, and for the transverse mass bin i. Since the nuisance parameters θ_{ij} are Gaussianly distributed, it follows that the events yields will form a log-normal distribution. In the case of multiple uncorrelated nuisance parameters, the nuisance parameter values are obtained independently, whereas in the case of fully correlated nuisance parameters the random Gaussian number must be the same for all of them, to account for their interdependence. The systematic uncertainties from a specific source within a given row in Table 4.45 were taken to be 100% correlated between all events yields. Conversely, systematic uncertainties from different sources from different rows in Table 4.45 were taken to be uncorrelated.

Using the definition in Eq. (4.100), the test-statistic used can be expressed as

$$q_{\mu} \;=\; -2\ln\left[\frac{\mathcal{L}(\text{data}|\mu,\hat{\vec{\theta}})}{\mathcal{L}(\text{data}|\mu=0,\hat{\vec{\theta}})}\right] \tag{4.103}$$

or more explicitly as

$$q_\mu = -2\ln\left[\frac{\prod_i^{\text{All } m_T \text{ bins}} \frac{\left[s_i(\mu,\vec{\theta})+b_i(\mu,\vec{\theta})\right]^{N_i^{\text{obs}}}}{N_i^{\text{obs}}!} e^{-\left[s_i(\mu,\vec{\theta})+b_i(\mu,\vec{\theta})\right]}}{\prod_i^{\text{All } m_T \text{ bins}} \frac{\left[b_i(\mu=0,\vec{\theta})\right]^{N_i^{\text{obs}}}}{N_i^{\text{obs}}!} e^{-\left[b_i(\mu=0,\vec{\theta})\right]}}\right]. \tag{4.104}$$

This test-statistic was used to determine the observed and expected limits, as described in Section 4.10.1.2 and Section 4.10.1.3, respectively. Schematic overviews of the procedures employed are shown in Fig. 4.98 and Fig. 4.99, for the observed and expected limits calculations, respectively. Given that the test-statistic distributions for a given signal strength modifier μ are independent on the toy MC pseudo-data used, the latter were computed only once instead of generating new ones for each μ trial. Thus, the computation of the p-values for each toy MC pseudo-data set required that the test-statistic was only evaluated once for each trial μ, which significantly reduced the amount of resources required for the limits computations. The aforementioned operation was repeated for each of the light charged Higgs boson mass points considered, in order to obtain exclusion limits for each individual signal+background hypotheses.

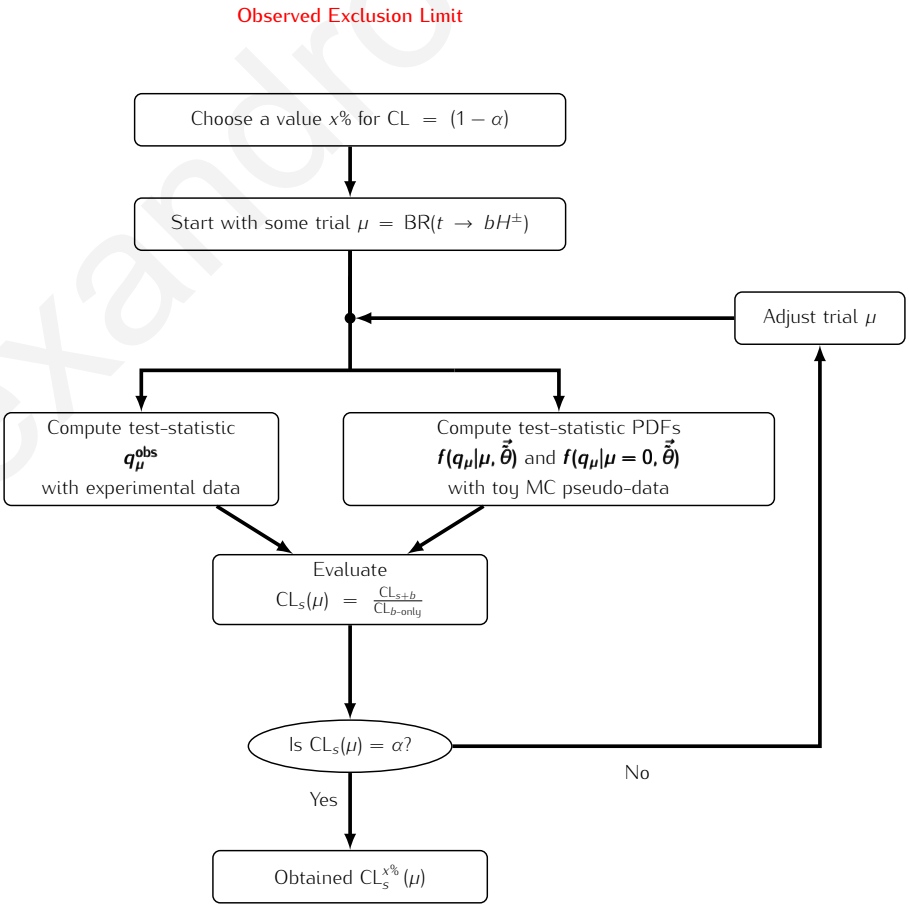

Figure 4.98: Schematic overview of the procedure for calculating the observed exclusion limits on $\mu = \text{BR}(H^\pm \to \tau^\pm \nu_\tau)$.

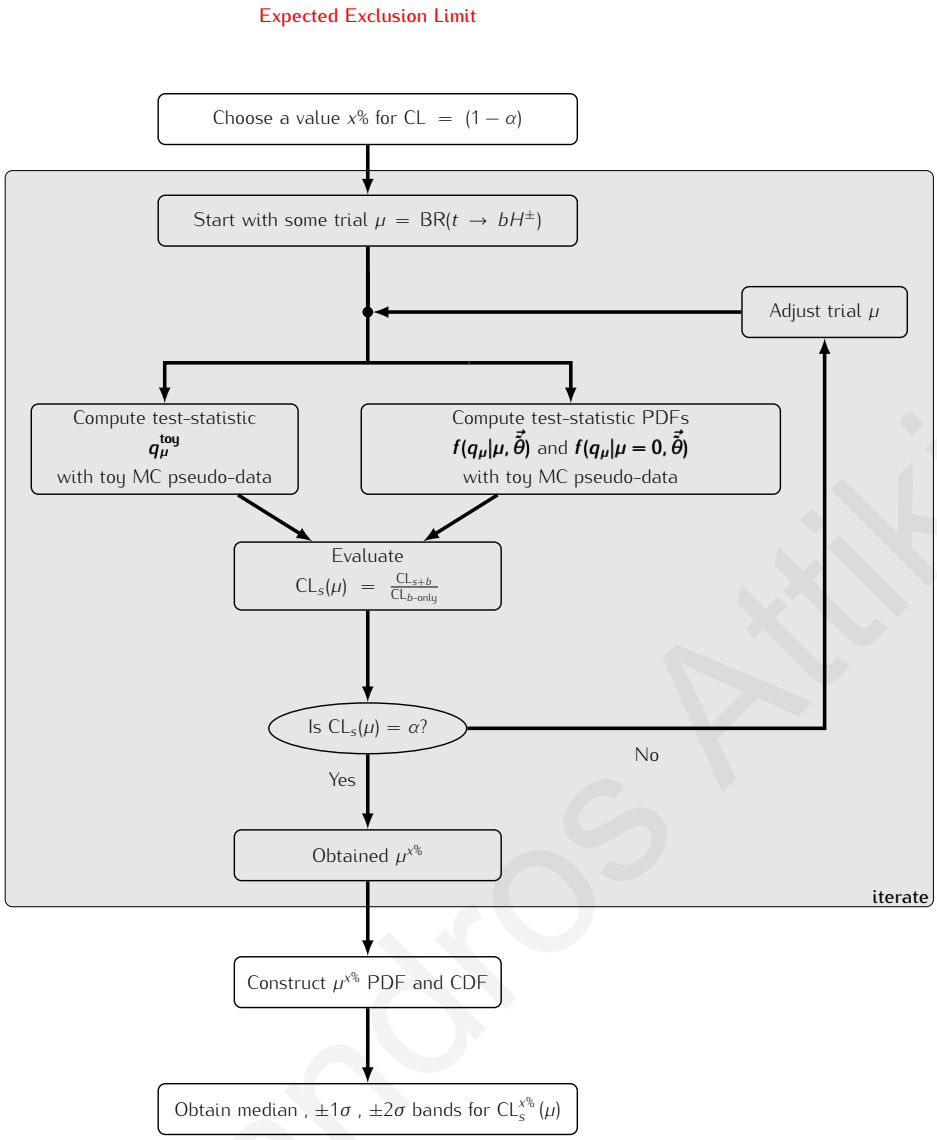

Figure 4.99: Schematic overview of the procedure for calculating the observed exclusion limits on $\mu = \text{BR}(H^\pm \to \tau^\pm \nu_\tau)$.

4.10.2.2 Treatment of systematic uncertainties

All related background and signal uncertainties, described in Section 4.9.3, were modelled with log-normal PDFs (denoted as lnN in the LandS data-cards), except for 3 special cases, as indicated in the LandS data-cards attached in Appendix H. Firstly, the uncertainty of the transverse mass shape due to JES effects was taken into account as a shape uncertainty, by using the template morphing technique (denoted as ShapeQ in the LandS data-cards), as described in Ref. [146]. The JES affects the transverse mass shapes of all simulation samples, due to effects that the hadronic jets/τ-jet energy scale have on the $E_{\text{T}}^{\text{miss}}$ and the overall event yield. In order to account for this, multiple instances of the transverse mass shape are produced from the simulated samples, by varying the JES and re-calculating the resultant clustered and un-clustered $E_{\text{T}}^{\text{miss}}$, as described in Section 4.7.3. Thus, the nominal event yield for a given simulated sample in transverse mass bin i, denoted N_i, is re-expressed as

a function of the nuisance parameter θ as follows

$$N_i(\theta) \quad = \quad N_i + \left[\alpha(\theta) \cdot N_i^{\text{JES}+} + \beta(\theta) \cdot N_i + \gamma(\theta) \cdot N_i^{\text{JES}-}\right] \tag{4.105}$$

where N_i denotes the nominal event yield in transverse mass bin i, and $N_i^{\text{JES}+}$ and $N_i^{\text{JES}-}$ denote the corresponding event yields obtained by scaling up and scaling down the JES, respectively. The nuisance parameter values are again sampled from a Gaussian distribution with a mean $\tilde{\theta} = 0$ and a unit standard deviation $\sigma_{\tilde{\theta}} = 1$. The parameters $\alpha(\theta)$, $\beta(\theta)$ and $\gamma(\theta)$ are defined as follows

$$\left.\begin{aligned} \alpha(\theta) &= \theta \text{ if } \theta > 0 \\ &= 0 \text{ if } \theta < 0 \\ \beta(\theta) &= -|\theta| \\ \gamma(\theta) &= 0 \text{ if } \theta > 0 \\ &= -\theta \text{ if } \theta < 0 \end{aligned}\right\} \quad |\theta| > 1, \tag{4.106}$$

for the case where $|\theta| > 1$. However, for the case where $|\theta| \leq 1$, they take the form

$$\left.\begin{aligned} \alpha(\theta) &= \frac{\theta}{2} \cdot (\theta + 1) \\ \beta(\theta) &= -\theta^2 \\ \gamma(\theta) &= \frac{\theta}{2} \cdot (\theta - 1) \end{aligned}\right\} \quad |\theta| \leq 1, \tag{4.107}$$

to avoid the discontinuities in the derivatives at $\theta = 0$ for Eq. (4.106). In this way, for $|\theta| > 1$ the morphing is conducted by the linear interpolation defined by Eq. (4.105) and (4.106), whereas for $|\theta| \leq 1$ the morphing is conducted by the quadratic interpolation defined by Eq. (4.105) and (4.107). An example of how an event yield would be distributed according to the aforementioned description is presented in Fig. 4.100.

The other 2 uncertainties that were not modelled with log-normal PDFs, were the statistical uncertainties from the 2 data-driven background measurements, QCD multi-jet and EWK+$t\bar{t}$ genuine τ. These were taken into account as a bin-by-bin uncertainty, denoted as ShapeStat in the LandS data-card. Either uncorrelated or fully correlated effects to individual processes were then taken into account [145]. In particular, as can be seen in Appendix H, each data-card row corresponds to a systematic uncertainty or nuisance parameter and all systematic errors along any single row were assumed to be independent of other rows (0% correlated), but within each row the systematic uncertainties were assumed to be fully correlated (100% correlated).

4.10.2.3 Results

The expected upper limits on the branching ratio BR($t \to bH^{\pm}$) are shown in Fig. 4.101 for the various signal+background hypotheses and under the assumption BR($H^{\pm} \to \tau^{\pm}\nu_{\tau}$) = 1,

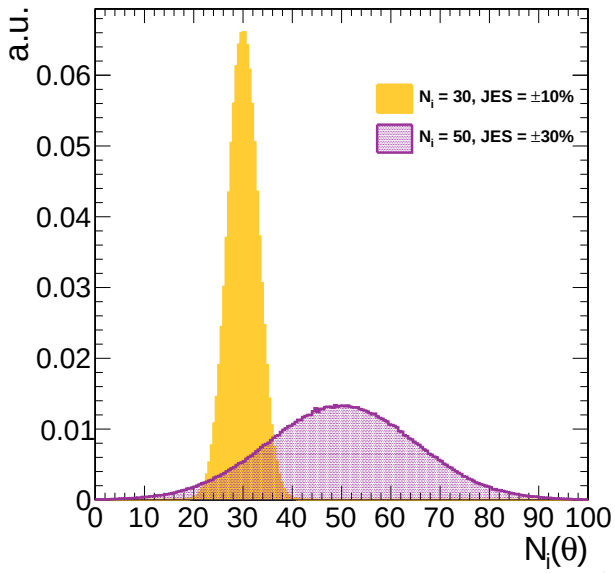

Figure 4.100: Example of how an event wield is distributed, when treated by the morphing technique, through Eq. (4.105), (4.106) and (4.107).

for the 3 $\Delta\phi\left(\tau \text{ jet}, E_{\mathrm{T}}^{\mathrm{miss}}\right)$ options: without $\Delta\phi$ cut, $\Delta\phi < 160°$ and $\Delta\phi < 130°$. A set of 500 toy MC pseudo-data were used to produce the expected limits, while the PDFs of the test-statistics $f(q_\mu|\mu, \vec{\hat{\theta}})$ and $f(q_\mu|\mu = 0, \vec{\hat{\theta}})$ were constructed with 10^4 toy MC pseudo-data. The selection with $\Delta\phi < 160°$ was chosen for the final results because it gives better expected limits than the selection without a $\Delta\phi$ cut for all studied signal+background hypotheses. The selection with $\Delta\phi < 130°$ appears to give slightly better expected limits in the $m_{H^\pm} \geq 100\,\mathrm{GeV}/c^2$ region, but it was disfavoured in order to have a measurable amount of QCD multi-jet background, and because the uncertainties of the expected limits were increased compared to the $\Delta\phi < 160°$ cut option.

The expected and observed upper limits on the branching ratio $\mathrm{BR}(t \to bH^\pm)$ for $\Delta\phi < 160°$ are shown in Fig. 4.102 for the various signal+background hypotheses with the assumption $\mathrm{BR}(H^\pm \to \tau^\pm\nu_\tau) = 1$. The dotted line indicates the expected median 95% CL upper limit on the signal strength modifier $\mu = \mathrm{BR}(t \to bH^\pm)$, while the green and yellow bands represent the corresponding $\pm1\sigma$ (68%) and $\pm2\sigma$ (95%) confidence bounds. The solid line represents the observed limits as obtained directly from the experimental data and it appears to be contained within the $\pm2\sigma$ band for the full mass range considered, indicating good agreement with the expected limits. Upon scrutiny, the exclusion curves reveal that there appears to be superior performance at the high-edge of the mass-spectrum under consideration, which can be partly understood from the standalone and combined signal selection efficiencies, first shown in Fig. 4.28 on page 159 and Fig. 4.27 on page 159, respectively. The combined selection efficiencies for the signal process $t\bar{t} \to bW^\pm bH^\mp$ ($t\bar{t} \to bH^\pm bH^\mp$) is an increasing (decreasing) function of the light charged Higgs boson mass ($m_{H^\mp}$). For the $t\bar{t} \to bW^\pm bH^\mp$ process, which contributes the vast majority of events to the signal event yield, the combined signal selection efficiency increases linearly from small to large masses, a feature which is reflected in the exclusion plot in Fig. 4.102. The higher the signal event

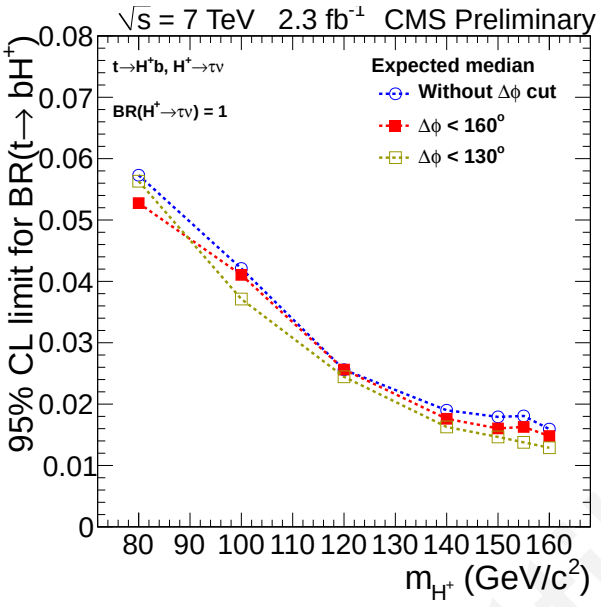

Figure 4.101: Expected upper limits on the branching ratio BR($t \to bH^{\pm}$) for the signal+background hypotheses in the mass region $m_{H^{\pm}} = 80 - 160\,\text{GeV}/c^2$ and assuming BR($H^{\pm} \to \tau^{\pm}\nu_{\tau}$) = 1, for 3 $\Delta\phi\left(\tau\text{ jet}, E_{\text{T}}^{\text{miss}}\right)$ options: without $\Delta\phi$ cut, $\Delta\phi < 160°$ and $\Delta\phi < 130°$.

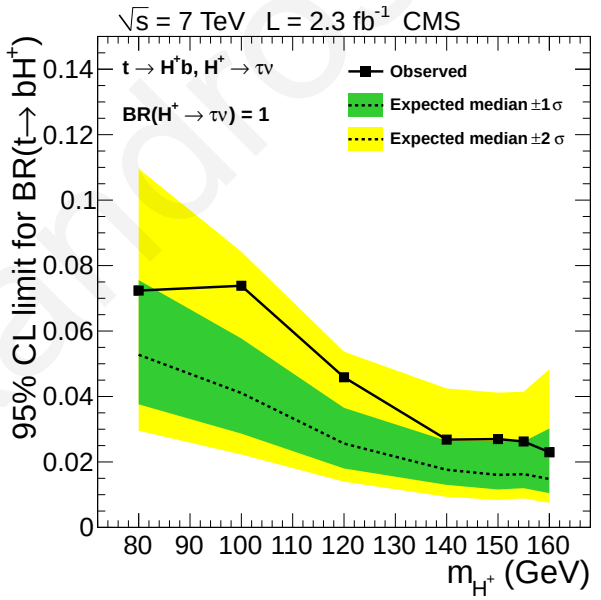

Figure 4.102: Observed and expected limits on the branching ratio BR($t \to bH^{\pm}$), for the signal+background hypotheses in the mass region $m_{H^{\pm}} = 80 - 160\,\text{GeV}/c^2$ and assuming BR($H^{\pm} \to \tau^{\pm}\nu_{\tau}$) = 1, for $\Delta\phi(\tau\text{ jet}, E_{\text{T}}^{\text{miss}}) < 160°$.

yield is, it follows that the more easy it will be to apply more stringent restrictions to the signal+background hypothesis.

Another contributing factor attributing to the exhibited exclusion limit behaviour, is the fact that at larger values of $m_{H^{\pm}}$ the transverse mass shape of the signal is expected to be shifted to higher values. Although the Jacobian peak of the transverse mass, which ideally is expected at $m_{\text{T}} = m_{H^{\pm}}$, is not fully resolved due to a combination of smearing effects caused

by the signal selection requirement and detector resolution effects, it is however expected that at larger values of $m_{H^\pm}$ the distribution will tend to shift towards larger values, thus providing an additional discriminating power over the SM background. For values of $m_{H^\pm}$ much closer to the $W^\pm$ mass ($m_{W^\pm}$ =80.399 GeV/c^2 [15]) the corresponding transverse mass of the signal events will closely follow that of background, limiting the ability to provide more stringent limits on the signal strength modifier $\mu = \mathrm{BR}(t \to bH^\pm)$.

The FeynHiggs [100] software, with input parameters defined in the LHC Higgs cross-sections Working Group [8], was used to calculate the branching ratios $\mathrm{BR}(t \to bH^\pm)$ and $\mathrm{BR}(H^\pm \to \tau^\pm \nu_\tau)$ for various $\tan\beta$ values, in order to transform the upper limit of $\mathrm{BR}(t \to bH^\pm)$ in Fig. 4.102 to limits in the $\tan\beta$ plane. The upper limits in the ($\tan\beta$, m_{A^0}) and ($\tan\beta$, $m_{H^\pm}$) parameter-space for μ = 200 are shown in Fig. 4.103 (a) and Fig. 4.103 (b), respectively. Finally, in Fig. 4.104 the observed limits with MSSM μ parameter values of −1000, −200, 200, and 1000 GeV/c^2 are also illustrated.

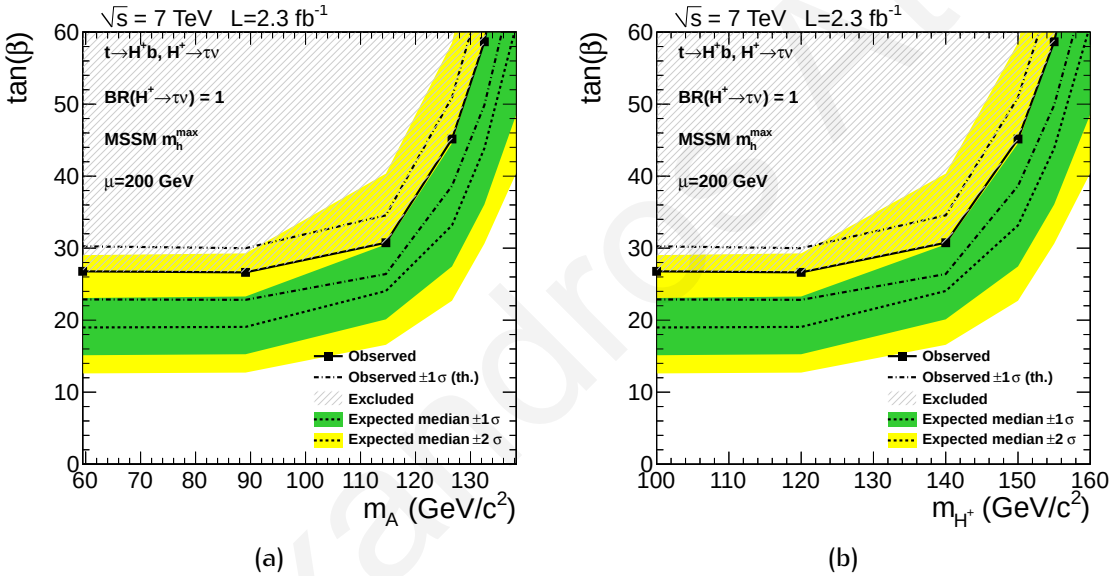

Figure 4.103: Upper limits on the branching ratio $\mathrm{BR}(t \to bH^\pm)$ in Fig. 4.102 transformed to the ($\tan\beta$, $m_{H^\pm}$) and ($\tan\beta$, m_{A^0}) spaces of the MSSM m_h^{max} scenario (μ = 200 GeV) and for the $\Delta\phi\left(\tau \text{ jet}, E_{\mathrm{T}}^{\mathrm{miss}}\right) < 160°$.

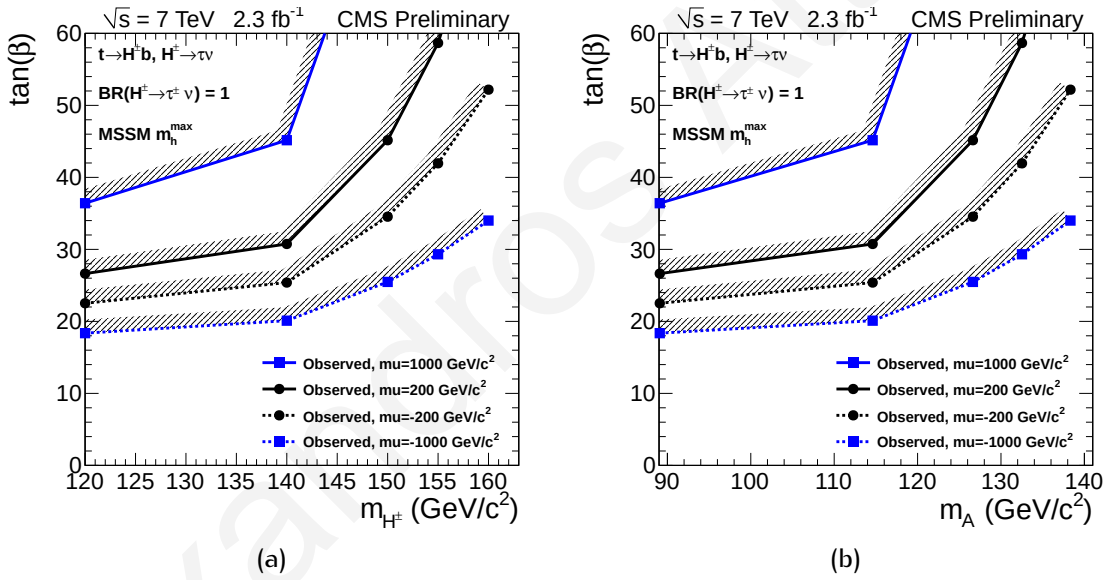

Figure 4.104: Variations of μ for the upper limits on branching ratio BR($t \to bH^{\pm}$) of Fig. 4.103.

Chapter 5

Comparison with other analyses, conclusions and outlook

In this thesis, results have been presented on a search for a light charged Higgs boson that can be produced in $t \to bH^{\pm}$ decays, with the $H^{\pm} \to \tau^{\pm}\nu_{\tau}$ decay. In particular, the fully hadronic final state was studied, whereby the $W^{\pm}$ boson decays to quarks through $W^{\pm} \to q\bar{q}'$, and the τ-lepton decays into hadrons and a neutrino (henceforth denoted as τ_h). In parallel with the present analysis, the CMS collaboration has conducted analyses on additional final states, all requiring the presence of a τ-lepton from the $H^{\pm}$ decay, missing transverse energy and multiple jets, with all analyses consequently combined into a single study, as documented in Ref. [79]. The analysed data corresponded to an integrated luminosity of $\sim 2\,\text{fb}^{-1}$, recorded in proton-proton collisions at $\sqrt{s} = 7$ TeV. More specifically, in additional to the production of τ_h and jets (referred to as τ_h+jets) shown in Fig. 5.1 (a), 3 additional final states were studied; the τ_h production in association with an electron or a muon (referred to as eτ_h and $\mu\tau_h$, respectively) shown in Fig. 5.1 (b), and the production of an electron and a muon (referred to a eμ) as shown Fig. 5.1 (c). Unlike the preset study, the analyses for the 3 additional final states eτ_h, $\mu\tau_h$, and eμ used event counting to obtain the upper limits. For these ℓ+jets final states, the presence of an additional neutrino through the decay $W^{\pm} \to \ell\nu_{\ell}$ spoiled the selection power of the transverse mass, and consequently a shape analysis on this variable was not considered as an option.

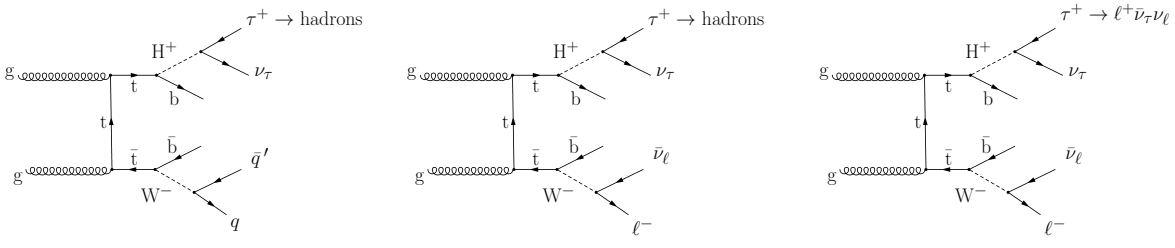

Figure 5.1: Representative Feynman diagrams for the τ_h+jets (a), e(μ)τ_h (b) and eμ (c) final states, used for the combined analysis performed by CMS Collaboration in the search for a light charged Higgs boson [79].

The upper limits obtained by the CMS collaboration on BR($t \to bH^{\pm}$), for all aforementioned final states are shown in Fig. 5.2, as a function of $m_{H^{\pm}}$. These can be compared to the upper limits obtained on BR($t \to bH^{\pm}$) for the present study, which were first shown in Fig. 4.102 on page 241, but are shown again here to enable the direct comparison of results. Upon comparing the expected limits between all final states, it is evident to see

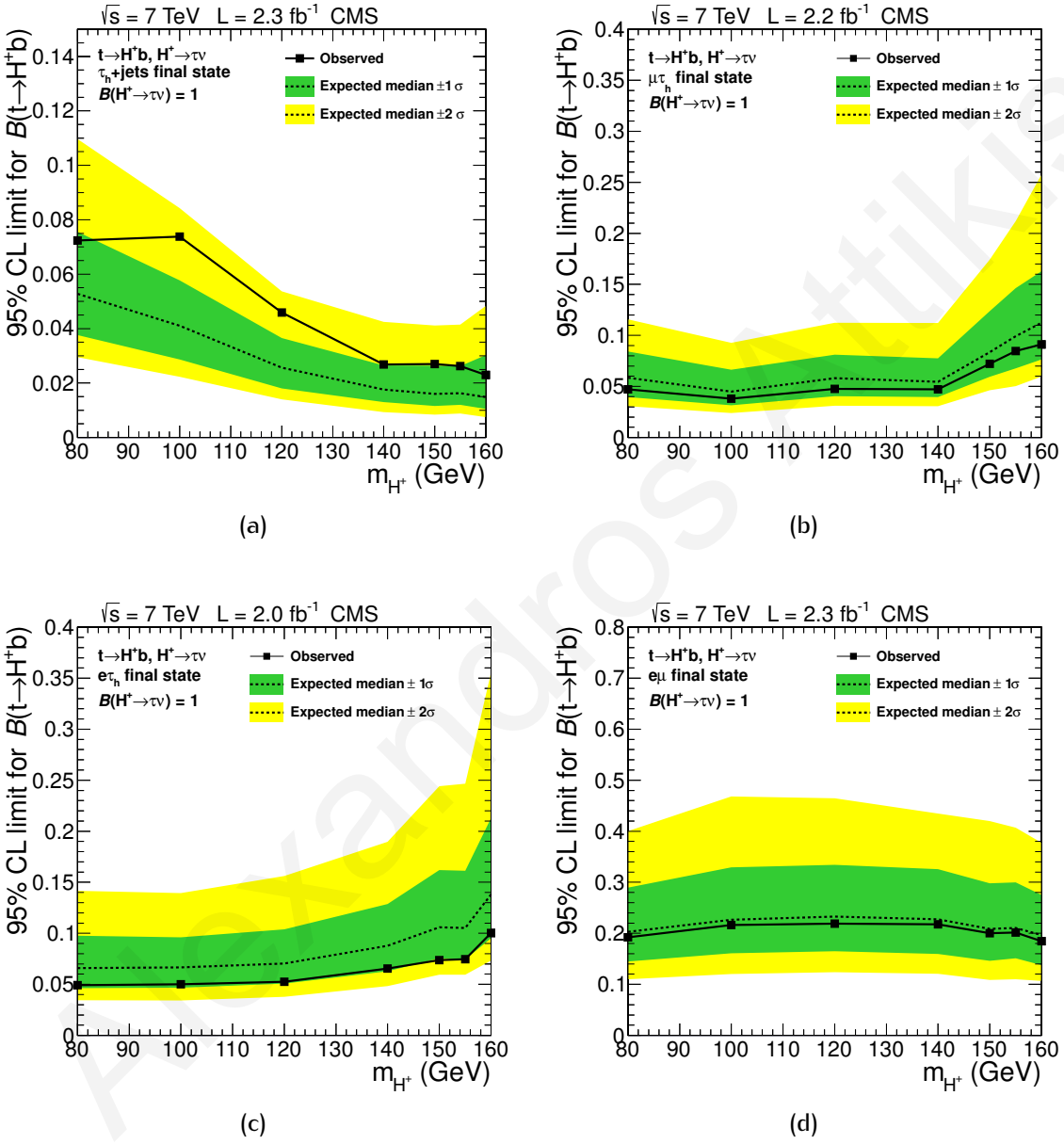

Figure 5.2: Upper limit on BR($t \to bH^{\pm}$), as a function of $m_{H^{\pm}}$, for the all final states considered in the CMS search for a light charged Higgs boson, that can be produced in $t \to bH^{\pm}$ decays, and which in turn decay through $H^{\pm} \to \tau^{\pm}\nu_{\tau}$; τ_h+jets (a), $\mu\tau_h$ (b), eτ_h (c) and eμ(d). The $\pm 1\sigma$ and $\pm 2\sigma$ bands around the expected limit are also shown. Taken from Ref. [79].

that the present analysis (τ_h+jets) has the edge over all the other 3 final states analyses. In particular, apart from the mass point $m_{H^{\pm}} = 80\,\text{GeV}/c^2$, where $\mu\tau_h$ performance is perhaps on a par with that from τ_h+jets, in the rest of the $m_{H^{\pm}}$ spectrum the τ_h+jets final state provides better limits on BR($t \to bH^{\pm}$), especially in the high-mass regions.

The reasons behind this behaviour are multi-fold. Firstly, a major difference between the τ_h+jets and the rest of the final state analyses is the fact that the limits for the former are extracted in a binned maximum likelihood fit on the transverse mass shape $m_{\mathrm{T}}(\tau \text{ jet}, E_{\mathrm{T}}^{\mathrm{miss}})$, while the latter use event counting for setting the limits. This provides the τ_h+jets final state analysis the edge over other final states, especially for values of $m_{H^{\pm}}$ closer to m_t where the signal becomes much cleaner to extract. Thus, the presence of additional neutrinos in the eτ_h, $\mu\tau_h$ and eμ final states prevents the utilisation of the powerful m_{T} (τ jet,$E_{\mathrm{T}}^{\mathrm{miss}}$) shape fit in extracting the limits.

Secondly, perhaps an equally contributing factor is the fact that the present analysis employs data-driven methods for measuring both major backgrounds, namely Quantum Chromodynamics (QCD) multi-jet and EWK+$t\bar{t}$ genuine τ, while the other final state analyses rely more heavily on Monte-Carlo (MC) simulations to determined the associated backgrounds. This is especially true for the eμ final state where all backgrounds are measured from MC simulations, which partly explains why the analysis is not at all competing with the rest of the final states. The reliance on MC simulations in determining backgrounds is a serious confinement on the power of any analysis, due to the fact that it ultimately becomes restricted on systematics effects. In these particular analyses, the sources of systematic uncertainties are mostly related to data-to-simulation corrections of trigger scale factors, Jet Energy Scale (JES), Jet Energy Resolution (JER) and $E_{\mathrm{T}}^{\mathrm{miss}}$ scale, b-tagging and pile-up corrections. Each of the aforementioned sources of systematic uncertainties are not needed when performing data-driven measurements, which is why such methods are commonly preferred in any kind of analysis. Indicatively, for the eμ final state

Thirdly, as already discussed in Section 4.5.9, the performance of the τ_h+jets final state increases at large values of $m_{H^{\pm}}$, due to increased trigger and τ-jet identification efficiency. This is because the heavier the $H^{\pm}$ is, the harder the τ-lepton will emerge in $H^{\pm} \to \tau^{\pm}\nu_{\tau}$ decays. This effect is dominating the limits on BR($t \to bH^{\pm}$) through the entire mass spectrum of $H^{\pm}$ and is in fact what causes the downwards sloping feature of the limits curve, as it can be seen in Fig. 5.2 (a).

Finally, the hadronic jet selection employed by the individual analyses also plays a significant role in explaining the characteristics of the limits plots at the high edge of the $m_{H^{\pm}}$ spectrum. As it can be seen in Fig. 5.1 (a), the τ_h+jets final state is characterised by the presence of at least 4 hadronic jets (of which 2 are b-jets) in addition to the τ jet, yet the signal selection requirements only require the presence of 3 such jets. Conversely, in the eτ_h and $\mu\tau_h$ analyses shown in Fig. 5.1 (b), the final states are characterised by the presence of 2 hadronic jets (both of which are b-jets), which is exactly the required number of jets asked for in the corresponding offline selections. What this means is that, as the mass of the light charged Higgs boson approaches that of the top quark, the b-quark produced in the $t \to bH^{\pm}$ decay becomes increasingly soft due to the reduction of the available phase-space. As a result, it becomes increasingly probable that the particular b-jet will not be successfully reconstructed, implying the effective loss of 1 jet from the final state. This effect is mitigated in the τ_h+jets analysis due to the fact that only 3 from the expected 4

jets are required to be present in the final state. Conversely, the $e\tau_h$ and $\mu\tau_h$ analyses, which require at least as many jets as expected in the final state, appear to be suffering in performance due to the loss of 1 of these jets. This can in principle explain why the limits in both $e\tau_h$ and $\mu\tau_h$ analyses deteriorate for values of $m_{H^\pm} \geq 140\,\text{GeV}/c^2$. For the τ_h+jets final state however, the softer hadronic jet selection requirement, in combination with the increased trigger and τ jet identification efficiency actually results in the opposite effect.

The upper limit on BR($t \to bH^\pm$) obtained from the combination of all final states investigated by the CMS collaboration is shown in Fig. 5.3 (a), as a function of $m_{H^\pm}$. The corresponding combined upper limits in ($\tan\beta, m_{H^\pm}$) parameter-space for the Minimal Supersymmetric Standard Model (MSSM) m_h^{max} are shown Fig. 5.3 (b). The latter figure can be directly compared with Fig. 4.103 on page 242, which shows the exclusion obtained from the τ_h+jets final state alone. Upon considering the individual contribution from all final states, it is evident that the fully hadronic finally state plays a dominant role in both the independent and model-depended limits obtained from the combined analysis. Overall, the combined upper limit on BR($t \to bH^\pm$) appears to be relatively flat over the whole mass spectrum considered, providing a model-independent upper limit on BR($t \to bH^\pm$) in the range of $2-3\%$ for the mass range $80 \leq m_{H^\pm} \leq 160\,\text{GeV}/c^2$, under the assumption that BR($H^\pm \to \tau^\pm \nu_\tau$) = 1.

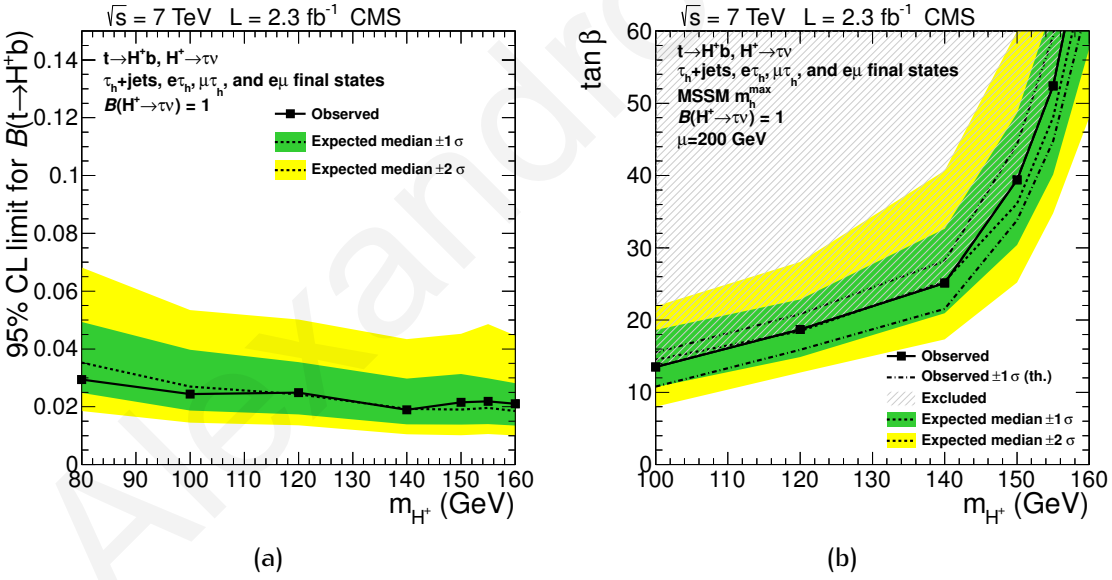

Figure 5.3: (a) Upper limit on BR($t \to bH^\pm$), as a function of $m_{H^\pm}$ obtained from the combination of the all final states; fully hadronic, the semi-leptonic ($e\tau_h$ and $\mu\tau_h$) and di-lepton $e\mu$. (b) The exclusion region in the MSSM ($\tan\beta, m_{H^\pm}$) parameter space, obtained from the combined analysis for the MSSM m_h^{max} scenario is also shown. The $\pm1\sigma$ and $\pm2\sigma$ bands around the expected limit are also shown. Taken from Ref. [79].

As already mentioned in Section 4.1, the ATLAS experiment has also recently presented results on a search for a light charged Higgs boson, that can be produced in $t \to bH^\pm$ decays, and which in turn decay through $H^\pm \to \tau^\pm \nu_\tau$ [75]. The analysis set an upper limit on the BR($t \to bH^\pm$) between $5-1\%$ for charged Higgs boson masses in the mass range $90 < m_{H^\pm} < 160\,\text{GeV}/c^2$ and assuming BR($H^\pm \to \tau^\pm \nu_\tau$) = 1 [75], as was shown in

Fig. 4.3 on page 101. The combined analysis was based on 4.6 fb^{-1} of integrated luminosity, double than that used in the corresponding CMS study, and incorporated results from the the ℓ+jets, the τ_h+lepton, and the τ_h+jets final states. In similar fashion to the CMS analyses, the individual ATLAS analyses generically relied on the presence of a τ-lepton from the $H^{\pm}$ decay, missing transverse energy and multiple jets. Comparing the results obtained by CMS with those obtained by ATLAS, reveals that both experiments set the same expected upper limit on BR($t \to bH^{\pm}$), despite the fact that the results from the ATLAS collaboration correspond to almost 2 times more integrated luminosity. It is both noteworthy and beneficial to understand the reason behind this.

The most sensitive channel for both experiments is the τ_h+jets final state, which in both studies contributes significantly in the limits imposed on BR($t \to bH^{\pm}$). In this particular channel, the CMS study appears to provide better results, even-though the signal selection requirements and trigger settings are very similar between the 2 analyses. The main difference in the analyses are focused on a more relaxed $\tau + E_{\text{T}}^{\text{miss}}$ trigger threshold for the ATLAS analysis, which is possible due to a better calorimeter performance noise-wise. Furthermore, the ATLAS analysis employs a looser τ jet identification requirement, which results in about double the number of signal events after all selections compared to the CMS analysis. Also, unlike the present study, although the ATLAS analysis employs top-mass reconstruction as a discriminating variable $m_{\text{jjb}} \in [120, 240]$[1] it does not employ a $\Delta\phi(\tau \text{ jet}, E_{\text{T}}^{\text{miss}})$ requirement to control the QCD multi-jet contribution in the signal region. Both analyses are based on a binned maximum likelihood fit on the transverse mass shape obtained from the τ jet and $E_{\text{T}}^{\text{miss}}$ objects, $m_{\text{T}}(\tau \text{ jet}, E_{\text{T}}^{\text{miss}})$. Therefore, the absence of a $\Delta\phi(\tau \text{ jet}, E_{\text{T}}^{\text{miss}})$ requirement is particularly important due to the QCD multi-jet "bump" appearing in the transverse mass shape around $m_{\text{T}} \simeq 100\,\text{GeV}/c^2$, which can hide the Jacobian peak expected from signal processes (see Section 4.9.2).

Another crucial difference between the 2 analyses, is the choice of data-driven method in determining the EWK+$t\bar{t}$ genuine τ and QCD multi-jet backgrounds. Similarly to the present study, the ATLAS analysis employed the τ-embedding method for determining the EWK+$t\bar{t}$ genuine τ in the signal region. However, the systematic uncertainties related to this measurement were found to be larger than those associated with the present study, mainly attributed to the trigger efficiency measurement. Concerning the QCD multi-jet background determination, the present analysis employed factorisation techniques in estimating its contribution to the signal region, and for obtaining the corresponding m_{T} (τ jet, $E_{\text{T}}^{\text{miss}}$) shape. Instead, the ATLAS collaboration opted for measuring the QCD multi-jet background by fitting its $E_{\text{T}}^{\text{miss}}$ shape to data. This was achieved by defining a control region where the τ jet identification and b-tagging are modified, by requiring that τ jet candidates pass a loose identification but fail a tight one and that no b-tagged jets are present. Assuming that the $E_{\text{T}}^{\text{miss}}$ shape is the same in the control and signal regions, the $E_{\text{T}}^{\text{miss}}$ shape for QCD multi-jet processes was obtained in the control region after subtracting the simulated con-

[1] Preliminary studies showed that the top-mass reconstruction did not provide good discriminating power. Consequently, the decision was made to not incorporate this variable in the signal selection requirements.

tributions from other processes. Thus, the $E_{\mathrm{T}}^{\mathrm{miss}}$ shape measured in the data was fitted using this QCD multi-jet shape and the sum of other processes taken from simulation. However, this technique yielded a much larger associated systematic uncertainty for the QCD multi-jet event yield, of about 50%.

Therefore, upon comparing the ATLAS and CMS analyses, the performance of the latter appears to be better due to 2 main reasons. The first major reason is a smaller systematic uncertainty related to the QCD multi-jet and EWK+$t\bar{t}$ genuine τ data-driven measurements. The reason for the reduced systematics is that, for the QCD multi-jet measurement a different approach is used for event yield prediction and the m_{T} shape extraction from data, which in the CMS analysis is performed in p_{T} bins of the τ jet candidates. Also, for the EWK+$t\bar{t}$ genuine τ data-driven measurement, the uncertainty related to the normalisation factor is much smaller for CMS, due to the smaller trigger efficiency and muon isolation uncertainties. The second major reason is the absence of a QCD multi-jet "bump" in the m_{T} (τ jet, $E_{\mathrm{T}}^{\mathrm{miss}}$) distribution of the CMS analysis, right under the position where one would expect the Jacobian peak for the signal. The CMS analysis achieves this "bump"- removal in the τ_h+jets final state by the introduction of a $\Delta\phi(\tau\text{ jet}, E_{\mathrm{T}}^{\mathrm{miss}}) < 160^{\circ}$ requirement.

The present study was concerned with the search for light charged Higgs bosons in the $t \to bH^{\pm}$ decay, with $H^{\pm} \to \tau^{\pm}\nu_{\tau}$ and the fully hadronic final state, whereby the τ-lepton decays hadronically. The search was based on the first 2.3 fb^{-1} of data recorded with the CMS detector during 2011. The analysis was performed using events selected with a trigger requiring the presence of a τ jet with $p_{\mathrm{T}} > 35$ GeV/c and large calorimetric missing transverse energy, $E_{\mathrm{T}}^{\mathrm{miss}} > 60$ GeV. Furthermore, the τ jet trigger selection included the requirement that the leading charged particle satisfied $p_{\mathrm{T}}^{\text{Ldg. Trk.}} > 20$ GeV/c. The offline signal selection requirements included the presence of a single τ jet successfully identified with the Hadron plus Strips (HPS) algorithm with $p_{\mathrm{T}} > 40$ GeV and $|\eta| < 2.1$, at least 3 other hadronic jets with $p_{\mathrm{T}} > 30$ GeV/c and $|\eta| < 2.4$, and with at least 1 of these jets identified as a b-jet with the Track Counting High Efficiency (TCHE) b-tagging algorithm.

In order to suppress the reducible QCD multi-jet background, selection criteria were imposed on the missing transverse energy, PF $E_{\mathrm{T}}^{\mathrm{miss}} > 50$ GeV, and on the azimuthal angle between the $E_{\mathrm{T}}^{\mathrm{miss}}$ object and the τ jet, $\Delta\phi(\tau\text{ jet}, E_{\mathrm{T}}^{\mathrm{miss}}) < 160^{\circ}$. Furthermore, only τ jets with 1 charged hadron (1-prong) with tranverse momentum $p_{\mathrm{T}}^{\text{Ldg. Trk.}} > 20$ GeV/c were considered. In order to ensure that the final state was orthogonal to final states containing leptons, events containing an isolated electron or a muon with $p_{\mathrm{T}} > 15$ GeV/c were rejected. Finally, the signal selection requirements exploited the different polarisations of τ-leptons originating from $H^{\pm}$ or $W^{\pm}$ decays, to reject backgrounds with genuine τ-leptons originating from $W^{\pm} \to \tau^{\pm}\nu_{\tau}$ decays, by requiring that the $R_{\tau} = \frac{p^{\text{Ldg. Trk.}}}{p^{\tau\text{ jet}}}$ satisfied $R_{\tau} > 0.7$.

The dominant backgrounds were found to be attributed to QCD multi-jet and EWK+$t\bar{t}$ genuine τ processes, both of which were determined with data-driven techniques. The less-contributing EWK+$t\bar{t}$ fake τ background processes, consisting of events with no τ-leptons in the final state (e/μ mis-identified as a τ jet), or with τ-leptons outside the acceptance,

were evaluated through simulations.

The light charged Higgs boson transverse mass, reconstructed from the selected τ jet and the $E_{\mathrm{T}}^{\mathrm{miss}}$ objects, was employed in a binned maximum likelihood fit to experimental data, after all signal selection requirements. As a result, model-independent upper limits were determined for the branching ratio BR($t \to bH^{\pm}$), as a function of the light charged Higgs boson mass ($m_{H^{\pm}}$). The observed and expected upper limits were found to be $2.2 - 7.3\%$ and $1.5 - 5.2\%$, respectively, for the mass range $80\,\mathrm{GeV}/c^2 \leq m_{H^{\pm}} \leq 160\,\mathrm{GeV}/c^2$. These limits were transformed in the $(\tan\beta, m_{H^{\pm}})$ and $(\tan\beta, m_{A^0})$ plane of the MSSM maximal mixing scenario $m_{\mathrm{h}}^{\mathrm{max}}$, and were found to exclude a significant region of the parameter space that had previously remained unexplored.

Nevertheless, the search for a charged Higgs boson is all but concluded. Although the restart of the Large Hadron Collider (LHC) will come with an increase in beam energy from the 2011 beam setting of 3.5 TeV to 4 TeV, it is nevertheless possible to combine both sets of data in a single analysis. The target set by LHC for an integrated luminosity of $\sim 20\,\mathrm{fb}^{-1}$ for 2012 opens up the possibility of also probing the heavy charged Higgs boson, which so far has been unavailable due to the much smaller production cross-section, relative to the light charged Higgs boson. Indicatevely, for a heavy charged Higgs boson of mass $m_{H^{\pm}} = 171.6\,(300.9)\,\mathrm{GeV}/c^2$, the Next-to-Leading Order (NLO) production cross-section for the Leading Order (LO) process $gb \to tH^{\pm}$ is about $2.128\,(0.687)\,\mathrm{pb}$ for $\tan\beta = 30$. Multiplying the aforementioned cross-sections with BR($H^{\pm} \to \tau^{\pm}\nu_{\tau}$) $= 0.983\,(0.264)$ and BR$(\tau^{\pm} \to \text{hadrons}\,\nu_{\tau}) \simeq 0.65$ yields $1359.2\,(118.3)\,\mathrm{fb}$ for the process $gb \to tH^{\pm}$, $H^{\pm} \to \tau^{\pm}\nu_{\tau}$, $\tau^{\pm} \to \text{hadrons}\,\nu_{\tau}$ [147, 148, 149].

Thus, a new yet similar analysis possibility arises; that of the heavy charged Higgs through the production process $gb \to tH^{\pm}$, and part of its NLO corrections $gg \to tbH^{\pm}$. For the fully hadronic final state, this implies the decays $t \to bqq$, $H^{\pm} \to \tau^{\pm}\nu_{\tau}$ and $\tau^{\pm} \to \text{hadrons} + \nu_{\tau}$. The $H^{\pm} \to tb$ decay channel is another possible discovery channel, as it becomes the dominant mode when the mass of the heavy charged Higgs exceeds the sum of masses of top and bottom quarks, but is not heavy enough that the Supersymmetric decay channels become significant. Therefore, for the immediate future, 2 research objectives can be aimed for. The first objective is concerned with the continuation of the search for a light charged Higgs boson, by incorporating the significant amount of collision data collected after the early part of 2011 data-taking period, and those collected during 2012. The second objective is extending the analysis to include the search for a heavy charged Higgs boson, also in the fully hadronic final state. The two searches can be conducted using similar techniques, even-though the production process and background composition can differ significantly between these two channels.

In order to incorporate all available integrated luminosity into the present analysis, the difficult task of understanding and controlling the dynamically changing collision environment conditions is presented. The data collected by CMS towards the end of 2011 and the data recorded during the 2012 runs are characterised by increased pile-up, resulting from

the higher instantaneous luminosity of LHC operation. This has a multi-fold effect, especially in terms of the trigger used and the isolation criteria of the physics objects employed. As a result, in-depth studies must be performed dedicated in estimating the new trigger efficiencies and scale factors for the late 2011 and 2012 data. For the future 2012 runs, the development of a trigger menu such that the rate and efficiency are kept at an acceptable level will also be required. Moreover, the effects of increased pile-up are expected to significantly affect the offline signal selection requirements, and their effectiveness in suppressing backgrounds and extracting the signal. It will thus be imperative that dedicated studies are undertaken that will concentrate on addressing these issues and dictate a way of adapting the analysis accordingly. On a related issue, the increase in beam energy to 4 TeV, despite being a subtle 0.5 TeV increase compared to the 3.5 TeV beams used during the 2011 runs, implies that a full re-optimisation of the kinematical selection cuts will be required, new MC samples would need to be produced and all cross-sections recalculated accordingly. Indicatively, the signal production cross-section is expected to increase by about $\sim$ 40%, due to an increase in the $t\bar{t}$ production cross-section from 165 pb to about 234 pb [150]. Moreover, a recommissioning of all the background measurement methods will be required, as well as their extension and improvement where and if necessary.

Despite all the changes in the collision environment however, it is anticipated that the core of the present study can be used with relatively minor adjustments to conduct an updated analysis that will incorporate the full 2011 and 2012 integrated luminosity, expected to be around 5 and 20 fb^{-1}, respectively. This is a major advantage, since the available resources can be focused on developing new data-driven methods of estimating the various backgrounds and discriminating variables for the signal extraction. In particular, techniques for extracting the signal from the data might include revisiting the possibility of utilising top-mass reconstruction, investigating the possibility to use the full charged Higgs mass reconstruction and tighter b-tagging criteria. Furthemore, the possibility of applying an explicit veto for the presence of a second τ jet in the event with loose criteria can also be explored. An additional option would be to investigate whether the utilisation of various multivariate techniques can be exploited in extracting the signal from the background.

To conclude, the ultimate goal for the immediate future is either the discovery of a light/heavy charged Higgs boson, or their exclusion. Ideally, the imminent analysis of all accumulated data will result in the discovery of light/heavy Charged Higgs boson, although their exclusion will be equally significant. Whatever the outcome however, both scenarios will be of paramount importance in closing in on the solution to the mystery surrounding the Electroweak (EWK) symmetry breaking mechanism, with significant consequences for the future of particle physics in general.

Bibliography

[1] A. Pich, "The Standard Model of Electroweak Interactions", 2005. arXiv.org:hep-ph/0502010.

[2] Y. Nambu, "Quasi-Particles and Gauge Invariance in the Theory of Superconductivity", *Phys. Rev.* **117** (Feb, 1960) 648–663. doi:10.1103/PhysRev.117.648.

[3] J. Goldstone, "Field Theories with Superconductor Solutions", *Nuovo Cim.* **19** (1961) 154–164. doi:10.1007/BF02812722.

[4] J. Goldstone, A. Salam, and S. Weinberg, "Broken Symmetries", *Phys. Rev.* **127** (Aug, 1962) 965–970. doi:10.1103/PhysRev.127.965.

[5] S. Weinberg, "A Model of Leptons", *Phys. Rev. Lett.* **19** (Nov, 1967) 1264–1266. doi:10.1103/PhysRevLett.19.1264.

[6] A. Pich, "The Standard Model, Parts 1-8", *CERN Summer Student Lecture Programme Course* (Jul, 2008).

[7] A. Pich, "The Standard Model of Electroweak Interactions", 2012. arxiv.org/abs/1201.0537v1.

[8] LHC Higgs Cross Section Working Group Collaboration, "Handbook of LHC Higgs Cross Sections: 1. Inclusive Observables", arXiv:1101.0593.

[9] ALEPH Collaboration, CDF Collaboration, D0 Collaboration, DELPHI Collaboration, L3 Collaboration, OPAL Collaboration, SLD Collaboration, LEP Electroweak Working Group, Tevatron Electroweak Working Group, SLD Electroweak and Heavy Flavour Groups Collaboration, "Precision Electroweak Measurements and Constraints on the Standard Model", arXiv:1012.2367. 18 pages.

[10] LEP Working Group for Higgs boson searches Collaboration, "Search for the standard model Higgs boson at LEP", *Phys. Lett.* **B565** (2003) 61–75, arXiv:hep-ex/0306033. doi:10.1016/S0370-2693(03)00614-2.

[11] CDF Collaboration and D0 Collaboration Collaboration, "Combination of Tevatron Searches for the Standard Model Higgs Boson in the W^+W^- Decay Mode", *Phys. Rev. Lett.* **104** (Feb, 2010) 061802. doi:10.1103/PhysRevLett.104.061802.

[12] A. Collaboration, "Combination of Higgs Boson Searches with up to 4.9 fb^{-1} of pp Collisions Data Taken at a center-of-mass energy of 7 TeV with the ATLAS Experiment at the LHC", Technical Report ATLAS-CONF-2011-163, CERN, Geneva, (Dec, 2011).

[13] CMS Collaboration Collaboration, "Combination of SM Higgs Searches",.

[14] U. Amaldi, W. de Boer, and H. Furstenau, "Comparison of grand unified theories with electroweak and strong coupling constants measured at LEP", *Phys. Lett.* **B260** (1991) 447–455. doi:10.1016/0370-2693(91)91641-8.

[15] Particle Data Group Collaboration, "Review of particle physics", *J. Phys.* **G37** (2010) 075021. doi:10.1088/0954-3899/37/7A/075021.

[16] P. Fayet, "Supergauge Invariant Extension of the Higgs Mechanism and a Model for the Electron and Its Neutrino", *Nucl. Phys.* **B90** (1975) 104. doi:10.1016/0550-3213(75)90636-7.

[17] P. Fayet, "Supersymmetry and Weak, Electromagnetic and Strong Interactions", *Phys. Lett.* **B64** (1976) 159. doi:10.1016/0370-2693(76)90319-1.

[18] P. Fayet, "Spontaneously Broken Supersymmetric Theories of Weak, Electromagnetic and Strong Interactions", *Phys. Lett.* **B69** (1977) 489. doi:10.1016/0370-2693(77)90852-8.

[19] S. Dimopoulos and H. Georgi, "Softly Broken Supersymmetry and SU(5)", *Nucl. Phys.* **B193** (1981) 150. doi:10.1016/0550-3213(81)90522-8.

[20] N. Sakai, "Naturalness in Supersymmetric Guts", *Z. Phys.* **C11** (1981) 153. doi:10.1007/BF01573998.

[21] K. Inoue, A. Kakuto, H. Komatsu et al., "Low-Energy Parameters and Particle Masses in a Supersymmetric Grand Unified Model", *Prog. Theor. Phys.* **67** (1982) 1889. Revised version. doi:10.1143/PTP.67.1889.

[22] K. Inoue, A. Kakuto, H. Komatsu et al., "Aspects of Grand Unified Models with Softly Broken Supersymmetry", *Prog. Theor. Phys.* **68** (1982) 927. doi:10.1143/PTP.68.927.

[23] K. Inoue, A. Kakuto, H. Komatsu et al., "Renormalization of Supersymmetry Breaking Parameters Revisited", *Prog. Theor. Phys.* **71** (1984) 413. doi:10.1143/PTP.71.413.

[24] C. T. Hill and E. H. Simmons, "Strong dynamics and electroweak symmetry breaking", *Physics Reports* **381** (2003), no. 4-6, 235 – 402. doi:10.1016/S0370-1573(03)00140-6.

[25] K. Lane, "Two lectures on technicolor", arXiv:hep-ph/0202255.

[26] A. Martin, "Technicolor Signals at the LHC", arXiv:0812.1841.

[27] A. Djouadi, "The anatomy of electro-weak symmetry breaking. II. The Higgs bosons in the minimal supersymmetric model", *Phys. Rept.* **459** (2008) 1, arXiv:hep-ph/0503173. doi:10.1016/j.physrep.2007.10.005.

[28] S. P. Martin, "A Supersymmetry Primer", arXiv:hep-ph/9709356.

[29] I. Simonsen, "A Review of minimal supersymmetric electroweak theory", arXiv:hep-ph/9506369. Latex, 112 pages.

[30] M. Kuroda, "Complete Lagrangian of MSSM", arXiv:hep-ph/9902340.

[31] M. S. Carena, S. Heinemeyer, C. E. M. Wagner et al., "Suggestions for benchmark scenarios for MSSM Higgs boson searches at hadron colliders", *Eur. Phys. J.* **C26** (2003) 601–607, arXiv:hep-ph/0202167. doi:10.1140/epjc/s2002-01084-3.

[32] LHC Higgs Cross Section Working Group, S. Dittmaier, C. Mariotti et al., "Handbook of LHC Higgs Cross Sections: 2. Differential Distributions", *CERN-2012-002* (CERN, Geneva, 2012) arXiv:1201.3084.

[33] LHC Higgs Cross Section Working Group, S. Dittmaier, C. Mariotti et al., "Handbook of LHC Higgs Cross Sections: 1. Inclusive Observables", *CERN-2011-002* (CERN, Geneva, 2011) arXiv:1101.0593.

[34] L. Wendland, "Identification of Hadronically Decaying Tau Leptons in Searches for Heavy MSSM Higgs Bosons with the CMS Detector at the CERN LHC". PhD thesis, University of Helsinki, University of Helsinki, 2009. Presented on 2009.

[35] https://twiki.cern.ch/twiki/bin/view/LHCPhysics/MSSMCharged/.

[36] L. Evans and P. Bryant, "LHC Machine", *Journal of Instrumentation* **3** (2008) S08001. doi:10.1088/1748-0221/3/08/S08001.

[37] O. S. BrÃijning, P. Collier, P. Lebrun et al., "LHC Design Report". CERN, Geneva, 2004.

[38] D. Kovalskyi, M. Tadel, A. Mrak-Tadel et al., "Fireworks: A Physics Event Display for CMS. oai:cds.cern.ch:1196116", Technical Report CMS-CR-2009-111, CERN, Geneva, (May, 2009).

[39] CMS Collaboration, "The Compact Muon Solenoid Technical Proposal", *CERN/LHCC* **1994-38** (December, 1994).

[40] CMS Collaboration, "CMS Physics Technical Design Report, Volume I: Detector Performance and software", *CERN/LHCC* **2006-001** (February, 2006).

[41] CMS Collaboration, "CMS Physics Technical Design Report, Volume II: Physics Performance", *J. Phys. G: Nucl. Part. Phys.* **34** (2007) 995–1579.

[42] CMS Collaboration, "The CMS experiment at the CERN LHC", *JINST* **3** (2008) S08004. doi:10.1088/1748-0221/3/08/S08004.

[43] CMS Collaboration, "The CMS experiment at the CERN LHC", *Journal of Instrumentation* **3** (2008) S08004. doi:10.1088/1748-0221/3/08/S08004.

[44] CMS Collaboration, "Total cross-section, elastic scattering and diffraction dissociation at the Large Hadron Collider at CERN: TOTEM Technical Design Report". Technical Design Report TOTEM. CERN, Geneva, 2004.

[45] CMS Collaboration, "CMS Physics Technical Design Report Volume I: Detector Performance and Software". Technical Design Report CMS. CERN, Geneva, 2006. There is an error on cover due to a technical problem for some items.

[46] CMS Collaboration, "CMS: The Tracker Project Technical Design Report", *CERN/LHCC* **1998-6** (February, 1998).

[47] CMS Collaboration, "The CMS tracker: addendum to the Technical Design Report". Technical Design Report CMS. CERN, Geneva, 2000.

[48] CMS Collaboration, "Alignment of the CMS silicon tracker during commissioning with cosmic rays", *Journal of Instrumentation* **5** (2010), no. 03, T03009.

[49] I. T. et al., "Description and Performance of the CMS Track Reconstruction", *CMS AN* **2011/172** (2011).

[50] CMS Colla boration, "CMS Trigger and Data-Acquisition System Project Technical Design Report", *CERN/LHCC* **2000-38** (December, 2000).

[51] P. Merkel, "Experience with mass production bump bonding with outside vendors in the CMS FPIX project", *Nucl. Instrum. Meth.* **A582** (2007) 771–775. doi:10.1016/j.nima.2007.07.089.

[52] K. Stenson, "Tracking and Particle ID", in *2011 CERN-Fermilab Hadron Collider Physics Summer School, CERN, Geneva, Switzerland*. 2011.

[53] D. H. Perkins, "Introduction to High Energy Physics". Cambridge University Press, 4th. edition, 2000.

[54] K. Kleinknecht, "Detectors for Particle Radiation; 2nd ed.". Cambridge Univ. Press, Cambridge, 1998.

[55] CMS Collaboration, "The CMS electromagnetic calorimeter project: Technical Design Report". Technical Design Report CMS. CERN, Geneva, 1997.

[56] CMS Collaboration, "Changes to CMS ECAL electronics: addendum to the Technical Design Report". Technical Design Report CMS. CERN, Geneva, 2002.

[57] CMS Collaboration, "The CMS hadron calorimeter project: Technical Design Report". Technical Design Report CMS. CERN, Geneva, 1997.

[58] W. Frass, "Passage Of Particles Through Matter", (2009). Oxford University.

[59] H. Pi, P. Avery, D. Green et al., "Measurement of Missing Transverse Energy With the CMS Detector at the LHC", Technical Report CMS-NOTE-2006-035, CERN, Geneva, (Feb, 2006).

[60] A. Heister, O. Kodolova, V. Konoplyanikov et al., "Measurement of Jets with the CMS Detector at the LHC", Technical Report CMS-NOTE-2006-036, CERN, Geneva, (Feb, 2006).

[61] CMS Collaboration, "The CMS muon project: Technical Design Report". Technical Design Report CMS. CERN, Geneva, 1997.

[62] S. Lacaprara, "The CMS Muon System and Physics Performance. oai:cds.cern.ch:687850", Technical Report CMS-CR-2003-025, CERN, Geneva, (Jul, 2003).

[63] F. Thyssen, "Performance of the Resistive Plate Chambers in the CMS experiment", *Journal of Instrumentation* **7** (2012), no. 01, C01104. doi:10.1088/1748-0221/7/01/C01104.

[64] CMS Collaboration, "Performance of the CMS Drift Tube Chambers with Cosmic Rays", *J. Instrum.* **5** (Nov, 2009) T03015 . 47 p. doi:10.1088/1748-0221/5/03/T03015.

[65] J. Gilmore, "The CMS Muon System", in *CMS101*, Ohio State University. 2007.

[66] C. Collaboration, "Performance of the CMS hadron calorimeter with cosmic ray muons and LHC beam data", *Journal of Instrumentation* **5** (2010), no. 03, T03012.

[67] C. Collaboration, "Design, Performance, and Calibration of CMS Hadron-Barrel Calorimeter Wedges", Technical Report CMS-NOTE-2006-138, CERN, Geneva, (May, 2007).

[68] CMS Collaboration, "CMS Trigger and Data-Acquisition project, Volume I: The Level-1 Trigger". Technical Design Report CMS. CERN, Geneva, 2000.

[69] CMS Collaboration, "CMS Trigger and Data-Acquisition project, Volume II: Data Acquisition & High-Level Trigger". Technical Design Report CMS. CERN, Geneva, 2002.

[70] http://root.cern.ch/drupal/.

[71] J. F. Gunion, H. E. Haber, G. L. Kane et al., "The Higgs Hunters' Guide", *Front.Phys.* **80** (2000) 1.

[72] LEP Higgs Working Group for Higgs boson searches, ALEPH, DELPHI, L3, OPAL Collaboration, "Search for charged Higgs bosons: Preliminary combined results using LEP data collected at energies up to 209-GeV", arXiv:hep-ex/0107031.

[73] CDF Collaboration, "Search for charged Higgs bosons from top quark decays in $p\bar{p}$ collisions at $\sqrt{s} = 1.96$-TeV", *Phys. Rev. Lett.* **96** (2006) 042003, arXiv:hep-ex/0510065. doi:10.1103/PhysRevLett.96.042003.

[74] DØ Collaboration, "Search for charged Higgs bosons in top quark decays", *Phys. Lett.* **B682** (2009) 278, arXiv:0908.1811. doi:10.1016/j.physletb.2009.11.016.

[75] ATLAS Collaboration Collaboration, "Search for charged Higgs bosons decaying via $H^{\pm} \to \tau^{\pm}\nu_{\tau}$ in top quark pair events using pp collision data at $\sqrt{s} = 7$ TeV with the ATLAS detector", arXiv:1204.2760.

[76] A. Attikis et al., "Search for the light charged MSSM Higgs bosons with the $H^{\pm} \to \tau^{\pm}\nu_{\tau}$ decay in fully hadronic final state", *CMS AN* **2011/126** (2011).

[77] CMS Collaboration, "Search for the charged Higgs boson with $H^{+} \to \tau^{+}\nu$ decay mode in top quark decays", *CMS PAS* **HIG-11-008** (2011).

[78] CMS Collaboration, "Search for the charged Higgs boson in top quark decays in pp collisions at $\sqrt{s} = 7$ TeV", *CMS PAS* **HIG-11-019** (2011).

[79] CMS Collaboration Collaboration, "Search for a light charged Higgs boson in top quark decays in pp collisions at $\sqrt{s} = 7$ TeV", arXiv:1205.5736.

[80] T. Ohl and T. H. Darmstadt, "feynMF: Drawing Feynman Diagrams with LATEX and METAFONT", 1995.

[81] C. A. et al. (Particle Data Group), "Review of Particle Physics", *Physics Letters* **B667** (2008), no. 1,.

[82] D. P. Roy, "The Hadronic tau decay signature of a heavy charged Higgs boson at LHC", *Phys. Lett.* **B459** (1999) 607, arXiv:hep-ph/9905542. doi:10.1016/S0370-2693(99)00724-8.

[83] M. Guchait, R. Kinnunen, and D. P. Roy, "Signature of heavy charged Higgs boson at LHC in the 1 and 3 prong hadronic tau decay channels", *Eur. Phys. J.* **C52** (2007) 665–672, arXiv:hep-ph/0608324. doi:10.1140/epjc/s10052-007-0396-2.

[84] R. Godbole, M. Guchait, and D. Roy, "Using tau polarization to discriminate between SUSY models and determine SUSY parameters at ILC", *Phys.Lett.* **B618** (2005) 193–200, arXiv:hep-ph/0411306. doi:10.1016/j.physletb.2005.05.035.

[85] V. Rapsevicius and the CMS DQM Group, "CMS Run Registry: Data Certification Bookkeeping and Publication System", *Journal of Physics: Conference Series* **331** (2011), no. 4, 042038.

[86] http://cmssdt.cern.ch/SDT/doxygen/CMSSW_4_2_8_patch2/doc/html/.

[87] http://cms-conddb.cern.ch/gtlist/?GlobalTag=GR_R_42_V20.

[88] https://twiki.cern.ch/twiki/bin/viewauth/CMS/Collisions2010Recipes, revision 52.

[89] S. Agostinelli et al., "Geant4 – A simulation Toolkit", *Nucl. Inst. Meth. A* **506** (2003) 250–303.

[90] T. Sjostrand, L. Lonnblad, S. Mrenna et al., "Pythia 6.3 Physics and Manual", *LU TP* **03-38** (2003) arXiv:hep-ph/0308153.

[91] CMS Collaboration, "Measurement of the Underlying Event Activity at the LHC with at $\sqrt{s} = 7$ TeV and Comparison with $\sqrt{s} = 0.9$ TeV", *JHEP* **2011** (9, 2011) 109, arXiv:1107.0330. doi:10.1007/JHEP09(2011)109.

[92] CMS Collaboration, "Measurement of the Underlying Event Activity at the LHC with $\sqrt{s}$=7 TeV", *CMS PAS* **QCD-10-010** (2010).

[93] S. Jadach, Z. Was, R. Decker et al., "The tau decay library TAUOLA: Version 2.4", *Comput. Phys. Commun.* **76** (1993) 361–380. doi:10.1016/0010-4655(93)90061-G.

[94] F. Maltoni and T. Stelzer, "MadEvent: Automatic event generation with MadGraph", *JHEP* **02** (2003) 027, arXiv:hep-ph/0208156.

[95] P. Nason, "A new method for combining NLO QCD with shower Monte Carlo algorithms", *JHEP 0411* **040** (2004) arXiv:hep-ph/0409146. doi:10.1088/1126-6708/2004/11/040.

[96] S. Fixione, P. Nason, and C. Oleari, "Matching NLO QCD computations with Parton Shower simulations: the POWHEG method", *JHEP 0711* **070** (2007) arXiv:0709.2092. doi:10.1088/1126-6708/2007/11/070.

[97] S. Alioli, P. Nason, C. Oleari et al., "A general framework for implementing NLO calculations in shower Monte Carlo programs: the POWHEG BOX", *JHEP 1006* **043** (2010) arXiv:1002.2581. doi:10.1088/1126-6708/2010/06/043.

[98] S. Alioli, P. Nason, C. Oleari et al., "NLO single-top production matched with shower in POWHEG: s- and t-channel contributions", *JHEP 0909* **111** (2009) arXiv:0907.4076. doi:10.1088/1126-6708/2009/09/111.

[99] E. Re, "Single-top Wt-channel production matched with parton showers using the POWHEG method", *Eur. Phys. J.* **C71** (2011) 1547, arXiv:1009.2450. doi:10.1140/epjc/s10052-011-1547-z.

[100] S. Heinemeyer, W. Hollik, and G. Weiglein, "FeynHiggs: A program for the calculation of the masses of the neutral CP-even Higgs bosons in the MSSM", *Comput. Phys. Commun.* **124** (2000) 76–89, arXiv:hep-ph/9812320. doi:10.1016/S0010-4655(99)00364-1.

[101] N. Kidonakis, "Higher-order corrections to top-antitop pair and single top quark production", arXiv:0909.0037.

[102] N. Kidonakis, "Next-to-next-to-leading-order collinear and soft gluon corrections for t-channel single top quark production", *Phys. Rev. D* **83** (2011) 091503, arXiv:1103.2792. doi:10.1103/PhysRevD.83.091503.

[103] N. Kidonakis, "Two-loop soft anomalous dimensions for single top quark associated production with a W^- or H^-", *Phys. Rev. D* **82** (2010) 054018, arXiv:1005.4451. doi:10.1103/PhysRevD.82.054018.

[104] N. Kidonakis, "NNLL resummation for s-channel single top quark production", *Phys. Rev. D* **81** (2010) 054028, arXiv:1001.5034. doi:10.1103/PhysRevD.81.054028.

[105] CMS Collaboration, "Measurement of the $\mathrm{t\bar{t}}$ production cross section in the tau+jets channel in pp collisions at $\sqrt{s} = 7$ TeV", *CMS PAS* **TOP-11-004** (2012).

[106] M. Bachtis, L. Bianchini, C. Calabria et al., "Performance of tau reconstruction algorithms in 2011 data collected with CMS", *CMS AN* **2011/239** (2011).

[107] CMS Collaboration, "Performance of muon identification in pp collisions at $\sqrt{s} = 7$ TeV", *CMS PAS* **MUO-10-002** (2010).

[108] C. J. Clopper and S. Pearson, "The use of confidence or fiducial limits illustrated in the case of the binomial", *Biometrika* **26** (1934) 404–413.

[109] R. D. Cousins, K. E. Hymes, and J. Tucker, "Frequentist evaluation of intervals estimated for a binomial parameter and for the ratio of Poisson means", *Nucl. Instr. and Meth. A* **612** (2010), no. 2, 388–398, arXiv:0905.3831. doi:10.1016/j.nima.2009.10.156.

[110] CMS Collaboration, "Particle-Flow Event Reconstruction in CMS and Performance for Jets, Taus, and MET",.

[111] CMS Collaboration, "Commissioning of the Particle-Flow Reconstruction in Minimum-Bias and Jet Events from pp Collisions at 7 TeV", *CMS PAS* **PFT-10-002** (2010).

[112] M. Bachtis et al., "Commissioning of the particle-flow event reconstruction with leptons from J/Psi and W decays at 7 TeV", *CMS AN* **2010/210** (2010).

[113] W. Erdmann, "Offline Primary Vertex Reconstruction with Deterministic Annealing Clustering", *CMS IN-2011/014* (2011).

[114] M. Bachtis, "PhD thesis - Heavy Neutral Particle Decays to Tau Pairs in Proton Collisions at $\sqrt{s} = 7$ TeV with CMS at the CERN Large Hadron Collider". PhD thesis, University of Wisconsin - Madison, 2012. Presented on 04/24/2012.

[115] CMS Collaboration, "Performance of τ-lepton reconstruction and identification in CMS", *JINST* **7** (2012) P01001, arXiv:1109.6034. doi:10.1088/1748-0221/7/01/P01001.

[116] CMS Collaboration, "Electron reconstruction and identification at $\sqrt{s} = 7$ TeV", *CMS PAS* **EGM-10-004** (2010).

[117] M. Cacciari, G. P. Salam, and G. Soyez, "The anti-k_T jet clustering algorithm", *JHEP* **04** (2008) 063. doi:10.1088/1126-6708/2008/04/063.

[118] CMS Collaboration, "Determination of Jet Energy Calibration and Transverse Momentum Resolution in CMS", *CMS PAPER* **JME-10-011** (2011) arXiv:1107.4277.

[119] CMS Collaboration, "CMS Commissioning of b-jet identification with pp collisions at $\sqrt{s} = 7$ TeV", *CMS PAS* **BTV-11-001** (2011).

[120] https://twiki.cern.ch/twiki/bin/view/CMS/PileupMCReweightingUtilities, revision 17.

[121] https://twiki.cern.ch/twiki/bin/view/CMS/Pileup_2011_Reweighting.

[122] https://twiki.cern.ch/twiki/bin/view/CMSPublic/WorkBookJetEnergyCorrections, 9.6.2011.

[123] https://twiki.cern.ch/twiki/bin/view/CMS/MissingETUncertaintyPrescription, 9.6.2011.

[124] https://twiki.cern.ch/twiki/bin/view/LHCPhysics/MSSMCharged, revision 8.

[125] CMS Collaboration, "Absolute Calibration of the Luminosity Measurement at CMS: Winter2012 Update", *CMS PAS* **SMP-12-008** (2012).

[126] CMS Collaboration, "Absolute Calibration of the CMS Luminosity Measurement: Summer 2011 Update", *CMS PAS* **EWK-11-001** (2011).

[127] CMS Collaboration, "Towards the measurement of the ttbar cross section in the e-tau and mu-tau dilepton channels in pp collisions at sqrt(s)=14 TeV", *CMS PAS* **TOP-08-004** (2009).

[128] CMS Collaboration, "Selection of Top-Like Events in the Dilepton and Lepton-plus-Jets Channels in Early 7 TeV Data", *CMS PAS* **TOP-10-004** (2010).

[129] CMS Collaboration, "Performance of Methods for Data-Driven Background Estimation in SUSY Searches", *CMS PAS* **SUS-10-001** (2010).

[130] ATLAS Collaboration, "Search for Charged Higgs Bosons in the τ+jets Final State in $t\bar{t}$ Decays with 1.03 fb^{-1} of pp Collision Data Recorded at $\sqrt{s} = 7$ TeV with the ATLAS Experiment", Technical Report ATLAS-CONF-2011-138, CERN, Geneva, (Sep, 2011).

[131] M. Bluj, A. Burgmeier, T. Früboes et al., "Modelling of $\tau\tau$ final states by embedding τ pairs in $Z \to \mu\mu$ events", *CMS AN* **2011/020** (2011).

[132] ATLAS Collaboration, "Data-driven estimation of the background to charged Higgs boson searches using hadronically-decaying τ final states in ATLAS", *ATLAS-CONF-2011-051* (2011).

[133] A. Attikis et al., "Search for light charged Higgs bosons with the $H^{\pm} \to \tau^{\pm}\nu_{\tau}$ decay in the fully hadronic final state", *CMS AN* **2011/470** (2012).

[134] M. J. Kortelainen, "PhD thesis (in preparation)". PhD thesis, University of Helsinki, 2012. Will be presented in September 2012.

[135] https://twiki.cern.ch/twiki/bin/viewauth/CMS/TopLeptonPlusJetsRefSel_mu.

[136] K. Nakamura et al. (Particle Data Group), "The Review of Particle Physics", *J. Phys. G* **37** (2010) 075021.

[137] C. D. Pardos et al., "Establishing the method to measure the single muon efficiency from $Z \to \mu\mu$ events with the first data", *CMS AN* **2010/233** (2010).

[138] A. L. Read, "Modified frequentist analysis of search results (the CL_s method). oai:cds.cern.ch:451614",.

[139] A. L. Read, "Presentation of search results: the CL s technique", *Journal of Physics G: Nuclear and Particle Physics* **28** (2002), no. 10, 2693.

[140] T. Junk, "Confidence level computation for combining searches with small statistics", *Nucl.Instrum.Meth.* **A434** (1999) 435–443, arXiv:hep-ex/9902006. doi:10.1016/S0168-9002(99)00498-2.

[141] T. ATLAS, "Procedure for the LHC Higgs boson search combination in Summer 2011", Technical Report CMS-NOTE-2011-005, CERN, Geneva, (Aug, 2011).

[142] A. L. Read, "Modified frequentist analysis of search results (the CLs method)", *CERN Yellow Report* **CERN-2000-005** (2000) 81.

[143] T. Junk, "Confidence level computation for combining searches with small statistics", *Nucl.Instrum.Meth. A* **434** (1999) 435.

[144] The ATLAS Collaboration, The CMS Collaboration, The LHC Higgs Combination Group, "Procedure for the LHC Higgs boson search combination in Summer 2011", *CMS Note* **2011/005** (2011).

[145] C. Mingshui and A. Korytov. http://mschen.web.cern.ch/mschen/lands/, version of 25.2.2011.

[146] M. B. et al., "Search for neutral Higgs boson decaying into tau pairs with $35pb^{-1}$ at $\sqrt{s} = 7$ TeV using HPS tau identification algorithm", *CMS AN* **2010/430** (2011).

[147] R. Kinnunen, "Search for the Heavy Charged MSSM Higgs bosons with the $H^{\pm} \to \tau^{\pm}\nu_{\tau}$ Decay Mode in Fully Hadronic Final State", Technical Report CMS-NOTE-2006-100, CERN, Geneva, (May, 2006).

[148] E. L. Berger, T. Han, J. Jiang et al., "Associated production of a top quark and a charged Higgs boson", *Phys. Rev. D* **71** (Jun, 2005) 115012. doi:10.1103/PhysRevD.71.115012.

[149] T. Plehn, "Charged Higgs boson production in bottom gluon fusion", *Phys.Rev.* **D67** (2003) 014018, arXiv:hep-ph/0206121. doi:10.1103/PhysRevD.67.014018.

[150] N. Kidonakis, "Differential and total cross sections for top pair and single top production", arXiv:1205.3453.

[151] I. J. R. Aitchison and A. J. G. Hey, "Gauge Theories in Particle Physics, Volume I: From Relativistic Quantum Mechanics to QED". Taylor & Francis, 2004.

[152] M. E. Peskin and D. V. Schroeder, "An Introduction to Quantum Field Theory". Westview Press ABP, 1995.

[153] A. Pich, "Effective Field Theory", 1998.

[154] I. J. R. Aitchison and A. J. G. Hey, "Gauge Theories in Particle Physics, Volume II: QCD and the Electroweak Theory". Taylor & Francis, 2004.

[155] N. R. Martin and G. Shaw, "Particle Physics". John Wiley & Sons, second edition, 2000.

[156] C. G. Callan and D. J. Gross, "High-Energy Electroproduction and the Constitution of the Electric Current", *Phys. Rev. Lett.* **22** (1969), no. 4, 156–159. doi:10.1103/PhysRev.179.1547.

[157] A. Pich, "Aspects of Quantum Chromodynamics", 2000. arXiv.org:hep-ph/0001118.

Appendix A

Lagrangian formalism

The Standard Model (SM) is a Quantum Field Theory (QFT), which employs a Lagrangian formalism in deriving the equations of motion for the fundamental particles it describes, and for describing their interactions with force fields. In general, the Euler-Lagrange equations of motion can be derived by minimising the Action ($\mathcal{S}$), a classical fundamental quantity which is defined to be

$$\mathcal{S} = \int dt \int d^3x \mathcal{L}\left[\phi_i(x), \partial_\mu \phi_i(x)\right] = \int d^4x \, \mathcal{L}\left[\phi_i(x), \partial_\mu \phi_i(x)\right]. \tag{A.1}$$

The symbol $\mathcal{L}$ is the Lagrangian density or simply Lagrangian, and is a functional of one or more fields $\phi_i(x)$ and their derivatives $\partial_\mu \phi_i(x)$. The integral over the space-time coordinates preserves relativistic invariance, whereas the space integral $L = \int \mathcal{L} d^3x$ is the classical Lagrangian.

The principle of least action states that for a system evolving from a given configuration to another from time t_1 to time t_2, the path followed is such as the variation of the actions $\delta\mathcal{S}$ is an extremum; the first-order change in the value of $\mathcal{S}$, when you distort the path, is zero, albeit not necessarily a minimum. This is mathematically expressed as

$$\delta\mathcal{S} = \int d^4x \left[\frac{\partial \mathcal{L}}{\partial \phi_i(x)} \delta\phi_i(x) + \frac{\partial \mathcal{L}}{\partial\left(\partial_\mu \phi_i(x)\right)} \delta\left(\partial_\mu \phi_i(x)\right)\right] = 0. \tag{A.2}$$

The second term, $\frac{\partial \mathcal{L}}{\partial\left(\partial_\mu \phi_i(x)\right)} \delta\left(\partial_\mu \phi_i(x)\right)$, can be rewritten as

$$\frac{\partial \mathcal{L}}{\partial\left(\partial_\mu \phi_i(x)\right)} \delta\left(\partial_\mu \phi_i(x)\right) = \partial_\mu \left(\frac{\partial \mathcal{L}}{\partial\left(\partial_\mu \phi_i(x)\right)} \delta\phi_i(x)\right) - \partial_\mu \left(\frac{\partial \mathcal{L}}{\partial(\partial_\mu \phi_i(x))}\right) \delta\phi_i(x) \tag{A.3}$$

and Eq. (A.2) can be now re-written as

$$\delta\mathcal{S} = \int d^4x \left[\frac{\partial \mathcal{L}}{\partial \phi_i(x)} \delta\phi_i(x) + \partial_\mu \left(\frac{\partial \mathcal{L}}{\partial\left(\partial_\mu \phi_i(x)\right)} \delta\phi_i(x)\right) - \partial_\mu \left(\frac{\partial \mathcal{L}}{\partial(\partial_\mu \phi_i(x))}\right) \delta\phi_i(x)\right] = 0. \tag{A.4}$$

The second term of Eq. (A.4) vanishes, if one turns it into a surface integral over the boundary

of the 4-dimensional space-time region of integration. Given that the initial and final field configurations are known, $\delta\phi_i(x)$ vanishes outside this bounded region. The principle of least action now simplifies to

$$\delta\mathcal{S} = \int d^4x \left[\frac{\partial\mathcal{L}}{\partial\phi_i(x)}\delta\phi_i(x) - \partial_\mu \left(\frac{\partial\mathcal{L}}{\partial(\partial_\mu\phi_i(x))} \right) \delta\phi_i(x) \right] = 0 \tag{A.5}$$

$$\delta\mathcal{S} = \int d^4x \left[\frac{\partial\mathcal{L}}{\partial\phi_i(x)} - \partial_\mu \left(\frac{\partial\mathcal{L}}{\partial(\partial_\mu\phi_i(x))} \right) \right] \delta\phi_i(x) = 0. \tag{A.6}$$

This result must be true for arbitrary fluctuations of the fields $\delta\phi_i(x)$, so the quantity that multiplies this term must vanish at all points giving the result

$$\frac{\partial\mathcal{L}}{\partial\phi_i(x)} = \partial_\mu \left(\frac{\partial\mathcal{L}}{\partial(\partial_\mu\phi_i(x))} \right) \tag{A.7}$$

which is the Euler-Lagrange equation of motion for the field $\phi_i(x)$, in a relativistically invariant form. This equation is also valid for the hermitian conjugated field $\phi_i(x)^*$

Appendix B

Quantum Electrodynamics

B.1 The QED Lagrangian

The SM is a QFT, which employs a Lagrangian formalism as summarised in Appendix A, in deriving the equations of motion for the fundamental particles it describes, and for describing their interactions with force fields. The Lagrangian which describes the Electromagnetic (EM) interaction, denoted $\mathcal{L}_{\text{QED}}$, can be derived by first writing down the Lorentz-invariant Lagrangian describing a free Dirac fermion [1, 151, 152]

$$\mathcal{L}_{\text{Dirac}} = \bar{\psi}(x)(i\partial\!\!\!/ - m)\psi(x) \tag{B.1}$$

for which the Feynman or Dirac slash notation $\partial\!\!\!/ = \gamma^\mu \partial_\mu$ has been used, while $\bar{\psi}(x) = \psi^\dagger(x)\gamma^0$. The matrix γ^0 is included to guarantee the proper behaviour under Lorentz Transformations (LTs). Since the phase of the Dirac spinor $\psi(x)$, which describes a relativistic spin-1/2 field, is not an observable but instead a purely convention-dependent quantity without any physical meaning, the Lagrangian should remain invariant under arbitrary Global Phase Transformation (GPT)

$$\psi(x) \xrightarrow{\text{U(1)}_{\text{global}}} \psi'(x) \equiv e^{iQ\theta}\psi(x) \tag{B.2}$$

where $Q\theta$ is an arbitrary real constant. It can be easily checked that GPT leave the free fermion Lagrangian unchanged

$$\mathcal{L}_{\text{Dirac}} \xrightarrow{\text{U(1)}_{\text{global}}} \mathcal{L}'_{\text{Dirac}} \equiv \bar{\psi}'(x)(i\partial\!\!\!/ - m)\psi'(x) = \mathcal{L}_{\text{Dirac}}$$

However, if one applies a Local Phase Transformation (LPT) to the Dirac spinor, in which the phase is allowed to depend on the space-time coordinate $x^\mu \equiv x = (t, \vec{x})$ such that $\theta = \theta(x)$

$$\psi(x) \xrightarrow{\text{U(1)}_{\text{local}}} \psi'(x) \equiv e^{iQ\theta(x)}\psi(x), \tag{B.3}$$

the free fermion Lagrangian is no longer invariant

$$\mathcal{L}_{\text{Dirac}} \xrightarrow{\text{U(1)}_{\text{local}}} \mathcal{L}'_{\text{Dirac}} \equiv \bar{\psi}'(x)(i\partial\!\!\!/ - m)\psi'(x) = \mathcal{L}_{\text{Dirac}} - Q\bar{\psi}(x)\psi(x)\partial\!\!\!/\theta(x) \tag{B.4}$$

This result is unphysical, since it means that if a phase convection has been chosen at a reference point in space-time, the same convection must also be taken at all space-time coordinates. The extra term that appears in the Lagrangian can be eliminated by adopting the gauge principle, which is the requirement that the free Lagrangian remains invariant under LPT. In order to impose the condition that the Dirac Lagrangian is invariant under LPT, a gauge covariant derivative must be defined that takes the form

$$D_\mu \equiv \partial_\mu - ieQA_\mu(x), \tag{B.5}$$

in which a new spin-1 field $A_\mu(x) = (\phi, \vec{A})$ has been introduced. This spin-1 field is identified as the EM field, and under LPT transforms as

$$A_\mu(x) \xrightarrow{\text{U(1)}_{\text{local}}} A'_\mu(x) \equiv A_\mu(x) + \frac{1}{e}\partial_\mu\theta(x). \tag{B.6}$$

Using the results from Eq. (B.3) and (B.6), the LPT of the covariant derivative can now be written as

$$\begin{aligned} D_\mu\psi(x) \xrightarrow{\text{U(1)}_{\text{local}}} (D_\mu\psi)'(x) &\equiv \left[\partial_\mu - ieQA'_\mu(x)\right]\psi'(x) = e^{iQ\theta(x)}\left[\partial_\mu - ieQA_\mu\right]\psi(x) \\ \Rightarrow (D_\mu\psi)'(x) &\equiv e^{iQ\theta(x)}D_\mu\psi(x). \end{aligned} \tag{B.7}$$

If the 4-derivative ∂_μ in the Dirac Lagrangian is now replaced by the covariant derivative D_μ, the modified Lagrangian takes the form

$$\begin{aligned} \mathcal{L} &\equiv \bar{\psi}(x)(iD\!\!\!/ - m)\psi(x) = \mathcal{L}_{\text{Dirac}} + eQA_\mu(x)\bar{\psi}(x)\gamma^\mu\psi(x) \\ \Rightarrow \mathcal{L} &= \mathcal{L}_{\text{Dirac}} + \mathcal{L}_{\text{int}}, \end{aligned} \tag{B.8}$$

which now includes the extra term $\mathcal{L}_{\text{int}}$ and is now also invariant under LPT

$$\begin{aligned} \mathcal{L} \xrightarrow{\text{U(1)}_{\text{local}}} \mathcal{L}' &\equiv \bar{\psi}'(x)[i(D\!\!\!/\psi)'(x) - m\psi'(x)] = e^{-iQ\theta(x)}e^{iQ\theta(x)}\bar{\psi}(x)(iD\!\!\!/ - m)\psi(x) \\ \Rightarrow \mathcal{L}' &= \mathcal{L}. \end{aligned} \tag{B.9}$$

Therefore, by imposing the condition that the free Dirac fermion Lagrangian must remain invariant under both GPT and LPT, an interaction term $\mathcal{L}_{\text{int}} = eQA_\mu(x)\bar{\psi}(x)\gamma^\mu\psi(x)$ between the Dirac spinor and the gauge field $A_\mu(x)$ has been generated. The gauge principle, which requires invariance under a local symmetry, has thus given rise to what is known as the vertex of Quantum Electrodynamics (QED). The arbitrary constant Q, which was first introduced in Eq. (B.2) has no connection with the EM field but instead is a property of the fermion field $\psi(x)$; its EM charge. Conversely, the term e is indeed a property of the EM field $A_\mu(x)$ and describes the strength with which it interacts.

The final step in obtaining the full QED Lagrangian is the inclusion of a gauge-invariant and Lorentz-invariant kinetic term

$$\mathcal{L}_{\text{Maxwell}} = -\frac{1}{4}\left(F_{\mu\nu}\right)^2 = -\frac{1}{4}\left(\partial_\mu A_\nu - \partial_\nu A_\mu\right)^2 \tag{B.10}$$

which will enable the EM field to be a true propagating field. The term $F_{\mu\nu}$ is just the EM field strength tensor,[1] whose inner product gives the Lorentz-invariant quantity

$$F_{\mu\nu}F^{\mu\nu} = 2\left(B^2 - \frac{E^2}{c^2}\right). \tag{B.11}$$

The QED Lagrangian can now be written in its final form as

$$\mathcal{L}_{\text{QED}} = \mathcal{L}_{\text{Dirac}} + \mathcal{L}_{\text{int}} + \mathcal{L}_{\text{Maxwell}} \tag{B.12}$$

$$\mathcal{L}_{\text{QED}} = \bar{\psi}(x)\left(i\partial\!\!\!/ - m\right)\psi(x) + eQA_\mu(x)\bar{\psi}(x)\gamma^\mu\psi(x) - \frac{1}{4}\left(F_{\mu\nu}\right)^2 \tag{B.13}$$

$$\Rightarrow \mathcal{L}_{\text{QED}} = \bar{\psi}(x)\left(iD\!\!\!/ - m\right)\psi(x) - \frac{1}{4}\left(F_{\mu\nu}\right)^2. \tag{B.14}$$

The first term of the QED Lagrangian in Eq. (B.13) describes the free evolution of a spinor field, the second term describes the EM interaction between the spinor field and the EM field, while the last term is the kinetic term of the EM field and describes the propagation of the EM field, as shown in Fig. B.1.

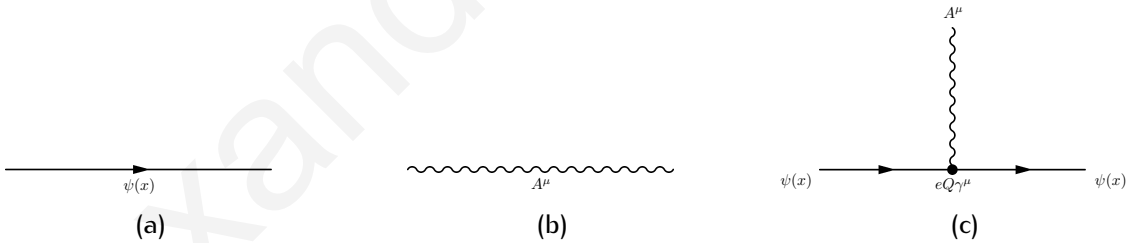

Figure B.1: QED interaction vertices, showing the free propagation of a spinor field (a), the free propagation of the EM field (b), and the EM interaction between the EM field and the spinor field (c).

By imposing the condition that the free-fermion Dirac Lagrangian must be gauge-invariant, the QED Lagrangian was readily derived, providing the full power of classical electrodynamics. Under the application of the Euler-Lagrange equation for $\bar{\psi}(x)$, the QED Lagrangian generates the Dirac equation with a fermion coupled to the EM field

$$\left(iD\!\!\!/ - m\right)\psi(x) = 0, \tag{B.15}$$

while the Euler-Lagrange equation for $\psi(x)$ gives the same equation in Hermitian-conjugate form. Alternatively, the Euler-Lagrange equation for the EM field A_ν generates the Maxwell

[1] Also known as the Faraday tensor or the Maxwell bivector.

source equations

$$\partial_\mu F^{\mu\nu} = e\bar{\psi}(x)\,\gamma^\nu\psi(x) = J^\nu_{\text{em}} \tag{B.16}$$

with $J^\nu_{\text{em}} = (c\rho, \vec{J})$ being the EM 4-current; a Lorentz-covariant 4-vector that replaces the EM current density. It is interesting to note that the addition of a possible mass term for the EM field in Eq. (B.14)

$$\mathcal{L}_{\text{mass}} = \frac{1}{2}m^2 A^\mu A_\mu \tag{B.17}$$

violates gauge invariance and is thus forbidden. In this way the EM field, which interacts with all non-zero electrically charged fermions, is predicted to be massless in remarkable agreement with experimental results which place the photon mass to be $m_\gamma < 1 \times 10^{-18}$ eV/c^2 [81].

B.2 Charge screening and running coupling

Lets consider now the interaction of 2 electrons through the exchange of a photon. In classical electrodynamics, only the direct photon exchange is allowed, which is the first diagram of the right-hand side of Fig. B.2. In QED however, the photon field is able to create at a

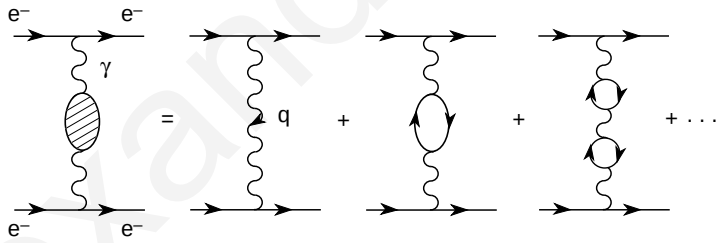

Figure B.2: Feynman diagrams for photon self-energy contribution to e^-e^-. Taken from Ref. [153].

given point in space-time an electron-positron pair e^+e^-, which live for a very short amount of time, thus respecting the principle of energy conservation and momenta or in general the Heisenberg Uncertainty Principle. The e^+e^- pair annihilates to create a photon again, which reaches the other electron, as it is the end outcome in classical electrodynamics. The addition of this process with respect to the LO diagrams which contains no quantum loops, introduces an additional factor of 2 powers of the EM coupling g^2 in the amplitude calculation. The inclusion of a second loop introduces an extra additional factor g^2 and so on for even higher orders, in an infinite geometrical series of EM quantum corrections, which result in a physical scattering amplitude at a given momentum transfer $q^2 = -Q^2$ [153]

$$T\left(q^2\right) \sim -\frac{\alpha}{Q^2}\left[1 + \Pi(Q^2) + \Pi(Q^2)^2 + \Pi(Q^2)^4 + \dots\right] \sim \frac{\alpha\left(Q^2\right)}{Q^2}. \tag{B.18}$$

The term $\Pi(Q^2)$ is a correction term that depends on the momentum transfer carried by the propagator. The quantity $\alpha\left(Q^2\right)$ is known as the QED running coupling, while the fine structure constant $\alpha \approx 1/137$ corresponds to a very low $Q^2 = -m_e^2$. The QED running coupling, which is now an effective coupling, takes the form [153]

$$\alpha\left(Q^2\right) = \frac{\alpha\left(Q_0^2\right)}{1 - \frac{\beta_1 \alpha\left(Q_0^2\right)}{2\pi} \log\left(\frac{Q^2}{Q_0^2}\right)} \tag{B.19}$$

where $Q_0^2 = m_e^2$ and $\beta_1 > 0$. What is evident is that the QED quantum corrections have corrected the effective coupling that the electron sees. In effect, the EM charge decreases at large distances

$$\lim_{Q^2 > Q_0^2} \quad \alpha\left(Q^2\right) > \alpha\left(Q_0^2\right) \tag{B.20}$$

$$\lim_{Q^2 \to 0} \quad \alpha\left(Q^2\right) = 0, \tag{B.21}$$

and the QED running coupling increases with the energy scale. Intuitively, this can be understood as a screening effect of the virtual fermion-anti-fermion pairs ($f\bar{f}$) generated through quantum effects, around the electron charge. The EM vacuum is thus not empty, but is instead filled with energy, which results in e^+e^- pairs appearing and disappearing continuously, making the EM vacuum an collection of dipoles. In this way the physical QED vacuum behaves as a polarised dielectric medium.At large distances (small Q^2) the number of dipoles screening the bare electric charge is large, which translates to seeing a small electric charge. Conversely, at increasingly smaller distances (large Q^2) less dipoles are screening the electron charge and so the strength of EM interaction increases accordingly. Applying the same concept of quantum corrections to QCD however, will yield surprising results.

Appendix C

Quantum Chromodynamics

C.1 Quarks, Colour Confinement and Asymptotic Freedom

Strongly interacting particles are explained in terms of quarks, the elementary constituents of matter. They are fermions, carry fractional electric charge and come in six flavours; up (u), down (d), charm (c), strange (s), top (t) and bottom (b). These fermions are the constituents of the known mesonic and baryonic states, that comprise the hadronic spectrum. Mesons are the bound state of a quark (q) and an anti-quark ($\bar{q}$), while baryons have 3 quark constituents.

The observation of the Δ^{++} resonance, a spin-3/2 baryon of 3 u-quarks with their spins aligned, was evidence of the existence of a new quantum number; colour. Although at first it appeared that the introduction of the colour quantum number was just an artificial mathematical device to classify the hadronic world, to-date there is substantial evidence to support that this is an intrinsic degree of freedom of quarks. Such examples include the measurement of the cross-section ratio [81, 53]

$$R_{e^+e^-} = \frac{\sigma\left(e^+e^- \to \text{hadrons}\right)}{\sigma\left(e^+e^- \to \mu^+\mu^-\right)} \tag{C.1}$$

whose value depends on the centre-of-mass energy of the production process, the calculation of the neutral pion decay channel $\pi^0 \to \gamma\gamma$ [154] and the branching ratio of the processes $\tau^- \to e^-\bar{\nu}_e\nu_\tau$, $q\bar{q} \to \ell\bar{\ell}$ and $W^- \to e^-\bar{\nu}_e$ also provide evidence for the existence of colour.

The introduction of the colour quantum number resolved the Δ^{++} problem with Fermi-Dirac statistics, but it required an additional postulate to explain the fact that colour multiplicity of hadronic states is not observed in nature; extra states with non-zero colour are not observed, but instead all asymptotic states are singlets under rotations in colour-space. This fact implies that the inter-quark force depends on colour, since this force has to produce quark configurations which are restricted by the observed hadron spectrum. This is the confinement hypothesis which assumes that the quark colour degree of freedom is confined to colour-singlet bound states.

The size and structure of the proton has been studied through the elastic and inelastic reactions $\ell^- p \to \ell^- p$ and $\ell^- p \to \ell^- X$, respectively. Elastic scattering led to the first measurements of the size of the proton, which is of the order of 1 fm, while inelastic scattering experiments provided the first evidence for the quark constituents within the proton. The Bjorken scaling or scale invariance [53, 154, 155], which was observed in proton inelastic experiments, suggested that the structure functions, which are a measure of the partonic structure of hadrons, are unchanged by a scale transformation in which particle masses, energy and momenta are multiplied by a scale factor. This scaling behaviour was the first dynamical evidence for the existence of quarks as point-like constituents of the proton, whereas the experimental verification of the Callan-Gross relation [156] also proved that they are spin-1/2 particles.

The aforementioned successful predictions suggested that, quarks are free and independent point-like partons inside the proton, despite the fact that quarks are supposed to be confined in colourless combinations by the Strong interaction. The Bjorken scaling, suggests that the Strong interaction has the property of asymptotic freedom. That is, Strong interactions become weaker at short distances thus allowing the quarks to behave as free particles in the limit that $Q^2 \to \infty$. Considering also the fact that the experimental data for $R_{e^+e^-}$ were more accurate at high energies, one must conclude that the quark confinement only applies at low energies, whereas at high energies the quarks can be seen as free and unconfined particles.

C.2 Quark colour as an SU(3) group

While the quark flavour is associated with the Weak interaction and the fermion electric charges are related to the EM interaction, the Strong interaction appears to be flavour-conserving and flavour-independent. Moreover, the quark colour is not associated with any of the gauge bosons of the EWK interaction γ, Z^0 and $W^\pm$. It thus seems natural to attempt to associate the colour charge with the Strong interaction and try to construct a QFT based on it, analogous to QED. The experimental observations described in Section C.1 are crucial restrictions that have to be implemented in the theory of colour interactions; the number of colour is 3, Colour multiplicity of hadronic states is not observed, colour/confinement and quarks asymptotic freedom must hold, and quarks and anti-quarks are different states.

The simplest representation is the $SU(3)_c$ triplet, in which case the quark colour wavefunction transformation is realised by a special unitary 3×3 matrix parametrised as

$$U = \exp\{i\frac{\lambda^a}{2}\theta_a\} \qquad (a = 1, 2, \ldots, 8), \tag{C.2}$$

As shown in Appendix E, the λ^a are the 8 Gell-Mann matrices and θ_a are arbitrary phase angles. Therefore, the quark colour wavefunction q_α is represented by a 3-component column

vector

$$q_\alpha = \begin{pmatrix} q_1 \\ q_2 \\ q_3 \end{pmatrix} \tag{C.3}$$

and transforms as

$$q_\alpha \to q'_\alpha = U q_\alpha \tag{C.4}$$

The transpose of its complex conjugate $(q^*)^T = q^\dagger$ transforms as

$$q^\dagger_\alpha \to q'^\dagger_\alpha = (U q_\alpha)^\dagger = q^\dagger_\alpha U^\dagger \tag{C.5}$$

In this way the meson combination $q^\dagger_\alpha q_\alpha$ is invariant under $\mathrm{SU}(3)_c$ transformations

$$q^\dagger_\alpha q_\alpha \xrightarrow{\mathrm{SU}(3)_c} q'^\dagger_\alpha q'_\alpha \;\; = \;\; q^\dagger_\alpha U^\dagger U q_\alpha = q^\dagger_\alpha q_\alpha \tag{C.6}$$

which follows from the fact that the U matrices of $\mathrm{SU}(3)_c$ are unitary, as shown in Appendix E. Similarly, the baryon combination qqq remains invariant under an $\mathrm{SU}(3)_c$ transformation

$$\begin{aligned} \epsilon^{\alpha\beta\gamma} q_\alpha q_\beta q_\gamma \xrightarrow{\mathrm{SU}(3)_c} \epsilon^{\alpha\beta\gamma} q'_\alpha q'_\beta q'_\gamma \;\; &= \;\; \epsilon^{\alpha\beta\gamma} U^{\alpha k} U^{\beta\lambda} U^{\gamma\mu} q_k q_\lambda q_\mu = \epsilon^{k\lambda\mu} \det U \; q_k q_\lambda q_\mu \\ \Rightarrow \epsilon^{\alpha\beta\gamma} q'_\alpha q'_\beta q'_\gamma \;\; &= \;\; \epsilon^{k\lambda\mu} q_k q_\lambda q_\mu \end{aligned} \tag{C.7}$$

However, it is not possible to form $\mathrm{SU}(3)_c$ colour singlet combinations of diquarks (qq), anti-diquarks $(\bar{q}\bar{q})$, tetraquarks $(qqqq)$ or anti-tetraquarks $(\bar{q}\bar{q}\bar{q}\bar{q})$. Even-though the requirements for confinement and asymptotic freedom are still not explained, it seems to be the right choice for describing the theory of colour interactions.

C.3 The QCD Lagrangian

The colour symmetry had no obvious physical role and so it was natural to identify this with a gauge group, with the colours being the gauge quantum numbers of the quarks. The Strong interaction was consequently understood to be a system of quarks of 6 flavours, each assigned to the fundamental representation of the local gauge group $\mathrm{SU}(3)$, with the quanta of the $\mathrm{SU}(3)$ gauge field named gluons and the resulting theory QCD. It is tempting to suppose that the gluons are vector particles like the photons in QED, and construct a free Lagrangian analogous to Eq. (B.1), which describes the $\mathrm{SU}(3)_c$ covariant colour interactions [154, 157]

$$\mathcal{L}_{\text{quark}} = \sum_f \bar{q}_f \left(i\partial\!\!\!/ - m_f \right) q_f \tag{C.8}$$

where for simplicity, a vector notation is adopted in which

$$q_f = \begin{pmatrix} q_f^1 \\ q_f^2 \\ q_f^3 \end{pmatrix} \quad , \quad q_f^T = \left(q_f^1,\, q_f^2,\, q_f^3\right) \tag{C.9}$$

denotes a quark of flavour f as a triplet of fields in colour space. Since colour is an exact symmetry, the Lagrangian in Eq. (C.8) should be invariant under global $\mathrm{SU}(3)_c$ transformations in colour space

$$q_f^\alpha \xrightarrow{\mathrm{SU}(3)_c} (q_f^\alpha)' = U_\beta^\alpha\, q_f^\beta. \tag{C.10}$$

The $\mathrm{SU}(3)_c$ matrices for finite transformations take the form

$$U \;=\; \exp\{ig_s\frac{\lambda^a}{2}\theta_a\} \qquad (a = 1,\, 2,\, \ldots,\, 8) \tag{C.11}$$

as shown in Appendix E, while its infinitesimal version being

$$U_{\mathrm{inf}} \;=\; \left(\mathbb{I}_3 + ig_s\frac{\lambda^a}{2}\delta\theta_a\right) \qquad (a = 1,\, 2,\, \ldots,\, 8) \tag{C.12}$$

with $\mathbb{I}_3$ being the 3-dimensional unit matrix. The term g_s is the coupling constant of the Strong interactions, θ_a are arbitrary phase angles, $\delta\theta_a$ are infinitesimal arbitrary phase angles. The terms $\frac{\lambda^a}{2}$ are the generators of the fundamental representation of the $\mathrm{SU}(3)_c$ algebra, whose properties are given in Section E.3.

Although the free QCD Lagrangian is indeed invariant under global $\mathrm{SU}(3)_c$ transformations

$$\mathcal{L}_{\mathrm{quark}} \xrightarrow{\mathrm{SU}(3)_{c_{\mathrm{global}}}} \mathcal{L}'_{\mathrm{quark}} \;\equiv\; \sum_f \bar{q}'_f\,(i\partial\!\!\!/ - m_f)\,q'_f = \mathcal{L}_{\mathrm{quark}}, \tag{C.13}$$

it is however not invariant under local $\mathrm{SU}(3)_c$ transformations, in which the arbitrary parameters θ_a are allowed to have space-time dependence $\theta_a \equiv \theta_a(x)$

$$\mathcal{L}_{\mathrm{quark}} \xrightarrow{\mathrm{SU}(3)_{c_{\mathrm{local}}}} \mathcal{L}'_{\mathrm{quark}} \;\equiv\; \sum_f \bar{q}'_f\,(i\partial\!\!\!/ - m_f)\,q'_f = \mathcal{L}_{\mathrm{quark}} - \sum_f \bar{q}_f\frac{\lambda^a}{2}\partial\!\!\!/\theta_a(x) q_f \tag{C.14}$$

$$\tag{C.15}$$

Using the same reasoning as with the QED Lagrangian in Appendix B, the quark derivatives need to be replaced by covariant objects to eliminate the extra term generated by the LPT. However, unlike in QED where only 1 independent gauge parameters are required, in QCD there are 8 independent gauge parameters required and hence 8 different gauge bosons $G_a^\mu(x)$; the gluons. The $\mathrm{SU}(3)_c$ covariant derivative is defined as

$$D^\mu \equiv \partial^\mu + ig_s\frac{\lambda^a}{2}G_a^\mu(x) \equiv \partial^\mu + ig_s G^\mu(x) \tag{C.16}$$

where $G_1^\mu, G_2^\mu, \ldots, G_8^\mu$ are the eight gluon fields and g_s is the coupling of the Strong interaction. For simplicity the compact matrix notation

$$[G^\mu(x)]_{\alpha\beta} \equiv \left(\frac{\lambda^a}{2}\right)_{\alpha\beta} G_a^\mu(x) \tag{C.17}$$

can be used. As was the case with QED, the transformation properties of the gauge fields can be fixed such that the covariant derivative in Eq. (C.16) transforms in the same way as the colour-vector q_f

$$D^\mu q_f \overset{\mathrm{SU(3)_{c_{local}}}}{\longrightarrow} (D_\mu q_f)'(x) \equiv \left[\partial_\mu + ig_s\frac{\lambda^a}{2}(G^\mu)'\right] q_f' = e^{i\frac{\lambda^a}{2}\theta_a(x)} D^\mu q_f \tag{C.18}$$

The infinitesimal form of Eq. (C.18) is given by

$$D^\mu q_f \overset{\mathrm{SU(3)_{c_{local}}}}{\longrightarrow} (D_\mu q_f)'(x) = \left(\mathbb{I}_3 + ig_s\frac{\lambda^a}{2}\delta\theta_a\right) D^\mu q_f \tag{C.19}$$

Using Eq. (C.19), the transformation properties of the gauge fields are derived. The gauge fields transformation can be written in the form $(G_a^\mu)' = G_a^\mu + \delta G_a^\mu$ and solving for δG_a^μ, while neglecting second order terms involving the product of δG_a^μ and $\delta\theta_a(x)$, the result obtained is

$$ig_s\left[\left(\frac{\lambda^b}{2}\delta\theta_b(x)\right)\left(\frac{\lambda^c}{2}G_c^\mu\right) - \left(\frac{\lambda^c}{2}G_c^\mu\right)\left(\frac{\lambda^b}{2}\delta\theta_b(x)\right)\right] q_f \tag{C.20}$$

Using the commutator properties of the generators in Eq. (E.45), this result can be written in the more compact form

$$\begin{aligned}
\left(\frac{\lambda^a}{2}\delta G_a^\mu\right) q_f &= -\frac{\lambda^a}{2}\left(\partial^\mu\delta\theta_a(x)\right) q_f + ig_s\left[\frac{\lambda^b}{2}, \frac{\lambda^c}{2}\right]\delta\theta_b(x) G_c^\mu q_f \\
&= -\frac{\lambda^a}{2}\left(\partial^\mu\delta\theta_a(x)\right) q_f + ig_s\left(if^{bca}\frac{\lambda^a}{2}\right)\delta\theta_b(x) G_c^\mu q_f \\
&= -\frac{\lambda^a}{2}\left(\partial^\mu\delta\theta_a(x)\right) q_f - g_s\frac{\lambda^a}{2} f^{bca}\delta\theta_b(x) G_c^\mu q_f \\
\Rightarrow \delta G_a^\mu &= -\left(\partial^\mu\delta\theta_a(x)\right) - g_s f^{bca}\delta\theta_b(x) G_c^\mu .
\end{aligned} \tag{C.21}$$

Therefore, this result has fixed the general infinitesimal gauge transformation for the octet of gauge fields G_a^μ

$$(G_a^\mu)' = G_a^\mu - \partial^\mu\delta\theta_a(x) - g_s f^{abc}\delta\theta_b(x) G_c^\mu \tag{C.22}$$

and its corresponding finite transformation law

$$(G^\mu)' = UG^\mu U^\dagger + \frac{i}{g_s}\left(\partial^\mu U\right) U^\dagger \tag{C.23}$$

Likewise, the infinitesimal $SU(3)_c$ transformation of the colour-vector q_f is given by

$$(q_f^\alpha)' = q_f^\alpha + ig_s \left(\frac{\lambda^a}{2}\right)_{\alpha\beta} \delta\theta_a(x) q_f^\beta \tag{C.24}$$

while its corresponding finite transformation law is

$$(q_f^\alpha)' = U_\beta^\alpha q_f^\alpha \tag{C.25}$$

Comparing the gauge transformation of the gluon field G_a^μ in Eq. (C.22) with the gauge transformation of the photon field $A_\mu(x)$ in Eq. (B.6) it is clear that, the non-commutativity of the $SU(3)_c$ matrices has given rise to the non-Abelian extra term $g_s f^{abc} \delta\theta_b(x) G_c^\mu$ which contains the gluon fields. Therefore the gluon fields G_a^μ, which transform as an SU(3) octet in terms of the structure constants f^{abc}, belong to the adjoint representation of the colour group, which is described in Appendix E. A free Dirac equation for an SU(3) triplet q_f which is covariant under SU(3) transformations can now be written down by replacing ∂^μ in Eq. (C.8) by D^μ to get

$$\begin{aligned} \mathcal{L} &= \sum_f \bar{q}_f \left(i\not{D} - m_f\right) q_f = \mathcal{L}_{\text{quark}} - g_s G_a^\mu \sum_f \bar{q}_f \gamma_\mu \frac{\lambda^a}{2} q_f \\ \Rightarrow \mathcal{L} &= \mathcal{L}_{\text{quark}} + \mathcal{L}_{\text{int}_{q-g}}, \end{aligned} \tag{C.26}$$

which is invariant under LPTs. Therefore, as with the QED Lagrangian in Eq. (B.8), the requirement that the free Dirac Lagrangian for quarks remains invariant under LPT has generated a colour interaction term between the quarks and the gluons $\mathcal{L}_{\text{int}_{q-g}}$.

Analogously to the Maxwell term of the QED Lagrangian $\frac{1}{4} F_{\mu\nu} F^{\mu\nu}$ in Eq. (B.10), and by taking the proper normalisation for the gluon kinetic term, the gauge-invariant quantity of the gluon field can be written in the form

$$\mathcal{L}_{\text{gluon}} = -\frac{1}{4} G_a^{\mu\nu} G^a_{\mu\nu}. \tag{C.27}$$

By adding this gluon kinetic term to the Lagrangian in Eq. (C.26), the $SU(3)_c$ invariant QCD Lagrangian can finally be written

$$\begin{aligned} \mathcal{L}_{\text{QCD}} &= \mathcal{L}_{\text{quark}} + \mathcal{L}_{\text{int}_{q-g}} + \mathcal{L}_{\text{gluon}} \\ \mathcal{L}_{\text{QCD}} &= \sum_f \bar{q}_f \left(i\not{\partial} - m_f\right) q_f - g_s G_a^\mu \sum_f \bar{q}_f \gamma_\mu \frac{\lambda^a}{2} q_f - \frac{1}{4} G_a^{\mu\nu} G^a_{\mu\nu} \\ \Rightarrow \mathcal{L}_{\text{QCD}} &= \sum_f \bar{q}_f \left(i\not{D} - m_f\right) q_f - \frac{1}{4} G_a^{\mu\nu} G^a_{\mu\nu}, \end{aligned} \tag{C.28}$$

which can be expanded to a more explicit form

$$\begin{aligned}\mathcal{L}_{\text{QCD}} &= \sum_f \bar{q}_f^{\alpha}\left(i\partial\!\!\!/ - m_f\right) q_f^{\alpha} - \frac{1}{4}\left(\partial^{\mu}G_a^{\nu} - \partial^{\nu}G_a^{\mu}\right)\left(\partial_{\mu}G_{\nu}^{a} - \partial_{\nu}G_{\mu}^{a}\right) \\ &+ g_s G_a^{\mu}\sum_f \bar{q}_f^{\alpha}\gamma_{\mu}\left(\frac{\lambda^a}{2}\right)_{\alpha\beta} q_f^{\beta} \\ &- \frac{g_s}{2}f^{abc}\left(\partial^{\mu}G_a^{\nu} - \partial^{\nu}G_a^{\mu}\right)G_{\mu}^{b}G_{\nu}^{c} - \frac{g_s^2}{4}f^{abc}f_{ade}G_b^{\mu}G_c^{\nu}G_{\mu}^{d}G_{\nu}^{e}.\end{aligned} \tag{C.29}$$

Repeated indices are summed over; α and β are $\mathrm{SU}(3)_c$ triplet indices that run from 1 to 3 while a and b are $\mathrm{SU}(3)_c$ octet indices running from 1 to 8. The first line of the

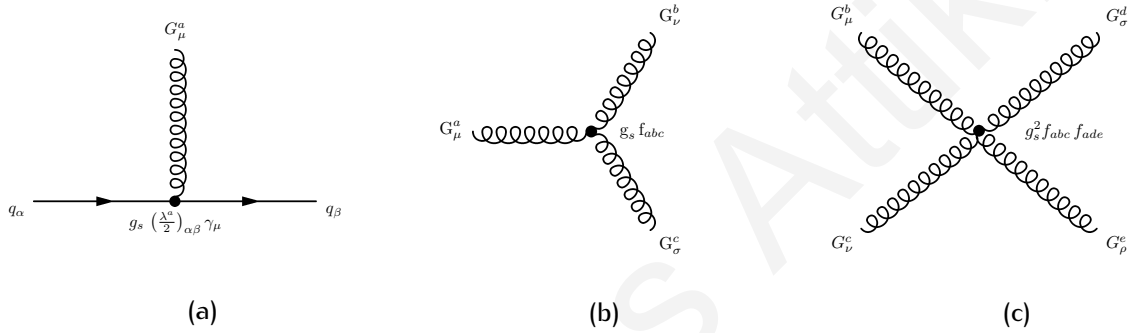

Figure C.1: QCD interaction vertices, showing the emission of a gluon from a quark (a), cubic gluon self-interaction (b) and quartic gluon self-interaction (c).

equation contains the kinetic terms for the quark and gluon fields, which give rise to their corresponding propagators. The next 2 lines describe the interaction vertices of QCD, which are shown in Fig. C.1. The term in the second line, which includes the $\mathrm{SU}(3)_c$ generators, describes the colour interactions between quarks and gluons, as shown in Fig. C.1 (a). The strength of these interactions is characterised by the coupling constant g_s.

The most interesting part of the QCD Lagrangian is revealed in the last line where, due to the non-Abelian structure of the SU(3) colour group, gluon self-interactions arise. In particular, the first term describes cubic gluon self-interactions as shown in Fig. C.1 (b) while the second term quartic gluon self-interactions as shown in Fig. C.1 (c). These features were not observed in QED because instead of one phase, the LPT of the QCD Lagrangian is associated with a matrix of phases. In QED the phase transformations were said to be equivalent to rotations in a plane. However, in QCD the rotations in colour space are equivalent to rotations in 3-dimensional space which, as any matrix multiplication, do not commute and they are said to have a non-Abelian structure.

Another interesting fact is that, only one free parameter is required in QCD; the coupling constant g_s, which characterises all Strong interactions. This is in contrast with the EM force, in which each electrically charged field interacts with the gauge field A^{μ} via a coupling whose strength depends on the EM charge. This difference is another manifestation of the non-Abelian character of the colour group, and it is a consequence of the commutation relations of the $\mathrm{SU}(3)_c$ generators, in Eq. (E.45). Therefore, although in QED it is possible to assign

different EM charges to the different fermions, it is not possible in QCD.

C.4 Charge anti-screening and running coupling

If we now consider the interaction of 2 quarks through the exchange of a gluon, as shown in Fig. C.2 and as previously done for QED, similar arguments will lead to the conclusion that, the gluon field is able to create at a given point in space-time a quark-antiquark pair ($q\bar{q}$). These quarks, which live for a very short amount of time, annihilate to create a gluon again

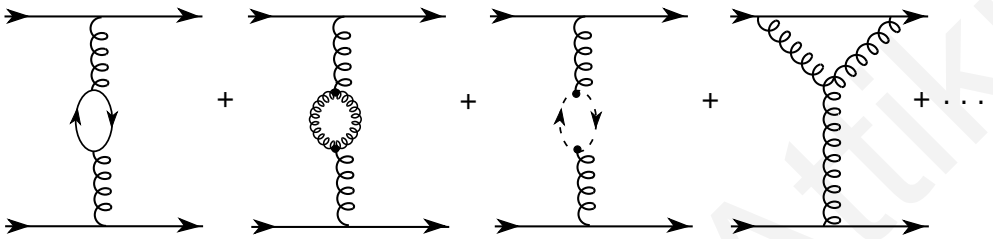

Figure C.2: Feynman diagrams contributing to the Renormalisation of the strong coupling. Taken from Ref. [153].

which reaches the other quark. However, there is a big difference with respect to what was observed in QED. In QCD there are self-interactions between the gluon fields, a consequence of the matrix structure of SU(3) and the non-commutativity of the gluon fields. Thus, the gluon field can couple to 2 gluon fields, since the gluon is its own anti-particle, which can annihilate to give a gluon again. Other configurations are also possible in which gluons solely interact, and the end result is that you get an effective QCD coupling which depends on the momentum transfer of the propagator ($Q^2 = -m_e^2$) and has a form very similar to its QED counterpart [153]

$$\alpha_s\left(Q^2\right) = \frac{\alpha_s\left(Q_0^2\right)}{1 - \frac{\beta_1 \alpha_s\left(Q_0^2\right)}{2\pi} \log\left(\frac{Q^2}{Q_0^2}\right)}. \tag{C.30}$$

However, unlike QED, the term β_1 a negative sign such that $\beta_1 < 0$ and can be expressed as

$$\beta_1 = \frac{1}{3}N_f - \frac{11}{6}N_c \tag{C.31}$$

where $N_f = 6$ and $N_c = 3$. Therefore, β_1 is negative because the contribution from gluon-interactions exceeds that from quark-interaction in the QCD quantum corrections. Since the term β_1 in QCD has an opposite sign than in QED, the QCD coupling running must also be opposite to QED. Therefore, the QCD running coupling decreases at short distances (large Q^2) and increases at large distances (small Q^2)

$$\lim_{Q^2 \to \infty} \quad \alpha_s\left(Q^2\right) = 0 \tag{C.32}$$

$$\lim_{Q^2 \to 0} \quad \alpha_s\left(Q^2\right) = \infty. \tag{C.33}$$

The gluons are generating an anti-screening of the colour charge which makes the QCD coupling to depend on the probing distance or Q^2. Just like in QED, the QCD vacuum is not empty, but instead is filled with energy which results in gluons generating $q\bar{q}$ pairs that appear and disappear continuously. Gauge field self-interaction were not however possible in QED, because photons do not carry electric charge. Only non-Abelian gauge theories, where the intermediate gauge bosons are self-interacting particles, have this anti-screening property. Therefore, Eq. (C.32) describes the fact that QCD has the property of asymptotic freedom; Quarks interact weakly at high energies, allowing for perturbative calculations. Conversely, Eq. (C.33) describes confinement hypothesis; at low energies quarks are confined to colour-singlet bound states thus preventing the unbinding of baryons mesons. Characteristically, at 1 GeV the QCD effective coupling strength is of the order of $\alpha_s \simeq \mathcal{O}(1)$, making perturbative calculations impossible.

Appendix D

Electroweak unification

D.1 The $SU(2)_L \otimes U(1)_Y$ gauge group

Although the QED and QCD full Lagrangians were determined by applying gauge invariance to free Lagrangians, a more elaborated structure is required for Weak interactions in order to properly describe and incorporate the experimental facts. More specifically, the several fermionic flavours and the different properties exhibited for left- and right-handed fields are among the most significant constraints, imposing the need for the left-handed fermions to appear in doublets, while the right-handed fermions in singlets. Obviously, the theory would have to allow for massive gauge bosons $W^{\pm}$ and Z^0 in addition to the massless photon (γ). The simplest possible group with doublet representations is $SU(2)$, while, to also incorporate EM interactions the $U(1)$ group is also required. The resultant symmetry group is $SU(2)_L \otimes U(1)_Y$, where the subscript L refers to left-handed fields and the subscript Y stands for hypercharge. To keep things simple, only a single family of quarks is considered with the notation shown in Table D.1, while the discussion is also equivalent for the lepton sector.

Table D.1: Adopted notation for EWK unification.

Field	$\psi_1(x)$	$\psi_2(x)$	$\psi_3(x)$
Quarks	$\begin{pmatrix} u \\ d \end{pmatrix}_L$	u_R	d_R
Leptons	$\begin{pmatrix} \nu_e \\ e^- \end{pmatrix}_L$	ν_{eR}	e^-_R

As in QCD and QED, the construction of the EWK Lagrangian starts from a free Lagrangian for a massless fermion

$$\mathcal{L}_0 = \sum_{j=1}^{3} i\bar{\psi}_j(x)\,\gamma^\mu \partial_\mu \psi_j(x) \tag{D.1}$$

where the index j ensures that the Lagrangian includes the left-handed doublet $\psi_1(x)$, the right-handed quark singlet $\psi_2(x)$ and the other right-handed quark singlet $\psi_3(x)$. As before, in order to extract something useful from this free Lagrangian, one must impose symmetry conditions. One such example would be flavour symmetry, whereby the field and its complex conjugate can be re-defined using phases and the Lagrangian should remain invariant under such re-definitions. This applies to all 3 fields, giving

$$\psi_1(x) \overset{SU(2)_L \otimes U(1)_Y|_{\text{global}}}{\longrightarrow} \psi_1'(x) \equiv e^{iy_1\beta}\, U_L\, \psi_1(x) \tag{D.2}$$

$$\psi_2(x) \overset{SU(2)_L \otimes U(1)_Y|_{\text{global}}}{\longrightarrow} \psi_2'(x) \equiv e^{iy_2\beta}\, \psi_2(x) \tag{D.3}$$

$$\psi_3(x) \overset{SU(2)_L \otimes U(1)_Y|_{\text{global}}}{\longrightarrow} \psi_3'(x) \equiv e^{iy_3\beta}\, \psi_3(x)\ , \tag{D.4}$$

where for the singlets $\psi_2(x)$ and $\psi_3(x)$ exactly the same transformations as for the QED fields are required, while for the doublet field $\psi_1(x)$ the $SU(2)_L$ transformation is required with

$$U_L \equiv \exp\{i\,\frac{\sigma_i}{2}\,\alpha^i\} \qquad (i=1,2,3) \tag{D.5}$$

where σ_i are the well known Pauli matrices. As in QCD, the matrix transformation U_L is non-Abelian. The parameters y_i are called hypercharges for the reason that, the $U(1)_Y$ phase transformation for fields $\psi_2(x)$ and $\psi_3(x)$ in Eq. (D.3) and Eq. (D.4) is analogous to the QED one in Eq. (B.2). One crucial difference from QED and QCD is that, here it is impossible to include a mass term in the free Lagrangian in Eq. (D.1) as it would mix the left- and right-handed fields, therefore spoiling the symmetry considerations in Eq. (D.2)-Eq. (D.4).

$$\mathcal{L}_0 = \bar{\psi}_L(x)\, i\gamma^\mu \partial_\mu \psi_L(x) + \bar{\psi}_R(x)\, i\gamma^\mu \partial_\mu \psi_R(x) - m\left[\bar{\psi}_L(x)\,\psi_R(x) + \bar{\psi}_R(x)\,\psi_L(x)\right]. \tag{D.6}$$

The terms α^i and β introduced above are just constants, but one can now impose that they can take different convections at different space-time coordinates. That is, the free Lagrangian in Eq. (D.1) is now required to be invariant under local $SU(2)_L \otimes U(1)_Y$ gauge transformations with

$$\alpha^i = \alpha^i(x) \quad , \quad \beta = \beta(x)\,. \tag{D.7}$$

This can only be achieved by replacing the fermion 4-derivatives ∂_μ by covariant derivatives

$$D_\mu \psi_1(x) \equiv \left[\partial_\mu + i\,g\,\widetilde{W}_\mu(x) + i\,g'\,y_1\,B_\mu(x)\right]\,\psi_1(x)\ , \tag{D.8}$$

$$D_\mu \psi_2(x) \equiv \left[\partial_\mu + i\,g'\,y_2\,B_\mu(x)\right]\,\psi_2(x)\ , \tag{D.9}$$

$$D_\mu \psi_3(x) \equiv \left[\partial_\mu + i\,g'\,y_3\,B_\mu(x)\right]\,\psi_3(x)\ , \tag{D.10}$$

where

$$\widetilde{W}_\mu(x) \equiv \frac{\sigma_i}{2} W_\mu^i(x). \tag{D.11}$$

denotes a $\mathrm{SU}(2)_L$ matrix field which is equivalent to the $\mathrm{SU}(3)_c$ matrix field of QCD in Eq. (C.17). The transformation properties for the field derivatives $D_\mu\psi_j(x)$ must be exactly the same as for the fields themselves $\psi_j(x)$, which fixes the transformation properties of the gauge fields as

$$B_\mu(x) \overset{\mathrm{SU}(2)_L\otimes\mathrm{U}(1)_Y|_{\mathrm{local}}}{\longrightarrow} B'_\mu(x) \equiv B_\mu(x) - \frac{1}{g'}\partial_\mu\beta(x), \tag{D.12}$$

$$\widetilde{W}_\mu \overset{\mathrm{SU}(2)_L\otimes\mathrm{U}(1)_Y|_{\mathrm{local}}}{\longrightarrow} \widetilde{W}'_\mu \equiv U_L(x)\,\widetilde{W}_\mu\,U_L^\dagger(x) + \frac{i}{g}\,\partial_\mu U_L(x)\,U_L^\dagger(x). \tag{D.13}$$

The transformation properties of the field $B_\mu(x)$ in Eq. (D.12) appear to be identical to the transformation properties of the photon field $A_\mu(x)$ in Eq. (B.6). Similarly, the $\mathrm{SU}(2)_L$ W_μ^i fields appear to transform in similar fashion to the gluon fields in QCD, as was found in Eq. (C.23). However, instead of 8 gluon fields that are predicted by the dimension of the $\mathrm{SU}(3)_c$ group with $N^2-1=8$, there are now $N^2-1=3$ W_μ's, namely W_μ^1, W_μ^2 and W_μ^3. Also, since the $\mathrm{SU}(2)_L$ is a group of non-commuting matrices, the infinitesimal transformations of W_μ must contain the structure constants of the $\mathrm{SU}(2)_L$

$$\delta W_\mu^i = -\frac{1}{g}\partial_\mu\left(\delta\alpha^i\right) - \epsilon^{ijk}\delta\alpha^j W_\mu^k, \tag{D.14}$$

which originate from the Pauli matrices commutation and anti-commutation relations shown in Eq. (E.12) and Eq. (E.13), respectively. The $\psi_j(x)$ couplings to B_μ are completely free as in QED, meaning that the hypercharges y_j can be arbitrary parameters. Conversely, due to the non-commutative nature of $\mathrm{SU}(2)_L$, this freedom does not exist for the W_μ^i for which there is only a unique $\mathrm{SU}(2)_L$ coupling g. Therefore, from the free Lagrangian of massless fermions in Eq. (D.1), one that remains invariant under local $\mathrm{SU}(2)_L\otimes\mathrm{U}(1)_Y$ transformations can now be written

$$\mathcal{L}_0 = \sum_{j=1}^{3} i\bar{\psi}_j(x)\,\gamma^\mu D_\mu\psi_j(x) \tag{D.15}$$

where 4 massless gauge bosons appear to be available, $W_\mu^\pm, W_\mu^3, B_\mu^0$; 1 from the $\mathrm{U}(1)_Y$ symmetry group and 3 from the $\mathrm{SU}(2)_L$ symmetry group. In order to build the gauge-invariant kinetic term for the gauge fields, the corresponding field strengths are introduced

$$B_{\mu\nu} \equiv \partial_\mu B_\nu - \partial_\nu B_\mu \tag{D.16}$$

$$\widetilde{W}_{\mu\nu} \equiv -\frac{i}{g}\left[\left(\partial_\mu + ig\widetilde{W}_\mu\right), \left(\partial_\nu + ig\widetilde{W}_\nu\right)\right] = \partial_\mu\widetilde{W}_\nu - \partial_\nu\widetilde{W}_\mu + ig\left[W_\mu, W_\nu\right] \tag{D.17}$$

$$\widetilde{W}_{\mu\nu} \equiv \frac{\sigma_i}{2}W_{\mu\nu}^i \quad , \quad W_{\mu\nu}^i = \partial_\mu W_\nu^i - \partial_\nu W_\mu^i - g\epsilon^{ijk}W_\mu^j W_\nu^k. \tag{D.18}$$

Therefore, the properly normalised kinetic Lagrangian is given by

$$\mathcal{L}_{\text{kinetic}} = -\frac{1}{4}B_{\mu\nu}B^{\mu\nu} - \frac{1}{2}\text{Tr}\left[\widetilde{W}_{\mu\nu}\widetilde{W}^{\mu\nu}\right] = -\frac{1}{4}B_{\mu\nu}B^{\mu\nu} - \frac{1}{4}W^{i}_{\mu\nu}W_{i}^{\mu\nu}, \tag{D.19}$$

which appears to give rise to cubic and quartic self-interactions among the gauge fields, a consequence of the fact that the field strengths $W^{i}_{\mu\nu}$ contain a quadratic piece. The strength of these interactions is given by the same $\text{SU}(2)_L$ coupling g which appears in the fermionic piece of the Lagrangian. It is noteworthy that the gauge symmetry forbids the inclusion of a mass term for the gauge bosons, while fermionic masses are also not possible because they would communicate the left- and right-handed fields, which from experiment it is known not to be true. Moreover, left- and right-handed fields have different transformation properties which would therefore produce an explicit breaking of the gauge symmetry. Thus, the $\text{SU}(2)_L \otimes \text{U}(1)_Y$ Lagrangian in Eq. (D.15) and (D.19) can for the moment only contain massless fields.

D.2 Charged-current interactions

The Lagrangian in Eq. (D.15), which remained invariant under local $\text{SU}(2)_L \otimes \text{U}(1)_Y$ gauge transformations, contains interactions of the fermion fields with the gauge bosons

$$\mathcal{L}_0 = \sum_{j=1}^{3} i\bar{\psi}_j(x)\,\gamma^{\mu}D_{\mu}\psi_j(x) \tag{D.20}$$

$$\mathcal{L}_0 = -g\bar{\psi}_1(x)\,\gamma^{\mu}\widetilde{W}_{\mu}\psi_1(x) - g'B_{\mu}\sum_{j=1}^{3} y_j\bar{\psi}_j\gamma^{\mu}\psi_j + i\sum_{j=1}^{3}\bar{\psi}_j(x)\,\gamma^{\mu}\partial_{\mu}\psi_j(x) \tag{D.21}$$

The term containing the $\text{SU}(2)_L$ matrix

$$\widetilde{W}_{\mu} = \frac{\sigma^{i}}{2}W^{i}_{\mu} = \frac{1}{2}\begin{pmatrix} W^{3}_{\mu} & \sqrt{2}W^{\dagger}_{\mu} \\ \sqrt{2}W_{\mu} & -W^{3}_{\mu} \end{pmatrix} \tag{D.22}$$

gives rise to charged-current interactions with the boson field $W_{\mu} \equiv (W^{1}_{\mu} + iW^{2}_{\mu})/\sqrt{2}$ and its complex-conjugate $W^{\dagger}_{\mu} \equiv (W^{1}_{\mu} - iW^{2}_{\mu})/\sqrt{2}$, as shown in Fig. D.1. For a single family of quarks and leptons, the Lagrangian which describes charged-current interactions is

$$\mathcal{L}_{CC} = -\frac{g}{2\sqrt{2}}\left\{W^{\dagger}_{\mu}\left[\bar{u}\gamma^{\mu}(1-\gamma_5)d + \bar{\nu}_e\gamma^{\mu}(1-\gamma_5)e\right] + \text{h.c.}\right\}, \tag{D.23}$$

where the $(1-\gamma_5)$ structure ensures that only left-handed interactions are allowed. The first term couples the upper component of $\psi_1(x)$ with the lower component of $\psi_1(x)$ and similarly for the second term. Therefore, the Lagrangian in Eq. (D.23) appears to have the right properties as it involves only left-handed interactions and has quark/lepton universality manifested through a unique single coupling g to the gauge boson W_{μ}. Since it involves an

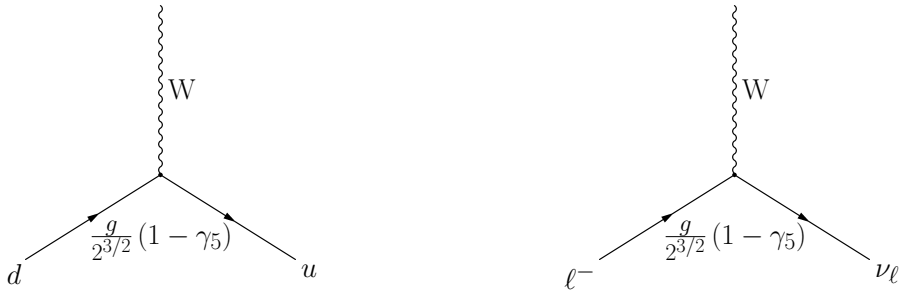

Figure D.1: Charged-current interaction vertices. The $W^{\pm}$ boson couples with a universal interaction strength g, but it only couples to left-handed fermions a feature which is manifested through its $(1-\gamma_5)$ structure.

$\mathrm{SU}(2)_L$ symmetry there are no charges, therefore the interaction is universal.

It is now evident that the universality of quark and lepton interactions is a direct consequence of the assumed gauge symmetry. However, as convincing and elegant as the Lagrangian in Eq. (D.23) might look, it cannot describe the observed dynamics. This is because the gauge bosons described are massless which corresponds to long-range forces, unlike the massive $W^{\pm}$ and Z^0 forces which are known to mediate a short-ranged Weak force.

D.3 Neutral-current interactions

The Lagrangian in Eq. (D.15) also contains interactions with the neutral gauge fields W^3_μ and B_μ. It would perhaps be convenient to identify these bosons with the Z^0 and the γ. This however proves to be impossible, due to the fact that the photon has the same interaction with both fermion chiralities, and so the singlet gauge boson B_μ cannot be equal to the EM field. That would require $y_1 = y_2 = y_3$ and $g' y_j = eQ_j$, which cannot be simultaneously true. Since however both fields are neutral, it is possible to attempt to make a new field which is an arbitrary combination of the 2 fields

$$\begin{pmatrix} W^3_\mu \\ B_\mu \end{pmatrix} \equiv \begin{pmatrix} \cos\theta_W & \sin\theta_W \\ -\sin\theta_W & \cos\theta_W \end{pmatrix} \begin{pmatrix} Z_\mu \\ A_\mu \end{pmatrix}, \tag{D.24}$$

where θ_W is known as the Weak mixing angle or the Weinberg angle. The physical Z^0 boson has a mass different from zero, which is forbidden by the local gauge symmetry. For the moment, it can only be assumed that something breaks the symmetry which generates a mass for the Z^0 boson, and that the neutral mass eigenstates are a mixture of the triplet and singlet $\mathrm{SU}(2)_L$ fields. In terms of the fields Z^0 and γ, the neutral-current Lagrangian is

given by

$$\mathcal{L}_{NC} = -\sum_j \bar{\psi}_j \gamma^\mu \left\{ A_\mu \left[g \frac{\sigma_3}{2} \sin\theta_W + g' y_j \cos\theta_W \right] + Z_\mu \left[g \frac{\sigma_3}{2} \cos\theta_W - g' y_j \sin\theta_W \right] \right\} \psi_j. \tag{D.25}$$

providing the neutral-current vertices as shown in Fig. D.2. In order to get QED from the

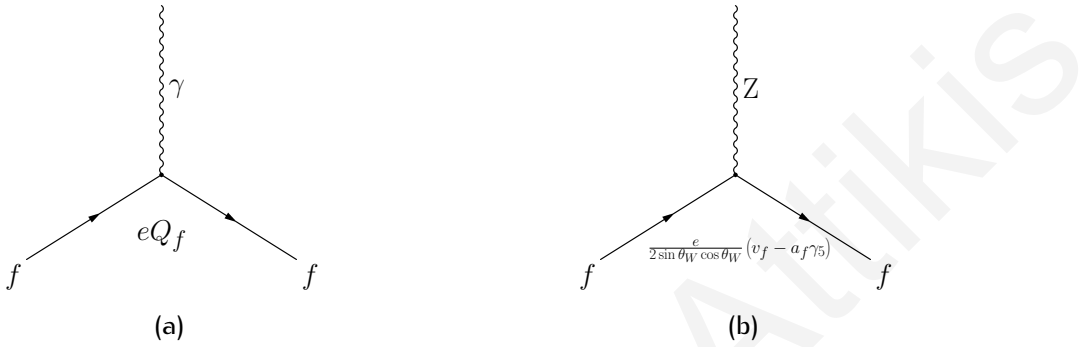

Figure D.2: neutral-current interaction vertices. The photon couples to all fermions through EM interactions with a strength that depends on e and the electric charge of the fermion Q_f. The Z^0 couples to all fermions with an interaction that depends on $\frac{e}{2\sin\theta_W\cos\theta_W}(v_f - a_f\gamma_5)$.

A_μ piece, one needs to impose the conditions

$$g \sin\theta_W = g' \cos\theta_W = \mathrm{e} \tag{D.26}$$

$$Y = Q - T_3, \tag{D.27}$$

where $T_3 \equiv \frac{\sigma_3}{2}$ and Q denotes the EM charge operator

$$Q_1 \equiv \begin{pmatrix} Q_{u/\nu} & 0 \\ 0 & Q_{d/e} \end{pmatrix}, \qquad Q_2 = Q_{u/\nu}, \qquad Q_3 = Q_{d/e}. \tag{D.28}$$

The EWK unification is essentially achieved with Eq. (D.26), whereby a relation between the EM and Weak couplings, g and g', is established. The equality in Eq. (D.26) relates the $\mathrm{SU}(2)_L$ and $\mathrm{U}(1)_Y$ couplings to the EM coupling, providing a unification of the EM and Weak interactions into the EWK interactions. The identity in Eq. (D.27) fixes the fermion hypercharges in terms of their electric charge (Q) and weak isospin quantum numbers (T_3)

$$\text{Quarks:} \quad y_1 = Q_u - \tfrac{1}{2} = Q_d + \tfrac{1}{2} = \tfrac{1}{6}, \qquad y_2 = Q_u = \tfrac{2}{3}, \qquad y_3 = Q_d = -\tfrac{1}{3},$$

$$\text{Leptons:} \quad y_1 = Q_\nu - \tfrac{1}{2} = Q_e + \tfrac{1}{2} = -\tfrac{1}{2}, \qquad y_2 = Q_\nu = 0, \qquad y_3 = Q_e = -1.$$

For neutrinos and leptons, similar behaviour also applies.

Therefore, the unique conditions imposed on the mixing parameter θ_W and the hypercharges (Y) in Eq. (D.26) and (D.27), respectively, have enabled for the Lagrangian of QED to

be reproduced, giving the neutral-current Lagrangian as

$$\mathcal{L}_{NC} = \mathcal{L}_{\text{QED}} + \mathcal{L}_{NC}^{Z} \tag{D.29}$$

where

$$\mathcal{L}_{\text{QED}} = -eA_\mu \sum_j \bar{\psi}_j \gamma^\mu Q_j \psi_j \equiv -eA_\mu J^\mu_{\text{em}} \tag{D.30}$$

is the usual QED Lagrangian and

$$\mathcal{L}_{NC}^{Z} = -\frac{e}{2\sin\theta_W \cos\theta_W} Z_\mu \sum_f \bar{f}\gamma^\mu (v_f - a_f\gamma_5) f\,, \tag{D.31}$$

takes the famous V-A form where $a_f = T_3^f$ and $v_f = T_3^f\left(1 - 4|Q_f|\sin^2\theta_W\right)$. All the interactions of fermions with the Z^0 are fixed in terms of the electric charge e and the mixing angle θ_W. The interactions are however no longer restricted to left-handed fields like the $W^\pm$ boson interactions, but instead it is an interaction that mixes a vector piece γ^μ with an axial piece $\gamma^\mu\gamma_5$. The neutral-current couplings of the different fermions with the Z^0 boson are tabulated in Table D.2.

Table D.2: neutral-current couplings.

	u	d	ν_e	e
$2v_f$	$1 - \frac{8}{3}\sin^2\theta_W$	$-1 + \frac{4}{3}\sin^2\theta_W$	1	$-1 + 4\sin^2\theta_W$
$2a_f$	1	-1	1	-1

In addition to the usual kinetic terms, the kinetic Lagrangian in Eq. (D.19) generates cubic and quartic self-interactions between the gauge bosons [1]

$$\begin{aligned}\mathcal{L}_3 = {} & ie\cot\theta_W \left\{\left(\partial^\mu W^\nu - \partial^\nu W^\mu\right) W_\mu^\dagger Z_\nu - \left(\partial^\mu W^{\nu\dagger} - \partial^\nu W^{\mu\dagger}\right) W_\mu Z_\nu + W_\mu W_\nu^\dagger \left(\partial^\mu Z^\nu - \partial^\nu Z^\mu\right)\right\} \\ & + ie\left\{\left(\partial^\mu W^\nu - \partial^\nu W^\mu\right) W_\mu^\dagger A_\nu - \left(\partial^\mu W^{\nu\dagger} - \partial^\nu W^{\mu\dagger}\right) W_\mu A_\nu + W_\mu W_\nu^\dagger \left(\partial^\mu A^\nu - \partial^\nu A^\mu\right)\right\} \end{aligned} \tag{D.32}$$

$$\begin{aligned}\mathcal{L}_4 = {} & -\frac{e^2}{2\sin^2\theta_W}\left\{\left(W_\mu^\dagger W^\mu\right)^2 - W_\mu^\dagger W^{\mu\dagger} W_\nu W^\nu\right\} - e^2\cot^2\theta_W \left\{W_\mu^\dagger W^\mu Z_\nu Z^\nu - W_\mu^\dagger Z^\mu W_\nu Z^\nu\right\} \\ & - e^2\cot\theta_W \left\{2W_\mu^\dagger W^\mu Z_\nu A^\nu - W_\mu^\dagger Z^\mu W_\nu A^\nu - W_\mu^\dagger A^\mu W_\nu Z^\nu\right\} \\ & - e^2\left\{W_\mu^\dagger W^\mu A_\nu A^\nu - W_\mu^\dagger A^\mu W_\nu A^\nu\right\}. \end{aligned} \tag{D.33}$$

as shown in Fig. D.3. It is worth noting that at least a pair of $W^\pm$ bosons is always present in the Gauge boson self-interaction vertices, meaning that the $\text{SU}(2)_L$ algebra does not generate any neutral vertex with only photons and Z^0 bosons.

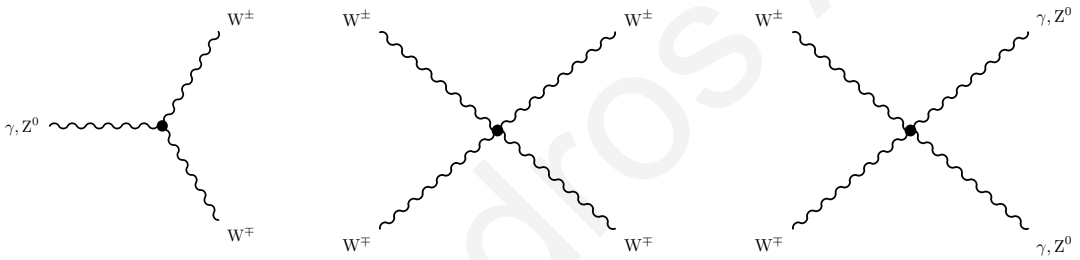

Figure D.3: Gauge boson self-interaction vertices. In all cases, the interaction vertices involve at least a pair of $W^{\pm}$ bosons.

Appendix E

SU(N) algebra

The Special Unitary group of degree N, denoted SU(N), is a group of $N \times N$ Special, Unitary matrices. The SU(N) is a real matrix Lie group of dimension $N^2 - 1$ whose matrices are Special in the sense that they all have

$$\det U = 1 \tag{E.1}$$

and Unitary because

$$UU^\dagger = U^\dagger U = 1 \tag{E.2}$$

where $U^\dagger = (U^*)^T$. Any SU(N) matrix can be written in the form

$$U = e^{iT^a\theta_a} \qquad\qquad a = 1, 2, \ldots, N^2 - 1 \tag{E.3}$$

where θ_a are the arbitrary parameters of the transformation and the $T^a = \frac{\lambda^a}{2}$ are the generators of the SU(N) algebra and are represented by traceless Hermitian matrices satisfying

$$\mathrm{Tr}(T^a) = 0 \tag{E.4}$$

$$(T^a)^\dagger = T^a \tag{E.5}$$

Their commuation relations are, which define the SU(N) algebra are given by

$$\left[T^a,\ T^b\right] = if^{abc}T^c \tag{E.6}$$

The $N \times N$ matrices $T^a = \frac{\lambda^a}{2}$ are the basis generators for the fundamental representation of the SU(N) algebra. The basis generators $\frac{\lambda^a}{2}$ can be chosen so that the structure constants f^{abc} are real and totally antisymmetric. The commutation relations in Eq. (E.6) and the identity

$$\left[T^a, \left[T^b, T^c\right]\right] + \left[T^b, \left[T^c, T^a\right]\right] + \left[T^c, \left[T^a, T^b\right]\right] = 0 \tag{E.7}$$

give the Jacobi identity

$$f^{ade}f^{bcd} + f^{bde}f^{cad} + f^{cde}f^{abd} = 0 \tag{E.8}$$

E.1 Adjoint representation of SU(N)

The adjoint representation of the SU(N) is given by the $\left(N^2-1\right)\left(N^2-1\right)$ matrices which take the form $\left(T_A^a\right)_{bc} = -if^{abc}$. The SU(N) invariants T_F, C_F and C_A are defined by the relations

$$\begin{aligned} &Tr\left(\lambda^a\lambda^b\right) = 4T_f\delta_{ab}, && T_F = \frac{1}{2}, \\ &\left(\lambda^a\lambda^b\right)_{\alpha\beta} = 4C_F\delta_{\alpha\beta}, && C_F = \frac{N^2-1}{2N}, \\ &Tr\left(T_A^aT_A^b\right) = f^{acd}f^{bcd} = C_A\delta_{ab}, && C_A = N, \end{aligned} \tag{E.9}$$

Some other useful properties are given below

$$\begin{aligned} &\left(\lambda^a\right)_{\alpha\beta}\left(\lambda^a\right)_{\gamma\delta} = 2\delta_{\alpha\delta}\delta_{\beta\gamma} - \frac{2}{N}\delta_{\alpha\beta}\delta_{\gamma\delta}, && Tr\left(\lambda^a\lambda^b\lambda^c\right) = 2\left(d^{abc} + if^{abc}\right), \\ &Tr\left(T_A^aT_A^bT_A^c\right) = i\frac{N}{2}f^{abc}, && \sum_b d^{abb} = 0, \\ &f^{abe}f^{cde} + f^{ace}f^{dbe} + f^{ade}f^{bce} = 0, && f^{abe}d^{cde} + f^{ace}d^{dbe} + f^{ade}d^{bce} = 0, \\ &d^{abc}d^{ebc} = \left(N - \frac{4}{N}\right)\delta_{ae}, \end{aligned} \tag{E.10}$$

E.2 SU(2)

The Special Unitary group of degree N=2, denoted SU(2), is an example of a Lie group with 2×2 Special, Unitary matrices. It has dimension $N^2-1=3$ and the basis generators λ^a are the well known Pauli matrices; a set of 2×2 traceless, Hermitian and Unitary matrices

$$\sigma^1 = \sigma^x = \begin{pmatrix} 0 & 1 \\ 1 & 0 \end{pmatrix}, \qquad \sigma^2 = \sigma^y = \begin{pmatrix} 0 & -i \\ i & 0 \end{pmatrix}, \qquad \sigma^3 = \sigma^z = \begin{pmatrix} 1 & 0 \\ 0 & -1 \end{pmatrix}, \tag{E.11}$$

have the following commutation relations

$$\left[\sigma^i, \sigma^j\right] = \sigma^i\sigma^j - \sigma^j\sigma^i = 2i\,\epsilon^{ijk}\sigma^k \tag{E.12}$$

and the following anti-commutation relations

$$\left\{\sigma^i, \sigma^j\right\} = \sigma^i\sigma^j + \sigma^j\sigma^i = 2\delta^{ij} \tag{E.13}$$

The structure constants for SU(2) are defined by the Levi-Civita tensor, a completely anti-symmetric tensor which in 3 dimensions takes the values

$$\epsilon^{ijk} = \begin{cases} 0 & \text{if any 2 of } i,j,k \text{ are equal} \\ 1 & \text{if } i,j,k \text{ is an even permutation} \\ -1 & \text{if } i,j,k \text{ is an odd permutation} \end{cases} \tag{E.14}$$

In addition, the trace of the product of two Pauli matrices gives

$$Tr\left(\sigma^i \sigma^j\right) = 2\delta^{ij} \tag{E.15}$$

The physical consenquences of SU(2) are more obvious by considering infinitesimal transformations in which the transformation matrix V differs only slightly from the 2×2 identity matrix $\mathbb{I}_2$

$$V_{inf} = \mathbb{I}_2 + i\xi = \begin{pmatrix} 1 + i\xi_{11} & i\xi_{12} \\ i\xi_{21} & 1 + i\xi_{22} \end{pmatrix} \tag{E.16}$$

$$\tag{E.17}$$

The term ξ is a 2×2 matrix whose entries are first-order small quantities. The condition now that V_{inf} is Special reduces to

$$\det V_{inf} = (1 + i\xi_{11})(1 + i\xi_{22}) - i^2 \xi_{12} i\xi_{21} = 1 \tag{E.18}$$

Now, neglecting second-order terms $\mathcal{O}(\xi^2)$

$$\begin{aligned} \det V_{inf} &\approx 1 + i(\xi_{11} + \xi_{22}) = 1 && \text{(E.19)} \\ \det V_{inf} &\approx 1 + iTr[\xi] = 1 && \text{(E.20)} \\ \Rightarrow Tr[\xi] &= 0 && \text{(E.21)} \end{aligned}$$

Moreover, the unitarity condition imposed on the SU(2) matrix V imposes the requirement that the matrix ξ is also Hermitian

$$\xi = \xi^\dagger \tag{E.22}$$

This is demonstrated below (again neglecting second-order terms $\mathcal{O}(\xi^2)$)

$$\begin{aligned} VV^\dagger &= (\mathbb{I}_2 + i\xi)\left(\mathbb{I}_2 - i\xi^\dagger\right) = \mathbb{I}_2 && \text{(E.23)} \\ &= \left(\mathbb{I}_2 + i\xi\mathbb{I}_2 - i\xi^\dagger\mathbb{I}_2\right) = \mathbb{I}_2 && \text{(E.24)} \\ &= \mathbb{I}_2 + i\left(\xi - \xi^\dagger\right)\mathbb{I}_2 = \mathbb{I}_2 && \text{(E.25)} \\ \Rightarrow \xi - \xi^\dagger &= 0 && \text{(E.26)} \end{aligned}$$

Therefore, the conditions imposed on V to be a Special and Unitary 2×2 matrix has

resulted in ξ being a traceless (Eq. (E.21)) Hermitian (Eq. (E.22) matrix whose elements are the infinitesimal parameters a, b and c

$$\xi = \begin{pmatrix} a & b - ic \\ b + ic & -a \end{pmatrix} \tag{E.27}$$

This result can be but in a more revealing form by employing the Pauli matrices. First we write

$$a = \frac{\epsilon_3}{2}, \qquad b = \frac{\epsilon_1}{2}, \qquad c = \frac{\epsilon_2}{2} \tag{E.28}$$

and so the matrix in Eq. (E.27) can be expressed as

$$\xi = \frac{\epsilon_a \sigma^a}{2} \qquad a = 1, 2, 3 \tag{E.29}$$

where $\epsilon_a = (\epsilon_1, \epsilon_2, \epsilon_3)$ and $\sigma^a = \left(\sigma^1, \sigma^2, \sigma^3\right)$ is simply the Pauli vector composed of the Pauli matrices. This representation of the ξ matrix is a compact form of the one given in Eq. (E.27), as shown below

$$\xi = \frac{\epsilon_a \sigma^a}{2} = \frac{\epsilon_1}{2}\sigma_1 + \frac{\epsilon_2}{2}\sigma_2 + \frac{\epsilon_1}{3}\sigma_3 \tag{E.30}$$

$$= \frac{\epsilon_1}{2}\begin{pmatrix} 0 & 1 \\ 1 & 0 \end{pmatrix} + \frac{\epsilon_2}{2}\begin{pmatrix} 0 & -i \\ i & 0 \end{pmatrix} + \frac{\epsilon_1}{2}\begin{pmatrix} 1 & 0 \\ 0 & -1 \end{pmatrix} \tag{E.31}$$

$$= b\begin{pmatrix} 0 & 1 \\ 1 & 0 \end{pmatrix} + c\begin{pmatrix} 0 & -i \\ i & 0 \end{pmatrix} + a\begin{pmatrix} 1 & 0 \\ 0 & -1 \end{pmatrix} \tag{E.32}$$

$$\Rightarrow \xi = \begin{pmatrix} a & b - ic \\ b + ic & -a \end{pmatrix} \tag{E.33}$$

Using this result, the general form for an infinitesimal SU(2) matrix takes the form

$$V_{inf} = \left(\mathbb{I}_2 + i\frac{\epsilon_a \sigma^a}{2}\right) \tag{E.34}$$

The infinitesimal form of the SU(2) transformation in Eq. (E.34) can be used to obtain the finite SU(2) transformation by employing the result

$$\lim_{n\to\infty}\left(1 + \frac{A}{n}\right)^n = e^A \tag{E.35}$$

generalised to matrices. The first-order small quantities $\epsilon_1, \epsilon_2, \epsilon_3$ are now replaced by three real but finite (instead of infinitesimal) parameters $\theta_1, \theta_2, \theta_3$ so that $\epsilon_a = \frac{\theta_a}{n}$. The infinitesimal transformation is then applied n times with $n \to \infty$ to give the finite SU(2) transformation

$$V = e^{i\frac{\sigma^a}{2}\theta_a} \qquad a = 1, 2, 3 \tag{E.36}$$

in accordance with the N-dimensional form in Eq. (E.3). This finite SU(2) transformation

has three phase angles θ_a and three non-commuting matrix operators - the Pauli matrices - in the exponent. Moreover, this exponential form of the finite transformations makes the Unitary condition more explicit

$$\begin{aligned} VV^\dagger &= e^{i\frac{\sigma^a}{2}\theta_a}\left(e^{i\frac{\sigma^a}{2}\theta_a}\right)^\dagger && \text{(E.37)}\\ &= e^{i\frac{\sigma^a}{2}\theta_a}e^{-i\left(\frac{\sigma^a}{2}\theta_a\right)^\dagger} && \text{(E.38)}\\ &= e^{i\frac{\sigma^a}{2}\theta_a}e^{-i\frac{\sigma^a}{2}\theta_a} && \text{(E.39)}\\ &= e^0 && \text{(E.40)}\\ \Rightarrow VV^\dagger &= \mathbb{I}_2 && \text{(E.41)} \end{aligned}$$

where we have used the fact that the Pauli matrices are Hermitian and the three θ parameters are real. Comparing the result in Eq. (E.41) with the group axiom we see that the conjugate transpose of the transformation matrix V is simply the inverse transformation matrix V^{-1}

$$V^\dagger = V^{-1} \qquad \text{(E.42)}$$

E.3 SU(3)

The Special Unitary group of degree N=3 is denoted SU(3) and is a group of 3×3 Special, Unitary matrices. It has dimension $N^2-1=8$ and the basis generators λ^a are the well known Gell-Mann matrices

$$\lambda^1=\begin{pmatrix}0&1&0\\1&0&0\\0&0&0\end{pmatrix},\quad \lambda^2=\begin{pmatrix}0&-i&0\\i&0&0\\0&0&0\end{pmatrix},\quad \lambda^3=\begin{pmatrix}1&0&0\\0&-1&0\\0&0&0\end{pmatrix},\quad \lambda^4=\begin{pmatrix}0&0&1\\0&0&0\\1&0&0\end{pmatrix},$$

$$\lambda^5=\begin{pmatrix}0&0&-i\\0&0&0\\i&0&0\end{pmatrix},\quad \lambda^6=\begin{pmatrix}0&0&0\\0&0&1\\0&1&0\end{pmatrix},\quad \lambda^7=\begin{pmatrix}0&0&0\\0&0&-i\\0&i&0\end{pmatrix},\quad \lambda^8=\frac{1}{\sqrt{3}}\begin{pmatrix}1&0&0\\0&1&0\\0&0&-2\end{pmatrix}, \qquad \text{(E.43)}$$

which all have a trace

$$\mathrm{Tr}[\lambda^a] = 0. \qquad \text{(E.44)}$$

Their commutation relations take the form

$$\left[\frac{\lambda^a}{2},\frac{\lambda^b}{2}\right] = if^{abc}\frac{\lambda^c}{2} \qquad \text{(E.45)}$$

where f^{abc} are the $SU(3)_c$ structure constants, which are real and anti-symmetric. Their corresponding anti-commutation relations are given by

$$\{\lambda^a, \lambda^b\} = \frac{4}{N}\delta^{ab}\mathbb{I}_N + 2d^{abc}\lambda^c. \tag{E.46}$$

The term $\mathbb{I}_N$ stands for the N-dimensional unit matrix

$$\mathbb{I}_2 = \begin{bmatrix} 1 & 0 \\ 0 & 1 \end{bmatrix}, \qquad \mathbb{I}_3 = \begin{bmatrix} 1 & 0 & 0 \\ 0 & 1 & 0 \\ 0 & 0 & 1 \end{bmatrix}, \qquad \mathbb{I}_N = \begin{bmatrix} 1 & 0 & \cdots & 0 \\ 0 & 1 & \cdots & 0 \\ \vdots & \vdots & \ddots & \vdots \\ 0 & 0 & \cdots & 1 \end{bmatrix}, \tag{E.47}$$

while the constants d^{abc} are totally symmetric and the only non-zero terms (up to permutations) are

$$d^{146} = d^{157} = -d^{247} = d^{256} = d^{344} = d^{355} = -d^{366} = -d^{377} = \frac{1}{2} \tag{E.48}$$

$$d^{118} = d^{228} = d^{338} = -2d^{448} = -2d^{558} = -2d^{668} = -2d^{778} = -d^{888} = \frac{1}{\sqrt{3}} \tag{E.49}$$

The SU(3) algebra is

$$\left[T^a, T^b\right] = if^{abc}T^c \qquad\qquad a, b, c = 1, 2, \ldots, 8 \tag{E.50}$$

the non-vanishing structure constants f^{abc} are

$$\frac{1}{2}f^{123} = f^{147} = -f^{156} = f^{246} = f^{257} = f^{345} = -f^{367} = \frac{1}{\sqrt{3}}f^{458} = \frac{1}{\sqrt{3}}f^{678} = \frac{1}{2} \tag{E.51}$$

These structure constants are anti-symmetric in all pair of indices.

Appendix F

MSSM Higgs boson branching ratios

The branching ratios of the lighter $\mathcal{CP}$-even MSSM Higgs boson h^0, the heavier $\mathcal{CP}$-even MSSM Higgs boson H^0, the $\mathcal{CP}$-odd MSSM Higgs boson A^0 and the charged MSSM Higgs boson $H^\pm$ are presented in Figs. F.1-F.4. The branching ratio values, taken from Ref. [27], were calculated with the parameters shown in Table F.1.

Table F.1: The MSSM parameters used in Ref. [27] for obtaining the MSSM Higgs boson branching ratios.

Parameter	Value
M_{SUSY}	2 TeV
X_t	$A_t - \mu \cot\beta$
μ	-400 GeV
$m_{\tilde{g}}$	$0.8 M_{\text{SUSY}}$
M_2	+400 GeV
A_t	$\sqrt{6} M_{\text{SUSY}}$
A_b	$\sqrt{6} M_{\text{SUSY}}$
$\tan\beta$	3 , 30

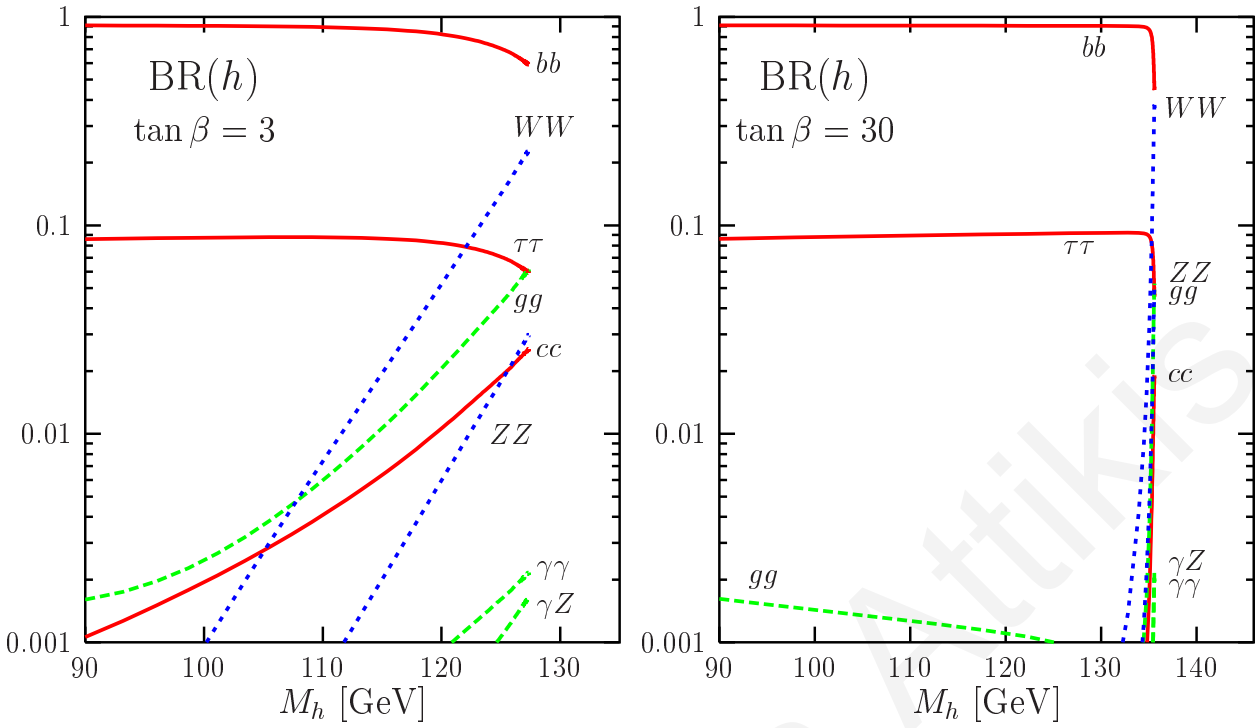

Figure F.1: The decay branching ratios of the $\mathcal{CP}$-even MSSM Higgs boson h^0 as a function of its mass, $\tan\beta = 3$ (**left**) and $\tan\beta = 30$ (**right**). Taken from Ref. [27].

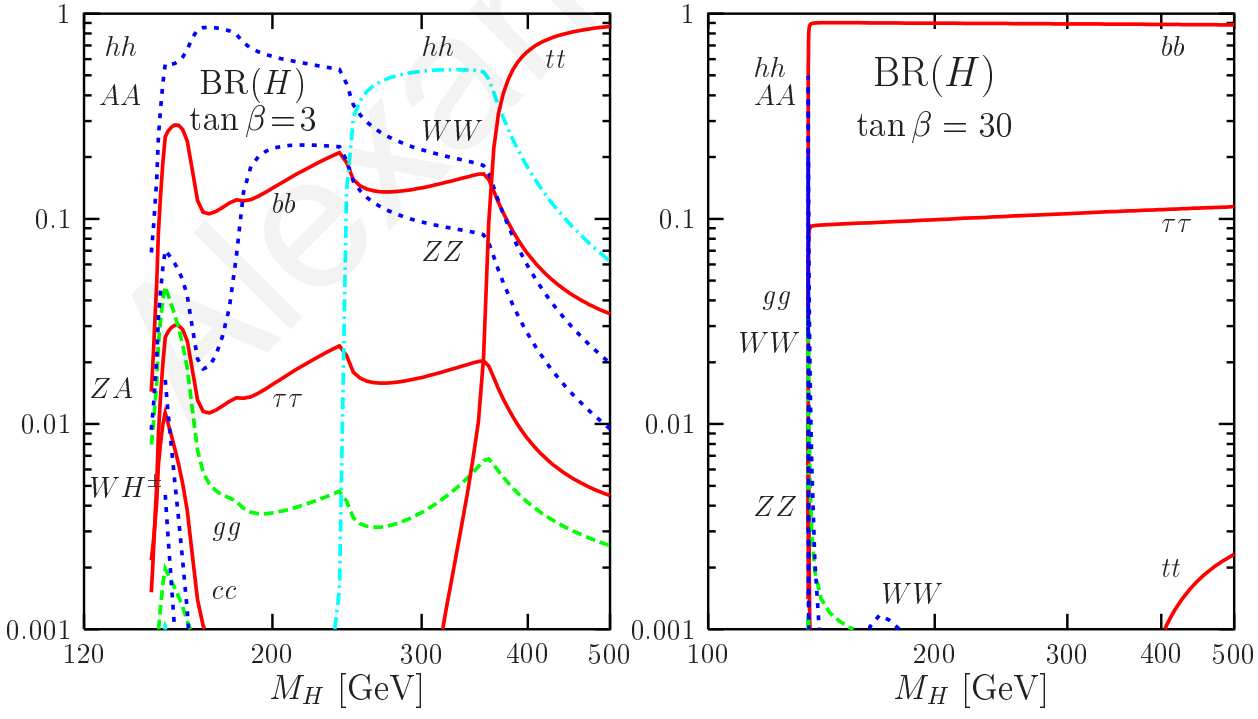

Figure F.2: The decay branching ratios of the heavier $\mathcal{CP}$-even MSSM Higgs boson h^0 as a function of its mass, $\tan\beta = 3$ (**left**) and $\tan\beta = 30$ (**right**). Taken from Ref. [27].

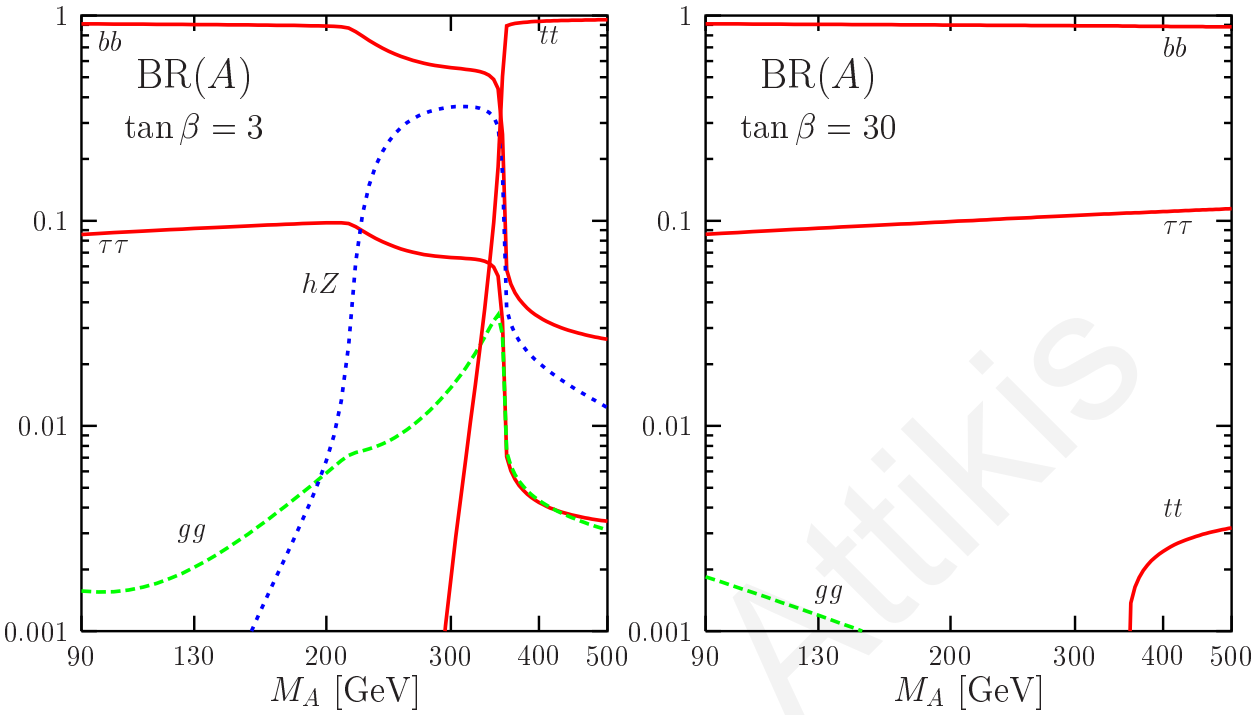

Figure F.3: The decay branching ratios of the heavier $\mathcal{CP}$-even MSSM Higgs boson h^0, as a function of its mass, $\tan\beta = 3$ (**left**) and $\tan\beta = 30$ (**right**). Taken from Ref. [27].

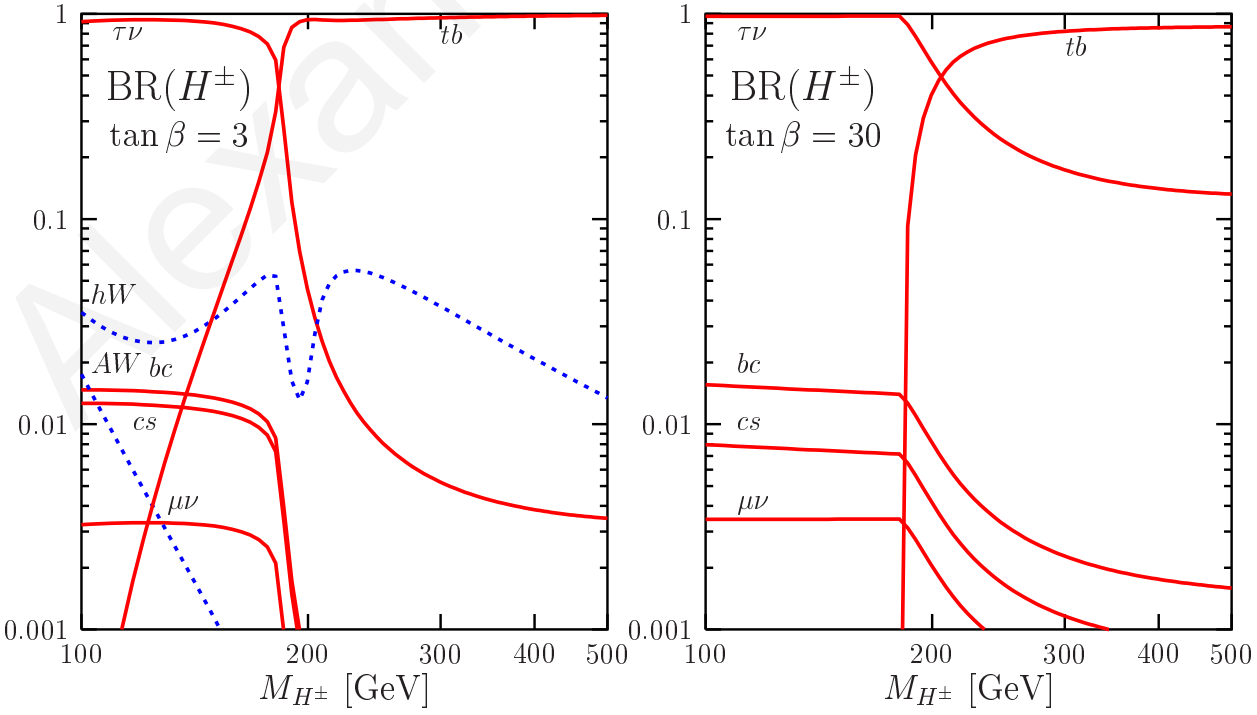

Figure F.4: The decay branching ratios of the charged MSSM Higgs boson $H^{\pm}$, as a function of its mass, $\tan\beta = 3$ (**left**) and $\tan\beta = 30$ (**right**). Taken from Ref. [27].

Appendix G

CMSSW software version and tags used

The analysis was done with the CMSSW_4_2_8_patch2 release and the following tags

```
addpkg RecoTauTag/Configuration   V01-02-03
addpkg RecoTauTag/RecoTau         V01-02-07
addpkg RecoTauTag/TauTagTools     V01-02-00

addpkg DataFormats/PatCandidates  V06-04-19-01
addpkg PhysicsTools/PatAlgos      V08-06-41
addpkg PhysicsTools/PatExamples   V00-05-22
addpkg PhysicsTools/SelectorUtils V00-03-17

addpkg RecoJets/Configuration     V02-04-17

addpkg RecoLuminosity/LumiDB      V03-03-02
```

Appendix H

Datacards used for LandS

The following Limits and Signifcance (LandS) datacard was used for the mass point $m_{H^{\pm}} = 80\,\text{GeV}/c^2$ for $\Delta\phi(\tau\text{ jet}, E_{\text{T}}^{\text{miss}}) < 160°$. Each row corresponds to a systematic unertainty or nuisance parameter which is assumed to be independent of other rows, or 0% correlated. However, within each row the uncertainties are assumed to be 100% correlated. Therefore, different sources of systematic uncertainties are assumed to be completely uncorrelated between each other, while systematic uncertainties of same origin are assumed to be completely correlated between different event yields or measurements.

```
Description: LandS datacard (auto generated) mass=80, luminosity=2.273 1/fb, fully_hadronic_2011A_MET50_withRtau_DeltaPhi160
Date: Thu Mar 22 12:28:00 2012
-------------------------------------------------------------------------------------------------------------------------------
imax    1       number of channels
jmax    *       number of backgrounds
kmax    39      number of nuisance parameters
-------------------------------------------------------------------------------------------------------------------------------
shapes * * lands_histograms_hplushadronic_m80.root $PROCESS $PROCESS_$SYSTEMATIC
-------------------------------------------------------------------------------------------------------------------------------
Observation     130
-------------------------------------------------------------------------------------------------------------------------------
bin             1       1       1       1       1       1       1       1       1       1
process         HH80_1  HW80_1  fake_tt res.    QCD     EWK_Tau EWK_DYx EWK_VVx fake_W  fake_t
process         -1      0       1       2       3       4       5       6       7       8
-------------------------------------------------------------------------------------------------------------------------------
rate            733.758 324.653 2.109   0.000   26.392  78.429  7.003   0.351   4.190   0.163
-------------------------------------------------------------------------------------------------------------------------------
1       lnN     1.122   1.126   1.120   1       1       1.113   1.121   1.112   1.137   1.109   tau+MET trg scale factor
2       lnN     1       1       1       1       1       1       1       1       1       1       reserved for leptonic
3       lnN     1.060   1.060   1       1       1       1.060   1.060   1.060   1       1       tau-jet ID (no Rtau)
4       lnN     1       1       1.150   1       1       1       1       1       1.150   1.150   tau-jet mis-ID (no Rtau)
5       lnN     1       1       1       1       1       1       1       1       1       1       reserved for leptonic
6       lnN     1       1       1       1       1       1       1       1       1       1       reserved for leptonic
7       shapeQ  1       1       1       0       0       1       1       1       1       1       JES/JER/MET/Rtau effect on mT shape
8       lnN     1       1       1       1       1       1       1       1       1       1       reserved for leptonic
9       lnN     1.003   1.007   1.008   1       1       1       1.009   1.012   1.003   1.005   lepton veto
10      lnN     1.015   1.018   1.014   1       1       1       1       1       1       1.016   btagging
11      lnN     1       1       1       1       1       1       1.020   1.026   1.044   1       mis-btagging
12      shapeStat       0       0       0       0       0       1       0       0       0       0       QCD stat.
13      lnN     1       1       1       1       1.040   1       1       1       1       1       QCD syst.
14      lnN     1       1       1       1       1       1.012   1       1       1       1       EWK with taus QCD contamination
15      lnN     1       1       1       1       1       1.007   1.001   1.001   1       1       EWK with taus W->tau->mu
16      lnN     1       1       1       1       1       1.005   1.001   1.001   1       1       EWK with taus muon selection
17      lnN     1.067   1       1       1       1       1       1       1       1       1       HH MC stat.
18      lnN     1       1.103   1       1       1       1       1       1       1       1       HW MC stat.
19      shapeStat       0       0       0       0       0       1       0       0       0       0       EWK with taus stat.
20      lnN     1       1       1       1       1       1       1       1       1       1       reserved for leptonic
21      lnN     1       1       1       1       1       1       1       1       1       1       reserved for leptonic
22      lnN     1       1       1       1       1       1       1       1       1       1       tt->jjtau MC stat.
23      lnN     1       1       1       1       1       1       1       1       1       1       reserved for leptonic
24      lnN     1       1       1       1       1       1       1.292   1       1       1       Z->tautau MC stat
25      lnN     1       1       1       1       1       1       1       1       1       1       W+jets MC stat.
26      lnN     1       1       1       1       1       1       1       1       1       1       Single top MC stat.
27      lnN     1       1       1       1       1       1       1       1.659   1       1       diboson MC stat
28      lnN     0.904/1.070     0.904/1.070     0.904/1.070     1       1       1       1       1       1       ttbar cross section
29      lnN     1       1       1       1       1       1       1       1       1.050   1       W+jets cross section
```

```
30      lnN     1       1       1       1       1       1       1       1       1       1.080   single top cross section
31      lnN     1       1       1       1       1       1       1.040   1       1       1       Z->ll cross section
32      lnN     1       1       1       1       1       1       1       1.040   1       1       diboson cross section
33      lnN     1.022   1.022   1.022   1       1       1       1.022   1.022   1.022   1.022   luminosity
34      lnN     1.034   1.007   1.071   1       1       1       1.076   1.039   1.101   1.147   pileup
35      lnN     1       1       1.280   1       1       1       1       1       1       1       ttbar fake tau MC stat.
36      lnN     1       1       1       1       1       1       1       1       1       1       Z->tautau fake tau MC stat.
37      lnN     1       1       1       1       1       1       1       1       1.713   1       W+jets fake tau MC stat.
38      lnN     1       1       1       1       1       1       1       1       1       1.493   single top fake tau MC stat.
39      lnN     1       1       1       1       1       1       1       1       1       1       diboson fake tau MC stat.
```

The following LandS datacard was used for the mass point $m_{H^\pm} = 100\,\text{GeV}/c^2$ for $\Delta\phi(\tau\,\text{jet}, E_\text{T}^\text{miss}) < 160°$. Each row corresponds to a systematic unertainty or nuisance parameter which is assumed to be independent of other rows, or 0% correlated. However, within each row the uncertainties are assumed to be 100% correlated. Therefore, different sources of systematic uncertainties are assumed to be completely uncorrelated between each other, while systematic uncertainties of same origin are assumed to be completely correlated between different event yields or measurements.

```
Description: LandS datacard (auto generated) mass=100, luminosity=2.273 1/fb, fully_hadronic_2011A_MET50_withRtau_DeltaPhi160
Date: Thu Mar 22 12:28:00 2012
-------------------------------------------------------------------------------------------------------------------------------
imax    1       number of channels
jmax    *       number of backgrounds
kmax    39      number of nuisance parameters
-------------------------------------------------------------------------------------------------------------------------------
shapes * * lands_histograms_hplushadronic_m100.root $PROCESS $PROCESS_$SYSTEMATIC
-------------------------------------------------------------------------------------------------------------------------------
Observation     130
-------------------------------------------------------------------------------------------------------------------------------
bin             1       1       1       1       1       1       1       1       1       1
process         HH100_1 HW100_1 fake_tt res.    QCD     EWK_Tau EWK_DYx EWK_VVx fake_W  fake_t
process         -1      0       1       2       3       4       5       6       7       8
-------------------------------------------------------------------------------------------------------------------------------
rate            863.629 359.781 2.109   0.000   26.392  78.429  7.003   0.351   4.190   0.163
-------------------------------------------------------------------------------------------------------------------------------
1       lnN     1.130   1.125   1.120   1       1       1.113   1.121   1.112   1.137   1.109   tau+MET trg scale factor
2       lnN     1       1       1       1       1       1       1       1       1       1       reserved for leptonic
3       lnN     1.060   1.060   1       1       1       1.060   1.060   1.060   1       1       tau-jet ID (no Rtau)
4       lnN     1       1       1.150   1       1       1       1       1       1.150   1.150   tau-jet mis-ID (no Rtau)
5       lnN     1       1       1       1       1       1       1       1       1       1       reserved for leptonic
6       lnN     1       1       1       1       1       1       1       1       1       1       reserved for leptonic
7       shapeQ  1       1       1       0       0       1       1       1       1       1       JES/JER/MET/Rtau effect on mT shape
8       lnN     1       1       1       1       1       1       1       1       1       1       reserved for leptonic
9       lnN     1.003   1.007   1.008   1       1       1       1.009   1.012   1.003   1.005   lepton veto
10      lnN     1.017   1.017   1.014   1       1       1       1       1       1       1.016   btagging
11      lnN     1       1       1       1       1       1       1.020   1.026   1.044   1       mis-btagging
12      shapeStat       0       0       0       0       1       0       0       0       0       0       QCD stat.
13      lnN     1       1       1       1       1.040   1       1       1       1       1       QCD syst.
14      lnN     1       1       1       1       1       1.012   1       1       1       1       EWK with taus QCD contamination
15      lnN     1       1       1       1       1       1.007   1.001   1.001   1       1       EWK with taus W->tau->mu
16      lnN     1       1       1       1       1       1.005   1.001   1.001   1       1       EWK with taus muon selection
17      lnN     1.062   1       1       1       1       1       1       1       1       1       HH MC stat.
18      lnN     1       1.098   1       1       1       1       1       1       1       1       HW MC stat.
19      shapeStat       0       0       0       0       0       1       0       0       0       0       EWK with taus stat.
20      lnN     1       1       1       1       1       1       1       1       1       1       reserved for leptonic
21      lnN     1       1       1       1       1       1       1       1       1       1       reserved for leptonic
22      lnN     1       1       1       1       1       1       1       1       1       1       tt->jjtau MC stat.
23      lnN     1       1       1       1       1       1       1       1       1       1       reserved for leptonic
24      lnN     1       1       1       1       1       1       1.292   1       1       1       Z->tautau MC stat
25      lnN     1       1       1       1       1       1       1       1       1       1       W+jets MC stat.
26      lnN     1       1       1       1       1       1       1       1       1       1       Single top MC stat.
27      lnN     1       1       1       1       1       1       1       1.659   1       1       diboson MC stat
28      lnN     0.904/1.070     0.904/1.070     0.904/1.070     1       1       1       1       1       1       ttbar cross section
29      lnN     1       1       1       1       1       1       1       1       1.050   1       W+jets cross section
30      lnN     1       1       1       1       1       1       1       1       1       1.080   single top cross section
31      lnN     1       1       1       1       1       1       1.040   1       1       1       Z->ll cross section
32      lnN     1       1       1       1       1       1       1       1.040   1       1       diboson cross section
33      lnN     1.022   1.022   1.022   1       1       1       1.022   1.022   1.022   1.022   luminosity
34      lnN     1.003   1.052   1.071   1       1       1       1.076   1.039   1.101   1.147   pileup
35      lnN     1       1       1.280   1       1       1       1       1       1       1       ttbar fake tau MC stat.
36      lnN     1       1       1       1       1       1       1       1       1       1       Z->tautau fake tau MC stat.
37      lnN     1       1       1       1       1       1       1       1       1.713   1       W+jets fake tau MC stat.
38      lnN     1       1       1       1       1       1       1       1       1       1.493   single top fake tau MC stat.
39      lnN     1       1       1       1       1       1       1       1       1       1       diboson fake tau MC stat.
```

The following LandS datacard was used for the mass point $m_{H^\pm} = 120\,\text{GeV}/c^2$ for $\Delta\phi(\tau\,\text{jet}, E_\text{T}^\text{miss}) < 160°$. Each row corresponds to a systematic unertainty or nuisance parameter which is assumed to be independent of other rows, or 0% correlated. However, within each row the uncertainties are assumed to be 100% correlated. Therefore, different sources of systematic uncertainties are assumed to be completely uncorrelated between each other, while systematic uncertainties of same origin are assumed to be completely correlated between different event yields or measurements.

```
Description: LandS datacard (auto generated) mass=120, luminosity=2.273 1/fb, fully_hadronic_2011A_MET50_withRtau_DeltaPhi160
Date: Thu Mar 22 12:28:00 2012
-------------------------------------------------------------------------------------------------------------------------------
imax    1       number of channels
jmax    *       number of backgrounds
kmax    39      number of nuisance parameters
-------------------------------------------------------------------------------------------------------------------------------
shapes * * lands_histograms_hplushadronic_m120.root $PROCESS $PROCESS_$SYSTEMATIC
-------------------------------------------------------------------------------------------------------------------------------
Observation     130
-------------------------------------------------------------------------------------------------------------------------------
bin             1       1       1       1       1       1       1       1       1       1
process         HH120_1 HW120_1 fake_tt res.    QCD     EWK_Tau EWK_DYx EWK_VVx fake_W  fake_t
process         -1      0       1       2       3       4       5       6       7       8
-------------------------------------------------------------------------------------------------------------------------------
rate            882.446 513.739 2.109   0.000   26.392  78.429  7.003   0.351   4.190   0.163
-------------------------------------------------------------------------------------------------------------------------------
1       lnN     1.132   1.125   1.120   1       1       1.113   1.121   1.112   1.137   1.109   tau+MET trg scale factor
2       lnN     1       1       1       1       1       1       1       1       1       1       reserved for leptonic
3       lnN     1.060   1.060   1       1       1       1.060   1.060   1.060   1       1       tau-jet ID (no Rtau)
4       lnN     1       1       1.150   1       1       1       1       1       1.150   1.150   tau-jet mis-ID (no Rtau)
5       lnN     1       1       1       1       1       1       1       1       1       1       reserved for leptonic
6       lnN     1       1       1       1       1       1       1       1       1       1       reserved for leptonic
7       shapeQ  1       1       1       0       0       1       1       1       1       1       JES/JER/MET/Rtau effect on mT shape
8       lnN     1       1       1       1       1       1       1       1       1       1       reserved for leptonic
9       lnN     1.004   1.006   1.008   1       1       1       1.009   1.012   1.003   1.005   lepton veto
10      lnN     1.012   1.012   1.014   1       1       1       1       1       1       1.016   btagging
11      lnN     1       1       1       1       1       1       1.020   1.026   1.044   1       mis-btagging
12      shapeStat       0       0       0       0       1       0       0       0       0       0       QCD stat.
13      lnN     1       1       1       1       1.040   1       1       1       1       1       QCD syst.
14      lnN     1       1       1       1       1       1.012   1       1       1       1       EWK with taus QCD contamination
15      lnN     1       1       1       1       1       1.007   1.001   1.001   1       1       EWK with taus W->tau->mu
16      lnN     1       1       1       1       1       1.005   1.001   1.001   1       1       EWK with taus muon selection
17      lnN     1.063   1       1       1       1       1       1       1       1       1       HH MC stat.
18      lnN     1       1.081   1       1       1       1       1       1       1       1       HW MC stat.
19      shapeStat       0       0       0       0       0       1       0       0       0       0       EWK with taus stat.
20      lnN     1       1       1       1       1       1       1       1       1       1       reserved for leptonic
21      lnN     1       1       1       1       1       1       1       1       1       1       reserved for leptonic
22      lnN     1       1       1       1       1       1       1       1       1       1       tt->jjtau MC stat.
23      lnN     1       1       1       1       1       1       1       1       1       1       reserved for leptonic
24      lnN     1       1       1       1       1       1       1.292   1       1       1       Z->tautau MC stat
25      lnN     1       1       1       1       1       1       1       1       1       1       W+jets MC stat.
26      lnN     1       1       1       1       1       1       1       1       1       1       Single top MC stat.
27      lnN     1       1       1       1       1       1       1       1.659   1       1       diboson MC stat
28      lnN     0.904/1.070     0.904/1.070     0.904/1.070     1       1       1       1       1       ttbar cross section
29      lnN     1       1       1       1       1       1       1       1       1.050   1       W+jets cross section
30      lnN     1       1       1       1       1       1       1       1       1       1.080   single top cross section
31      lnN     1       1       1       1       1       1       1.040   1       1       1       Z->ll cross section
32      lnN     1       1       1       1       1       1       1       1.040   1       1       diboson cross section
33      lnN     1.022   1.022   1.022   1       1       1       1.022   1.022   1.022   1.022   luminosity
34      lnN     1.009   1.008   1.071   1       1       1       1.076   1.039   1.101   1.147   pileup
35      lnN     1       1       1.280   1       1       1       1       1       1       1       ttbar fake tau MC stat.
36      lnN     1       1       1       1       1       1       1       1       1       1       Z->tautau fake tau MC stat.
37      lnN     1       1       1       1       1       1       1       1       1.713   1       W+jets fake tau MC stat.
38      lnN     1       1       1       1       1       1       1       1       1       1.493   single top fake tau MC stat.
39      lnN     1       1       1       1       1       1       1       1       1       1       diboson fake tau MC stat.
```

The following LandS datacard was used for the mass point $m_{H^\pm} = 140\,\text{GeV}/c^2$ for $\Delta\phi(\tau\,\text{jet}, E_\text{T}^\text{miss}) < 160°$. Each row corresponds to a systematic unertainty or nuisance parameter which is assumed to be independent of other rows, or 0% correlated. However, within each row the uncertainties are assumed to be 100% correlated. Therefore, different sources of systematic uncertainties are assumed to be completely uncorrelated between each other, while systematic uncertainties of same origin are assumed to be completely correlated between different event yields or measurements.

```
Description: LandS datacard (auto generated) mass=140, luminosity=2.273 1/fb, fully_hadronic_2011A_MET50_withRtau_DeltaPhi160
Date: Thu Mar 22 12:28:00 2012
-------------------------------------------------------------------------------------------------------------------------------
imax    1       number of channels
jmax    *       number of backgrounds
kmax    39      number of nuisance parameters
-------------------------------------------------------------------------------------------------------------------------------
shapes * * lands_histograms_hplushadronic_m140.root $PROCESS $PROCESS_$SYSTEMATIC
-------------------------------------------------------------------------------------------------------------------------------
Observation     130
-------------------------------------------------------------------------------------------------------------------------------
bin             1       1       1       1       1       1       1       1       1       1
process         HH140_1 HW140_1 fake_tt res.    QCD     EWK_Tau EWK_DYx EWK_VVx fake_W  fake_t
process         -1      0       1       2       3       4       5       6       7       8
-------------------------------------------------------------------------------------------------------------------------------
rate            745.910 593.838 2.109   0.000   26.392  78.429  7.003   0.351   4.190   0.163
-------------------------------------------------------------------------------------------------------------------------------
1       lnN     1.130   1.127   1.120   1       1       1.113   1.121   1.112   1.137   1.109   tau+MET trg scale factor
2       lnN     1       1       1       1       1       1       1       1       1       1       reserved for leptonic
3       lnN     1.060   1.060   1       1       1       1.060   1.060   1.060   1       1       tau-jet ID (no Rtau)
4       lnN     1       1       1.150   1       1       1       1       1       1.150   1.150   tau-jet mis-ID (no Rtau)
5       lnN     1       1       1       1       1       1       1       1       1       1       reserved for leptonic
6       lnN     1       1       1       1       1       1       1       1       1       1       reserved for leptonic
7       shapeQ  1       1       1       0       0       1       1       1       1       1       JES/JER/MET/Rtau effect on mT shape
8       lnN     1       1       1       1       1       1       1       1       1       1       reserved for leptonic
9       lnN     1.004   1.006   1.008   1       1       1       1.009   1.012   1.003   1.005   lepton veto
10      lnN     1.011   1.013   1.014   1       1       1       1       1       1       1.016   btagging
11      lnN     1       1       1       1       1       1       1.020   1.026   1.044   1       mis-btagging
12      shapeStat       0       0       0       0       1       0       0       0       0       0       QCD stat.
13      lnN     1       1       1       1       1.040   1       1       1       1       1       QCD syst.
14      lnN     1       1       1       1       1       1.012   1       1       1       1       EWK with taus QCD contamination
15      lnN     1       1       1       1       1       1.007   1.001   1.001   1       1       EWK with taus W->tau->mu
16      lnN     1       1       1       1       1       1.005   1.001   1.001   1       1       EWK with taus muon selection
17      lnN     1.066   1       1       1       1       1       1       1       1       1       HH MC stat.
18      lnN     1       1.076   1       1       1       1       1       1       1       1       HW MC stat.
19      shapeStat       0       0       0       0       0       1       0       0       0       0       EWK with taus stat.
20      lnN     1       1       1       1       1       1       1       1       1       1       reserved for leptonic
21      lnN     1       1       1       1       1       1       1       1       1       1       reserved for leptonic
22      lnN     1       1       1       1       1       1       1       1       1       1       tt->jjtau MC stat.
23      lnN     1       1       1       1       1       1       1       1       1       1       reserved for leptonic
24      lnN     1       1       1       1       1       1       1.292   1       1       1       Z->tautau MC stat
25      lnN     1       1       1       1       1       1       1       1       1       1       W+jets MC stat.
26      lnN     1       1       1       1       1       1       1       1       1       1       Single top MC stat.
27      lnN     1       1       1       1       1       1       1       1.659   1       1       diboson MC stat
28      lnN     0.904/1.070     0.904/1.070     0.904/1.070     1       1       1       1       1       1       ttbar cross section
29      lnN     1       1       1       1       1       1       1       1       1.050   1       W+jets cross section
30      lnN     1       1       1       1       1       1       1       1       1       1.080   single top cross section
31      lnN     1       1       1       1       1       1       1.040   1       1       1       Z->ll cross section
32      lnN     1       1       1       1       1       1       1       1.040   1       1       diboson cross section
33      lnN     1.022   1.022   1.022   1       1       1       1.022   1.022   1.022   1.022   luminosity
34      lnN     1.024   1.012   1.071   1       1       1       1.076   1.039   1.101   1.147   pileup
35      lnN     1       1       1.280   1       1       1       1       1       1       1       ttbar fake tau MC stat.
36      lnN     1       1       1       1       1       1       1       1       1       1       Z->tautau fake tau MC stat.
37      lnN     1       1       1       1       1       1       1       1       1.713   1       W+jets fake tau MC stat.
38      lnN     1       1       1       1       1       1       1       1       1       1.493   single top fake tau MC stat.
39      lnN     1       1       1       1       1       1       1       1       1       1       diboson fake tau MC stat.
```

The following LandS datacard was used for the mass point $m_{H^\pm} = 150\,\text{GeV}/c^2$ for $\Delta\phi(\tau\,\text{jet}, E_\text{T}^\text{miss}) < 160°$. Each row corresponds to a systematic unertainty or nuisance parameter which is assumed to be independent of other rows, or 0% correlated. However, within each row the uncertainties are assumed to be 100% correlated. Therefore, different sources of systematic uncertainties are assumed to be completely uncorrelated between each other, while systematic uncertainties of same origin are assumed to be completely correlated between different event yields or measurements.

```
Description: LandS datacard (auto generated) mass=150, luminosity=2.273 1/fb, fully_hadronic_2011A_MET50_withRtau_DeltaPhi160
Date: Thu Mar 22 12:28:00 2012
-------------------------------------------------------------------------------------------------------------------------------
imax    1       number of channels
jmax    *       number of backgrounds
kmax    39      number of nuisance parameters
-------------------------------------------------------------------------------------------------------------------------------
shapes * * lands_histograms_hplushadronic_m150.root $PROCESS $PROCESS_$SYSTEMATIC
-------------------------------------------------------------------------------------------------------------------------------
Observation     130
-------------------------------------------------------------------------------------------------------------------------------
bin             1       1       1       1       1       1       1       1       1       1
```

```
process         HH150_1 HW150_1 fake_tt res.    QCD     EWK_Tau EWK_DYx EWK_VVx fake_W  fake_t
process         -1      0       1       2       3       4       5       6       7       8
-------------------------------------------------------------------------------------------------------------------------------
rate            510.609 675.326 2.109   0.000   26.392  78.429  7.003   0.351   4.190   0.163
-------------------------------------------------------------------------------------------------------------------------------
1       lnN     1.132   1.130   1.120   1       1       1.113   1.121   1.112   1.137   1.109   tau+MET trg scale factor
2       lnN     1       1       1       1       1       1       1       1       1       1       reserved for leptonic
3       lnN     1.060   1.060   1       1       1       1.060   1.060   1.060   1       1       tau-jet ID (no Rtau)
4       lnN     1       1       1.150   1       1       1       1       1       1.150   1.150   tau-jet mis-ID (no Rtau)
5       lnN     1       1       1       1       1       1       1       1       1       1       reserved for leptonic
6       lnN     1       1       1       1       1       1       1       1       1       1       reserved for leptonic
7       shapeQ  1       1       1       0       0       1       1       1       1       1       JES/JER/MET/Rtau effect on mT shape
8       lnN     1       1       1       1       1       1       1       1       1       1       reserved for leptonic
9       lnN     1.004   1.005   1.008   1       1       1       1.009   1.012   1.003   1.005   lepton veto
10      lnN     1.011   1.010   1.014   1       1       1       1       1       1       1.016   btagging
11      lnN     1       1       1       1       1       1       1.020   1.026   1.044   1       mis-btagging
12      shapeStat       0       0       0       0       1       0       0       0       0       0       QCD stat.
13      lnN     1       1       1       1       1.040   1       1       1       1       1       QCD syst.
14      lnN     1       1       1       1       1       1.012   1       1       1       1       EWK with taus QCD contamination
15      lnN     1       1       1       1       1       1.007   1.001   1.001   1       1       EWK with taus W->tau->mu
16      lnN     1       1       1       1       1       1.005   1.001   1.001   1       1       EWK with taus muon selection
17      lnN     1.081   1       1       1       1       1       1       1       1       1       HH MC stat.
18      lnN     1       1.070   1       1       1       1       1       1       1       1       HW MC stat.
19      shapeStat       0       0       0       0       0       1       0       0       0       0       EWK with taus stat.
20      lnN     1       1       1       1       1       1       1       1       1       1       reserved for leptonic
21      lnN     1       1       1       1       1       1       1       1       1       1       reserved for leptonic
22      lnN     1       1       1       1       1       1       1       1       1       1       tt->jjtau MC stat.
23      lnN     1       1       1       1       1       1       1       1       1       1       reserved for leptonic
24      lnN     1       1       1       1       1       1       1.292   1       1       1       Z->tautau MC stat
25      lnN     1       1       1       1       1       1       1       1       1       1       W+jets MC stat.
26      lnN     1       1       1       1       1       1       1       1       1       1       Single top MC stat.
27      lnN     1       1       1       1       1       1       1       1.659   1       1       diboson MC stat
28      lnN     0.904/1.070     0.904/1.070     0.904/1.070     1       1       1       1       1       ttbar cross section
29      lnN     1       1       1       1       1       1       1       1       1.050   1       W+jets cross section
30      lnN     1       1       1       1       1       1       1       1       1       1.080   single top cross section
31      lnN     1       1       1       1       1       1       1.040   1       1       1       Z->ll cross section
32      lnN     1       1       1       1       1       1       1       1.040   1       1       diboson cross section
33      lnN     1.022   1.022   1.022   1       1       1       1.022   1.022   1.022   1.022   luminosity
34      lnN     1.019   1.010   1.071   1       1       1       1.076   1.039   1.101   1.147   pileup
35      lnN     1       1       1.280   1       1       1       1       1       1       1       ttbar fake tau MC stat.
36      lnN     1       1       1       1       1       1       1       1       1       1       Z->tautau fake tau MC stat.
37      lnN     1       1       1       1       1       1       1       1       1.713   1       W+jets fake tau MC stat.
38      lnN     1       1       1       1       1       1       1       1       1       1.493   single top fake tau MC stat.
39      lnN     1       1       1       1       1       1       1       1       1       1       diboson fake tau MC stat.
```

The following LandS datacard was used for the mass point $m_{H^\pm} = 155\,\text{GeV}/c^2$ for $\Delta\phi(\tau\,\text{jet}, E_\text{T}^\text{miss}) < 160^\circ$. Each row corresponds to a systematic unertainty or nuisance parameter which is assumed to be independent of other rows, or 0% correlated. However, within each row the uncertainties are assumed to be 100% correlated. Therefore, different sources of systematic uncertainties are assumed to be completely uncorrelated between each other, while systematic uncertainties of same origin are assumed to be completely correlated between different event yields or measurements.

```
Description: LandS datacard (auto generated) mass=155, luminosity=2.273 1/fb, fully_hadronic_2011A_MET50_withRtau_DeltaPhi160
Date: Thu Mar 22 12:28:00 2012
-------------------------------------------------------------------------------------------------------------------------------
imax    1       number of channels
jmax    *       number of backgrounds
kmax    39      number of nuisance parameters
-------------------------------------------------------------------------------------------------------------------------------
shapes * * lands_histograms_hplushadronic_m155.root $PROCESS $PROCESS_$SYSTEMATIC
-------------------------------------------------------------------------------------------------------------------------------
Observation     130
-------------------------------------------------------------------------------------------------------------------------------
bin             1       1       1       1       1       1       1       1       1       1
process         HH155_1 HW155_1 fake_tt res.    QCD     EWK_Tau EWK_DYx EWK_VVx fake_W  fake_t
process         -1      0       1       2       3       4       5       6       7       8
-------------------------------------------------------------------------------------------------------------------------------
rate            345.023 676.082 2.109   0.000   26.392  78.429  7.003   0.351   4.190   0.163
-------------------------------------------------------------------------------------------------------------------------------
1       lnN     1.126   1.127   1.120   1       1       1.113   1.121   1.112   1.137   1.109   tau+MET trg scale factor
2       lnN     1       1       1       1       1       1       1       1       1       1       reserved for leptonic
3       lnN     1.060   1.060   1       1       1       1.060   1.060   1.060   1       1       tau-jet ID (no Rtau)
4       lnN     1       1       1.150   1       1       1       1       1       1.150   1.150   tau-jet mis-ID (no Rtau)
5       lnN     1       1       1       1       1       1       1       1       1       1       reserved for leptonic
6       lnN     1       1       1       1       1       1       1       1       1       1       reserved for leptonic
7       shapeQ  1       1       1       0       0       1       1       1       1       1       JES/JER/MET/Rtau effect on mT shape
```

```
8       lnN     1       1       1       1       1       1       1       1       1       1       reserved for leptonic
9       lnN     1.004   1.006   1.008   1       1       1       1.009   1.012   1.003   1.005   lepton veto
10      lnN     1.014   1.011   1.014   1       1       1       1       1       1       1.016   btagging
11      lnN     1       1       1       1       1       1       1.020   1.026   1.044   1       mis-btagging
12      shapeStat       0       0       0       0       1       0       0       0       0       0       QCD stat.
13      lnN     1       1       1       1       1.040   1       1       1       1       1       QCD syst.
14      lnN     1       1       1       1       1       1.012   1       1       1       1       EWK with taus QCD contamination
15      lnN     1       1       1       1       1       1.007   1.001   1.001   1       1       EWK with taus W->tau->mu
16      lnN     1       1       1       1       1       1.005   1.001   1.001   1       1       EWK with taus muon selection
17      lnN     1.100   1       1       1       1       1       1       1       1       1       HH MC stat.
18      lnN     1       1.071   1       1       1       1       1       1       1       1       HW MC stat.
19      shapeStat       0       0       0       0       0       1       0       0       0       0       EWK with taus stat.
20      lnN     1       1       1       1       1       1       1       1       1       1       reserved for leptonic
21      lnN     1       1       1       1       1       1       1       1       1       1       reserved for leptonic
22      lnN     1       1       1       1       1       1       1       1       1       1       tt->jjtau MC stat.
23      lnN     1       1       1       1       1       1       1       1       1       1       reserved for leptonic
24      lnN     1       1       1       1       1       1       1.292   1       1       1       Z->tautau MC stat
25      lnN     1       1       1       1       1       1       1       1       1       1       W+jets MC stat.
26      lnN     1       1       1       1       1       1       1       1       1       1       Single top MC stat.
27      lnN     1       1       1       1       1       1       1       1.659   1       1       diboson MC stat
28      lnN     0.904/1.070     0.904/1.070     0.904/1.070     1       1       1       1       1       1       ttbar cross section
29      lnN     1       1       1       1       1       1       1       1       1.050   1       W+jets cross section
30      lnN     1       1       1       1       1       1       1       1       1       1.080   single top cross section
31      lnN     1       1       1       1       1       1       1.040   1       1       1       Z->ll cross section
32      lnN     1       1       1       1       1       1       1       1.040   1       1       diboson cross section
33      lnN     1.022   1.022   1.022   1       1       1       1.022   1.022   1.022   1.022   luminosity
34      lnN     1.028   1.011   1.071   1       1       1       1.076   1.039   1.101   1.147   pileup
35      lnN     1       1       1.280   1       1       1       1       1       1       1       ttbar fake tau MC stat.
36      lnN     1       1       1       1       1       1       1       1       1       1       Z->tautau fake tau MC stat.
37      lnN     1       1       1       1       1       1       1       1       1.713   1       W+jets fake tau MC stat.
38      lnN     1       1       1       1       1       1       1       1       1       1.493   single top fake tau MC stat.
39      lnN     1       1       1       1       1       1       1       1       1       1       diboson fake tau MC stat.
```

The following LandS datacard was used for the mass point $m_{H^\pm} = 160\,\text{GeV}/c^2$ for $\Delta\phi(\tau\,\text{jet}, E_\text{T}^\text{miss}) < 160°$. Each row corresponds to a systematic unertainty or nuisance parameter which is assumed to be independent of other rows, or 0% correlated. However, within each row the uncertainties are assumed to be 100% correlated. Therefore, different sources of systematic uncertainties are assumed to be completely uncorrelated between each other, while systematic uncertainties of same origin are assumed to be completely correlated between different event yields or measurements.

```
Description: LandS datacard (auto generated) mass=160, luminosity=2.273 1/fb, fully_hadronic_2011A_MET50_withRtau_DeltaPhi160
Date: Thu Mar 22 12:28:00 2012
-------------------------------------------------------------------------------------------------------------------------------
imax    1       number of channels
jmax    *       number of backgrounds
kmax    39      number of nuisance parameters
-------------------------------------------------------------------------------------------------------------------------------
shapes * * lands_histograms_hplushadronic_m160.root $PROCESS $PROCESS_$SYSTEMATIC
-------------------------------------------------------------------------------------------------------------------------------
Observation     130
-------------------------------------------------------------------------------------------------------------------------------
bin             1       1       1       1       1       1       1       1       1       1
process         HH160_1 HW160_1 fake_tt res.    QCD     EWK_Tau EWK_DYx EWK_VVx fake_W  fake_t
process         -1      0       1       2       3       4       5       6       7       8
-------------------------------------------------------------------------------------------------------------------------------
rate            310.913 708.799 2.109   0.000   26.392  78.429  7.003   0.351   4.190   0.163
-------------------------------------------------------------------------------------------------------------------------------
1       lnN     1.134   1.129   1.120   1       1       1.113   1.121   1.112   1.137   1.109   tau+MET trg scale factor
2       lnN     1       1       1       1       1       1       1       1       1       1       reserved for leptonic
3       lnN     1.060   1.060   1       1       1       1.060   1.060   1.060   1       1       tau-jet ID (no Rtau)
4       lnN     1       1       1.150   1       1       1       1       1       1.150   1.150   tau-jet mis-ID (no Rtau)
5       lnN     1       1       1       1       1       1       1       1       1       1       reserved for leptonic
6       lnN     1       1       1       1       1       1       1       1       1       1       reserved for leptonic
7       shapeQ  1       1       1       0       0       1       1       1       1       1       JES/JER/MET/Rtau effect on mT shape
8       lnN     1       1       1       1       1       1       1       1       1       1       reserved for leptonic
9       lnN     1.004   1.005   1.008   1       1       1       1.009   1.012   1.003   1.005   lepton veto
10      lnN     1.021   1.011   1.014   1       1       1       1       1       1       1.016   btagging
11      lnN     1       1       1       1       1       1       1.020   1.026   1.044   1       mis-btagging
12      shapeStat       0       0       0       0       1       0       0       0       0       0       QCD stat.
13      lnN     1       1       1       1       1.040   1       1       1       1       1       QCD syst.
14      lnN     1       1       1       1       1       1.012   1       1       1       1       EWK with taus QCD contamination
15      lnN     1       1       1       1       1       1.007   1.001   1.001   1       1       EWK with taus W->tau->mu
16      lnN     1       1       1       1       1       1.005   1.001   1.001   1       1       EWK with taus muon selection
17      lnN     1.105   1       1       1       1       1       1       1       1       1       HH MC stat.
18      lnN     1       1.070   1       1       1       1       1       1       1       1       HW MC stat.
19      shapeStat       0       0       0       0       0       1       0       0       0       0       EWK with taus stat.
```

20	lnN	1	1	1	1	1	1	1	1	1	1	reserved for leptonic
21	lnN	1	1	1	1	1	1	1	1	1	1	reserved for leptonic
22	lnN	1	1	1	1	1	1	1	1	1	1	tt->jjtau MC stat.
23	lnN	1	1	1	1	1	1	1	1	1	1	reserved for leptonic
24	lnN	1	1	1	1	1	1	1.292	1	1	1	Z->tautau MC stat
25	lnN	1	1	1	1	1	1	1	1	1	1	W+jets MC stat.
26	lnN	1	1	1	1	1	1	1	1	1	1	Single top MC stat.
27	lnN	1	1	1	1	1	1	1	1.659	1	1	diboson MC stat
28	lnN	0.904/1.070		0.904/1.070		0.904/1.070		1	1	1	1	1 1 1 ttbar cross section
29	lnN	1	1	1	1	1	1	1	1	1.050	1	W+jets cross section
30	lnN	1	1	1	1	1	1	1	1	1	1.080	single top cross section
31	lnN	1	1	1	1	1	1	1.040	1	1	1	Z->ll cross section
32	lnN	1	1	1	1	1	1	1	1.040	1	1	diboson cross section
33	lnN	1.022	1.022	1.022	1	1	1	1.022	1.022	1.022	1.022	luminosity
34	lnN	1.038	1.006	1.071	1	1	1	1.076	1.039	1.101	1.147	pileup
35	lnN	1	1	1.280	1	1	1	1	1	1	1	ttbar fake tau MC stat.
36	lnN	1	1	1	1	1	1	1	1	1	1	Z->tautau fake tau MC stat.
37	lnN	1	1	1	1	1	1	1	1	1.713	1	W+jets fake tau MC stat.
38	lnN	1	1	1	1	1	1	1	1	1	1.493	single top fake tau MC stat.
39	lnN	1	1	1	1	1	1	1	1	1	1	diboson fake tau MC stat.

Appendix I

Event displays of signal-candidate events

In Figs. I.1-I.5, event displays from signal-candidate events are presented in the r-ϕ, r-z, 3D-Tower and Lego views [(a)-(d)], as reconstructed by Fireworks [38], the official Compact Muon Solenoid (CMS) event-display for event visualisation. These events survived all signal selection requirements, and were also required to satisfy the additional requirements $\Delta\phi\left(\tau \text{ jet}, E_{\mathrm{T}}^{\mathrm{miss}}\right) < 60^{\circ}$ and $m_{\mathrm{T}}(\tau \text{ jet}, E_{\mathrm{T}}^{\mathrm{miss}}) > 40\,\mathrm{GeV}/c^2$. Only tracks with $p_{\mathrm{T}} > 1\,\mathrm{GeV}/c$ are displayed. The HPS τ jet is represented by the black dotted-line, $E_{\mathrm{T}}^{\mathrm{miss}}$ by the red arrow, the hadronic jets by golden cones and the b-jets by dark-blue cones. The Electromagnetic Calorimeter (ECAL) and Hadronic Calorimeter (HCAL) energy deposits are represented in red and blue, respectively.

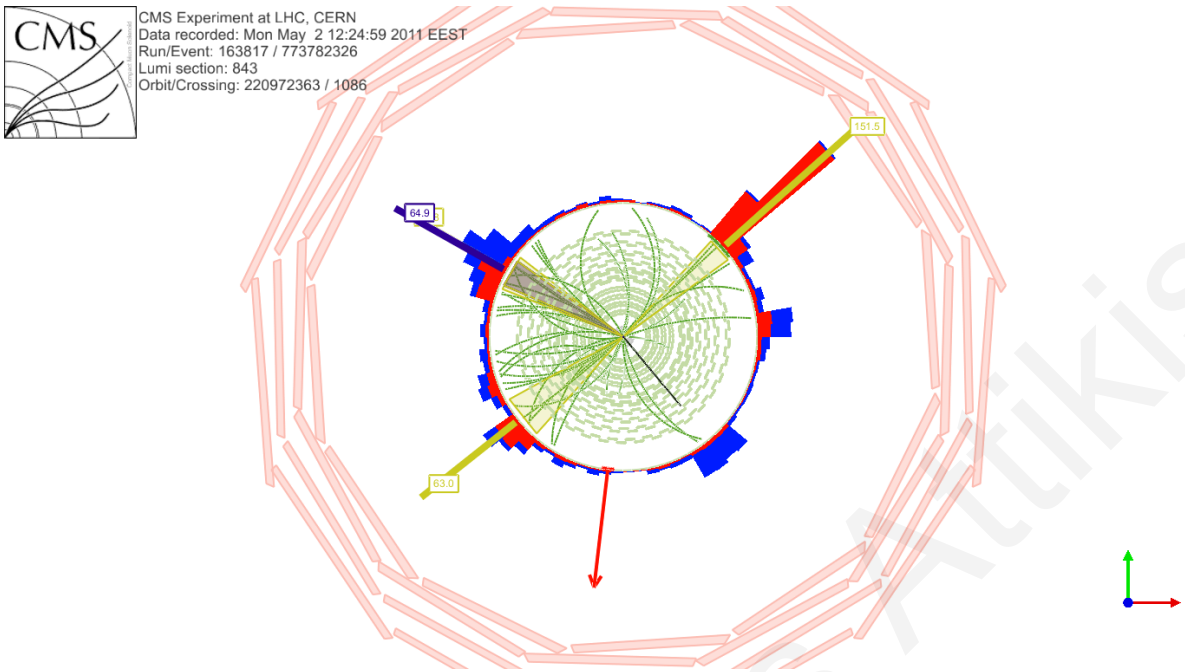

(a)

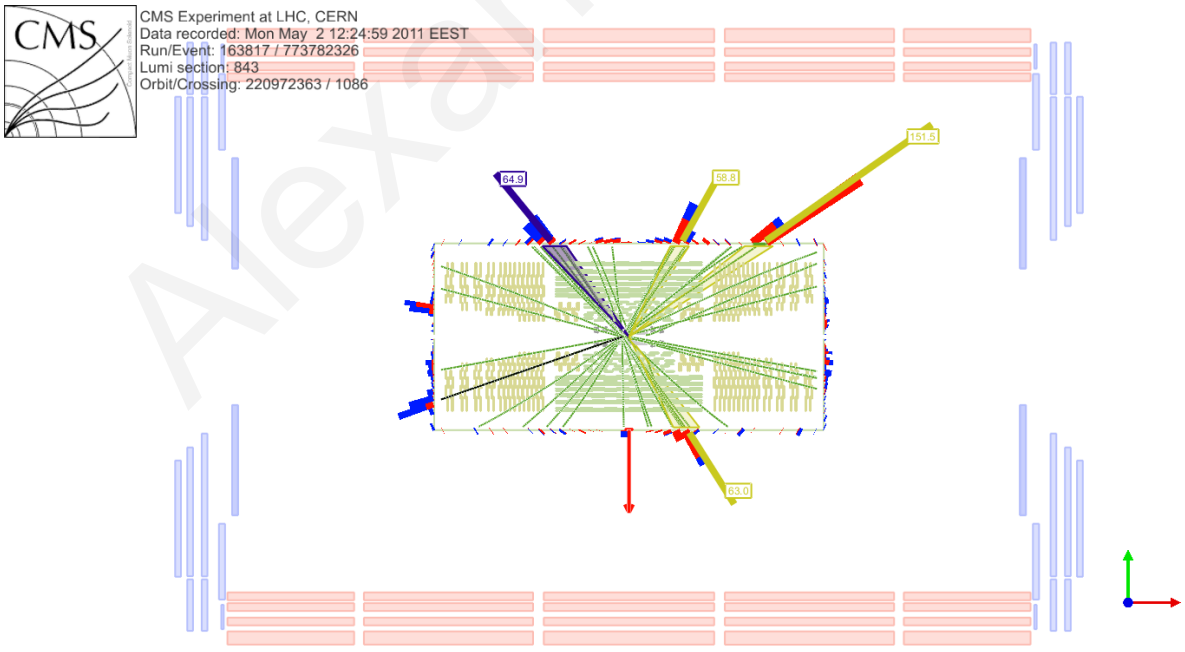

(b)

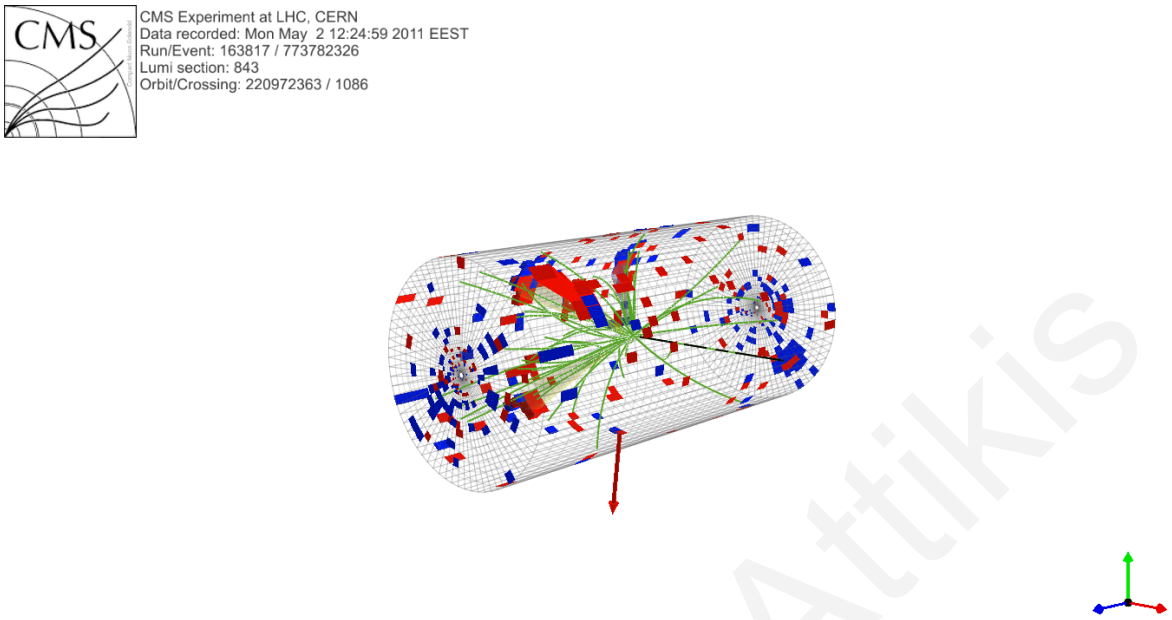

(c)

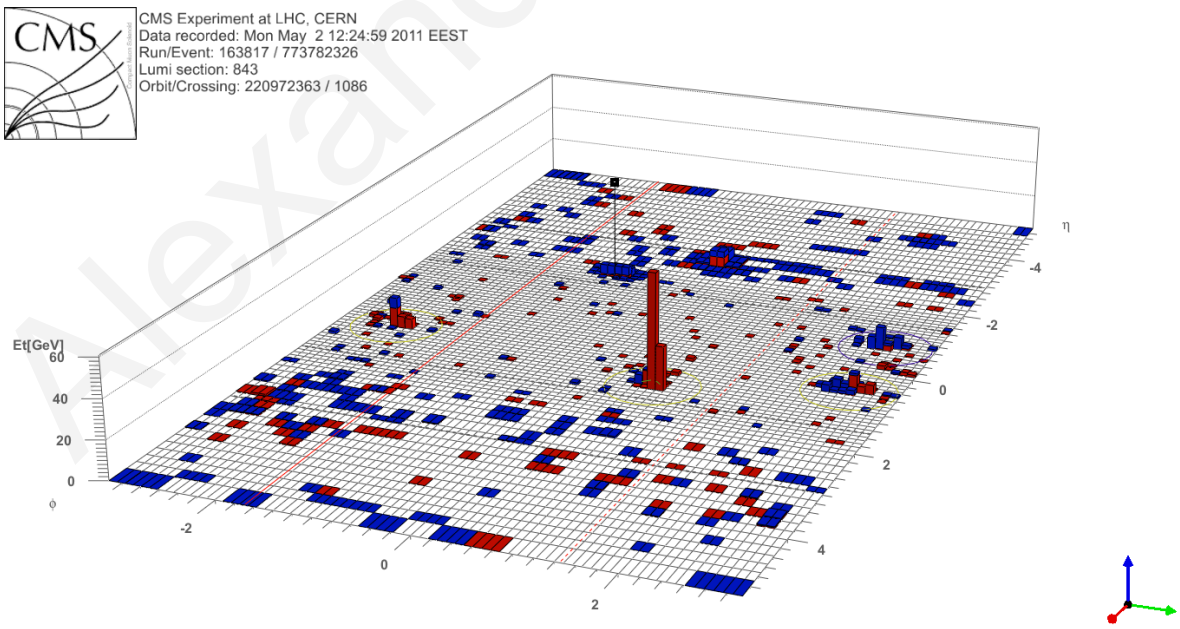

(d)

Figure I.1: Signal-candidate event from Run 163817 in the r-ϕ (a), r-z (b), 3D-Tower (c), and Lego (d) views.

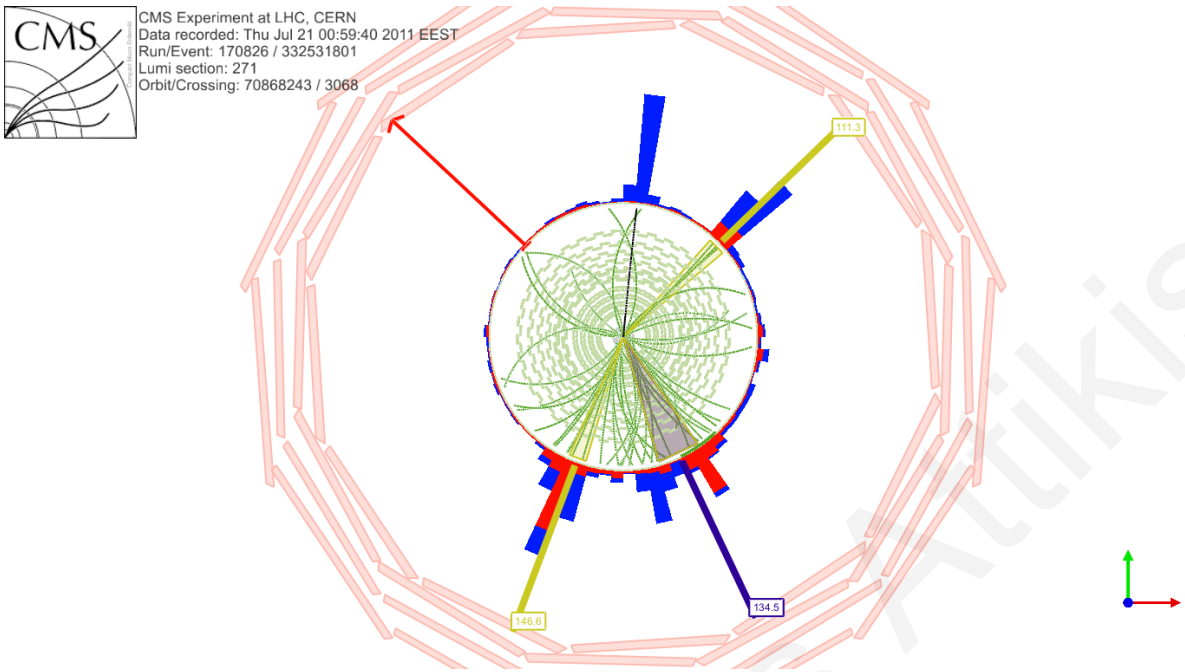

(a)

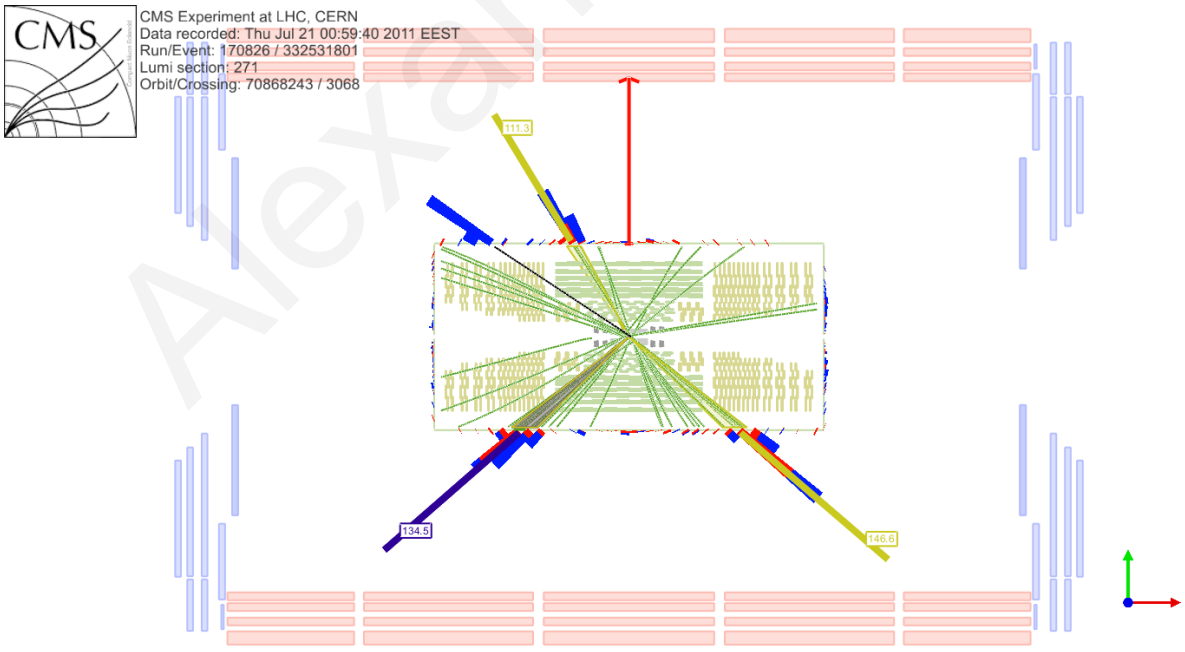

(b)

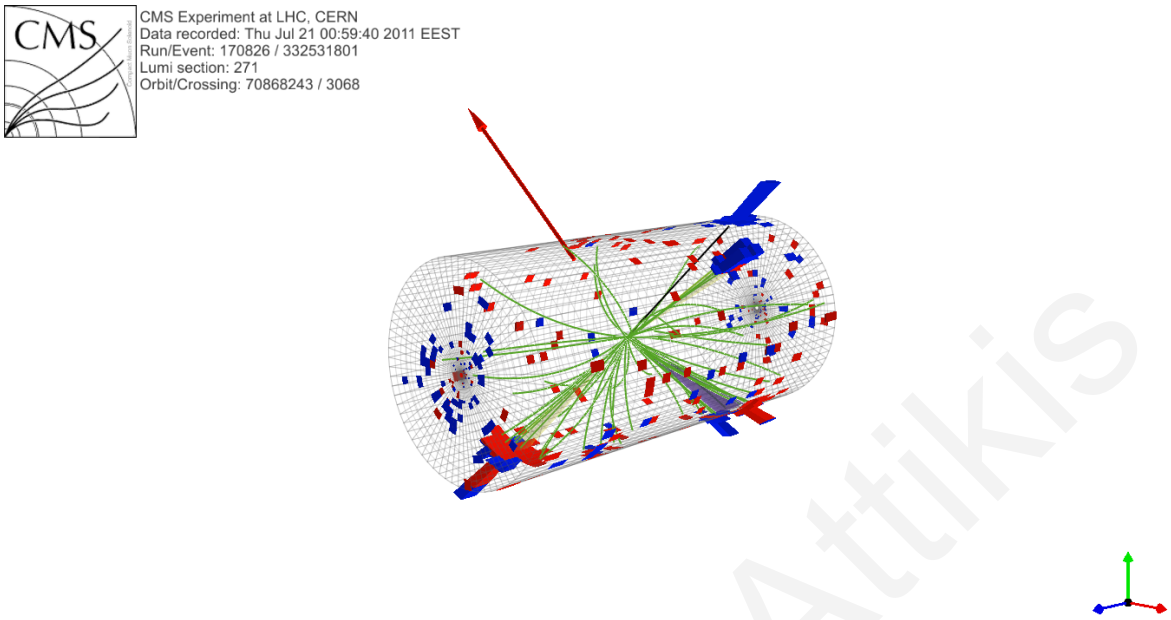

(c)

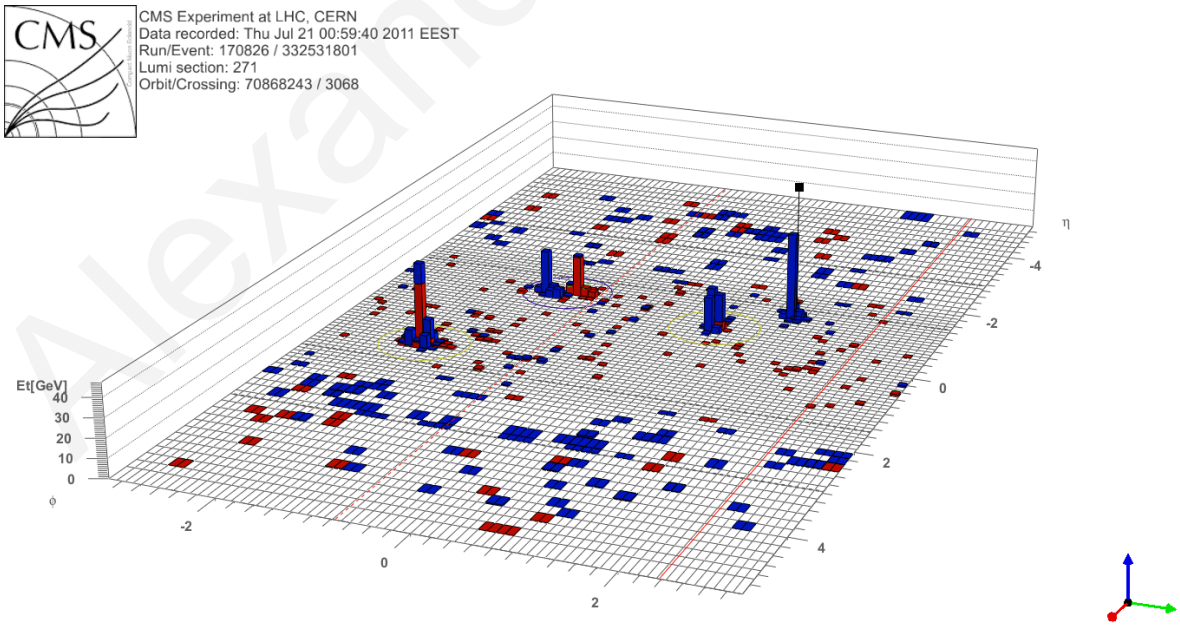

(d)

Figure I.2: Signal-candidate event from Run 170826 in the r-ϕ (a), r-z (b), 3D-Tower (c), and Lego (d) views.

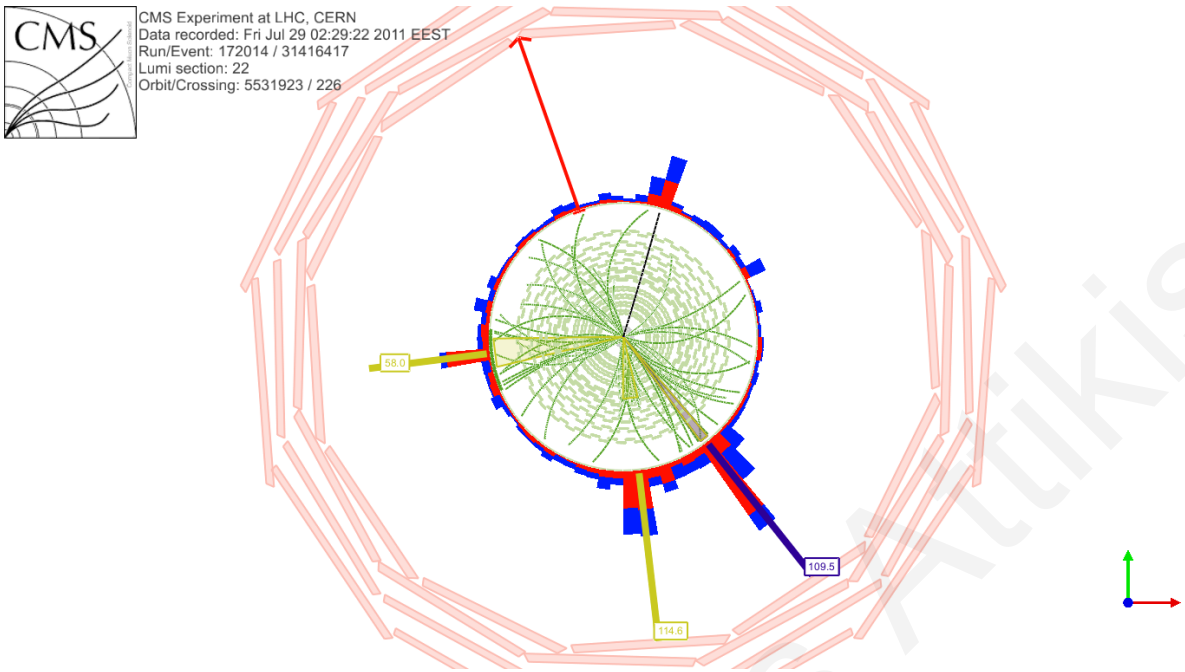

(a)

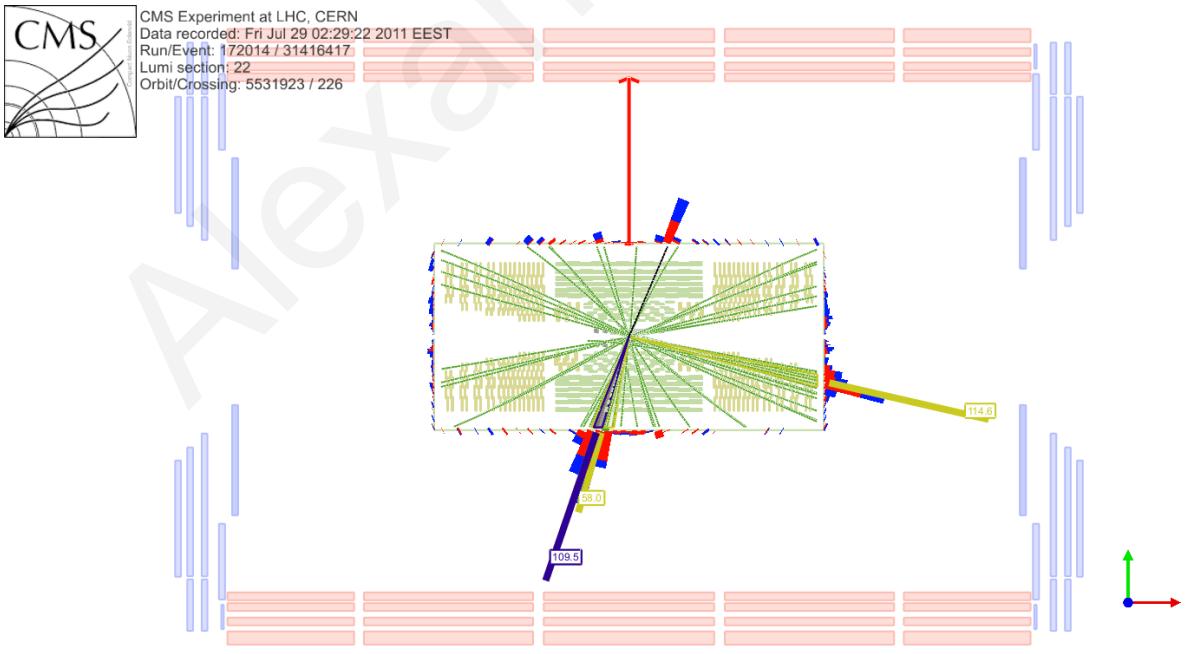

(b)

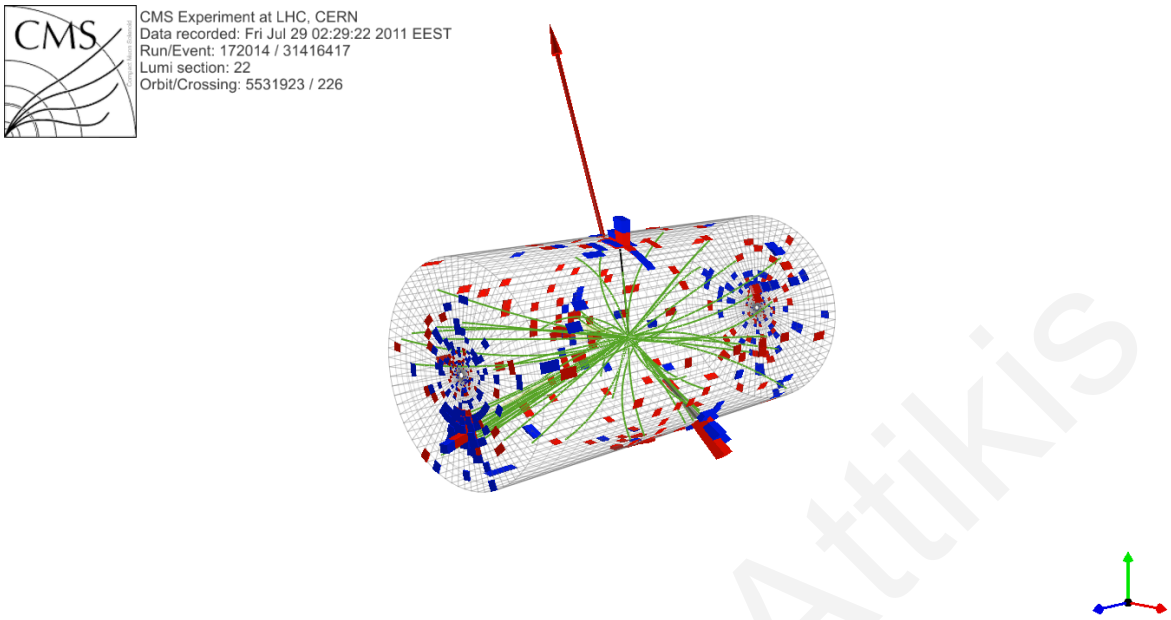

(c)

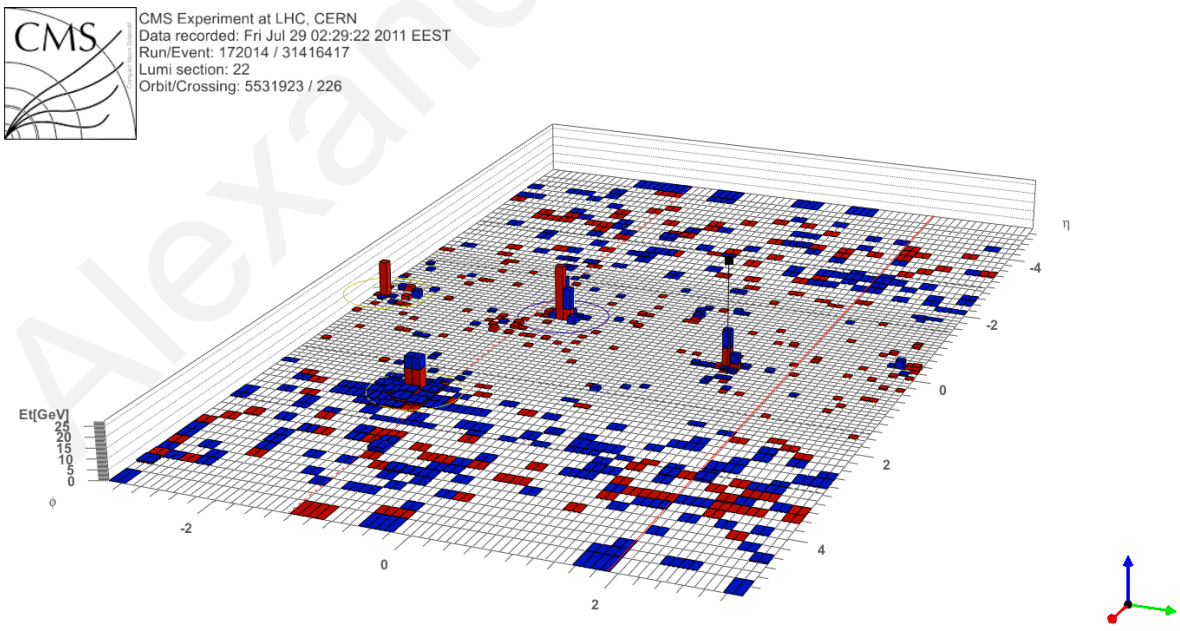

(d)

Figure I.3: Signal-candidate event from Run 172014 in the r-ϕ (a), r-z (b), 3D-Tower (c), and Lego (d) views.

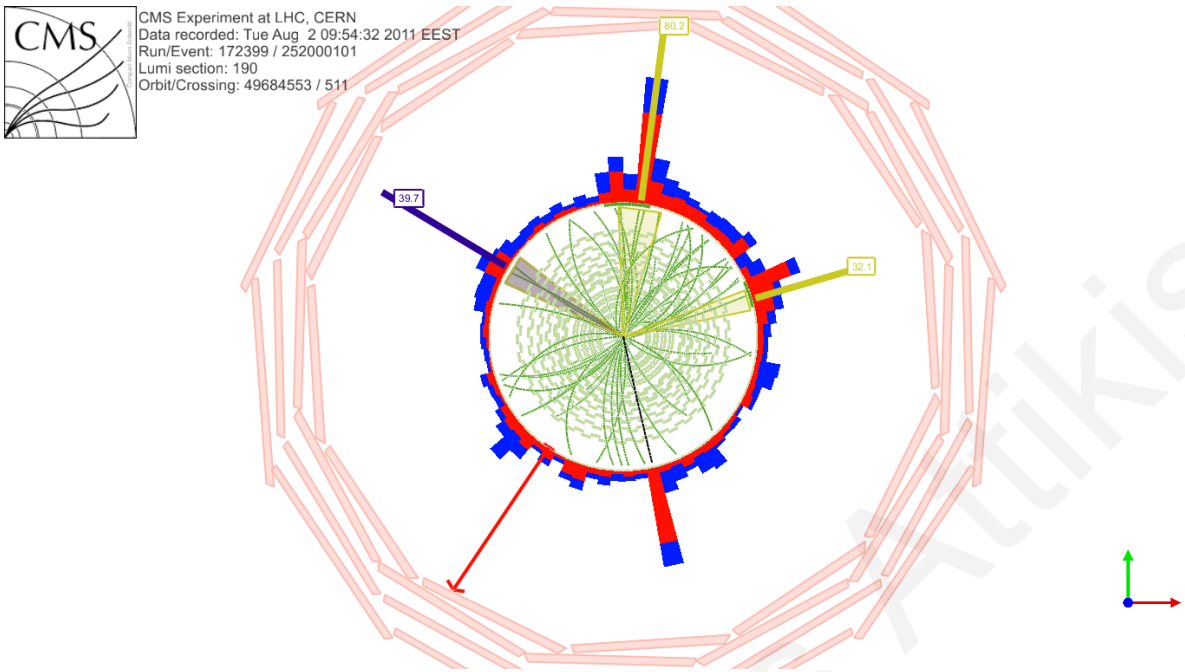

(a)

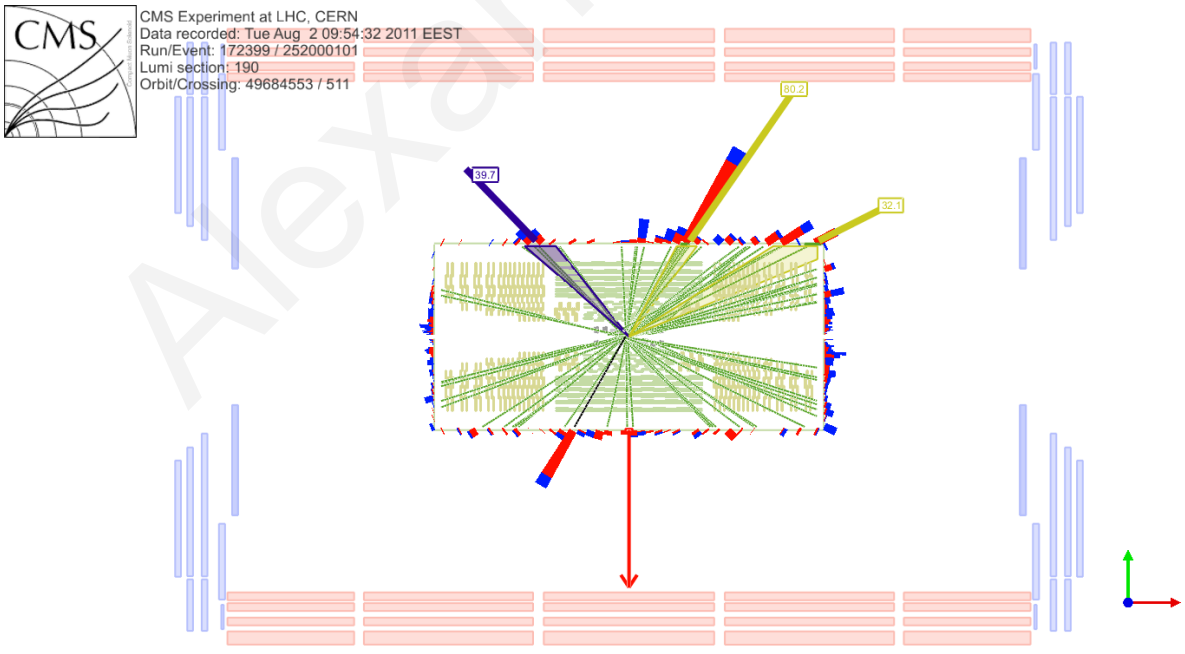

(b)

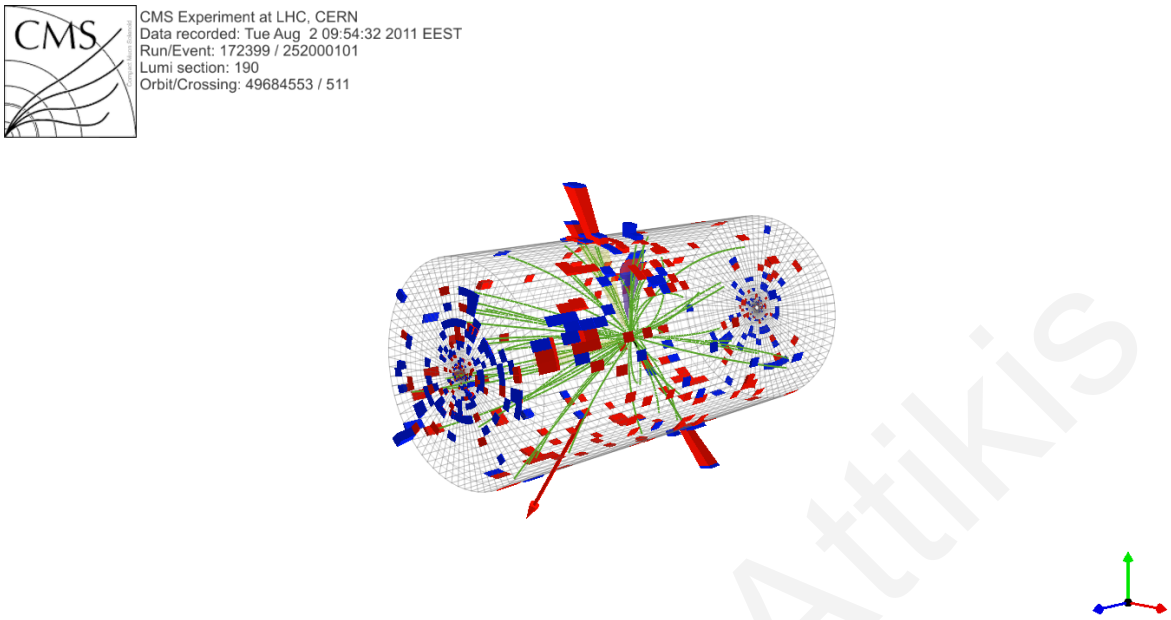

(c)

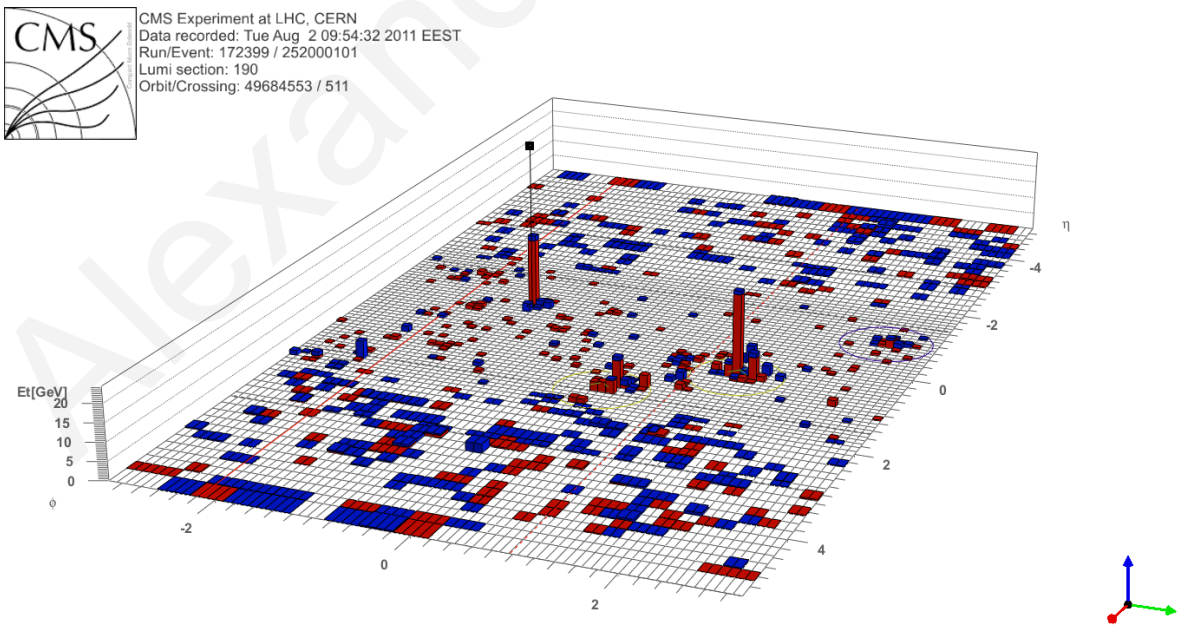

(d)

Figure I.4: Signal-candidate event from Run 172399 in the r-ϕ (a), r-z (b), 3D-Tower (c), and Lego (d) views.

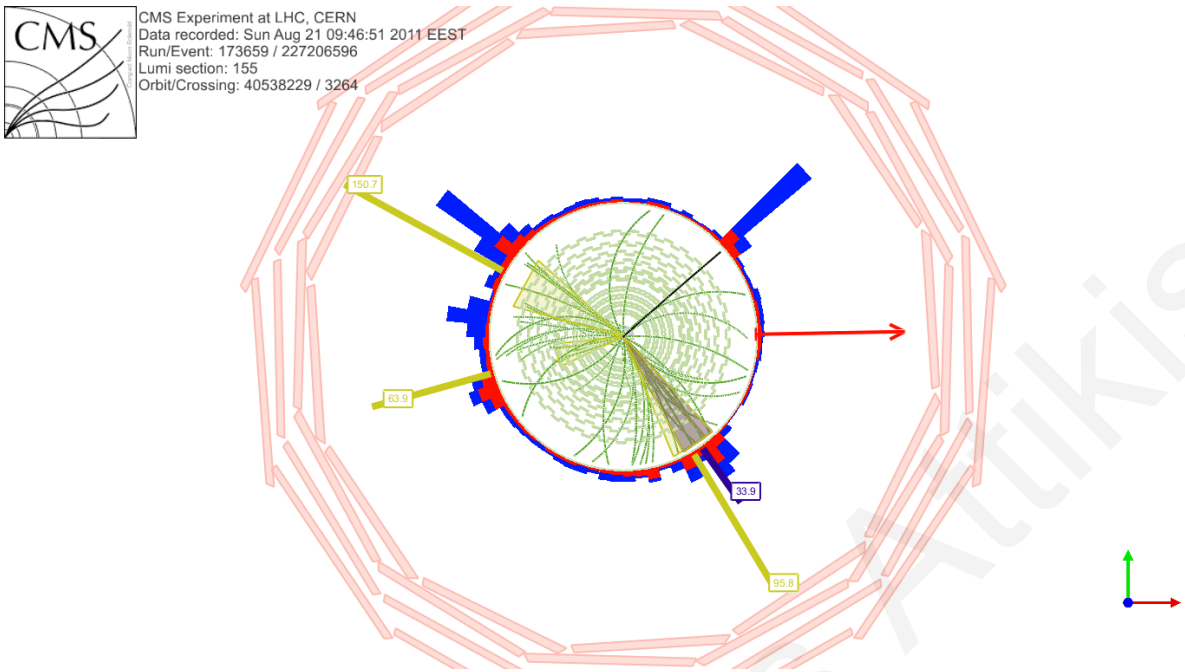

(a)

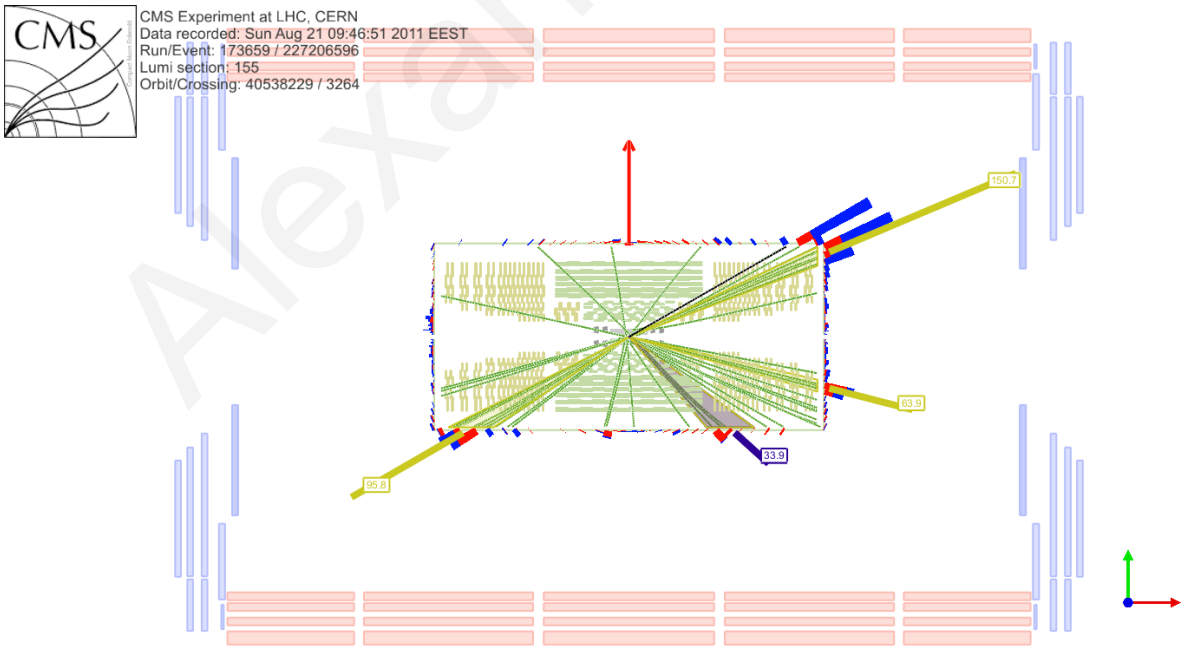

(b)

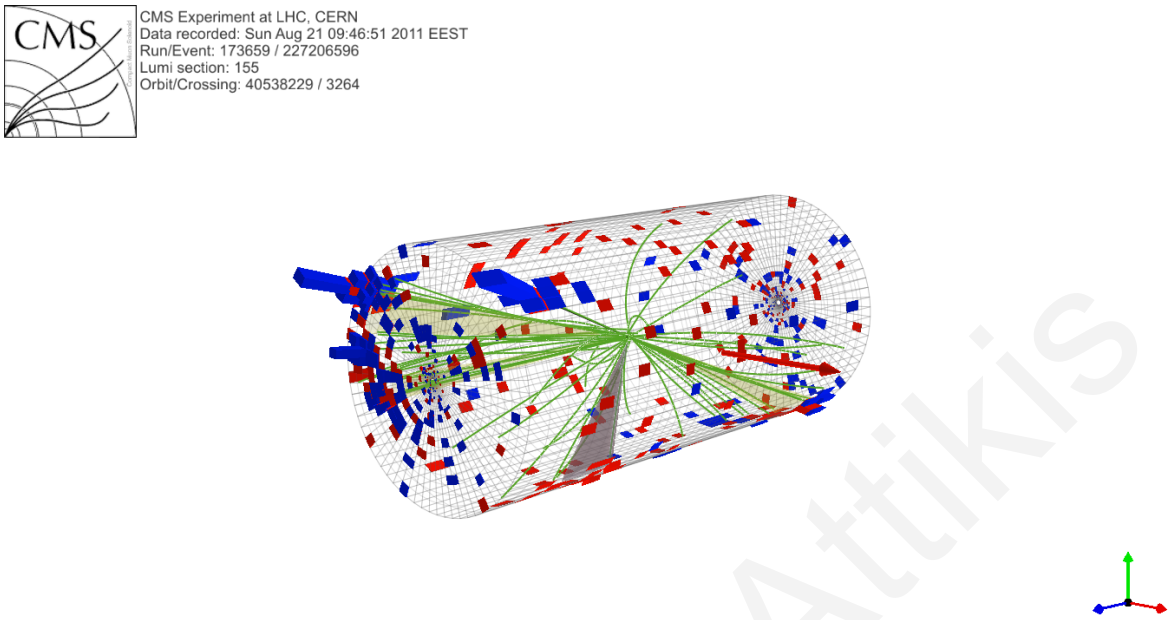

(c)

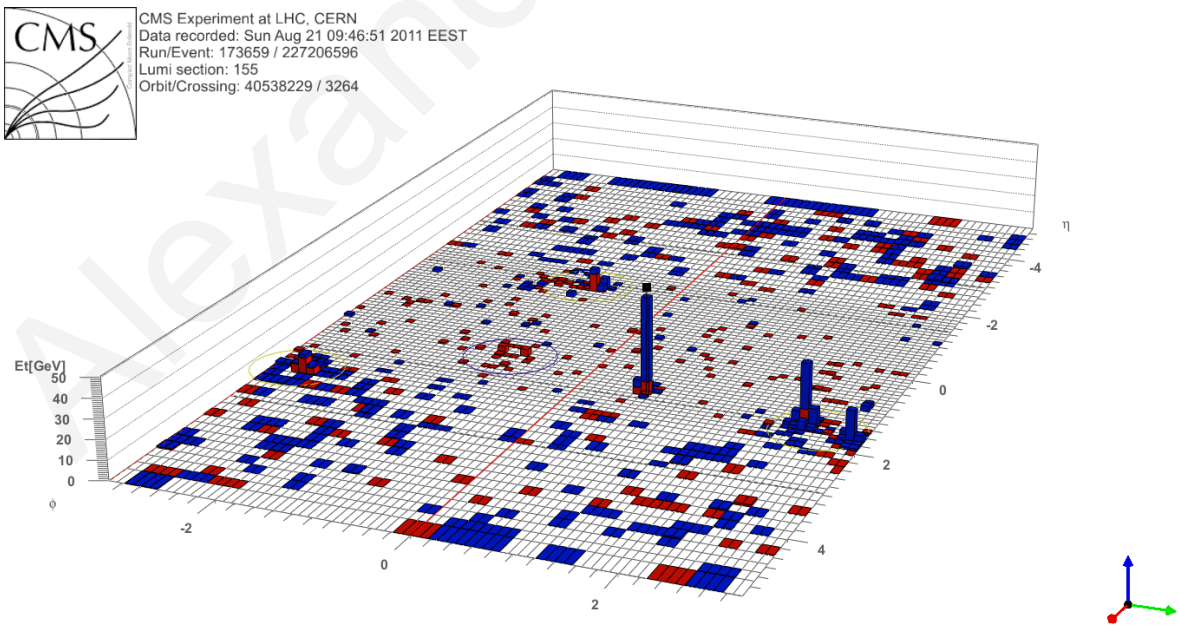

(d)

Figure I.5: Signal-candidate event from Run 173659 in the r-ϕ (a), r-z (b), 3D-Tower (c), and Lego (d) views.